U.S. DEPARTMENT OF ENERGY | Energy Efficiency & Renewable Energy

Lightweight Materials 2016 Annual Report

October 2017

Disclaimer

VTO competitively awards funding through funding opportunity announcement (FOA) selections and projects are fully funded through the duration of the project in the year the funding is awarded. The future direction for direct-funded work at the national laboratories is subject to change based on annual appropriations.

Foreword

The Materials Technology program supports the mission of the U.S. Department of Energy, Vehicles Technologies Office to reduce petroleum consumption while meeting or exceeding vehicle performance and safety requirements. For structural components, the market is shifting from traditional steel to lighter weight materials such as advanced high-strength steels, aluminum alloys, magnesium alloys, and carbon fiber composites. These materials will enable improvements in fuel economy by providing properties that are equal to or better than traditional materials and by providing flexibility in design that enables additional lightweighting. Because it takes less energy to accelerate a lighter vehicle, designing for and manufacturing with lightweight materials reduces a vehicle's fuel consumption compared to vehicles made from heavier cast iron and traditional steel components. Lightweighting of an electric vehicle could enable a farther travel distance with the same charge or enable a downsized battery for an equivalent range.

One of the Materials Technology program goals is to enable a 25% reduction of glider weight by 2025 compared to a 2012 baseline vehicle at less than $5 /lb weight saved. Considering that a 10% reduction in vehicle weight results in a 6-8% reduction in fuel consumption, achieving this 25% weight reduction goal could result in a 15-20% decrease in fuel consumption.

Many technology gaps still prevent widespread adoption of these lightweight metals including high cost, lack of an adequate supply chain, and inadequate materials properties to meet the requirements of specific applications. Earlier stage lightweight materials, specifically magnesium and carbon fiber composites, have the potential to save greater weight than the more mature advanced high-strength steels and aluminum; however, technology gaps that limit the use of these materials include the high cost of carbon fiber precursor materials, scaling up raw material production, and validating their use in automotive applications. Cost, manufacturability, formability, and compatibility are additional challenges that must be overcome.

The Materials Technology program supports research and development to provide innovative and feasible solutions to address the many technology gaps. The papers included in this report illustrate progress against these gaps. The lightweight materials research projects are organized by automotive metals, carbon fiber and composites, multi-material joining, and crosscutting research. Within these families of materials and technologies, the taxonomy is categorized by three sub-areas: (1) properties and manufacturing, (2) multi-material enabling, and (3) modeling and computational science. Properties and manufacturing research aims to improve material mechanical properties and performance, where manufacturability R&D addresses formability, cycle time, ductility, and cost.

The multi-material joining efforts target original, strikingly new, unusual, or different from anything seen or known before processes, designs, materials, and technologies that enable assembly of disparate material systems (dissimilar metals and composites to metals) into lightweight structures. Understanding corrosion and how to mitigate it is also a focus for this area. The developed technologies seek to enable effortless integration and joining of components into a vehicle system while avoiding performance degradation, corrosion, and other compatibility issues.

Computational materials science and integrated computational materials engineering continue to mature predictive tools to speed up the development to deployment cycle. These tools predict the performance of lightweight structures, such as energy absorption during a crash, by integrating validated models on structure/property and process/property relationships while taking into account uncertainty from materials processing and manufacturing. Ultimately, this area seeks to integrate materials development from composition through processing and performance. The challenges for integrating and validating materials models are addressed directly in the work documented in this report.

Preface

The following report documents the progress made during Fiscal Year 2016 to overcome the technical barriers preventing widespread use of lightweight structural materials in vehicles. The areas of research are organized by material type: Automotive Metals, Carbon Fiber and Polymer Composites, Multi-Material Joining, and Cross-cutting research. From early stage research to industrially relevant demonstrations, Materials Technology is laying the foundation for improved lightweight materials to significantly reduce fuel consumption.

Acknowledgements

First and foremost, we acknowledge the principal investigators and their teams from industry, academia, and the national laboratories. It is their innovative ideas and efforts to deploy them broadly in vehicles that will enable increased fuel economy and reduced environmental impact

Thank you to the project managers at the National Energy Technology Laboratory for their continued support in administering these projects.

We would also like to acknowledge Energetics Incorporated for their support in preparing and publishing, and the Idaho National Laboratory technical staff for their efforts managing the compilation of this report.

H. Felix Wu, Ph.D.
Program Manager, Materials Technology
Vehicle Technologies Office

Carol Schutte, Ph.D.
Technology Development Manager, Composites
Vehicle Technologies Office

Will Joost, Ph.D.
Technology Development Manager, Metals
Vehicle Technologies Office

Sarah Kleinbaum
Technology Development Manager, Joining
Vehicle Technologies Office

Acronyms and Abbreviations

α	resin degree of cure in the Kamal-Sourour kinetic model
Δ*h*	total enthalpy of polymerization of resin in the Kamal-Sourour kinetic model
ε"	imaginary part of permittivity called the loss factor or lossiness
γ	solid/liquid interfacial energy in the Pan Solidification module
ρ	symbol for density
υ	Poisson's ratio
1.5kx, 4kx	1,500 times and 4,000 times magnification
2D	two-dimensional
3D	three-dimensional
3DRVEs	three-dimensional representative volume elements
3G	third-generation
3GAHSS	third-generation advanced high-strength steel
5xxx	series designation of Al alloyed with Mg
6xxx	series designation for Al alloyed with Mg and Si
7xxx	series designation for Al alloyed with Zn

A

a_{11} or A_{11}, etc.	fiber orientation tensor or degree of orientation at end of injection molding process
A-42	DowAska 12K carbon fiber filler and reinforcement material having tensile strength of 610 ksi (4,200 MPa), tensile modulus of 34.8 Msi (240 GPa), strain of 1.8%, density 0.064 lb/in^3 (1.78 g/cm^3), and yield 0.931 ft/lb (1,600 g/1,000 m)
AA	Aluminum Association
AA5182	wrought work hardenable Al alloy in the 5000 series containing 4.5% Mg and 0.35% Mn
AA6022	heat treatable low copper precipitation hardenable Al sheet alloy containing 0.8 to 1.5% Si and 0.45 to 0.70% Mg
AA6061	precipitation hardening Al alloy containing 0.8 to 1.2% Mg and 0.4 to 0.8% Si as its major alloying elements
AA7075	aluminum alloy with strength comparable to many steels, good fatigue strength, and average machinability
AA7085	an aerospace grade Al alloy containing 7.15% Al, 1.75% Mg, 1.45% Cu, 0.12% Zr, 0.06% Fe, and 0.02% Si.
Abaqus	software suite for finite element analysis and computer-aided engineering
AC1101	DowAska chopped carbon fiber with a bulk density of 550 g/L for thermoset applications
AE42	die-cast magnesium alloy with good strength and creep resistance up to 150°C (316°F)
AE44	Mg alloy with high-temperature mechanical properties, diecastability, and corrosion resistance
AET Integration	Advanced Research, Engineering and Testing Integration
Ag	silver
AHSS	advanced high-strength steel
AK Steel	producer of flat-rolled carbon, stainless, and electrical steel products
Al	aluminum
Al 3003	alloy in the wrought Al-Mn family (3000 or 3xxx series)
Al 6013	weldable high strength 6XXX series alloy exhibiting 7XXX strength levels in the T6 temper
Al:Cu_2O	aluminum: copper (I) oxide

AlMn	aluminum-manganese
Al_2O_3	aluminum oxide
Alodine® 5200	chromium-free treatment for Al and its alloys
AM	Mg alloy designation with Al and Mn as principal alloying metals
AM50	Mg alloy 5.0% Al and less than 0.5% Mn
AM60	Mg alloy 5.6 to 6.5% Al and less than 0.25% Mn
$AmSO_4$	ammonium sulfate
amps	amperes
AN	acrylonitrile
ANL	Argonne National Laboratory
ANSYS	specialists in finite element analysis, computational fluid dynamics, electronics, semiconductors, embedded software and design optimization
ARD-RSC	anisotropic rotary diffusion/reduced strain closure
ASMI	Autodesk® Simulation Moldflow® Insight
A/SP	Auto/Steel Partnership
ASTM	American Society for Testing and Materials International
AT72	magnesium alloy comprised of 7% Al and 2% Sn
ATS	aluminum-tin-silicon
AU	arbitrary units
AWD	all-wheel drive
AZ31B	most widely available Mg grade alloy, high strength to weight ratio with 2.5 to 3.5% Al and 0.7 to 1.3% Zn
AZ91	Mg alloy with 9 weight% Al and 1 weight% Zn

B

BASF	largest chemical company in the world
BETAFORCE™	Dow Chemical Company two-component composite bonding adhesive
BIW	body-in-white
BLM	boundary layer mesh
BM	ball milled
BM+D	ball milled with diluent added
BMW	Bayerische Motoren Werke AG; a German luxury automobile, motorcycle, and engine manufacturing company
BSE	backscattered electron
BU	Brown University
BYU	Brigham Young University

C

C	carbon
Ci	coefficient of interaction in the Folgar-Tucker model
C_p	specific heat
Ca	calcium
CAD	computer-aided design
CAE	computer-aided engineering
CAFÉ	corporate average fuel economy
CALPHAD	CALculation of PHAse Diagrams
CARC	chemical agent-resistant coating
CATIA	computer aided three-dimensional interactive application
Ce	cerium
CEM	computational electromagnetic

CF	carbon fiber
CFRP	carbon fiber reinforced polymer
CFTF	Carbon Fiber Technology Facility
Chomarat	international, privately-owned, textile group producing textile and plastic coatings, textile finishing, and special reinforcement materials
CO_2	carbon dioxide
CompuTherm	University of Wisconsin-Madison spin-off company
COV	coefficient of variation
cP	centipoise
CPEC	close proximity electromagnetic carbonization
Cr	chromium
CR	cooling rate
CRADA	cooperative research and development agreement
C-RTM	continuous (or compression) resin transfer molding
c/s	counts per second
CSM	Colorado School of Mines
CSP	Continental Structural Plastics
CST	Computer Simulation Technology (3D electromagnetic simulation software from Dassault Systèms)
CT	computed tomography
CTS	cross-tension strength
Cu	copper
CU	Clemson University
CuO	copper(II) oxide or cupric oxide
Cu_2O	copper(I) oxide or cuprous oxide
CUV	crossover utility vehicle
CV	coefficient of variation

D

D	deuterium
D_2O	deuterium oxide
$D_2{}^{16}O$	atomic oxygen isotope of deuterated water
DCB	double cantilever beam
DIC	digital image correlation
DICTRA	Diffusion Module within Thermo-Calc for accurate simulation of diffusion-controlled reactions in multicomponent alloy systems
Digimat®	nonlinear multi-scale material and structure modeling platform by MSC Software
DIW	door in white
D-LFT	direct-injection long-fiber technology molding process
DOE	U.S. Department of Energy
Dow	Dow Chemical Company
DowAksa	large-scale, full-service, fully integrated provider of carbon fiber solutions for industrial applications
DP	dual phase
DPB	dual phase base
DPT	dual phase tempered
DP590	advanced high-strength formable steel for inner body side, inner quarter panel, rear rails, and rear shock reinforcements
DP980	dual-phase steel consisting of a ferrite matrix containing a hard second phase

DP1180	high-ductility, dual-phase, ultra-high-strength steel with an ultimate tensile strength greater than or equal 1180 MPa
DRI	Dynamic Research Incorporated
DSC	differential scanning calorimeter
DSpace	open source, turnkey, online repository application

E

E717	high formability magnesium sheet by Magnesium Elektron North America
EBSD	electron backscatter diffraction
EC	electromagnetic carbonization
E. coli	Escherichia coli
EDAG	Engineering + Design AG Inc.
EDS or EDX	energy dispersive spectroscopy or energy dispersive x-ray spectroscope
EERE	Energy Efficiency and Renewable Energy
e.g.	abbreviation meaning “for example”
EM	electromagnetic
EMTA-NLA	Eshelby-Mori-Tanaka Approach to Non-Linear Analysis
EPA	Environmental Protection Agency
EPIKOTE™	EPIKOTE™ Resin 05475; a medium viscous epoxy resin
EPMA	electron probe microanalysis
Epon 825™	high-purity bisphenol A-epichlorohydrin epoxy resin
ESI	Engineered Solutions, Inc.
et al.	abbreviation meaning “and others”
Excel	spreadsheet software featuring calculation, graphing tools, pivot tables, and a macro programming language for applications

F

F_R	range of frequency
FBCC	front bumper and crash can
FBJ	friction bit joining
FCA US LLC	Fiat Chrysler Automobiles U.S. LLC
Fe	iron
FE	finite element
FEA	finite element analysis
Fibersim	software by Siemens for composites engineering in the aerospace, automotive, marine, and wind energy industries
FIT	finite integral time
fit2D	general purpose and specialist 1 and 2 dimensional data analysis program
FLD	fiber-length distribution
FLD	forming (or formability) limit diagrams
FMVSS	Federal Motor Vehicle Safety Standards
FO	fiber orientation
FOA	funding opportunity announcement
FOD	fiber orientation distribution
Folgar-Tucker	mathematical model for predicting the orientation distribution function of rigid fibers
FRP	fiber-reinforced polymer
f_s	fraction solid
FSS	friction stir scribe
FSST	friction stir scribe technology
FSSW	friction stir spot welding

FSW	friction stir welding
ft	foot or feet
FY	fiscal year

G

g	gram(s)
G	thermal gradient
G_{Ic}	critical strain energy release rate
g/cc	gram(s) per cubic centimeter
g/L	gram(s) per liter
Gd	gadolinium
GEN	generation
GENOA-MCQ	GENOA Material Characterization and Qualifications composites suite
GF	glass fiber
GM	General Motors
G-NAC	GTEKT North American Corporation
Go/No-Go	determination to proceed with or abandon a plan or project
GPa	gigapascals
GVWR	gross vehicle weight rating

H

h or hr	hour(s)
h	thickness of the diffusion boundary layer in the Nernst-Brunner equation
H	hydrogen
H	latent heat
H13	versatile chromium-molybdenum steel for hot and cold work tooling applications
$H_2{}^{18}O$	atomic oxygen isotope of water
HBM Prenscia (HBM)	company providing sensors, transducers, strain gauges, amplifiers, data acquisition systems, and software for structural durability investigations, tests, and analysis
HCP or hcp	hexagonal close-packed
H/D	ratio of hydrogen to deuterium
HER	hole expansion (extrusion) ratio
HEXRD	high-energy x-ray diffraction
HPDC	high-pressure die casting
HP-RTM	high-pressure resin transfer molding
HRA	Honda R&D America
HSA	high-strength Al
HSBS	hot stamped boron steel
HyperMesh	multi-disciplinary finite element pre-processor with advanced model assembly tools

I

i3, i8	i3 – five-door urban electric vehicle; i8 – coupe with an advanced plug-in hybrid drivetrain
IA	inter-critical annealing
IBIS	IBIS Associates, Inc.
ICME	integrated computational materials engineering
ICP-OES	inductively coupled plasma-optical emission spectroscopy
ICWE	integrated computational welding engineering
i.e.	abbreviation meaning “that is”

IIHS	Insurance Institute for Highway Safety
IM7	carbon fiber with an intermediate modulus of 7 GPa
in situ	onsite or in place

J

J/kg	joules per kilogram

K

$K_{x(y)(z)}$	reinforcement permeability tensor values
k	thermal conductivity tensor in the Kamal-Sourour kinetic model
K_{Ic}	critical Mode-I stress intensity factor
k_{race}	permeability for a simulated race-tracking region in fluid flow calculations
k_v	velocity-dependent partition coefficient
Kampmann-Wagner	numerical model adopted as a precipitation modeling framework accounting for concurrent nucleation, growth, and coarsening kinetics and to predict the as-cast grain size of inoculated multicomponent aluminum alloys
Kevlar®	registered trademark for a para-aramid synthetic fiber
kg	kilogram
kJ	kilojoules
kN	kilonewton
1K/s	K/s with a number before it referring to solidification rate
Ksi, ksi, and kpsi	kilopound per square inch
kWh	kilowatt hour(s)

L

L_w	weighted fiber length
L&L Products	technology driven business-to-business company with unique expertise in static sealing, acoustics, vibration reduction, structural reinforcements, and composite components
LabVIEW	Laboratory Virtual Instrument Engineering Workbench
LBNL	Lawrence Berkeley National Laboratory
lb	pound(s)
LBS100	value for 100 lb of weight reduction in crash models
LCA	life-cycle assessment
LCCF	low-cost carbon fiber
LCF	long carbon fiber
l/d	length/diameter
LDH	limiting dome height
LFT	long fiber-reinforced thermoplastic
LGF	long glass fiber
LIN	local interconnect network
Linkham TS1500	research tool for studying ceramics, metallurgy, materials, geology, and high-temperature polymers at both high and low heating and cooling rates
LLC	Limited Liability Company
LS-DYNA	advanced, general-purpose, multi-physics simulation software package
LSTC	Livermore Software Technology Corporation
LT	light truck
LTC	low-temperature carbonization

M

MAGMASOFT®	modular simulation software for casting process simulation
Mag-tec	company offering full service die casting in Mg, Al, and Zn
MaSp1	major ampullate spidroin 1 - spidroin, the main protein in a spider's dragline silk, with a very low proline content
MaSp2	major ampullate spidroin 2 - spidroin, the main protein in a spider's dragline silk, with a significant proline content
MAT 278	a curing model in LS-DYNA
MATLAB	MATrix LABoratory, a multi-paradigm numerical computing environment and programming language
MC933	stitch-bonded quadraxial fabric
MD	molecular dynamic(s)
MDS	multiscale design system
MENA	Magnesium Elektron North America
Mg	magnesium
MGC or MgC	plasma electrolytic deposition process for depositing a ceramic layer of Mg oxide allowing advanced corrosion protection of the Mg surface
$MgCl_2$	magnesium chloride
MgO	magnesium oxide
$Mg(OH)_2$	magnesium hydroxide
mHz	megahertz
MICRESS	MICRostructure Evolution Simulation Software
Micromill™	Alcoa-patented process for changing the microstructure of the metal and producing an Al alloy that has 40% greater formability and 30% greater strength
min	minute(s)
mm	millimeters
mm^2	square millimeters
Mn	manganese
modeFRONTIER®	software for streamlining the design process with workflows, innovative algorithms, and sophisticated post-processing tools
Moldex3D	professional plastic injection molding simulation software
Moldflow	high-end plastic injection molding computer-aided engineering software
MPa	megapascals
mph	miles per hour
MPS	material and process systems
MSC	MacNeal-Schwendler Corporation
msec	millisecond
MSI or Msi	million pounds per square inch
MultiScale Designer	software for development and simulation of multiscale material models of continuous, woven, and/or chopped fiber composites, honeycomb cores, reinforced concrete, soil, bones, and various other heterogeneous materials
MY	model year

N

N	newtons
NASTRAN	multidisciplinary structural analysis application for performing static, dynamic, and thermal analysis across the linear and nonlinear domains
NCF	non–crimped fabric
nCode	engineering data analysis tool with special concentration in fatigue and durability
Nd	neodymium

Nd_2O_3	neodymium oxide
NETL	National Energy Technology Laboratory
NHTSA	National Highway Traffic Safety Administration
NIST	National Institute of Standards and Technology
nm	nanometers
NRC	National Research Council
NVH	noise, vibration, and harshness
NWU or NU	Northwestern University

O

O	oxygen
OEM	original equipment manufacturer
OMEGA	optimization model for reducing emissions of greenhouse gases from automobiles
ORNL	Oak Ridge National Laboratory
OSU	Ohio State University
OVERWT00	value for mass reduction in heavier-than-average cars

P

PA	polyamide
PA66	polyamide 6,6
PAM-CRASH	software package for crash simulation and design of occupant safety systems
PAM-CURE	module of PAM-RTM software for modeling the curing process
PAM-DISTORTION	software package for prediction of manufacturing-induced residual stresses and shape distortion of composites parts
PAM-RTM	pluggable authentication module-resin transfer molding
PAM-FORM	software program enabling realistic and predictive simulation of dry textiles or prepregs forming processes
PAN	polyacrylonitrile
Pandat™	integrated computational tool for multi-component phase diagram calculation and materials property simulation
PanMagnesium	thermodynamic and atomic mobility database for Mg
PanPrecipitation	module in the Pandat™ software simulating precipitation kinetics during heat treatment process
PanSolidification	micromodel in the Pandat™ software incorporating back diffusion and cooling rate
PCE	polynomial chaos expansion
PDF	probability density function
PDS	process development system
PE	polyethylene (when referring to polymers)
PE	predictive engineering (when referring to a modeling tool)
PlastiComp	supplier of stronger, tougher, and lighter benefits of long fiber reinforcement technology
PNNL	Pacific Northwest National Laboratory
PP	polypropylene
prepreg	“pre-impregnated” composite fibers
PRISMS	PRedictive Integrated Structural Materials Science
PVD	physical vapor deposition used in vapor phase processing
Pyrofil	commercially available material compatible with epoxy prepreg

Q

Q&P	quench and partition
QP980	Baosteel Group Corporation's ultra-high strength galvanized steel with resistance to corrosion for use in automotive applications

R

r	designation for resin in the Kamal-Sourour kinetic model
RA	retained austenite
R&D	research and development
RADIOSS	multidisciplinary finite element solver for both linear and non-linear problems using implicit and explicit integration schemes
RAVF	retained austenite volume fraction
RE	rare earth
Redox	reduction-oxidation
RF	radio frequency
RMX	RMX Technologies, an advanced materials technology company with ceramics and various commercialized products
RPM or rpm	revolution(s) per minute
R-ratio	compressive strength divided by ultimate tensile strength
RTM	resin transfer molding
RVE	representative volume element

S

s.d.	standard deviation
SABIC	Saudi Arabia Basic Industries Corporation
SAIE	shear-assisted indirect extrusion
SANS	small angle neutron scattering
SC685	five-harness satin woven material
SCC	stress corrosion cracking
Scheil Model	model for describing the microsegregation present in primary phase dendritic growth and directional solidification
SciDAC	scientific discovery through advanced computing
SD	shear direction
SDAS	secondary dendrite arm spacing
SEM	scanning electron microscope (or microscopy)
ShAPE	shear-assisted processing and extrusion
SIMS	secondary ion mass spectrometry
SINCAP	Side Impact New Car Assessment Program
SLME	self-learning metabasin escape
SMART	partnership between Swatch and Mercedes (s+m) and their design of an "artful" little car
SMC	sheet molding compound
SMDI	Steel Market Development Institute
Sn	tin
SNS	spallation neutron source
Sobol indices	variance of conditional expectation of output given the value of an input
SPN or SPD	shear plane normal direction
SPR	self-pierce riveting or self-piercing rivets
Sr	strontium

STDEV	standard deviation
STEM	scanning transmission electron microscope (or microscopy)
SUV	sports utility vehicle
SVDC	super vacuum die casting

T

T_{ad}	adiabatic temperature
T_h	holding temperature
T5	temper designation for cooled from hot working and artificially aged (at elevated temperature)
T6	temper designation for solution heat-treated and artificially aged Al alloy
T700 or T800	carbon fiber designation with a tensile strength around 700 or 800 ksi
tan (δ)	dielectric loss or dissipation of electromagnetic energy parameterized in terms of either the loss angle δ or the corresponding loss tangent, tan δ
TARDEC	U.S. Army Tank Automotive Research Development and Engineering Center
TC411	2x2 twill woven material
TEM	transmission electron microscope (or microscopy)
TenCate	thermoplastic composite and thermoset composite supplier of aerospace composites, prepregs, and radom materials
TGA	thermogravimetric analysis
Thermo-Calc	software package for thermodynamic calculations
TOF	time-of-flight
TP	thermoplastic
TPI	TPI Composites, Inc.
TRIP	transformation-induced plasticity
TSS	tensile shear strength
TTI Metals	company with special cutting tools to the metalworking industry and provider of supply chain management services
TWB	tailor-welded blanks

U

UCR	upset cast riveting
UCR	University of California, Riverside
UD	unidirectional
UD-CCM	University of Delaware Center for Composite Materials
UHP	ultra-high purity
UHSS	ultra-high strength steel
UIUC	University of Illinois at Urbana-Champaign
UM	University of Michigan-Dearborn
UMAT	User Material Subroutine
UNDRWT00	value for mass reduction in lighter-than-average cars
UPJ	upset protrusion joining
UPLC	ultra performance liquid chromatography
USAMP	United States Automotive Materials Partnership
USC	University of Southern California
UTS	ultimate tensile strength

V

v or V	solidification front velocity in micro-segregation models

viz	synonym for “namely,” “that is to say,” and “as follows”
VMM	validation of materials and models
VMT	vehicle mile(s) of travel
von Mises	yield criterion suggesting that yielding of materials begins when second deviatoric stress invariant reaches a critical value
Voronoi	partitioning of a plane into regions based on distance to points in a specific subset of the plane
vs	versus
VTO	Vehicle Technologies Office

W

WDS	wavelength dispersive x-ray spectroscopy
WE43	high strength casting alloy used in temperatures of up to 300°C (572°F)
W/g	watts per gram (heat flow)
WIRS	weighted interval rank and sort
Wks	weeks
WSU	Wayne State University
wt%	percent by weight

X

x	alloy composition
XPS	x-ray photoelectron spectroscopy

Y

Y	yttrium

Z

z/h	normalized thickness
ZEK100 (ZE10A)	novel magnesium alloy with reduced content of rare earth metals
ZK60	magnesium wrought alloy consisting of primary matrix α (Mg) and the eutectic
Zn	zinc
Zr	zirconium

Table of Contents

I. Executive Summary

The automotive structural components market is shifting from traditional steel to lighter weight materials such as advanced high-strength steels, aluminum alloys, magnesium alloys, and carbon fiber composites. These material technologies allow for lighter structural components with properties of low density, high strength, and high stiffness while meeting requirements for performance and safety. One Materials Technology program goal is to enable a 25% glider weight reduction for light-duty vehicles including body, chassis, and interior as compared to a 2012 baseline vehicle at no more than a $5/lb-saved increase in cost.

Research for improving automotive metals addresses third-generation advanced high strength steel and lighter weight metals such as aluminum and magnesium. Advanced high strength steel is the most mature material in terms of widespread use in industry due to its compatibility with existing manufacturing infrastructure and vehicle materials. However, research is needed to address issues with dual phase advanced high strength steels, such as enhanced sheared edge stretchability, which occurs during parts fabrication. Application of third generation high strength steel has the potential to reduce component weight by up to 25%, particularly in strength-limited designs. Material strength targets have been established for two different property sets: (1) exceptional strength and high ductility (greater than 1,500 MPa ultimate tensile strength, greater than 1,200 MPa yield strength, and greater than 25% elongation) and high strength and exceptional ductility (greater than 1,200 MPa ultimate tensile strength, >800 MPa yield strength, and >30% elongation). In FY 2016, production of a medium manganese quench and partition steel was completed by United States Automotive Materials Partnership, LLC which is the first of two third generation advanced high strength steels developed. The integrated computational materials engineering approach used to deliver results will accelerate development and widespread deployment of third generation advanced high strength steels and other lightweight materials through modeling of multi-scale physical properties and mechanical processes.

Aluminum and magnesium both have the potential to significantly reduce vehicle component weight by 55% or greater; however, there are several significant technical barriers preventing increased use of these materials in vehicle designs. Aluminum has the issues of material cost, room temperature formability, and limitations within the existing manufacturing infrastructure. Magnesium has high raw material costs and price volatility, relatively low specific stiffness, difficulty in forming sheet at low temperatures, low ductility of finished components, and a limited alloy set, among others. High performance cast magnesium alloys with improved strength and corrosion resistances are desirable for automotive applications; however, a major technical gap exists in the scientific foundation for developing such materials. Several funded projects investigated advancing manufacturing methods in both forming and welding to enable further use of aluminum and for supporting improved scientific comprehension in the area of phase transformation kinetics, liquid-solid diffusion couples, and novel extrusion techniques for magnesium. In FY 2016, early-stage research was performed on high-strength electroformed nanostructured aluminum and research continued for the development of low-cost, high-strength automotive aluminum sheet. FY 2016 research efforts produced a magnesium alloy that contains no rare earth elements and has energy adsorption similar to standard 6061 series aluminum with a 20% mass savings over 6061 series aluminum.

Carbon fiber composites have the potential to reduce component weight by more than 60%. The main barriers to widespread carbon fiber use are the high cost of the raw material (precursor) and the energy-intensive manufacturing process of oxidizing and carbonizing the precursor to produce the carbon fiber. The Oak Ridge National Laboratory's Carbon Fiber Technology Facility continues to work with companies and execute intellectual property licenses that support high throughput processes for carbon fiber technology. Research continued in FY 2016 to develop spider silk protein as an unconventional, non-petroleum precursor with attributes of high-strength, low-cost, and high-yield for producing carbon fiber more efficiently. Spider silk protein fibers were successfully carbonized at 1,700°C. The resulting fibers maintained a useable fiber with excellent tensile strength.

In order to optimize carbon fiber composites for cost and performance, industry needs reliable predictive tools for both part design performance prediction. Predictive engineering tools for injection-molded long carbon fiber thermoplastic composites were developed that allow comparison of fiber orientation predictions and

experimental data. A part-to-part weight reduction analysis was performed, with assistance from a vehicle manufacturer, which used three-point bending simulations to compare long carbon fiber and polyamide 6,6 blends to steel. Results estimated a weight savings of 43.2% relative to steel for a complex three-dimensional part. Predictions for front bumper and crash can prototypes fabricated with composite materials demonstrated the critical role that non-destructive evaluation plays in enabling successful product development and application of carbon fiber composites for structural components. A detailed non-destructive evaluation methodology was demonstrated for characterization of the fabricated composite front bumper and crash can prototypes and adhesive joining techniques. When fully developed, these tools will integrate models from the microscale to the macroscale, predicting structure/property and process/property relationships while taking into account uncertainty (e.g., fiber misalignment, defects, and the probabilistic nature of materials) that ultimately allows accurate pre-assessments of the performance of the structural component in a crash.

When various lightweight structural materials with different strengths and weaknesses are used, the resulting multi-material structures have challenges of their own. Traditional joining methods used in automotive assembly, such as resistance spot welding and riveting, are inefficient for joining of dissimilar metals. In the near term, friction stir scribe welding is showing promising advances for joining of advanced high strength steel and aluminum (the more mature lightweight metals). As the barriers to introduction of magnesium and carbon fiber are overcome, breakthroughs in joining technology are also necessary. Current efforts address solutions for dissimilar joining of light metal to light metal and light metal to carbon fiber composites. Friction stir scribe joining of aluminum to steel remains a focus area for further development. In FY 2016, effects of hook morphology in aluminum-steel friction stir scribe joints as related to mechanical property and fracture mode were investigated. An optimum joining parameter window and tooling requirements for curvilinear high-speed friction stir welding in both similar and dissimilar aluminum alloy combinations were demonstrated at a supplier facility, using a commercial production friction stir welding machine. Also, the continued development of a novel composite foil for brazing dissimilar metals resulted in the reduction of the solidification temperature on cooling by over 100°C by replacing the copper diluent with silver, thereby producing a braze alloy and stronger bonds.

Finally, lightweight material crosscutting endeavors must include evaluations of safety and costs. An ongoing analysis of the relationship between vehicle weight, size (footprint), and societal fatality risk per vehicle miles of travel illuminates the impact of mass reduction on vehicle safety, risk, and vehicle footprint based on real-world crash data. Other crosscutting projects address the manufacture and demonstration of three different ultra-light hybrid door designs with a cost-effective means of realizing a vehicle mass reduction if all four doors utilized lightweight materials while maintaining the fit, functionality, safety and performance of the baseline production vehicle. A mid-sized sport utility vehicle's door with an assumed production volume of 20,000 vehicles annually is the basis of design for one prototype that is 15.6 kg, or 40.4%, lighter than the baseline driver-side door. The incremental cost associated with this design was estimated to be $2.59 per pound saved versus a target of $5/lb.

The products of funded research for advanced lightweight materials and their joining processes have been, and will continue to be, accepted by the automotive industry because of their economic and manufacturing benefits in addition to their ability to decrease vehicle energy use. The Materials Technology program continues to successfully provide the products and technologies that meet or surpass the requirements of traditional materials used in vehicle manufacturing.

II. Major Accomplishments for Fiscal Year 2016

II.1 Industry Impact

- Produced a Mg-Nd master alloy with a molten salt electrolysis process using magnesium oxide (MgO) and neodymium oxide (Nd_2O_3) as raw materials and blended the master alloy with Mg metal and other alloying elements to produce and ship 507 lb of an AE42 alloy to an automotive partner for die casting automotive parts.
- Completed production of Canada Centre for Mineral and Energy Technology Materials (CMAT) medium manganese quench and partition steel, which is the final version of the first of two 3GAHSS materials.
- Completed benchmark testing of a reference assembly in the 2016 Chevrolet Malibu to derive the performance requirements for a carbon fiber assembly and developed preliminary design ideas for the carbon fiber assembly with unique advantages for composite manufacturability.
- Implemented an orthotropic closure model that achieves a 50% improvement in accuracy for fiber orientation and mechanical property prediction that is used in modeling of complex ribbed and non-ribbed vehicle parts. This model is now available in commercial versions of the Autodesk® Simulation Moldflow® Insight software. Toyota has estimated a potential primary weight reduction of 22.5% for the vehicle body system, including the body-in-white, closures, fenders, and bumpers with 50 wt% long carbon fiber/PA66 in applicable steel parts.
- Linked a Moldflow analysis, multi-scale material model, and structural analysis for optimized design of structural parts with results of 18% weight savings in a subframe built with sheet molding compound and more than 40% weight savings in a unidirectional laminated design compared to the steel baseline.
- Selected five companies to negotiate intellectual property with LeMond Composites related to increased throughput of textile acrylic fiber.
- Transferred welding parameter sets and tooling designs to produce dissimilar thickness, aluminum alloy, friction stir weld joints to General Motors and Alcoa for demonstration trials with production equipment.

II.2 Technology Pipeline

- Initiated a major thrust through three independent projects to design, manufacture and demonstrate an ultra-light hybrid door with a cost-effective means of realizing a 56-kg full vehicle mass reduction if all four doors of a 4-door, C-segment vehicle were lightweighted while maintaining the fit, functionality, safety and performance of the baseline production vehicle. An expected cost increase of less than $5/lb in weight saved is the target. A 2013 mid-sized sport utility vehicle's door from a vehicle manufacturer with an assumed production volume of 20,000 vehicles annually was the basis for design. One prototype design is 15.6 kg, or 40.4%, lighter than the baseline driver-side door. The incremental cost associated with this design is estimated to be $2.59 per pound saved.

- Completed integrated computational materials engineering models and methodology for preforming, sheet compound molding, and curing analyses. Established multi-scale representative volume element models for unidirectional, woven, and chopped fiber composites. Improved computer-aided engineering models for crash analysis. Integrated all models for design optimization.
- Developed the ability to predict phase transformations as a function of strain in multi-phase steel, which is expected to dramatically improve the predictive capability of a 3GAHSS ICME model.
- Successfully carbonized spider silk protein fibers to 1,700°C and still maintained a useable fiber with excellent tensile strength as a novel precursor for carbon fiber. A techno-economic model was created that describes the relative percent costs of all the inputs to spider silk protein production via fermentation with the latest modifications to the process.
- Processed Mg alloy containing no rare earth elements for fine grain size using low cost Shear Assisted Processing and Extrusion (SHAPE). Results showed the alloy absorb energy similar to 6061 aluminum with a 20% mass savings over 6061.
- Produced friction stir scribe joints between cast Al and mild steel and supplied joint coupons to a vehicle manufacturer for individual evaluation, including corrosion and impact testing. Established welding parameters and tool design to produce friction stir scribe joints with quasi-static strength greater than 70% of weaker base metal for dissimilar joints between an Al alloy and transformation-induced plasticity (TRIP 590) steel for body and chassis applications.
- Developed correlations between welded and naturally aged tailor-weld blank panels (similar thickness precipitation-strengthened alloy) at the supplier's facility to address the ability to adequately evaluate welds in high-volume production environments. Produced and provided welded joint panels to General Motors for Barlat coefficient determination in the weld region.
- Completed initial experimentation using vibrational neutron spectroscopy to identify H speciation in aqueous-exposed pure Mg and Mg RE-modified alloy E717. Such techniques have not previously been applied in this manner to Mg corrosion.
- Demonstrated initial success of a thermal buckling modeling tool to understand and predict thermally induced buckling of spot-weld and adhesively bonded Al-steel components due to mismatch of the coefficient of thermal expansion.
- Evaluated the use of a military specification chemical agent-resistant coating and a new commercially available pretreatment to determine if these coatings could provide improved galvanic isolation between steel and Mg samples and improved corrosion performance of Mg compared to previously evaluated conventional automotive coatings.
- Continued research for brazing dissimilar metals with a novel composite foil by identifying Cu vapor as the gaseous species during propagation of reactions within ball-milled, mechanically processed redox foils. Produced vapor-deposited Al:Cu_2O:Cu foils with five different diluent amounts to identify an idealized microstructure. Reduced the solidification temperature on cooling by over 100°C by replacing the Cu diluent with silver (Ag), thereby producing a braze alloy and stronger bonds.

III. Automotive Metals

III.1 Advancing Properties, Processes, and Enabling Tools for Lightweight Metals – Pacific Northwest National Laboratory

Project Details

Darrell Herling, Technical Field Monitor
Pacific Northwest National Laboratory
902 Battelle Boulevard
Richland, WA 99352
Phone: 509-375-6905
E-mail: Darrell.herling@pnnl.gov

Sarah Kleinbaum, Technology Area Development Manager
U.S. Department of Energy
1000 Independence Avenue, SW
Washington, DC 20585
Phone: 202-586-8027
E-mail: sarah.ollila@ee.doe.gov

Contractor: Pacific Northwest National Laboratory
Contract No.: DE-AC05-00OR22725 and DE-AC06-76RL01830

Executive Summary

This project consists of three tasks that are focused on research and development activities advancing the basic mechanical properties, manufacturability, and cost of lightweight materials toward the levels needed for increased implementation in automotive applications. The specific tasks include the following:

- Enhancing sheared edge stretchability of advanced high-strength steel (AHSS)/ultra-high-strength steel (UHSS).
- Extruding non-rare earth high-performance wrought magnesium (Mg) alloys
- Optimizing heat treatment parameters for third generation AHSS with high throughput in-situ experiments and integrated modeling frameworks.

The following three sections outline specific task work conducted at PNNL in the areas of predictive engineering, process development, and enabling technologies for metals that have low density and high strength-to-weight ratios and associated manufacturing processes. Each task supports one or more goals within the Vehicle Technologies Office's project agreement as outlined in the following subsections.

III.1.1 Enhancing Sheared Edge Stretchability of AHSS/UHSS through Integrated Manufacturing Process Simulations

Project Details

Xin Sun, Principal Investigator
Pacific Northwest National Laboratory
902 Battelle Boulevard
Richland, WA 99352
Phone: 509-372-6489
E-mail: xin.sun@pnnl.gov

Constantin Chiriac and Raj Sohmshetty, Industry Partners
Ford Motor Corporation
16800 Executive Plaza Drive North
Dearborn, MI 48124
Phone: 313-390-0839
E-mail: cchiriac@ford.com
Phone: 313-317-9035
E-mail: rsohmshe@ford.com

Ming Shi and Brandon Hance, Industry Partners
U.S. Steel
5850 New King Court
Troy, MI 48098
Phone: 248-267-2610
E-mail: mfshi@uss.com
Phone: 248-267-2564
E-mail: bhance@uss.com

Kavesary Raghaven, Industry Partner
AK Steel Corp.
9227 Centre Pointe Dr.
West Chester, OH 45069
Phone: 513-425-2922
E-mail: kaversary.raghaven@aksteel.com

Yu-wei Wang, Industry Partner
AK Steel Corp.
4001 Miller Rd.
Dearborn, MI 48120
Phone: 313-317-1301
E-mail: yu-wei.wang@aksteel.com

Sergey Golovashchenko, University Partner
Oakland University
248 Dodge Hall
Rochester, MI 48309-4401
Phone: 248-370-4051
E-mail: golovash@oakland.edu

Accomplishments

- Generated two different dual phase (DP) steels (i.e., AK Steel DP980 dual phase baseline [DPB] and dual phase tempered [DPT]) with different phase properties by applying a tempering heat treatment.
- Performed hole expansion/extrusion tests with DPB/DPT steels to examine the effects of phase properties on their performance.
- Characterized the DPB/DPT steels using mechanical and microstructural examination techniques.
- Performed a shearing and tensile stretchability test with DPB steel.
- Set up a simulation method for predicting the hole expansion/extrusion ratio (HER) of DPB/DPT steels.
- Set up a simulation scheme to predict the tensile stretchability of sheared DP steels based on material information of U.S. Steel DP980 steel (i.e., UDP).
- Estimated the fracture strain curves for the macro shearing model and the microstructure-based model using computational/experimental methods.
- Examined the effects of material heterogeneity on variation of the sheared edge shape.
- Examined the effects of representative volume element (RVE) size on its fracture strain to be used as information for the models with a different element size.

Future Directions

- Perform accumulated rolling and tension test and shearing and stretchability test with UDP steel.
- Validate the simulation scheme for the tensile stretchability prediction against experimental data.
- Upgrade the computational models with finely calibrated material parameters based on new experimental results.
- Examine edge fracture and damage by metallography and three-dimensional high energy x-ray diffraction (3D HEXRD) tomography.

Technology Assessment

- Target: Enhance the sheared edge stretchability of AHSS/UHSS by developing quantitative and predictive understanding of microstructure effects on sheared edge fracture and stretchability.
- Gap: The experimental data currently available from open literature are typically only valid for the specific material under the specific combination of edge preparation and stretching conditions due to the lack of fundamental understanding of microstructure effects on sheared edge stretchability.

Introduction

During cold stamping of AHSS/UHSS parts, the most commonly observed failure mode is edge splitting. The sheared edge stretchability appears to depend on a combination of factors, including edge stretching mode, edge shearing/trimming conditions, and initial sheet properties defined by microstructural characteristics and damage occurrence in the steel sheets. The contributions of these various factors to the material edge stretchability are not well understood due to the complex interactions of these factors during edge preparation and subsequent forming operations.

It is generally accepted that edge damage caused by a piercing operation depends on the microstructure of the material, and the difference in the edge stretching limit between different dual phase steels of the same

ultimate tensile strength (UTS) level could be due to different levels of edge damage produced by the hole-piercing operation. However, quantitative and predictive capabilities linking the microstructure characteristics to the sheared edge stretchability under different loading modes (i.e., tensile stretching or hole expansion) are not available. Moreover, experimental data available from open literature are typically only valid for the specific material under the specific combination of edge preparation and stretching conditions due to the lack of a fundamental understanding of microstructure effects on sheared edge stretchability. There is a keen interest from steel producers for more fundamental understanding on key microstructure features that influence macroscopic properties (i.e., tensile properties, HER, and localized formability of AHSS/UHSS) during their steel development process. On the other hand, there is an urgent need from automotive original equipment manufacturers to obtain a quantitative and predictive understanding of whether a specific type of macroscopic test result can be used to infer these steels' in-die behaviors in their efforts to establish robust manufacturing processes for the new generations of AHSS/UHSS.

The purpose of this project is to enhance the sheared edge stretchability of AHSS/UHSS by developing quantitative and predictive understandings of the microstructure effects on sheared edge fracture and stretchability; therefore, accelerating development of next generation advanced high-strength steels and enabling a rapid and cost-effective implementation of AHSS/UHSS in vehicle structures for substantial mass savings.

Approach

During this project, a combined experimental and modeling approach has been adopted to develop a quantitative understanding and a predictive capability about the effects of microstructure features on sheared edge fracture and stretchability for AHSS/UHSS sheet steels with a UTS of 980MPa. We proposed to focus on two or three UHSS sheets with a minimum UTS of 980 MPa (referred to as DP980 hereafter) as our example material system; however, the overall approach should be extendable to other AHSS/UHSS grades.

During Fiscal Year (FY) 2016, for the experimental approach, hole expansion/extrusion tests were mainly focused on assessing the effects of constituent phase properties on edge stretchability. For this purpose, tempering treatment was first conducted on AK DP980 steel (i.e., DPB) to generate a new DP980 steel (i.e., DPT) with different phase properties. Various experiments (e.g., the tensile test, HEXRD test, and so forth) were subsequently performed with these materials for material characterization. A tensile stretchability test was also performed with the DPB to assess the effects of clearance, between the two shear blades, on the stretchability of its sheared samples. For the modeling approach, two different modeling methods have been developed in order to simulate the processes of the hole piercing/expansion test and the tensile stretchability test. More modeling works were also performed to have further fundamental understanding about the sheared edge fracture and stretchability of DP980 steels.

Results and Discussion

DPT steel was generated by performing a tempering treatment on DPB steel. The purpose of this heat treatment was to decrease the strength disparity between the ferrite and martensite and then to examine its effects on performance in the hole expansion/extrusion tests. Figures III.1.1-1(a) and 1(b) compare the microstructures of the two steels. As shown in the figures, their microstructures are quite similar to each other in terms of martensite volume fraction, and grain size. However, DPT steels generally shows a lower strength and ductility when compared to the DPB steel due to the tempering effect (see the stress-strain curves in Figure III.1.1-1(c)).

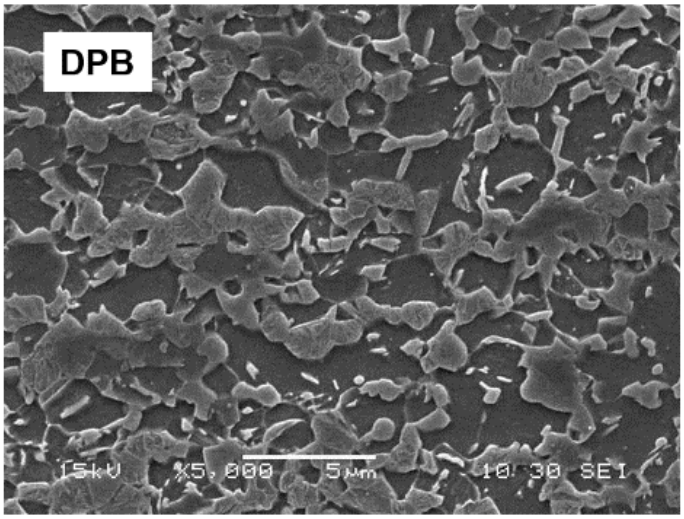

(a)

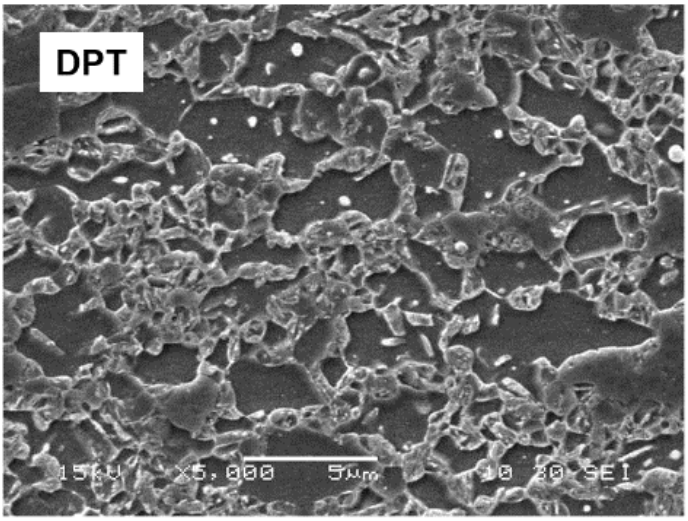

(b)

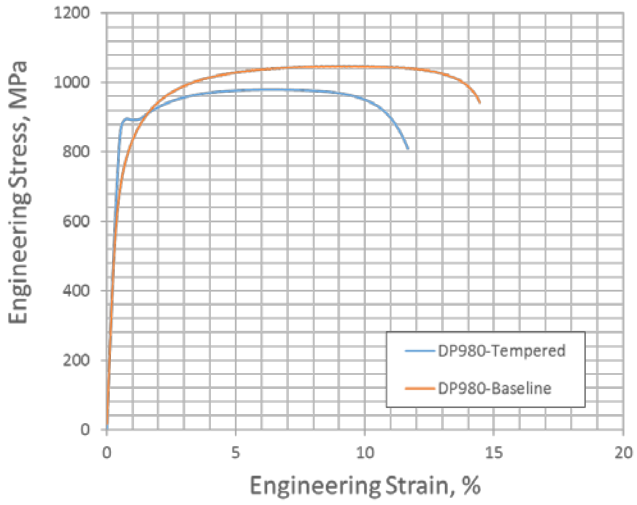

(c)

Figure III.1.1-1. A scanning electron microscopy micrograph of (a) DPB (baseline steel) and (b) DPT (tempered steel). (c) Stress-strain curves for the two DP980 steels.

Figure III.1.1-2 compares the large-strain flow stresses and constituent phase properties between the two steels. The large-strain flow stresses were obtained from accumulated rolling and tension tests and the constituent phase properties were estimated from a HEXRD test with an elasto-plastic self-consistent model. As shown in Figures III.1.1-2(b) and 2(d), DPT steel shows less strength disparity between the two phases than the DPB steel, which appears to be due to softening of the martensite phase. Similar to Figure III.1.1-1(c), the large-strain flow stress of DPT steel is also lower than that of DPB steel. Note that large-strain flow stresses are used as input properties in the macro-shearing model.

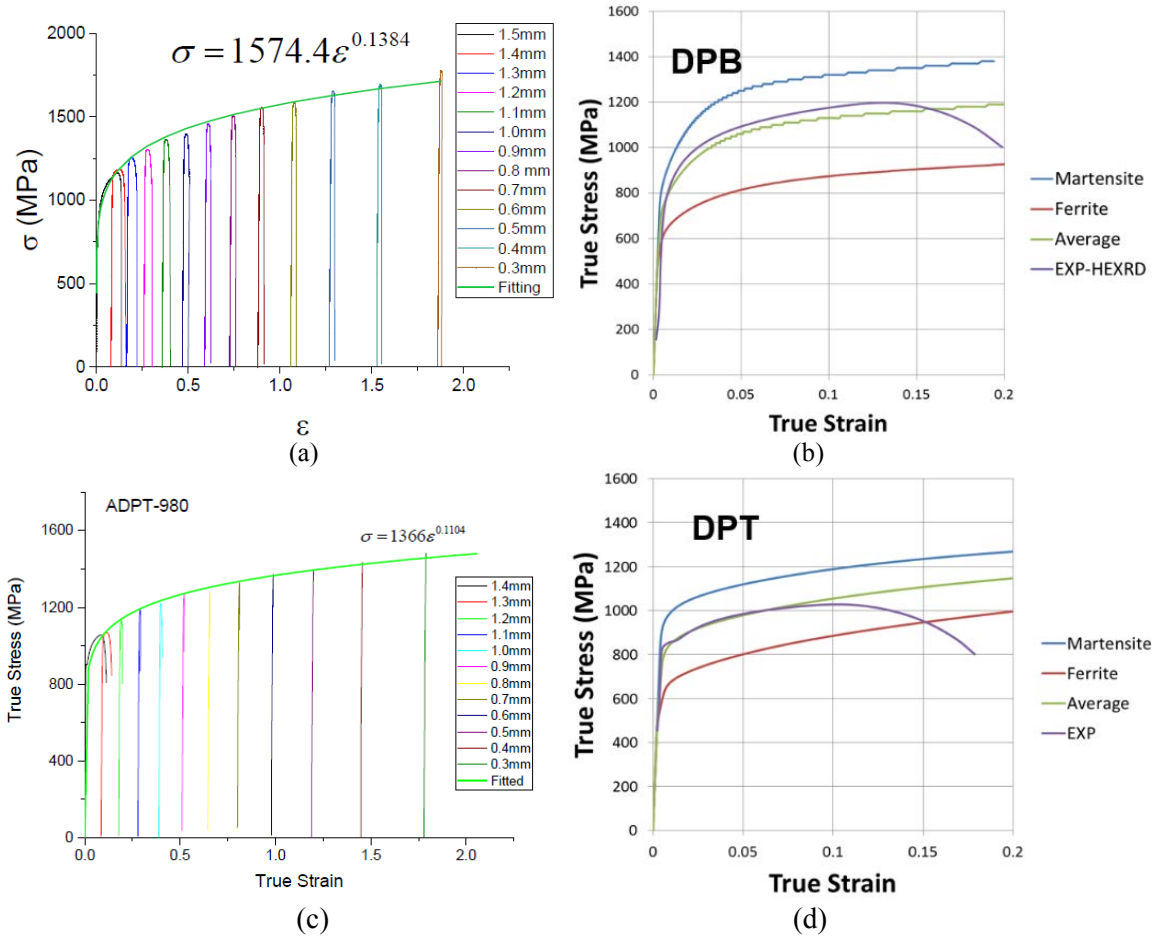

Figure III.1.1-2. Flow stresses at large strain and individual phase properties of (a) and (b) DPB and (c) and (d) DPT steels.

Hole extrusion/expansion tests were performed with the DPB and DPT steels. As an example of experimental results, Figure III.1.1-3 compares HER between the two steels. In the tests, a 60-degree conical die extrudes the pierced blank with the burr away from the punch until a through-thickness crack is observed. HER is defined as the percentage change in the diameter of pierced hole. As show in Figure III.1.1-3(d), DPT steels show about 100% improvement in HER when compared to DPB steel. This improvements is due to the lowered strength disparity induced by softening of the martensite phase. Note also that the softened martensite phase in the DPT steel may have higher fracture strain compared to that in the DPB steel.

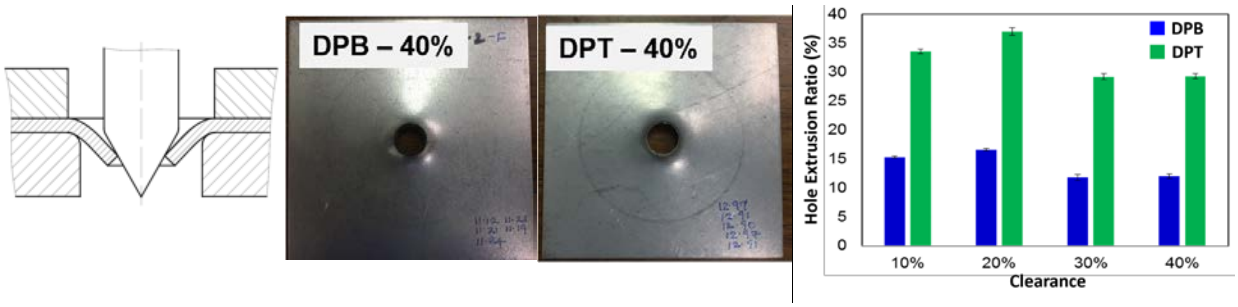

(a) (b) (c) (d)

Figure III.1.1-3. (a) Schematics of hole extrusion test, (b) and (c) tested samples with 40% clearance and (d) comparison of HER between the DPB and DPT steels.

Figure III.1.1-4 shows the computational model for assessing the effects of tempering heat treatment on HER. A two-dimensional (2D) axisymmetric model was first developed so the predicted sheared edge shape can be similar to those observed in experiments (Figures III.1.1-4(a), 4(b), and 4(c)). A 3D hole extrusion model was developed based on the sheared edge profile and the field variable information obtained from 2D simulations. Note that information on material heterogeneity (e.g., phase properties, phase volume fraction, phase fracture, and texture) was also incorporated into the 3D model. As shown in Figures III.1.1-4(d) and 4(e), the developed 3D model can predict the significantly improved HER for DPT steel (i.e., 20.6% versus 13.8%) as observed in the experiment. The 2D/3D models may be further calibrated when new materials' parameters are available from various sources.

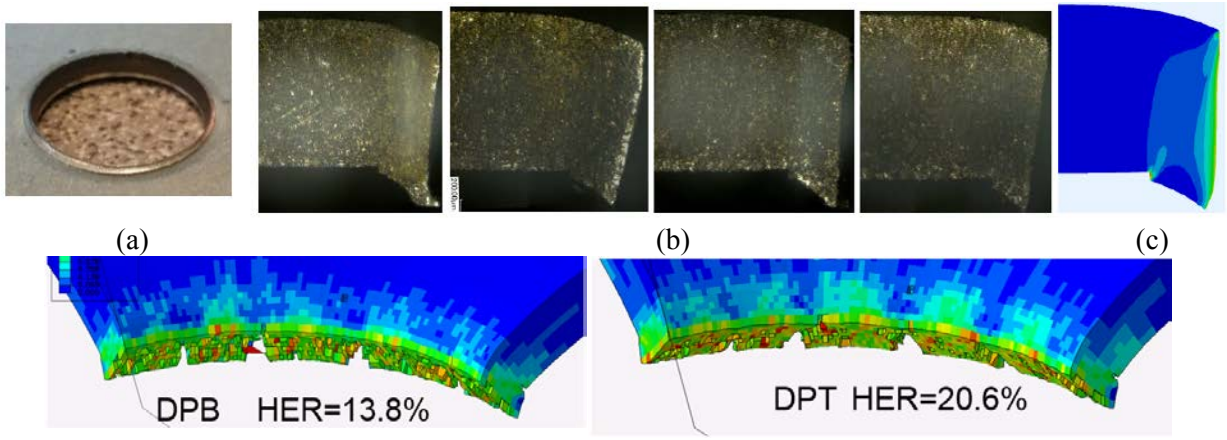

(a) (b) (c)

(d) (e)

Figure III.1.1-4. (a) Hole pierced with 40% clearance, (b) sheared edge shapes at four different locations along the hole circumference, (c) result of 2D axisymmetric shearing simulation for 40% clearance, and (d) and (e) predicted HER from the 3D hole extrusion model.

Tensile stretchability tests were also performed with the DPB steels. Figure III.1.1-5 shows the schematics of the conventional shearing process and the results of tensile stretchability tests for the sheared DPB samples. Figure III.1.1-5(b) shows the three different failure modes observed from the DPB steel [1]. Depending on the distance of the grid from the fracture, the measured local strains may be classified as fractured, localized (or necked), and safe [2]. Figure III.1.1-5(c) shows stretchability in the form of major strain as a function of clearance. The lower boundary of all fractured or localized data points may represent the fracture limit (red line) and the upper boundary of all safe data points may represent the safe forming limit (green line). In general, clearance appears not to have a significant influence on the fracture limit. Figure III.1.1-6 shows the computational scheme developed for prediction of tensile stretchability of sheared DP steels. In short, 2D macroscopic shearing simulation and sub-model simulations using a microstructure-based model are performed to obtain the plastic strain distributions and internal cracking/voids near/along the sheared edge (Figure III.1.1-6(a)). The obtained damage information is then incorporated into the 3D tensile stretchability model (Figure III.1.1-6(b)). Figures III.1.1-6(c) and 6(d) show some simulation results of failure mode and

predicted stress-strain curve. Further simulations will be performed to validate the developed computational scheme against experimental results.

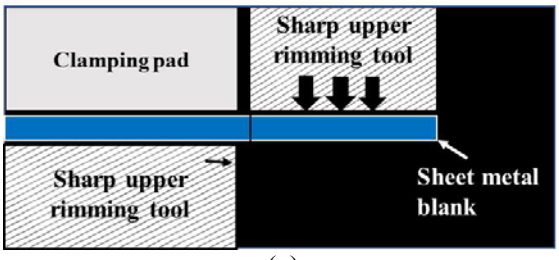

(a)

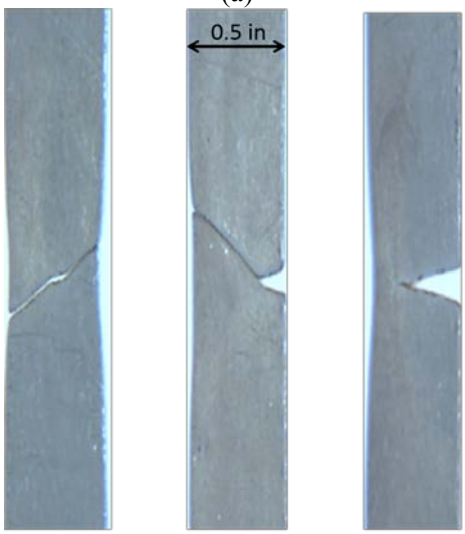

(b)

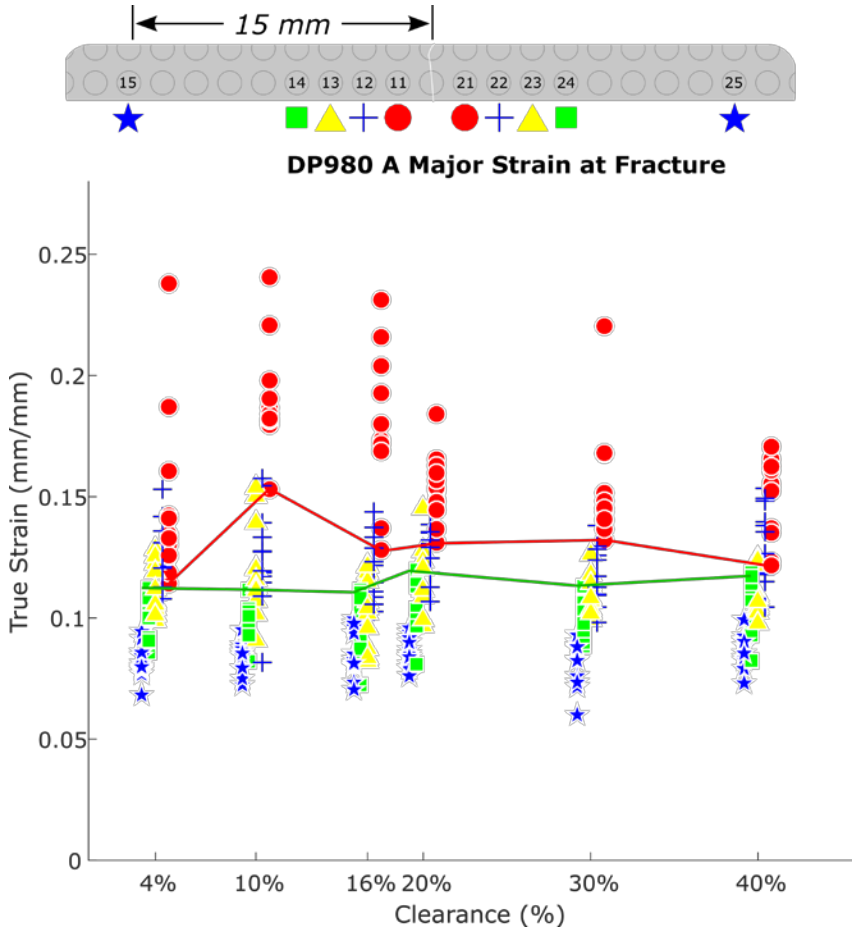

(c)

Figure III.1.1-5. (a) Schematic of conventional shearing process, (b) in-plane failure modes under tension of sheared samples, and (c) tensile stretchability for the sheared DPB steel.

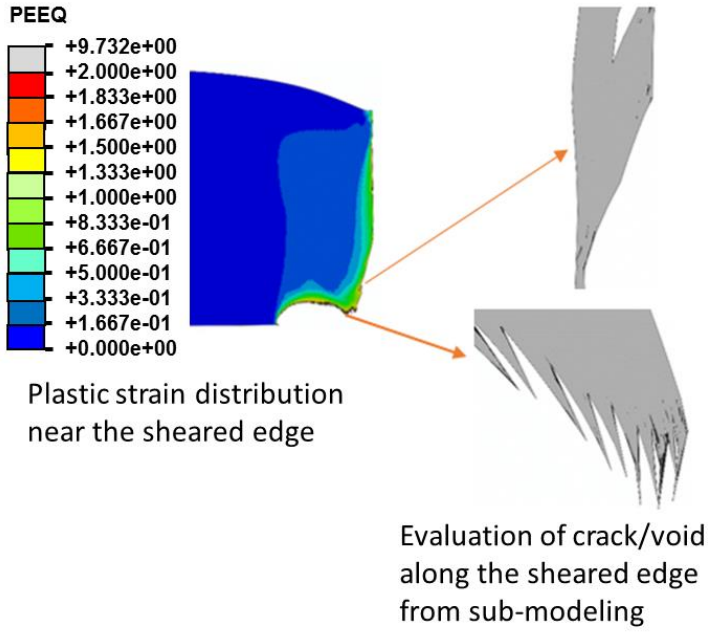

(a)

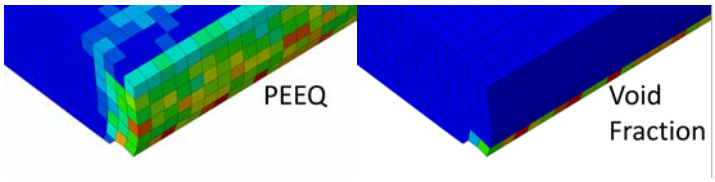

(b)

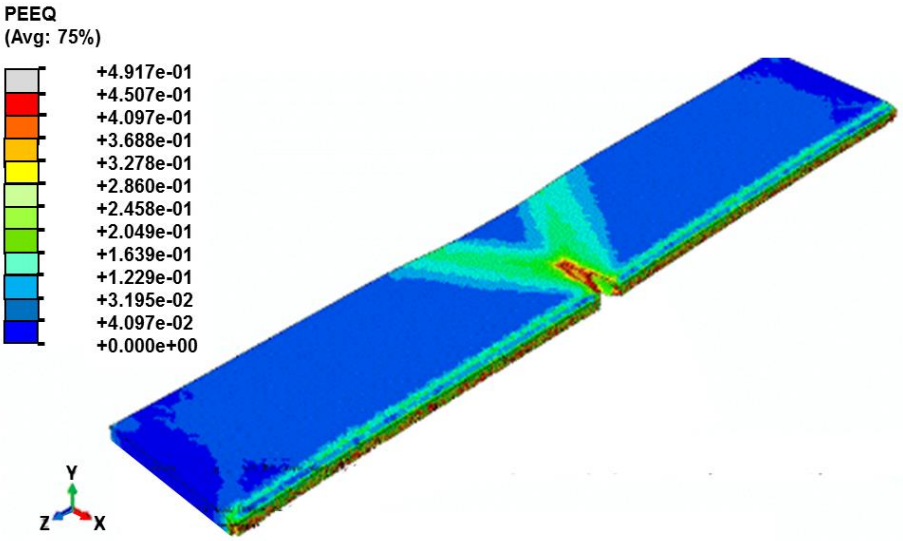

(c)

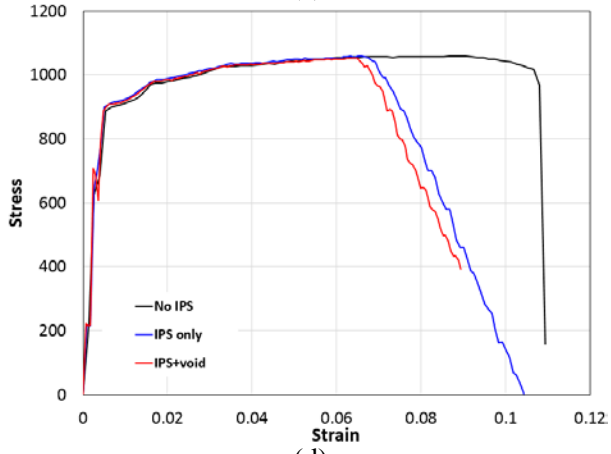

(d)

Figure III.1.1-6. Modeling for prediction of tensile stretchability: (a) plastic strain distribution from shearing simulation and crack/void distributions from sub-model simulations, (b) integration of shearing simulation results into the 3D tensile model, and (c) and (d) examples of simulation results (i.e., failure mode and stress-stain curves) for the case of 40% clearance (IPS represents initial plastic strain).

Fracture strain curves (versus stress triaxiality) for the macroscopic material and the constituent phases play an important role in these modeling works. Both computational and experimental methods have been adopted in this work in order to estimate a more accurate fracture strain level that is needed for the simulations. For example, the fracture strain curve for the macroscopic material of the UDP steel was estimated by comparing the sheared edge shapes between the simulations and experiments (Figure III.1.1-7(a)) [3]. Note that the predicted edge shapes in terms of the sizes of burnish, rollover, and fracture are quite similar to those measured from the experiment (Figure III.1.1-7(b)). Grain deformations near the sheared edge were also measured for estimating the fracture strain level of the materials (Figure III.1.1-8). The fracture strain level estimated from the grain deformation measurement was found to be similar to that estimated from the simulation method shown in Figure III.1.1-8.

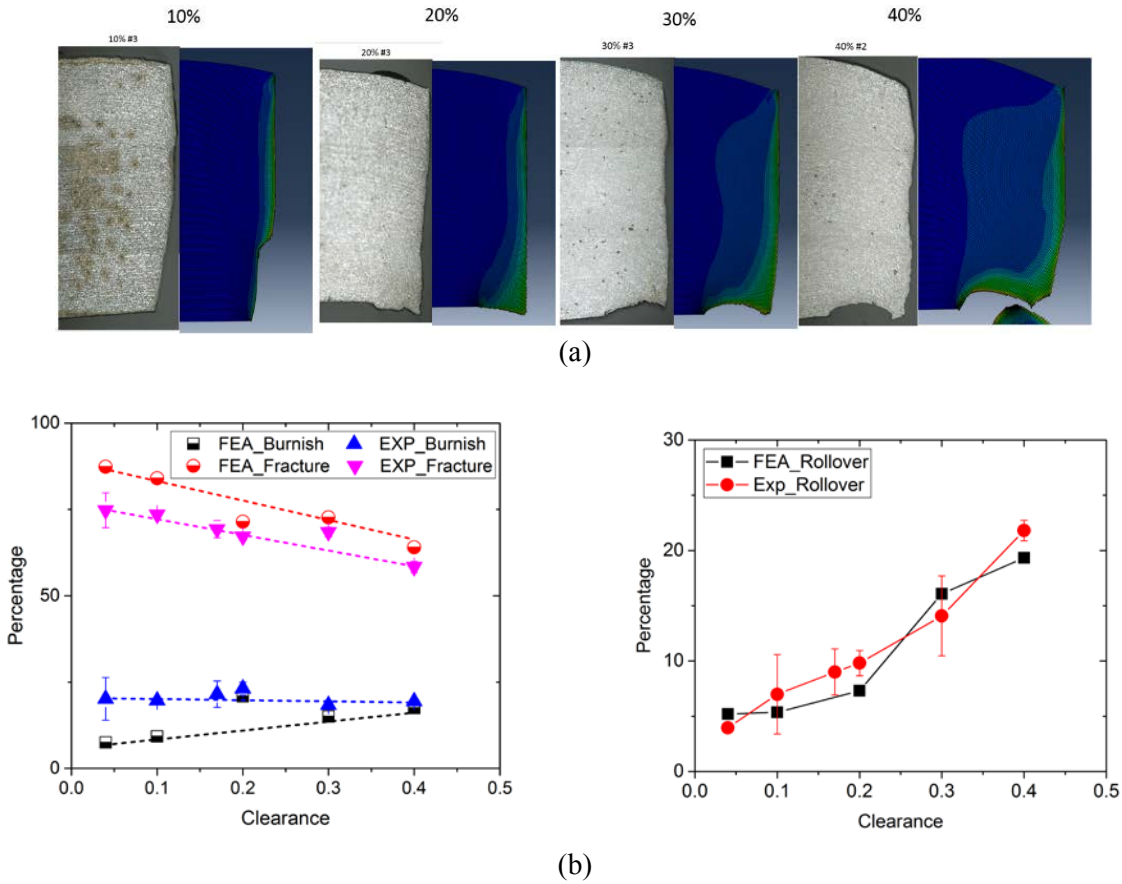

Figure III.1.1-7. (a) Comparison of sheared edge shapes between experiment and simulations and (b) comparison between measured data and simulation results for UDP steel.

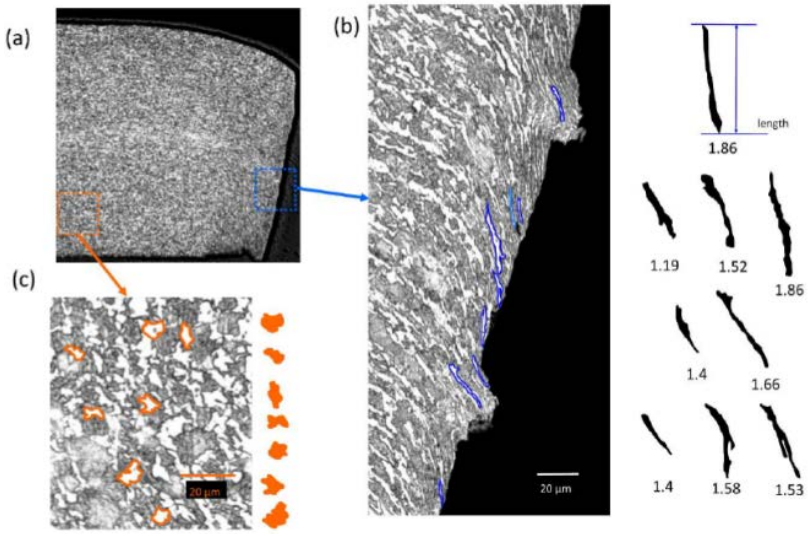

Figure III.1.1-8. Fracture strain estimation based on grain deformation measurement near the sheared edge.

Large edge variability was observed along the sheared edge of UDP steel as shown in the burr height variation for the case of 40% clearance in Figure III.1.1-9(a). Note that DPB steel does not show the burr height variation in Figure III.1.1-9(a). However, DPB steel still shows the burr height variation along the circumference of the pierced hole for some clearance (Figure III.1.1-10(b)). Computational models were adopted to understand the possible source for edge variability of these materials. For the UDP steel, large microstructural heterogeneity was observed in terms of local martensite volume fraction. Therefore, several 2D

models with different heterogeneous microstructure distributions were generated/used to examine its effects on edge variability. Figure III.1.1-9(b) shows that microstructural heterogeneity may be an important source for edge variability for the UDP steel. The 3D piercing simulation was also performed for the DPB steel. Off-center punching might result in edge variability for the DPB steel (Figure III.1.1-10(c)).

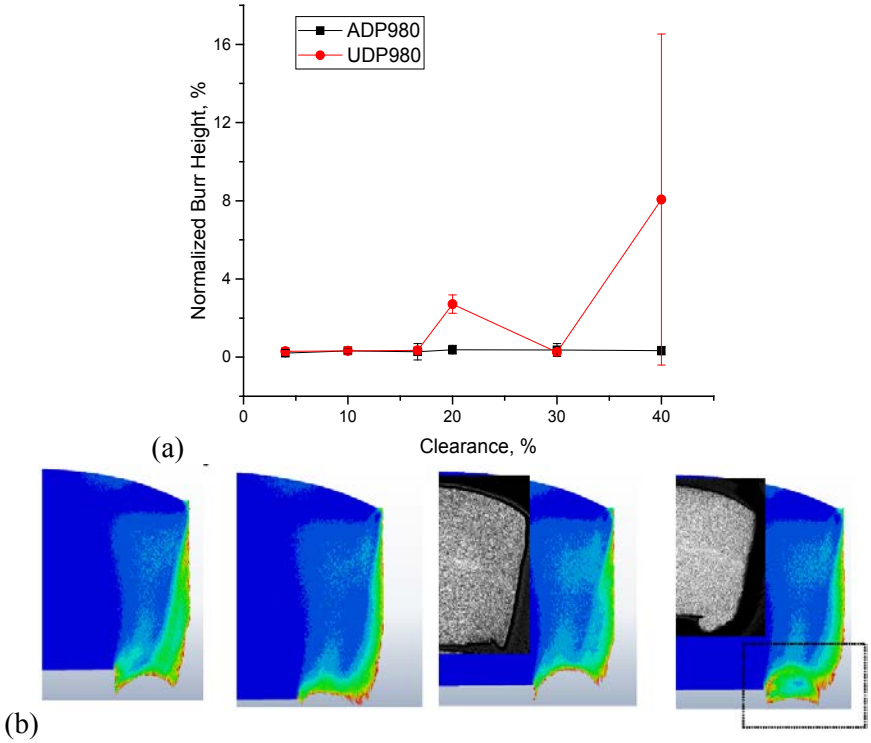

Figure III.1.1-9. (a) Normalized burr height versus clearances for the DPB (ADP980) and UDP (UDP980) steels and (b) burr height variation shown in the simulations with heterogeneous microstructure distributions.

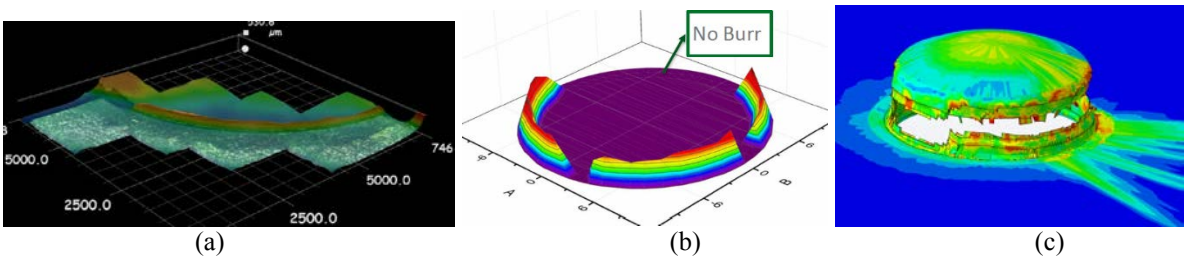

Figure III.1.1-10. (a) 3D image showing the burr near the pierced hole, (b) burr height variation along the hole circumference of DPB steel, and (c) an example of a 3D hole piercing simulation showing burr height variation.

Mesh-size dependency is a well-known difficulty in modeling material failure with finite element analysis. In this work, 2D/3D models with different mesh sizes have been adopted to simulate failure behaviors of the DP steels under different deformation processes of interest. Therefore, RVE size effects on its fracture strain were examined using the actual microstructure-based finite element model and a possible quantitative relationship between the RVE size and its fracture strain was obtained (Figure III.1.1-11). The information shown in Figure III.1.1-11 may be used as a guideline to determine the appropriate fracture strain level for the finite element models of DP steels with different mesh sizes as adopted in this work.

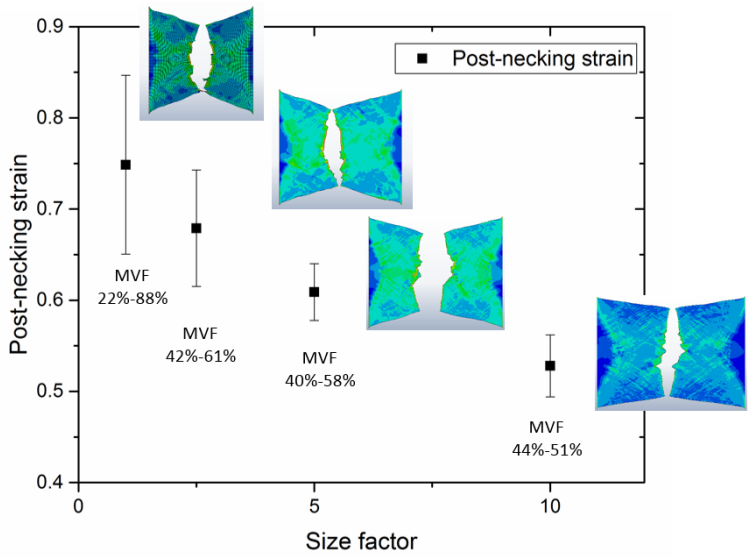

Figure III.1.1-11. RVE size effects on fracture strain (MVF represents martensite volume fraction).

Technology Transfer Path

Technology transfer of this project will be directly through Ford Motor Company and their Tier 1 suppliers. Broader commercialization of the technology through the Tier 1 suppliers will reach the entire automotive original equipment manufacturer industry. We also plan to present and publish our findings in the Society of Automotive Engineers and/or other engineering journals to further disseminate our research results.

Conclusions

The effects of a smaller strength disparity between the constituent phases on HER of DP980 steels were examined by applying a tempering heat treatment to a DP980 steel. The experimental results show that less strength disparity can contribute to significant improvement of HER. According to tensile stretchability tests, shearing clearance does not appear to have a substantial influence on the fracture limit of DP980 steels.

Computational models were developed in order to simulate the processes of the hole piercing/expansion test and the tensile stretchability test and to understand the key factors influencing edge stretchability of DP980 steels. The developed models may provide explanations about experimental observations of interest and will continue to be upgraded with experimental validations and more accurate material parameters.

III.1.2 Cost-Effective Magnesium Extrusion

Project Details

Curt A. Lavender, Principal Investigator
Pacific Northwest National Laboratory
902 Battelle Boulevard Richland, WA 99352
Phone: 509-372-6770
E-mail: curt.lavendar@pnnl.gov

Tim Skszek, Principal Investigator
Magna Cosma International
1807 East Maple Road Troy, MI 48083
Phone: 248-689-5512
E-mail: tim.skszek@cosmaeng.com

Introduction

The Pacific Northwest National Laboratory (PNNL) and Magna Cosma International have been actively collaborating on technologies relevant to the automotive industry that support the U.S. Department of Energy's mission of improving process and product efficiencies while reducing the weight of automobiles. The use of high-performance Mg alloys in the automotive industry is presently limited due to the addition of costly rare-earth elements and the slow rate of the processing (i.e., conventional extrusion techniques). Current work aims to eliminate the need for rare earth additives, while simultaneously improving the processing rate and energy efficiency.

The application of Mg alloys in bumper beams, crush tips, and intrusion beams has been demonstrated to result in significant vehicle weight savings. However, to increase the structural use of Mg alloys, development of cost-effective bulk metal forming methods are necessary. In this regard, extrusion techniques, which are typically used to produce bars, tubes, or more complex cross-sections at a fairly rapid speed, are a promising metal-forming method to investigate. Several researchers have studied the role of different process variables during extrusion of Mg alloys. However, during all of these studies, extrusion experiments were conducted at elevated temperatures because Mg alloys suffer from limited room temperature ductility due to limited slip systems. In order to minimize grain size at these high temperatures, the feed rate during extrusion is kept low or needs to be followed by severe plastic deformation processes to refine grain size. This project aims to develop and demonstrate low-cost extruded Mg alloys that do not rely on rare earth alloying elements for their strength, ductility, and energy absorption properties. A novel low-cost, high-speed processing method, in conjunction with Mg alloys containing rare earth substitutes, will be developed to produce the microstructure and properties needed for automotive applications in a cost-effective manner.

Accomplishments

- A scaled-up version of the novel extrusion system, Shear Assisted Processing and Extrusion (ShAPE), has been developed to produce fine-grained Mg alloy tubes:
  - Demonstrated the process is energy efficient and repeatable
  - Produced a 50.8-mm diameter tube with 1.5-mm and 3-mm wall thickness
  - Developed the ability to control texture as a function of feed rate and rotational speed
  - Filed a continuation-in-part application patent for the process with the U.S. Patent and Trademark Office complimenting/supporting the original application [4].

- The ZK60 Mg alloy was cast and extruded to produce high-performance Mg alloys with fine grain sizes with the following features:
  - Grain sizes appear to be less than 5 μm
  - Dispersions near 15 nm interact with dislocations.
- A Mg alloy containing no rare earth elements that was processed for fine grain size using low-cost, ShAPE was shown to absorb energy similar to 6061 aluminum:
  - Resulted in a 20% mass savings over 6061
  - Initiated thermal modeling to understand processing parameters.

Future Directions

- Establish commercial goals for non-tubular Mg alloy extrusions and demonstrate high strength in prototypic-size components.

Technology Assessment

- Target: Develop high energy absorption Mg alloys that can replace aluminum extrusions at a mass savings of 20% (based on density).
- Target: Use inverse process modeling to develop a low-cost process for producing microstructures required for high performance at a low cost, making Mg extrusion viable for automotive applications.
- Gap: The current system extrudes only tubular components and this will be addressed by designing a bridge die that will help in extruding the Mg structures relevant to the automotive industry.

Approach

The objective of this project is to develop a low-cost method for extruding Mg alloys with highly refined grain structures. We will investigate the use of a shearing process where the Mg ingot is rotated to induce a plasticized region at the Mg/die interface. This process is now commonly referred to as ShAPE. Small-scale exploratory experiments at PNNL have shown that extrusion force can be greatly reduced using this method; however, it is unclear whether or not this process can be scaled up to larger extrusions. Advantages may include enhanced grain refinement, leading to better material properties, higher material throughput, and lower extrusion forces that lead to smaller tonnage equipment and lower process energy consumption.

This project will progress in two distinct phases. Phase I focuses on scaling up the existing shear-assisted indirect extrusion technology, while Phase II moves beyond indirect ShAPE to direct ShAPE, which will eliminate the need for boring or piercing the Mg billet. The technical scope for both phases of this project includes four key components: (1) modeling and simulation, (2) process parameter development, (3) materials characterization, and (4) extrusion at a scale relevant to industry.

Phase I**:** PNNL will perform modeling and simulation to guide tooling design, rotation speed, and thermal transport impacts on scale-up of the 7.5-mm/6.0-mm outside diameter to inside diameter (OD/ID) proof-of-concept tubing that was demonstrated using ShAPE in FY 2014. Model results will then be used to inform design of the ram, die, bolster, container housing, and other components of the extrusion system that can produce indirect extrusions at a scale relevant to industry. Once the extrusion system has been established, we will determine the processing parameters and conditions necessary to produce non-rare earth Mg alloy extrusions at a high rate with material properties suitable for structural automotive applications. Materials characterization will be conducted for important properties (e.g., grain size, precipitate size, texture, compression, and tension yield stress). A key part of the scope is demonstration of the ShAPE process at a scale that is relevant to industry. This project will avoid the pitfall of demonstrations that are too far from an

industrial process to induce confidence in scale up. The target for Phase I of the project is to demonstrate an extrusion that is approximately 2.0-in. OD by 1.5-mm wall thickness by 24-in. long. Phase II will incorporate a bridge die technique to form similarly sized tubing.

Phase II: Using a bridge die to form tubing is advantageous because the billet does not have to be bored or pierced prior to or during extrusion, which can result in substantial cost savings compared to indirect extrusion. During the second phase of this project, PNNL will move from indirect extrusion to direct extrusion of Mg alloy tubing using a bridge die approach. Because of the expected complexity of combining a direct bridge die approach with friction-assisted extrusion, we anticipate that developing ShAPE will be a substantial effort encompassing the majority of FY 2016 and all of FY 2017. Similar to Phase I, research activities will generally include modeling and simulation, bridge die system design and implementation, process development, materials characterization, and model validation. The target for Phase II of the project is to demonstrate a square extrusion that is approximately 2.0-in. by 2.0-in. by 24-in. long and having a wall thickness on the order of 1.5 mm.

Results and Discussion

During the ShAPE process, a rotating billet is forced into a stationary extrusion die, where significant heating occurs due to friction at the billet/die interface (Figure III.1.2-1). The amount of heat generation is controlled by the applied torque, rotational speed, and chilled water flow rate through the mandrel. As temperature increases, the billet face softens and plastically flows through the spiral scroll features inward toward the extrusion orifice. Material streams within multiple scrolls are consolidated between the mandrel and bearing surface prior to exiting through the die relief. Recrystallization occurs within the deforming material and, when shear and temperature are suddenly reduced, a refined microstructure can be obtained [5, 6] in the extrudate. Because of the complex shear and thermal conditions present during ShAPE, crystallographic texture is thought to develop as a combination of recrystallization mechanisms [7, 8] due to the interplay between rotational speed, extrusion rate, and thermal conditions. As such, the ShAPE process may offer unique control over grain refinement and crystallographic orientation and material property improvements beyond conventional extrusion techniques. During embodiment of the ShAPE process (Figure III.1.2-1), the extrusion die is held in a fixed position and the rotating components translate from right to left. Therefore, the tube is extruded in the direction of billet translation and is classified as a direct extrusion. In this configuration, the extrudate is spinning along with the rotating components, but the ShAPE process can be easily configured where the extrusion die is the only rotating component and the extrudate would not spin.

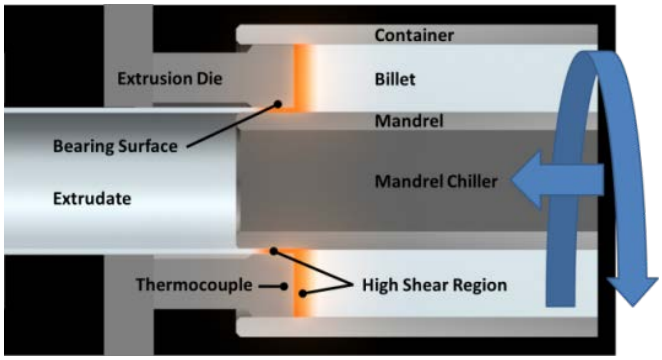

Figure III.1.2-1. Cross section of the hardware showing a direct extrusion embodiment of the ShAPE process.

The ShAPE extrusion hardware consists of four components: (1) an extrusion die, (2) billet, (3) container/mandrel assembly, and (4) mandrel chiller (Figure III.1.2-2). The extrusion die is fabricated from H13 tool steel and has an ID of 50.8 mm, which defines the OD of the extrudate. Two spiral scrolls are machined into the face of the die to aid material flow into the extrusion orifice. For this study, the scroll channels have a width of 2.72 mm, depth of 0.47 mm, and pitch of 4.04 mm, with each of the two starts completing 2.25 turns. A gently tapered relief of the die throat occurs after a 12.7-mm bearing surface.

Temperature measurements are made using a type-K thermocouple embedded 1 mm from the scrolled face midway between the ID and OD of the die face. The container/mandrel assembly is machined from an American National Standards Institute 8620 steel CAT-50 bar blank to obtain a mandrel OD of 47.8 mm and container ID of 88.9 mm. The difference in radius between the extrusion die ID and mandrel OD is 1.52 mm and defines the extrudate wall thickness. An A316 stainless chiller assembly is inserted within the mandrel to provide cooling water during the process. Hollow billets are machined from extruded ZK60A-T5 (henceforth referred to as ZK60) round bar stock to an OD of 88.8 mm, ID of 47.9 mm, and length of 113 mm. Four cylindrical pockets are machined into one end of the billet and keyed to the container to prevent relative motion during processing. The extrusion ratio is 17.7 for the configuration used in this work. The extrusion components are mounted into a Transformational Technology, Inc. LS2-2.5 friction stir welding machine capable of 120-kN axial force while applying 1,000-N-m of torque at 2,000 rpm.

Figure III.1.2-2. Components for extruding thin-walled ZK60 tubing using the ShAPE process.

Numerical modeling was used to characterize the thermal and structural characteristics of ShAPE, guide design of the tooling geometry, and understand observations from physical experiments. The modeling activity focused primarily on characterization of thermal losses during extrusion. Thermal losses must be small to reduce the machine power requirement for frictional heat generation and be carefully managed to ensure temperature in the die region is sufficiently high to facilitate plastic material flow, but sufficiently low in the billet and extrudate to maintain structural integrity. An axisymmetric model of a simplified geometry was constructed using the commercial finite element analysis software, ANSYS. The thermal model considered conduction, convection, and radiation heat transfer mechanisms to characterize transient heating on startup and steady-state thermal performance during extrusion. Various sensitivity analyses were performed to do the following:

- Quantify distribution of thermal losses to the die, mandrel, and environment
- Quantify the heat generation rate required to maintain a sufficient extrusion temperature
- Determine the effect of billet geometry on thermal distribution
- Quantify applied loads required to initiate plastic strain in the billet
- Determine mandrel geometry modifications and operating conditions to avoid billet shear
- Determine deflections of the die
- Characterize the effect of active spray cooling to the interior and/or exterior billet surfaces.

The results of these scoping analyses aided, in part, definition of the actively cooled tooling design ultimately used in the Phase I experiments. A detailed axisymmetric finite element analysis model of this design

(Figure III.1.2-3(a)) was constructed and used during further thermal and structural evaluations to do the following:

- Quantify reduction of thermal losses through the improved die and mandrel design
- Quantify the effect of cooling insert geometry and flow rate on temperature (Figure III.1.2-3b)
- Compare predicted transient temperature history to actual thermocouple measurements from experiments to verify the model sufficiently captures heat transfer mechanisms
- Understand how closure of the billet/mandrel radial gap, due to billet plastic deformation, changes heat transfer losses and maximum temperature.

Efforts were also initiated to numerically quantify the mechanical loading history and influence the die/scroll geometry on the extrusion quality; however, these models are more complex and remain in progress.

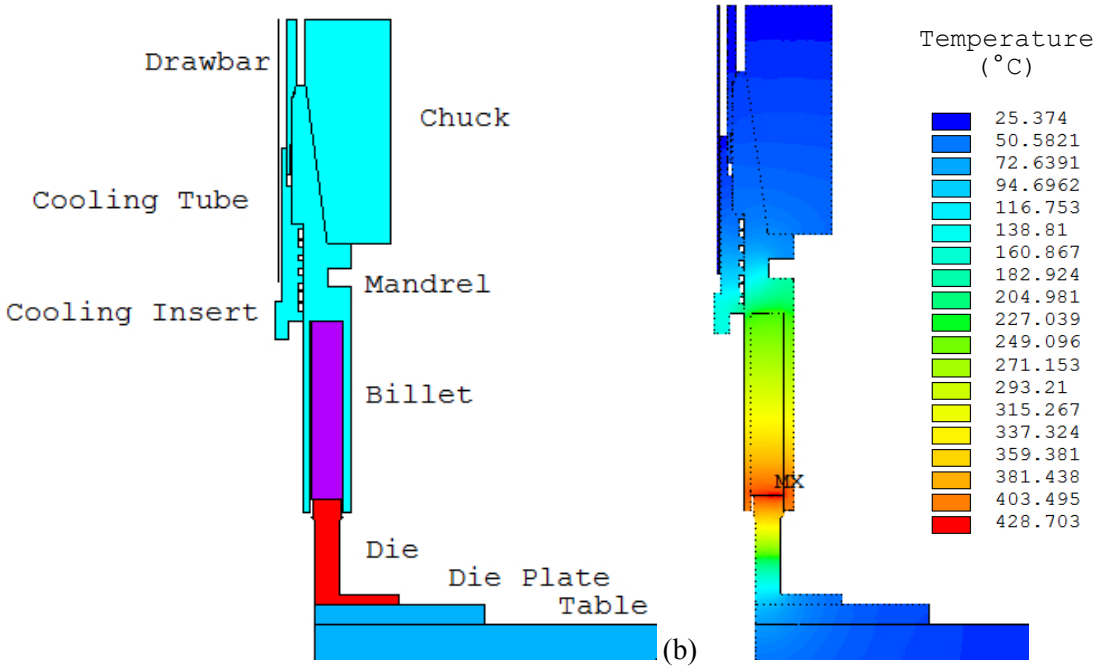

Figure III.1.2-3. (a) Axisymmetric ANSYS finite element analysis model geometry and (b) predicted temperature field for the friction extrusion test assuming 2000W heat generation.

Several runs were made at different rpms and feed rates to produce the tube. For simplification, only the results for one set of extrusion conditions will be provided. During this preliminary study, the ZK60 billet was rotated at 250 rpm and rammed against the extrusion die at a constant rate of 3.81 mm/minute. Ram force and torque build rapidly (Figure III.1.2-4), rising to their peaks of 47.1 kN and 697 N-m roughly 20 seconds after contact is made between the billet and die. The thermocouple reading corresponding to the peak ram force and torque is 230°C. During this initial phase, the scrolls essentially machine the billet, creating shavings with a “steel wool” consistency and no extrusion is formed yet. Once the peak force is reached, force and torque fall off sharply, indicating that material has begun to soften and extrude through the die. Tool speed was then reduced to 200 rpm for the remainder of the process and the thermocouple temperature eventually stabilized near 475°C. This temperature was chosen as a target because early trials showed that hot shortness occurred at thermocouple temperatures above 550°C. During the last 2 minutes of the process (i.e., operating condition), the ram force and torque averaged 40 kN and 550 N-m, respectively, and the electrical power consumption of the spindle motor was 11.5 kW at 20 rpm. The high-frequency oscillations in the torque and force data were attributed to small amounts of non-uniform, intermittent flashing observed between the die OD and container ID.

Figure III.1.2-5 shows a picture of the ZK60 extrusion cross-section having an OD = 50.8 mm and a nominal wall thickness of 1.52 mm. A representative 30-cm length is also shown. The ram force of 40 kN and k-factor of 3.33 MPa required to extrude this tube are remarkably low compared to conventionally extruded material. Assuming a k-factor in the range of 68.9 to 137.9 MPa [9] for a conventionally extruded Mg alloy, the ram force required is estimated to be 800 to 1,655 kN. Therefore, the ShAPE process achieves a greater than ten times reduction in ram force compared to conventional extrusion due to a k-factor of just 3.33 MPa. To put this in perspective, the ShAPE process requires the electrical power (i.e., 11.5 kW) consumed by a typical residential oven and the force (i.e., 40 kN) generated by a small benchtop hydraulic press.

This speaks to the combined benefits of (1) heat only being generated where it is necessary to soften the material and (2) scroll features assisting in material flow toward the extrusion orifice. Some light galling is present on the exterior surface of the tube, which is attributed to pressure variations between the mandrel and die bearing surface caused by compliance in the Transformational Technology, Inc. metals motor spindle (i.e., "walking"). However, using a more stable and robust motor spindle, which will be executed in future work, can eliminate the galling.

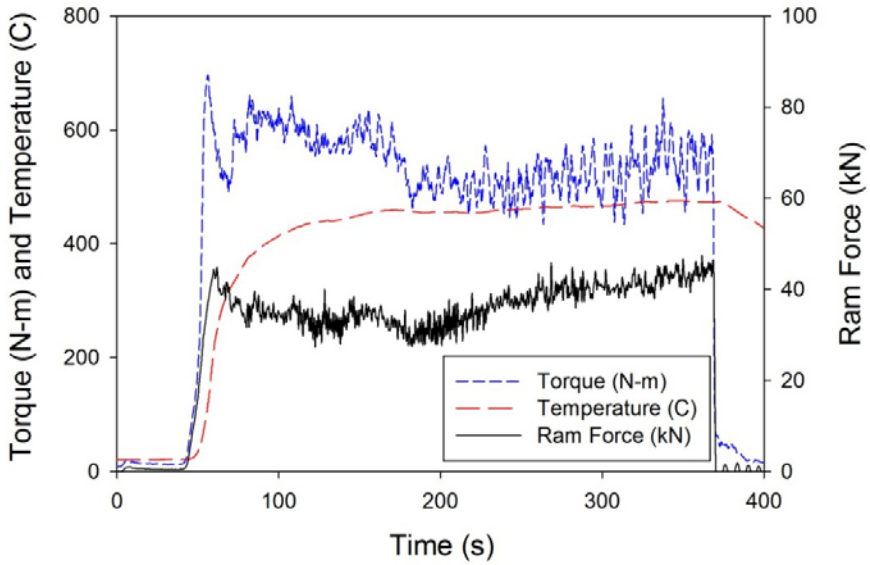

Figure III.1.2-4. Force, torque, and temperature data while extruding ZK60 tubing using the ShAPE process.

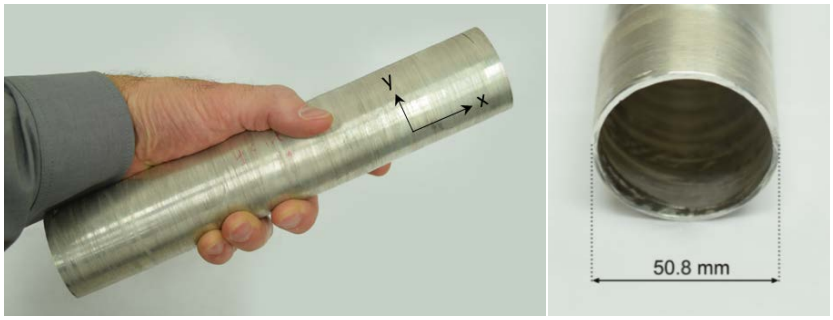

Figure III.1.2-5. A 30-cm length of ZK60 tubing extruded using the ShAPE process, along with a cross-section showing the 1.52-mm nominal wall thickness.

Following extrusion, the tubing was cut and polished in the longitudinal direction for microstructural evaluation. A through-thickness micrograph of the tubing wall is shown in Figure III.1.2-6. The top side of the specimen was in contact with the die bearing surface while the bottom side contacted the rotating mandrel. During processing, the combined axial and torsional shear, together with material movement aided by scroll features on the die face, result in complex material flow within the extrudate. Evidence of this effect can be seen in the specimen cross-section where distinct flow lines indicate how the grain structure follows the direction of working in the extrudate.

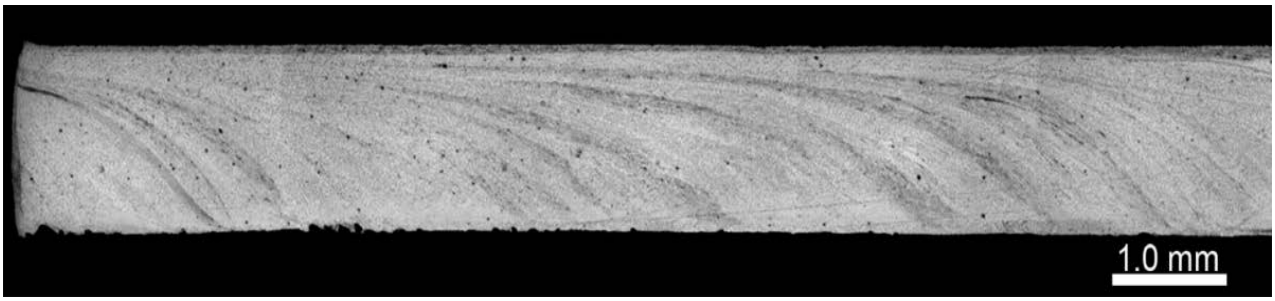

Figure III.1.2-6. Optical micrograph showing flow lines formed during the ShAPE process. The bottom side of the tube wall was in contact with the mandrel surface and the top side contacted the die bearing surface. Extrusion direction is from left to right.

Two primary sources of working are thought to generate the observed flow line configuration. First, the mandrel (i.e., contacting bottom of specimen) is moving linearly from left to right relative to the die bearing surface (i.e., contacting top of specimen). As such, a gradient in material velocity across the wall thickness can result in formation of flow lines. Second, the two scroll features on the die face are feeding material (within two separate channels) into the space between the mandrel and die-bearing surface. In this space, the two material flows are consolidated as overlapping spirals, which works the material and contributes to development of the flow line pattern. This mechanism has been observed and described in depth by Young et al. for indirect shear extrusion techniques [10] and Li et al. for friction stir back extrusion [11]. The orientation of these flow lines suggest that off-axis texture may be developing, which could aid in reducing property asymmetry in ZK60 extrusions.

Electron backscatter diffraction was performed on the center region of the tube cross-section (Figure III.1.2-6) to determine grain size at the mid-point of the wall thickness and orientation of the (0001) basal planes. The left side of Figure III.1.2-7(a) shows the scanning electron microscopic images of the specimen reference region and the direction of the flow lines. The red block is the electron backscatter diffraction area which is enhanced on the right side of Figure III.1.2-7(a). A histogram for the analysis of grain size is shown in Figure III.1.2-7(b). The analysis found that 75% of the mapped grains were less than 5 μm in diameter, with the average being 3.8 μm ±2.1 μm. A cursory scan across the entire wall thickness revealed that grain size was relatively uniform throughout. These data demonstrate that severe plastic deformation intrinsic to the ShAPE process is effective at developing refined microstructures in ZK60.

A pole figure was generated from the electron backscatter diffraction dataset to determine if the ShAPE process was effective at developing texture in the extrudate. The basal texture shown in Figure III.1.2-8 is primarily aligned in the y-direction (through thickness), but is slightly off-axis as referenced to the axis convention in Figure III.1.2-6. The importance of this result is that texture development would likely lead to anisotropic deformation properties. This is important for applications where energy absorption is critical such as automotive crush tips, bumpers, and door beams.

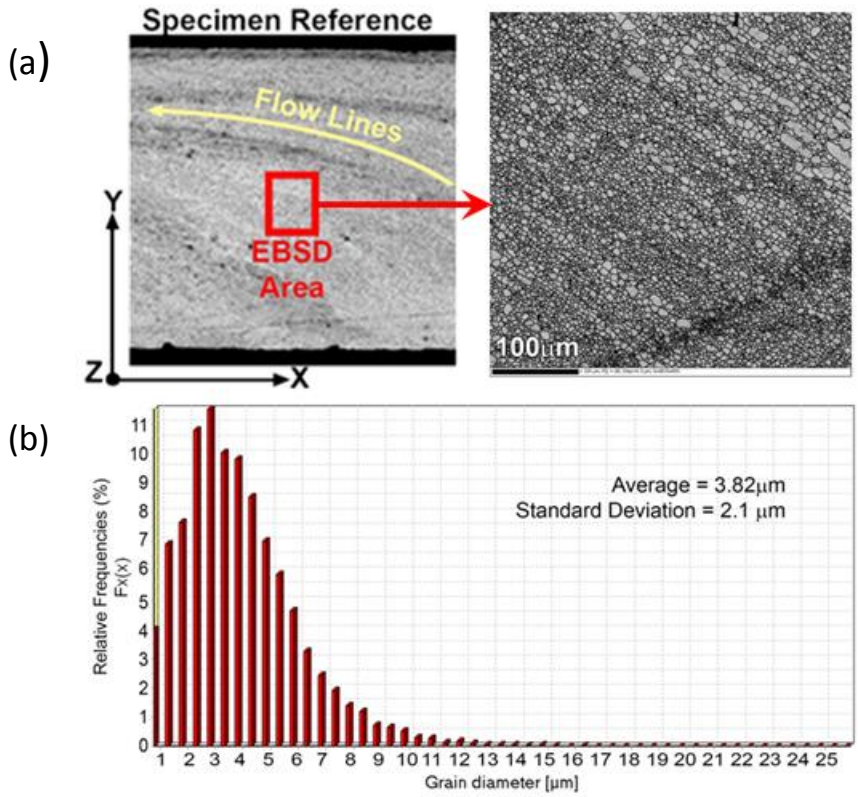

Figure III.1.2-7. (a) Scanning electron microscopy image of the region where grain size analysis was performed to determine average grain diameter at the mid-point of the wall thickness. (b) The average grain diameter was measured to be 3.8 μm with 75% of the mapped grains being less than 5 μm in diameter.

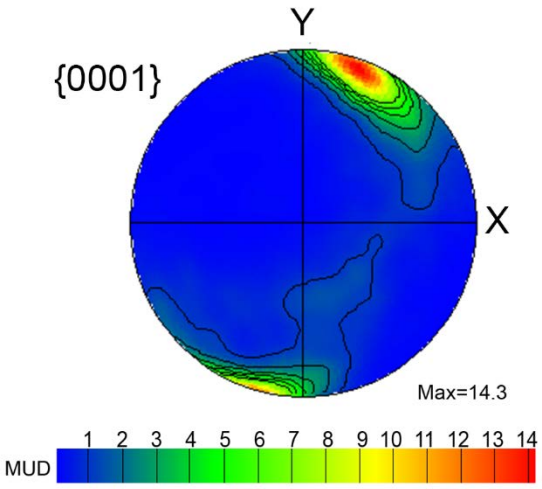

Figure III.1.2-8. Pole figure showing strong basal texture oriented with plane normal directions aligned with through thickness (y-direction).

Tensile testing was performed by Metcut Research Associates, Inc. per American Society of Testing and Materials E-8 on small-scale dog-bone specimens having an effective gage length of 7.85 mm and average thickness of 1.67 mm. From the tube in Figure III.1.2-4, nine specimens were cut in the longitudinal (x) direction, eleven in the transverse (y) direction, and six at 45 degrees between the (x) and (y) directions; all at various locations along the length of the tube. Results for UTS and elongation are shown in Table III.1.2-1. By comparison, typical industry values for ZK60A-T5 bar in the extrusion direction are UTS = 300 MPa and elongation = 13% (averaged from various supplier data sheets).

Table III.1.2-1. Tensile Test Data for UTS and Elongation in the Longitudinal (x), Transverse (y), and 45 Degree Between (x) and (y)

Test Direction	UTS (MPa)	Elongation (%)
Longitudinal (x)	254.4	20.1
Transverse (y)	297.2	25.0
45 Degree Between (x) and (y)	279.9	21.2

Compared to industry values, UTS is 15% lower in the extrusion direction, but elongation was increased by roughly 50%. We hypothesize that the lower strengths are primarily the result of texture development, where basal slip would be aligned nearly parallel to the extrusion direction (Figure III.1.2-7) [12, 13]. Literature also suggests texture development is dominant over strengthening due to grain refinement [14, 15], which can explain the lower strength in the longitudinal direction despite a grain size of 3.8 μm. UTS is on par with industry material in the transverse and 45-degree directions, while elongation is roughly twice as high in the transverse direction. Higher strength and elongation in the transverse (i.e., y) direction compared to the longitudinal (i.e., x) direction adds further evidence that texture development is playing an important role in bulk properties. As a result, texture development in ShAPE-processed Mg alloys is being extensively studied in ongoing investigations. Additionally, specimens are being heat treated to the T5 and T6 conditions to determine if strength can be increased without sacrificing ductility in ShAPE-processed ZK60 tubing.

Technology Transfer Path

The technology transfer for this project will occur late during Phase 2. The initial phase will focus on laboratory development and understanding the Mg alloys from a mechanistic standpoint. After processing is understood, technology transfer will occur to produce and deliver tubes to Magna Cosma for evaluation.

Conclusion

There are several advantages of the ShAPE process that lend well to potential cost reduction and scale-up for industry. First, the ram force required for this study is greater than a ten time reduction from what is required for similarly sized tubing fabricated using conventional direct extrusion. This is because material flow induced by the scroll features plays an important role in feeding material into the extrusion orifice. This large reduction in force would enable substantially smaller machinery, thus lowering capital expenditure and operational costs.

An additional advantage of the ShAPE process is that frictional heat generated at the billet/die interface is the only process heat required to soften the material and maintain temperature. In short, heat is generated only where it is needed. As such, the overall energy input to the process and, therefore, cost can be greatly reduced compared to conventional heating approaches such as billet preheating or container heating.

Finally, ShAPE is a single-step process that can lead to cost reduction compared to other multi-step severe plastic deformation processes such as Equal Channel Angular Extrusion, Accumulative Roll Bonding, High-Pressure Torsion and Cyclic Extrusion Compression. In fact, the authors are exploring the possibility of going directly from a ZK60 casting to a final extruded product using the ShAPE process. In addition to these potentially significant cost and scalability advantages, the ShAPE process also holds promise for improved mechanical properties.

In this work, the ShAPE process refined the microstructure in ZK60 to an average grain diameter to 3.8 μm, while simultaneously developing texture off-axis from the extrusion direction. Longitudinal tensile specimens cut from a 50.8-mm diameter tube having a nominal wall thickness of 1.52 mm displayed an elongation of 20.1% and UTS of 254.4 MPa. Transverse tensile specimens had an elongation of 25.0% with an UTS of 297.2 MPa.

Optimization of ShAPE process variables and subsequent heat treatments may lead to further improvement in bulk mechanical properties.

III.1.3 Optimizing Heat Treatment Parameters for 3rd Generation AHSS with High Throughput In-Situ Experiments and Integrated Modeling Frameworks

Project Details

Xin Sun, Principal Investigator
Pacific Northwest National Laboratory
902 Battelle Boulevard Richland, WA 99352
Phone: 509-372-6489
E-mail: xin.sun@pnnl.gov

Emmanuel De Moor, Principal Investigator
Advanced Steel Processing and Products Research Center
Colorado School of Mines
1500 Illinois Street
Golden, CO 80401
Phone: 303-273 3624
E-mail: edemoor@mines.edu

Accomplishments

- Awarded a university fellowship to the doctoral student with the Advanced Steel Processing and Products Research Center at Colorado School of Mines who is performing research on this project.
- Acquired two commercial software packages, Thermo-Calc and MICRESS, for use on this project. The software packages allow for users to conduct predictive modeling of microstructure evolution using the most current database and simulation techniques.
- Performed high-throughput, in-situ synchrotron-based, high-energy x-ray measurement of phase transformation during inter-critical annealing (IA) experiments for 7-Mn and 10-Mn steels.
- Analyzed austenite volume fractions, lattice parameter changes during the IA treatment from the in-situ HEXRD test.
- Performed initial Thermo-Calc simulation to calculate the equilibrium austenite volume fraction at annealing temperatures and retained austenite volume fraction after cooling down to room temperature.
- Completed initial Thermo-Calc/DICTRA simulation for austenite to martensite transformation at elevated temperature.

Future Directions

- Perform dilatometry tests and compare the results with in-situ HEXRD results during IA treatment.
- Correlate the lattice strain evolution data with chemical composition changes subjected to IA thermal histories.
- Attempt calculation of thermodynamic parameters of phases present in the medium Mn steels, using the above information, through the analysis of the HEXRD data and thermodynamic calculations. These parameters include carbon (C) or Mn diffusivity in various phases and enthalpies and entropies.
- Develop a phase-field-based modeling capability to predict the volume fraction, morphology, and stability of the austenite formed during the IA process.
- Link the predicted microstructure, including the austenite volume fraction retained after cooling, stability, and morphology, to the mechanical properties.

- Optimize strength and ductility of medium Mn transformation induced plasticity (TRIP) steels by judicious IA temperature selection.

Technology Assessment

- Target: Obtain thermodynamic parameters for model predictions of transformation kinetics and microstructures of constituent phases for thermal calculation and phase field modeling.
- Gap: Links need to be developed for correlating the lattice parameters obtained from HEXRD to the chemical composition in the ferrite-like phases and austenite. The relationship between HEXRD measured transformation kinetics, dilatometric measurement, and traditional experimental heat treatment and metallography need to be correlated.

Introduction

Medium Mn TRIP steels represent potentially important products for achieving the performance requirements of third generation AHSS in efforts to lightweight vehicles for improved fuel efficiency while meeting or exceeding safety regulations.

Medium Mn steels typically contain 5 to 10 wt.% Mn and other alloying elements similar to those used in selected current AHSS grades. It is well known that the mechanical properties of these steels are extremely sensitive to chemical compositions (i.e., C and Mn content) and IA temperatures, which, in turn, determine the volume fraction and thermodynamic stability of the retained austenite (RA) in the corresponding microstructures. Given a certain microstructure of the multi-phase steel (i.e., volume fraction, morphology, and stability of the RA), our team's prior work has established an integrated experimental and computational approach linking the microstructures to the corresponding mechanical properties [16, 17].

However, traditional experimental heat treatment and characterization techniques applied in optimizing the heat treatment parameters for strength and ductility combinations are often laborious and time consuming. Complete descriptions, efficient experimental characterization techniques, and predictive capabilities and the applications of these to describe relationships between chemical compositions, initial microstructures, heat treatment parameters, and subsequent RA volume fraction, RA stability, and mechanical properties have not been established.

Approach

During this project, four focus objectives were proposed: (1) develop an in-situ characterization technique to determine the austenite formation kinetics of medium Mn TRIP steels on heating and during IA to enable the accelerated development of future third generation AHSS; (2) develop a phase-field-based modeling capability to predict the volume fraction, morphology (including grain size), and stability (i.e., C and Mn concentration) of the austenite formed during the IA process; (3) link the predicted microstructures, including the austenite volume fraction retained after cooling, stability and morphology, to the mechanical properties; and (4) optimize the strength and ductility of medium Mn TRIP steels by judicious IA temperature selection.

Results and Discussion

For the first project objective, a high throughput in situ HEXRD experimental procedure was developed to obtain the kinetics of phase transformations during heating and cooling cycles of medium 7-Mn and 10-Mn steels under different IA heat-treatment. This experiment utilized the high-energy synchrotron source at beamline 11-D-C at the Advanced Photon Source of the Argonne National Laboratory and a Linkam TS1500 heating stage (Figure III.1.3-1(a)).

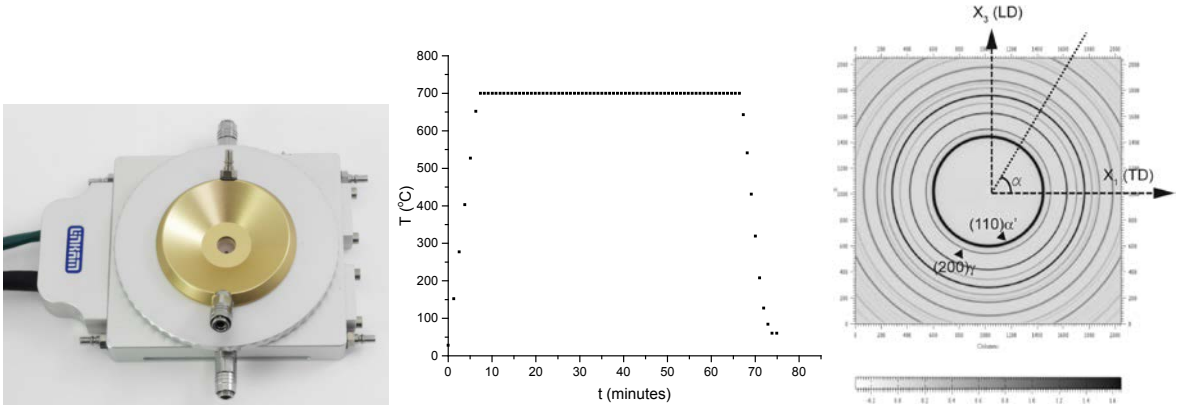

(a) Linkam TS1500 heating device (b) A typical thermal cycle (c) A typical x-ray diffraction pattern

Figure III.1.3-1. The high throughput HEXRD experiments for a 7Mn steel.

During the experiment, a small sample was placed inside the chamber of the Linkam heating device with argon as the inert gas to protect the sample from oxidation during experiments. The heating cycle consisted of heating, holding, and cooling stages. Figure III.1.3-1(b) is a typical thermal cycle, where the sample is heated at a heating rate of 200°C/second, then held at a temperature of 700°C for 1 hour, followed by cooling to room temperature at the 150°C/second cooling rate. During the thermal cycle, the synchrotron beam keeps radiating the center of the sample and the diffraction patterns are recorded at a set interval of time. The diffraction patterns are then analyzed by a fit 2D data analysis program and origin software to obtain volume fraction variation of various phases [18] with temperature and time.

The evolution of lattice parameters variation with temperature and holding time are also analyzed and shown in Figure III.1.3-2. In addition to the thermal cycle with holding temperature (T_h) of 700°C performed for the 7Mn steels, a series of similar experiments have been performed at T_h = 600, 650, 700, and 750°C for both 7Mn and 10Mn steel. The phase volume fractions and lattice parameters obtained from these experiments will be used to calibrate thermodynamic parameters (e.g., temperature-dependent C and Mn diffusivity in the various phases) and energy criteria for phase transformations. These parameters will be used in subsequent tasks of materials design; selecting the chemistry and the associated thermomechanical processes to achieve the performance requirements of the third generation AHSS.

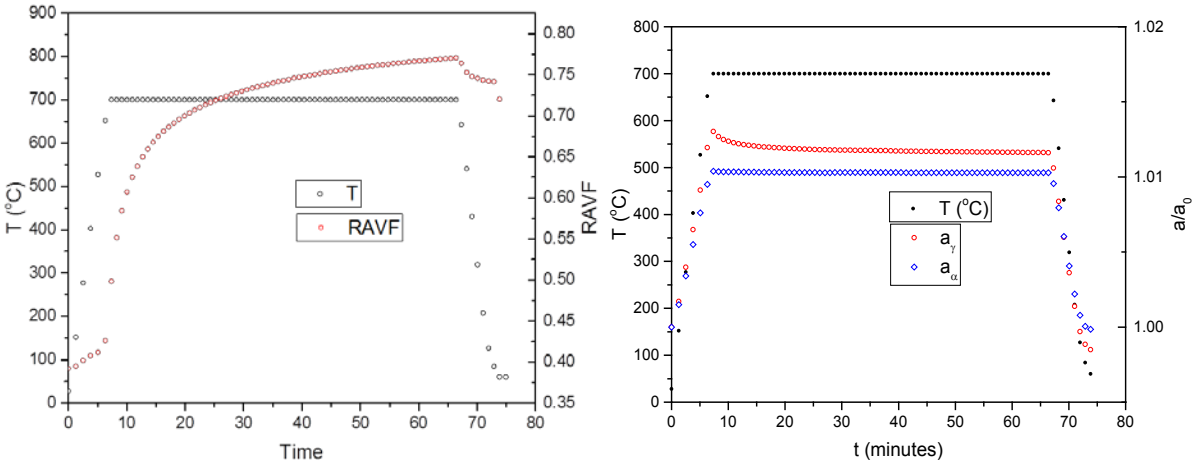

Figure III.1.3-2. The results of (a) austenite volume fraction and (b) normalized lattice parameters during the thermal cycles of a 7Mn steel.

Modeling efforts using Thermo-Calc to predict phase fractions after IA have been initiated and are currently ongoing. The model follows the procedure developed by De Moor et al. [19]. Thermo-Calc is used to calculate equilibrium phase fractions and solute concentrations within phases for various compositions and annealing temperatures. By coupling the equilibrium austenite fraction with annealing temperature and austenite

composition, the fraction of fresh martensite upon cooling can be calculated and the final equilibrium phase fraction of austenite is known. Figure III.1.3-3 illustrates simulated equilibrium phase fractions as a function of IA temperature.

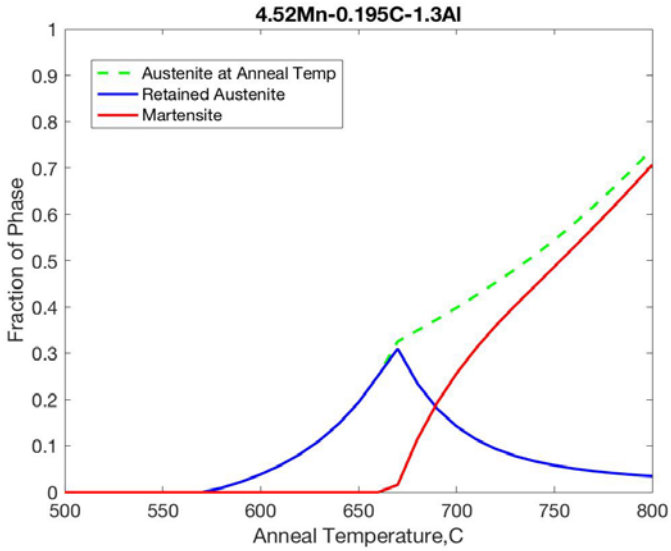

Figure III.1.3-3. Thermo-Calc simulated equilibrium phase fractions as a function of IA temperature for a 0.195C-4.52Mn-1.3Al composition.

The DICTRA module within Thermo-Calc is also being used to model the partitioning kinetics of austenite stabilizing solute during an IA process. A simulation of manganese partitioning is given in Figure III.1.3-4. An initial approach to model solute partitioning kinetics and phase boundary migration has been performed for various compositions, annealing times, and annealing temperatures. This simulation predicts concentration gradients of C and Mn and austenite growth during an IA. The initial phases intended to be present during the partitioning kinetics simulation are martensite and austenite. However, the simulations are limited by information in the Thermo-Calc databases.

The mobility of Mn in martensite has not been studied fundamentally and is not present in the Thermo-Calc mobility databases. Instead, martensite is approximated as ferrite in DICTRA simulations. It is believed that the mobility of substitutional solute varies greatly between martensite and ferrite. A recent publication comparing a DICTRA-simulated austenite-ferrite phase boundary migration to atom probe tomography data for a high-Mn steel undergoing a thermal treatment suggests that Mn mobility in martensite far exceeds that of the ferrite approximated model [20].

Additionally, other recent studies concerning austenite stabilization in medium-Mn steels via IA have found that austenite is stabilized to room temperature with shorter annealing times then predicted, suggesting that the mobility of Mn in martensite is much more rapid than in ferrite [21, 22].

While the mobility of martensite remains to be experimentally verified, the Mn mobility in the initial solute partitioning model was altered in the ferrite phase by a mobility enhancement factor available in the DICTRA module of Thermo-Calc. The model predicts the mobility of Mn impacts on austenite formation kinetics (Figure III.1.3-5).

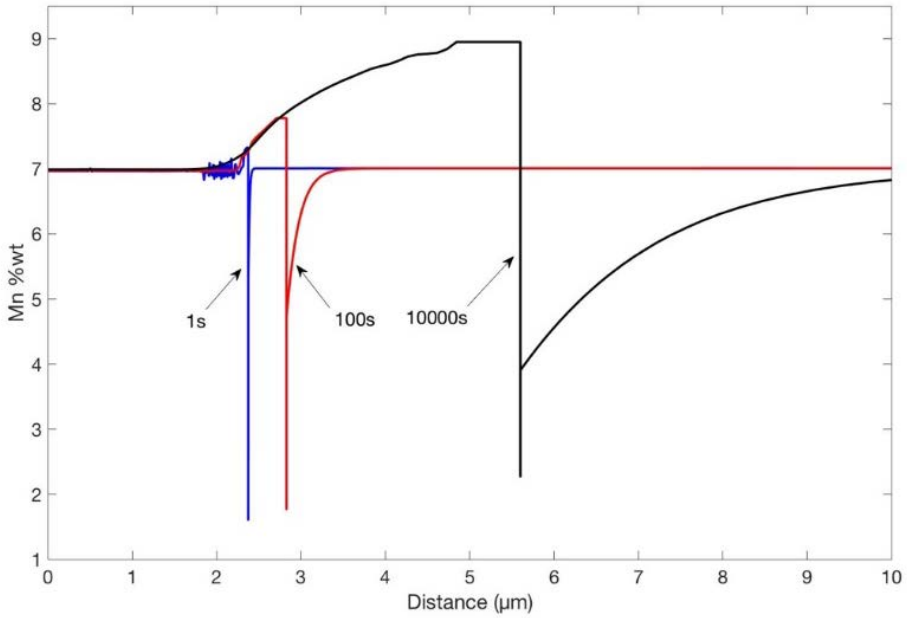

Figure III.1.3-4. DICTRA simulation of Mn partitioning during an IA at 650ºC for a 0.1C-7Mn steel. Curves correspond to different annealing times as labeled.

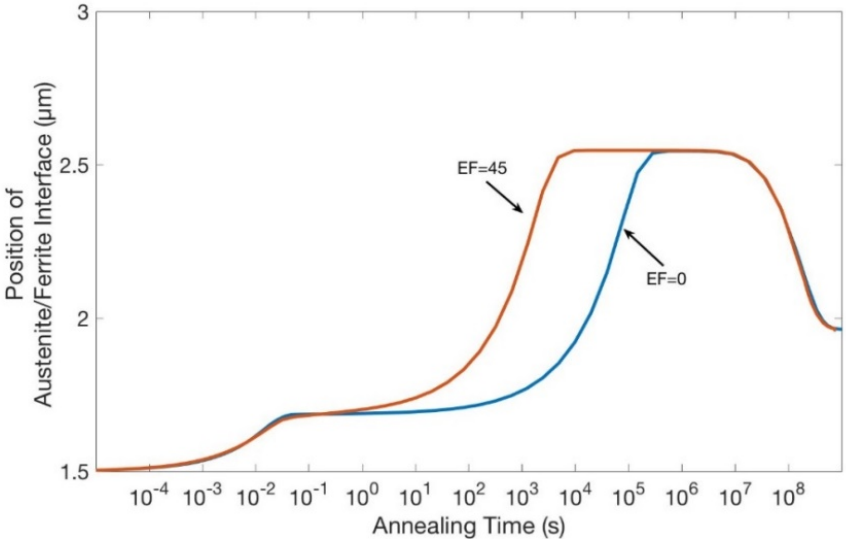

Figure III.1.3-5. DICTRA simulation of the growth of austenite with increasing annealing time for a 0.1C-7Mn steel inter-critically annealed at 650ºC EF is the mobility enhancement factor applied to manganese in ferrite.

Technology Transfer Path

The deliverables of this project will be transferred to original equipment manufacturer companies and steel producers during regularly scheduled semi-annual review meetings of the Advanced Steel Processing and Products Research Center (i.e., an industry/university cooperative research center at the Colorado School of Mines). The modeling methodology and modeling results will also be published in peer-reviewed technical journals so they are freely available to a broader engineering community.

Conclusion

Medium Mn TRIP steel was selected as model steel for development of an integrated experimental and modeling framework in optimizing heat treatment parameters for third generation AHSS. Once developed, the proposed work will not only gain predictive understanding in the phase transformation and diffusion processes during the IA process for medium Mn steels; it is also expected to provide a general capability in high-throughput characterization and prediction of evolving phase boundaries and carbon concentration gradients during other thermomechanical processes (e.g., the quenching and partitioning process).

Project Conclusions

This project is focused on research and development activities for advancing the basic mechanical properties, manufacturability, and cost of lightweight materials toward levels needed for increased implementation in automotive applications.

Highlights of these tasks and conclusion of results from the FY 2016 activities were captured in the previous sections. Ultimately, these three tasks, with unique scope and leadership, address an aspect of the materials challenges, limiting implementation of advanced high-strength steels and Mg as lightweight metals solutions for future automotive applications.

References

[1] Golovashchenko, S. F., 2008, "Quality of Trimming and its Effect on Stretch Flanging of Automotive Panels," *Journal of Materials Engineering and Performance* 17: 316-325.

[2] Le, Q. B., J. A. deVries, S. F. Golovashchenko, and J. J. F. Bonnen, 2014, "Analysis of Sheared Edge Formability of Aluminum," *Journal of Materials Processing Technology* 214: 876-891.

[3] Hu, X., K. S. Choi, X. Sun, and S. F. Golovashchenko, 2014, "Edge Fracture Prediction of Traditional and Advanced Trimming Processes for AA6111-T4 Sheets," *Journal of Manufacturing Science and Engineering* 136: 021016-1-021016-1.

[4] Lavender, C., V. Joshi, D. Paxton, S. Jana, G. Grant, D. Herling, and R. Davies, 2014, "System and Process for Formation of Extrusion Structures," U.S. Patent Application, 2014/0283574 A1.

[5] Joshi, V., S. Jana, D. Li, H. Garmestani, E. Nyberg, and C. Lavender, 2014, "High Shear Deformation to Produce High Strength and Energy Absorption in Mg Alloys," *Magnesium Technology*: 83-88.

[6] Whalen, S., S. Jana, D. Catalini, N. Overman, and J. Sharp, 2016, "Friction Consolidation Processing of n-Type Bismuth Telluride Thermoelectric Material," *Journal of Electronic Materials* 45(7): 3390-3399.

[7] McQueen, H., 2004, "Development of Dynamic Recrystallization Theory," *Materials Science and Engineering A* 387: 203-208.

[8] McQueen, H. and C. Imbert, 2004, "Dynamic Recrystallization: Plasticity Enhancing Structural Development," *Journal of Alloys and Compounds* 378(1): 35-43.

[9] Hu, H., D. Zhang, F. Pan, and M. Yang, 2008, "Analysis of the Cracks Formation on Surface of Extruded Magnesium Rod Based on Numerical Modeling and Experimental Verification," *Acta Metallurgica Sinica* 22(5): 353-364.

[10] Young, J., 2015, "The Production of Fine Grained Magnesium Alloys Through Thermomechanical Processing for the Optimization of Microstructural and Mechanical Properties," Ph.D. Thesis, Washington State University.

[11] Li, X., W. Tang, and A. Reynolds, 2013, "Material Flow and Texture in Friction Extruded Wire," *Friction Stir Welding and Processing VII*, John Wiley & Sons, Inc.: 339-347.

[12] Agnew, S., J. Horton, T. Lillo, and D. Brown, 2004, "Enhanced Ductility in Strongly Textured Magnesium Produced by Equal Channel Angular Pressing," *Scripta Materialia* 50: 377-381.

[13] Meyer, L., M. Hockauf, B. Zillmann, and I. Schneider, 2009, "Strength, Ductility and Impact Toughness of the Magnesium Alloy AZ31B After Equal-Channel Angular Pressing," *International Journal of Material Forming* 2(1): 61-64.

[14] Kim, K. and W. Kim, 2004, "Microstructural Instability and Strength of an AZ31 Mg Alloy After Severe Plastic Deformation," *Materials Science and Engineering A* 385: 300-308.

[15] Kim, W., S. Hong, Y. Kim, S. Min, H. Jeong, and J. Lee, 2003, "Texture Development and its Effects on Mechanical Properties of an AZ61 Mg Alloy Fabricated by Equal Channel Angular Pressing," *Acta Materialia* 51:3293-3307.

[16] Choi, K. S., A. Soulami, W. N. Liu, X. Sun, and M. A. Khaleel, 2010, "Influence of various material design parameters on deformation behaviors of TRIP steels," *Computational Materials Science* 50: 720-730.

[17] Choi, K. S., W. N. Liu, X. Sun, M. A. Khaleel, Y. Ren, and Y. D. Wang, 2008, "Advanced Micromechanical Model for Transformation-Induced Plasticity Steels with Application of In-Situ High-Energy X-Ray Diffraction Method," *Metallurgical and Materials Transactions A-Physical Metallurgy and Materials Science* 39A: 3089-3096.

[18] Hu, X. H., K. S. Choi, X. Sun, Y. Ren, and Y. D. Wang, 2016, "Determining individual phase flow properties in a Quench and Partitioning steel with in-situ high energy X-ray diffraction and multi-phase elasto-plastic self-consistent method," *Metallurgical and Materials Transactions A* 47, DOI:10.1007/s11661-016-3373-2.

[19] De Moor, E., D. K. Matlock, J. G. Speer, and M. J. Merwin, 2011, "Austenite stabilization through manganese enrichment," *Scripta Materialia* 64: 185-188.

[20] Dmitrieva, O., D. Ponge, G. Inden, J. Millan, P. Choi, J. Sietsma, and D. Raabe, 2011, "Chemical gradients across phase boundaries between martensite and austenite in steel studied by atom probe tomography and simulation," *Acta Materialia* 59: 364-374.

[21] Lee, S., S. J. Lee, and B. C. De Cooman, 2011, "Austenite stability of ultrafine-grained transformation-induced plasticity steel with Mn partitioning," *Scripta Materialia* 65: 225-228.

[22] De Moor, E., S. G. Kang, J. G. Speer, and D. K. Matlock, 2014, "Manganese Diffusion in Third Generation Advanced High Strength Steels," presented at *International Conference on Mining, Material and Metallurgical Engineering*.

Bibliography

Hu, X. H., K. S. Choi, X. Sun, Y. Ren, and Y. D. Wang, 2016, "Determining individual phase flow properties in a Quench and Partitioning steel with in-situ high energy X-ray diffraction and multi-phase elasto-plastic self-consistent method," *Metallurgical and Materials Transactions A* 47(12): 5733-5749, DOI:10.1007/s11661-016-3373-2.

Raghavan, K. S., X. Sun, X. Hu, K. S. Choi, and G. Cheng, 2016, "Linking Constituent Phase Properties to Edge Stretchability in Dual Phase 980 Steel," presented at *MS&T 2106 Symposium*, Salt Lake City, Utah, October 23 through 27, 2016.

Whalen, S., S. Jana, D. Catalini, N. Overman, and J. Sharp, 2016, "Friction Consolidation Processing of n-Type Bismuth Telluride Thermoelectric Material," *Journal of Electronic Materials* 45(7): 3390-3399.

III.2 Integrated Computational Materials Engineering Approach to Development of Lightweight 3GAHSS Vehicle Assembly (ICME 3GAHSS) – United States Automotive Materials Partnership, LLC

Project Details

Dr. Louis Hector, Jr., Principal Investigator
General Motors R&D Center (GM)
Mail Code 480-106-RL1
30500 Mound Road
Warren, MI 48090-9055
Phone: (586) 651-2628
e-mail: Louis.hector@gm.com

Dr. Jody Hall, Principal Investigator
Steel Market Development Institute
Vice President, Automotive Market
2000 Town Center, Suite 320
Southfield, MI 48075
Phone: (248) 945-4761
e-mail: rhall@steel.org

David Ollett, Technology Project Officer
National Energy Technology Laboratory
Department of Energy (DOE)/National Energy Technology Laboratory /PMC/VTP Division
626 Cochrans Mill Road
Pittsburgh, PA 15236-0940
Phone: 412.386.7339
e-mail: david.ollett@netl.doe.gov

William Joost, Technology Development Manager
U.S Department of Energy
1000 Independence Ave., S.W.
Washington, DC 20585
Phone: (202) 287-6020
e-mail: william.joost@ee.doe.gov

Contractor: United States Automotive Materials Partnership LLC
Contract No.: DOE DE-EE0005976

Executive Summary

The goal of the program is to successfully demonstrate the applicability of integrated computational materials engineering (ICME) for development and deployment of third generation advanced high strength steels (3GAHSS) for immediate weight reduction in passenger vehicles. The ICME approach will integrate results from well-established computational and experimental methodologies to develop a suite of material constitutive models (i.e., deformation and failure), manufacturing processes, and performance simulation modules, as well as the computational environment linking them together for both performance prediction and material optimization. The project officially started on February 1, 2013, and will be complete on January 31, 2017.

Accomplishments

3GAHSS Coupon Manufacturing

- Developed a steel nomenclature to track baseline steel and 3GAHSS process iterations.
- Completed production of Canada Centre for Mineral and Energy Technology Materials (CMAT) medium manganese (Mn) 2.2 steel, which is the final version of the first of two 3GAHSS materials created by this project.
- Produced CMAT quench and partitioning (Q&P) 2.3 coupons with properties comparable to those developed by the Colorado School of Mines (CSM) (i.e. 1,542 MPa tensile strength and 16.3% total elongation versus 1,538 MPa tensile strength and 19.2% total elongation).

Experimental

- Measured the fracture behavior of the baseline QP980 and CMAT medium Mn 2.2 steel at the Argonne National Laboratory (ANL) beamline 1 with x-ray microtomography.
- Demonstrated that austenite transformation is sensitive to the deformation mode and strain path through combined three-camera strain field measurements at AK Steel and austenite volume fraction measurements at ANL beam line 11 of the QP980 and CMAT medium Mn 2 steel on formed T-components from both materials; the results were contrasted against uniaxial tensile test results.
- Conducted high strain rate (0.5/s – 500/s) tensile measurements of the QP980 and CMAT medium Mn 2.2 steel.
- For Clemson University (CU), the following was accomplished:
  - Completed extraction of the full-forming limit curves for QP980.
  - Completed cyclic loading tests for tension/compression for QP980.
  - Measured the retained austenite volume fraction evolution with plastic strain for QP980 (in situ of tensile deformation and digital image correlation [DIC]).
  - Measured the retained austenite volume fraction evolution with plastic strain for 10% Mn steel (in situ tensile deformation and DIC).
  - Characterized the tensile flow behavior for the 10% Mn steels developed within this project (CSM/AK Steel and CMAT).
  - Characterized the initial microstructure and texture for all steels used in this project (QP980, CSM/AK Steel 10% Mn steel, and CMAT 10% Mn steel).
  - Completed a set of flow curves for QP980 at different strain rates from quasi-static to very high rate.

Computational

- Calibrated the Brown University (BU) fracture model for the baseline QP980 steel.
- Exercised the ICME model, including the T-shaped forming test.
- Calculated solute-dependent lattice constants and elasticity tensor components using an atomistic approach for bottom-centered cubic, face-centered cubic, hexagonal close-packed, and body-centered tetragonal iron and transferred the results to Ohio State University for crystal plasticity modeling.

- Applied a crystal plasticity approach that was developed and demonstrated on the baseline QP980 steel to manipulate the 3GAHSS microstructures for increased strength and ductility. The process has been applied to the CMAT Q&P 2.2 steel to determine the microstructure volume fractions needed to obtain 25% total elongation.
- Developed state variable models at Pacific Northwest National Laboratory for the baseline QP980 and CMAT medium Mn 2.2 steel.
- Developed the ability to predict phase transformations as a function of strain in a multi-phase steel, which is expected to dramatically improve the predictive capability of the 3GAHSS ICME model.

Design Optimization

- Completed the estimated joint properties milestone for all new design iterations of a chosen subassembly that is generated by employing the same joint strategy as the baseline vehicle subassembly models to enable better comparison of the material substitution effect on overall vehicle performance.
- Produced Iteration 9, which applied shape optimization and is a performance neutral side-structure design that meets stiffness targets with a mass savings of 30% and represents an 11% improvement in mass savings over the previous iteration.

Data Model

- Developed a data ontology for curating and storing experimental data and models in the National Institute of Science and Technology (NIST) dSpace ICME 3GAHSS Data Repository. Upon project completion, the data repository will be the data model deliverable.

Future Directions

- Focus in Fiscal Year (FY) 2017 on characterizing the CMAT Q&P 2.3 in order to calibrate the material models, forming model, and assembled ICME model, which will result in a material card and flow curve that will be compared against experimental work to validate the models' predictions.
- Develop and calibrate microstructure-based fracture models for both 3GAHSS materials at BU that allow future integration with the ICME model.
- Manufacture partial T components from the CMAT Q&P 2.3 steel because the blank size is too small for a full T component and, if possible, excise specimens from the T components for analysis at ANL to assess microstructure as a function of strain and strain path and to compare against model predictions to validate the material and forming models for the CMAT Q&P 2.3 steel.
- Continue to optimize the 3GAHSS side structure design, attempting to derive a crash performance-neutral design that meets both the stiffness and mass savings target.
- Update the final optimized 3GAHSS side structure design with the ICME model's validated material cards that were originally developed for the AK Steel version for the CMAT-produced versions.
- Focus on the primary project deliverables for the project ending on January 31, 2017, which are an ICME model, a user guide, and a data model, and the secondary project deliverables, which are ICME model-predicted 3GAHSS microstructures that meet the DOE Funding Opportunity Announcement (FOA) targets and an optimized 3GAHSS side structure design.

Technology Assessment

- Target: Model elements must be within 15% of experimental results and the optimized 3GAHSS assembly must achieve 35% weight savings at no more than $3.18 cost per pound of weight savings.
- Gap: An ICME framework that ties together all length-scale computer models with forming simulation, fracture modeling, and vehicle design optimization, especially with low and high-level optimization loops, does not exist. Although a linear input/output connectivity can be achieved between the length-scale material models, optimization loops will require significant coding that may be complicated by disparate codes used in the individual models.
- Gap: Boundary conditions have been applied to model elements to facilitate assembly and integration within the project's 4-year duration. For example, the number of solutes to be evaluated has been limited, inclusions and precipitates are largely ignored (although they have been measured with atom probe tomography at Pacific Northwest National Laboratory for QP980), and dislocation dynamics are superficially treated. These are all opportunities for future work and model improvement, but these boundary conditions (and dissipative processes such as friction in stamping) may adversely affect model accuracy. Friction constitutive model development should be pursued for Gen 3 steel stamping process simulations.
- Gap: The mass savings targets are aggressive. Work to date has shown that developing a 3GAHSS crash neutral design that meets the 35% mass savings target is not a challenge, but developing a design that meets both the stiffness and mass savings targets is challenging. Furthermore, optimizing a subassembly design in isolation is not a typical automotive practice where crash performance and stiffness are holistic vehicle metrics. The ability to achieve these metrics would be facilitated by whole vehicle optimization, which is outside the scope of this project. Future opportunity rests with the ability to access Government lab supercomputing resources, as was done for the side body structure optimizations in this project.
- Gap: No known material models exist for the stress/strain behavior of multi-phase microstructures with one or more metastable phases (e.g. austenite and epsilon martensite). Modeling of post-yield behavior of advanced high strength steel is a maturing science for relatively stable single and multi-phase structures. The addition of variable phase transformation in response to strain and a strain path coupled with complex deformation and hardening mechanisms (such as twinning) have not been previously modeled. Furthermore, experimental methodologies may not exist to develop sufficient constitutive information for modeling leaving an open opportunity for other length scale models as surrogates for experiments. The project will adapt the models to accommodate the gaps and document any unresolved technical gaps as opportunities for future work.
- Target: Two different 3GAHSS are defined by the FOA: (1) exceptional strength and high ductility (i.e., >1,500 MPa ultimate tensile strength, >1,200 MPa yield strength, and >25% total elongation) and (2) high strength and exceptional ductility (i.e., >1,200 MPa ultimate tensile strength, >800 MPa yield strength, and >30% total elongation).
- Gap: The ICME model will predict the microstructural constituents needed to meet the target mechanical properties; however, process development (e.g., melting, rolling, intermediate heat treatments, and finishing) may be needed to produce sheet steel with the predicted microstructure. The project will leverage the expertise of the steel industry participants to guide process development using laboratory-size heats to develop a process that can achieve the predicted microstructure.

Introduction

The goal of the program is to successfully demonstrate the applicability of ICME for development and deployment of 3GAHSS for immediate weight reduction in passenger vehicles. The ICME approach used in this project will accelerate development and widespread deployment of 3GAHSS through modeling of

multi-scale metallurgical, thermal, and mechanical processes in coil sheet development to automotive part and assembly manufacturing and, ultimately, vehicle performance. By integrating a suite of comprehensive, science-based, computational models at different length scales in the ICME environment, this project will demonstrate to end users in both the automotive and steel industries that immediate cost-effective weight savings can be achieved with 3GAHSS, and the ICME framework will support a reduced development-to-deployment lead time in all lightweight materials systems. The product of this proposed effort will be a simulation toolset and computational infrastructure composed of material models and associated validation data at different length scales, along with the software and application programming interfaces developed by the project team.

The project faces three distinct challenges: (1) to develop an ICME model, (2) to develop viable 3GAHSS sheet, and (3) to optimize an automotive design concept for a material that does not yet exist. Figure III.2-1 illustrates the relative values and Table III.2-1 provides the target mechanical properties for the two DOE-proposed grades. Neither of two proposed grades exist in the commercial domain; therefore, they were unavailable to provide the constitutive material properties information needed for effective modeling.

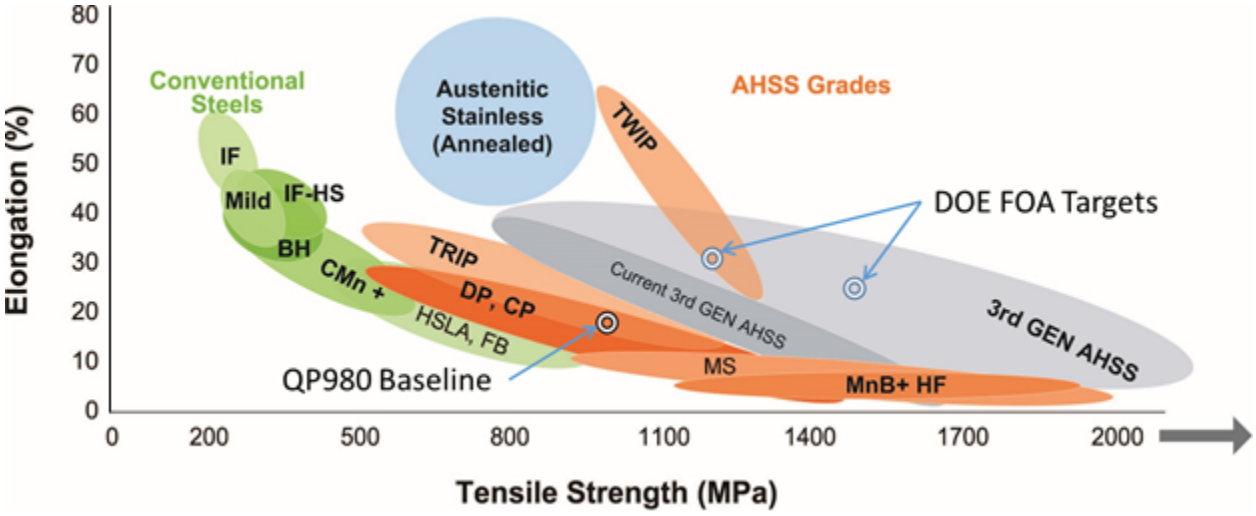

Figure III.2-1. 3GAHSS mechanical properties with baseline QP980 steel and DOE FOA 3GAHSS targets.

Table III.2-1. 3GAHSS Types Specified in FOA

Ferrous Sheet Metal Type	Yield Strength (MPa)	Tensile Strength (MPa)	Total Elongation (Uniaxial Strain to Failure)	Uniform Elongation
High Strength, Exceptional Elongation	≥800	≥1,200	≥30%	≥20%
Exceptional Strength, High Ductility	≥1,200	≥1,500	≥25%	≥8%

A baseline subassembly from a 2008 model year original equipment manufacturer production vehicle was identified to demonstrate the potential benefits of the 3GAHSS in reducing automotive component and assembly weight. The baseline assembly was fully characterized in terms of assembled components, performance, and individual component weight and cost. An iterative design optimization process of gauge and shape optimization has been applied to the baseline assembly, substituting 3GAHSS for advanced high strength steel and developing 3GAHSS designs that can meet the proposed mass savings target listed in Table III.2-2. Forming modeling and simulation, fracture modeling and simulation, and technical cost modeling are coupled with design optimization to assess the manufacturability, performance, and cost of the different design iterations with a goal of achieving the cost target listed in Table III.2-2 and without compromising component and assembly performance.

Table III.2-2. DOE FOA Weight and Cost Targets

Vehicle System	System Definition	Weight Reduction Target (%)	Cost per Pound of Weight Saved ($/lb. saved)
Body	Body-in-white, closures, windows, fenders, and bumpers	≥35	≤3.18

Integrating the material, forming, fracture, and cost models with design optimization will span the entire length of the program. The primary project deliverable includes an ICME model, user guide to enable users to run the model, and a data model. The objective is to create an ICME model that is capable of predicting part and assembly properties from the sheet properties and process history within 15% accuracy at all length scales that will enable the baseline structure to meet the specified weight and cost targets.

The challenges of this program require significant academic and cross-industry expertise and regular communication and collaboration between these parties to make the integration component of the project successful. The project is highly leveraged, with expertise from participants shown in Table III.2-3 supporting the entire life cycle of material, process, and product development. Prior collaboration between these project participants through the United States Automotive Materials Partnership and the Auto/Steel Partnership provides a unique and successful foundation for addressing the technical challenges of this program.

Table III.2-3. Project Participants

Universities/National Laboratories	Industry	Consortiums
BU	FCA US LLC	Auto/Steel Partnership
CU	Ford Motor Company	United States Automotive
CSM	GM	Material Partnership
Pacific Northwest National Laboratory	ArcelorMittal	
Ohio State University	AK Steel Corporation	
University of Illinois Urbana-Champagne	Nucor Steel Corporation	
	U.S. Steel	

Approach

The approach used in this project will accelerate development and widespread deployment of 3GAHSS through modeling of multi-scale metallurgical, thermal, and mechanical processes from sheet metal development to automotive part manufacturing and, ultimately, assembly into vehicle performance. An ICME approach will integrate results from well-established computational and experimental methodologies to develop a suite of material constitutive models (i.e., deformation and failure), manufacturing processes, and performance simulation modules, as well as the computational environment linking them together for both performance prediction and material optimization.

The project has been structured with seven tasks as follows:

- Task 1: Project Management and Planning
- Task 2: Model Development and Model-Level Validation
- Task 3: Forming: Component-Scale Performance Prediction and Validation
- Task 4: Assembly
- Task 5: Design Optimization
- Task 6: Integration
- Task 7: Technical Cost Modeling.

The development, calibration, and validation of an ICME 3GAHSS Model is a simultaneous six-stage process that is as follows:

1. The first stage is calibration and assembly of material and forming models based on a baseline steel with mechanical properties close to that of 3GAHSS. This project selected QP980 as the baseline steel, which has properties just outside the tensile strength/elongation space that defines 3GAHSS (refer back to Figure III.2-1).
2. The second stage was to produce steels with mechanical properties that meet the definition of 3GAHSS in order to further develop and calibrate the material and forming models for 3GAHSS.
3. The third stage was to calibrate material and forming models for 3GAHSS and assemble them into a rudimentary ICME model. This work is complete for the baseline QP980 and CMAT medium Mn 2.2 steels; however, work continues for the CMAT Q&P 2.3 steel.
4. The fourth stage was to use the ICME model to predict the microstructures needed for two 3GAHSS steels specified in the DOE FOA: (1) an exceptional strength, high ductility steel (i.e., 1,500 MPa tensile strength and 25% total elongation) and (2) a high strength, exceptional ductility steel (i.e., 1,200 MPa tensile strength and 30% total elongation).
5. The fifth stage was to validate the ICME model by producing 3GAHSS steels according to model predictions. However, steel process development time and the cost for obtaining steels with the predicted microstructures were prohibitive; therefore, this stage was cancelled. Fortunately, the recipes developed for the 3GHASS steels used for model development and calibration had properties at or close to the target 3GAHSS properties, enabling the project to have confidence in the eventual ICME model predictions.
6. The sixth stage was for the project to demonstrate the mass savings potential of the 3GAHSS by optimizing the design of a minimum of four advanced high-strength steel components in a 2006 model year or later as a baseline assembly. The optimized design must achieve a 35% or greater mass savings at no more than $3.18 per pound weight saved. This project selected the side-structure from a 2008 model year production vehicle as the baseline assembly.

Results and Discussion

To enable the reader to put into context the FY 2016 project results, the discussion will include work summaries from prior years. Because of the complex inter-relations between the tasks and models, the discussion will follow the project task outline, minus Project Management and Planning.

Model Development and Model-Level Validation

As discussed in the introduction, the project needed constitutive material property information to develop 3GAHSS material models. Because no commercial 3GHASS were available, the project selected QP980 as the baseline material, which had mechanical properties on the cusp of 3GAHSS. The QP980 steel, with its mixed ferrite, martensite, and metastable retained austenite microstructure, facilitated identification of relevant constitutive parameters for each length scale material model, provided a means for validating these models, and helped define the microstructural elements that will be needed for 3GAHSS. However, additional steels, with mechanical properties within the tensile strength/elongation space, were needed to calibrate the developed models for 3GAHSS.

Using prior literature studies, CSM identified two pathways (i.e., a Q&P process and a transformation-induced plasticity process) that were expected to produce 3GAHSS with the mechanical properties of specified DOE FOA 3GAHSS steels (refer back to Table III.2-1). AK Steel produced small volume heats from those recipes, resulting in two 3GAHSS grades with properties at or near the DOE targets. Unfortunately, the AK Steel heats were limited in terms of strip width and amount. The project then contracted CMAT, who had the capability to make wider strip widths sufficient for more comprehensive characterization and for forming/stamping small components. CMAT successfully cast, hot rolled, and cold rolled the two recipes received from CSM and validated by AK Steel. The mechanical properties were similar, but slightly different, between those made at CMAT and those made at AK Steel; however, all were definitively within the tensile strength and elongation

space that defines 3GAHSS (see Figure III.2-2 and Table III.2-4). This accomplishment showed that the 3GAHSS recipes were scalable from AK Steel's 50 lb. heats to CMAT's 450-lb heats. Furthermore, CMAT's processing equipment was closer to production equipment, suggesting the potential that these alloys could be manufactured on a commercial scale.

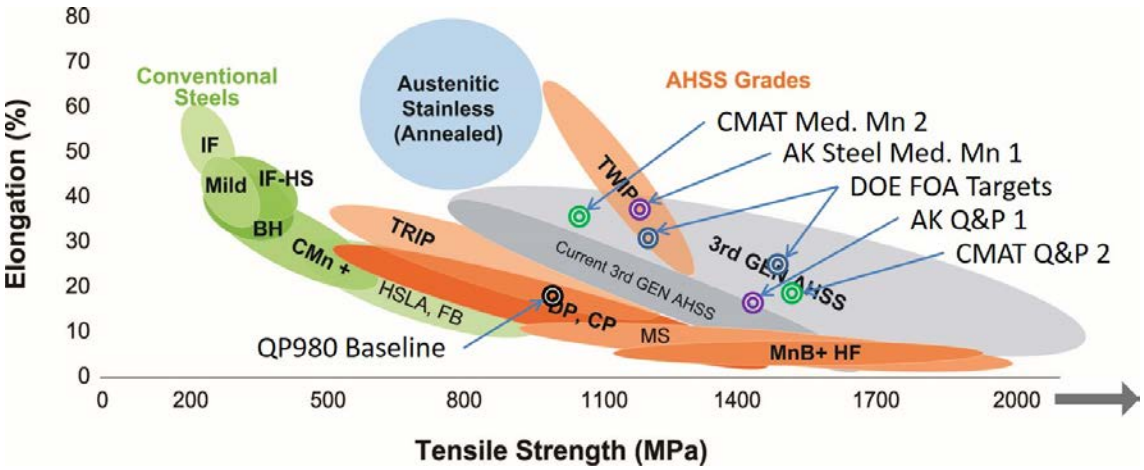

Figure III.2-2. 3GAHSS mechanical properties with baseline QP980 steel and DOE FOA 3GAHSS targets.

Table III.2-4. Summary of AK Steel and CMAT 3GAHSS Mechanical Properties

Steel Alloy	Yield Strength MPa	Ultimate Tensile Strength (MPa)	Tensile Elongation	Uniform Elongation
High Strength, Exceptional Ductility	≥800	≥1,200	≥30%	≥20%
AK Steel Medium Mn 1	750	1,200	37%	34
CMAT Medium Mn 2	693	1,042	35%	
Exceptional Strength, High Ductility	≥1200	≥1,500	≥25%	≥8%
AK Steel Q&P 1	830	1,432	17%	
CMAT Q&P 2	1,218	1,538	19%	15%
	Color Code	Target	Below target	Met target

During FY 2016, the project completed production of the CMAT medium Mn 2.2 blanks. Production of the CMAT Q&P 2 steel, which is the final version of the second of two 3GAHSS materials created by this project, was delayed because CMAT had inadequate heat treat equipment to quench and temper the steel and the CSM salt bath process was restricted to small coupon sizes. McMaster University was contracted to develop a Q&P process using an annealing simulator, which is capable of producing larger coupons (i.e., 120 mm x 200 mm) sufficient for more comprehensive material characterization and forming of T components. After a couple of process development iterations, the team successfully developed the similar annealing process to obtain the mechanical properties like those produced by AK Steel and CSM. McMaster University delivered 103 CMAT Q&P 2.3 blanks, which were distributed to GM for characterization and AK Steel for T component manufacturing.

Because of the number of process iterations needed to produce 3GAHSS, a steel nomenclature to track baseline steel and 3GAHSS process iterations was developed as shown in Table III.2-5.

Table III.2-5. Steel Nomenclature

Material	Rolling Mill	Heat Treater	Sequence	Material Designation
AK Steel				
10% Mn TRIP Steel	AK Steel	AK Steel	Hydrogen Annealed	AK Steel Medium Mn 1.1
	AK Steel	AK Steel	Nitrogen Annealed	AK Steel Medium Mn 1.2
	AK Steel	CSM	Nitrogen Annealed	AK Steel Medium Mn 1.3
3% Mn Q&P Steel	AK Steel	AK Steel		AK Steel Q&P 1.1
	AK Steel	CSM		AK Steel Q&P 1.2
CANMETMaterials				
10% Mn TRIP Steel	CMAT	CMAT	Phase 1	CMAT Medium Mn 2.1
	CMAT	CMAT	Phase 2	CMAT Medium Mn 2.2
3% Mn Q&P Steel	CMAT	CSM	Phase 1	CMAT Q&P 2.1
	CMAT	CSM	Phase 2	CMAT Q&P 2.2
	CMAT	McMaster University	Phase 2	CMAT Q&P 2.3

Early work at BU using micro-pillar compression and electron backscatter detection testing of the baseline QP980 and AK Steel produced 3GAHSS (AK Steel medium Mn 1.3 and AK Steel Q&P 1.2) enabled Ohio State University to develop three-dimensional representative volume elements (3DRVEs). Initial 3DRVEs were developed for the baseline steel and later for the AK Steel medium Mn 1.3 and the CMAT medium Mn 2.3. Efforts continued on the 3DRVEs for the CMAT Q&P 2.3. The 3DRVEs are expected to improve the accuracy of the crystal plasticity model and eventual ICME model by enabling the models to accommodate process-induced anisotropy.

CU performed the majority of the baseline and 3GAHSS materials characterization. This included uniaxial tension with DIC, rapid strain rate testing at NIST, and biaxial testing. Interspersed with the CU-derived data were results from GM, AK Steel, CMAT, and BU. During FY 2015 and FY 2016, Pacific Northwest National Laboratory, CU, and GM have collaborated to combine DIC with high-energy x-ray diffraction testing to measure the in situ transformation of retained austenite to martensite as a function of strain for three materials: (1) QP980, (2) CMAT medium Mn 2, and (3) CMAT Q&P 2. The ability to predict phase transformations as a function of strain in a multi-phase steel is a first and is expected to dramatically improve the predictive capability of the eventual 3GAHSS ICME model.

The data derived from experimentation were used to refine and calibrate the material models (i.e., the crystal plasticity model and state variable model). In the first couple of years of this project, Ohio State University and Pacific Northwest National Laboratory developed and calibrated their crystal plasticity and state variable models, respectively, for the baseline QP980 steel. Separate cards were developed to include phase transformation and strain rate dependency. In FY 2016, the models have expanded to include the CMAT medium Mn 2.2 steels. Only one material card has been developed for this steel, which includes phase transformation. The material cards for both materials have strong agreement with experimental test data.

Figure III.2-3 shows both the crystal plasticity model prediction for the material stress-strain curve (red) with experimental tensile test results (black) for the CMAT Q&P 2 steel. Figure III.2-4 provides the composite representative volume element model (labeled RVE1) for this steel with the phase volume fractions listed in Table III.2-5. There is general agreement between the model and experimental results with respect to the yield, ultimate tensile strengths and work hardening behavior. Disparities at the high strains are due to the absence of a fracture constitutive model in the simulation.

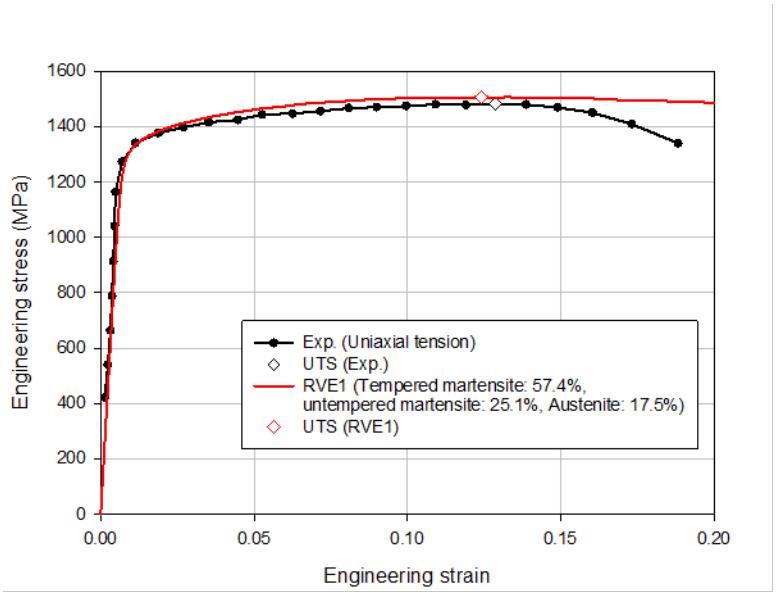

Figure III.2-3. Simulated Stress-Strain Curve (RVE1) versus experimental test results (Exp.) for the CMAT Q&P 2 steel.

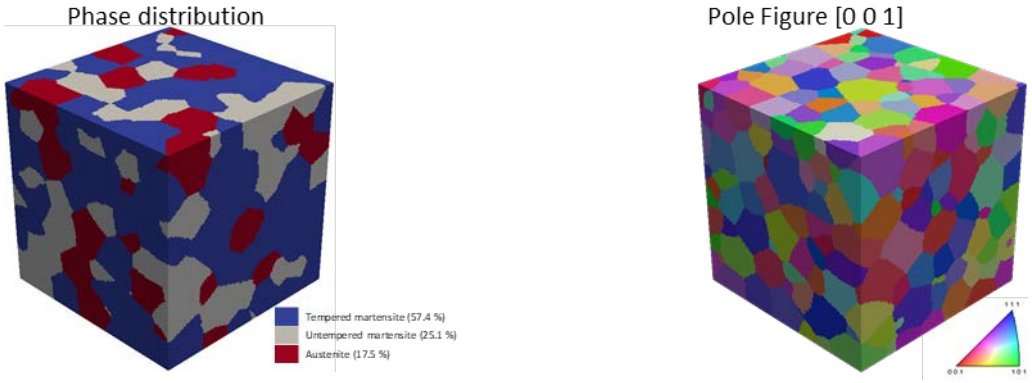

Figure III.2-4. 3-D representative volume element for the CMAT Q&P 2 steel (RVE1).

Table III.2-6. Volume Phase Fractions for the CMAT Q&P 2 and a Hypothetical Q&P Steels

Phase	Actual RVE for CMAT Q&P 2 Steel (see Figure III.2-4, RVE1)	RVE for a hypothetical Q&P steel (see Figure III.2-6, RVE2)
Tempered Martensite (α'_1)	57.4%	63.3%
Untempered Martensite (α'_2)	25.1%	19.0%
Retained Austenite (γ)	17.5%	17.7%

Taking the model a step further, a fictional hypothetical Q&P microstructure is postulated (labeled RVE2) with phase volume fractions shown in the third column to the right of Table III.2-4. The amount of tempered martensite is increased by approximately 6% with a corresponding decrease in untempered martensite and a marginal impact on the percentage of retained austenite. The model then simulates the expected stress-strain curve for this steel, which is shown in Figure III.2-5 (dashed blue curve) as contrasted against the actual simulated and experimental stress-strain curve for the CMAT Q&P 2 steel. The result is a predicted decrease in ultimate tensile strength with minimal impact on yield strength as a result of increasing the volume fraction of tempered martensite and corresponding decrease in untempered martensite. The composite representative volume element for the fictional Q&P steel is shown in Figure III.2-6. This demonstrates one of the foundational aspects of ICME which is generate hypothetical microstructures which can then be tested with the ICME model/process from simulation of coupon level experiments to simulation of forming to simulation of

vehicle performance. Many additional such hypothetical microstructures can be generated and tested and hence the RVE2 microstructure is by no means definitive.

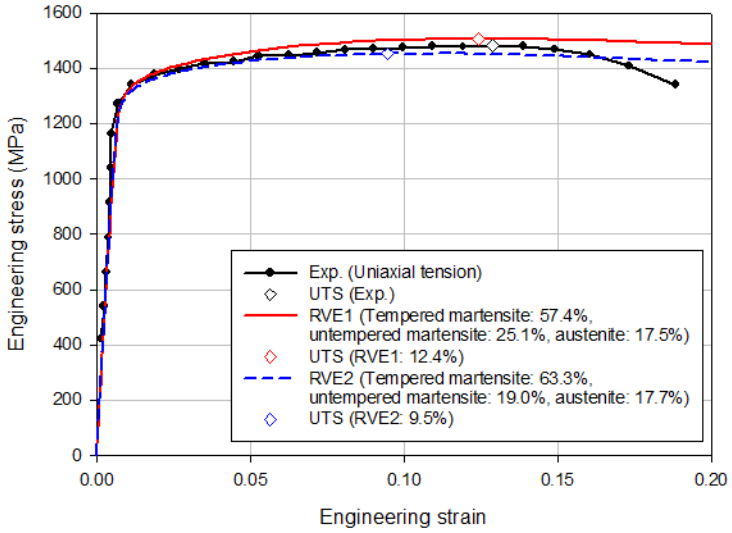

Figure III.2-5. Simulated Stress-Strain Curves of the hypothetical Q&P steel (RVE2) versus contrasted against the actual Q&P 2 steel simulated (RVE1) and experimental (Exp.) stress-strain curves.

Figure III.2-6. Hypothetical 3-D representative volume element for a hypothetical Q&P steel (RVE2).

Unlike the CMAT Q&P 2 steel, the CMAT Medium Mn 2 steel is more difficult to model and similar results shown for the Q&P steel were not available at the time of this report. The CMAT medium Mn 2.2 steel exhibits very complex inhomogeneous plasticity and phase transformation. Uniaxial tensile testing coupled with DIC at CU and at the ANL beamline have shown that retained austenite transforms as a function of strain. Furthermore, electron backscatter detection testing at BU and CU have shown the emergence of epsilon martensite as a transition phase from martensite to pre-tempered martensite. Complicating this is the observation of some twinning. The team concluded that additional work is needed to fully understand the deformation behavior of this steel in order to develop more accurate models.

Forming: Component-Scale Performance Prediction and Validation

Task 3 for forming began in FY 2014. The primary goal was to identify and develop a 3GAHSS forming simulation that would enable validation of the assembled material models. The assembled material model outputs are a flow curve and material card for each 3GAHSS material. Therefore, the forming model would have to be able to predict both the mechanical properties and microstructure of a formed component. The team then focused on identifying a component that would best represent an automotive component and be sufficiently complex to accommodate both linear and nonlinear strain paths. The team developed a

T component design with features similar to that of a B-pillar, which was fully inclusive of all expected forming scenarios (e.g., stretch, bending, stretch-bending, and biaxial stretch) (see Figure III.2-7).

Figure III.2-7. CMAT medium Mn 2.2 T component.

In FY 2015, the team designed and built a T component die and installed it at AK Steel in Dearborn, Michigan. AK Steel first ran T component forming simulations for both the baseline QP980 and medium Mn 2.2 steel to develop blank designs that would produce good parts (i.e., parts that met all dimensional requirements without cracks) and bad parts (i.e., parts designed to crack in a specific area). AK Steel then produced T components from both steels and confirmed that the forming model accurately predicted (1) part dimensions, (2) part thinning, and (3) part failure.

In FY 2016, the project excised coupons from regions of interest (i.e., regions of varying strain and strain path). The coupons were tested at CU using electron backscatter detection and at ANL's beamline using x-ray microtomography to determine the volume fractions of the microstructural constituents, including retained austenite. The results were compared and contrasted against the uniaxial tensile test results, which showed that the amount of retained austenite is dependent on strain and strain path.

T components for the second 3GAHSS, CMAT Q&P 2.3, were not produced due to delays in getting blanks. The team expects to make CMAT Q&P 2.3 T components and conduct similar testing of these T components to verify material and forming model predictions.

Assembly

The crystal plasticity model and state variable model were originally ABAQUS-based User Material Subroutine (called UMAT) solid finite element material models. In cooperation with Livermore Software Technology Corporation, the models were translated into LS-DYNA in preparation for assembly in Task 4. The state variable model was a finite element-based model that was originally constructed for solid elements. To enable the model's use in performance modeling, the team adapted the model for shell elements.

Toward the end of FY 2014, Livermore Software Technology Corporation began the process of assembling the material models using a standalone design optimization and probabilistic analysis package with interface to LS-DYNA called LS-OPT. This software system is capable of integrating computer models. The assembled material models have generated forming curves and material cards for both materials, which were passed on to the Task 3, Forming, and the Task 5, Design Optimization, teams. The assembled material models were then coupled with the forming model, resulting in a preliminary ICME model. The model was calibrated for the baseline steel and the CMAT medium Mn 2.2 steel and verified by use of T component testing. The Task 4 team will calibrate the model to the CMAT Q&P 2.3 steel and validate the model if time allows through T component production, testing, and analysis.

Design Optimization

Under Task 5, Engineering + Design AG Inc. and the Auto/Steel Partnership identified the 2008 model year side-structure subassembly from a production original equipment manufacturer donor vehicle as the baseline assembly for demonstrating the potential of 3GAHSS materials to lightweight automotive components and assemblies without compromising vehicle performance. To eliminate joining as a variable in design optimization, the team decided to apply spot welding with a 25-mm pitch for both the baseline and 3GAHSS designs. During the second fiscal year of the project, the Task 5 team defined the load cases for the side structure and assessed the performance of the side structure against the defined load cases.

The Task 5 team began preparations for design optimization by conducting a sensitivity analysis to determine each individual side structure component's contribution to assembly stiffness. This analysis assisted the design team in identifying those components that can be reduced in gauge and those that might need to be increased in gauge to facilitate gauge reduction in other components. Upon completion of the sensitivity analysis, the team began substituting the two 3GAHSS materials into the side-structure assembly.

During the third fiscal year, Engineering + Design AG Inc. generated a 3GAHSS design, labeled "Iteration 3," that had the same crash performance as the baseline design, but it achieved a 35.8% mass savings (i.e., exceeding the FOA target) with an approximately 10% and 20% reduction in torsional and bending stiffness, respectively. During FY 2016, the team produced several additional iterations. For Iteration 7, a crash neutral design was developed using gauge reduction and joint and component reduction that met the stiffness requirements but achieved a 19% mass savings. This is still an impressive achievement; however, it is far short of the DOE target. Subsequent iterations applied shape optimization to the Iteration 7 design, with the objective of maintaining crash performance and stiffness while recovering mass savings. The last iteration to be developed was Iteration 9, which achieved a 30% mass savings by expanding the side structure to include the rear rail and wheel arch assembly. Figure III.2-8 shows the results of the last three design iterations for the original 3GAHSS structure and the 3GAHSS structure including the rear rail and wheel arch.

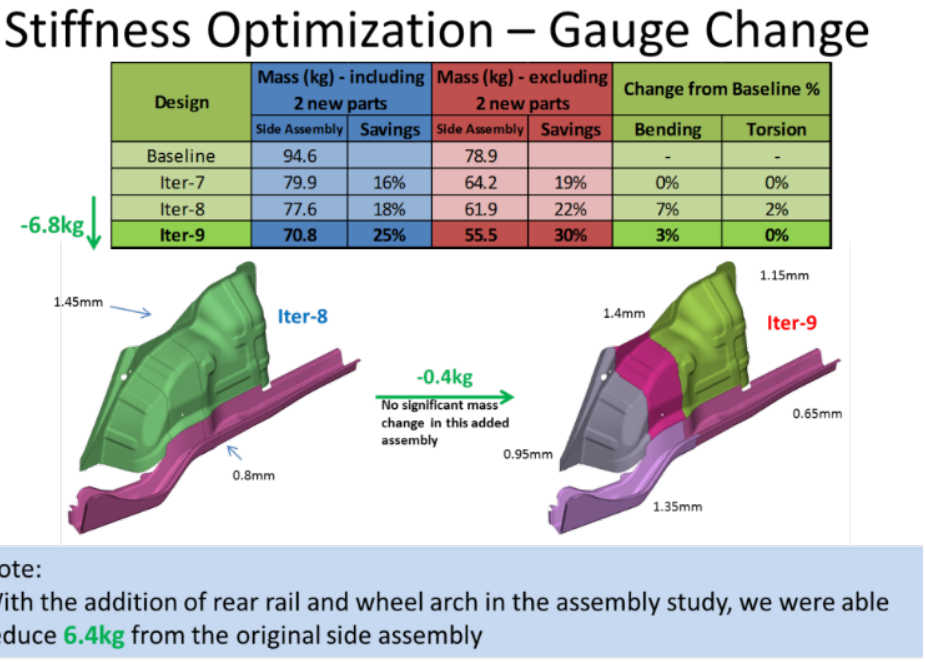

Figure III.2-8. Side structure design Iterations 7 through 9.

Work continues on optimization of the 3GAHSS side structure. The team was approved to use the National Renewable Energy Laboratories high-performance computational center to do the next optimization run, which hopefully will enable a converged design solution that meets the DOE targets. Use of the National Renewable Energy Laboratory's high performance computation center is expected to facilitate a converged design solution

that meets all crash performance and stiffness targets with maximum weight savings. However, the team does not expect to be able to produce a converged crash neutral design solution that meets both the stiffness requirements and mass savings target without expanding the target assembly to include other body-in-white components. This is outside the scope of the project; therefore, it is expected that mass savings will be between 25 and 35%. Meanwhile, as shown in Figure III.2-9, the current Iteration 9 design performs better than the baseline design with a respectable 30% mass savings.

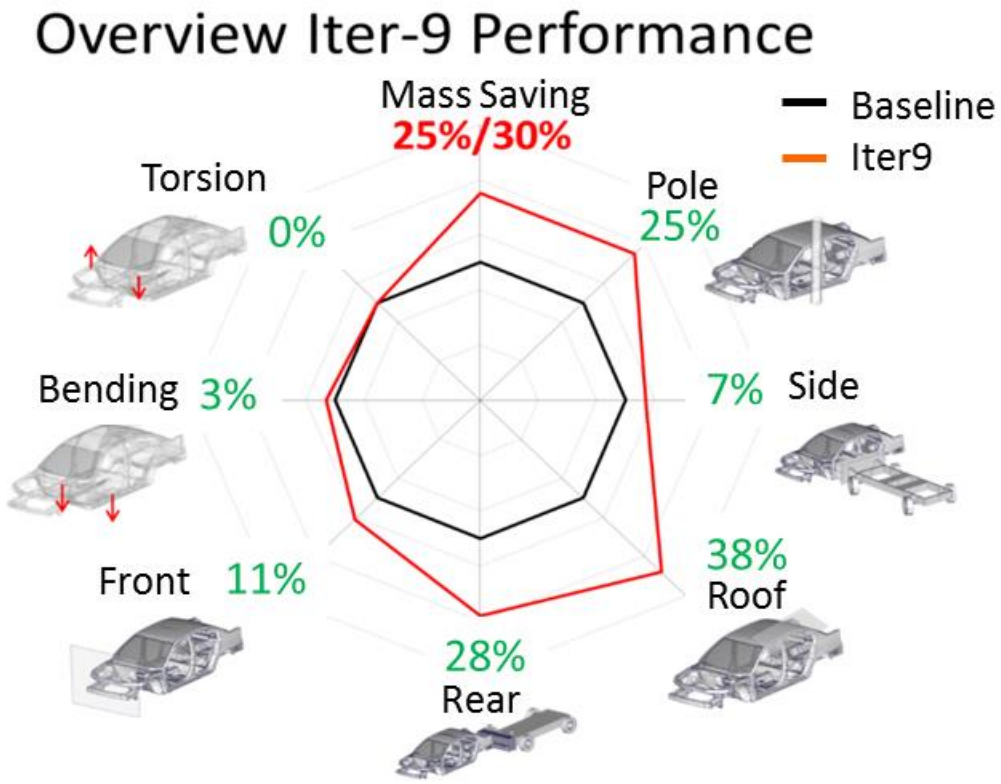

Figure III.2-9. Overview of Iteration 9 performance.

Integration

During FY 2015, the United States Automotive Materials Partnership signed a cooperative research and development agreement with the NIST to utilize the NIST dSpace data repository for curating and storage of project data. The project intends for this repository, which will be made public after project completion, to be the "ICME material database;" this is a primary project deliverable specified in the FOA. This fiscal year, the project defined an ontology and facilitated entry of project data from sub-recipients. By project close, the data repository will be populated with all project data and models accumulated and developed over the 4-year project duration.

Technical Cost Modeling

During the second fiscal year, the Task 7 team developed a technical cost model and applied it to the baseline assembly. Once a final 3GAHSS side structure design is produced during Task 5, the Task 7 team will apply the technical cost model and determine if the costs meet the DOE FOA requirements of less than $3.18 per pound of weight saved.

Technology Transfer Path

The primary deliverable of this program is an integrated computer model with a user guide. The software will include a high-level description of the integrated models, along with a description of input variables, output variables, state variables, and relational databases implemented within the final software deliverable. The user's manual will provide an overall description of the user implementation approach for the software.

During development of the ICME model, the project will be developing test methodologies for evaluating and characterizing 3GAHSS (e.g., nano-hardness testing, micro-pillar, bulge testing, sheet tension-compression, and measurement of austenite-to-martensite transformation with strain). If the results from these tests can be correlated to macroscopic bulk materials properties testing, then these tests are expected to be adopted for future work and, potentially, for industry standardization.

Additionally, if the individual length-scale material models show a high degree of accuracy, then these models will be adopted by industry and academia for expansion and refinement to cover additional steel processing paths. Primary users of the technology are the partners that are engaged in this project, which is expected to speed implementation of results and lessons learned.

Conclusion

The project is on schedule to meet all project milestones and deliverables by the completion date. The project team expects to deliver the primary deliverables (i.e., the ICME model, user guide, and data model). However, the team does not expect to meet all project metrics with respect to the secondary project deliverables. There are concerns that the mass savings target will not be fully met with the optimized 3GAHSS side structure design and the fracture models will not be able to be integrated into the ICME model by the project end date. Additionally, the project has insufficient resources and time to manufacture 3GAHSS heats to verify ICME model predictions for both DOE FOA target steels.

Still, the project has several notable achievements of which only a few are discussed in this report. The project successfully created two 3GAHSS materials with properties at or close to the DOE FOA targets. 3DRVEs were created for these materials to improve crystal plasticity model predictions. New test methodologies were applied to both coupons and components to measure microstructural volume fractions in complex multi-phase steels with meta-stable austenite. A pseudo automotive component was developed, tooling was manufactured, and parts made to validate material and forming model simulations for multiple strain paths. Less tangible but essential to the project's success has been significant communication and collaboration between project participants.

Work during the remaining 4 months of the project targets completion for (1) characterization of the CMAT Q&P 2.3 steel, (2) the manufacturing of T components from the CMAT Q&P 2.3 steel, (3) calibration of the material, forming, and ICME models for the CMAT Q&P 2.3 steel, and (4) completion of all of the following remaining milestones:

- Milestone #5: 3GAHSS Forming Model
- Milestone #8: Optimized Design
- Milestone #9: ICME Model and User Guide
- Milestone #10: Data Model
- Milestone #11: Technical Cost Model.

The project was targeted to end on January 31, 2017 but was granted a no cost extension to March 31, 2017. The ICME model is essentially complete, with work focused on developing the user guide. the data model is the ICME 3GAHSS NIST dSpace Data Repository, which will be updated with all experimental data and computational models. The last design optimization iteration 3GAHSS side structure is expected with the work

at the National Renewable Energy Laboratory and will be complete with application of the CMAT-produced 3GAHSS material cards.

Bibliography

Cheng, G., K. S. Choi, X. Hu, and X. Sun, 2016, "Determining Individual Phase Properties of a Multi-Phase Q&P Steel Using Multi-Scale Indentation Tests," *Materials Science and Engineering A*: 384-395.

Fellinger, M., 2016, "First Principles Calculations of Lattice Parameters and Elastic Constants of Fe Phases Containing Solutes," presented at the at the *2016 TMS Annual Meeting.*

Fellinger, M. A., L. Hector, Jr., and D. R. Trinkle, 2016, "Ab Initio Calculations of the Lattice Parameter and Elastic Stiffness Coefficients of bcc Fe with Solutes," *Computational Materials Science*.

Hector, Jr., Lou, 2015, "Integrated Computational Materials Engineering (ICME) Approach to Development of Lightweight 3GAHSS Vehicle Assembly," Auto/Steel Partnership Technology Day, Livonia, Michigan, October 2015.

Hu, X., K. S. Choi, X. Sun, Y. Ren, and Y. D. Wang, 2015, "Determining Individual Phase Flow Properties in a Quench and Partitioning Steel with In-Situ High Energy X-Ray Diffraction and Multi-Phase Elasto-Plastic Self-Consistent Method," *Materials and Metallurgical Transaction A*.

Poling, W. A., V. Savic, L. G. Hector, A. K. Sachdev, X. H. Hu, A. Devaraj, X. Sun, and Abu-Farha, 2016, "Combined Synchrotron X-ray Diffraction and Digital Image Correlation Technique for Measurement of Austenite Transformation with Strain in TRIP-assisted Steels," Society of Automotive Engineering Technical Paper.

Rana, R., E. De Moor, J. G. Speer, and D. K. Matlock, 2016, "Microstructures and Properties of Medium Manganese Sheet Steels - Strategies and Opportunities," presentation for *Shaping, Forming, and Modeling of Advanced High Strength Steels Symposium,* held as part of MS&T 2015.

Singh, H., V. Savic, and H. Ezzat, 2016, "Design Optimization with 3rd Generation AHSS. Validation Phase of: Integrated Computational Materials Engineering Approach to Development of Lightweight 3GAHSS Vehicle Assembly (ICME 3GAHSS)," presented at the *2016 Great Designs in Steel*.

Wang, Y., 2016, "Investigation of AHSS Formability Using a Customized T-Shaped Panel with ex-situ DIC," Presented at the *2016 Great Designs in Steel.*

III.3 Industrial Scale-Up of Low-Cost Zero Emmissions Magnesium by Electroylsis — Infinium, Inc.

Project Details

Adam C. Powell, IV, Principal Investigator
INFINIUM, Inc.
3 Huron Drive
Natick, MA 01760
Phone: 781-898-3430
E-mail: apowell@infiniummetals.com

Aaron Yocum, Program Officer
National Energy Technology Laboratory
3610 Collins Ferry Road
Morgantown, WV 26507
Phone: (304) 285-4852
Email: Aaron.Yocum@netl.doe.gov

William Joost, Technology Development Manager
U.S. Department of Energy (DOE)
1000 Independence Ave., S.W.
Washington, DC 20585
Phone: (202) 287-6020
e-mail: william.joost@ee.doe.gov

Contractor: INFINIUM, Inc.
Contract No.: DE-EE0005547

Executive Summary

The objective of this project is to bring INFINIUM's magnesium-rare earth (Mg-RE) master alloy production system to the threshold of commercial production. This energy-efficient process produces high-purity magnesium-neodymium (Mg-Nd) master alloy directly from abundant, domestic industrial magnesia and domestic neodymium oxide in a single step at very high current efficiency.

Project success could lead to commercial production, reducing costs, energy use, and emissions associated with current Mg-RE master alloy production. Vehicle manufacturers will also realize their goals of reduced vehicle weight and increased efficiency due to a secure domestic production route for high-performance Mg-RE alloys. Increased use of Mg can also improve vehicle recyclability by increasing the value of post-consumer automotive scrap metal.

Accomplishments

- Revised project plan to produce master alloy for 500 lb of AE42 alloy, which is an Mg alloy containing REs.
- Produced 30 kg of Mg-Nd master alloy with an approximate composition of 50% Mg-50% Nd by weight by molten salt electrolysis using magnesium oxide (MgO) and neodymium oxide (Nd_2O_3) as raw materials.
- Achieved current yield of over 90% in many Mg-Nd master alloy production runs.

- Automated oxide feed using variable-rate feeder.
- Automated much of the electrolysis cell operation using a programmable logic controller, enabling a single operator to potentially run several cells.
- Developed method for inductively coupled plasma-optical emission spectroscopy (ICP-OES) bath composition analysis.
- Blended Mg-Nd master alloy with Mg metal and other alloying elements to produce 590 lb AE42 alloy cast ingots.
- Shipped 507 lb of AE42 alloy to a partner for die casting automotive parts.

Future Directions

- Complete die casting and testing of representative automotive parts using AE42.

Technology Assessment

- Target: Process for low-cost production of Mg-RE master alloys to meet the needs of the automotive industry.
- Gap: Production of the current master alloy production cell is low (0.5 kg per 8-hour shift); there is need to increase that rate to lower production cost.
- Gap: Need to demonstrate use of this technology for master alloys beyond Mg-Nd, such as Mg-Ce, Mg-Y, Mg-Gd, and so forth.

Introduction

Mg is an important material for long-term vehicle light-weighting, because it is easily die cast and exhibits significantly higher stiffness/weight than aluminum. Indeed, the Magna International-Ford Motor Company Multi-Material Lightweight Vehicle Project's Mach II design achieves a 50% vehicle weight reduction versus a 2005 Ford Taurus, in large part, by using more than 50% Mg by weight in the chassis and body-in-white, chassis, closures, and subframes [**1**].

Unfortunately, energy use and carbon emissions associated with Mg's primary production are both much higher than for aluminum. In addition, China's produces 85% of the world's Mg, which leads to supply risk. These conditions prevent Mg's widespread adoption in motor vehicles today.

Master alloy, often called "hardener," is essential for production of Mg alloys containing RE metals (typically 0.5 to 7 wt%). These alloys exhibit high strength and low creep rate, including at high temperature, and are also more formable and less flammable than other Mg alloys. However, rare earth metal dissolution kinetics in liquid Mg are very slow, much slower than other alloying elements such as aluminum, zinc, and tin, which results in a long mixing time and low capital utilization for alloying furnaces. With fine structure, master alloys containing 20 to 50% RE disintegrate quickly in liquid Mg and small RE precipitates dissolve in seconds rather than tens of minutes. For a die casting or sheet production operation, the much faster-dissolving master alloy can go straight into production equipment, thus lowering cost.

The objective of this project is to bring INFINIUM's Mg-RE master alloy production system to the threshold of commercial production. This energy-efficient process produces high-purity Mg-Nd master alloy directly from abundant, domestic industrial magnesia and domestic Nd_2O_3 into a single step at very high current efficiency.

Project success could lead to commercial production, reducing costs, energy use, and emissions associated with current Mg-RE master alloy production. Vehicle manufacturers will also realize their goals of reduced vehicle weight and increased efficiency due to a secure domestic production route for master alloys used in high-performance Mg-RE alloys. Increased use of Mg can also improve vehicle recyclability by increasing the value of post-consumer automotive scrap metal.

Approach

INFINIUM is scaling up a breakthrough process for direct electrolytic production of Mg-RE master alloys from their very low cost oxides. As shown in Figure III.3-1, this approach dramatically simplifies the flow sheet for master alloy production, which in turn reduces cost, energy use, and emissions accordingly. In particular, this technology eliminates hydrogen fluoride (HF) and perfluorocarbon emissions associated with RE metal production, making it compatible with the U.S. Occupational Health and Safety Administration and the Organization for Economic Co-operation and Development workplace safety and environmental standards. For Mg, there are two production approaches today: (1) the extremely labor, energy, and emissions-intensive Pidgeon process from MgO or (2) fused salt electrolysis of anhydrous MgCl2, whose production from MgO by carbochlorination leads to dangerous dioxin and furan emissions. Table III.3-1 summarizes energy use and emissions associated with today's master alloy production.

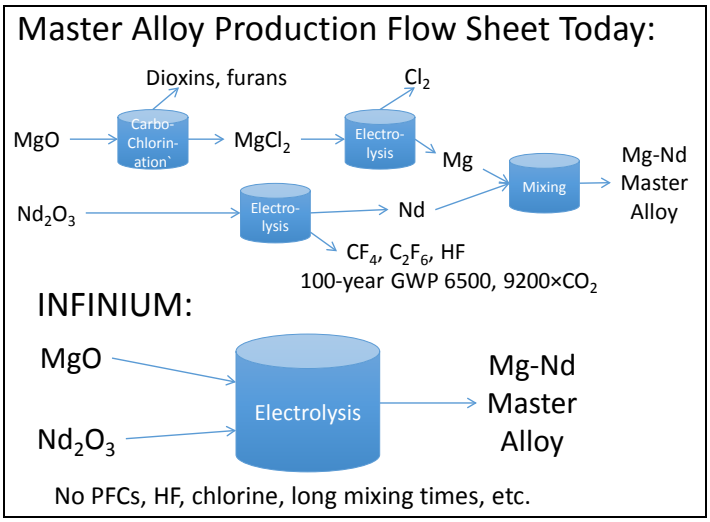

Figure III.3-1. Simplification of magnesium master alloy production flow sheet using INFINIUM technology.

Table III.3-1. Comparison of Energy Use and Emissions Associated with Today's Production of Master Alloy versus INFINIUM Technology

Product	Energy use, kWh/kg product	Emissions, kg CO_2/kg product
Pure Mg (Pidgeon)	100	25
Pure Mg ($MgCl_2$ electrolysis)	35	2
Pure Nd today	5.6	103 to 181
50-50 Mg-Nd master alloy today	20	52 to 92
INFINIUM 50-50 Mg-Nd	5 to 7	5.3 to 6

For this project, INFINIUM has produced 50-50 by weight Mg-Nd master alloy to be used in 500 lb of AE42 (Mg-4% Al 2% Nd) (i.e., an automotive die casting alloy). A project partner has blended this with other required elements to produce over 500 lb of that AE42 alloy. INFINIUM has shipped that alloy to our automotive partner for testing in a die cast part to evaluate fitness for motor vehicle use. At the end of this project, this technology will be proven at pilot scale and ready to scale up for use in automotive, aerospace, and other applications.

Results and Discussion

During Fiscal Year 2016, INFINIUM scaled up the Mg-Nd alloy co-deposition method developed in Fiscal Year 2015. An experimental campaign was conducted that varied cell parameters to identify the limiting factors of the scale up and production campaign, including the following:

- Anode current density
- Cathode design and current density
- Bath size
- Feed composition
- Voltage.

Based on the results of this investigation, the initial production cells were designed and a production campaign was planned. Bath volume increased three-fold with a new large-area electrode configuration and a new metal collection assembly. This configuration significantly increased cell current efficiency from 60 to over 90% and increased production rate ten-fold with a negligible change in anode current density (Figure III.3-2). The cathode material also changed from a high-cost industry standard material to a much lower-cost alternative. Other innovations focused on improving uptime for continuous production with automated feeding, including unattended production overnight and improving product purity.

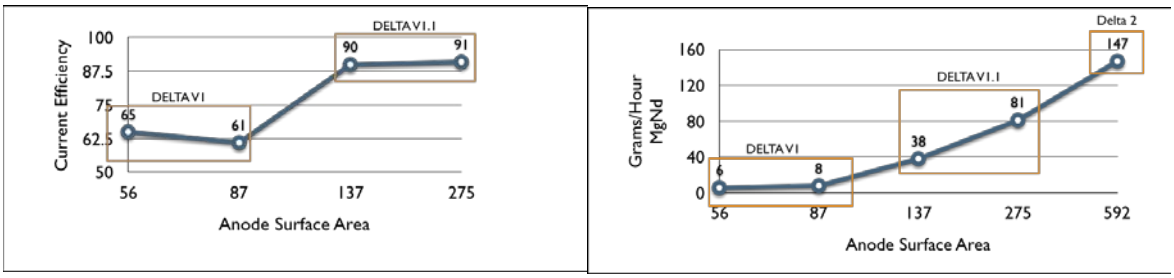

Figure III.3-2. Current efficiency (left) and production rate (right) for various cell configurations.

Continuous Production

A central focus for INFINIUM's production campaign centered on maintaining a level of continuous production in the renovated MgNd electrolysis cell. Continuous and predictable production allowed INFINIUM to expand total operating hours from a single shift operation to a two shift, 7 days a week production schedule. Expanding shifts required training of several operators to run the cell to ensure there was coverage through any absences. Several major obstacles were overcome to realize this, including electrolyte bath chemistry stability and transport properties. In the end, it was possible to maintain consistent electrolysis at approximately 120 amps in the small pilot cell and 275 amps in the larger production cell.

Automated Feeding

Adding oxide into the electrolyte to sustain production was the most time intensive process associated for a cell operator. Over the course of a run, an operator was opening the cell to add oxide up to six times to sustain a relatively constant production rate. This periodic addition of oxide results in current drift from 120 amps initially to 90 amps between oxide feeds.

To reduce operator involvement and improve average current, INFINIUM developed an automated feeder that continuously adds oxide during electrolysis. The feeder (Figure III.3-3) consists of three major sections: (1) the removable cover with drive assembly, (2) the hopper, and (3) the auger shaft.

The top of the feeder is a removable flange. A high torque National Electrical Manufacturers Association-17 stepper motor is mounted on top of the flange. The motor runs at a constant speed controlled by an Arduino

controller and motor shield. The controller is located inside a plastic casing to protect the controller from the dust and other matter in the laboratory. Power to the unit is controlled by a simple toggle switch. This allows the stepper motor to be powered down before removing the lid to fill the hopper with the desired oxide mixture. The feeder is calibrated to feed a precise amount of oxide mixture into the cell to support a resulting current of 120 amps.

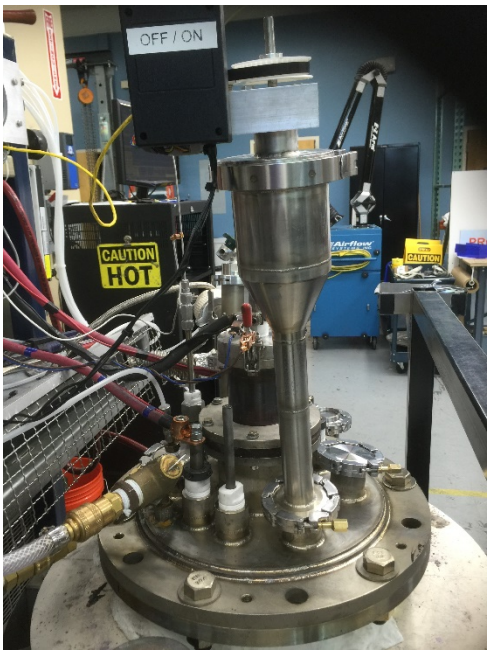

Figure III.3-3. INFINIUM semi-continuous feeder

The hopper is a cylinder with a conical bottom to funnel the flow of powder down to the auger shaft. The hopper can hold enough feed stock to produce upward of 1lb of MgNd alloy. If the cell operates at 100% current yield, it would take approximately 6 hours to produce 1 lb of metal.

Addition of the automated feeder significantly reduces operator intervention during electrolysis. The operator now is only required to load the hopper, periodically check the cell, and extract metal at the end of the run. In addition to reduced involvement, the feeder allows the system to run at a constant current of 120 amps, which stabilizes the kinetics of the system and creates a more consistent product.

Overnight Electrolysis

INFINIUM has successfully conducted several unattended overnight runs to produce MgNd during the pilot. This is a result of two major improvements in the process. The crucible containing the electrolyte had begun to degrade under electrolysis, which covered the surface of the electrolyte in conductive powder. This powder would short the anodes to the dam and the crucible wall. The shorting of the system reverted any product metal back into oxide. To solve this issue, the crucible configuration was altered. Immediately following this change, the dust was no longer observed on the surface and no shorting was observed over extended periods of electrolysis.

After resolving the surface shorting in the cell, the current efficiency decreased with increasing runtime. This was resolved by a change to the cathode assembly configuration.

Commissioning of a Production MgNd Cell

INFINIUM commissioned and ran a small production cell (Figure III.3-4). The unit features four anodes of similar size to two in the pilot. Anode surface is the limiting factor in the overall production rate. This unit

features the same cathode configuration as the pilot. The feeder assembly is also very similar to that of the pilot to capitalize on both use of standard parts and previous successes.

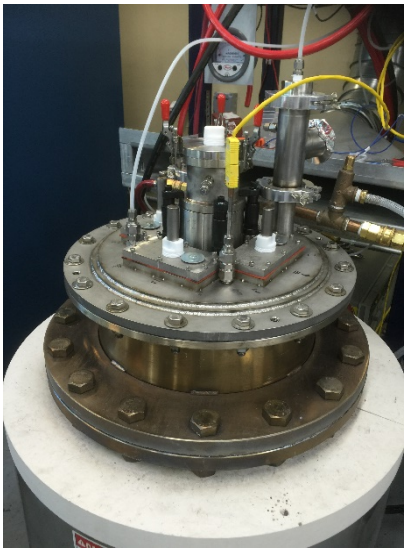

Figure III.3-4. Production cell.

Two major improvements over the pilot configuration revolve around total bath size and the anodes. First, the production cell contains approximately twice as much total electrolyte. The second major improvement is the ability to remove and replace the INFINIUM proprietary anodes in less than 10% of the time required in the pilot.

Product Purity

Over the life of the pilot production cell, several roadblocks were encountered that effected both production rate and metal purity. After approximately 4 months of continuous production, the internals of the cell began to show significant signs of wear, mainly the heat shield (Figure III.3-5). Degradation of the heat shield ultimately led to a decrease in overall product purity. After approximately 1 month of subpar and inconsistent production, INFINIUM decided to decommission the pilot cell and reuse the internals to prolong the life of the more efficient production cell.

Figure III.3-5. Degraded heat shield following electrolysis for 4 months.

In addition, as the heat shield degraded, more heat was absorbed by the top plate. This increased the load on the water cooling and made it far more difficult to operate. Changing heat shield materials increased its longevity by a factor of 2 to 3. This component could stand further improvement moving forward.

All metal produced at INFINIUM was analyzed using ICP-OES to track both the Mg content and the impurities within the produced metal. The Mg-Nd samples produced during commissioning of both the pilot and production cells were approximately 45% Mg by weight. The composition of the metal was dialed in at 50 to 55% Mg by weight as proper current densities and an aspect ratio of electrodes were developed. The major impurities found in the hardener were cathode, insulation, and electrolyte materials. In addition to these three impurities, there were other impurities unaccounted for because detection via ICP-OES was not feasible.

INFINIUM did not implement any material changes. The AE42 produced using the hardener (see Figure III.3-6) was in specification for all major impurities because the sources of each impurity were determined. The ingots poured from the production furnaces were up to 200 g in size. Each ingot poured was covered in electrolyte and it appeared that the top few millimeters of the ingot contained the electrolyte. This layer formed on top of each poured ingot, regardless of size or aspect ratio. Therefore, if the pours were to increase in size, the electrolyte impurity should decrease.

Figure III.3-6. 270 lb of AE42 produced using INFINIUM hardener.

While a process change would be sufficient to reduce the electrolyte impurity, material changes to the cathode and insulation are required to reduce other impurities.

Production Rate

Following commission of the production cell, INFINIUM worked to increase its production rate. One critical parameter identified was cathode seasoning. A new cathode can support a current of 100 amps. Anything above that results in a grey deposit and transport problems that are difficult to recover. However, after suitable treatment, the cathodes can support currents up to 350 amps, more than tripling the production rate. This enables production at a very high rate, even when utilizing a batch process where the oxide is added in between runs after the metal harvest.

While the batch process is effective, it requires several hours of downtime during each shift while the operator waits for oxide to dissolve. This process equates to approximately 1 hour of downtime after each run. Given that the operators can fit three runs into a shift, the cell is down for 3 hours. The addition of a feeder (Figure III.3-7), reduces downtime to 30 minutes per shift and increases production time by 50%.

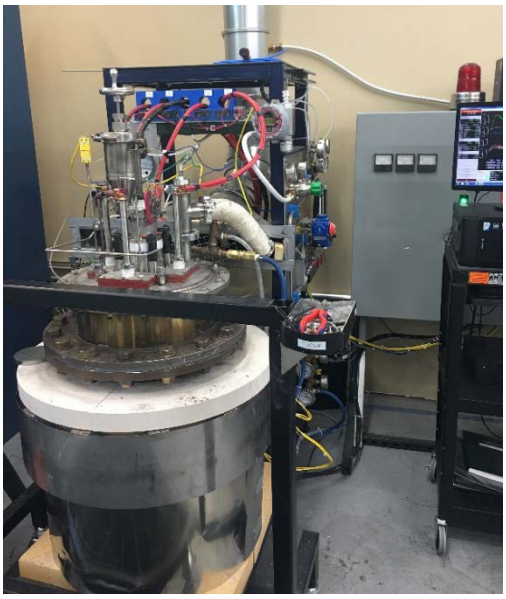

Figure III.3-7. Production cell with feeder.

Metal Production

INFINIUM first shipped 30 kg of Mg-Nd hardener to their alloying partner. From this hardener, the alloying partner cast 270 lb of AE42 alloy (Figure III.3-6). Unfortunately, this was the first cast of AE42 for the partner and a large amount of material was left behind in the heel of the pot.

INFINIUM shipped the remainder of the hardener to the alloying partner, where the remaining 350 lb of AE42 were cast in the form of 2-lb ingots and shipped back to INFINIUM. Five random ingots where removed from the lot to be analyzed via ICP-OES. Table III.3-2 gives the certificate of analysis generated for the lot.

Table III.3-2. Certificate of Analysis for INFINIUM AE42

Elements	Concentration (%)	Specification (%)
Aluminum	3.070	4
Neodymium	1.177	2.5*
Manganese	0.092	0.1
Iron	0.003	<0.01
Copper	0.004	<0.005
Nickel	0.001	<0.001
Zinc	0.060	<0.2
Lanthanum	0.073	*
Cerium	0.140	*
Praseodymium	0.008	*
Samarium	0.002	*
Magnesium	Balance	Balance
*Included in 2.5% total rare earths, usually mostly cerium.		

Once the material chemistry was verified, the material was packaged on a pallet. The poor form factor of the small 2-lb ingots made it necessary to package the material within a heavy duty bag to prevent any material from being lost during shipping. Figure III.3-8 illustrates the packaging method for the shipment to Vehma for casting into test parts. In particular, the MMLV front kick down rail (Figure III.3-6) is the candidate part that will be cast.

Figure III.3-8. 507 lb of AE42 alloy using INFINIUM hardener.

Figure III.3-9. MMLV front kick down rail candidate part for casting INFINIUM AE42 alloy.

Technology Transfer Path

In the short term, the technology transfer plan involves scaling up this technology for low-cost production of Mg-RE master alloys. This is a very important market segment that provides material for high-performance Mg alloys. RE metals have several important effects on Mg, including improved high-temperature tensile and creep strength, reduced corrosion, and reduced flammability. For example, the Corvette engine cradle used AE44 with 4% by weight RE metals, because of these advantages. Moving forward, many are talking about using ZEK100 alloy sheet for automotive closures; this will require Mg-Nd master alloys priced at $100 to $200 per kilogram.

Beyond this, production of other Mg-RE alloys such as Mg-Y and Mg-Gd should follow in a relatively straightforward manner. The ability to produce directly from oxides can result in a very significant cost advantage compared with today's producers of master alloys and allow large-scale production with much lower energy use and emissions.

Conclusions

INFINIUM has completed Mg-Nd master alloy production during this project and has reached some important milestones in the past year. The technology has much lower cost, energy use, and emissions than today's available technology. Unlike other oxide reduction technologies, it is compatible with U.S. Occupational Health and Safety Administration and the Organization for Economic Co-operation and Development workplace safety and environmental regulations. We demonstrated much higher current efficiency, much higher current production rate, longer furnace uptime, continuous automated feeding of oxide raw material, and overnight unattended operation. Our partner used the master alloy from our cells to produce well over 500 lb of AE42 alloy for testing. The developed technology is close to commercial readiness and will continue to advance as we use it for commercial production.

References

[1] Skszek, T., D. Wagner, J. Conklin, and M. Zaluzek, 2015, "Multi-Material Lightweight Vehicles," presentation at DOE Vehicle Technologies Office Annual Merit Review, Washington, DC, June 11, 2015.

Bibliography

Das, S., 2011, "Technical Cost Modeling – Life Cycle Analysis Basis for Program Focus," presentation at DOE Vehicle Technologies Office Annual Merit Review, May 11, 2011.

Kippouros, G. and D. Sadoway, 2001, "A thermochemical analysis of the production of anhydrous MgCl2," Journal of Light Metals 1: 111–117, DOI: 10.1016/51471-5317(01)00004-9.

Powell, A. and S. Derezinski, 2016, "Scale-Up of Magnesium Production by INFINIUM Electrolysis," DOE VTO Annual Merit Review, Washington, DC, June 8, 2016.

III.4 High-Strength Electroformed Nanostructured Aluminum for Lightweight Automotive Applications – Xtalic Corporation

Project Details

Robert Hilty, Principal Investigator
Xtalic Corporation
260 Cedar Hill Street
Marlborough, MA 01752
Phone: 508-485-9730
E-mail: sruan@xtalic.com

William Joost, DOE Technology Area Development Manager
U.S. Department of Energy
1000 Independence Ave., S.W.
Washington, DC 20585
Phone: 202-287-6020
E-mail: william.joost@ee.doe.gov

Executive Summary

The overall project goal is to electroform high-strength nanostructured aluminum (nano-Al) alloys for lightweight automotive applications. During Fiscal Year (FY) 2016, Xtalic fabricated the pilot plating line to demonstrate ability to scale the process. They fabricated 6 x 6-in. sheets of nano-Al from the pilot system, verified mechanical properties, and further optimized the plating chemistry to boost the thickness capability to produce a dense and pore free structure.

Accomplishments

- Built a prototype continuous plating system for nano-Al.
- Designed, built, and tested flow-controlled plating cells.
- Validated the cost model and assumptions.
- Built 6 x 6-in. sheets of composite nano-Al structures.

Future Directions

- Apply static flow cell knowledge to the continuous sheet plating cell.
- Optimize the sheet fabrication rate and bath lifetime.
- Fabricate and test nano-Al sheets, optimize properties, and down-select preferred alloy composition.
- Develop and refine the economic cost model.

Technology Assessment

- Target: Validate the nano-Al sheet manufacturing process on an industrial scale.
- Gap: The nano-Al electrolytic bath chemistry and process are unique. The prototype system bridges some of the gap, but technical risks remain.

- Target: Materials need to meet the full specifications required for target application.
- Gap: Properties are good for rack-plated parts, but remain unproven for a continuously made product.
- Target: Integrate nano-Al material into the vehicle component manufacturing process.
- Gap: Potential concerns regarding post-fabrication steps (e.g., spring-back during stamping). Fiat Chrysler Automobiles US, LLC (FCA) will help with analysis of forming the sheet using conventional stamping processes.
- Target: Achieve target cost of $2/lb of weight saved.
- Gap: The cost model shows a viable path towards $2/lb saved. However, the path requires technical improvements in strength, plating bath age, and plating rate in order to meet the goal.

Introduction

Xtalic's electrodeposition process is a transformative, disruptive technology that has produced nano-Al sheet materials that dramatically outperform traditional high-strength Al (Table VI.4-1a) and achieve weight-normalized properties not otherwise available in engineering metals (Figure III.4-1b) [1, 2]. These new materials can enable weight reductions of 50% or more in strength-critical applications.

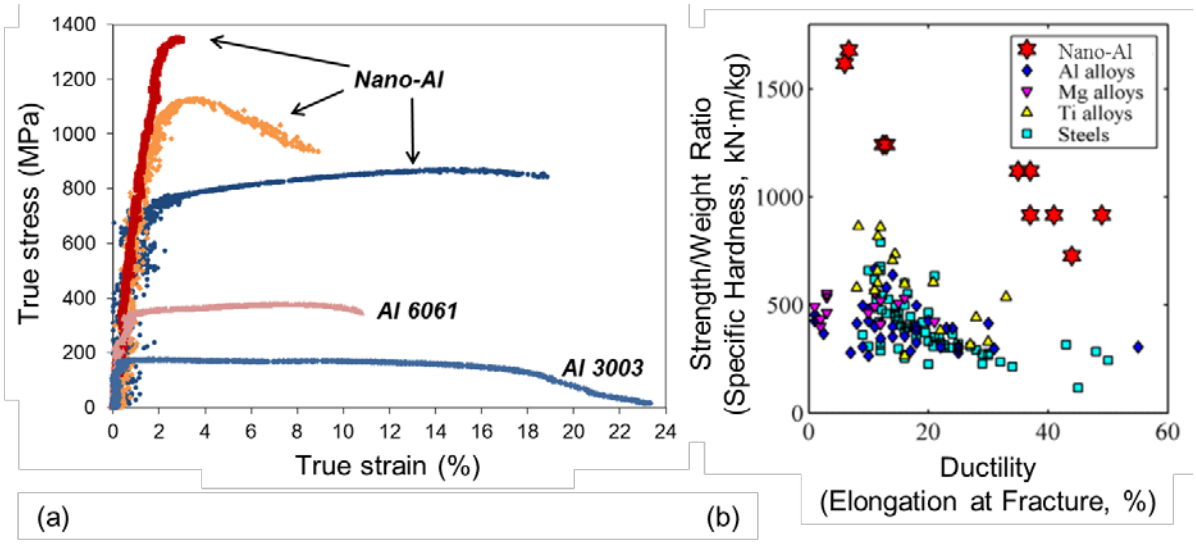

Figure III.4-1. Properties of nano-Al alloys: (a) stress versus strain in comparison with a typical 6xxx Al alloy and (b) weight-normalized strength versus ductility in comparison with traditional structural metals.

The objectives for this project are to develop a commercial process for manufacturing high-strength nano-Al sheet and simulate the use of nano-Al in a prototype automotive component. The expected outcomes are (1) a commercial-grade process for fabricating nano-Al sheet, (2) confirmation that nano-Al materials properties are maintained when produced by the new process, (3) simulation of the new alloy material in specific vehicle components, and (4) economic validation that the new material and process are cost competitive for vehicle components.

Approach

The tasks associated with achieving the four main outcomes listed in the previous section include (1) design and build a pilot-scale electroforming system for nano-Al sheets, (2) fabricate nano-Al sheets from the new electroforming system, (3) fabricate alloys and test and optimize sheet properties, and (4) develop and refine an economic model for identifying cost drivers and assessing commercial viability. Table III.4-1 provides an overview of the tasks that will be performed systematically over the course of the 4-year program.

Table III.4-1. Overview of Tasks that will be Performed Over the Course of the 4-Year Program

Tasks	Year 1	2	3	4
Optimize process output and consistency				
Develop continuous electroforming system				
Go/no-go: Engineering feasibility of design				
Build and validate pilot line				
Go/no-go: Verify system functionality, deliver 1 sample of 6-in x 6-in sheet				
Fabricate alloys, optimize properties, downselect				
Demonstrate conditions for economic viability				
Go/no-go: Economic viability of nano-Al sheet production				
Fabricate preferred alloy(s), test against full specs				
Economic modeling				
Management and reporting				

The approach and tasks identified in Table III.4-1 were somewhat modified from the original plan due to changes in the project team. FCA has continued to support the project, but is no longer able to produce the test panels originally proposed. FCA's skill sets will be leveraged to computationally characterize performance of the alloys in stamping processes instead of making physical parts. This change in plan will allow the project to focus more on the challenging economic viability of the $2/lb saved target and the processes required to hit that target.

During FY 2016 (Budget Period 2), the main focus was to build and validate the pilot line. At the end of the budget period, multiple 6 x 6-in sheets were produced from the new system. Because of some resource constraints, the project was extended by one quarter with no cost extension. Table III.4-2 summarizes the planned tasks and milestones for Budget Period 2.

Table III.4-2. List of Tasks and Milestone for Budget Period 2, including the No Cost Extension

Tasks	Program Quarter 1 Oct-Dec	2 Jan-Mar	3 Apr-Jun	4 Jul-Sep	(No-Cost Extension) Oct-Dec
Build and validate pilot line					
• Acquire components (Milestone 5)					
• Begin installing electroforming system (Milestone 6)					
• System test					
• Pilot line commissioning					
• Go/no go: fabricate nano-Al sheet from new system					

Results and Discussion

Build and Validate Pilot Line

During FY 2016, the project worked to scale the plating process to larger sample sizes and plating volumes. Two distinct steps accomplished this: (1) 2 x 2-in. sheets and (2) full-scale 6 x 6-in. sheets. For the 2 x 2-in. samples, a 20-L reactor was used. The larger tank volume of this reactor provided the opportunity to establish the ongoing process consistency of the plating process. A sample rocker arm was added, which provides lateral movement of the plating workpiece and improves mass transport of the plating solution at the cathode. Mass transport of the electrolyte was further supported by a sparger system at the base of the reactor. The rocker arm and tank are depicted in Figure III.4-2. The project designed and built polytetrafluoroethylene fixtures for the 2 x 2-in. samples and iterated on this design to produce high-quality samples for tensile testing and characterization.

Figure III.4-2. 20-L plating reactor for nano-Al used to produce 2 x 2-in. sheet samples as part of the scale-up effort.

The project used the 2 x 2-in. fixture to produce many sheets of varying thickness. The system proved to be capable of repeatable thickness with good surface finish. The new additive systems are now producing high-quality deposits with minimal surface roughness. Some local thickening occurred at the extreme edge of the sample due to local current density high-flux regions, which produced a locally high plating rate. This can be corrected in a production cell through more controlled anode shape optimization and thieving current collectors near the edges. The measured thickness across the deposits were within the target thickness range of 400 µm. Figure III.4-3 shows a representative 2 x 2-in sample, where the thickness values are tabulated at five locations on the sample. The measurement locations are shown on the image with the values tabulated on the right. While the thickness variations are larger than wanted, the ability to produce thick deposits was proven. This is a single-sided plated part, but the process could be mirrored to produce a double-sided part that is 1-mm thick.

Solution flow is critical to the deposit performance. As part of the scale up, the project designed a 6-in x6-in plating cell which would allow for flexibility in the flow of the electrolyte. The plating cell, shown in Figure III.4-4, included up to 38 flow nozzles which are adjustable for their flow rate, flow direction and proximity to the cathode. By adjusting these factors, the flow for production rate and metal quality can be optimized. Because each flow cell is independent, adjustments were made for small variabilities in the flow rates across the sample by adjusting each individual nozzle.

The plating cell (see Figure III.4-4) is configured so anode material can be placed in the interstitial regions between the nozzles. The anode material is pure Al and is in the form of 3 x 6-mm rods. Small particulate contamination can be prevented in the plating chemistry by covering the anode with a layer of Kevlar® fabric, fabricated with holes to surround the nozzles but reduce particulate flow into the active plating zone.

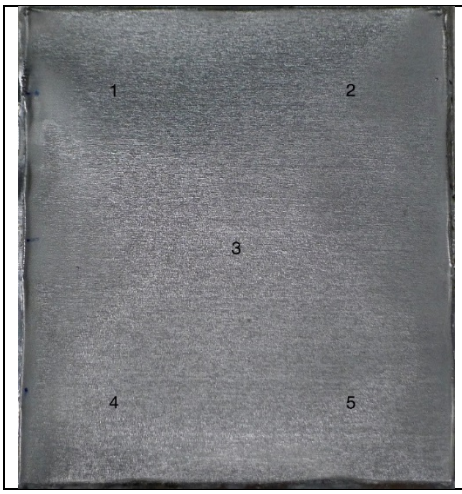

Location	Thickness (µm)
1	480
2	470
3	380
4	480
5	460

Figure III.4-3. Surface of a 50 x 50-mm plated sheet of nan-Al-manganese, plated to approximately 0.5-mm thick. The numbers indicate the point of measurement for the thickness in the chart.

The electrolyte is pumped through the nozzles to create the flow field. Figure III.4-5 shows the plating cell with the flow field activated. Electrolyte flows from the nozzles onto the workpiece (being held by the engineer in Figure III.4-5) then flows laterally over weirs and into the return plumbing. Excess electrolyte is held in a plating sump below the cell. The cell is fabricated from polytetrafluoroethylene and titanium, with additional plumbing features made from perfluoroalkoxy.

Powerful pumps moved the electrolyte through the filtration systems used to remove unwanted particulate. The electrolyte is more viscous than water. Increases in the temperature of the electrolyte were measured due to viscous shear heating. Heaters are often used to help control the plating bath temperature. While a heater is included in the plating cell design, the bath reaches operating temperatures quickly through a combination of shear heating and excess heat from the amperage used to plate. Experiments to the data evaluated the plating rates that require up to 51 amps of current. At full production rates, the process would use 149 amps, which will add heat to the system. To mitigate the risk of overheating the bath, a cooling system was added to the sump. This is a bit tricky because both the cooling system and the cooling media must be compatible with the electrolyte. Perfluoroalkoxy tubing plumbed with a silicone oil was chosen. While both of these materials are compatible, the heat exchange rates are low and will not be able to control the temperature when larger currents are applied. During Budget Period 3, a modification will be made to the cooler in order to boost temperature control capability.

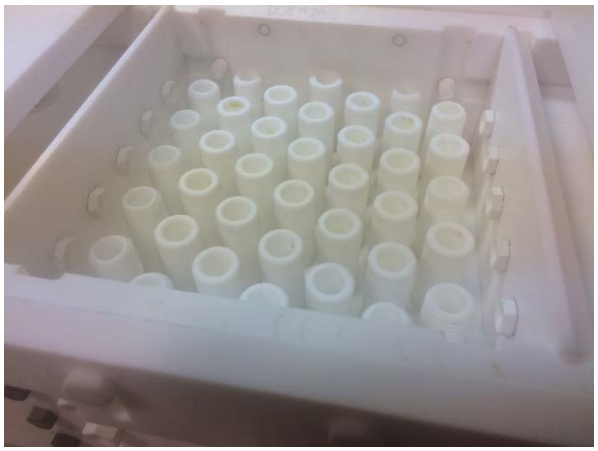

Figure III.4-4. A 6 x 6-in. flow cell showing the adjustable nozzle configuration.

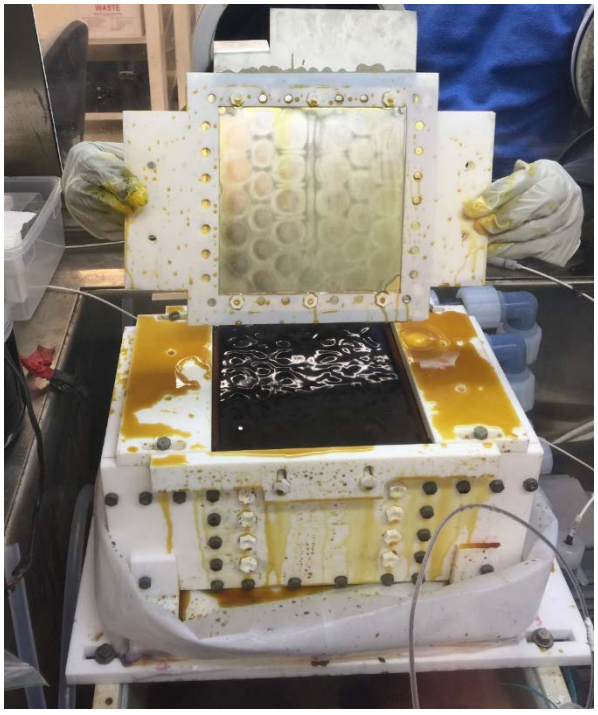

Figure III.4-5. Plating cell with nozzles activated to show the solution flow. The cathode workpiece is being held by the engineer and is placed on top of the cell for plating.

The thickness uniformity and effectiveness of the flow cell configuration were gauged by measuring the thickness of the deposit during the early stages of deposition. Figure III.4-6 shows the thickness of the nano-Al layers plated onto a brass plate as made in the flow cell. The thicknesses are given in µm for each location in the 6 x 6-in. plate. The thickness variation in this sample is ±15%, showing the need to make adjustments to the flow configuration and the flow rate. Unplated sections are seen in the corners due to insufficient jet flow from the nozzles such that the entire workpiece was not wet by the plating solution.

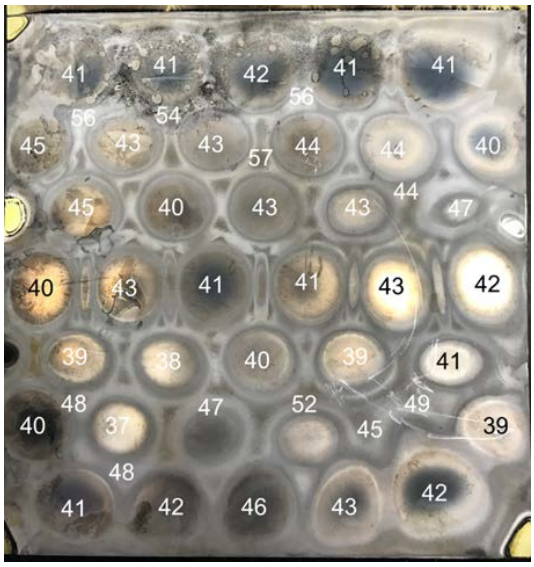

Figure III.4-6. Thickness distribution across the 6 x 6-in. plate during plating initiation. Thickness values are in µm.

During Budget Period 1, the project designed the continuous plating system. During Budget Period 2, the project fabricated the continuous thickening station. Figure III.4-7 shows the continuous system as installed in the glove box protective environment, which features roller payoff and a system that will be used to feed 0.2-mm thick AA6XXX as a substrate for the composite structure. The substrate passes over an insulating roller, then over an activation roller. The activation roller has an electrical connection to the rectifier and is electrically isolated from the plating system itself. This first roller will be used to provide the pulse waveforms used to active that Al alloy before plating. The plating cell is next (not pictured here) in line and is 12 in. in length. The second larger roller is the rectifier connection point for active plating. The last roller is a pinch roller that is adjustable for thickness to help guide the material out of the plating system.

The material then traverses a set of rollers. A linear actuator was added to drive the system, pulling the material through the machine while the nano-Al is being plated. This was required in order to fit the system into the glove box environment; the linear actuator could be replaced by a continuous roller take-up system when needed. The photo in Figure III.4-7 also shows the strip configured with a copper substrate. Copper foil handling is well known; therefore, this material was used as an interim step to building and qualifying the line.

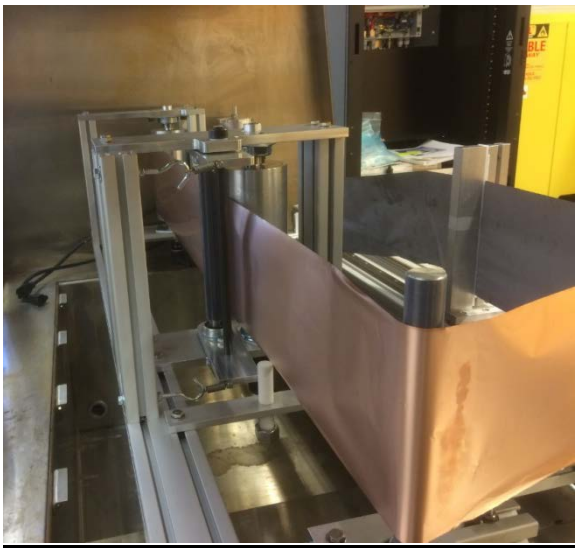

Figure III.4-7. Continuous thickening station for reel-to-reel plating on nano-Al.

The pilot line plating cell was used to create a series of 6 x 6-in samples for proof-of-concept. Ten samples were produced as double-sided coatings onto either brass or AA6061 substrates. The system is capable of activating the Al substrate, generating good adhesion, and plating uniformity across the sample. Plating thicknesses on the 6 x 6-in substrate were 50 µm per side and can be scaled to greater thicknesses during Budget Period 3.

Optimize Process Output and Consistency

As the thickness of the plated deposit increases, there is greater risk for the surface roughness to become more nodular and dendritic. As small nodules inevitably form on the surface, the increased surface area can concentrate the electric fields and lead to faster electrodeposition on the nodule. This can become a runaway situation, where the nodules grow at the expense of the balance of the surface to be coated. Plating additives are typically organic species added to the plating bath to suppress deposition on the nodule, leveling out the plating as it grows. Additives that are well known to the aqueous plating industry generally do not apply to ionic liquid plating electrolytes, thus new additives were required.

During the first 2 years of the project, effort was invested to determine the best plating additives for building thick, dense, and pore-free coatings. While several new additives had been developed, the chemistry of their reaction at the surface had been unknown and required study. Figure III.4-8 shows the surface of a nano-Al coating that was made with a surface-leveling additive. The image shows larger plating clusters (i.e., collections of plated grains where the collective grain boundary can be seen in the surface topography) and a large number of pores on the surface. The project found that in certain overdosing situations, the additive can lead to porosity in the deposit. While the pores here are relatively small, they have a deleterious effect on the strength and ductility of the deposit. Further refinement of additive chemistry was required. A formulation that worked well and a plated series of brass rods with thick layers of nano-Al were found (see Figure III.4-9). These rods had thicknesses in our target range (the one shown is about 350 µm). The deposit shows little to no porosity and a generally smooth finish.

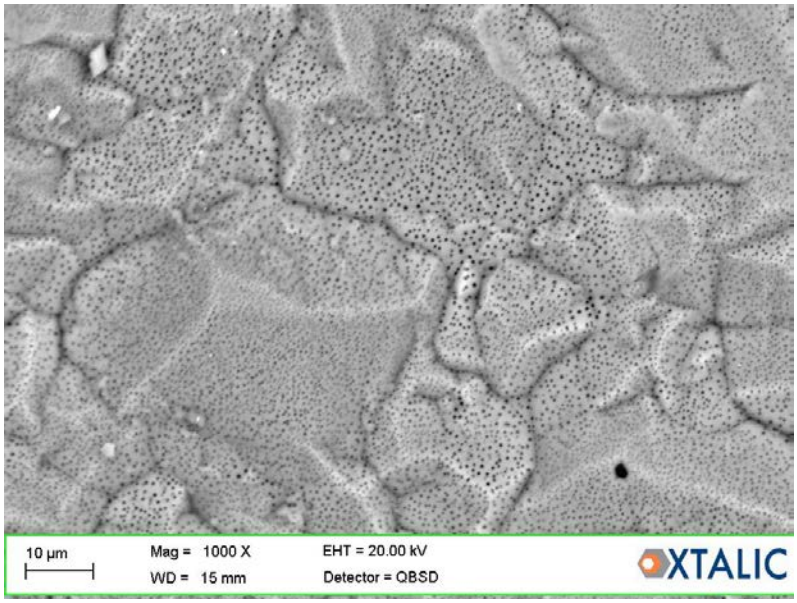

Figure III.4-8. Porosity in the nano-Al layer due to excessive additive in the electrolyte.

Figure III.4-9. Thick deposit (i.e., about 350 µm) of nano-Al on a rod substrate with no evidence of porosity.

With the additive system set, 2 x 2-in. samples were constructed for tensile testing to verify the nano-Al properties. The material was tested as free-standing nano-Al and as a composite structure. The free-standing parts were made by electroforming nano-Al onto a substrate layer, then physically removing them from the substrate. These sheets could be cut into tensile bars for mechanical testing. Composite parts were fabricated by plating thick layers of nano-Al onto an Al substrate.

The results of the representative tensile tests are shown in Figures III.4-10 and 11. Figure III.4-10 shows the results from composite samples. There are five replicates in this batch, which show tensile strengths varying from 580 to 675 MPa. Ductility in each case is more than 8% elongation. These are excellent results demonstrating the strength and ductility capability of these alloys.

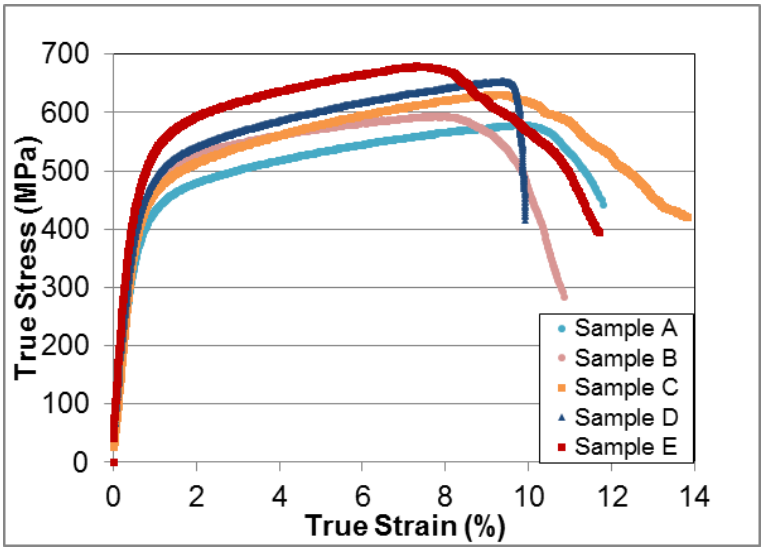

Figure III.4-10. Tensile data on composite nano-Al structures showing strength, ductility, and repeatability of performance.

Figure III.4-11 shows the performance of free standing nano-Al alloys. In this case, the sheets are thinner and there is more variability in the performance, generally resulting from surface defects on the plated or machined test samples. Despite these challenges, many of the results show strong nano-Al properties. The performance of the substrate is shown for reference; these samples were tested without a substrate layer. For several of the samples, there is good repeatability of the initial loading curve through the point of yielding. After yielding, the surface defects can give rise to premature failure due to local stress concentrations. These defects can be

eliminated through more careful surface preparation of the machined test parts and improved filtration of the plating electrolyte.

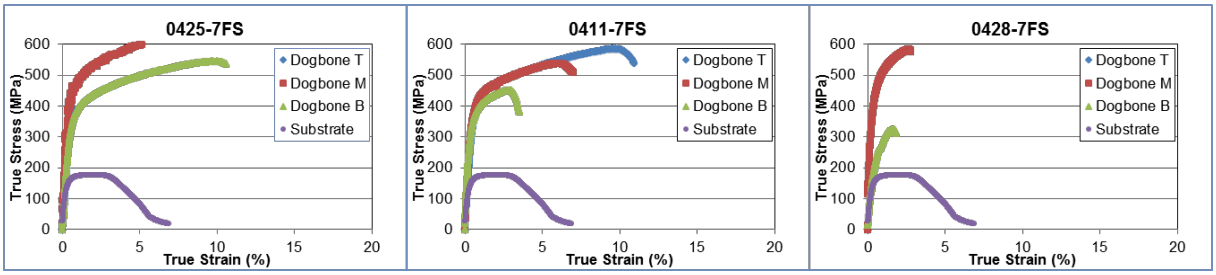

Figure III.4-11. Tensile data on free-standing nano-Al samples showing strengths up to 600 MPa for some samples. Poor ductility can often be attributed to sample preparation and surface roughness.

Cost Model

One of the key deliverables of the project is to produce a viable material at an acceptable cost. The project has engaged IBIS as partners to assist with cost modeling of the plating process. The cost model is extensive, taking into account many process variables and leveraging real equipment price quoting to ensure model accuracy and viability.

The plating process can be modeled as a series of manufacturing steps following a process flow diagram (see Figure III.4-12). The Al plating process is water sensitive; therefore, these portions of the process must occur within a controlled environment. We believe that a dry-room environment, such as those used in Li-ion battery fabrication, should be satisfactory to meet the environmental conditions. This approach was used as a basis for the cost modeling effort. As Figure III.4-12 shows, some operations can be performed outside the dry-room environment (e.g., degreasing the substrate and inspection). In a full production environment, with economy of scale, a plating tank for nano-Al is fairly long at about 19 m. A line of this length can fit into a commercially available dry room (for which price quotes have been received). Many other elements are included in the model, including plating rate, energy cost, capital costs, tank size, electrolyte cost, metal costs, labor rates, and labor intensity. Figure III.4-13 shows a pie chart of the fractional costs of making nano-Al on a high-volume manufacturing basis in one particular plating scenario. An examination of Figure III.4-13 reveals that the major costs for producing nano-Al are plating bath, energy, and equipment (capital). Labor cost is a small fraction of the total cost, even when modeled as being fabricated in the United States. The relatively high fractional cost of energy makes fabrication of nano-Al in the United States particularly attractive because the energy costs are relatively low and the labor costs represent a small fraction of the total.

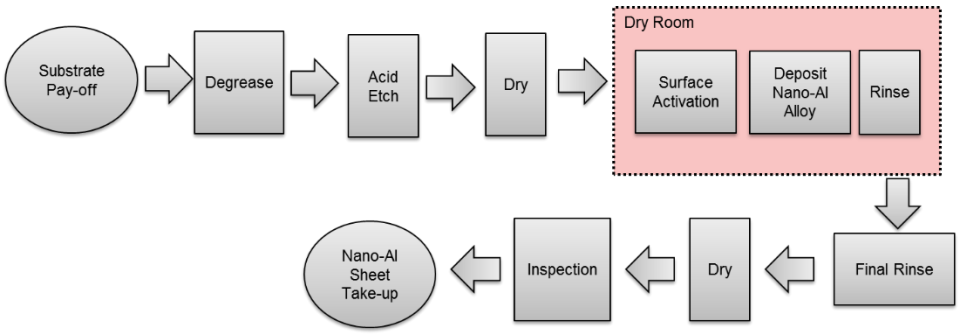

Figure III.4-12. Schematic process flow map for plating of nano-Al.

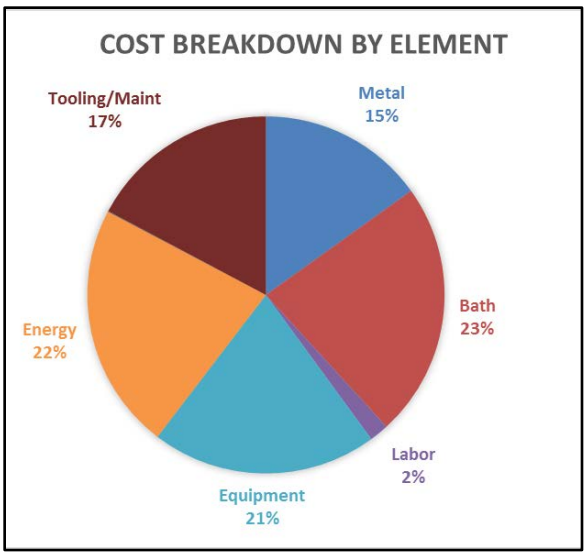

Figure III.4-13. Cost breakdown for plating of nano-Al in the United States. Energy and plating bath costs dominate, while labor cost is low.

Technology Transfer Path

Xtalic's business model includes working with manufacturing partners to produce nano-crystalline electrodeposited metal products by providing manufacturing process design specifications and onsite engineering support and raw materials to its manufacturing partners. Xtalic will work with Tri-Arrows Aluminum, Inc. or another manufacturing partner to fabricate, install, and operate the nano-Al sheet lines.

Xtalic is actively working with top-tier automotive original equipment manufacturer suppliers to identify suitable entry-point applications. For this project, Xtalic is collaborating with FCA to simulate formation of prototype component parts. This project is the first step in the process of technology development within FCA. Throughout the duration of this project, FCA will monitor technical progress, experimental results, and economic analysis to evaluate the technology's potential to meet their product performance requirements and economic goals for future vehicle applications. FCA will determine the technology's suitability to proceed to the next phase of their internal technology development stage-gate process.

Conclusions

During FY 2016, the project fabricated and qualified the plating systems to produce 6 x 6-in. nano-Al sheets. Plating additives were developed improved to produce plating thicknesses at the target thickness of 400 µm. These can be combined with a 200-µm thick AA6XXX substrate to produce a final thickness of 1 mm, with strengths in excess of 600 MPa and elongation greater than 8%. Multiple samples of 6 x 6-in. sheets were produced from the plating cell and the flow configurations required for continuous plating were further developed. A cost model was developed that includes elements for plating rate, energy cost, capital costs, tank size, electrolyte cost, metal costs, labor rates, and labor intensity. High-volume manufacturing for one particular plating scenario revealed that major costs for producing nano-Al are plating bath, energy, and equipment (capital). Labor cost is a small fraction of the total cost. Xtalic successfully accomplished all milestones and completed the deliverable for Budget Period 2.

References

[1] Ruan, S. and C. A. Schuh, 2009, "Electrodeposited Alloys and Methods of Making Same Using Power Pulses," U.S. Patent Application No. 12/579,062, filed October 14, 2009.

[2] Ruan, S., W. Paw, H. Martin, C. A. Schuh, and A. Lund, 2013, "Systems and Methods for Electrodepositing Aluminum Alloys," U.S. Patent Application No. 13/830,531, filed March 14, 2013.

Bibliography

Abbott, J. G. and E. Freydina, 2016, "Utilizing Acid to Control Process Chemistry for Electrodeposition of Aluminum from Chloroaluminate Ionic Liquids," presented at the 2*6th EUCHEM Conference on Molten Salts and Ionic Liquids*, Vienna, Austria, http://www.euchem2016.org/programme/confirmed-poster-presentations/.

Freydina, E. and J. G. Abbott, 2016, "Red-Ox Reactions in Ionic Liquids and Their Impact on Electrodeposition of Metals and Alloys," *Electro Chemical Society Transactions* 75(15): 639-648, http://ecst.ecsdl.org/content/75/15/639.

Hilty, R., 2016, "High-Strength Electroformed Nanostructured Aluminum for Lightweight Automotive Applications," presented at the *Department of Energy Vehicle Technologies Program Annual Merit Review*, June 2016, https://energy.gov/eere/vehicles/vehicle-technologies-office-annual-merit-review-presentations.

III.5 Development of Low-Cost, High-Strength Automotive Aluminum Sheet - Arconic

Project Details

Russell Long, Principal Investigator
100 Technical Drive
New Kensington, PA 15069
Phone: 724 337-5420
e-mail: russell.long@arconic.com

John Newman, Principal Investigator
100 Technical Drive
New Kensington, PA 15069
Phone: 724 337-2689
e-mail: John.newman@arconic.com

Charles Alsup, Project Manager
National Energy Technology Laboratory
3610 Collins Ferry Rd
Morgantown, WV 26507
Phone: 304 285-5432
e-mail: Charles.alsup@netl.doe.gov

William Joost, DOE Technology Area Development Manager
U.S. Department of Energy
1000 Independence Ave. S.W.
Washington, DC 20585
Phone: 202 287-6020
e-mail: William.Joost@ee.doe.gov

Contractor: Arconic
Contract No.: DE-EE0006847

Executive Summary

The goal of the project is to develop an automotive high-strength 7xxx aluminum alloy and demonstrate its ability to replace an ultra high-strength component with significant weight savings at a cost of $2 per pound saved.

Arconic, in partnership with Oak Ridge National Laboratory and our industrial partners Honda R&D Americas, Inc. (Honda) and Cosma, leads this project to productively reduce weight in vehicles in a cost-effective manner. This effort of increasing strength of a 7xxx material while reducing costs can only be successfully performed by a team that includes a Tier 1 automotive supplier (i.e., Cosma) an original equipment manufacturer (i.e., Honda), and an aluminum producer. Honda will provide the requirements for the vehicle component and Cosma will develop the warm forming tooling and procedures for forming the baseline component. Oak Ridge National Laboratory will develop the method required to tailoring welded blanks to further reduce material usage. The proposed alloy developments will be done initially in laboratory-scale trials and then in full-scale trials at Alcoa. Once the full-scale trial material is available, full-scale forming trials will be conducted with and without tailor-welded blanks. The material will be evaluated for strength, formability, and corrosion based on stringent Honda requirements.

Accomplishments

- Tested all the ingot-based and Micromill™ produced trial materials following a warm forming simulation and paint bake treatment. These mechanical properties are being used to select the composition for full-scale trials. Corrosion testing has been completed on a subset of these experimental materials.
- Completed forming characterization of the baseline 7055 material and it is also underway on a subset of the experimental alloys.
- Designed the demonstration part and refined using forming simulation. The 7055 baseline material forming characterization was used for this refinement.
- Designed and built the warm forming tooling. This tooling has been installed in a press line.
- Designed and built an oven to heat the blanks for the forming trials. This has been installed in the pressline.
- Began forming trials on the 7055 baseline material and four new 7xxx series alloys.

Future Directions

- Refine forming temperature profile and incoming material temper to provide the largest forming process window to reach the program's strength targets.
- Mechanically test the properties of the warm-formed parts and compare to the previous testing.
- Conduct corrosion testing of samples cut from the formed parts and compare to previous results.
- Conduct component tests on the straight portion of the formed part in three-point bending.
- Produce and conduct forming trials on tailor-welded blanks.
- Complete cost study on part costs to access the cost per pound saved over the baseline steel part.

Technology Assessment

- Target: Achieve the 600-MPa ultimate strength and 8% elongation targets following warm forming simulation and paint bake cycles on several ingot cast and Micromill™-produced experimental alloys.
- Gap: The 600-MPa ultimate strength and 8% elongation target has been reached for several experimental alloys after a simulated warm forming cycle and paint bake. The next step is to test the properties from samples cut from warm-formed parts.
- Gap: The formability of the material is increased with higher forming temperatures; however, the higher temperatures can overage the material, resulting in lower strengths. The formability of the experimental alloy is being tested during the forming trial.
- Target: Produce sound tailor-welded blanks on sample materials using friction stir welding and successfully form the parts without weld fracture.
- Gap: Can blanks with sound friction stir welds be formed without weld fractures? The forming trials of the experimental alloys with tailor-welded blanks will be done during the next year. The location of the friction stir weld could be moved to areas of lower forming strains.

Introduction

The goal of the project is to develop an automotive high-strength 7xxx aluminum alloy and demonstrate its ability to replace an ultra high-strength component with significant weight savings at a cost of $2 per pound saved.

The initial phase is based on alloy development to reach the stated targets. Corrosion and forming requirements are being developed by Honda and Cosma, respectively. Alloy development trials will target the properties stated and the added corrosion and formability requirements.

In addition, the team has defined a demonstration part that includes the critical features of the current production hot stamped steel component. This part geometry has been evaluated for forming simulations using the material properties developed during the alloy development phase. Demonstration part tooling has been built along with the oven to heat the blanks. The tooling and oven are installed in a press line and the forming trials of the new alloys are underway.

Oak Ridge National Laboratory has evaluated the properties of tailor-welded blanks produced using friction stir welding in these experimental alloys. Oak Ridge National Laboratory friction stir welding procedures will be used to produce full tailor-welded blanks of these alloys for next year's forming trials.

Approach

The first year of the contract provided definition of the detailed requirements. These specifications were targeted during the alloy development phase. Multiple new alloys were produced at a laboratory scale. These alloy development trials were used to define a number of alloys, which were produced at full-scale in existing Alcoa facilities. A demonstration part has been developed by Honda and Cosma to include all critical features of the current production ultra high-strength steel part (see Figure III.5-1).

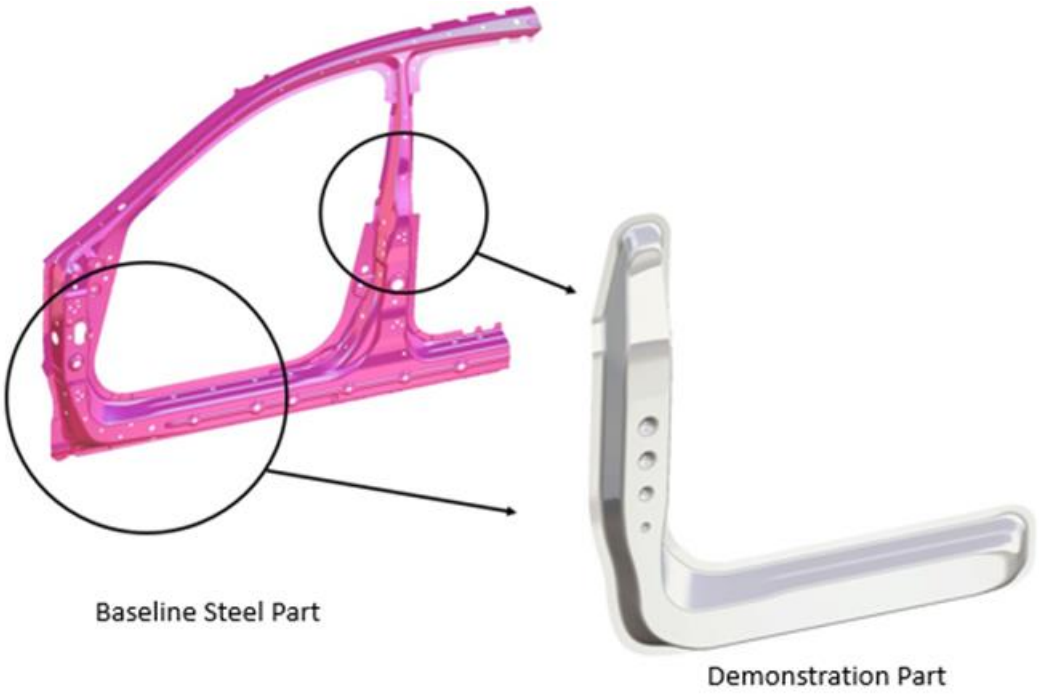

Figure III.5-1. Demonstration part geometry.

The forming tooling was designed and built to form this part at elevated temperatures. A warm forming oven that can heat a single blank with rapid heat up times will also be built as part of the project.

Results and Discussion

There are several different paths for forming 7xxx materials. For roll formed or simple shapes, a room temperature forming path can be used on tempered materials. The complex stamped shape of the baseline steel parts cannot be formed at room temperature in these alloys. This shape could be hot formed using procedures similar to those used for hot forming steel, but with much lower temperatures. The other alternative is to warm form, which means the material forming temperature is less than the solution heat treat temperature of the alloy. This project also stipulated that forming be done at a maximum temperature of 225°C, which falls into the warm forming range. Therefore, the 7xxx alloy would be provided temper with a strength level close to the final requirement and the blank will be heated to no more than 225°C. The impact of time at elevated temperatures relative to the ultimate tensile strength was evaluated using a baseline 7055 material (see Figure III.5-2). This plot includes the warm forming (referred to as WF in Figure III.5-2) temperature at various times with a paint bake (referred to as PB in Figure III.5-2) cycle.

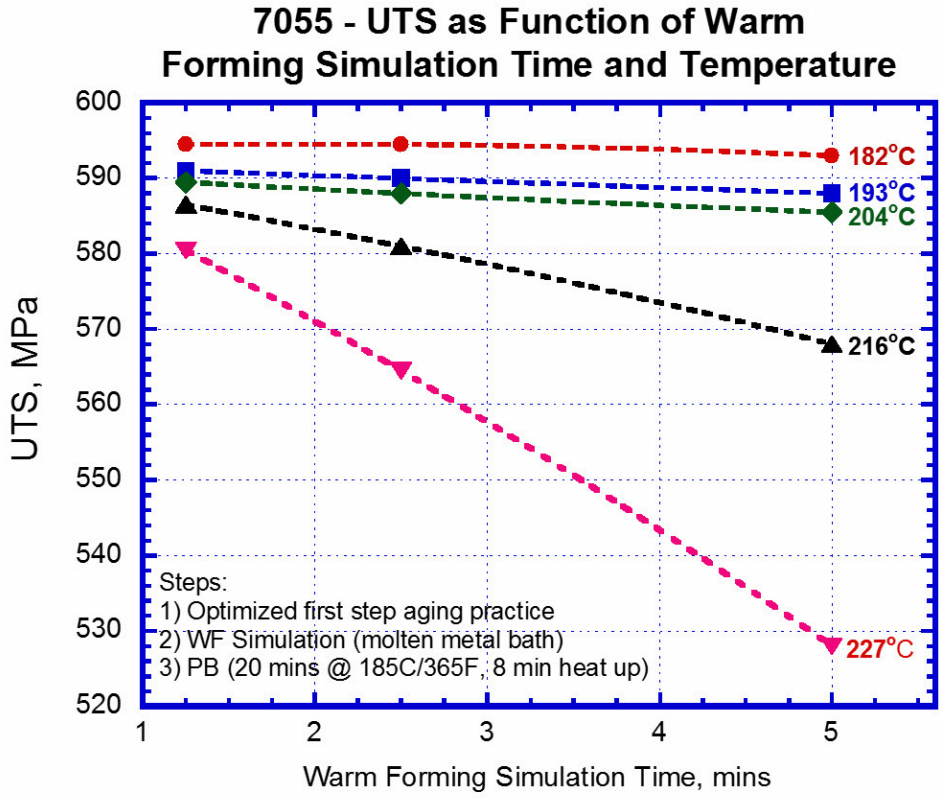

Figure III.5-2. Impact of warm forming temperature and time on ultimate tensile strength of 7055.

Both direct chill ingot approach and the Arconic Micromill™ (continuous casting) produced alloys that would meet the material properties in the vehicle after warm forming and paint bake cycles.

All experimental alloys exceeded the strength of the plant-processed 7055-T76, which is the highest strength 7xxx alloy commercially available. The measured mechanical properties of some of the development alloys are shown in Figure III.5-3.

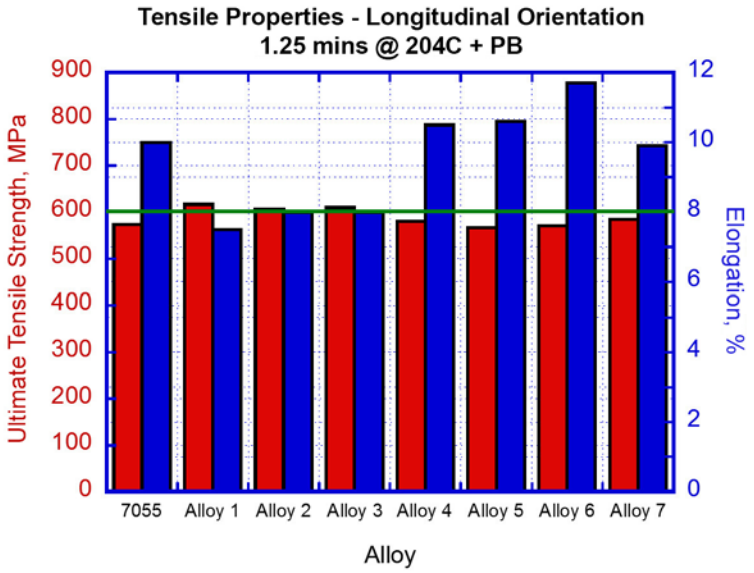

Figure III.5-3. Experimental alloy tensile properties – L orientation - warm formed for 1.25 minutes at 204°C + paint bake cycle.

These property measurements were conducted at a specific warm forming time and temperature, followed by the paint bake cycle. The impact of the different warm forming times and temperature has been used in developing the furnace specification. The furnace must have a rapid heat up rate to prevent reductions in properties. This has been labeled as warm forming time, but it should be thought of as time versus temperature during forming operation. An oven was designed to heat the blanks (see Figure III.5-4).

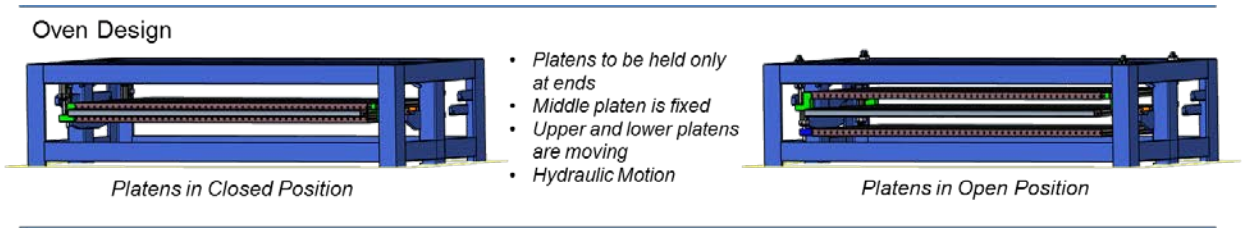

Figure III.5-4. Oven design.

Because the 7xxx material will be warm formed, it will be supplied in a near final temper; therefore, the time the blank is held in the oven must be controlled to prevent overaging. The oven was designed to accommodate a maximum blank size of 2,200 mm x 1,900 mm, based on the full door ring part with temperature control within 5˚C. The blank is in contact with the platens for rapid heat up and good control. The oven design is modular; therefore, multiple copies of the oven could be stacked for high rate production.

The oven has been built, shipped to Eagle Bend Manufacturing, and installed in an existing press line. The oven and robotic loading and unloading system have been tested.

All promising experimental alloys have also been evaluated based on several different corrosion tests. These samples were all tested uncoated. This testing includes an evaluation of exfoliation using American Society of Testing and Materials (ASTM) G110, with results shown in Figure III.5-5. The depth of attack obtained for the experimental alloys is considered acceptable in this case because it is less than 200 µm. These alloys were also evaluated using ASTM G44 for stress corrosion cracking. These results are shown in Table III.5-1. All samples were stressed to 75% of the tensile yield strength and subjected to salt spray. Table III.5-1 indicates the days to failure under accelerated testing. Samples noted as OK221 indicate samples were pulled from test without failure after 221 days. Alloy selection for full-scale trials was based on the combination of corrosion and strength.

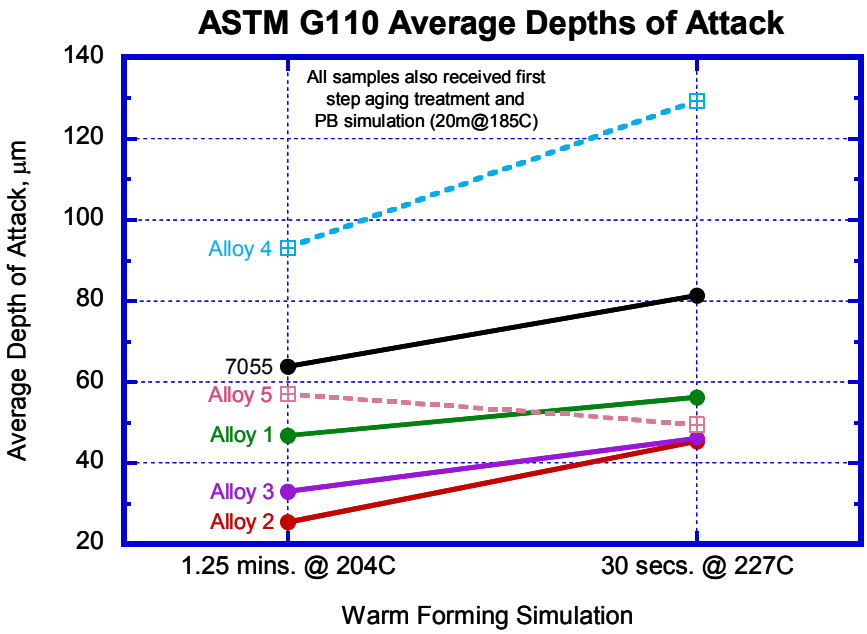

Figure III.5-5. ASTM G110 average depth of attack results for the experimental alloys.

Table III.5-1. ASTM G44 "Mini-Direct" Stress Corrosion Cracking Test Results for Experimental Alloys

Alloy	Stress Level (% of TYS)	Days to Failure 1.25 mins @ 204°C			Days to Failure 30 secs @ 232°C		
7055	75	23	31	34	154	89	31
Alloy 1	75	20	51	41	44	31	30
Alloy 2	75	OK221	162	OK221	OK221	47	72
Alloy 3	75	23	41	35	26	41	OK221
Alloy 4	75	47	37	40	OK90	OK90	37
Alloy 5	75	57	30	33	47	37	57
Alloy 6	75	26	26	37	34	37	45
Alloy 7	75	29	29	29	26	26	26

Four new alloys (i.e., 2, 4, 5, and 6) have been produced for use during the forming trial and 7055 will be included in the trial as a baseline material. Forming tooling has been completed (see Figure III.5-6).

Forming trials will explore the impact of forming temperature, lubricant, and tooling temperature on each alloy. The goal of a trial is to develop robust procedures to produce this part and evaluate the performance of each alloy. Ultimately, the forming trial will determine which alloy is the most formable. Then the parts produced using each experimental alloy will be cut up and mechanically tested. Coupons cut from these parts also will be subjected to corrosion tests to verify that earlier test results are representative of performance in the final part.

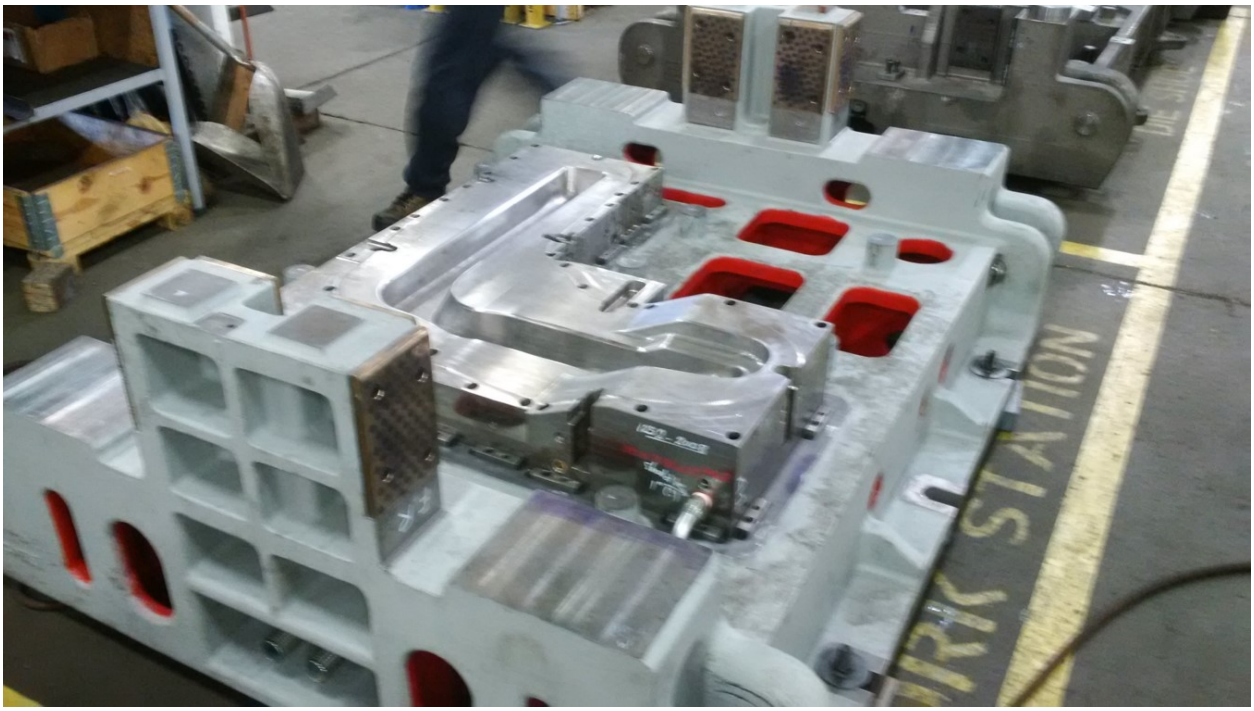

Figure III.5-6. Demonstration part tooling.

Technology Transfer Path

The project is based on an existing ultra high-strength door ring in Honda vehicles. The project will demonstrate the weight reduction, production method, and cost implications of converting this component to high-strength aluminum. The new alloy will be produced at Arconic's existing production facilities. The forming trials will be conducted at Cosma (i.e., the current production supplier of hot-stamped steel components). Both Arconic and Cosma are committed to production of high-strength aluminum components. This project serves as a means of developing the part requirements with Honda and information needed to demonstrate the feasibility of this approach. Arconic will produce the experimental alloy for supply to the automotive industry once strength, formability, and cost feasibility is demonstrated.

Conclusion

During the second year of the contract, multiple experimental alloys were characterized following a simulated warm forming cycle and paint bake cycle. Several candidate alloys were identified as reaching the specifications. These alloys have undergone corrosion testing and formability characterization. The forming tooling and oven for heating the blanks have been fabricated and installed on a pressline. Four experimental materials were provided in full-scale blanks for the forming trials. The forming trials are beginning and, once complete, the properties within the formed part will be tested. The forming trials will also better define the temperature profile and verify the forming simulation.

III.6 High-Throughput Study of Diffusion and Phase Transformation Kinetics of Magnesium-Based Systems for Automotive Cast Magnesium Alloys – Ohio State University

Project Details

Alan A. Luo, Principle Investigator
Ohio State University
137 Fontana Labs, 116 W. 19th Ave.
Columbus, OH 43210
Phone: 614-292-5629
E-mail: luo.445@osu.edu

Ji-Cheng Zhao, Principle Investigator
Ohio State University
286 Watts Hall, 116 W. 19th Ave.
Columbus, OH 43210
Phone: 614-292-9462
E-mail: zhao.199@osu.edu

Adrienne Riggi, Project Officer
National Energy Technology Laboratory
3610 Collins Ferry Road P.O. Box 880
Morgantown, WV 26507-0880
Phone: 304-285-5223
E-mail: Adrienne.riggi@netl.doe.gov

William Joost, DOE Technology Development Manager
U.S. Department of Energy
1000 Independence Ave., S.W.
Washington, DC 20585
Phone: 202-287-6020
E-mail: william.joost@ee.doe.gov

Contractor: Ohio State University, CompuTherm LLC (Madison, WI)
Contract No.: DE-EE0006450

Executive Summary

The objective of the proposed study is to establish a scientific foundation for kinetic modeling of diffusion, phase precipitation, and casting/solidification in order to accelerate design and optimization of cast magnesium (Mg) alloys for weight reduction of the U.S. automotive fleet. The team will (1) study diffusion kinetics of six Mg-containing binary systems using high-throughput diffusion multiples to establish reliable diffusivity and mobility databases for the Mg-aluminum (Al)-zinc (Zn)-tin (Sn)-calcium (Ca)-strontium (Sr)-manganese (Mn) system; (2) study precipitation kinetics (i.e., nucleation, growth, and coarsening) using both innovative dual-anneal diffusion multiples and cast model alloys to provide large amounts of kinetic data (including interfacial energy) and microstructure atlases to enable implementation of the Kampmann-Wagner numerical model to simulate phase transformation kinetics of non-spherical/non-cuboidal precipitates in Mg alloys; (3) implement a micromodel to take into account back diffusion in the solid phase in order to predict microstructure and micro-segregation in multicomponent Mg alloys during dendritic solidification, especially under high pressure die-casting (HPDC) conditions; and (4) widely disseminate data, knowledge, and information using the

Materials Genome Initiative infrastructure (http://www.mgidata.org) and publications and digital data sharing to enable researchers to identify new pathways/routes for better casting Mg alloys.

Accomplishments

- Prepared liquid-solid diffusion couples, including Mg-MgY, MgGd, MgCe, MgMn, and Li systems. Heat treatments were conducted at various temperatures to generate diffusion profiles for electron probe microanalysis (EPMA) (Fiscal Year [FY] 2016).
- Employed forward-simulation analysis to extract diffusion coefficients from diffusion profiles measured by EPMA. Diffusion data for Mg-Al, Zn, and Sn systems were further optimized. Diffusion data for the Mg-Y system were extracted. The first set of experimental diffusion data for the Mg-Ca system was obtained (FY 2016).
- Developed the first version of Mg atomic mobility database, using the CALculation of PHAse Diagrams (CALPHAD) approach, based on a CALPHAD assessment and optimization of data from experiments within this project and literature. This version includes 11 elements and has been extended to include attractive rare earth elements Ce, Gd, La, Nd, and Y. It was used in design of a solution treatment for AT72 (Mg-7Al-2Sn, wt.%) and ATS (Mg-7Al-2Sn-xSi) alloys and precipitation and solidification simulations (FY 2016).
- Updated previous precipitation simulations on AZ91 alloy (Mg-9Al-1Zn) and Mg-Sn alloys using the PanPrecipitation module developed in the Pandat™ software package and this new atomic mobility database. The PanPrecipitation module and a simple method for treating non-spherical/non-cuboidal precipitates have been reasonably and successfully tested on single precipitate precipitation (such as $Mg_{17}Al_{12}$ in AZ91 alloy and Mg_2Sn in Mg-Sn alloys) (FY 2016).
- Micro-alloyed AT72 alloy with elements, including Zn, Ag, Ca, and Cu and the age hardening responses were investigated (FY 2016).
- Compiled the micro-segregation data for Mg-Al, Mg-Al-Ca, and Mg-Al-Ca-Sn alloys from literature and our experiments. The PanSolidification module (i.e., micromodel incorporating back diffusion and cooling rate) was further developed and used to simulate solidifications of several binary Mg-Al and ternary Mg-Al-Ca alloys prepared by directional solidification (FY 2016).
- Prepared the HPDC AT72 alloy for characterization of micro-segregation to provide data for extension of the PanSolidification module to be applicable to simulations on the industrial solidification process (FY 2016).

Future Directions

- Extract diffusion coefficients from newly heat-treated diffusion samples of Mg-Ce, Gd, Mn, and Li systems (FY 2017).
- Further characterize precipitation of the AT72 alloy during aging and improve the previous results. The PanPrecipitation module will be further developed on concurrent precipitation of two precipitates in the AT72 alloy (FY 2017).
- Collect and analyze micro-segregation data from the HPDC AT72 alloy to provide micro-segregation profiles for simulations using PanSolidification module. Further develop the PanSolidification module to make it applicable to simulations not only on multi-component Mg alloys prepared by directional solidification, but also to simulations on alloys prepared by the industrial HPDC process(FY 2017).

Technology Assessment

- Target: Experimentally establish a complete Mg diffusivity/mobility database, including key alloying elements Al, Zn, Sn, Ca, Mn, Sr, and Zr, as well as rare earth elements Y, Ce, and Gd.
- Gap: Some elements are difficult to deal with in experiments. Reliable diffusion profiles cannot be measured using EPMA due to the extremely low solubility of Sr in Mg. Interactions between elements with high melting points and Mg are weak at interfaces because Mn and Zr do not form eutectic with Mg. Rare earth elements are prone to oxidation and Mg-rare earth master alloys are needed.
- Target: Investigate precipitation of the AT72 alloy during aging through a combination of experimentation and simulation.
- Gap: Based on previous experiments, the AT72 alloy is prone to corrosion with twin jet polishing used for making transmission electron microscopy (TEM) samples.
- Target: Develop the PanSolidification module for simulating solidification of multi-component Mg alloys.
- Gap: Issues such as applicability of the model to simulate alloys prepared by industrial casting processes with higher cooling rate need to be investigated and resolved.

Introduction

The lack of diffusivity data for Mg alloys is hindering the computational design of high-performance Mg alloys using integrated computational materials engineering approaches. Compared with Al alloys, information on precipitation kinetics (i.e., nucleation, growth, and coarsening) of Mg alloys is not sufficient and needs to be investigated through a combination of experimentation and simulation. A micro-model incorporating back diffusion and cooling rate is important for accurately simulating solidification of Mg alloys, especially those prepared by industrial casting processes. In FY 2016, solid-liquid diffusion couples for Mg-MgY, MgGd, MgCe, MgMn, and Li systems were prepared and heat treatments were conducted at various temperatures to generate diffusion profiles for EPMA measurement. Diffusivities for Al, Zn, Sn, Ca, and Y were extracted from diffusion profiles by the forward simulation method [1]. Using the CALPHAD approach [2], the first version of the Mg atomic mobility database was developed and used in design of a solution treatment schedule and precipitation and solidification simulations. Simulations on microstructure evolutions of AZ91 and Mg-Sn alloys during aging were updated with the new database. The AT72 alloy was micro-alloyed with Zn, Ag, Ca, and Cu and age hardening responses were measured. The micro-segregation data for the Mg-Al, Mg-Al-Ca, and Mg-Al-Ca-Sn alloys from literature and the current experiment were compiled. The PanSolidification module was used to simulate solidification of several binary Mg-Al and ternary Mg-Al-Ca alloys prepared by directional solidification. The HPDC AT72 alloy was prepared to provide micro-segregation data for further development of the PanSolidification module.

Approach

Diffusion

The novel experimental method, liquid-solid diffusion couple technique, which was designed last year, was fully developed and employed this year. The geometry of a typical liquid-solid diffusion couple and its cross section are shown in Figure III.6-1. Mg alloys(e.g., Mg-Ca and Mg-Y alloys) can be used to assemble liquid-solid diffusion couples besides the pure elements used before such as Al, Zn, and Sn. EPMA was used to measure diffusion profiles from liquid-solid diffusion couples and forward-simulation analysis was employed to extract diffusion coefficients. This year diffusion data of five solutes (i.e., Al, Zn, Sn, Ca, and Y) in Mg were reliably obtained and critically evaluated with available literature data, which lay the foundation for an Mg diffusivity database. Li, Gd, Ce, and Mn were also important alloying elements under study this year.

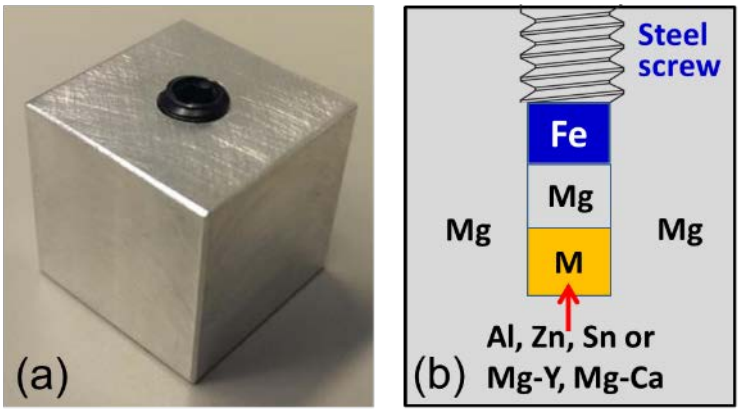

Figure III.6-1. Geometry of a liquid-solid diffusion couple: (a) photo (about 20 x 20 x 25 mm) and (b) schematic of a cross section.

Precipitation

In order to provide temperature and composition-dependent diffusion coefficients for precipitation and solidification simulations or other process designs through coupling to a CALPHAD-type Mg thermodynamic database, a CALPHAD-type Mg atomic mobility database is needed. Diffusion data from experiments in this project and literature were optimized using the CALPHAD approach [2] to generate atomic mobilities. Empirical methods were used to obtain the hypothetic atomic mobility parameters. The first version, including 11 elements, was developed this year. The solution treatment for the AT72 and ATS alloys and precipitations of the AZ91 and Mg-Sn alloys during aging were simulated with this new database. The Kampmann-Wagner-numerical model [3] implemented in the PanPrecipitation module of the Pandat™ software [4] was used in the precipitation simulation. In order to improve precipitation of the AT72 alloy, it was micro-alloyed with Zn, Ag, Ca, and Cu. Gravity casting was used in sample preparation and age hardening responses were measured. Continuing previous work, TEM was used to further characterize the precipitation of the AT72 samples that were prepared by ion milling, which provided better samples than the twin jet polishing method used last year.

Solidification

The estabilshed PanSolidification module was directly coupled with phase diagram calculations incorporating thermodynamic and diffusion effects such as undercooling, solid state back-diffusion, dendrite arm coarsening, and thermodynamic correction of the interface concentrations. Figure III.6-2 shows the flow chart of the PanSolidification module. The input variables for simulation are alloy composition (x), solidification velocity (V), thermal gradient (G), solid/liquid interfacial energy (γ), and latent heat (H). Cooling rate is automatically calculated as $CR=G\times V$. This year the PanSolidification module was used to simulate solidification of several Mg-Al alloys and was extended to simulations on ternary Mg-Al-Ca alloys.Currently, micro-segregations of alloying elements from current experiments and literature are obtained from the samples prepared by directional solidification, which is a well-controlled process and during which the cooling rate is generally below 1K/s. In order to provide data from samples prepared by a real industrial process for calibration of the PanSolidification model, the AT72 sample was prepared by HPDC. It was examined by scanning transmission electron microscope/energy-dispersive x-ray diffraction spectroscopy. Concentrations of Al, Sn, and Mg on 400 points uniformly distributed in an area will be measured by EPMA and the data will be analyzed to extract the micro-segregation profiles of Al and Sn in (Mg).

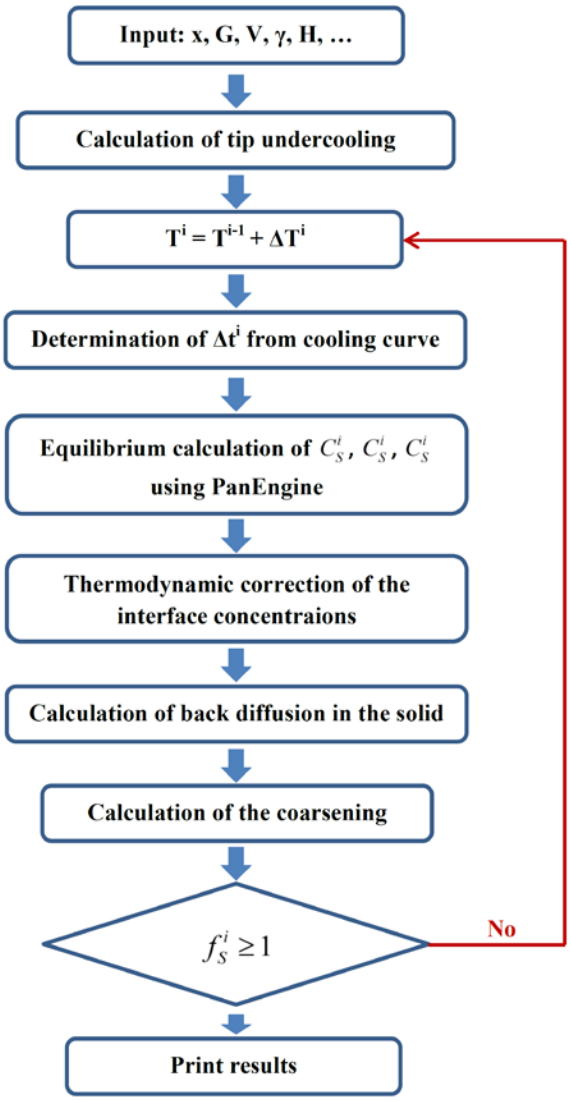

Figure III.6-2. Flow chart of the PanSolidification module.

Results and Discussion

Diffusion

The combined liquid-solid diffusion couples and the forward simulation method were employed to reliably extract diffusion coefficients of Al, Zn, Sn, Y, and Ca in Mg. Our results were critically evaluated with available literature data and also compared with first-principles calculation results. These results can serve as the foundation for reliable Mg alloy diffusion databases.

Diffusion data from Mg-Al, Zn, Sn, Y, and Ca systems and the consentaneous experimental impurity diffusion coefficients expressed by Arrhenius equations for these systems are shown as solid red lines in Figures III.6-3 through 7 and presented in Table III.6-1. These figures and the table also show the solubility of each solute in Mg at the annealing temperatures. Data for Al, Zn, and Sn were further optimized this year. The optimized equation for the Mg-Al system is based on our data; two other diffusion couple studies by Kammerer et al. [5] and Brennan et al. [6], excluding Das et al. [7]; and a study using the secondary ion mass spectrometry by Brennan et al. [8]. As for the Mg-Zn system, the final equation is based on our data; data from diffusion couple from Kammerer et al. [5]; and tracer data from Lal [9] and Čermák and Stloukal [10], excluding data from Das

et al. [11]. The equation for the Mg-Sn system is recommended by fitting our data and tracer data from Combronde and Brebec [12].

Because pure Y is very prone to oxidation, an Mg-25wt.%Y master alloy was used to assemble three Mg-Y liquid-solid diffusion couples, which were annealed at elevated temperatures. The interdiffusion coefficients are constant at each temperature; therefore, they are equal to the impurity diffusion coefficients of Y in Mg. Diffusion data reported by Das et al. [13] obtained from a multi-phase simulation analysis are again significantly lower than our trend values, which is similar to the situations for the Mg-Al and Zn systems. We performed the forward simulations on four original Mg-Y diffusion profiles provided by Das et al. [13] and obtained impurity and interdiffusion coefficients that agree well with our diffusion coefficients, indicating that their experimental profiles for Mg-Y are reliable; however, the analysis process may be problematic. The final Arrhenius equation is determined using our data and re-analyzed data from Das et al. [13].

An Mg-15 wt.% Ca master alloy is used to assemble four Mg-Ca liquid-solid diffusion couples due to the high reactivity of pure Ca. It is worthwhile to note that the solubility of Ca in Mg is extremely limited (as low as 0.08 at.% at 630°C), but is very accurately determined by EPMA composition profiling from these liquid-solid diffusion couples. At such low solubility values, it is reasonable to assume the interdiffusion coefficients are constant at each temperature and are equal to the impurity diffusion coefficients of Ca in Mg. Our data are the first set of experimental impurity diffusion coefficients reported.

Tracer experiments, though laborious and expensive to perform, are usually very reliable in determining the impurity diffusion coefficients. Three sets of tracer experiments were performed for Sn and Zn diffusion in Mg [9, 10, 12].There is excellent agreement between our data and the results of these tracer studies, demonstrating the reliability of our combined approach in obtaining accurate impurity diffusion coefficients.

There are three first-principles studies on impurity (dilute) diffusion coefficients in Mg [14–16] and the calculation results have been compared for each system in Figures III.6-3b, III.6-4b, and III.6-5 through III.6-7. The calculations of Zhou et al. [14] are a recent improvement over those of Ganeshan et al. [15]; therefore, the Ganeshan et al. [15] results are not used in the following comparison. Figure III.6-8 is a comprehensive comparison of all five elements, showing that recent calculations from Zhou et al. [14] and Wu et al. [16] have achieved an impressive accuracy for Al, Sn, and Zn. However, the calculated impurity coefficients of Ca in Mg from both groups are higher than our experimental values and the computed impurity coefficients of Y in Mg from Wu et al. [16] are also higher than our experimental values. The results for Y from Zhou et al. [14] agree well with our experimental data. The calculated diffusion coefficients along the basal plane and along the c-axis are averaged (2/3 basal + 1/3 c-axis) into a single impurity diffusion coefficient for this comparison according to literature [17]. This element-by-element comparison using reliable experimental data is very valuable in identifying ways for improving the reliability of future calculations.

Finally, Figure III.6-9 summarizes the best-judgement/consentaneous experimental impurity diffusion coefficients of Al, Ca, Sn, Y, and Zn in Mg in comparison with the self-diffusion coefficient of Mg [18]. (We again averaged diffusion coefficients along the basal plane and the c-axis into one Arrhenius equation $D_{Mg\ in\ Mg} = 1.66 \times 10^{-4} e^{-138440/RT}$ (m^2/s).) These impurity diffusion coefficients should be very reliable and applicable to a wide range of temperatures. These data and the interdiffusion coefficients obtained in this project and literature data will serve as the foundation for reliable diffusion (mobility) databases for Mg alloys. Among the five elements, Ca has the highest and Zn has the second highest impurity diffusion coefficient in Mg; both are higher than the Mg self-diffusion coefficient. In the absence of experimental diffusion data, Ca often has been assumed to be a slow diffuser in Mg as rare earth elements. However, our results clearly show that Ca diffusion in Mg is significantly faster than Mg self-diffusion, which is faster than Al diffusion in Mg. The fast Ca diffusion may be a disappointment to researchers who assumed slow Ca diffusion in Mg may help achieve high creep strength in Ca-alloyed Mg alloys for high-temperature applications. Both Al and Sn have very similar impurity diffusion coefficients in Mg and they diffuse slower than the Mg self-diffusion. Y diffusion in Mg is slightly slower than Al and Sn at high temperatures, but is about the same as Sn below 390°C. Therefore Y may not be as a potent of an element for enhancement of creep strength of Mg alloys as has been often expected.

Table III.6-1. Maximum Solubility of Al, Zn, Sn, Y, and Ca in Mg and Recommended Impurity Diffusion Coefficients as Arrhenius Equations (in m^2/s with Temperature T in Kelvin and the Gas Constant R = 8.314 J K–1 mol–1)

System	Solubility (at.%) of Solute at Annealing Temperature (°C)	Impurity Diffusion Coefficient as Arrhenius Equation
Mg-Al	10.3, 7.2, 4.6, 2.5 at.% Al at 450, 500, 550, 600 °C	$D_{Al\ in\ Mg} = 2.0 \times 10^{-4} e^{-146000/RT}$
Mg-Zn	3.5, 2.6, 1.7 at.% Zn at 450, 500, 550 °C	$D_{Zn\ in\ Ma} = 0.87 \times 10^{-4} e^{-125000/RT}$
Mg-Sn	0.8, 1.1, 2.0, 4.1, 2.6 at.% Sn at 375, 420, 500, 550, 600 °C	$D_{Sn\ in\ Ma} = 1.08 \times 10^{-4} e^{-140900/RT}$
Mg-Y	1.9, 1.0, 0.6 at.% Y at 590, 610, 630 °C	$D_{Y\ in\ Ma} = 0.08 \times 10^{-4} e^{-126700/RT}$
Mg-Ca	0.44, 0.26, 0.22, 0.08 at.% Ca at 530, 580, 600, 630 °C	$D_{CainMa} = 0.06 \times 10^{-4} e^{-103700/RT}$

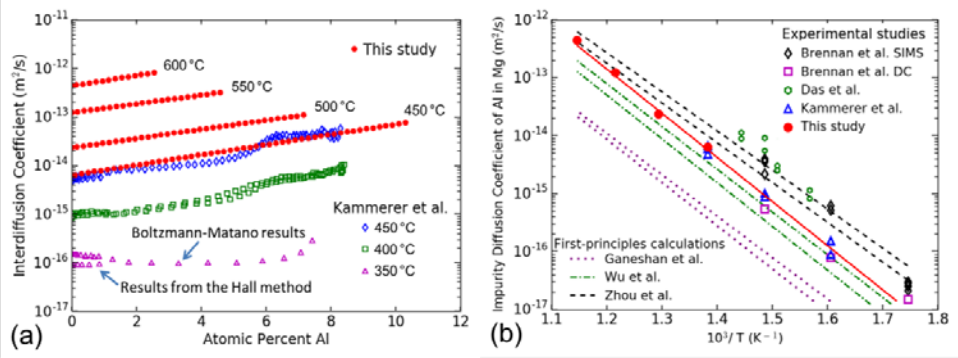

Figure III.6-3. Results for the Mg-Al system: (a) interdiffusion coefficients for the hexagonal close packed phase of the Mg-Al system and (b) comparison of experimental impurity diffusion coefficients of Al in Mg with first-principles calculations.

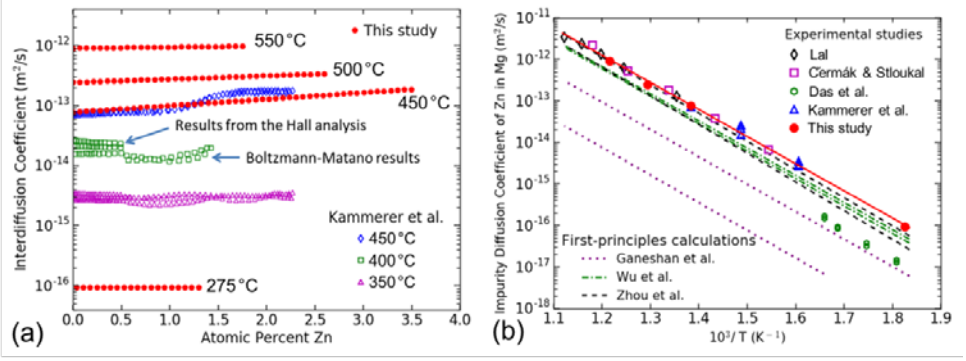

Figure III.6-4. Results for the Mg-Zn system: (a) interdiffusion coefficients for the hexagonal close-packed phase of the Mg-Zn system and (b) comparison of experimental impurity diffusion coefficients of Zn in Mg with first-principles calculations.

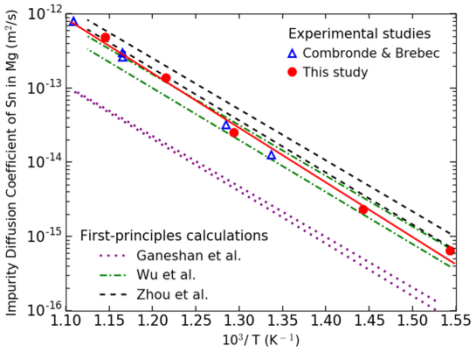

Figure III.6-5. Comparison of experimental impurity diffusion coefficients of Sn in Mg with first-principles calculations.

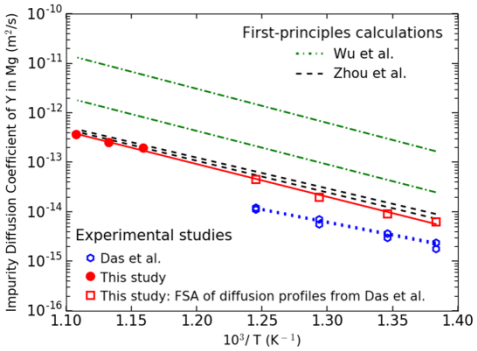

Figure III.6-6.Comparison of experimental impurity diffusion coefficients of Y in Mg with first-principles calculations.

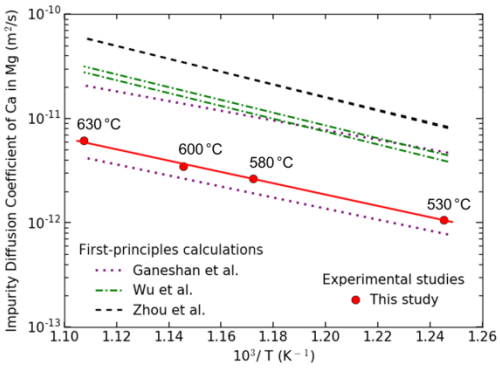

Figure III.6-7. Comparison of experimental impurity diffusion coefficients of Ca in Mg with first-principles calculations.

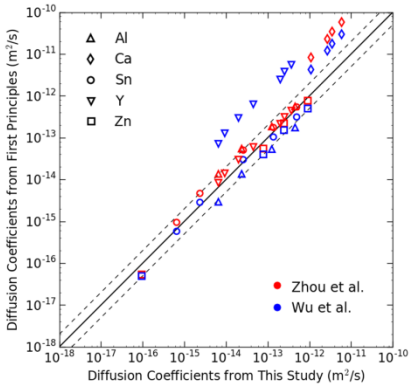

Figure III.6-8. Comparison of the experimental impurity diffusion coefficients with first-principles calculations (The dashed lines refer to values that are either twice as much or half the values).

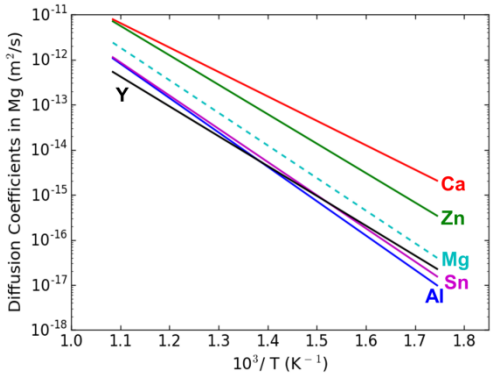

Figure III.6-9. Comparison of the best judgment impurity diffusion coefficients of Al, Zn, Sn, Y, and Ca in Mg with the self-diffusion coefficient of Mg.

Precipitation

The first version of CALPHAD-type Mg atomic mobility database for precipitation and solidification simulations includes not only common non-rare earth metals Al, Zn, Sn, Mn, Ca and Sr, but also has been extended to include attractive rare earth metals Ce, Gd, La, Nd and Y, which could significantly increase the strength of Mg alloys compared to non-rare earth Mg alloys. During the CALPHAD optimization, the experimental interdiffusion coefficients from this project and literature of Mg-Al, Zn, Y and Gd systems were used to optimize the interaction terms of the atomic mobility parameters. For Sr, the atomic mobility parameter related to impurity diffusion coefficient is directly obtained from first principles calculations [14] since the experiment data are not available. In addition, the interaction term of Al and Zn in Mg is also considered based on the experimental data for ternary MgAlZn systems [19]. This database is being used and tested in heat treatment design, precipitation and solidification simulations. Figures III.6-10 and III.6-11 show that the calculated diffusion coefficients from this atomic mobility database can reproduce most of the experimental results for Mg-Al-Zn [10, 19] and Mg-Gd alloys [19].

Figures III.6-12 and III.6-13 show one case of using the Mg atomic mobility database to assist the design of solution treatment schedule for Mg alloys. The as-cast microstructure of HPDC ATS alloy shown in Figure III.6-13a exhibits strong segregations of Al and Sn in the grain boundary. Figure III.6-12 shows the simulated composition profiles of Al and Sn in (Mg) during solution treatment at 420°C, which indicates that Al and Sn segregating in the boundary in the as-cast microstructure could be dissolved after 8 hours at 420°C. The as-annealed microstructure presented in Figure III.6-13b demonstrates that the segregation "cloud" in the as-cast microstructure disappears and the elements Al and Sn segregating in the boundary are dissolved into (Mg) matrix after 8 hours at 420°C.

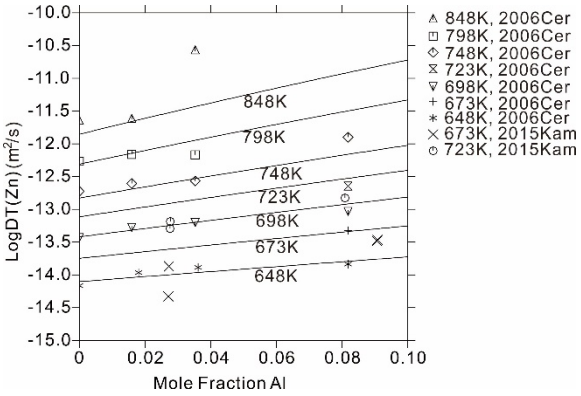

Figure III.6-10. Calculated impurity diffusion coefficients of Zn inMg-Al alloys with the experimental results [10, 19].

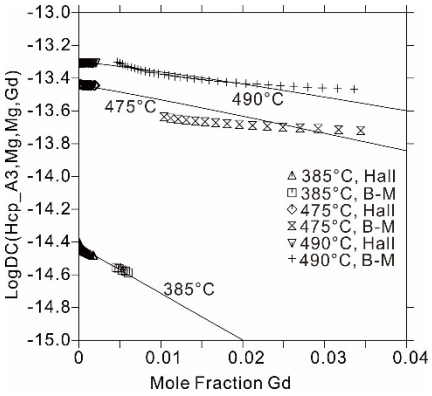

Figure III.6-11. Calculated interdiffusion coefficients in Mg-Gd alloys with the experimental results [19]. The abbreviation B-M represents Boltzmann-Matano method.

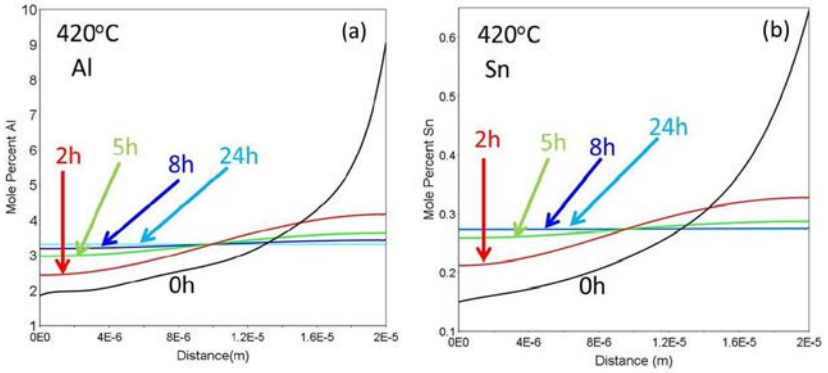

Figure III.6-12. Simulated composition profiles of Al (a) and Sn (b) in (Mg) matrix during solution treatment at 420°C.

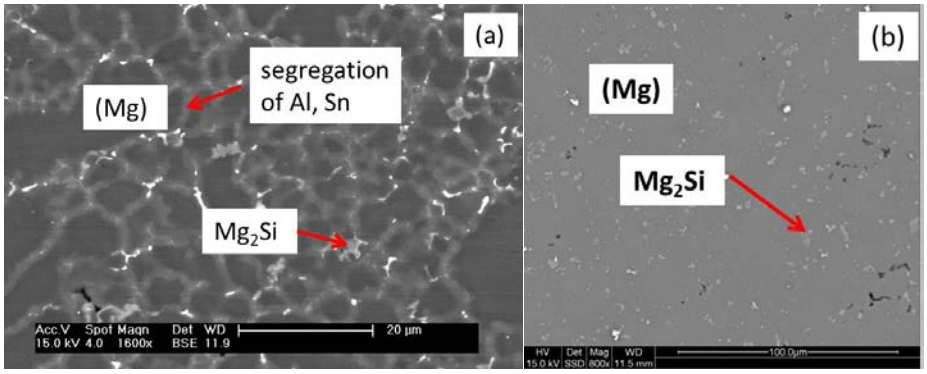

Figure III.6-13. Back scattered electron images of as-cast microstructure (a) and as-annealed microstructure at 420°C for 8 hours (b). The Mg_2Si is a highly stable phase and is not dissolved.

Figure III.6-14 shows the calculated diffusion coefficients at the common precipitation temperature of 200°C from currently more accurate new database are half of the previous calculated values as the Al composition is not large. Thus, the previous simulations on AZ91 and two Mg-Sn alloys were updated using the new database and the results are shown in Figures III.6-15 and III.6-16. The number density of $Mg_{17}Al_{12}$ in AZ91 alloy is between about 10^{19}-$10^{20}/m^3$. However, the precipitation of Mg_2Sn in binary Mg-Sn alloys is very sluggish. Not only the number density is as lower as $10^{18}/m^3$, but also the time to reach maximum number density is much longer. Previous investigation on precipitation of AT72 alloy shows that the precipitation of Mg_2Sn is enhanced as the Al may have positive effect on the precipitation of Mg_2Sn. During this year, the ion milling method was employed to replace twin jet polishing for TEM sample preparation. It is found that the quality of TEM sample is significantly improved. Figure III.6-17 shows the scanning transmission electron microscope/energy-dispersive x-ray diffraction spectroscopy characterization of HPDC AT72 microstructure

aged at 200°C for 72 hours, which clearly further demonstrates the precipitation of Mg_2Sn is enhanced and could be comparable to that of $Mg_{17}Al_{12}$. The counting and analysis of number density is going on and the data will be used to calibrate the simulation on precipitation of AT72 alloys.

The AT72 alloys micro-alloyed with Zn, Ag, Cu and Ca were prepared by gravity casting using steel mold. The age hardening responses are shown in Fig. 18. Small amount of Zn (0.6 wt.%) and Ag (0.7 wt.%) can accelerate the age hardening of AT72 alloys. Large amount of Ag (4 wt.%) further increases the hardness, but not significantly. Cu enhances the hardness, but doesn't accelerate the aging response. Ca has negative effect on the age hardening.

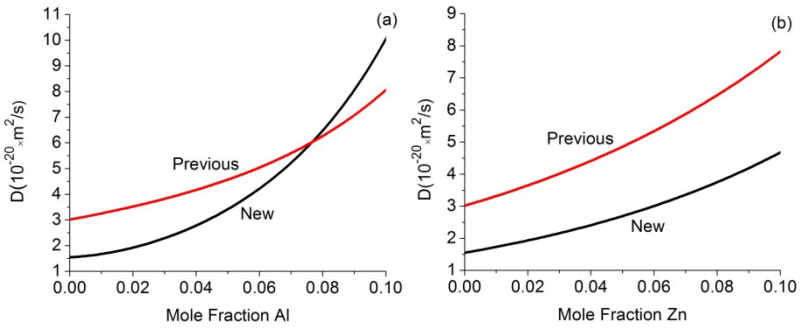

Figure III.6-14. Calculated interdiffusion coefficients of Mg-Al alloys (a) and impurity diffusion coefficients of Al in Mg-Zn alloys (b) at 200oC.

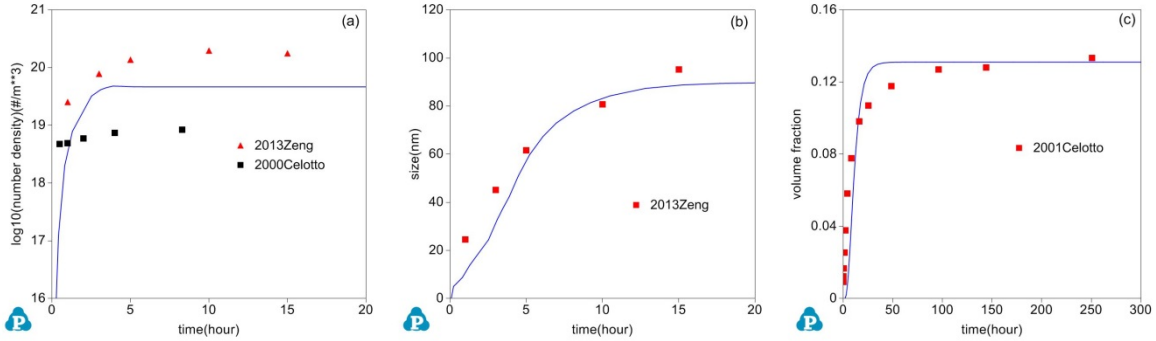

Figure III.6-15. Simulated microstructure of AZ91 alloys during aging at 200°C using the new databasewith experimental data [20-22]. (a) Number density; (b) Precipitate size; (c) Volume fraction.

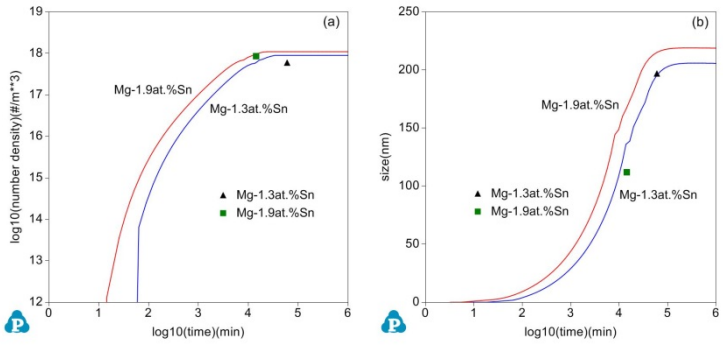

Figure III.6-16. Simulated microstructure of Mg-Sn alloys during aging at 200°C using the new database with experimental data [23]. (a) Number density; (b) Precipitate size.

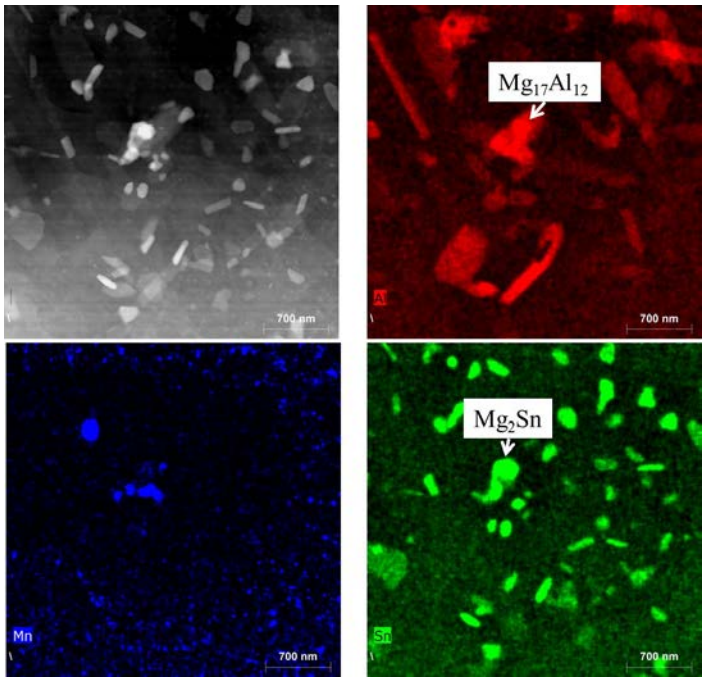

Figure III.6-17. Scanning transmission electron microscope/energy-dispersive x-ray diffraction spectroscopy characterization of HPDC AT72 microstructure aged at 200°C for 72 hours.

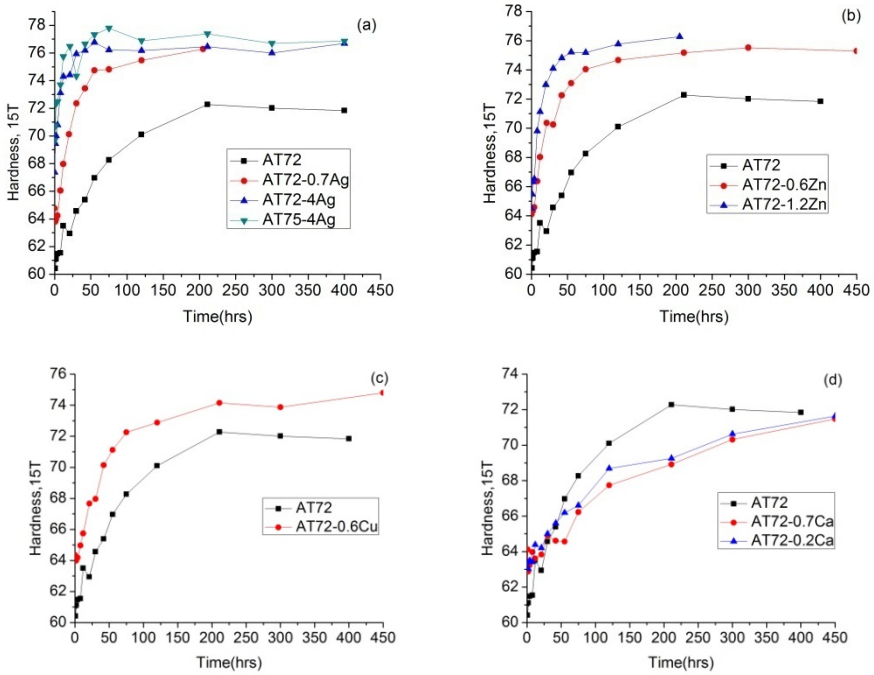

Figure III.6-18. Age hardening responses of AT72 alloys micro-alloyed with Ag, Zn, Cu and Ca. (a) Ag; (b) Zn; (c) Cu; (4) Ca.

Solidification

The micro-segregation data for Mg-Al, Mg-Al-Ca, and Mg-Al-Ca-Sn alloys that are prepared by directional solidification from literature [24-27] and current experiments were collected and compiled. Table III.6-2 lists the experimentally investigated Mg-Al and Mg-Al-Ca alloys in literature [24-27] under various cooling rates. Solidification simulations were carried out on these binary and ternary alloys this year.

Table III.6-2. Alloys Experimentally Investigated in Literature and Simulated during this Period

Alloy Composition (wt.%)	Thermal Gradient (K/m)	Solidification Velocity (m/s)
Mg-3Al	$7.5x10^3$	$5.0x10^{-5}$
Mg-3Al	$4.26x10^2$	$2.58x10^{-3}$
Mg-4Al	$4x10^3$	$5.0x10^{-5}$
Mg-4Al	$4x10^3$	$2.0x10^{-4}$
Mg-6Al	$7.5x10^3$	$5.0x10^{-5}$
Mg-6Al	$4.26x10^2$	$2.58x10^{-3}$
Mg-9Al	$7.5x10^3$	$5.0x10^{-5}$
Mg-9Al	$4.26x10^2$	$2.58x10^{-3}$
Mg-4Al-4Ca	$4x10^3$	$5.0x10^{-5}$
Mg-4Al-4Ca	$4x10^3$	$1.0x10^{-4}$
Mg-5Al-3Ca	$4x10^3$	$1.0x10^{-6}$
Mg-5Al-3Ca	$4x10^3$	$3.0x10^{-5}$
Mg-5Al-3Ca	$4x10^3$	$1.0x10^{-4}$

Figures III.6-19 and III.6-20 show the calculated concentration profiles using different models (i.e., Scheil, plate, cylinder, sphere) for the two Mg-Al binary alloys listed in Table III.6-2. Experimental data obtained [25] under different cooling rates are also plotted on these figures for comparison. Three dendrite arm geometries (i.e., plate, cylinder, and sphere) were considered in this present study. The morphology and scale of the dendrite structure are of crucial importance because they strongly influence the extent of back diffusion.

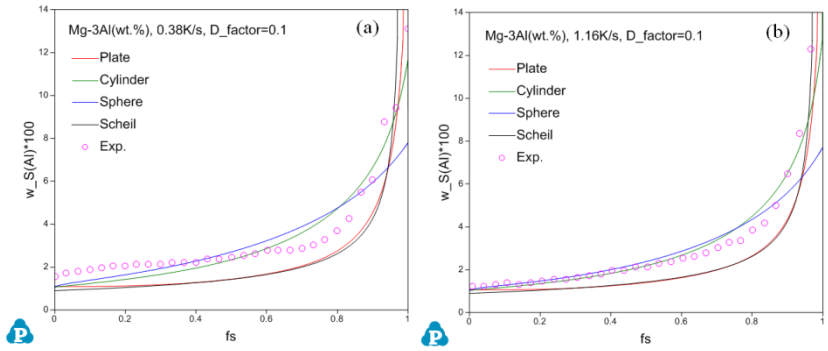

Figure III.6-19. Simulated concentration profiles of Mg-3wt.% Al using different models with experimental data under different cooling rates: (a) 0.38K/s and (b) 1.16K/s.

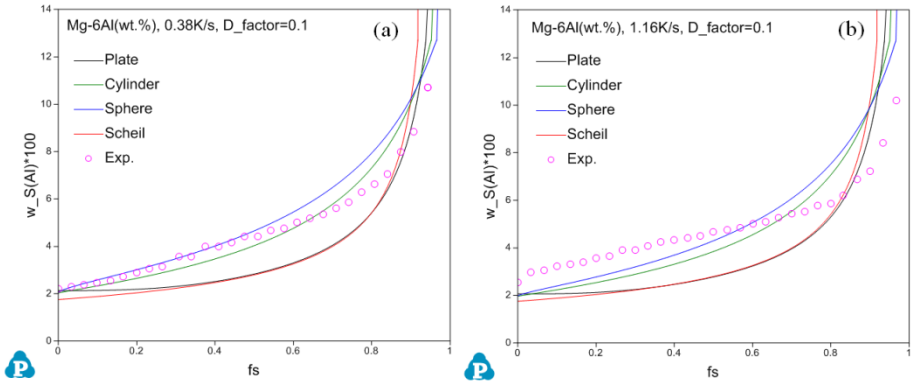

Figure III.6-20. Simulated concentration profiles of Mg-6wt.%Al using different models with experimental data under different cooling rates: (a) 0.38K/s and (b) 1.16K/s.

The results indicate that the calculated concentration profiles using the Scheil model show large discrepancies with the experimental measurements. With the back-diffusion effect, the calculated values show better agreement with the experiments. In most cases, the sphere model yields the best agreement with the experimental data, especially at the lower fractions of solid. On the other hand, calculated data using plate geometry are in better agreement with experimental data at higher fractions of solids. The trend of the cylinder

model is in the middle of both sphere and plate models. It is well known that the formation and growth of the secondary arms at the earlier stage is in particle shape, the dendrite arm lengths are limited, and the end effects play an important role. Therefore, the sphere arm morphology is the best to approximate the shape of the dendrite arms at this stage. As the dendrite arm continues to grow, the end effects become less important and the plate model is a better approximation. This is the reason none of these models can describe the experimental data perfectly during the whole process. However, development of a new morphology model for better describing the dendritic morphology at different solidification stages is far more complex and beyond the scope this project.

In addition to the concentration profiles, the simulated secondary dendrite arm spacing (SDAS) versus the measured values are shown in Figure III.6-21, which shows that the calculated SDAS values are slightly greater than the experimental measurements. This is because we use the constant interfacial energy for simplicity and extendibility of the current PanSolidification module. As discussed in [28], the interfacial energy decreases with an increasing Al concentration. The values used are the same as derived for 3wt.% Al, which is greater than that of higher Al concentrations (4, 6, and 9wt.%Al). Therefore, the calculated SDAS are slightly greater than the measured values. Comparison between the calculated and measured fraction of interdendritic phases is shown in Figure III.6-22. This indicates that the plate model works better for the lower Al concentration and the sphere model is better for the higher Al concentration.

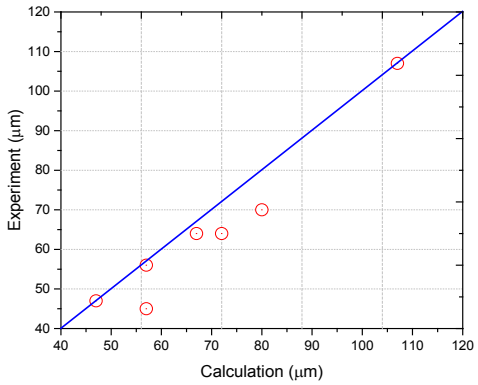

Figure III.6-21. Comparison between the measured and simulated SDAS of the Mg-Al binary alloys.

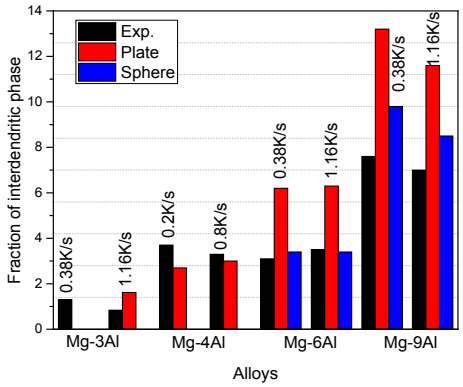

Figure III.6-22. Comparison between the measured and simulated fraction of the interdendritic phase region

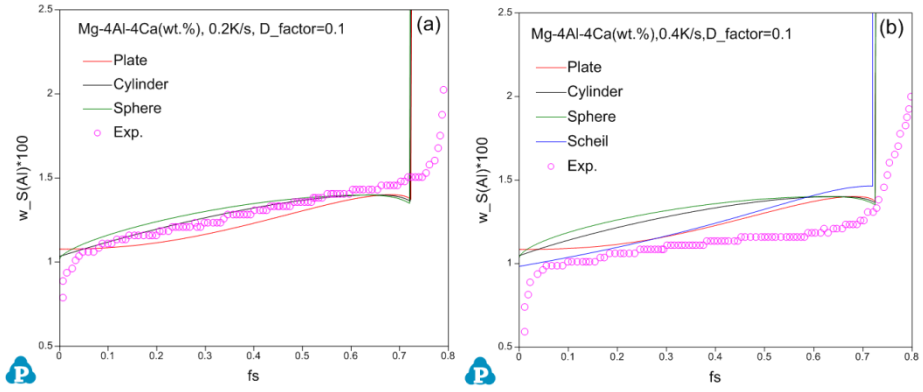

Figure III.6-23. Simulated concentration profiles of Mg-4Al-4Ca (wt.%) using different models with experimental data under different cooling rates: (a) 0.2K/s and (b) 0.4K/s.

Without adjusting any solidification parameters, the concentration profiles of the Mg-Al-Ca ternary alloys are simulated using various models (Figure III.6-23). The experimentally measured data are superimposed in Figure III.6-23 as well. As shown in Figure III.6-23a, the simulated concentration profiles are in good agreement with the experimental data for the Mg-4Al-4Ca alloy at the cooling rate of 0.2K/s, while a large discrepancy is found between the simulated data and experimental values at the cooling rate of 0.4K/s as

shown in Figure III.6-23b. Here, the experimentally measured concentration profile of Mg-4Al-4Ca at 0.4K/s is even lower than the Scheil simulations, which indicates experimental data may not be accurate. Comparison between the simulated and measured SDAS for the Mg-Al-Ca alloys is shown in Figure III.6-24, which indicates that the simulated values are in good agreement with the experimentally measured data.

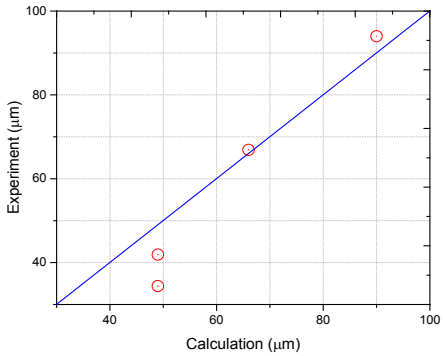

Figure III.6-24. Comparison between the measured and simulated SDAS of the Mg-Al-Ca ternary alloys.

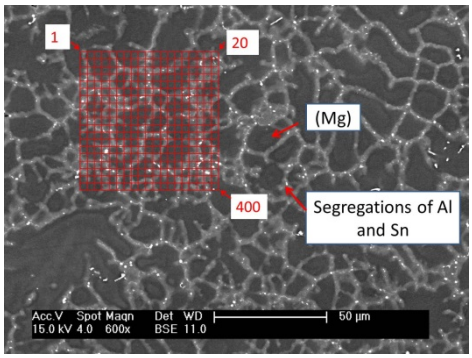

Figure III.6-25. Back-scattered electron image of the as-cast microstructure of the AT72 alloy prepared by HPDC and the EPMA measurement plan.

The above solidifications are performed on alloys prepared by directional solidification, which is a well controlled process and the cooling rate is usually below 1K/s. This directional solidification is far from an industrial solidification process (such as gravity casting with permanent mold and HPDC) during which the cooling rate is much higher. In order to further calibrate the PanPrecipitation module for prediction of solidification in an industrial process, the micro-segregation of alloying elements in the Mg alloys prepared by industrial process are needed. In this work, the AT72 was prepared by HPDC. As shown in Figure III.6-25, the microstructure exhibits strong segregation of alloying elements in the grain boundary, which is quite different from that of directional solidification. The compositions at 400 points uniformly distributed in an area covering several grains are measured by EPMA and the micro-segregation profiles of alloying elements will be extracted. Characterization is currently occurring on and results will be obtained soon. There is one issue regarding cooling rate during HPDC, which could not be measured experimentally during the casting process. Casting simulation software ProCAST was used to simulate the casting process and generate the cooling rate. The thermo-physical parameters (such as heat transfer coefficient) were calibrated by gravity casting using steel mold to guarantee the input parameters are valid for HPDC simulation.

Technology Transfer Path

The diffusivities measured during this work significantly improve the Mg alloys diffusivity database, which is rather inadequate when compared with that of Al alloys. These experimental data lay the foundation for investigation of diffusion of an alloying element in Mg and can assist the design of high-performance Mg alloys using an integrated computational materials engineering approach.

Through coupling to an Mg thermodynamic database, the established CALPHAD-type Mg atomic mobility database can conveniently calculate or extrapolate composition and temperature-dependent diffusion coefficients for precipitation and solidification simulations or other process designs. This database is currently test-run by CompuTherm for further improvement. The fully validated database will be published and submitted to the materials genome initiative repository at the National Institute of Standards and Technology.

Research on precipitation and micro-alloyingof the AT72 alloy indicates (1) precipitation of Mg_2Sn can be strengthened in the AT72 alloy and (2) Zn and Ag may further improve the age hardening response of the AT72 alloy. Zn may need to be controlled carefully to avoid hot cracking. These findings are being used in the optimization of Mg-Al-Sn-Si alloys for automotive applications in collaboration with General Motors.

The PanPrecipitation module developed during this project can be used to simulate the precipitation of Mg alloys during aging. This model can be used in integrated computational materials engineering design of new Mg alloys and their heat treatment process parameters.

The PanSolidification module can be used to more accurately predict the microstructure evolution of Mg alloys during casting processes such as solidification path, micro-segregation, and second arm spacing once fully developed.

Conclusions

Reliable diffusivities for Mg-Al, Zn, Sn, Ca, and Y systems were obtained through a combination of solid-liquid diffusion couples and forward simulations. Liquid-solid diffusion couples, including Mg-MgY, MgGd, MgCe, MgMn, and Li systems, were prepared. Heat treatments were conducted at various temperatures to generate diffusion profiles for EPMA.

The first version of the CALPHAD-type Mg atomic mobility database, including 11 elements within this project, was finished based on an assessment and optimization of data from experiments within this project and literature. This new database was used during design of a solution treatment schedule and precipitation and solidification simulations of Mg alloys.

Further characterization on precipitation of the AT72 alloy using ion-milled TEM samples demonstrates the precipitation of Mg_2Sn can be strengthened in the AT72 alloy. Micro-alloying experiments on the AT72 alloy show that Zn and Ag have a positive effect on the age-hardening response of AT72 alloys. The PanPrecipitation module and the simple method for treating non-spherical/non-cuboidal precipitates have been successfully tested on single precipitate precipitation in the AZ91 alloy and Mg-Sn alloys, respectively. The module is being developed on concurrent precipitation of two precipitates.

The PanSolidification module was further developed and used to simulate solidifications of several binary Mg-Al and Mg-Al-Ca alloys prepared by directional solidification. The HPDC AT72 alloy was prepared to provide micro-segregation data for extension of the PanSolidification module to be applicable to simulations on the industrial solidification process.

References

[1] Zhang, Q. and J. C. Zhao, 2013, "Extracting Interdiffusion Coefficients from Binary Diffusion Couples Using Traditional Methods and a Forward-Simulation Method," *Intermetallics*34: 132-141, http://www.sciencedirect.com/science/article/pii/S0966979512004293.

[2] Saunders, N. and A. P. Miodownik (eds.), 1998, *CALPHAD (Calculation of Phase Diagrams): A Comprehensive Guide*, Oxford: Pergemon Press.

[3] Kampmann, R. and R. Wagner, 1983, "Kinetics of Precipitation in Metastable Binary Alloys-theory and application to Cu-1.9 at % Ti and Ni-14 at % Al," *Decomposition of Alloys: the Early Stages, September 19-23, 1983,* Sonnenberg, Germany, Oxford: Pergamon Press:91-103.

[4] Zhang, C., W. Cao, S. L. Chen, J. Zhu, F. Zhang, A. A. Luo, and R. Schmid-Fetzer, 2014, "Precipitation Simulation of AZ91 Alloy, *"Journal of Materials* 66(3): 389-396, http://link.springer.com/article/10.1007/s11837-014-0879-1.

[5] Kammerer, C.C., N. S.Kulkarni, R. J. Warmack, and Y. H. Sohn, 2014,"Interdiffusion and Impurity Diffusion in Polycrystalline Mg Solid Solution with Al or Zn," *Journal of Alloys and Compounds* 617: 968-974, http://www.sciencedirect.com/science/article/pii/S092583881401826X,

[6] Brennan, S., K. Bermudez, N. S. Kulkarni, and Y. H.Sohn,2012,"Interdiffusion in the MG-Al System and Intrinsic Diffusion in β-Mg2Al3,"" *Metallurgical and Materials Transactions A* 43(11): 4043-4052, http://link.springer.com/article/10.1007/s11661-012-1248-8.

[7] Das, S.K., Y. M. Kim, T. K. Ha, R. Gauvin, and I. H. Jung, 2013,"Anisotropic Diffusion Behavior of Al in Mg: Diffusion Couple Study Using Mg Single Crystal," *Metallurgical and Materials Transactions A* 44(6): 2539-2547, http://link.springer.com/article/10.1007/s11661-013-1636-8.

[8] Brennan, S., A. P.Warren, K. R. Coffey, N. Kulkarni, P. Todd, M. Kilmov, and Y. H. Sohn, 2012,"Aluminum Impurity Diffusion in Magnesium," *Journal of Phase Equilibria and Diffusion* 33(2): 121-125, http://link.springer.com/article/10.1007/s11669-012-0007-2.

[9] Lal, K., 1967,*L'Étude de la diffusion de quelques éléments dans le magnesium,* Ph.D. Dissertation, Paris, France: University of Paris.

[10] Čermák, J. and I. Stloukal, 2006,"Diffusion of 65Zn in Mg and in Mg–x Al Solid Solutions," *Physica Status Solidi (a)*203(10): 2386-2392, http://onlinelibrary.wiley.com/doi/10.1002/pssa.200622219/pdf.

[11] Das, S.K., Y. M. Kim, T. K. Ha, and I. H. Jung, 2013,"Investigation of Anisotropic Diffusion Behavior of Zn in HCP Mg and Interdiffusion Coefficients of Intermediate Phases in the Mg–Zn System," *Calphad* 42: 51-58, http://www.sciencedirect.com/science/article/pii/S0364591613000576.

[12] Combronde, J. and G. Brebec, 1972,"Heterodiffusion de Ag, Cd, In, Sn et Sb dans le magnesium," *Acta Metallurgica* 20(1): 37-44, http://www.sciencedirect.com/science/article/pii/0001616072901113.

[13] Das, S.K., Y. B. Kang, T. K. Ha, and I. H. Jung, 2014,"Thermodynamic Modeling and Diffusion Kinetic Experiments of Binary Mg–Gd and Mg–Y Systems," *Acta Materialia* 71: 164-175, http://www.sciencedirect.com/science/article/pii/S1359645414001220.

[14] Zhou, B.C., S. L. Shang, Y. Wang, andZ. K. Liu, 2016,"Diffusion Coefficients of Alloying Elements in Dilute Mg Alloys: A Comprehensive First-principles Study," *Acta Materialia* 103: 573-586, http://www.sciencedirect.com/science/article/pii/S1359645415300112.

[15] Ganeshan, S., L. G. Hector, and Z. K. Liu, 2011,"First-Principles Calculations of Impurity Diffusion Coefficients in Dilute Mg Alloys Using the 8-Frequency Model," *Acta Materialia* 59(8): 3214-3228, http://www.sciencedirect.com/science/article/pii/S1359645411000784.

[16] Wu, H., T.Mayeshiba, and D. Morgan, 2016,"High-Throughput ab-initio Dilute Solute Diffusion Database," *arXiv preprint arXiv:1602.01725*.

[17] Nandipati, G., N. Govind, A. Andersen, and A. Rohatgi, 2016,"Self-Learning Kinetic Monte Carlo Simulations of Al Diffusion in Mg," *Journal of Physics: Condensed Matter* 28(15): 155001, http://iopscience.iop.org/article/10.1088/0953-8984/28/15/155001/pdf.

[18] Combronde, J. and G. Brebec, 1971,"Anisotropie d'autodiffusion du magnesium,"*Acta Metallurgica* 19(12): 1393-1399, http://www.sciencedirect.com/science/article/pii/0001616071900770.

[19] Kammerer, C.C., 2015,*The Influence of Alloying Additions on Diffusion and Strengthening of Magnesium,* Ph.D. Thesis, Orlando, Florida: University of Central Florida.

[20] Zeng R., 2013, *Precipitation Hardening in AZ91 Magnesium Alloy,* Ph.D. Thesis, Birmingham, United Kingdom: University of Birmingham.

[21] Celotto, S., 2000, "TEM Study of Continuous Precipitation in Mg–9 wt% Al–1 wt% Zn Alloy" *Acta Metallurgica* 48(8): 1775-1787, http://www.sciencedirect.com/science/article/pii/S1359645400000045.

[22] Celotto, S. and T. J. Bastow, 2001, "Study of Precipitation in Aged Binary Mg–Al and Ternary Mg–Al–Zn Alloys Using ^{27}Al NMR Spectroscopy," *Acta Metallurgica* 49(1): 41-51, http://www.sciencedirect.com/science/article/pii/S1359645400003050.

[23] Mendis, C. L.,C. J. Bettles, M. A. Gibson, S. Gorsse, and C. R. Hutchinson, 2006, "Refinement of Precipitate Distributions in an Age-Hardenable Mg–Sn Alloy through Microalloying," *Philosophical Magazine Letters* 86(7): 443-456, http://www.tandfonline.com/doi/abs/10.1080/09500830600871186?journalCode=tphl20.

[24] Zhang, C., D. Ma, K. S. Wu, H. B. Cao, G. P. Cao, S. Kou, Y. A. Chang, and X. Y. Yan, 2007, "Microstructure and microsegregation in directionally solidified Mg-4Al alloy," *Intermetallics*15(10): 1395-1400, http://www.sciencedirect.com/science/article/pii/S0966979507000623.

[25] Paliwal, M. and I. H. Jung, 2013, "The Evolution of the Growth Morphology in Mg–Al Alloys Depending on the Cooling Rate during Solidification," *Acta Metallurgica* 61(13): 4848-4860, http://www.sciencedirect.com/science/article/pii/S1359645413003480.

[26] Paliwal, M. 2013, *Microstructural Development in Mg Alloys during Solidification: An Experimental and Modeling Study,* Ph.D. Thesis, Montreal, Quebec: McGill University.

[27] Zheng, X.W.,A. A. Luo, C. Zhang, J. Dong, and R. A. Waldo, 2012, "Directional Solidification and Microsegregation in a Magnesium-Aluminum-Calcium Alloy," *Metallurgical and Materials Transactions A*43(9): 3239-3248, http://link.springer.com/article/10.1007/s11661-012-1159-8.

[28] Paliwal, M. and I. H. Jung, 2013, "Solid/Liquid Interfacial Energy of Mg-Al Alloys," *Metallurgical and Materials Transactions A*44(4): 1636-1640, http://link.springer.com/article/10.1007/s11661-013-1623-0.

Bibliography

Sun, W., X. Shi, E. Cinkilic, and A.A. Luo, 2016, "Investigation of the non-equilibrium solidification microstructure of a Mg-4Al-2RE (AE42) alloy," *Journal of Materials Science* 51: 6287-6294.

Xia, X., W. Sun, A.A. Luo, and D.S. Stone, 2016, "Precipitation evolution and hardening in Mg-Sm-Zn-Zr alloys," *Acta Materialia* 111:335-347.

Zhong, W. and J.C. Zhao, 2017, "First experimental measurement of calcium diffusion in magnesium using novel liquid-solid diffusion couples and forward-simulation analysis," *Scripta Materialia* 127: 92-96.

III.7 Phase Transformation Kinetics and Alloy Micro-Segregation in High-Pressure Die Cast Mg Alloys – University of Michigan

Project Details

John Allison, Principal Investigator
Materials Science and Engineering
University of Michigan (UM)
2200 Bonisteel Boulevard
Ann Arbor, MI 48104
Phone: 734-971-3989
E-mail: johnea@umich.edu

Aaron Yocum, Project Manager
National Energy Technology Laboratory (NETL)
P.O. Box 880
3610 Collins Ferry Road
Morgantown, WV 26507-0880
Phone: 304-285-4852
E-mail: aaron.yocum@netl.doe.gov

William Joost, Technology Area Development Manager
U.S. Department of Energy (DOE)
1000 Independence Ave., S.W.,
Washington, DC 20585
Phone: 202 287-6020
E-mail: William.Joost@ee.doe.gov

Contractor: University of Michigan
Contract No.: DE-EE0006434

Executive Summary

High-pressure die casting (HPDC) is the predominant manufacturing method for magnesium (Mg) alloy automotive components; however, the phase transformation kinetics that occur during this process are, at best, poorly understood. The cooling rates during solidification in HPDC are far from equilibrium and have not been the subject of significant quantitative research. Improved understanding of microstructural kinetics and alloy segregation are required to refine industrial processes and to develop new alloy systems. Improvements in this understanding will be accomplished by combining systematic and quantitative experiments and state-of-the-art modeling and simulation.

The primary objective of this project is to conduct a systematic, quantitative study of phase transformation kinetics and micro-segregation in high-pressure die cast Mg alloys in both as-cast and heat-treated conditions. Results will be used to develop and validate physics-based, phase transformation kinetics micro-models that quantitatively capture microstructural evolution and micro-segregation during HPDC and heat treatment of Mg alloys. Finally, this knowledge will be transferred to industry and the wider research community through these micro-models; experimental data will be stored in the National Institute of Standards and Technology (NIST)-DOE Energy Efficiency and Renewable Energy Advanced Automotive Cast Mg Alloys Repository and the UM-DOE Materials Commons. This is a new knowledge repository under development within the UM Center for PRedictive Integrated Structural Materials Science (PRISMS) funded by DOE Basic Energy Sciences.

To accomplish these goals a systematic and comprehensive experimental study is being combined with computational modeling and simulation.

UM is conducting all experimental characterization of microstructures and micro-segregation in the HPDC and super vacuum die casting (SVDC) materials. The microstructure and chemical compositions of as-cast HPDC Mg alloys are being quantitatively and systematically characterized using a combination of methods, including electron probe microanalysis (EPMA) and optical, scanning electron microscopy and transmission electron microscopy. This comprehensive characterization has been initiated in AM60 and AZ91 cast at Tsinghua University and in magnesium-aluminum-manganese (Mg-Al-Mn) ternaries (AM series) and Mg-Al binary plates provided by the Ford Research and Innovation Center at Mag-Tec Corporation. These initial results have shown that, while Scheil solidification kinetics appear to describe the Al segregation profile at mid-thickness in 2.5-mm and 5.0-mm plates, Scheil models do not describe the micro-segregation that occurs during rapid solidification at the edge of the plate. Continued characterization will provide new insights in understanding phase transformation kinetics during high cooling rate solidification, micro-segregation of different alloying elements, and the impact of casting parameters (e.g., cooling rate and casting thickness) on as-cast microstructure and microstructure evolution during subsequent heat treatment processes.

Based on quantitative experimental results, a solidification micro-model is being developed in close collaboration with Dr. Mei Li at Ford Motor Co to predict evolution of the primary microstructural features of as-cast HPDC Mg alloys. Micro-models will also be developed to predict the dissolution of eutectic phases and redistribution of alloying elements during solution treatment and precipitation of strengthening phases during aging. These micro-models will be validated using the quantitative results obtained on complex-shaped HPDC/SVDC casting of AM50 and AZ91.

This is a 4-year project that is planned as one phase, which consists of six tasks.

Accomplishments

- Produced plates of ternary Mg alloys AM60B, AM70, and AZ91 using a super vacuum HPDC technique (Fiscal Year [FY] 2014).
- Completed initial precision MAGMASOFT® HPDC simulation of the SVDC casting conditions and geometry (FY 2014).
- Established reliable and consistent EPMA and metallographic procedures on the above ternary alloys (FY 2014).
- Developed a Monte Carlo “Forward Model” simulation of micro-segregation behavior as measured by EPMA in HPDC Mg Alloys (FY 2014).
- Characterized micro-segregation behavior in HPDC AM60B (of two-plate thicknesses), AM70, and AZ91, as well as in Mg-9wt.%Al produced under different casting conditions (FY 2014).
- Completed quantitative characterization of β-$Mg_{17}Al_{12}$ area fraction in HPDC AM60B (FY 2014).
- Completed electron backscatter diffraction characterization of HPDC AM60B (of two-plate thicknesses) and AZ91 as-cast microstructure (FY 2014).
- Characterized micro-segregation behavior in HPDC AM40, AM50, AM60, and AM70 (of two-plate thicknesses) (FY 2015).
- Completed electron backscatter diffraction characterization of HPDC AM series alloys (of two-plate thickness) (FY 2015).
- Began characterization of externally solidified crystals in HPDC AM series alloys (FY 2015).
- Began to develop micro-model to predict micro-segregation as a function of solidification front velocity (FY 2015).
- Determined that macro-segregation of Al exists in the as-cast plates and persists through solution treatment (FY 2015).

- Produced plates of Mg-3wt.%Al, Mg-5wt.%Al, Mg-9wt.%Al, and Mg-12wt.%Al using a super vacuum HPDC technique (FY 2016).
- Performed about 190 EPMA scans to characterize segregation in about 120 conditions of as-cast and heat-treated HPDC Mg plates (FY 2016).
- Verified cooling rates from the MAGMASOFT® simulation by comparing grain size versus cooling rate in the HPDC Mg-Al alloys with the grain size versus cooling rate reported in the literature for Mg-Al-Mn and Mg-Al-Zn alloys (FY 2016).
- Uploaded over 400 files (about 3 GB) onto both the UM DOE PRISMS Materials Commons data site and the NIST DSpace Repository (FY 2016).
- Determined that plate thickness does not influence micro-segregation behavior in the range of 2.5 to 5.0 mm in either the Mg-Al-Mn or Mg-Al alloys (FY 2016).
- Determined that by using a solidification front, velocity-dependent partition coefficient, the Scheil equation can be modified to describe both the observed micro-segregation and macro-segregation (FY 2016).
- Used the EPMA forward model simulation to determine the apparent solidification front, velocity-dependent partition coefficients for three distances from the casting surface in the AM series alloys (FY 2016).
- Used Dictra, the Thermo-Calc diffusion simulation software, to predict changes in micro-segregation during solution treatment in AM70 and Mg-9wt.%Al (FY 2016).
- Used a MATLAB thresholding routine to quantify the amount of β-$Mg_{17}Al_{12}$ phase in the Mg-Al-Mn and Mg-Al alloys (FY 2016).

Future Directions

- Complete study of phase transformation kinetics and micro-segregation in as-cast Mg-Al binaries and Mg-Al-Mn ternaries (FY 2017).
- Complete study of precipitation kinetics and dissolution phase transformation and micro-segregation during heat treatment in Mg-9wt.%Al and develop model to describe evolution (FY 2017).
- Complete micro-model to predict micro-segregation in as-cast Mg-Al binaries and Mg-Al-Mn ternaries (FY 2017).
- Complete micro-model to predict changes in micro-segregation and dissolution phase transformation in Mg-Al binaries and Mg-Al-Mn ternaries (FY 2017).
- Incorporate final experimental data and models for Mg-Al binaries and Mg-Al-Mn ternaries into UM DOE PRISMS Materials Commons data site and the NIST DSpace Repository and release to public (FY 2017).

Technology Assessment

- Target: Improved predictive capabilities for HPDC Mg alloy microstructures and precipitation kinetics.
- Gap: There is a lack of quantitative information on phase transformations and micro-segregation in HPDC Mg alloys.

Introduction

HPDC is used to manufacture over 90% of the commercial Mg products [1]. This process is fast and economical and produces complex thin-wall Mg components that cannot be fabricated through other means. The cooling rate involved in HPDC and SVDC are extremely high and range from 10 to 1000°C/s [2, 3]. The solidification processes experienced in this region are far from equilibrium conditions. Under such extreme conditions, the solidification kinetics, phase transformations, and redistribution of alloying elements cannot be predicted using equilibrium thermodynamics or the typical modifications to predict alloy partitioning (e.g., those represented by a Scheil model) [4]. Essentially, there is no systematic, quantitative information on eutectic phase formation or micro-segregation in this region. This represents a major and distinct gap in our scientific understanding of this important manufacturing process.

Redistribution of alloying elements during non-equilibrium solidification leads to micro-scale segregation across the dendrite/cell and this micro-scale segregation is strongly dependent on the cooling rate. Although micro-segregation has been the subject of a limited number of investigations in Mg alloys [5 through 11], there is no known micro-segregation study for Mg alloys under HPDC conditions in open literature. Previous studies of micro-segregation in Mg alloys have been obtained in directionally solidified castings or in samples cast under moderate cooling rate conditions.

Research on heat treatment of die cast Mg alloys has been limited due to the blistering that occurs when entrapped air expands during solution treatment. A new processing technology, SVDC for Al and Mg alloy components [12, 13] significantly reduces or eliminates air entrapment, enabling heat treatment of die casting alloys and components. This advanced processing route offers new approaches for alloy development and improved Mg component properties. To date, studies of the dissolution of eutectic phases and precipitate evolution during heat treatment of die cast alloys has been very limited [14 through 16] and there has been no systematic investigation of alloying and processing effects.

Precipitation hardening has the potential to be a major strengthening mechanism in heat-treatable SVDC Mg alloys; however, SVDC Mg alloys have not yet been the subject of extensive studies. Gradients in alloy micro-segregation and eutectic phase transformation that will be exhibited during SVDC will likely have a key influence on development of new alloy systems. In addition, quantitative characterization of precipitation microstructure under different heat treatment conditions is crucial to optimize the effects of precipitation strengthening and building physics-based strengthening models.

Approach

Manufacture of High-Pressure Die Cast Plates and Complex-Shaped Castings and Simulation

The target alloy compositions used in this study are shown in Table III.7-1. The alloy matrix was selected to include a wide range of compositions that will provide for optimization of current commercial alloys AM50/AM60 and AZ91, as well as pave the way for development of advanced, high-temperature Mg-Al-Ca and Mg-Al-Sr alloys. The Ford Research and Innovation Center at Mag-Tec Corporation provided the castings. These castings are being processed using SVDC casting procedures.

Table III.7-1. Target Alloy Compositions Used in this Study (wt.%)

Mg	Al	Zn	Mn	Ca	Sr
bal	3				
bal	5				
bal	9				
bal	12				
bal	4		0.5		
bal	5		0.5		
bal	6		0.5		
bal	7		0.5		
bal	9	0.5			
bal	9	1			
bal	9	2			
bal	5			3	
bal	5				3

Die casting process controls linked with precision MAGMASOFT® HPDC simulation are being used to provide an estimate of the cooling rate as a function of location in casting and casting geometry. The simulations use a fine finite difference mesh (i.e., at least 5 to 10 elements through the cross section; however, some have been completed with 30 to 45 elements) and high-fidelity HPDC interfacial heat transfer coefficients for HPDC developed by Li and Allison and co-workers [17 through 19] to estimate cooling rate as a function of location.

Quantitative Characterization of Phase Transformation Kinetics and Micro-Segregation in High-Pressure Die Castings

Solidification phase transformation kinetics are being quantified using comprehensive microstructural characterization, including optical metallography and scanning electron microscopy coupled with advanced image analysis. The primary characteristics that are being quantified are eutectic volume fraction and grain size as a function of alloy, location, sample thickness, and process condition. Micro-segregation profiles of alloying elements (i.e., Al, Mn, Zn, Ca, and Sr) versus solidification fraction are being quantitatively characterized using the EPMA scan method [5 through 7]. These micro-segregation results are being compared with Calphad-based Scheil solidification estimates of alloy partitioning. Phase transformation kinetics and micro-segregation profiles will also be quantified in a complex casting of both AM50 and AZ91 to confirm the experimental findings and to validate the phase transformation kinetics micro-models described below.

Quantitative Characterization of Phase Transformation Kinetics and Micro-Segregation during Heat Treatment of SVDC

This task is to characterize quantitatively phase transformation kinetics and changes in micro-segregation profiles during heat treatment of SVDC plates. Eutectic phase dissolution and changes in micro-segregation are being characterized as a function of solution treatment time and temperature. Phase transformation kinetics are being quantified using quantitative microstructural characterization, including x-ray diffraction, optical metallography, and scanning electron microscopy. The primary characteristics that are being quantified are changes in eutectic volume fraction and size as a function of alloy, location, sample thickness, and process condition. Solution treatment-induced changes in micro-segregation profiles of alloying elements (i.e., Al, Mn, Zn, Ca, and Sr) are being quantitatively characterized using the electron microprobe area scan method. Precipitate evolution will be characterized in selected alloys using quantitative transmission electron

microscopy techniques [15]. Precipitate evolution will be captured in the form of isothermal transformation curves. Beta phase dissolution kinetics and changes in micro-segregation profiles will also be quantified in complex castings of AM50 and AZ91 to validate the phase transformation kinetics micro-models.

Develop Physics-Based Phase Transformation Kinetics Micro-Models that Quantitatively Capture Microstructural Evolution and Micro-Segregation during HPDC and Heat Treatment

The quantitative and systematic results described above are being used to develop state-of-the-art phase transformation kinetics micro-models for HPDC alloys. A comprehensive solidification kinetics micro-model is being developed that considers solute trapping, dendrite arm coarsening, and dendrite tip undercooling. It also couples these calculations directly with multi-component phase diagram computations. Given solidification conditions and alloy compositions, this micro-model will be capable of predicting secondary dendrite arm spacing, types, and fractions of various non-equilibrium phases, liquid concentrations, and solute concentration profiles in the primary Mg phase under the extreme high heat extraction conditions that exist in HPDC and SVDC. A dissolution kinetics micro-model will be developed to account for eutectic phase dissolution and compositional homogenization. In addition, an analytical precipitation kinetics micro-model for predicting precipitate kinetics will also be developed.

Transfer Project Knowledge to Industry and the Research Community through Micro-Models and Experimental Data Housed in the UM DOE PRISMS Materials Commons

The information produced in this study is being uploaded to the NIST-DOE Energy Efficiency and Renewable Energy Advanced Automotive Cast Mg Alloys Repository and the UM-DOE Materials Commons, which is a knowledge repository that is under development within the UM-DOE PRISMS Center.

Results and Discussion

The focus this past year has been on completing characterization of microstructure and micro-segregation in a set of HPDC AM series plates provided by the Ford Research and Innovation Center at Mag-Tec Corporation and shifting to characterizing Mg-Al binaries cast during this fiscal year. Scripts have been written to process and analyze the EPMA results and to facilitate comparing multiple conditions.

Scripts were written that allow for rapid consolidation and analysis of micro-segregation data and exporting the data for release onto UM DOE PRISMS Materials Commons and the NIST DSpace Repository. One script refers to an Excel spreadsheet where metadata for all EPMA scans are recorded and the relevant composition measurements are imported. These composition measurements are filtered and assigned to a fraction solid using the weighted interval rank and sort method described by Mirković et al. [5]. The script exports an Excel spreadsheet with the micro-segregation profiles (i.e. the composition assigned to each fraction solid). To provide a quick view of the data, the script also exports an image of the micro-segregation profiles.

A second set of scripts uploads the micro-segregation curves and plots them for rapid comparison between different locations within the same plate or between different plate thicknesses for the same alloy, location, and heat treatment. These plots are automatically exported to serve as a quick reference and for incorporation into the materials information repositories (i.e., NIST DSpace and Materials Commons). For all eight alloys studied, micro-segregation does not depend on casting thickness. All eight alloys show macro-segregation that results in an Al-rich skin on the casting surface.

Because the average grain diameter in the HPDC plates is approximately two times the electron beam interaction volume, the EPMA micro-segregation profiles are distorted. An EPMA forward model simulation is being used to determine the velocity-dependent partition coefficients (k_v), assuming the concentration of Al (C) as a function of fraction solid (f_s) follows a Scheil-based model:

$$C = k_v C_0 (1 - f_s)^{(k_v - 1)} \quad (1)$$

Optical emission spectroscopy results were used for the average Al composition, C_0. Apparent solidification front velocity-dependent partition coefficients were obtained for the AM series alloys by using a least-squares difference approach to compare the forward model simulation results for a selected partition coefficient to the experimental EPMA profiles. An example of forward model simulation results is plotted against the EPMA micro-segregation profiles from the 2.5-mm thick AM70 in Figure III.7-1.

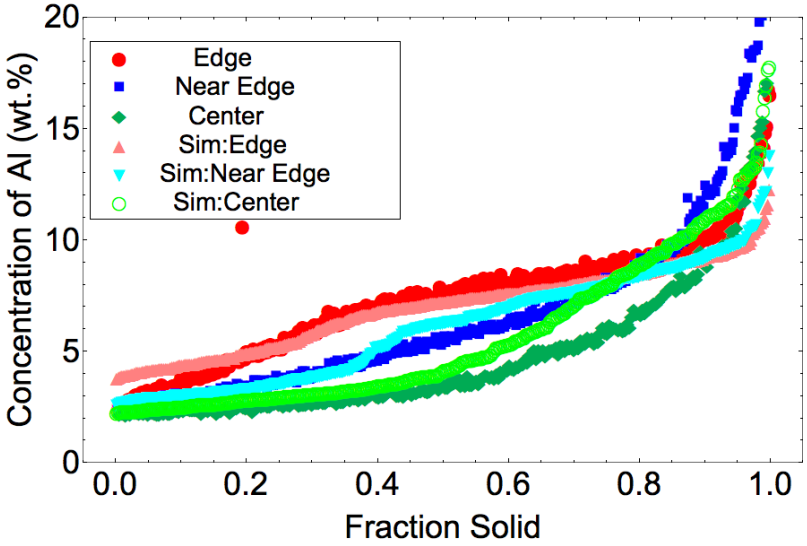

Figure III.7-1. EPMA micro-segregation curves compared to the forward model simulation results in the 2.5-mm thick AM70.

For the AM series alloys, a partition coefficient of 0.25 to 0.3 (i.e., close to the equilibrium partition coefficient) describes the micro-segregation behavior at the center of the plates; however, a higher partition coefficient is needed to describe micro-segregation about 300 µm from the casting surface or "near edge" (k_v~0.35) and at the surface of the castings (k_v~0.55). Analysis of the Mg-9wt.%Al indicates that similar location-dependent partition coefficients also will be appropriate in the Mg-Al binary alloys.

These apparent partition coefficients can be used to describe the through-thickness macro-segregation of Al. The EPMA grid analysis technique was performed on solution-treated samples of all eight alloys. After solution treatment, the β-phase is fully dissolved and very little micro-segregation remains, with the exception of the Mg-12wt.%Al samples. The average Al concentration at each location was calculated using all quality composition measurements within the grid.

Manipulation of the Scheil equation provides an understanding of how solute trapping impacts macro-segregation and the amount of eutectic phases. The average Al concentration as a function of the alloy composition, $C_{0,}$ can be estimated by fixing k_v and calculating the following:

$$C_{ave} = \int_0^a C_0 k_v (1-x)^{k_v-1} dx + \int_a^1 33.3 dx \quad (2)$$

Where x is the fraction solid and a is the fraction solid at which the eutectic begins to form. The composition where the eutectic precipitates is approximated at 13 wt.% , which is the maximum solubility of Al in Mg at the eutectic temperature. The second expression in the equation represents the total amount of Al in the β-phase, which has a composition of approximately 33 wt.% Al. The partition coefficients that lead to the best agreement with the measured average Al concentration are k_v=0.25 (center), 0.35 (near edge), and 0.55 (edge) (Figure III.7-2). These location-dependent partition coefficients are in good agreement with those determined by comparing the as-cast micro-segregation profiles with the forward model simulation results.

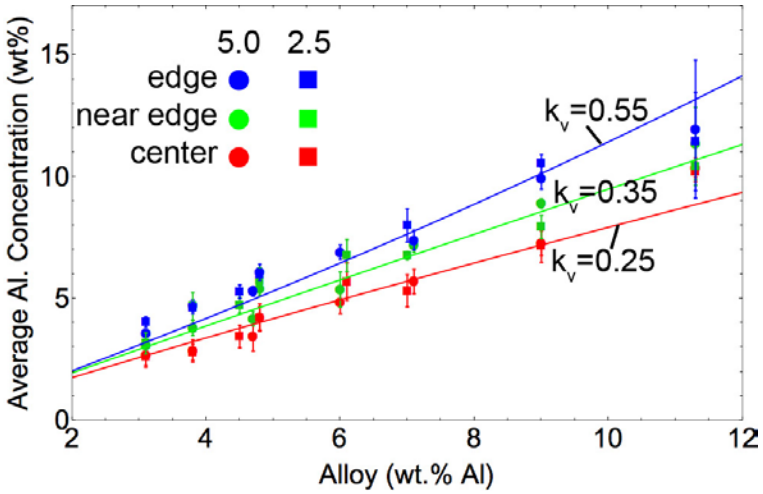

Figure III.7-2. Local average Al concentration as a function of alloy composition. The solid lines indicate the predicted average Al concentration for a fixed value of k_v. As noted in the legend, samples were either 5.0mm in thickness or 2.5mm in thickness.

Another focus of this reporting period has been continuing quantitative characterization of the β-phase volume in the as-cast conditions in addition to initial characterization on solution-treated Mg-9wt.%Al samples. Several improvements have been made to the MATLAB image thresholding routine that is used to calculate the β-phase volume fraction from the scanning electron microscope images. Issues with the previous version of the code include failure to accurately isolate the β-phase due to inconsistencies with brightness and contrast between samples and bright "halos" around the edges of pores. Figure III.7-3 shows a comparison of the (a) original micrograph and the output from the phase fraction MATLAB routine in the (b) previous version and (c) the newest version at the edge location for the 2.5-mm thick Mg-5wt.%Al. The intermetallic phases are bright/white in all three images. The red arrow highlights a "pore-halo." In the old output, due to the bright contrast, this halo was incorrectly selected as an intermetallic phase and shows up in the output. In the new version of the code, a routine that includes dilation of the pores and masking elements successfully eliminates the halo from the output. This leads to a decrease in the measured β-phase volume fraction and a decrease in measurement uncertainty.

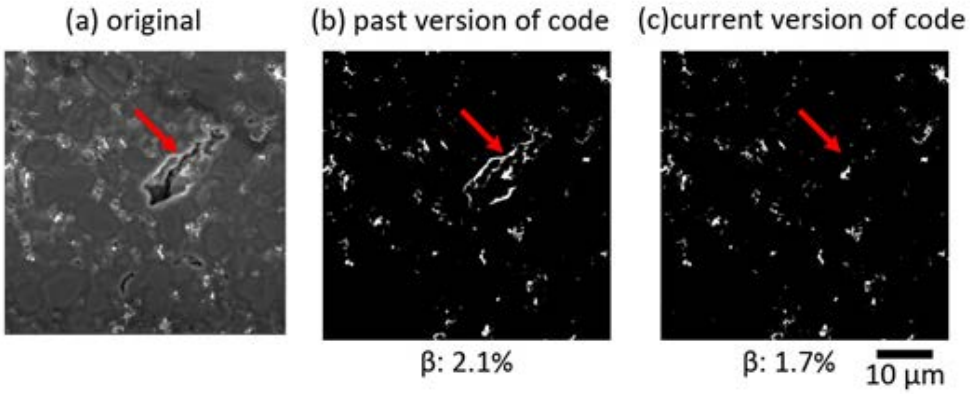

Figure III.7-3. Comparison of the (a) original scanning electron micrograph and the output from the phase fraction MATLAB routine in the (b) previous version and (c) newest version at the edge location for the 2.5-mm thick Mg-5wt.%Al.

One goal of this project is to model evolution of micro-segregation and phase transformation kinetics during solution treatment. Heat treatments have been performed on the Mg-9wt.%Al alloy at 380ºC, 400ºC, and 420ºC between 2 minutes and 2 hours duration. Figure III.7-4 shows the EPMA micro-segregation profiles from the samples treated at 400ºC. The results demonstrate that while the Al composition is becoming more homogenous as the length of the annealing treatment increases, 60 minutes is not sufficient to remove micro-segregation. Future work includes adapting the forward model simulation to facilitate comparison of simulated diffusion data with EPMA experimental results.

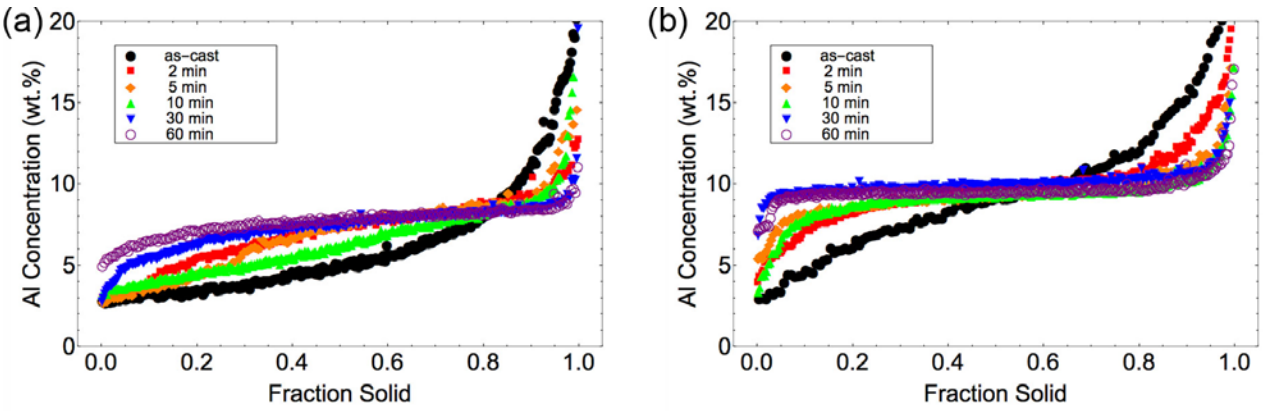

Figure III.7-4. Evolution of micro-segregation in 2.5-mm thick Mg-9wt.%Al during solution treatment at 400ºC at the (a) center and (b) edge.

Technology Transfer Path

Project knowledge, including experimental data and micro-models, will be transferred to industry and the research community through the NIST DOE Energy Efficiency and Renewable Energy Mg Kinetics Repository and UM DOE PRISMS Materials Commons. The database structure and content used for the Materials Commons is being constructed in coordination with national Materials Genome Initiative repository efforts lead by NIST. The project team has had several discussions with key repository experts. This will ensure the information developed in this program will be broadly accessible to the technical community. Templates specific to the EPMA data acquisition and analysis and electron backscatter diffraction data collection have been implemented into Material Commons. A dataset describing the microstructure and micro-segregation in the as-cast HPDC Mg-Al-Mn alloys was published on the Materials Commons public data site in August 2016.

Conclusion

It has been demonstrated that it is possible to characterize micro-segregation in fine-grained HPDC Mg-Al alloys through use of an EPMA forward model simulation that quantitatively predicts the effect of microstructure parameters and experimental conditions on measured micro-segregation behavior. Both micro-segregation and macro-segregation in Mg-Al plates can be described through use of a Scheil-based model that allows for solute trapping by introducing a solidification front velocity-dependent partition coefficient. Faster cooling at the surface of the castings leads to more solute trapping, resulting in a higher partition coefficient in the skin. This improved understanding of the through-thickness solute distribution, combined with dissolution phase kinetics and an understanding of micro-segregation evolution during solution treatment, will allow for optimization of aging treatments in heat-treatable SVDC Mg-Al components.

References

[1] Slade, S., 2010, "Mg : Bridging Diverse Metal Markets," in *Mg Technology,* S. R. Agnew, N. R. Neelameggham, E. A. Nyberg, and W. H. Sillekens (eds.), Wiley: 91–95.

[2] Gjestland, H. and H. Westengen, 2007, "Advancements in High Pressure Die Casting of Mg," *Advanced Engineering Materials* 9: 769–776.

[3] Kim, J. S., M. Isac, and R. I. L. Guthrie, 2004, "Metal-Mold Heat Transfer and Solidification of Mg Alloys in Belt Casting Processes," in *Mg Technology,* A. A. Lu (ed.), Metallurgical Society of AIME: 247–255.

[4] Porter, D. A. and K. E. Easterling, 1992, *Phase Transformations in Metals and Alloys,* second

edition, Nelson Thornes Ltd.: Cheltenham, United Kingdom.

[5] Mirković, D. and R. Schmid-Fetzer, 2009, "Directional Solidification of Mg-Al Alloys and Microsegregation Study of Mg Alloys AZ31 and AM50: Part I. Methodology," *Metallurgical and Materials Transactions A* 40: 958–973.

[6] TerBush, J. R., N. D. Saddock, J. W. Jones, and T. M. Pollock, 2010, "Partitioning of Solute to the Primary α-Mg Phase in Creep-Resistant Mg-Al-Ca–Based Cast Alloys," *Metallurgical and Materials Transactions A* 41: 2435–2442.

[7] Zheng, X., A. A. Luo, C. Zhang, J. Dong, and R. A. Waldo, 2012, "Directional Solidification and Microsegregation in a Mg-Al-Calcium Alloy," *Metallurgical and Materials Transactions A* 43: 3239–3248.

[8] Khan, M. I., A. O. Mostafa, and M. Aljarrah, E. Essadiqi, and M. Medraj, 2014, "Influence of Cooling Rate on Microsegregation Behavior of Mg Alloys," *Journal of Materials* 2014: 1–18.

[9] Zhang, C., D. Ma, K.-S. Wu, H.-B. Cao, G.-P. Cao, S. Kou, Y. A. Chang, and X.-Y. Yan, 2007, "Microstructure and Microsegregation in Directionally Solidified Mg–4Al Alloy," *Intermetallics* 15: 1,395–1400.

[10] Paliwal, M., D. H. Kang, E. Essadiqi, and I. H. Jung, 2014, "The Evolution of as-Cast Microstructure of Ternary Mg-Al-Zn Alloys: An Experimental and Modeling Study," *Metallurgical and Materials Transactions A* 45: 3596–3608.

[11] Liu, S., G. Yang, and W. Jie, 2014, "Microstructure, Microsegregation, and Mechanical Properties of Directional Solidified Mg–3.0Nd–1.5Gd Alloy," *Acta Metallurgica Sinica (English Letters)* 27: 1134–1143.

[12] Sadayappan, K., W. Kasprzak, Z. Brown, L. Quimet, and A. A. Luo, 2009, "Characterization of Mg Automotive Components Produced by Super-Vacuum Die Casting Process," *Materials Science Forum* 618–619: 381–386.

[13] Luo, A. A., 2010, "Advanced Casting Technologies for Lightweight Automotive Applications," *China Foundry* 7: 463–469.

[14] Li, M., R. Zhang, and J. Allison, 2010, "Modeling Casting and Heat Treatment Effects on Microstructure in Super Vacuum Die Casting (SVDC) AZ91 Mg Alloy," in *Mg Technology,* S. R. Agnew, N. R. Neelameggham, E. A. Nyberg, and W. H. Sillekens, (eds.), Wiley: 623–627.

[15] Miao, J., M. Li, and J. E. Allison, 2012, "Microstructure Evolution During Heat Treatment in a Super Vacuum Die Casting AZ91 Alloy," in *Mg: Proceedings of the 9th International Conference Mg Alloys and Their Applications,* W. J. Poole and K. U. Kainer (eds.), ICMAA2012: Vancouver, Canada: 493–498.

[16] Wang, J., M. Li, B. Ghaffari, L.-Q. Chen, J. Miao, and J. A. Allison, 2012, "Microstructural Evolution Model for $Mg_{17}Al_{12}$ Precipitates in AZ91," in *Mg Technology,* S. N. Mathaudhu, W. H. Sillekens, N. Hort, and N. R. Neelameggham (eds.), Wiley: 163–170.

[17] Guo, Z.-P., S.-M. Xiong, B.-C. Liu, M. Li, and J. Allison, 2008, "Effect of Process Parameters, Casting Thickness, and Alloys on the Interfacial Heat-Transfer Coefficient in the High-Pressure Die-Casting Process," *Metallurgical and Materials Transactions A* 39: 2896–2905.

[18] Guo, Z., S. Xiong, B. Liu, M. Li, and J. Allison, 2008, "Determination of the Heat Transfer Coefficient at Metal–die Interface of High Pressure Die Casting Process of AM50 Alloy," *Internationsl Journal of Heat and Mass Transfer* 51: 6032–6038.

[19] Li, S., S. Xiong, B. Liu, M. Li, and J. E. Allison, 2010, "Numerical Simulation of Flow-Induced Air Entrapment Defects in the High Pressure Die Casting Process," in *Mg Technology*, S. R. Agnew, N. R. Neelameggham, E. A. Nyberg, and W. H. Sillekens, (eds.) Wiley: 613–616.

IV. Carbon Fiber and Polymer Composites

IV.1 Close Proximity Electromagnetic Carbonization – Oak Ridge National Laboratory

Project Details

Felix Paulauskas, Principal Investigator
Materials Science and Technology Division
Oak Ridge National Laboratory (ORNL)
1 Bethel Valley Road
Oak Ridge, TN 37831-6053
Phone: 865-576-3785
E-mail: paulauskasfl@ornl.gov

H. Felix Wu, Program Manager
U.S. Department of Energy
1000 Independence Ave., S.W.
Washington, DC 20585
Phone: 202-586-4830
e-mail: felix.wu@ee.doe.gov

Contractor: ORNL
Contract No: DE-AC05-00OR22725

Executive Summary

Close proximity electromagnetic carbonization (CPEC) is a joint development project between RMX Technologies and ORNL that is funded by the U.S. Department of Energy. Preliminary work on electromagnetic carbonization was jointly conducted during the previous three years by both institutions and served as a precursor to this work. In 2013, preliminary work undertook by RMX Technologies and ORNL led to an initial design (i.e., CPEC-1) that demonstrated the possibility of carbonization of polyacrylonitrile (PAN) fiber in the near field of antennas using radiofrequency power; that work served as the precursor to this project. The carbonized area was non-uniform, leaving areas of the exposed material untreated. Based on these results, a model was used that would allow creating designs of the feed structure and antenna equipment and calculate the electromagnetic (EM) fields that they radiate.

The model allows prediction of the rise in a material's temperature given the electrical and thermal properties with respect to time and temperature. To prepare for this project, a significant effort has been dedicated to the PAN material and its electrical properties. This effort has been bibliographic and experimental (e.g., sample preparation, dielectric spectroscopy using impedance analyzers, and resistance measurements). Once the behavior of all variables of interest was known and appropriate approximations applied, the model was configured. The model was iterated until results matching expected performances were developed. The power supply is certainly the most expensive and most constraining subcomponent of CPEC because it has to comply with the requirements and limitations of an industrial setting. For the design of CPEC, these constraints on the power supply were taken into account.

This report describes progress on the CPEC project during Fiscal Year (FY) 2016. A major advance occurred during the first quarter when, based on new expertise, a computational EM (CEM) model was used rather than an improved replica of the former physical setup (i.e., CPEC-1). By the end of the third quarter, a new design based on successful CEM modeling was selected. CPEC-2 was a virtual device that was modeled and was used as the basis for construction of the CPEC-3 unit. At the end of June 2016, while additional models were solved

to determine the appropriate tolerance, construction of CPEC-3 started. The last quarter of FY 2016 was dedicated to fine-tuning the model and completing construction of the physical setup. As of September 30, construction of the CEM-based CPEC furnace was nearly complete. The first laboratory tests will begin early in FY 2017.

Accomplishments

- Developed simulation-based design using solid modeling and CEMs (FY 2016).
- Completed 160 measurements of 47 material samples to define permittivity and create a characteristic database that previously had been nonexistent (FY 2016).
- Completed benchmarking and acquisition of software for CEM (FY 2016).
- Completed optimization of the driving variables pertaining to CPEC (FY 2016).
- Confirmed that thermal representations predicted an acceptable uniformity across the tow width (FY 2016).
- Completed benchmarking radiofrequency power supply merchants that can meet operational requirements (FY 2016).
- Selected a final operations frequency band (FY 2016).
- Completed fine tuning of the model (FY 2016).
- Completed a three-dimensional, model–based full drawing package of the current design using SolidWorks 2016 (FY 2016).
- Completed construction of the physical setup on October 15, 2016, meeting the milestone schedule (FY 2016).

Approach

The CPEC Project was split in four major design and construction phases, with each phase related to an experimental setup. These phases are given in Table IV.1-1. This chart encompasses the project from its preliminary work (FY 2013) to its end (FY 2018). The phases emphasize the change of scientific approach that occurred early in FY 2016. There was a determination not to build the CPEC-2 (i.e., an upgrade of the original setup, CPEC-1) in favor of a more versatile model or CPEC-2V that allows visualization and optimization based on a proven CEM code (i.e., finite integral time domain) and further reduces total project risk. The object of this report is to describe achievements during FY 2016 that are related to Phase 2 and Phase 3 (i.e., elaboration on the CPEC-2V model and construction of CPEC-3).

Table IV.1-1. Description of the Major Phases of the CPEC Project

Phase	Name	Date	Status (Sept.2016)	Description
1	CPEC-1	FY 2013	Completed	Demonstration of feasibility (static mode)
2	CPEC-2	FY 2016	Aborted	Upgrade of CPEC-1 (with automatic impedance matching); abandoned in favor of CPEC-2V
	CPEC-2V	FY 2016	Completed	Optimization of the CPEC concept using a computational model
3	CPEC-3	FY 2016	Under construction	Physical construction of CPEC-2V (continuous process at lab-scale)
4	CPEC-4	FY 2017 FY 2018	To be done	Scale-up of CPEC-3 to a 1-ton/year furnace

Results and Discussion

The Cartesian coordinate system is used in this report to show results with respect to spatial orientation. The tow is consistently modeled along the y-axes. All figures are orientated based on the same frame of reference, which is displayed where needed (Figure IV.1-1).

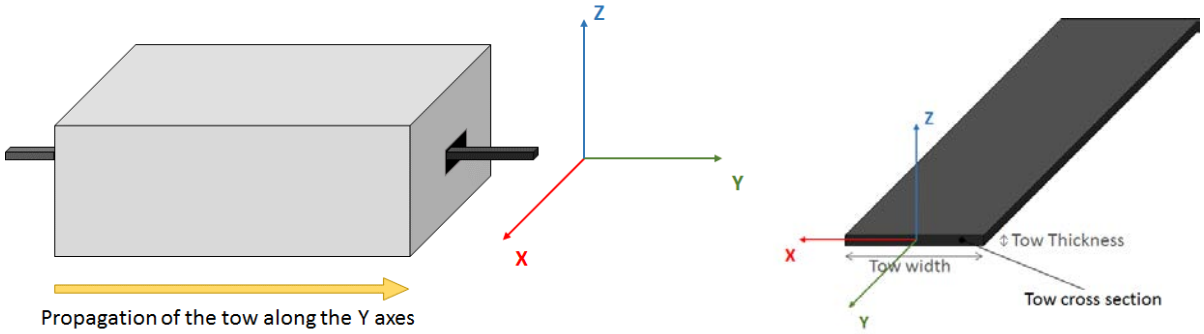

(a) (b)

Figure IV.1-1. Illustration of the Cartesian coordinate system used to represent results spatially: (a) an overview of the outside of the furnace prototype "CPEC-3"and (b) a representation of the tow using the same frame of reference. Y is collinear to the motion of the tow, X goes across the width of the tow, and Z to the top, with the original at the center of mass of the tow in all CEM models.

Measurements and Electrical Characterization of the Material

Previous efforts began in 2013 with a physical build and static testing. The results showed a tow that was carbonized in various spots. To further characterize the interaction between the high power electromagnetic fields and the oxidized PAN, CEM modeling was pursued. To begin this effort, the fiber first had to be electromagnetically characterized. At initiation of this phase, limited information pertaining to material permittivity was found in available literature.

Material characterization encompassing EM and thermal properties attained through measurement and literature searches is complete. PAN is now characterized to a previously unseen level in terms of EM properties. The final data set exceeds 160 measurements and more than 47 unique carbon fiber samples and spans a range in both temperature and frequency nonexistent in literature. The collected data show the behavior of several variables across the temperature range of low-temperature carbonization (LTC). It not only provides information directly related to this project, but also provides in-depth information for future endeavors. This effort has confirmed and given more knowledge about an effective area of operation throughout the LTC stages and the electrical properties of carbon fibers in general. The summary data set is reported in Table IV.1-2.

The loss tangent or tan (δ) has been calculated based on measurements that were conducted on Samples A through J. These samples have been partially carbonized to cover the operating temperature range of LTC. The set of data reveals the following:

- At low frequency, samples relating to a higher level of carbonization exhibit a high conductivity and show a higher loss.
- Samples related to the early stage of the process of carbonization show lower values for tan (δ), relative to highly conductive areas. This means this material is not easy to couple with radiators over the explored range of frequencies.

Conclusions based on these measurements are as follows:

- Partially carbonized PAN is not extremely lossy, outside of a highly conductive band, within the measured frequency range.

- Where the behavior of the material remains almost unchanged, the choice of frequency of operation will be driven by both cost and efficiency of energy coupling to the tow.

Table IV.1-2. Summary of the EM Measurements Conducted on Samples A through J (These samples have been partially carbonized at varying stages covering the full span of temperatures of LTC.)

Samples	Number of Measurements	Number of Unique Samples	Sample Minimum Temperature (°C)	Sample Maximum Temperature (°C)	Number of Samples without PE	Sample of Configurations	Number of Frequency Samples
A	35	11	-100	250	4	5	1,348
B	9	7	21	21	0	1	801
C	9	7	21	21	0	1	801
D	9	7	21	21	0	1	801
E	20	9	–100	250	2	2	801
F	1	1	21	21	0	1	801
G	1	1	21	21	0	1	801
H	1	1	21	21	0	1	801
I	1	1	21	21	0	1	801
J	10	2	21	250	1	2	801
Polyethylene	13	2	21	21	0	1	801
Polytetrafluoroethylene (Teflon)	4	2	21	21	2	1	801
Polyacrylonitrile	15	3	20	250	3	1	972
50-Ohm Calibration Standard	35	3	21	21	35	1	801
Totals	163	57					11,932

Thermal Fiber Properties

The heat capacity of the material is an influential parameter in the model. This variable is temperature dependent. A modulated differential scanning calorimeter was used to obtain these data. Because of equipment limitations, the measurement could only be performed on a part of the range of interest.

Thermal conductivity is the effectiveness of the material to conduct heat. From the literature, thermal conductivity is strongly temperature dependent [1]. In the context of the CPEC Project, where the goal is to heat up a material, a low value of thermal conductivity is preferable over high values. Indeed, a high thermal conductivity indicates the energy has a high trend of migrating out of the heating zone, making the material more difficult to heat up. According to the literature, this value is relatively low for similar carbonaceous material. By updating it accordingly, the model has been able to show several designs that are able to reach the expected temperature or more.

Emissivity is the property of a surface to emit EM radiation, or more specific to our situation, thermal radiation, mainly in the infrared region. It is a dimensionless variable that is color, surface, wavelength, and temperature dependent. Because of the material specificities (especially shape and surface) and changes along the process, this variable is not easy to measure. The wide range of temperatures involved in this process lead to emissivity needing to be considered as a variable. Nevertheless, due to technical reasons, the value of the emissivity selected for the model is set as a constant. Its value is a conservative assumption based on data available in the literature on comparable materials [2]. Furthermore, resolution of several models indicates that

temperature elevation is poorly dependent on the value of emissivity, as long as this one is selected in the proper span.

The Model and Approximation

Using a modeling software like Dassault Systems computer simulation technology software and finite integral time domain presents certain advantages (e.g., being able to represent a system and the field distribution it generates without having to build it or perform physical measurements). In the context of CPEC, it is particularly efficient in modifying the geometry of the system and optimizing coupling between radiators and the material.

Nevertheless, like any model, it is a simplification of reality. Not all variables of the system can be taken into account and some of them have to be set as constant (e.g., the weight loss of the tow across the process or modification of the environment due to off-gas). Additionally, because of technical reasons or calculation limitations, some geometrical approximation had to be done. The most important one is that tow has to be modeled by a parallelepiped instead of a bundle of fibers due to mesh size, minimum mesh step, and time of calculation.

Table IV.1-3 is a list of the approximations with an assessment of their impacts on the model versus reality. Among the approximations listed, the following four have greater effect and are emphasized in Table IV.1-3:

- Geometry of the tow will have an impact on heat distribution across the cross section.
- Lossiness (ε") occurs by fixing this parameter to its value at the early stage of the process. The model underestimates the induced EM loss, which is expected to rise and have a strong impact on the resultant temperature rise [3]. Furthermore, materials will generally become more lossy as the internal thermal energy rises, giving rise to greater loss and larger values of ε" at elevated temperatures. While the rise could be damaging the tow up to breakage, it could lead to a lower power requirement (due to the increased lossiness of the material).
- Thermal conductivity is underestimated because it is set as a constant (the selected value is the one at the beginning of the process). In reality, this value will increase with temperature and should act as a heat sink. This should help prevent damage due to the increase of coupling.
- Weight variation has not been taken into account in this model and should degrade the coupling by thickness reduction of the tow.

The model is static (i.e., the tow does not move). This could make a large difference between the model and reality. However, the model shows a fast temperature rise (i.e., less than 30 seconds). This indicates the process is relatively quick. In consequence, it can be assumed there are few differences between “static mode” and “slow motion mode,” which will be the condition of our first operational tests.

The major difference between the model and reality is thought to be a global rise in temperature, mostly driven by the major increase of ε"; the approximations of thermal conductivity and the weight variation mitigate this effect.

Consequently, the first of these four approximations generates an uncertainty on the temperature distribution in the cross section of the tow, whereas the last two introduce uncertainty on the average temperature elevation along the tow. None of the consequences of these approximations, which introduce an important uncertainty on the thermo-profiles, can be clearly assessed. Every effort has been made to carefully choose these approximations so a balance may be maintained concerning temperature rise within the tow or load. However, the model remains a powerful tool in predicting fields and thermal distribution, which is sufficient for identifying relative performance when comparing two sets of data and providing an optimized basis for a distributed matching network, cavity, and radiator design. With our current capabilities and timeframe, only experimental work will be able to fully characterize the LTC CPEC process.

Table IV.1-3. Summary of the Approximations Used to Model the Process of Carbonization at Low Temperature using CST Software (The five approximations that may have greater impact than the others have been highlighted.)

Variable Name	Nature of the Approximation	Expected Consequence on the Model Observation	Impact[a] (0–4)	Confidence in Approximation[a] (0–4)
Geometry of the tow, heat distribution	Parallelepiped instead of a bundle of fibers	Increase the non-homogeneity of the heat elevation crosswise	3	3
Geometry of the tow, average heat rise	Parallelepiped instead of a bundle of fibers	Moderate reduction of the temperature elevation	2	4
Lossiness (ε") of the material	ε" set constant using its value at 300°C or sample A	Important reduction of the temperature elevation of the material	4	4
Emissivity of the material	Estimated on its high side using values of similar materials at room temperature	Slight to negligible reduction of the temperature elevation of the material	0	4
Heat capacity of the material	Underestimation of the heat capacity: set constant using its value at 300°C	Moderate increase of the elevation of the temperature of the material and its pace	1	4
Thermal conductivity of the material	Underestimation of thermal conductivity: set constant using its value at 300°C	Significant increase of temperature elevation of the material	3	3
Weight variation of the material	Overestimation of the weight of the tow by setting its volume constant	Increase of the efficiency of the coupling, resulting in an increased temperature elevation of the material	3	2
Line speed	Static batch	Increasing the time of exposure of the material may provide a more uniformly carbonized tow	2	4
Gas mixture	100% N_2	No energy dissipation in the medium, which results in a moderate temperature elevation of the material	3	2
Condensation	No condensation of by products	No energy dissipation in the tare, which results in a negligible temperature elevation of the material	0	4
Radiator tolerance, realization	Perfect shape	Ideal resonance, which results in an optimal temperature rise of the material	1	4
Radiator tolerance, positioning	Ideal positioning	Ideal resonance, which results in an optimal temperature rise of the material	1	4
Connectors	Ideal power transmission	Small to negligible over estimation of the temperature rise of the material	0	4
Effect of off-gassing on coupling	Absent; must be experimentally determined	An increase of loss in the intermediate spacing within the bundle and its immediate surrounding area	3	3

[a]An impact of 0 is "Negligible" and 4 is "Significant." In terms of confidence, 0 would be "No Confidence" and 4 would be "High Confidence."

After running a significant number of models with varying designs, the thickness or cross-sectional area of the tow was observed to have a strong influence on the coupling and, consequently, on temperature elevation of the material. Generally, thicker tows are better, yielding a greater average temperature elevation. This project will deliver a 48,000-filament tow that has a thickness close to 0.3 mm when processed as a 25.4 mm strip.

The Selected Design

The CPEC-3 design has been down selected based on its simulated performance and the requirements of the FY 2016 second quarter milestone. The vessel encloses the tow with two narrow slots on opposite sides designed for the input and output of the tow (Figure IV.1-1). The tow will be exposed to radiation while inside the cavity. The RF power supply will be the most expensive part of the setup; however, the selected design is compatible with current industrial practices.

The selected design has been modeled using a band of frequencies, F_R. Despite a minor update to the cavity design and feed structure, these results remain valid to demonstrate the performance of this model, depicting a suitable gradient of induced temperature on the load or tow.

Results regarding temperature distribution across the tow showed in the previous section were generated by a model with a power source whose specification is compatible with currently available off-the-shelf power signal sources and with industrial requirements. The maximum temperature can be lowered by adjusting/reducing the input power into the system or increasing the line speed of the process. The model shows the required temperature can be achieved or even exceeded; this reflects reality as closely as possible while making the simplifications required in CEM. As a result, temperatures displayed by the model are not exact, but are within reasonable expected ranges.

Project efforts will focus on designs that give a better heat distribution over the cross section at the processing zones. Indeed, the colder zones may have lower or negligible effects on the process of conversion compared to the hot zones, especially if the material is exposed to the processing zones first. The selected design is the one that gave the most rectangular cross sections with limited boundary effects. Furthermore, its size is compact and heat dispersion is relatively low. This can be observed through post processed data not shown due to export control regulations, where the gradient of temperature between the tow and the environment is important. These sharp gradients indicate the energy transfer from the radiators to the tow is efficient and the energy transfer from the radiator or the tow to the environment remains relatively low.

Based on the model, about 65% of the hottest cross sections belonging to the tow are in the required ±2.5% temperature deviation. All of the tow would be encompassed within the range from −10.7% to +5.4%. However, these values are the result of a model and its approximations. More homogeneous temperature distributions are to be expected in the physical unit for the following reasons:

- Thermal conductivity is set as a fixed value in the model. In reality, it will rise as the material carbonizes and acts as a heat sink.
- Irradiating a parallelepiped, like the one modeled, with microwave energy has a tendency to warm the center more quickly than the surface due to thermal exchange with the surrounding environment. This phenomenon is magnified by the low ratio surface/bulk, whereas the irradiation of a bundle of thousands of filaments may have a strong and positive impact on the homogeneity of the process.
- Although static in the model, the tow will move through the furnace. This will allow another controllable aspect because it pertains to thermal migration along the material.
- A supplemental heat source may be connected, which should contribute to mitigating boundary effects while preventing off-gas condensation.

Building and Assembly of All Subcomponents

The radiofrequency source has been tested without load. With the exception of a short section of the waveguide (on order), all other elements related to generation or the propagation of the radiation (e.g., waveguides, circulators, and gaskets) are already available for assembly. Equipment for radiation measurement has been purchased or recalibrated.

An outside view of the furnace is shown in Figure IV.1-1 and is represented as installed in the experimental configuration in Figure IV.1-2. The model has been iterated several times to define the appropriate tolerance of

sensitive surfaces before machining. Low accuracy or rough surfaces could decrease performance; however, excessive precision has minimal benefit and would only lead to an unnecessary increase in cost.

A complete three-dimensional model and its drawing package have been completed (Figure IV.1-2). Because of export control regulations, critical details of the model presented here are not disclosed. Nevertheless, this figure shows the CPEC-3 furnace placed into a shielded enclosure. This setup includes the following:

- A chassis (complete)
- The power supply equipment (complete, not represented)
- A winding system (ready for assembly, not represented)
- All equipment required to manipulate CPEC-3 (ready for assembly)
- An exhaust system (in position, but not represented)
- Safety equipment (in position or available, but not represented).

All parts required for the fulfilment of the setup are available and assembly was finished in October 2016.

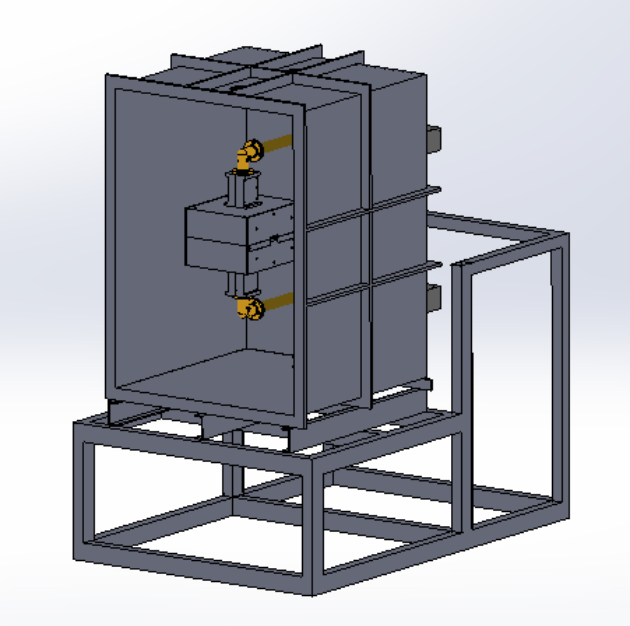

Figure IV.1-2. Isomeric view of CPEC-3 in a shielded enclosure. Because of export control regulations, some parts have been deliberately removed or hidden from this drawing.

Data will be collected via a reconfigurable input/output control system, managed, and saved in a computer running LabVIEW. An uninterruptible power supply will provide several minutes for action to save data in the case of an unexpected power outage. All equipment has been tested. The control box is currently under construction. The LabVIEW code is currently being written.

Technology Transfer Path

RMX Technologies is the industry partner on this project as a co-developer and co-inventor. RMX will scale up this technology to the pilot and production levels after completion of this work and will sell commercial furnaces to carbon fiber manufacturers. RMX has a record of accomplishment of successful scale-up, having commercialized the advanced oxidation technology previously developed by this team.

Conclusion

A large part of the year was dedicated to modeling (i.e., CPEC-2V). The results obtained from this model include:

- Confirming that carbonization of oxidized PAN fiber using EM energy is possible
- Leading the team to implement additional characterization of the material and its evolution
- Defining the most economical and realizable operating frequency
- Emphasizing how critical the geometry of this type of equipment is.

These four pieces of knowledge are of prime importance, especially the third and fourth ones, which indicate this type of design would be extremely difficult to achieve without a model.

Concretely, the model shows an acceptable homogeneity over the center of the cross section, which represents close to two-thirds of the tow and what parameters influence this result. The energy is localized about the tow, thanks to a unique patentable design. Consequently, the majority of the energy within the cavity reaches the tow and induces temperature elevation in the material. Nevertheless, several differences between the model and reality are expected. Thus, the temperature homogeneity of the real process can be expected to exceed that predicted within the model.

The CPEC-3 equipment setup was nearly complete at the end of FY 2016. It includes the oven and all its subcomponents (e.g., power supply, waveguides, safety enclosure, measurement system, and data control). The first tests on oxidized PAN fiber will happen at the beginning of FY 2017.

References

[1] Handermann, Alan, 2009, "Oxidized Polyacrylonitrile Fiber Properties, Products and Applications," Zoltek Corporation, X. Huang (ed.), "Fabrication and Properties of Carbon Fibers," *Materials* 2(4): 2369–2403.

[2] Thermoworks, "Emissivity for Carbon (candle soot): 0.95, Emissivity for Carbon (graphite, field surface): 0.98Table," http://www.thermoworks.com/learning/emissivity_table (accessed January 15, 2016).

[3] Paulauskas, F. L. and T. L. White, 2004, "Temperature-Dependent Dielectric Measurements of Polyacrylonitrile Fibers During Air Oxidation," presented at the *International SAMPE Symposium and Exhibition*, Long Beach, California, May 16 through 20, 2004, and published in the conference proceedings, available online at http://web.ornl.gov/~webworks/cppr/y2001/pres/119502.pdf.

IV.2 Carbon Fiber Technology Facility – Oak Ridge National Laboratory

Project Details

Alan Liby, Principal Investigator
Energy and Environmental Sciences
Oak Ridge National Laboratory (ORNL)
1 Bethel Valley Road
Oak Ridge, TN 37831
Phone: 865-576-4221
E-mail: libyal@ornl.gov

H. Felix Wu, Program Manager
U.S. Department of Energy
1000 Independence Ave., S.W.
Washington, DC 20585
Phone: 202-586-4830
e-mail: *felix.wu@ee.doe.gov*

Contractor: ORNL
Contract No: DE-AC05-00OR22725

Executive Summary

In March 2009, the U.S. Department of Energy Office of Energy Efficiency and Renewable Energy issued a competitive call for proposals to construct and operate a highly flexible, highly instrumented, low-cost carbon fiber (LCCF) technology facility for demonstrating and evaluating new low-cost manufacturing technologies at a pilot scale. ORNL responded to the call and was awarded the project. Construction of the Carbon Fiber Technology Facility (CFTF) began in March 2011 and the facility was commissioned for operations in March 2013.

CFTF offers a unique, highly flexible, highly instrumented carbon fiber line for demonstrating advanced technology scale-up and for producing market development volumes of prototypical carbon fibers. CFTF's unique capabilities, including the flexibility to process a range of feedstocks and product forms, are unmatched anywhere in the world. Designed to bridge the "valley of death" between laboratory research and commercial-scale deployment of LCCF technologies, CFTF fills a critical need for support for industrial competitiveness in the manufacturing of this nation's carbon fiber. The objectives of this project are to accomplish the safe and reliable operation of CFTF and to further U.S. Department of Energy objectives for large-scale commercialization of LCCFs. CFTF supports the Office of Energy Efficiency and Renewable Energy's efforts to transition technologies to industry, specifically with respect to cost-effective carbon fiber for composite materials in high-volume energy applications.

Activities funded under this project include development of process science for converting alternative precursor material into carbon fiber, production of sufficient quantities of carbon fiber from lower-cost precursor materials to provide LCCF to industry partners for development of prototypical composite applications, and establishment of a skilled workforce and training system that can be leveraged to assist industry in development of a skilled carbon fiber and composites workforce. No information in any section of this report is export controlled.

Accomplishments

- CFTF hosted 623 visitors, representing 118 organizations (FY 2016).
- Solicited interest from industry (by the ORNL Partnerships Office) to license intellectual property related to increased throughput of textile acrylic fiber. Five companies were selected for negotiations and a license has been executed with LeMond Composites for intellectual property related to increased throughput of textile acrylic fiber (FY 2016).
- Held the Annual Peer Review for CFTF in Oak Ridge, Tennessee, on August 18, 2016. Reviewers were positive about progress during the last year in bringing development of LCCF to a state of strong commercial interest. Deepened technical understanding of the role of precursor chemistries in increased material throughput was termed "great work." Continued research and development on precursor stretching effects, spin finish effects on oxidation kinetics and product properties, and melt-spinnable polyacrylonitrile (PAN and other precursors was strongly encouraged (FY 2016).
- Measured temperature uniformity across the belt in oxidation Ovens 1 and 3 with three different temperatures (i.e., 200°C, 215°C, and 230°C). Because of the location of the controlling thermocouple and the lower fan speed, the temperature uniformity is about 5°C lower than the stated temperature on the sides of the belt and 2°C lower in the middle portion of the belt. This information will help when determining oxidation rates of any material on the belt (FY 2016).
- Completed experiments to determine Kaltex textile PAN lot-to-lot variability. Lots TE4571150901 and TE4571151006 were run in September and October 2015, respectively. The material for both runs was Kaltex K20-HTU: 2.0 denier, high-tenacity, uncrimped fiber with 457 K tow/band size. Twelve specimens were prepared and tested for each band. Comparison of mechanical property data for both tensile strength and modulus showed only a small variation between the two lots (FY 2016).
- Completed thai acrylic pre-stretching trials. While observed tensile strength and modulus were low relative to the best results for the Kaltex precursor, the results were very encouraging considering the minimal number of development trials run in this initial evaluation (FY 2016).
- Completed trials on a second batch of Taekwang precursor with a higher acrylonitrile content (i.e., 93% range). This second batch behaved favorably during processing and the mechanical properties achieved were highly encouraging considering the limited development time and effort (FY 2016).
- Identified in situ monitoring and control techniques in four key areas (i.e., fiber oxidation state via visible polarized spectroscopy; fiber chemistry via vibration spectroscopy; infrared thermometry and/or thermography; and mass spectrometry) through proof of principle and selection of in-line measurement techniques (FY 2016).

Approach

CFTF is open for tours so that representatives from industry and others can see the technology and the process science under development to produce LCCF with industry-appropriate mechanical properties from alternative precursor materials. Currently, there is no commercial manufacturer of this particular type of LCCF; therefore, CFTF plans to produce enough of it for industry to evaluate, thus displaying the quality of the LCCF on a multitude of end user platforms. This work intends to produce industry demand for the technology. CFTF staff members continue to hold discussions with industrial partners that are interested in scaling up the processes under development at CFTF. The financial investment for industry to scale up the technology is significant; therefore, it is not quickly decided upon. One CFTF mission is to transition this technology to industry for scale-up, but numerous technical challenges remain that must be overcome to further reduce the risk for industry to implement the technology. CFTF addresses these technical challenges in collaboration with industry to reduce implementation risks. Some of these challenges are handling the large tow (300 K-610 K), increasing throughput, splicing and splitting the large tow, and developing appropriate sizing for the LCCF for

specific composite applications. CFTF continues to be a training ground for technical staff in the production of carbon fiber. Multiple tools were developed to establish a training program for future carbon fiber production facilities.

Results and Discussion

Verification of the Uniformity of the Thermal Profile in Oxidation Ovens 1 and 3

Temperature uniformity was measured across the belt with three different temperatures: 200°C, 215°C, and 230°C. Uniformity was measured at 2-ft increments on the control room side, middle, and operator side of the belt as shown in Tables IV.2-1 through IV.2-3.

Table IV.2-1. Temperature Uniformity in Oxidation Ovens 1 and 3 (Zones 1 and 3) at Different Locations (Oven Temperature set at 200°C)

Date	Fan Speed	Belt Speed	Temperature Set Points								
5/23/2016	25%	0.1	*Z1A*	*Z1B*	*Z3A*	*Z3B*					
			200	200	200	200					
Tow Band Position	**1**	**2**	**3**	**4**	**5**	**T**	**1**	**2**	**3**	**4**	**5**
Control Room Side											
Zone 1	154	182.5	186.4	188.5	189.7	191.9	193.2	193.6	192	191	190.4
Zone 3	189.5	191.7	193.7	194.8	193.6	195.2	194.6	193.5	191.7	191	188
Middle											
Zone 1	174.6	189.5	191.6	193	193.5	195.5	195.5	196.5	195.5	195.1	194.4
Zone 3	194.5	195.8	196.7	197.4	196.6	197.8	197	196.6	195.8	194.6	192.1
Operator Side											
Zone 1	178.6	192	194	193.7	195.9	194.5	197.3	196.1	195.1	193.9	193.6
Zone 3	194.6	195.9	197.2	198	197.1	198.3	197.6	197.3	196.3	195.3	194.6

Notes: Z1A = Zone 1, Heating Zone A; Z1B = Zone 1, Heating Zone B; Z3A = Zone 3, Heating Zone A; Z3B = Zone 3, Heating Zone B; and Section T of each oven is a transition section between each zone with only residual airflow.

Table IV.2-2. Temperature Uniformity in Oxidation Ovens 1 and 3 (Zones 1 and 3) at Different Locations (Oven Temperature set at 215°C)

Date	Fan Speed	Belt Speed	Temperature Set Points								
5/24/2016	25%	0.1	*Z1A*	*Z1B*	*Z3A*	*Z3B*					
			215	215	215	215					
Tow Band Position	**1**	**2**	**3**	**4**	**5**	**T**	**1**	**2**	**3**	**4**	**5**
Control Room Side											
Zone 1	181.1	186.5	183	201.2	199.9	203.9	202	207.1	207.6	207	207.6
Zone 3	199.7	198.5	200.2	206.8	203.8	208.4	207.2	207.4	201.1	206.8	205.6
Middle											
Zone 1	196.4	198.2	202.2	204.3	204.9	207.2	208.1	209.5	208.2	207.4	206.4
Zone 3	208.9	210	211.3	212	211	212	211.5	211.8	210.8	209.9	207.7
Operator Side											
Zone 1	173.4	200.4	203.6	205.5	206.1	208.8	205.1	210.5	209.5	208.3	207.5
Zone 3	206	208.3	209.5	210.6	211.3	211.1	210.6	210.2	209.4	208	204.5

Notes: Z1A = Zone 1, Heating Zone A; Z1B = Zone 1, Heating Zone B; Z3A = Zone 3, Heating Zone A; Z3B = Zone 3, Heating Zone B; and Section T of each oven is a transition section between each zone with only residual airflow.

Table IV.2-3. Temperature Uniformity in Oxidation Ovens 1 and 3 (Zones 1 and 3) at Different Locations (Oven Temperature set at 230°C)

Date	Fan Speed	Belt Speed	Temperature Set Points								
5/24/2016	25%	0.1	*Z1A*	*Z1B*	*Z3A*	*Z3B*					
			230	230	230	230					
Tow Band Position	**1**	**2**	**3**	**4**	**5**	**T**	**1**	**2**	**3**	**4**	**5**
Control Room Side											
Zone 1	204.6	216.7	218.5	218.8	219.8	220.8	221.3	224.6	223.5	223	222.3
Zone 3	202.3	217	219.6	221.9	224.1	224.3	224.2	225.4	224.4	224.8	223.3
Middle											
Zone 1	209.3	220.8	223	224	224.1	225.9	225.5	228	227.1	226.2	225.3
Zone 3	222	225	227	228.2	228.7	227.3	228.2	228	227.3	226.5	225.1
Operator Side											
Zone 1	189	210.6	215.5	218	218.9	221.8	221.1	223.6	222	221.3	219.5
Zone 3	209.3	214.7	220.6	222.4	223.4	224.2	226	225	224.3	223.4	222.5

Notes: Z1A = Zone 1, Heating Zone A; Z1B = Zone 1, Heating Zone B; Z3A = Zone 3, Heating Zone A; Z3B = Zone 3, Heating Zone B; and Section T of each oven is a transition section between each zone with only residual airflow.

As Tables IV.2-1 through IV.2-3 show, due to the location of the controlling thermocouple and the lower fan speed, the temperature uniformity is about 5°C lower than the stated temperature on the sides of the belt and 2°C lower in the middle portion of the belt. This drop in temperature needs factored into processing conditions when oxidizing anything using the belt.

Tables IV.2-4 and IV.2-5 show the allowable temperature delta between the zones with varying temperatures and fan speeds. As shown, a 15°C difference between each zone is the most the ovens are capable of between each connected oven zone. This will help when determining oxidation rates of any material on the belt.

Kaltex Lot-to-Lot Variability

Experiments to determine Kaltex textile PAN lot-to-lot variability were completed. Lots TE4571150901 and TE4571151006 were run in September and October 2015, respectively. Material for both runs was Kaltex K20-HTU: 2.0 denier, high-tenacity, uncrimped fiber with 457 K tow/band size. Twelve specimens were prepared and tested for each band. “Band location” in Tables IV.2-6 and IV.2-7 is the location of the five bands within the conversion line with Location 1 being closest to the control room. Comparison of mechanical property data for both tensile strength and modulus showed only a small variation between the two lots (Figure IV.2-1).

Table IV.2-4. Temperature Uniformity in Oxidation Ovens 1 and 3 (Zones 1 and 3) at Different Locations (Oven Temperature Varied Between 190°C and 250°C)

Date	Fan Speed	Belt Speed	Temperature Set Points								
5/25/2016	25%	0.1	*Z1A*	*Z1B*	*Z3A*	*Z3B*					
			190	210	230	250					
Section	A					T	B				
Increment (2 ft)	1	2	3	4	5		1	2	3	4	5
Zone 1	130.3	167.3	180.2	183.6	185	188	193.2	200.8	202.6	202.6	202
Zone 3	97.2	145.7	201.9	218	224.1	226.6	228.9	232.5	240.6	243	244.1
5/26/16	35%	0.1	*Z1A*	*Z1B*	*Z3A*	*Z3B*					
			190	210	230	250					
Zone 1	171.7	183	183.6	187.1	187.5	191.1	198.2	205.3	206	207	205.4
Zone 3	132.4	195.2	220.5	227.7	229.7	231	231.7	236.2	243.1	246.5	247.1
5/26/16	45%	0.1	*Z1A*	*Z1B*	*Z3A*	*Z3B*					
			190	210	230	250					
Zone 1	148.2	178.4	189	189.2	188.5	194.3	201.7	208.9	208.5	208.8	204.9
Zone 3	229.1	230.4	231.2	232.2	236.2	244.1	247	247.3	246.7	244.9	245.5

Notes: Z1A = Zone 1, Heating Zone A; Z1B = Zone 1, Heating Zone B; Z3A = Zone 3, Heating Zone A; Z3B = Zone 3, Heating Zone B; and Section T of each oven is a transition section between each zone with only residual airflow.

Table IV.2-5. Temperature Uniformity in Oxidation Ovens 1 and 3 (Zones 1 and 3) at Different Locations (Oven Temperature Varied Between 200°C and 260°C)

Date	Fan Speed	Belt Speed	Temperature Set Points								
5/25/2016	25%	0.1	*Z1A*	*Z1B*	*Z3A*	*Z3B*					
			200	220	240	260					
Section	A					T	B				
Increment (2 ft)	1	2	3	4	5		1	2	3	4	5
Zone 1	197.4	198.4	199.5	201.5	206.6	212.7	213.7	213.9	212	209.4	197.1
Zone 3	234.3	235.5	237.2	238.3	240.8	244.8	253.2	254.1	252.3	249.3	242.2
5/25/16	25%	0.1	*Z1A*	*Z1B*	*Z3A*	*Z3B*					
			210	230	250	260					
Zone 1	201.7	205.1	206.2	206.5	208.7	214.5	222.5	224.3	224	222.8	222.1
Zone 3	240.3	244.3	246.7	249.5	251.3	255.7	264.9	265.6	265.9	264.7	263.9
5/25/16	25%	0.1	*Z1A*	*Z1B*	*Z3A*	*Z3B*					
			200	220	240	260					
Zone 1	160.2	185.6	192.5	194.7	195.6	199.2	204.8	212.6	214.4	214.1	213.2
Zone 3	221.8	232.6	236.1	238.9	241.4	245.5	253.2	255.4	255.9	254.8	253.9

Notes: Z1A = Zone 1, Heating Zone A; Z1B = Zone 1, Heating Zone B; Z3A = Zone 3, Heating Zone A; Z3B = Zone 3, Heating Zone B; and Section T of each oven is a transition section between each zone with only residual airflow.

Table IV.2-6. Mechanical Properties of Kaltex Precursor Lot TE4571150901 (by Position along the Bandwidth after Conversion to Carbon Fiber at CFTF)

Lot	TE4571150901									
Band Location	1		2		3		4		5	
Series	15090914284901		15090914302902		15090914292403		15090914294204		15090914295505	
	Tensile Strength (ksi)	Modulus (msi)	Tensile Strength (ksi)	Modulus (msi)	Tensile Strength (ksi)	Modulus (msi)	Tensile Strength (ksi)	Modulus (msi)	Tensile Strength (ksi)	Modulus (msi)
1	376.2	39.95	372.7	39.11	434.9	40.30	406.8	39.52	421.2	38.97
2	368.4	39.26	407.5	39.04	416.4	40.05	387.5	40.77	433.8	40.41
3	395.0	39.90	381.0	39.07	388.0	38.78	422.5	40.50	424.1	40.26
4	373.7	39.69	363.6	38.90	394.0	40.46	433.5	40.61	433.4	39.86
5	384.5	40.09	350.6		438.0	39.90	390.0	40.29	424.5	39.58
6	402.4		370.5		409.5		400.6		414.0	
7	349.6		380.4		376.9		412.2		409.7	
8	368.7		349.4		377.8		408.9		398.4	
9	383.4		393.1		430.5		390.0		411.4	
10	387.7		402.2		398.5		423.4		432.5	
11	388.7		384.7		376.0		432.0		424.6	
12	380.1		425.1		431.6		424.6		436.5	
Average	379.9	39.78	381.7	39.03	406.0	39.90	411.0	40.34	422.0	39.82
STDEV	13.93	0.32	22.67	0.09	23.93	0.66	16.47	0.49	11.65	0.57
CV	3.67	0.81	5.94	0.23	5.90	1.66	4.01	1.21	2.76	1.44

Lot Average	Tensile Strength (ksi)	Modulus (msi)
Average	400.1	39.80
STDEV	24.40	0.60
CV	6.10	1.51

Table IV.2-7. Mechanical Properties of Kaltex Precursor Lot TE4571151006 (by Position along the Bandwidth after Conversion to Carbon Fiber at CFTF)

Lot	TE4571151006									
Band Location	1		2		3		4		5	
Series	15102710124301		15102710122002		15102710115803		15102710113004		15102710111005	
	Tensile Strength (ksi)	Modulus (msi)	Tensile Strength (ksi)	Modulus (msi)	Tensile Strength (ksi)	Modulus (msi)	Tensile Strength (ksi)	Modulus (msi)	Tensile Strength (ksi)	Modulus (msi)
1	397.1	38.655	345.0	38.685	435.3	40.288	410.3	39.392	428.0	39.351
2	377.5	38.615	351.5	39.793	420.7	39.053	427.6	39.502	383.4	39.796
3	337.8	38.853	411.2	38.396	431.9	40.733	384.0	38.56	417.4	39.368
4	375.2	38.862	422.8	38.701	417.4	40.560	395.8	38.809	423.8	
5	374.1	39.817	431.8	38.613	419.3	39.179	393.6	39.601	366.5	
6	384.9		407.1		425.1		411.7		413.6	
7	386.5		399.4		416.6		393.4		423.4	
8	378.1		381.7		355.4		400.7		421.3	
9	326.4		380.8		384.9		381.7		374.4	
10	375.9		395.9		370.8		396.2		408.5	
11	377.5		391.4		337.2		389.5		321.6	
12	436.5		378.7		405.9		398.8		368.8	
Average	377.3	38.96	391.4	38.84	401.7	39.96	398.6	39.17	395.9	39.51
STDEV	27.32	0.49	26.03	0.55	32.03	0.79	12.80	0.46	32.87	0.25
CV	7.24	1.26	6.65	1.41	7.97	1.98	3.21	1.18	8.30	0.64

Lot Average	Tensile Strength (ksi)	Modulus (msi)
Average	393.0	39.27
STDEV	27.62	0.66
CV	7.03	1.69

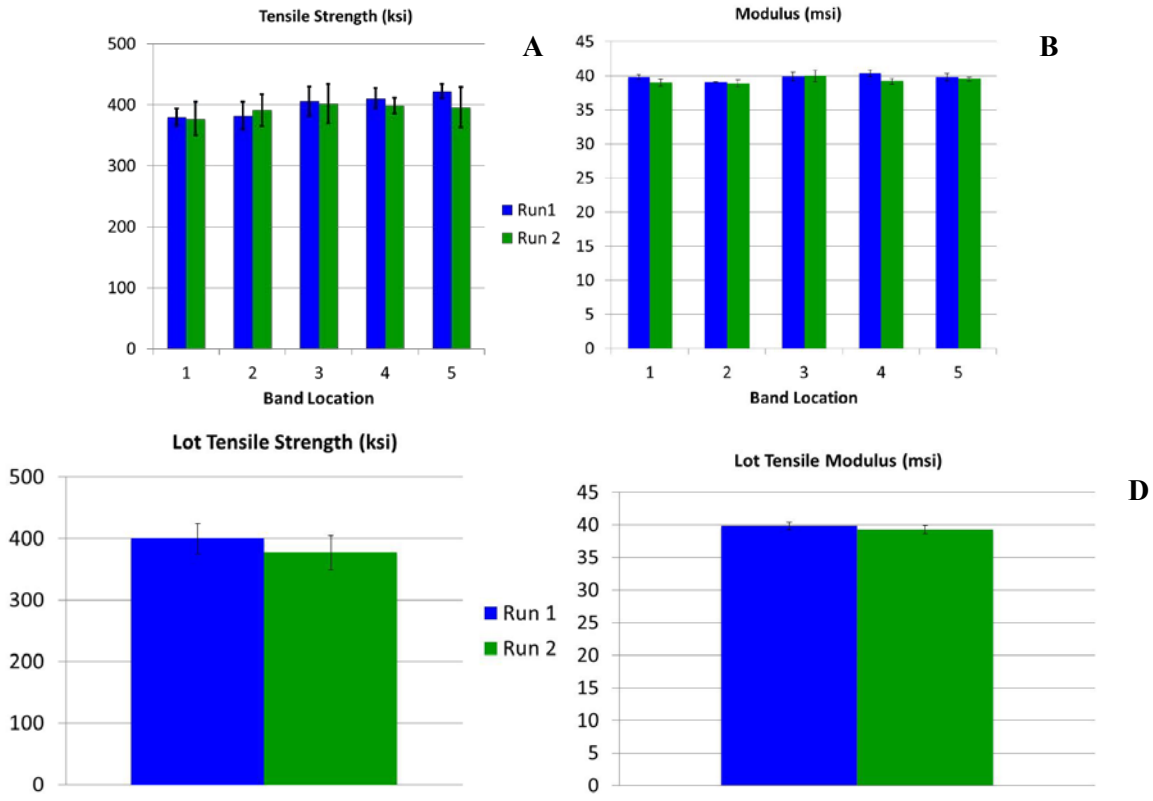

Figure IV.2-1. Mechanical property comparison between two Kaltex fiber lots (Lot Number TE4571151006 is Run 1 and Lot Number TE4571150901 is Run 2). (A) Tensile strength comparison at different positions along the bandwidth. (B) Tensile modulus comparison at different positions along the bandwidth. (C) Average tensile strength between the two different fiber lots. (D) Average modulus comparison between the two different fiber lots.

Development of the Thai Acrylic and Pre-Stretching Trials

Thai acrylic Lot TE7451160301 (two bands, TB15, EP834; 1.5 denier; 745 K tow) was used for this work. The Thai material was pre-stretched and heated by running through four oxidation ovens to improve fiber density and eliminate fiber fusing. The pre-stretch and heat treatment demonstrated the ability to increase oxidized fiber density from 1.2107 to 1.3566 g/cc (Table IV.2-8). Various temperature, speed, and stretch profiles were evaluated to obtain an appropriate density level for the carbonization process. Table IV.2-9 shows the resulting mechanical property data for Thai acrylic Lot TE7451160301 after carbonization.

Table IV.2-8. Thai Acrylic Pre-Stretch Data.

Lot TE7451160301		
Bale BA193077, BA193082		
Date	**Time**	**Zone 4 Density (g/cc)**
03/07/16	Start-Up	
03/07/16	7:58	1.2067
03/07/16	11:45	1.2072
03/08/16	7:45	1.2107
03/09/16	10:43	1.3191
03/09/16	16:11	1.3393
03/09/16	21:22	1.3450
03/10/16	4:30	1.3566

Table IV.2-9. Thai Acrylic Mechanical Property Data

Lot TE7451160301 — Bale BA193077, BA193082							
Date	Sample Set	Carbon Fiber Density (g/cc)	Linear Density with Size (g/meter)	Tensile Strength (ksi)	Tensile Modulus (msi)	Elongation (%)	Size Pickup (% by weight)
03/10/16	2	1.7475	21.26	245.2	24.52	1.00	1.61
03/10/16	2	1.7453	20.87	242.4	24.10	1.01	1.23
03/10/16	3	1.7009	17.67	212.5	23.63	0.90	1.67
03/10/16	3	1.7240	23.91	220.7	24.23	0.91	1.82
03/10/16	4	1.7269	25.86	242.1	23.98	1.01	1.82
03/10/16	4	1.7282	15.80	224.8	23.76	0.95	2.07

While observed tensile strength and modulus were low relative to the best results for the Kaltex precursor, the results were very encouraging considering the minimal number of development trials run during this initial evaluation.

Development of Taekwang Precursor

CFTF received a second batch of Taekwang precursor with a different spin finish and a higher PAN composition. This fiber showed much promise over the first batch upon initial oxidation; the initial carbonization (using ORNL's 1-ton, high-temperature furnace) showed tensile strengths in the 330-ksi range and tensile moduli in the 30-msi range.

The second batch of Taekwang had a higher acrylonitrile content (i.e., in the 93% range). The Taekwang T20-C precursor was oxidized at various speeds, temperatures, and stretch profiles in an attempt to optimize oxidation. Oxidized PAN fiber was collected for carbonization later. Continuous fiber was run through the low-temperature furnace and collected to allow for carbon fiber testing using the 1-ton pilot line's high-temperature furnace. The very early processing results of these trials are shown in Table IV.2-10.

Table IV.2-10. Summary Report for the Taekwang Precursor Trials (Conducted June 27 through July 1, 2016)

Lot: TN3631160602 (T20-C) 1 band													
Bale: ACR TOW NPB/906CTAA–0002													
				Oxidation Test Results				Carbon Fiber Results					
Date	Sample Set	Time	Series	Z1 Density (g/cc)	Z2 Density (g/cc)	Z3 Density (g/cc)	Z4 Density (g/cc)	Carbon Fiber Density (g/cc)	Linear Density w/Size (g/m)	Strand Tensile Strength (ksi)	Strand Tensile Modulus (msi)	Elongation (%)	Size Pickup (%)
06/07/16	T002	19:40	16060719400000	1.2062	1.2471	1.2936	1.3463	1.5450	19.05	66.5	NA	NA	NA
06/23/16	T002	16:30	16062316300000					1.7692	NA	328.2	29.11	1.13	1.64
06/27/16	T002	22:20	16062722200000					1.7585	12.72	330.1	30.89	1.07	0.90
06/13/15	T002	18:00	16061318000000					1.5575	20.04	61.2	NA	NA	NA
06/27/16	T002	19:30	16062719300000					1.7572	12.00	310.2	28.82	1.08	1.70

The Taekwang precursor with acrylonitrile content in the 93% range behaved favorably during processing and mechanical properties were highly encouraging considering the limited development time and effort.

Proof-of-Principle and Selection of In-Line Measurement Techniques

In-situ monitoring and control will be critical to improving the manufacturing of carbon fiber and increasing the adoption rate of carbon fiber in manufactured products. Process variables (e.g., time, temperature, tension, and gas flow) are closely monitored during manufacturing; however, the ability to monitor additional factors

(e.g., fiber chemical composition; defects; and crystal quantity, size, and orientation) would add significant value in carbon fiber manufacturing. This work has identified in situ monitoring and control techniques in the following four key areas.

1. Fiber oxidation state via visible polarized spectroscopy: Reflection characteristics change due to the degree of cross-linking; in-line verification can be used to optimize fiber tension and the heating process during oxidation to optimize fiber performance and energy consumption.
2. Fiber chemistry via vibration spectroscopy: Raman and/or Fourier transform infrared spectroscopy will enable measurement of specific fiber chemistry at all stages during conversion, providing the ability for closed loop control systems.
3. Process feedback via infrared thermometry and/or thermography: These techniques can be adapted to measure emissivity changes that may be associated with different states of fiber conversion on the path to full carbonization. Additionally, they enable measurement of fiber thermal conductivity and temperature, which can be linked to processing state.
4. Byproduct detection via mass spectrometry: This technique offers structurally descriptive detection of byproducts of the carbon fiber process during carbonization, which could aid in controlling uniformity of the process and product thereby, improving efficiency.

Technology Transfer Path

The ORNL Partnerships Office solicited interest from industry and publicly announced the opportunity to license intellectual property related to increased throughput of textile acrylic fiber. Five companies were selected for license negotiations based on the nine proposals submitted and a license has been executed with LeMond Composites.

Conclusions

Significant progress was made in developing processes to convert textile acrylic fiber to carbon fiber with mechanical properties suitable for use in vehicles and other industrial products. The results of developmental trials for precursor materials from two separate manufacturers showed favorable behavior during processing and were very encouraging considering the minimal number of development trials run in this initial evaluation. The opportunity to license provisional patents for production of carbon fiber from textile precursors was publicly announced and a license was executed with LeMond Composites. Although much process development work remains, a clear pathway to reduction of up to 50% of the cost of carbon fiber production relative to existing commercial operations using textile precursors has been established. CFTF also identified four key areas for in situ monitoring and control techniques.

Bibliography

Jackson, C. D., Naskar, A. K., 2015, “Method of Producing Carbon Fibers from Multipurpose Commercial Fibers,” US Provisional Patent Application 62/273,559, filed December 31, 2015.

Jackson, C.D.; Naskar, A.K., 2016, “Method of Producing Carbon Fibers from Multipurpose Commercial Fibers,” US Patent Application 62/305,232 0, filed March 8, 2016.

IV.3 Predictive Engineering Tools for Injection-Molded Long Carbon Fiber Thermoplastic Composites – Oak Ridge National Laboratory

Project Details

Vlastimil Kunc, Principle Investigator
Oak Ridge National Laboratory (ORNL)
1 Bethel Valley Road
Oak Ridge, TN 37831
Phone: 865-919-4595
Fax: 865-574-4357
E-mail: kuncv@ornl.gov

C. David Warren, Principal Investigator
ORNL
1 Bethel Valley Road
Oak Ridge, TN 37831
Phone: 865-574-9693
Fax: 865-574-6098
E-mail: warrencd@ornl.gov

Aaron Yocum, Contract Manager
National Energy Technology Laboratory
3610 Collins Ferry Road
Morgantown, WV 26507-0880s
Phone: 304-285-4852
Fax 304-285-4403
E-mail: aaron.yocum@netl.doe.gov

H. Felix Wu, Program Manager
U.S. Department of Energy
1000 Independence Ave., S.W.
Washington, DC 20585
Phone: 202-586-4830
Fax: 202-856-2476
E-mail:felix.wu@ee.doe.gov

Contractor: ORNL
Contract No.: DE-AC05-00OR22725

Executive Summary

The objective of this project is to validate three-dimensional (3D) models for long carbon fiber (CF)-reinforced, thermoplastic, injection-molded composites. Advanced characterization techniques are being used to generate a database of experimental results for CF orientation and CF length distribution within a component. Computational models are validated using a part with features representative of an automotive component and a database of results will be made available to the general public via the world-wide web. This predictive technology will be used to create a demonstration part that will lead to production implementation of a separate part by Ford Motor Company. ORNL is mainly responsible for generating and distributing experimental data with proven measurement techniques and coordinating the project. Ford Motor Company is responsible for system specification and weight-reduction analysis. BASF and PlastiComp are preparing and supplying materials for the project and assisting with part molding. Minco and BASF are responsible for

molding the final part. The University of Illinois - Champagne jointly assists by supporting model integration with Virginia Polytechnic Institute & State University. Moldex3D North America is responsible for implementation and commercialization of validated models.

Accomplishments

- Established acceptable temperatures for fiber-length sample pyrolysis in atmosphere and in nitrogen (Fiscal Year [FY] 2014).
- Qualified molding machines intended for plaque molding and complex part molding by performing fiber length distribution measurements on purges (FY 2014).
- Produced material for molding trial: polypropylene (PP) with 20% and 40% CF and polyamide (PA) with 20% and 40% CF (FY 2014).
- Established target molding parameters and molded plaque samples with all materials under target (FY 2014).
- Performed rheology measurements with cone and capillary rheometers and established model input rheology data for polypropylene materials (FY 2014).
- Performed preliminary flow analysis for the complex part (FY 2014).
- Modified the injection molding screw to achieve greater fiber lengths (FY 2015).
- Molded end-gated plaques with four materials with combinations of slow/fast fill speed and low/high back pressure (FY 2015).
- Molded complex parts with four materials using selected combinations of slow/fast fill speed and low/high back pressure (FY 2105).
- Performed fiber length measurements at three locations for each plaque type (FY 2015).
- Performed fiber orientation measurements at three locations for each plaque with five replicates performed at a central location (FY 2015).
- Completed plaque mold filling simulation using Moldex3D software and compared fiber orientation and fiber length to experimental data (FY 2015).
- Completed measurements of fiber length distribution in the complex part (FY 2015).
- Completed tensile and flexural stiffness predictions using experimental and predicted fiber orientation for plaque molded under the base condition: PA 40% CF, slow fill speed, and low back pressure (FY 2015).
- Completed calibration of models for plaques with Moldflow software (FY 2016).
- Completed prediction of complex part flow with Moldflow and Moldex3D (FY 2016).
- Completed fiber orientation measurements in the complex part (FY 2016).
- Completed comparison of fiber orientation predictions and experiments (FY 2016).

Future Directions

- Distribute results on world-wide web.
- Present full results in the final report.

Technology Assessment

- Target: Validate CF length to 15% of model prediction on flat plaques using the reduced order fiber breakage model.
- Target: Validate CF length to 15% of prediction for the complex part using the reduced order fiber breakage model.
- Target: Validate CF orientation to 15% of prediction for the complex part using the fiber orientation model.
- Gap: A reduced order fiber breakage model is not available in a commercial code. A reduced order model is not validated for injection-molded CF-reinforced thermoplastics.
- Gap: Fiber orientation and length models are not validated in commercial codes for injection-molded CF-reinforced thermoplastics.
- Gap: An experimental dataset for validation of fiber orientation and fiber length models specifically for CF is not available for parts with complex geometries.

Introduction

The objective of this project is to implement and validate computational tools for predicting fiber orientation distribution and fiber length distribution in injection-molded long CF (LCF) thermoplastic composites for automotive applications. Validation for a complex part with realistic features was conducted, and the experimental results are being made available to the public. The intent is to validate prediction tools on an actual 3D automotive part using an LCF thermoplastic material, resulting in weight savings at an acceptable cost.

The preliminary design indicates a potential for more than 50% weight reduction resulting from both part consolidation and material substitution. With the support of this project team, Ford Motor Company has committed to bringing the technology toward production implementation with an integrated LCF injection-molded thermoplastic system. During FY 2015, the team performed plaque and complex part molding trials, fiber length and fiber orientation measurements, Moldex3D and Moldflow software simulations, and stiffness predictions.

Approach

During FY 2016, the team completed all measurements on the complex part using modified techniques [1–4] and compared experimental results to predicted results. The predictions were made with Moldex 3D and Moldflow software without advanced knowledge of experimental results for the complex part. Model parameters for both software packages were calibrated using experimental results for flat plaques.

Results and Discussion

Simulation was performed with the Moldex3D and Moldflow software for 40% carbon fiber reinforced polyamide with density of 1.39 g/cm^2. With the plaque model ready in Moldflow, fiber orientation results were obtained. The anisotropic rotary diffusion/reduced strain closure (ARD-RSC) and the Folgar-Tucker model implemented in Moldflow were tested and compared to experimental results. Following the practice in Moldex3D simulations, the parameters in the fiber orientation models were determined through a fiber tuning process with the experimentally obtained fiber orientation tensor at Location #1 (Figure IV.3-1a) as the target. A range of the RSC parameter in the ARD-RSC model and the coefficient of interaction (Ci) value in the Folgar-Tucker model were tested. The ARD-RSC model matched with experimental data best when the RSC parameter was set to 0.8. For the Folgar-Tucker model, an automatic parameter determination procedure was available in Moldflow when tuning the parameter (i.e., Ci). The team compared the results using the Ci value recommended by this procedure and a range of user-designated Ci values; the best match was obtained with the Ci tuned automatically by Moldflow, which yields the Ci to be 2.39e-10.

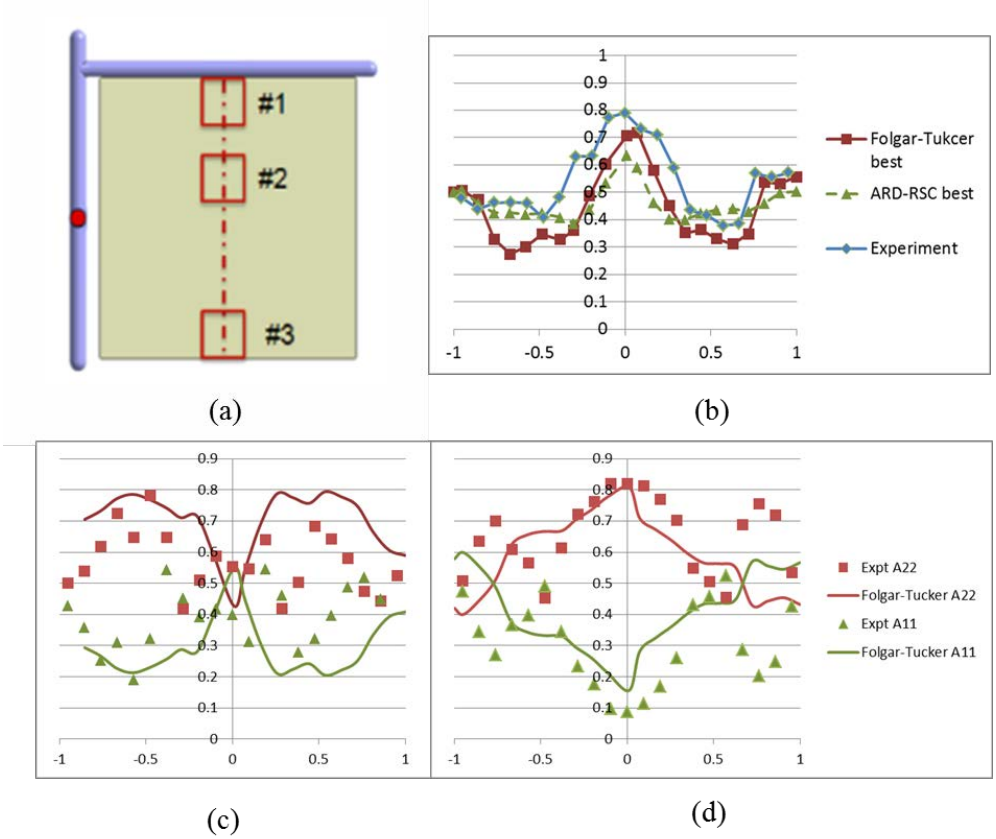

Figure IV.3-1. Fiber orientation model results predicted by Moldflow simulations. The fiber orientation results of Locations #1, #2, and #3 shown in (a) are extracted from the simulations. The fiber orientation data at Location #1 are taken as the target during the parameters tuning process. The best-fit fiber orientation results for a_{22} from both ARD-RSC and the Folgar-Tucker model are shown in (b), indicating that the Folgar-Tucker model gives a better match to experimental data. The comparison between experimental results and Folgar-Tucker model results of Locations #2 and #3 are shown in (c) and (d), respectively. The x-axis in (b), (c), and (d) give the normalized thickness, while the y-axis gives the values of the components.

The best results from both fiber orientation models and those from the experiment at Location #1 were compared as shown in Figure IV.3-1b. Because the flow is very close to a planar flow state, the fiber orientation tensors, a_{11} and a_{22}, are significantly higher than the component a_{33}, which quantifies the fiber alignment along the thickness direction. This indicates that the summation of a_{11} and a_{22} is close to 1 for the experiments and for both fiber orientation models. Therefore, comparison between a_{11} is only adequate for indicating the performance of the fiber orientation models. As in Figure IV.3-1b, the Folgar-Tucker model generally has a better match with experimental data for Location #1 compared with the ARD-RSC model. Comparisons between experimental results and Folgar-Tucker using the tuned Ci are shown in Figures IV.3-1c and 1d. The Folgar-Tucker model generally captures the trend of a_{11} and a_{22} variation through the thickness, yet deviations are still observed.

Complex Part Comparison

Model predictions for fiber orientation and fiber length distribution were compared at several strategically selected locations. The team identified features of interest and then selected comparison locations away from weld lines. The features of interest are shown in Figure IV.3-2 and include the following:

- Changes in thickness
- Ribs
- Holes

- Changes in direction.

Figure IV.3-2. Seatback and locations where measurements are taken.

Multiple measurements were performed at each feature of interest. Comparison of experimental and predicted data requires precise definition of the local coordinate system for each measurement location. Each location is assigned its local coordinate system in a global (model) coordinate system. Because of the complexity of the part, two additional datum systems were identified to physically isolate samples for measurements (see Figure IV.3-3).

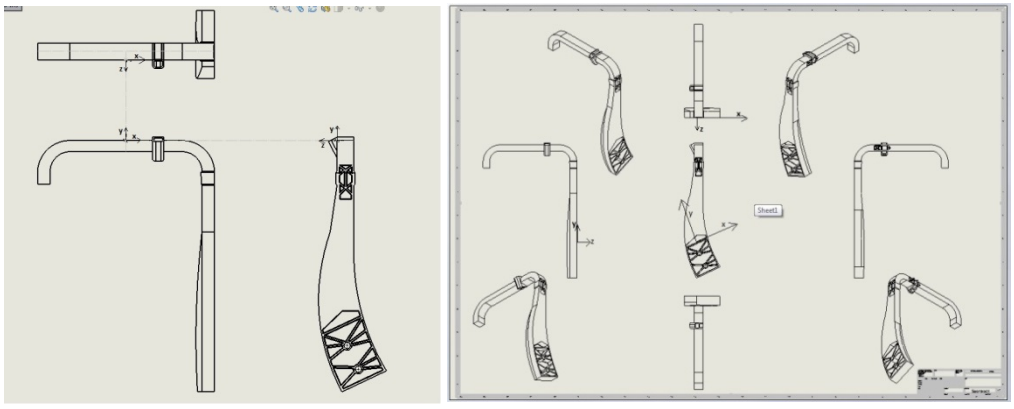

Figure IV.3-3. Datum coordinate system for measurement locations in a complex part.

The team then modeled cuts for isolation of samples and generated a set of local coordinate systems for each measurement location. Figure IV.3-4 shows an expanded view of a section of a seatback with several features isolated. Figure IV.3-5 shows an example of a rib isolated from the model and from the physical sample.

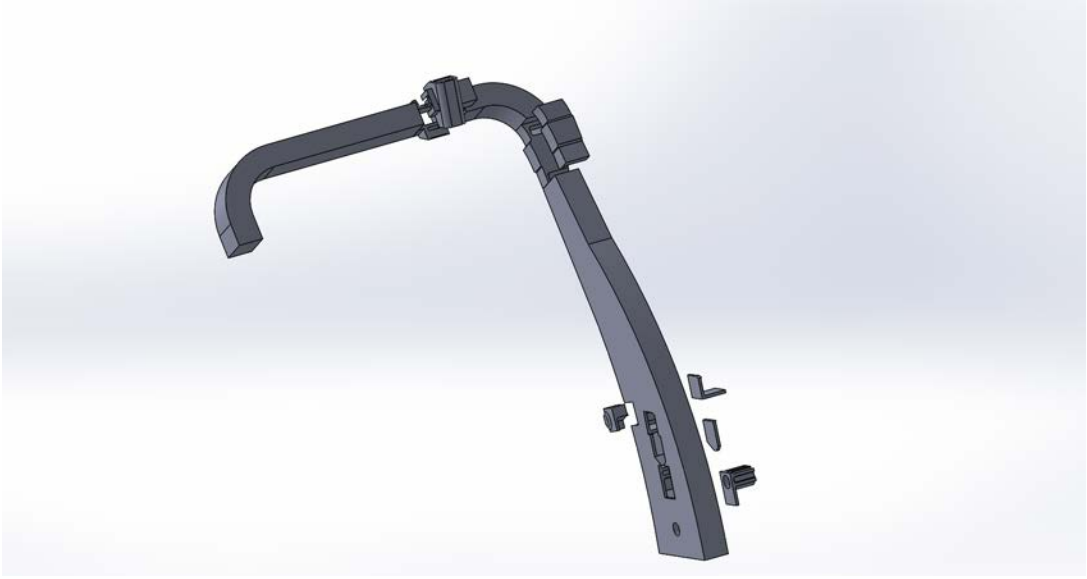

Figure IV.3-4. Expanded view of isolated samples in a section of the seatback.

Figure IV.3-5. Isolated rib sample from a model (left) and from a physical sample (right).

Once the features were isolated, the final specimens for fiber length and fiber orientation measurements were cut for the fiber orientation measurement. Figure IV.3-6 shows an example of a polished section of the seatback near a rib with the measurement location precisely identified in the low-resolution microscope image. Note the complexity of the flow in the transition of the feature.

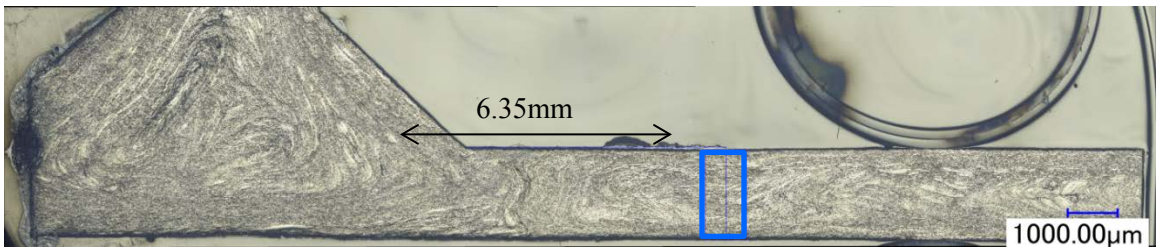

Figure IV.3-6. Low-resolution image of a rib fiber orientation sample. Measurement location for high-resolution imaging is precisely identified.

The actual high-resolution optical image for fiber orientation was then acquired within the area outlined by the blue rectangle in Figure IV.3-6. The area was determined by identifying features on the low-resolution image and finding the same features at high resolution. Moldex3D staff members then used the location information to determine the exact location in the finite element model for result extraction (see Figure IV.3-7). The coordinates were passed on to Ford so comparisons could be made at identical locations in Moldflow and Moldex3D.

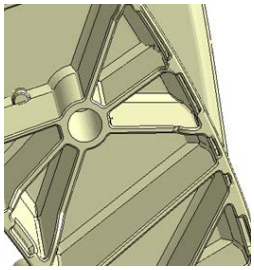

Figure IV.3-7. Rib sample location in Moldex3D finite element model.

All components of the second-order fiber orientation tensor were then extracted and maximum principal values were compared. In this particular rib location, the experimental principal value was 0.77, Moldflow prediction was 0.98, and Moldex3D prediction was 0.71. Therefore, the percentage deviation of prediction from the experimental value is 27.4% for Moldflow and 8.2% for Moldex3D. High principal value of the orientation tensor indicates a highly aligned state of fiber microstructure. Moldflow predicted a higher alignment in the part (Table IV.3-1).

Table IV.3-1. Model – Experiment Comparison of First Eigenvalue of Second Order Orientation Tensor for Polyamide with 40% CF Molded with Low Back Pressure and Slow Fill Speed

Location	Moldflow	Moldex3D	Experiment	Moldflow Prediction Deviation (%)	Moldex3D Prediction Deviation (%)
Direction Change 1	0.82	0.57	0.75	8.9	24.2
Direction Change 2	0.72	0.55	0.62	16.4	11.1
Direction Change 3	0.58	0.62	0.63	8.0	2.5
Thickness 1	0.96	0.76	0.72	32.7	5.1
Thickness 2	0.96	0.75	0.69	39.8	9.2
Rib	0.98	0.71	0.77	27.4	8.2
Flat Mutual Point	0.95	0.71	0.67	41.2	5.5
Hole 1	0.90	0.70	0.79	13.7	11.2
Hole 2	0.89	0.70	0.78	13.1	10.2

Eight of the nine predictions fall within 15% of experiments for Moldex3D, while four of nine Moldflow predictions fall within 15% of experiments.

Details of Moldex3D predictions for the complex part are summarized below. Figures IV.3-8 and IV.3-9 show Moldex3D's model and mesh of the seatback. Eight-layer boundary layer mesh was used to mesh the seatback model.

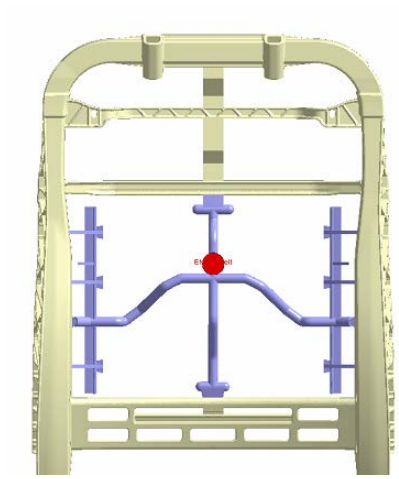

Figure IV.3-8. Moldex3D model of seatback.

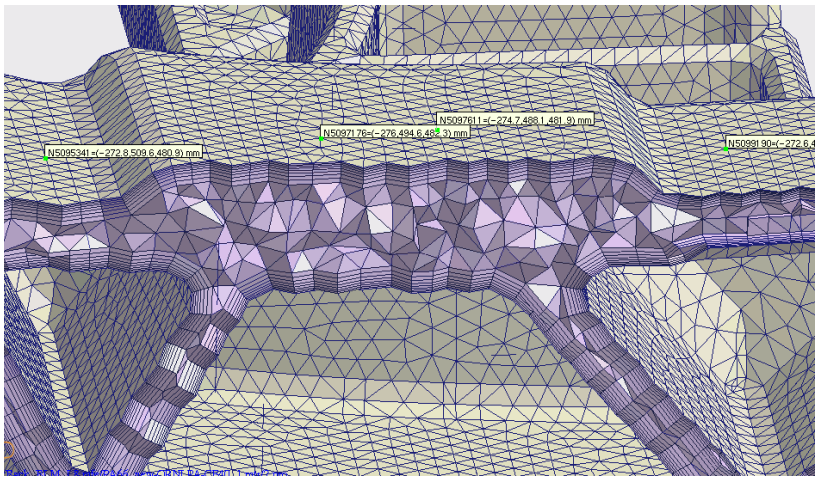

Figure IV.3-9. Moldex3D's boundary layer mesh for seatback.

Figure IV.3-10 shows Moldex3D fiber orientation predictions within the hole location and a graphical representation of the locations.

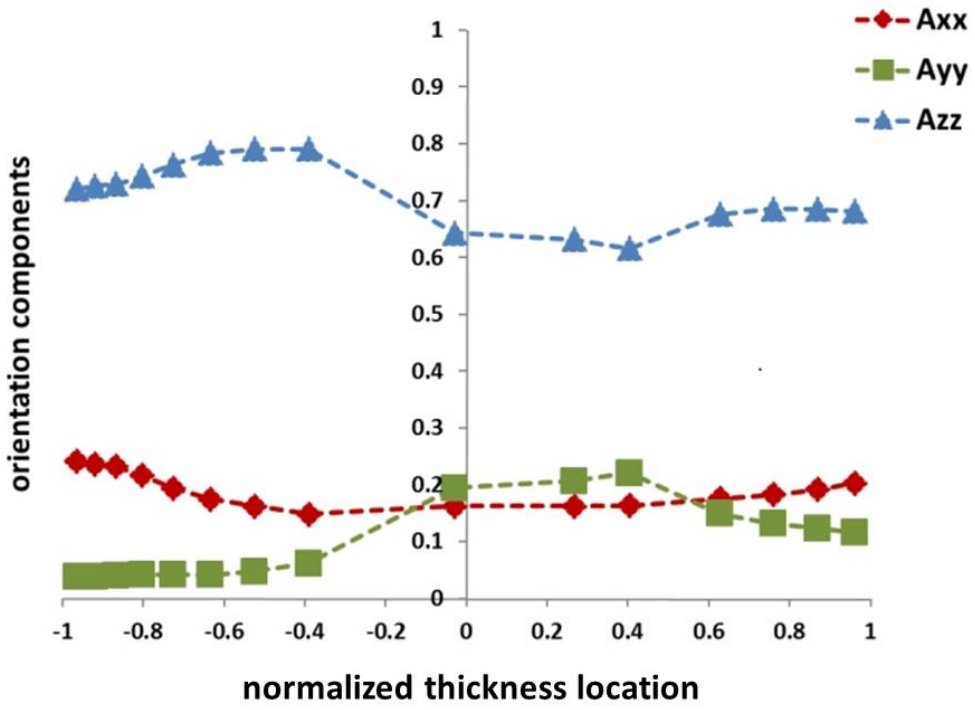

(a) Location 1

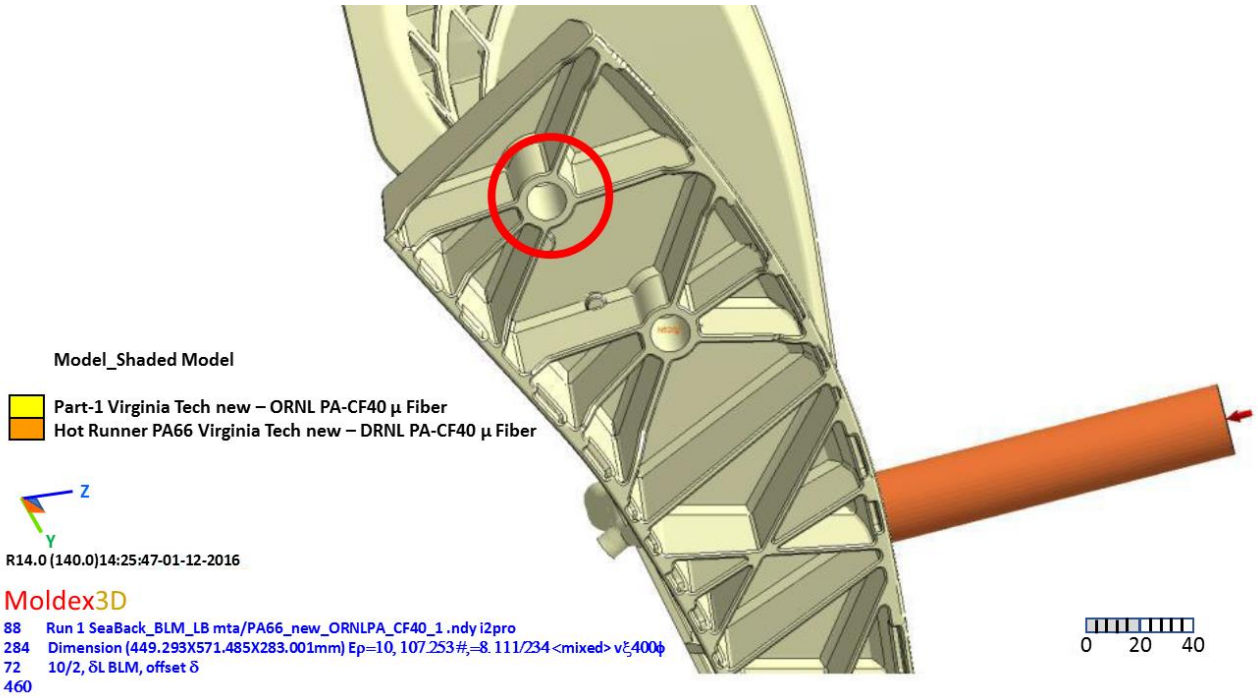

(a) continued

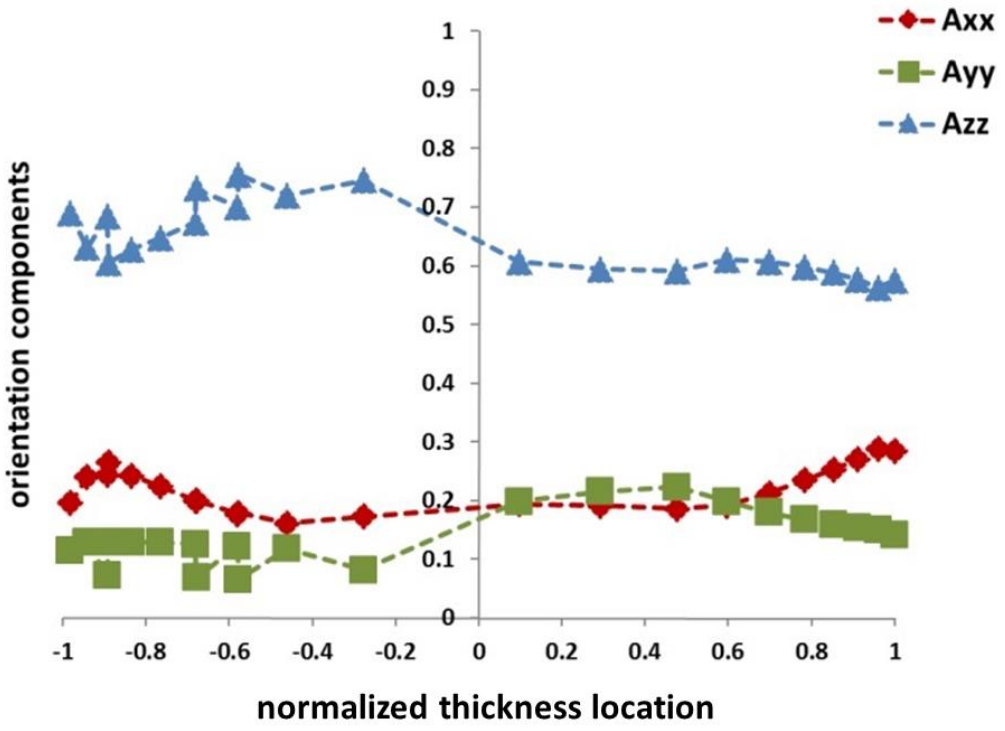

(b) Location 2

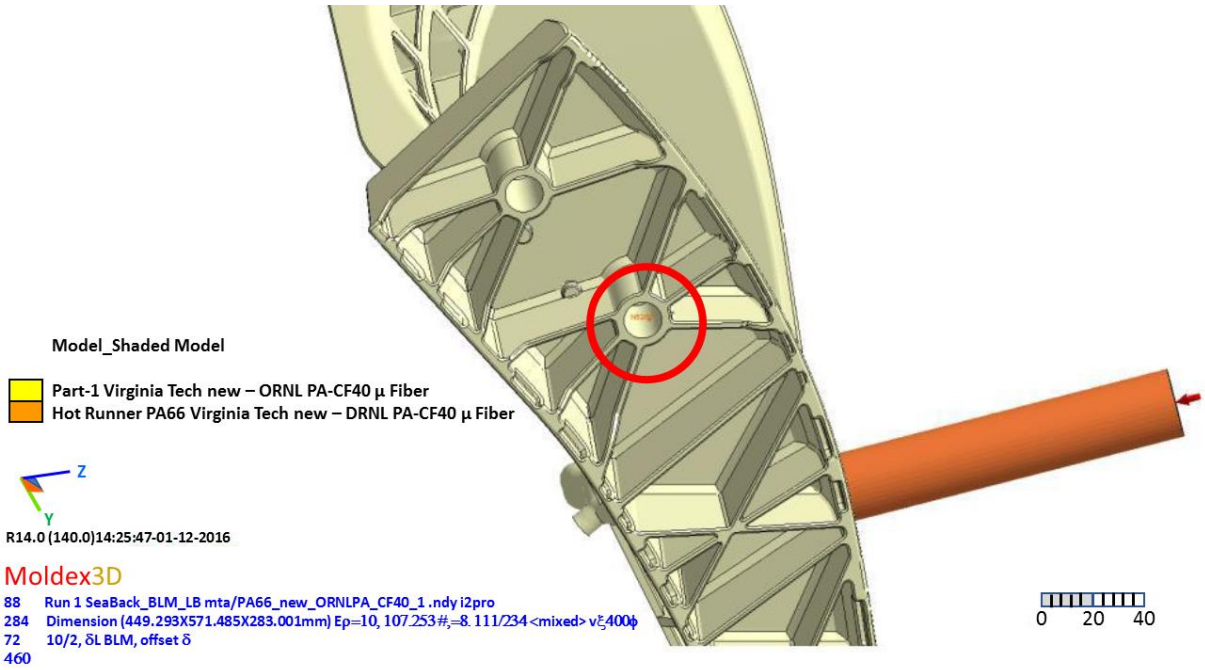

(b) cotinued

Figure IV.3-10. Fiber orientations in the hole region and the location where these measurements were taken.

Figure IV.3-11 shows Moldex3D fiber orientation predictions for a flat portion and a rib feature of the seatback sidewall. The flat portion is used as a common point to characterize the orientation state between the hole and the rib feature. Ideally, two locations closer to the rib and the hole are preferred; however, one common location was selected because the sample dimensions did not allow two experimental fiber length measurements. Figure IV.3-12 shows fiber orientation predictions in the thickness change location of the upper section of the seatback, and Figure IV.3-13 shows fiber orientations in the direction change region and the location where these measurements were taken.

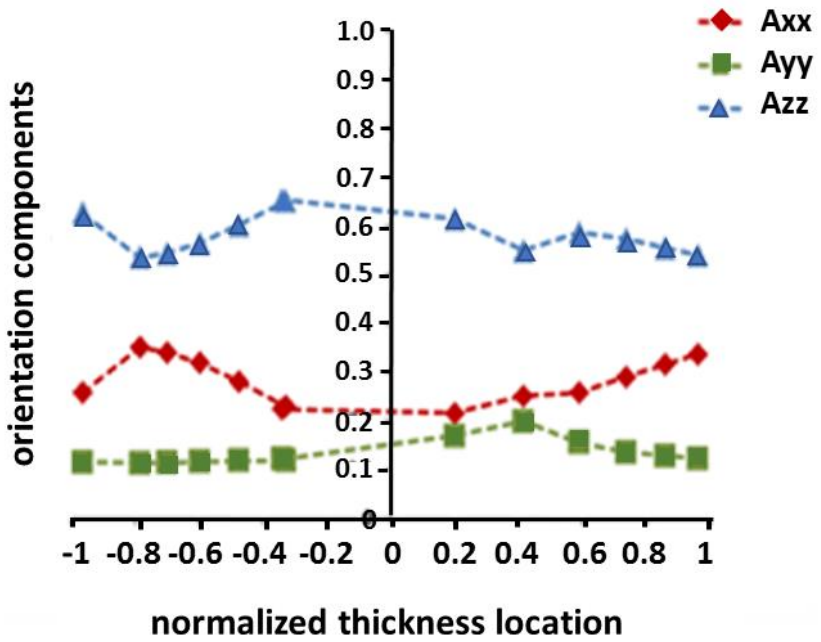

(a) Location 1

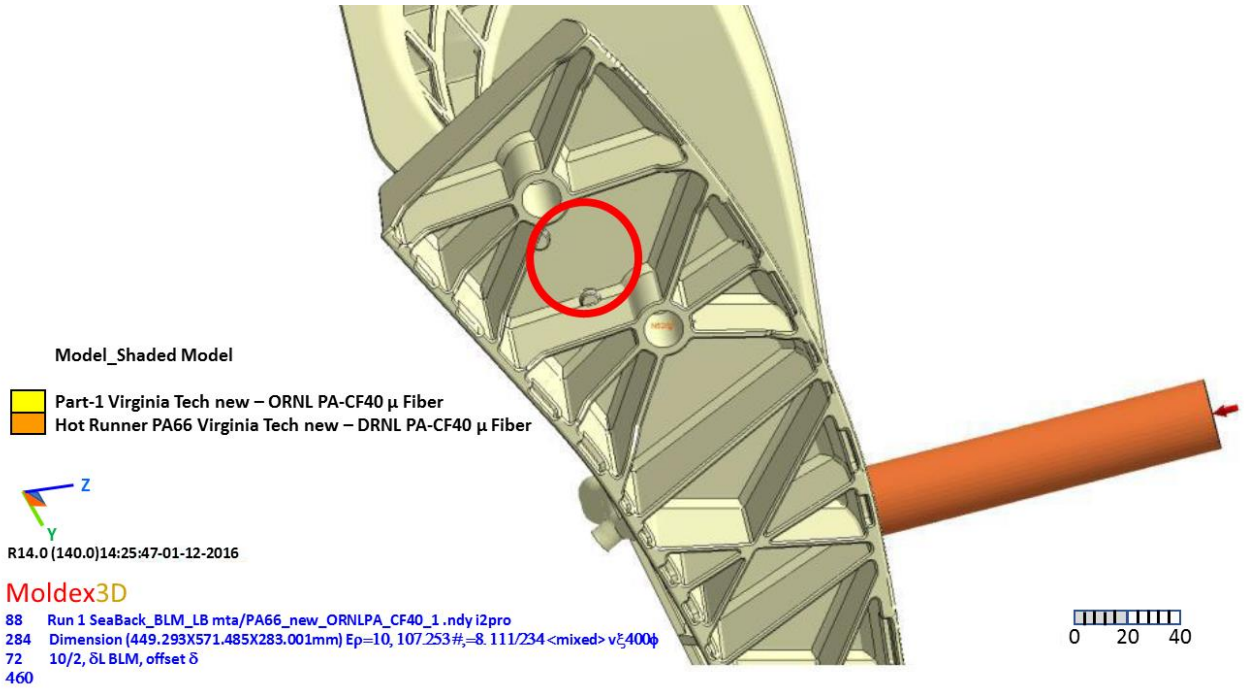

(a) continued

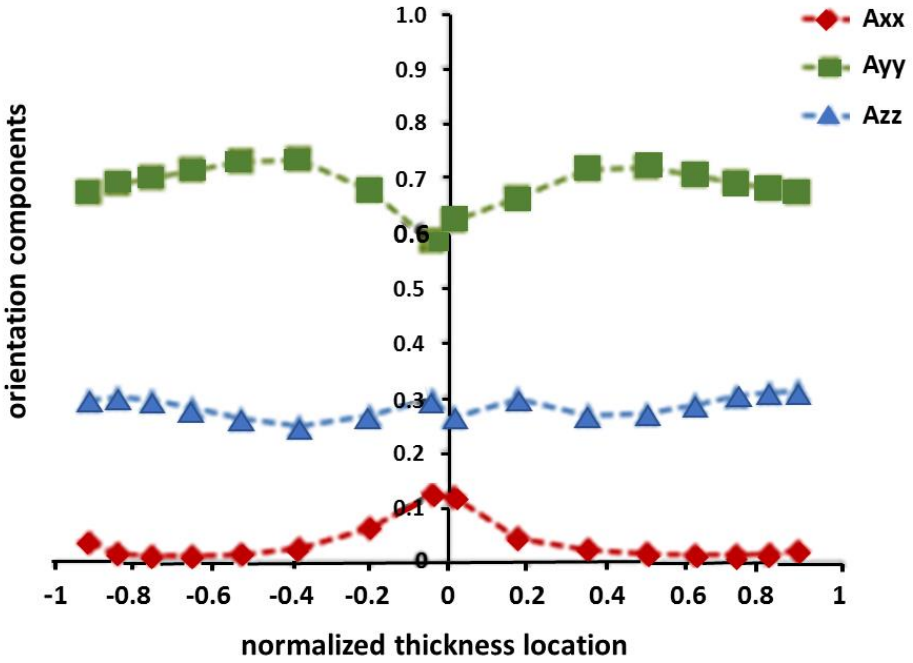

(b) Location 2

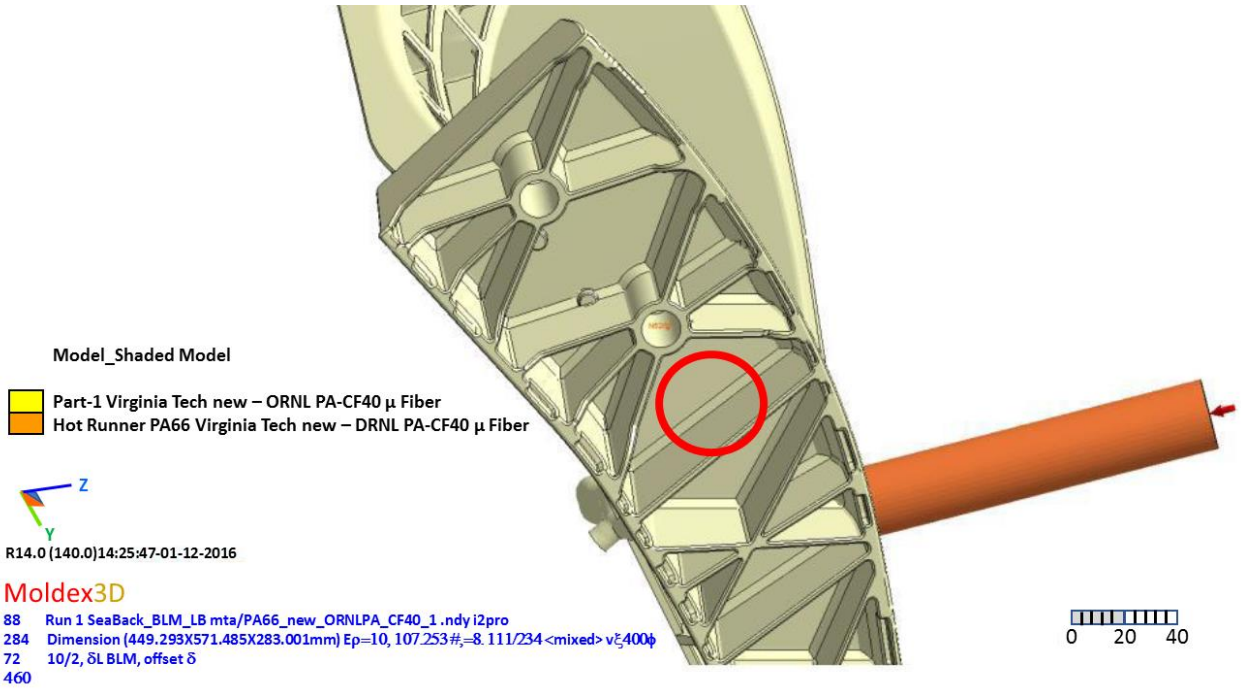

(b) cotinued

Figure IV.3-11. Fiber orientations in the rib region between the hole and the rib and the location where these measurements were taken.

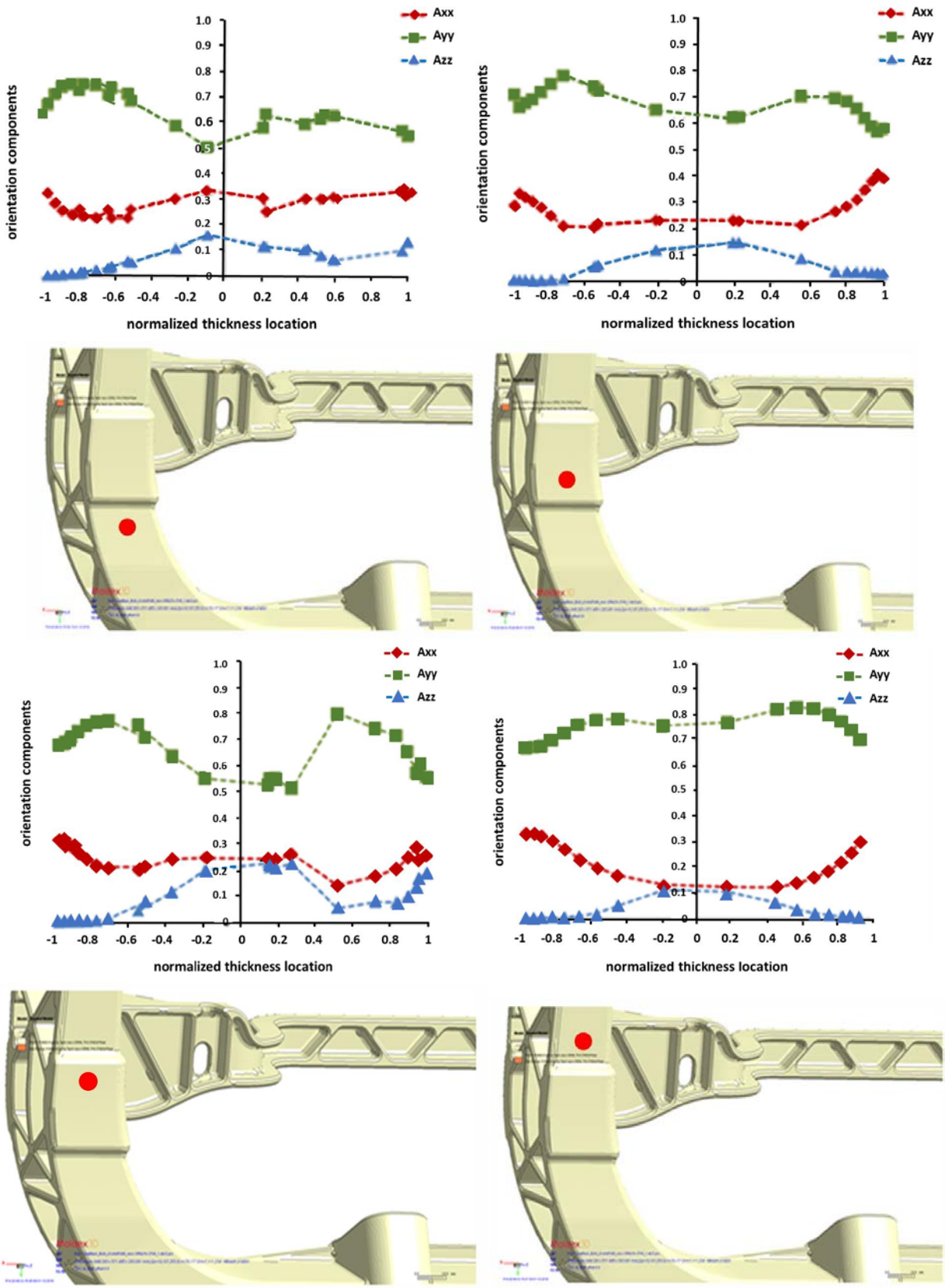

Figure IV.3-12. Fiber orientations in the thickness change region and the location where these measurements were taken.

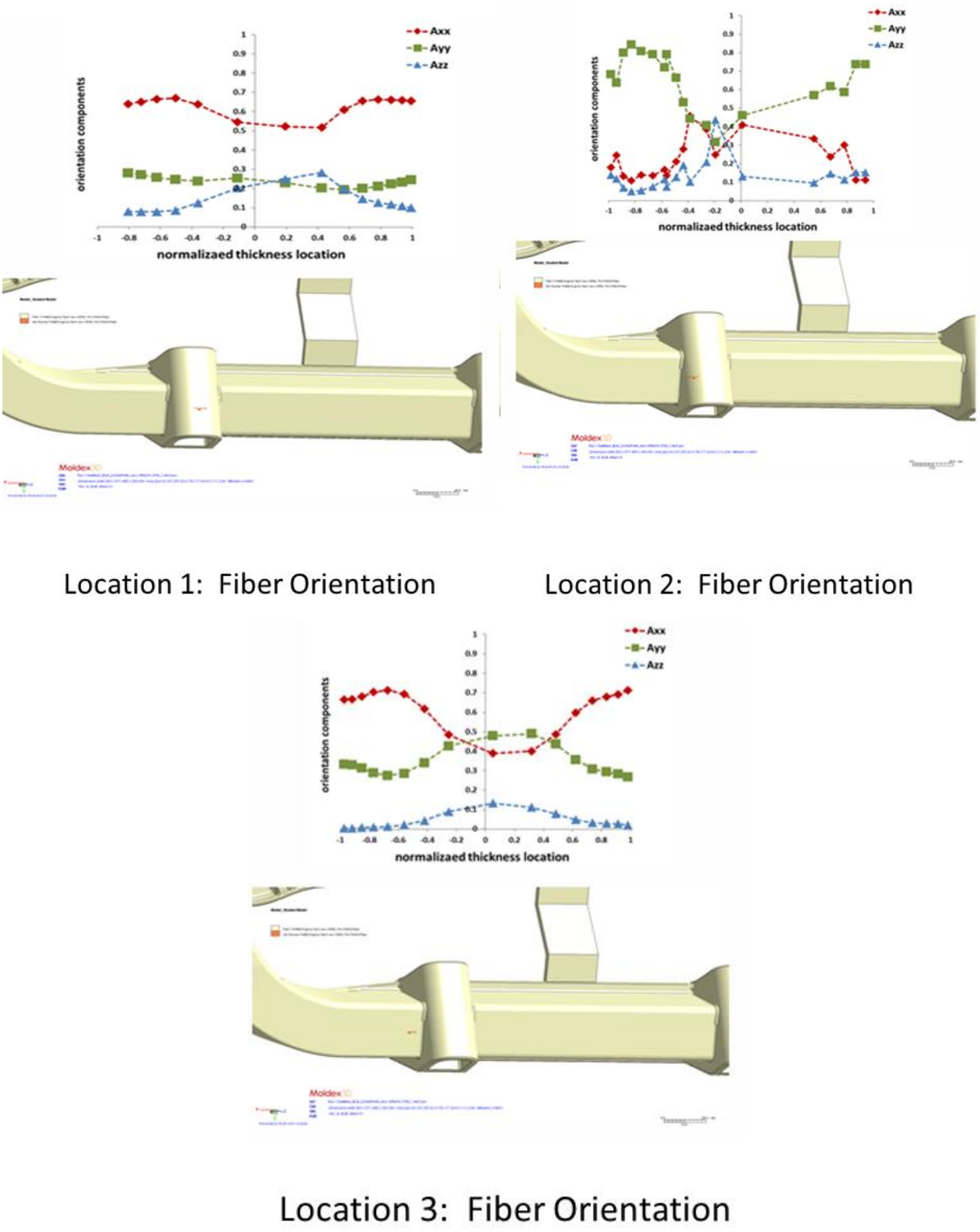

Figure IV.3-13. Fiber orientations in the direction change region and the location where these measurements were taken.

Experiments for modeling predictions were performed blindly, with experimental data being unavailable until after the predictions were released to the project team. The Moldex3D prediction was performed by Moldex3D

Northern America using the latest development code. Moldflow prediction was performed by Ford staff members using the latest available release of the software. Analysis and comparison of the data were performed by ORNL.

Cost and Mass Comparison

As the last step in completion of the project, the team was tasked with performing a comparison between part mass and part cost for the baseline (aluminum) part when compared to the PA66-40% LCF part. While the team had the produced samples to measure the mass of the PA66-40% LCF part, an optimized aluminum design was not available for comparison. The PA66-40% LCF has a density of 1.328 g/cm^3 and resulted in a part that weighed 1.75 kg. An equivalent aluminum part of the same dimensions would weight 3.56 kg, resulting in a 50.8 % mass reduction. There was no baseline cost for the aluminum par and the PA66 part cost could be roughly estimated, but specific details on tooling and manufacturing costs would have been very rough estimates at best.

While the project was being executed, Ford Motor Company was investigating using this technology for potential production of an oil pan. The oil pan uses the same composite material system (i.e., PA66-40% LCF) and replaces a die-cast aluminum oil pan. As a result, rather than performing a rough estimate of prototype and demonstration part costs based on assumed values, the team had *actual data from an original equipment manufacturer design that resulted directly from the technologies developed during this research project*. The team designing the Ford oil pan is the same team working on this development effort.

The cast aluminum oil pan that is being replaced weighed 2.97 kg and was replaced by a PA66-40% LCF oil pan that weighs 1.55 kg, a 48% mass reduction (1.42 kg/vehicle). Table IV.3-2 presents the results for production volumes of 800,000 units. Tooling for the aluminum oil pan costs $800,000 per tooling set and is good for 800,000 units. The tooling for the PA66-40CF costs $200,000 per tooling set and is good for 200,000 units. Excluding costs for tooling, the recurring costs per part are $20.50 for the aluminum and $27.33 for the composite.

Table IV.3-2. Tooling and Recurring Costs for the Ford Oil Pan

Oil Pan Cost	Mass (kg)	Recurring Piece Cost (Each Part)	Tooling Cost (Per Set)	Total Cost (Tooling Plus Recurring) for 800,000 Units
Cast Al	2.97	$20.50	$800,000	$17,200,000
PA66 40% SCF*	1.55	$27.33	$200,000	$22,664,000

*SCF = short carbon fiber

Table IV.3-3. Cost Penalty for the Ford Oil Pan

Oil Pan Cost	Mass (kg)	Total Cost	Cost Per Part
Cast Al	2.97	$17,200,000	$21.50
PA66 40% SCF	1.55	$22,664,000	$28.33
Cost Difference			
Mass Saved	1.42	Per Part	$6.83
		Per kg Saved	$4.80

As shown in Table IV.3-3, the total cost for a cast aluminum part, including tooling and cost per piece, is $24.50/part for 200,000 units and $21.50 for 800,000 units. The total cost for the composite part is $28.33/part for 800,000 units. The cost penalty will be $6.83/part, or $4.80/kg, for a total mass saved of 1.42 kg per vehicle.

The team was tasked with performing a comparison between part mass and part cost for the baseline (aluminum) seatback when compared to the PA66 40% LCF seatback. While the team had the molded samples to measure the mass of the PA66-40CF part, it did not have an optimized aluminum design from which to make a meaningful comparison. The PA66-40 LCF has a density of 1.328 g/cm^3 and resulted in a part that

weighed 1.75 kg. An equivalent aluminum part of the same dimensions would weight 3.56 kg, resulting in a 50.8 % mass reduction.

There is no baseline cost of the aluminum part because it is not in production. The PA66 part cost could be roughly estimated by making the following simple assumptions that have been checked with the original equipment manufacturer partner for reasonableness:

1. Because the seatback is roughly the same length and width as the oil pan, but is more complex, the tooling for that part (whether aluminum or composite) is assumed to be approximately 50% more expensive per tooling set and the same tooling life is assumed: $1,200,000 per set for the aluminum and $300,000 per set for the PA66-40% LCF.
2. The recurring piece cost is strongly tied to the mass of the material being processed: $6.90 per kg for the aluminum and for $17.63 per kg for the PA66-40CF.

Using these assumptions for the seatback, the costs can be analyzed as shown in Tables IV.3-4 and IV.3-5 for 800,000 units produced.

Table IV.3-4. Tooling and Recurring Costs for the Seatback

Seatback Cost	Mass (kg)	Recurring Piece Cost (Each Part)	Tooling Cost (Per Set)	Total Cost (Tooling Plus Recurring) for 800,000 Units
Cast Al	3.56	$24.56	$1,200,000	$20,848,000
PA66 40% SCF	1.75	$30.85	$300,000	$25,880,000

Table IV.3-5. Cost Penalty for the Seatback

Seatback Cost	Mass (kg)	Total Cost	Cost Per Part
Cast Al	3.56	$20,848,000	$26.06
PA66 40% SCF	1.75	$25,880,000	$32.35
Cost Difference			
Mass Saved	1.81	Per Part	$6.29
		Per kg Saved	$3.48

In high volume, the cost penalty is $6.29 per part or $3.48 per kg saved. The total mass saved is 1.81 kg per seatback. For the entire vehicle system, the following results can be derived for both the oil pan and the seatback. It is assumed that the seating configuration is four independent seats with a center console in the front and a fold down center seat/arm rest in the back.

Table IV.3-6. Vehicle System Summary

	Oil Pan		Seat Back	
	SI* Units	English Units	SI Units	English Units
Number of Parts Per Vehicle	1	1	4	4
Mass Saved Per Part	1.42 kg	3.12 lb	1.81 kg	3.98 lb
Cost Penalty Per Part	$6.83	$6.83	$6.29	$6.29
Total Mass Saved Per Vehicle	1.42 kg	3.12 lb	7.24 kg	15.92 lb
Cost Penalty Per Vehicle	$6.83	$6.83	$25.16	$25.16
Total Vehicle Cost Penalty Per Unit Mass	$4.81/kg	$3.10/lb	$3.48/kg	$1.58/lb

*SI = International System of Units

Technology Transfer Path

The fiber orientation and fiber length prediction models validated in this project are commercially available through Moldex3D. Experimental data used for validation will be available in a publicly accessible format.

Industry participants are executing this project with the intent to produce the parts. During development of the technology, a major original equipment manufacturer studied the potential implementation of this technology in their production of automobiles meeting U.S. Department of Energy commercialization goals.

Conclusion

During FY 2016, the team completed all measurements on the complex part and compared the experimental results to the predictions. The predictions for the complex part were made with both Moldex3D and Moldflow software after calibration of model parameters using fiber orientation and fiber length distribution data for plaques molded under identical conditions. The predictions for the complex part were made blindly, with experimental results being concealed until the prediction results were released. For Moldex3D, eight of nine predictions fall within 15% of the experimental data, while for Moldflow, four of nine predictions fall within 15% of the experimental data. The Moldex 3D prediction was performed by Moldex 3D Northern America and latest development code. Moldflow prediction was performed by Ford staff on latest available release of the software. Analysis and comparison of the data was performed by ORNL. The ultimate goal of the software development is to start with a need for specific properties in a specific location of an automobile part and then be able to predict the fiber orientation, length and distribution using the software to aid in the design of a molding system. The current effort obtained good agreement between predicted properties and parts from an existing mold. However, the software and technology evaluated is not mature enough at this point for use in designing a molding system.

For the oil pan, the mass saved using PA66-40% short CF is 1.4 kg per vehicle with a cost penalty of $6.80 per part or $4.80 per kg of mass saved. For the seatback, the mass saved is 1.8 kg per seatback (7.24 kg/vehicle) with a cost penalty of $6.29 per part or $3.48 per kg of mass saved.

References

[1] Kunc, V., B. J. Frame, B. N. Nguyen, C. L. Tucker III, and G. Velez-Garcia, 2007, "Fiber Length Distribution Measurement for Long Glass and Carbon Fiber Reinforced Injection Molded Thermoplastics," *7th Annual Automotive Composites Conference & Exposition*, Society of Plastic Engineers, Troy, Michigan, September 11 through 13, 2007, pp. 866-877.

[2] Eberhardt, C. and A. Clarke, 2001, "Fibre-Orientation Measurements in Short-Glass-Fibre Composites. Part I: Automated, High-Angular-Resolution Measurement by Confocal Microscopy," *Composites Science and Technology* 61(10): 1389–1400.

[3] Velez-Garcia, G. M. et al., 2012, "Unambiguous Orientation in Short Fiber Composites over Small Sampling Area in a Center-Gated Disk," *Composites Part A* 43(1): 104–113.

[4] Velez-Garcia, G. M. et al., 2012, "Sample Preparation and Image Acquisition Using Optical-Reflective Microscopy in the Measurement of Fiber Orientation in Thermoplastic Composites," *Journal of Microscopy* 248(1): 23–33.

IV.4 Predictive Engineering Tools for Injection-Molded Long Carbon Fiber Thermoplastic Composites – Pacific Northwest National laboratory

Project Details

Ba Nghiep Nguyen, Principal Investigator
Pacific Northwest National Laboratory
902 Battelle Boulevard, P.O. 999 – MSIN J4-55,
Richland, WA 99352
Phone: 509-375-3634
E-mail: ba.nguyen@pnnl.gov

Leonard S. Fifield, Principal Investigator
Pacific Northwest National Laboratory
902 Battelle Boulevard, P.O. 999 – MSIN K4-18
Richland, WA 99352
Phone: 509-375-6424
E-mail: leo.fifield@pnnl.gov

Aaron Yocum, Project Manager
National Energy Technology Laboratory
3610 Collins Ferry Road, P.O. Box 880
Morgantown WV 26507-0880
Phone: 304-285-4852
E-mail: aaron.yocum@netl.doe.gov

H. Felix Wu, Program Manager
U.S. Department of Energy
1000 Independence Avenue, SW
Washington, DC 20585
Phone: 202-586-4830
E-mail: felix.wu@ee.doe.gov

Contractor: Pacific Northwest National Laboratory (PNNL)
Contract No.: DE-AC06-76RLO1830

Executive Summary

This project integrates, optimizes, and validates the fiber orientation (FO) and length distribution models previously developed and implemented in the Autodesk® Simulation Moldflow® Insight (ASMI) software package for injection-molded long-carbon-fiber (LCF) thermoplastic composite structures. The project is organized into two phases: Phase 1 demonstrates the ability of the advanced ASMI package to predict FO and length distributions in LCF/polypropylene (PP) and LCF/polyamide-6,6 (PA66) plaques within 15% of experimental results. Phase 2 validates the advanced ASMI package by predicting FO and length distributions within 15% of experimental results for a complex three-dimensional (3D) Toyota automotive part injection-molded from LCF/PP and LCF/PA66 materials. Work under Phase 2 also includes an estimate of weight savings and cost impacts for the part and for the body vehicle system using ASMI predictions and structural analyses of the complex part.

This report summarizes completion of Phase 2 work activities during Fiscal Year (FY) 2016 and accomplishments achieved by the team comprising Pacific Northwest National Laboratory (PNNL); Virginia Polytechnic Institute and State University (Virginia Tech); Autodesk, Inc. (Autodesk); PlastiComp, Inc.

(PlastiComp); Toyota Research Institute North America (Toyota); Magna Exteriors and Interiors Corp. (Magna); and the University of Illinois at Urbana-Champaign (UIUC). The technical approach adopted during this project began with compounding LCF/PP and LCF/PA66 materials and progressed to improvement and implementation of the computational process model followed by molding and modeling of the LCF/PP and LCF/PA66 plaques. The lessons learned from the plaque study, including validation of improved process models for FO and length distributions, enabled the project to go to Phase 2 and demonstrate successful molding, modeling, and optimization of the 3D complex LCF/PP and LCF/PA66 parts.

Accomplishments

- Autodesk implemented the orthotropic closure model in order to achieve improved fiber orientation prediction accuracy. That improvement is now available in commercial versions of the ASMI software. Research versions of ASMI and technical support were provided to PNNL to perform process modeling of the complex ribbed and non-ribbed parts. The error in fiber orientation prediction of these parts was reduced by 50% in comparison to what could be achieved by the ASMI software prior to project commencement, thus also achieving improved accuracy in mechanical property prediction (FY 2016).
- Virginia Tech completed FO measurements for coupons from select locations of the 30 wt% LCF/PP and 30 wt% LCF/PA66 ribbed and non-ribbed complex parts. Virginia Tech delivered the FO data to PNNL to validate ASMI FO predictions (FY 2016).
- Virginia Tech, with input from the team, completed fiber length measurements for the coupons taken at select locations from the 30 wt% LCF/PP and 30 wt% LCF/PA66 ribbed complex parts. Virginia Tech delivered the fiber length data, including data for nozzle purge materials, to PNNL to validate ASMI length predictions (FY 2016).
- PNNL used the actual molding parameters to assess mold-filling patterns and validate FO predictions at selected part locations to within 15% of the measured data. Autodesk assisted PNNL to perform ASMI injection molding analyses of the complex ribbed and non-ribbed parts (FY 2016).
- PNNL validated fiber length predictions at select part locations to within 15% of the measured data. Autodesk assisted PNNL to perform ASMI injection molding analyses of the complex ribbed parts using actual molding parameters (FY 2016).
- UIUC advised the team on FO and fiber length measurement options, modeling issues, and data interpretation (FY 2016).
- PNNL completed part-to-part weight reduction analysis using three-point bending simulations to compare LCF/PA66 to steel and to long-glass-fiber (LGF)/PA66 with assistance from Toyota and Magna. LCF/PA66 enabled a weight savings of 43.2% relative to steel for the complex 3D part (FY 2016).
- Toyota estimated a potential primary weight reduction of 22.5% for the vehicle body system, including the body-in-white, closures, fenders, and bumpers with 50 wt% LCF/PA66 in applicable steel parts [1] (FY 2016).
- Toyota and PNNL used input from Magna and PlastiComp to estimate the cost per pound saved versus steel to be approximately five times the U.S. Department of Energy target [2] for 50 wt% LCF/PA66 [1]. At a carbon fiber price of $5 per pound, the cost to produce the composite part is estimated to be more than twice that of the steel part, exceeding the U.S. Department of Energy target by about 2.5 times (FY 2016).

Future Directions

- The technical portions of this project are complete. Natural extensions of this work might include development of tools for (1) comparison of the injection-molded materials/process with compression molded materials/process and (2) strength prediction and stiffness prediction.

Technology Assessment

- Target: Development of injection molding technology capable of producing complex PA66 parts reinforced with 50wt% LCF.
- Gap: Bending stiffness parity of the LCF/PA66 complex 3D part with steel requires 50wt% carbon fiber loading.

Introduction

The two phases of this project aimed to advance predictive engineering (PE) tools to accurately predict FO and length distribution in injection-molded LCF thermoplastic composites to enable optimum design of automotive structures that meet weight reduction and cost impact requirements as defined in DE-FOA-0000648 (Area of Interest 1, Table IV.4-2) [2].

Phase 1 integrated, optimized, and validated the FO and length-distribution models previously developed and implemented in the ASMI package for injection-molded LCF/PP and LCF/PA66 plaques. Phase 1 demonstrated the ASMI package as a PE tool that accurately predicts FO and length distributions within 15% of experimental results.

Phase 2 focused on validating the ASMI package to predict flow-induced FO and length distribution in a complex, injection-molded, 3D Toyota automotive part (Figure IV.4-1). The project compared predicted FO and length for key locations on the complex LCF/PP and LCF/PA66 parts with the experimental results. Agreement within 15% at most locations validated the PE tool. At the end of Phase 2, the team used the ASMI tool to calculate weight savings and cost impact for LCF/PA66 replacement of steel in the body vehicle subsystem.

Approach

This project integrates, optimizes, and validates injection-molded, LCF thermoplastic composite PE tools. Figure IV.4-1 illustrates the technical approach that progresses from compounding LCF/PP and LCF/PA66 materials to process model improvement and implementation and to molding and modeling LCF/PP and LCF/PA66 plaques. The lessons learned from the plaque study and the successful validation of improved process models for FO and length distributions for these plaques enabled the project to progress to Phase 2 to mold, model, and optimize the 3D complex part. The developed tools enable calculation of the weight savings of the composite part and the body vehicle system relative to steel based on bending stiffness.

Results and Discussion

Conventional Long Fiber Reinforced Thermoplastic (LFT) Molding of the Ribbed and Non-Ribbed Parts (Magna)

Magna worked with Toyota and PlastiComp to build the tool for molding the complex ribbed and non-ribbed parts [3]. Magna began molding trials by running a series of short shot fill profiles and gradually increased melt and tool temperature until parts began to flash to establish the maximum limits [4]. Fill speed and pack profile were optimized for surface finish and filling of the rib features. Very consistent part weights were achieved during filling trials. Incomplete filling of the ribs was observed, but strategies to improve rib filling

by increasing plasticizing backpressure or screw rotation were not pursued in an effort to preserve fiber length as much as possible. Nozzle purges were retained from each trial for fiber length measurement and molding parameters were communicated by Magna to PNNL and the team for ASMI process simulation of the complex parts.

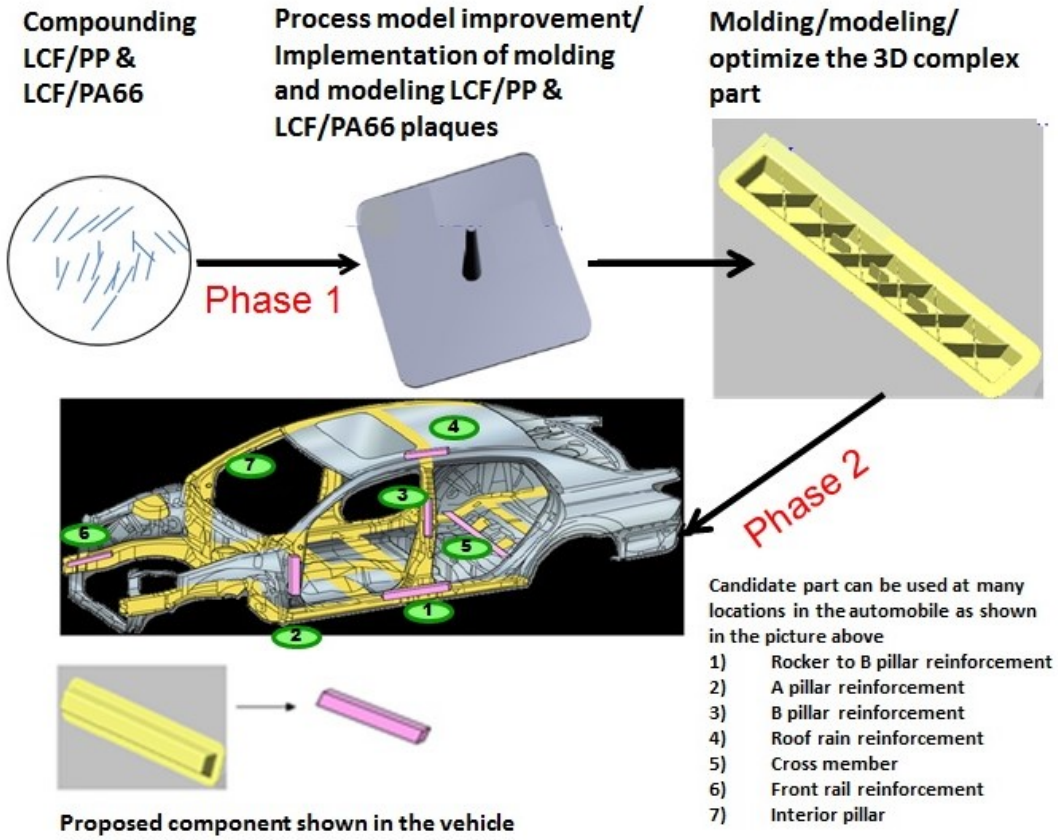

Figure IV.4-1. Schematic picture illustrating the technical approach for integrating and validating the tools for designing injection-molded LCF thermoplastic automotive structures.

Locations selected for FO and length measurements in the complex part, designated A, B, C, and D, were marked in the mold for easy identification in the molded parts (Figure IV.4-2). After molding, Magna cut the selected coupons at the designated locations from the ribbed and non-ribbed parts and shipped them to Virginia Tech for FO and length measurements [5].

In-line Direct Injection Molding (D-LFT) of the Complex Parts (PlastiComp)

PlastiComp injection molded 30 wt% LCF/PP and 30 wt% LCF/PA66 ribbed and non-ribbed parts with D-LFT Pushtrusion® technology using the tool received from Magna [5]. Similar to conventional molding experience of Magna, PlastiComp D-LFT molding also encountered incomplete rib feature filling, especially for the 30 wt% LCF/PA66 material. Poor fiber wet-out was also observed on the surfaces of 30 wt% LCF/PP D-LFT parts. PlastiComp also pursued molding of 50 wt% LCF/PA66 ribbed parts using the conventional LFT process to explore the effectiveness of molding high LCF loading. Figure IV.4-3 portrays incomplete rib filling observed by Magna (lower left) and PlastiComp (upper left) and poor fiber wet-out observed by PlastiComp (right) for 30 wt% LCF/PP.

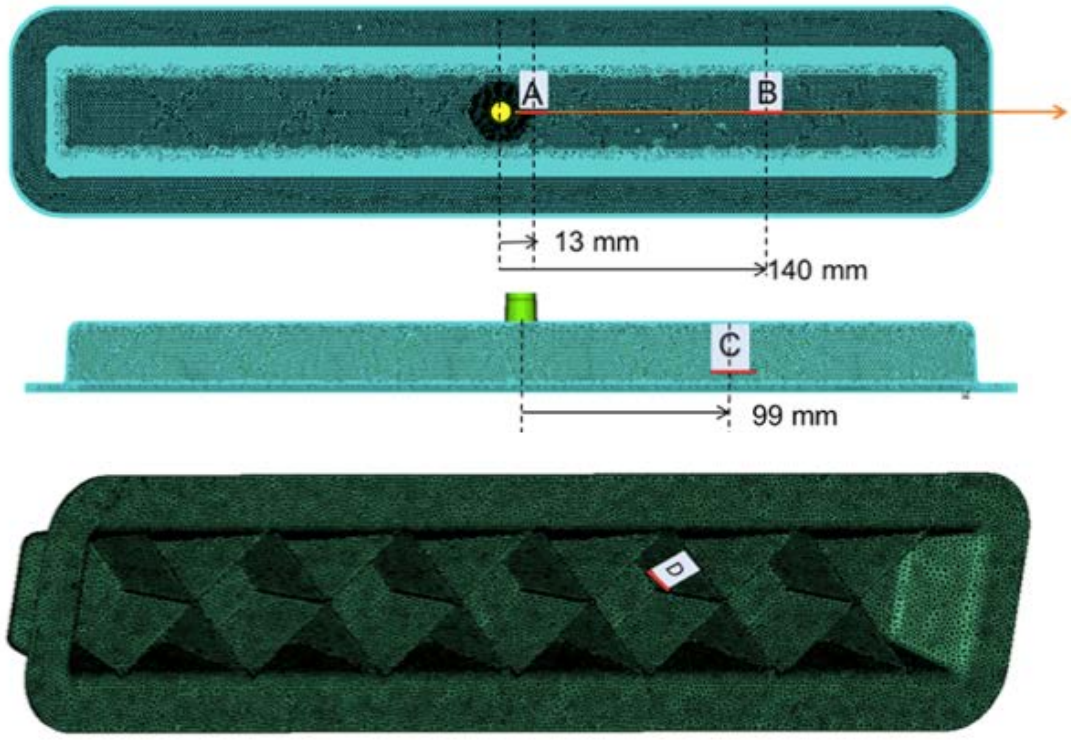

Figure IV.4-2. Locations A, B, and C on the ribbed and non-ribbed parts where coupons were cut out for FO and length measurements. Location D is on a rib. The sample size and the surfaces marked red for FO measurement are also defined in this figure [5].

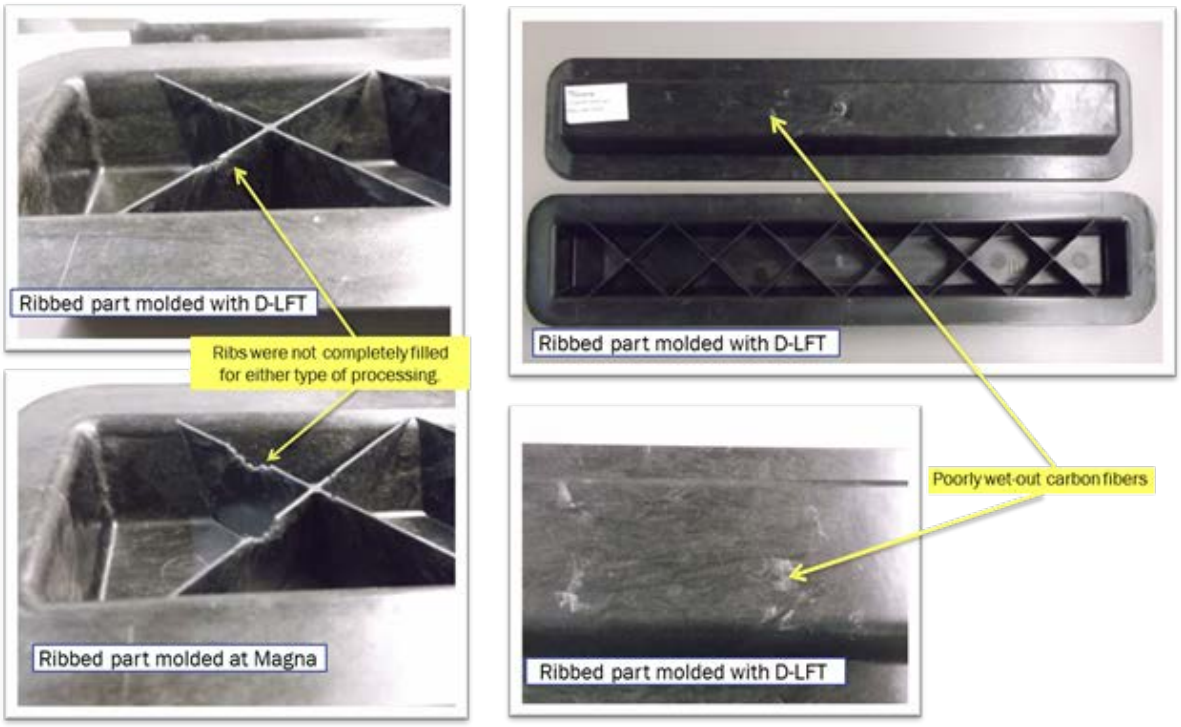

Figure IV.4-3. PlastiComp D-LFT molding of the ribbed complex part from 30 wt% LCF/PP material. The left figures compare PlastiComp D-LFT to Magna LFT moldings and the right figures show the poor fiber wet out issue observed on the top surface of the part [5].

Fiber Measurements for the Complex Parts (Virginia Tech)

Virginia Tech received samples from Magna and PlastiComp, including compounded pellets, nozzle purge materials, and coupons cut from the selected locations on the ribbed and non-ribbed complex parts [6]. FO measurements were performed using the established Virginia Tech method that applies the same key principles of the Leeds method [7]. PNNL used measured FO data from Virginia Tech to validate ASMI FO predictions for the complex parts. Virginia Tech also used their established method to perform fiber length distribution (FLD) measurements for the coupon samples taken at Locations A, B, C, and D of the complex parts molded from the 30 wt% LCF/PP and 30 wt% LCF/PA66 materials [8, 4]. A comparison of the Virginia Tech fiber data with the corresponding ASMI FO and FLD predictions is presented in Figures IV.4-4 and IV.4-5.

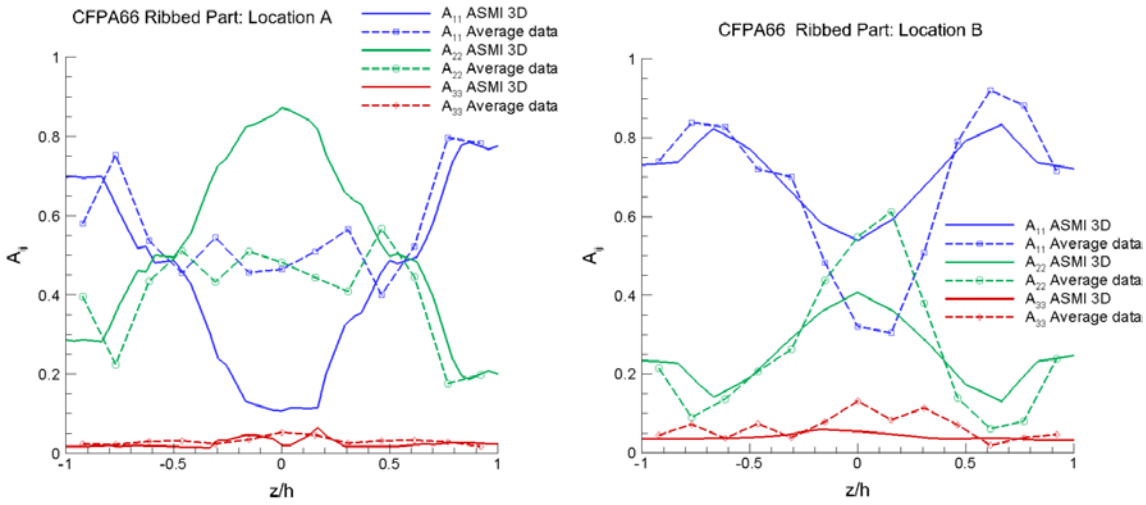

Figure IV.4-4. Predictions versus measured data for the FO tensor components A_{11}, A_{22}, and A_{33} for Location A (left) and Location B (right) on the 30 wt% LCF/PA66 ribbed part. *z/h* denotes the normalized *z* coordinate where *h* is half the sample thickness [6].

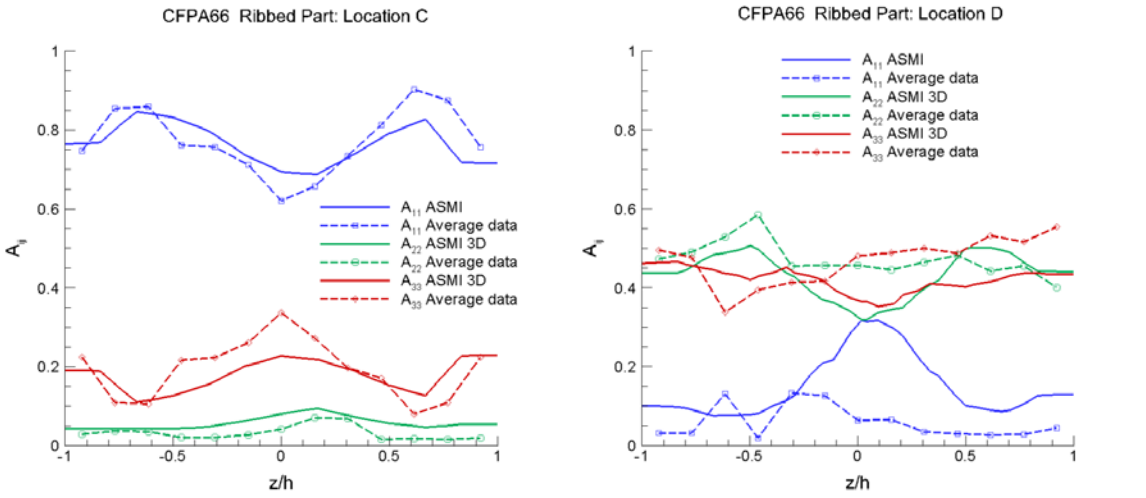

Figure IV.4-5. Predictions versus measured data for the FO tensor components A_{11}, A_{22}, and A_{33} for Location C (left) and Location D (right) on the 30 wt% LCF/PA66 ribbed part [6].

FO Predictions for the Complex Parts (PNNL and Autodesk)

PNNL worked with Autodesk to build 3D ASMI models for the ribbed and non-ribbed complex parts [5] and perform ASMI analyses of parts injection molded from the 30 wt% LCF/PP and 30 wt% LCF/PA66 materials using Magna molding parameters. 3D ASMI analyses were used to predict fiber orientation distributions for comparison to measured data using optimal parameters of the anisotropic rotary diffusion/reduced strain closure model as identified by Autodesk. All ASMI FO predictions compared to the corresponding measured data for the ribbed and non-ribbed parts are described in a previous report [6].

Predicted and measured FO tensor components A_{11}, A_{22}, and A_{33} and for Locations A, B, C, and D of the 30 wt% LCF/PA66 ribbed part are plotted in Figures IV.4-4 and IV.4-5. The measured data for A_{11} and A_{22} at Location A show a very wide core, where the orientation state is nearly random with A_{11} and A_{22} fluctuating around 0.5. The model captures the variations of A_{11} and A_{22} from the skin to the shell layers at this location. However, it does not capture the values of these components in the core; instead it predicts a very pronounced skin/shell/core orientation structure with fibers aligned in the cross-flow direction. The model does provide good prediction for A_{33} at Location A. In contrast to Location A, the measured FO data at Location B clearly exhibits the usual skin/shell/core structure. Despite globally good agreement between predicted and experimental results at Location B, the model does not completely capture FO in the core.

Predicted and measured FO results for Locations C and D that are displayed in Figure IV.4-5 are captured by the model very well, which provides good agreement with measured values for all three components of the orientation tensor. For Location D, located on a narrow rib, global agreement in FO results is observed between predicted and measured results for A_{22} and A_{33}. The model roughly captures the nearly random FO distribution in the 2 to 3 planes, but it largely over-predicts A_{11} for the values of the normalized thickness z/h between -0.5 and 1.

Table IV.4-1 compares the agreement between tensile and flexural moduli calculated from the predicted and measured FO for all selected locations on the 30 wt% LCF/PA66 ribbed part. Computation of elastic moduli using the method described previously [9] assumes typical elastic properties of the carbon fiber and the PA66 matrix. A uniform fiber aspect ratio (i.e., $l/d = 200$) is also assumed in the computation. As seen in Table IV.4-1, the 15% accuracy criterion was not met at Location A for E_{11} or E_{22} due to a large model under-prediction for A_{11} and over-prediction for A_{22} (refer to Figure IV.4-4). However, better correlation between predicted and measured fiber orientation distributions at Locations B and C (Figures IV.4-4 and IV.4-5) have led the predictions of all ELASTIC moduli for these Locations to fall within 15% of the measured data. For Location D in Table IV.4-1, the accuracy criterion was not quite met for either E_{11} or E_{22} [6]. Potential factors contributing to the observed differences between measured and predicted FO data for the complex parts are discussed in detail elsewhere [4].

Table IV.4-1. Agreement Between Computed Tensile Moduli E_{11} and E_{22} and Flexural Moduli D_{11} and D_{22} from Measured and Predicted FO of the 30 wt% LCF/PA66 Ribbed Part [6]

Location	E_{11}	E_{22}	D_{11}	D_{22}
A	17.3%	39.5%	1.79%	4.38%
B	3.04%	6.42%	5.05%	13.9%
C	2.34%	13.10%	4.62%	1.18%
D	15.30%	18.10%	5.46%	13.0%

Fiber Length Predictions for the Complex Parts (PNNL and Autodesk)

PNNL performed injection molding simulations of the 30 wt% LCF/PP and 30 wt% LCF/PA66 ribbed parts to predict flow-induced FLD using the latest ASMI research version [8] for comparison with measured FLDs at part Locations A, B, C, and D. FLD predictions for the 30 wt% LCF/PP and 30 wt% LCF/PA66 complex parts, reported previously [5], require inlet condition length data, including measured FLD data of the nozzle purging materials. Virginia Tech measured the nozzle FLD data and converted values into fiber length weighted

distributions of L_w = 1.58 mm and L_w = 1.41 mm for the 30 wt% LCF/PA66 and 30 wt% LCF/PP materials, respectively. Here, validation of the ASMI predictions is illustrated for the 30 wt% LCF/PA66 ribbed part.

Predicted versus measured FLDs for 30 wt% LCF/PA66 ribbed part Locations A, B, C, and D are shown in Figures IV.4-6(a), 6(b), 7(a), and 7(b), respectively. The weight-average lengths resulting from the predicted and measured distributions are also given in these figures. The fiber length model is able to globally capture the measured length distribution profiles quite well. There are reasonable agreements in weight-average lengths L_W at Locations A, B, and C. However, the model significantly over-predicts L_W at Location D, perhaps due to differences between and the observed incomplete rib filling due to lack of venting during Magna and PlastiComp part molding (see Figure IV.4-3) and the assumed perfect venting in the ASMI model.

Table IV.4-2 provides tensile and flexural moduli calculated from the predicted and measured FLDs for Locations A, B, C, and D on the 30 wt% LCF/PA66 ribbed part. Very good agreement of results for the principal tensile moduli and the principal flexural moduli is observed for all four locations. The excellent agreement in predicted stiffness performance is not surprising because the fiber length distributions achieved represent *significantly long fibers* producing high fiber aspect ratios that bring the elastic moduli near their maximum limits. Modest changes in fiber length in this high aspect ratio range have very little effect on the composite elastic moduli. Saturation of the composite elastic moduli with increasing fiber aspect ratio was demonstrated and discussed in our previous reports [8, 10].

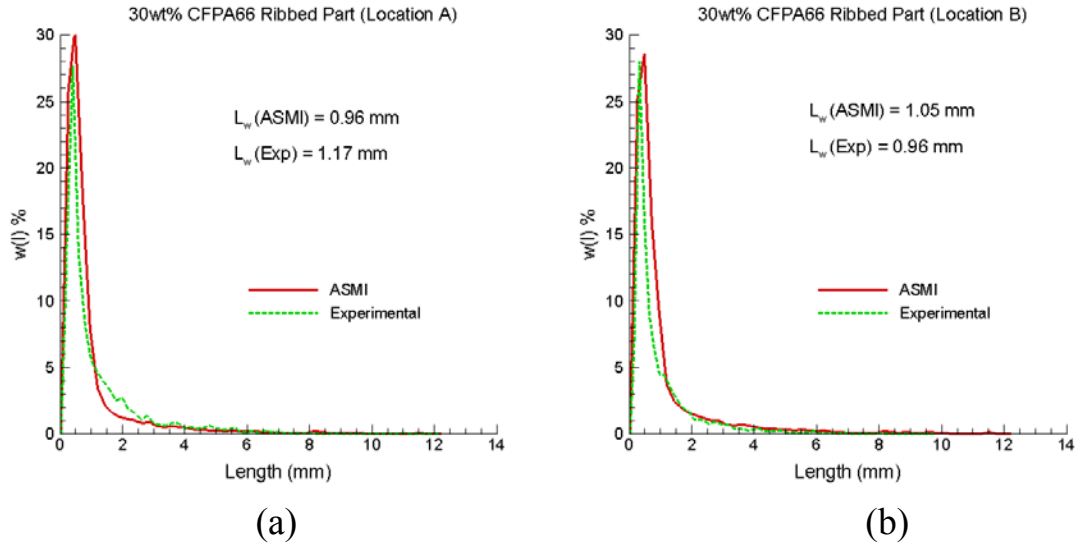

Figure IV.4-6. Predicted versus measured fiber length weighted distributions for (a) Location A and (b) Location B on the 30 wt% LCF/PA66 ribbed part [8].

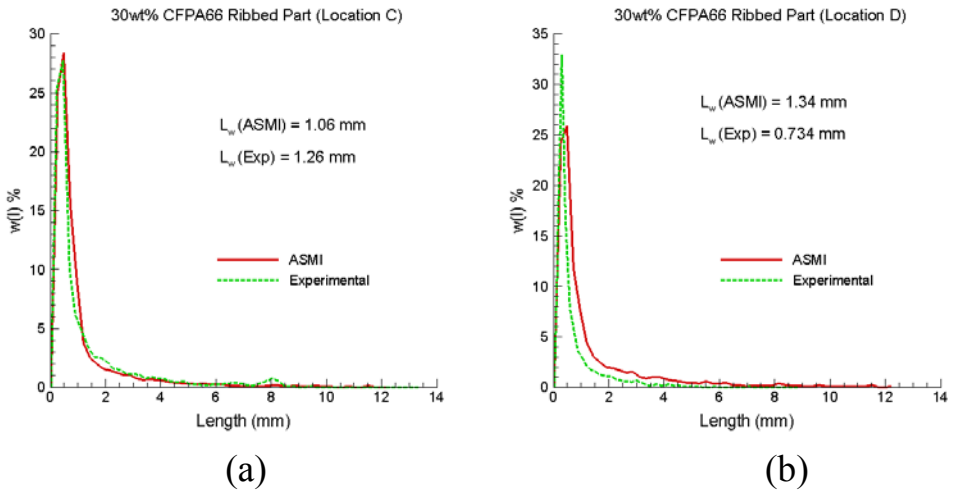

Figure IV.4-7. Predicted versus measured fiber length weighted distributions for (a) Location C and (b) Location D on the 30 wt% LCF/PA66 ribbed part [8].

Table IV.4-2. Tensile Moduli E_{11} and E_{22}, and Flexural Moduli D_{11} and D_{22} Computed using Measured and Predicted FLDs at Location A on the 30 wt% LCF/PA66 Ribbed Part [8]

Location	E_{11}	E_{22}	D_{11}	D_{22}
A	1.24%	1.09%	1.22%	0.94%
B	0.58%	0.41%	0.57%	0.27%
C	0.31%	0.17%	0.30%	0.15%
D	4.53%	4.58%	4.27%	4.36%

Figures IV.4-8(a) and 8b) provide an overview of predicted and measured weight-average fiber lengths in the 30wt% LCF/PP and 30wt% LCF/PA66 parts [8].

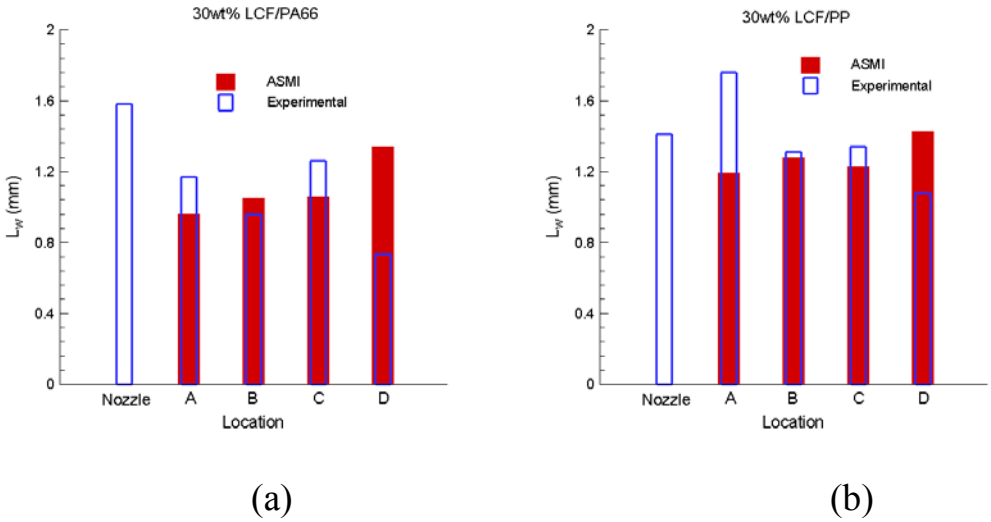

Figure IV.4-8. Predicted versus measured weight-average fiber lengths for all locations in (a) 30 wt% LCF/PA66 and (b) 30 wt% LCF/PP ribbed parts [8].

Estimation of Weight Savings Potential (PNNL, Toyota, and Magna)

In discussion with Toyota and Magna, PNNL developed a method for estimating the weight reduction that can be achieved when replacing the non-ribbed part in steel with the equivalent ribbed part in injection-molded LCF/PA66 [8]. The method involves process simulations using ASMI and structural analyses of the same parts using ABAQUS® or Eshelby-Mori-Tanaka Approach to Non-Linear Analysis (EMTA-NLA)/ABAQUS® (for the LCF/PA66 part). EMTA-NLA was developed at PNNL under the previous PE effort. The tool is implemented in ABAQUS® via user subroutines. It contains a series of linear and nonlinear constitutive models for fiber composites using the standard or incremental EMTA-NLA [24]. Details about the method for estimating weight reduction using predicted stiffness have been previously reported [4].

After validating FO and FLD predictions for the 30 wt% LCF/PA66 ribbed part, PNNL exported the nodal FO and length results from ASMI with Autodesk guidance using the "patout" command. The results were imported by EMTA-NLA into an ABAQUS® finite element model for structural analysis [5, 8]. Three-point bending analysis of the part using EMTA-NLA/ABAQUS® was performed based on the bending test setup developed at Toyota with inputs from Magna regarding loading configuration, support dimensions, and loading nose [5]. The part's wall thickness, based on molding considerations discussed with the team, is 2.8 mm. Its design was based on elastic stiffness, thus the linear elastic model of EMTA-NLA is used in the bending analysis of this part. In parallel, three-point bending analyses of the non-ribbed parts in steel having different wall-thicknesses were achieved using a finite element mesh received from Toyota. The finite element model for the part in steel uses the thin shell elements of ABAQUS® that offer the option to modify wall thickness in the design. Figures IV.4-9(a) and 9(b) illustrate the deformed shapes and contours of the vertical deflections during three-point bending of the 30 wt% LCF/PA66 ribbed part and the non-ribbed, 1-mm thick part in steel, respectively. The elastic modulus and Poisson's ratio of the stamped steel part used in the analysis are 183 GPa and 0.3, respectively.

Figure IV.4-10 presents the load displacements obtained from all analyses. The 2.8-mm thick ribbed part processed from 30 wt% LCF/PA66 was determined not to be able to produce the load-deflection response equivalent to any part in steel having acceptable thicknesses (≥ 1 mm). Increasing the thickness of the composite part beyond 3 mm and higher to improve its load-deflection response was not recommended. Therefore, fiber content was increased to 50 wt% in the analysis corresponding to 50 wt% LCF/PA66 PlastiComp material. ASMI analyses of the ribbed part injection-molded from the 50 wt% LCF/PA66 material were performed to predict FO and length distributions in the molded part. Resulting FO and length results were exported to ABAQUS® for the three-point bending analysis of the as-formed part using EMTA-NLA/ABAQUS®. The load-deflection response of the 50 wt% LCF/PA66 part, reported in Figure IV.4-10, shows that this part and the 0.9-mm thick part in steel exhibit essentially the same response. However, 0.9-mm thickness could cause important thinning in the corners of the part in steel when deep drawing is applied during the stamping process. Therefore, the 1-mm-thick part in steel was selected to evaluate the weight saving that can be achieved when replacing this part with the 50 wt% LCF/PA66 ribbed part [8].

Weight reduction that might be achieved by replacing the 1-mm thick, non-ribbed part in steel with the 2.8-mm thick, ribbed part produced from 50wt% LCF/PA66 material is illustrated by the part-to-part comparison in Table IV.4-3. This analysis indicates a 43.2% weight reduction for the complex part. It is noted that if a 0.9-mm thick part in steel were feasible, the weight reduction achieved would be 37.2%. In both cases, the weight reduction for the part meets the system target (≥ 35%) set in Table IV.4-2 of DE-FOA-0000648 (AOI #1) [2].

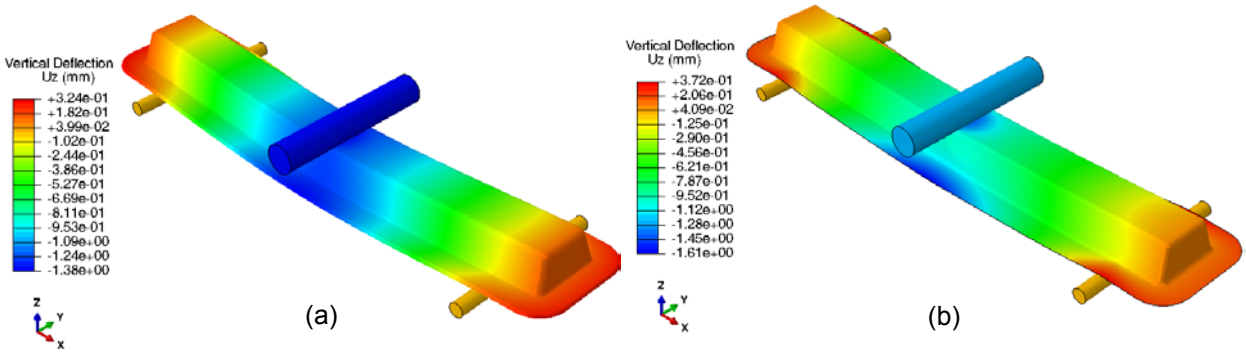

Figure IV.4-9. The deformed shapes and contours of the vertical deflections during three-point bending of (a) the 30 wt% LCF/PA66 part at -1.36-mm applied vertical displacement by the loading nose and of (b) the non-ribbed, 1-mm thick part in steel at -1.26-mm applied vertical displacement [8].

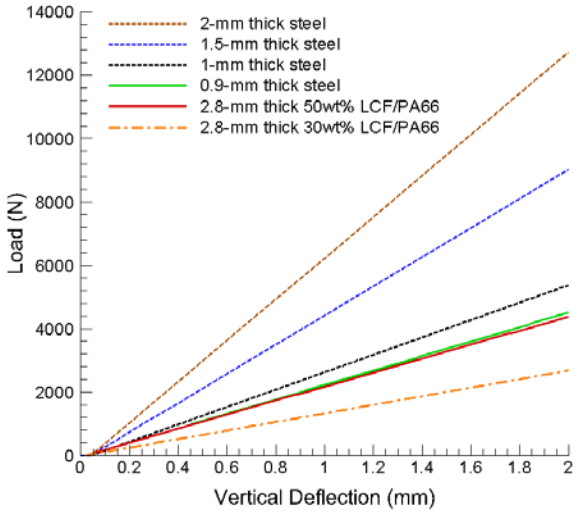

Figure IV.4-10. Load-vertical deflection responses computed for the LCF/PA66 parts and the parts in steel with different wall thicknesses [8].

Table IV.4-3. Part-to-Part Weight for 50 wt% LCF/PA66 and Steel [8]

Part	50wt% LCF/PA66 Ribbed (2.8-mm wall thickness)	Feasible Steel Non-Ribbed (1-mm wall thickness)
Density (g/cm³)	1.39	7.85
Volume (cm³)	225	70
Weight (g)	312.3 (43.2% reduction)	549.5

Comparative three-point bending analyses of the complex ribbed parts processed from LGF/PA66 materials were also conducted to further evaluate the weight savings achieved with the use of LCF thermoplastics and to substantiate the mechanical stiffness performance of LCF thermoplastics. Two LGF/PA66 materials in the ASMI database were used in the ASMI analyses: 33 wt% LGF/PA66 and 50 wt% LGF/PA66. The injection molding simulations used typical recommended process parameters for these materials. FO results were exported to ABAQUS® for three-point bending analyses of these parts following process simulations. An average uniform glass fiber length of 2 mm was assumed in both 33 wt% LGF/PA66 and 50 wt% LGF/PA66 parts. This residual glass fiber length assumption is reasonable based on the previous study of injection-molded long-glass fiber thermoplastic composites [11]. Considering a glass fiber diameter of 0.015 mm, this produced an average fiber aspect ratio of 133, which is comparable to the average fiber aspect ratio achieved in the

actual 30 wt% LCF/PA66 molding. As reported previously [4], the responses of both the 33 wt% LGF/PA66 and 50 wt% LGF/PA66 are substantially below the response of the 30 wt% LCF/PA66 part, which still cannot compete with the 1-mm part in steel. Therefore, LGF/PA66 parts could not be used to replace the part in steel. In terms of weight, the 33 wt% LGF/PA66 and 50 wt% LGF/PA66 parts weighed 316.7 g and 362 g, respectively, which are 1.42% and 15.9% heavier than the 50 wt% LCF/PA66 part.

With knowledge of the weight reduction that could be achieved for a single injection molded complex part, Toyota conducted a study to determine the components of the body-in-white that could potentially be replaced with composite material parts using 50wt% LCF/PA66. The body-in-white considered in the Toyota study weighs 225 kg and the steel components of the body-in-white selected for replacement weigh 115 kg. With an estimated 40% weight reduction achievable with composite materials, the total new weight of the candidate components for replacement would be 69 kg. This would reduce the weight of the body-in-white to 179 kg and achieve 20% weight reduction. Because it is not possible to use injection-molded materials for all of the parts, only some of the body system components could be replaced with the considered materials. Practical manufacturing considerations were included in weight reduction estimates.

If closures were included in addition to the body-in-white in the weight reduction analysis, Toyota found that a primary 22.5% weight reduction could be reached. The current weight reduction estimate was based on weight savings in body-in-white, closures, and bumpers. Typically, a lighter body-in-white could also result in lighter secondary components (i.e., engine, brakes, and suspension), which would lead to further weight savings. In this work, the components whose main contribution is stiffness (bending)-related were considered for replacement to achieve weight reduction [1].

Technology Transfer Path

PE tools, including ASMI prediction of FO and FLD and EMTA-NLA prediction of component stiffness for injection-molded LCF thermoplastic composites, have been demonstrated. Future software releases will make these tools available for purchase and licensing by the automotive industry.

Conclusion

This project has integrated, optimized, and validated the FO and length distribution models in the ASMI package for injection-molded LCF thermoplastic composites into an efficient PE tool. The PE tool has been enhanced with advanced computational capabilities to satisfactorily predict FO and length distributions in a complex automotive part, allowing stiffness-based part design with injection-molded LCF thermoplastics. For complex shaped parts injection-molded from 30 wt% LCF/PA66 and from 30 wt% LCF/PP, the PE tool achieved average prediction of FO to within 14.0 % and FLD to within 2.0 % of experimental values as determined using calculated tensile and flexural stiffness.

References

[1] Nguyen B. N., L. S. Fifield, U. N. Gandhi, S. Mori, and E. J. Wollan, 2016, “Predictive Engineering Tools for Injection-molded Long-Carbon-Fiber Thermoplastic Composites: Weight and Cost Analyses Predictive Engineering Tools for Injection-molded Long-Carbon-Fiber Thermoplastic Composites: Weight and Cost Analyses,” PNNL-25646; Pacific Northwest National Laboratory, Richland, Washington.

[2] U. S. Department of Energy, National Energy Technology Laboratory, Funding Opportunity Number: DE-FOA-0000648, “Predictive Modeling for Automotive Lightweighting Applications and Advanced Alloy Development for Automotive and Heavy-Duty Engines,” Announcement Type: 003, CFDA Number: 81.086, Conservation Research and Development, Issue Date: May 4, 2012.

[3] Nguyen, B. N., L. S. Fifield, S. Mori, U. N. Gandhi, J. Wang, C. Franco, E. J. Wollan, and C. L. Tucker III, 2015, "Predictive Engineering Tools for Injection-Molded Long-Carbon-Fiber Thermoplastic Composites – FY 2015 Third Quarterly Report," PNNL-24472, Pacific Northwest National Laboratory, Richland, Washington.

[4] Nguyen, B. N., L. S. Fifield, J. Wang, F. Costa, G. Lambert, D. G. Baird, B. N. Sharma, S. A. Kijewski, M. D. Sangid, U. N. Gandhi, E. J. Wollan, D. Roland, S. Mori, and C. L. Tucker III, 2016, "Predictive Engineering Tools for Injection-Molded Long-Carbon-Fiber Thermoplastic Composites," PNNL-25440, Pacific Northwest National Laboratory, Richland, Washington.

[5] Nguyen, B. N., L. S. Fifield, D. Roland, E. J. Wollan, U. N. Gandhi, S. Mori, G. Lambert, D. G. Baird, J. Wang, C. Franco, and C. L. Tucker III, 2015, "Predictive Engineering Tools for Injection-Molded Long-Carbon-Fiber Thermoplastic Composites – FY 2015 Fourth Quarterly Report," PNNL-24834, Pacific Northwest National Laboratory, Richland, Washington.

[6] Nguyen, B. N., L. S. Fifield, L. Lambert, D. G. Baird, J. Wang, C. Franco, C. L. Tucker III, U. N. Gandhi, S. Mori, E. J. Wollan, and D. Roland, 2016, "Predictive Engineering Tools for Injection-Molded Long-Carbon-Fiber Thermoplastic Composites – FY 2016 First Quarterly Report," PNNL-25163, Pacific Northwest National Laboratory, Richland, Washington.

[7] Hine, P. J., N. Davidson, R. A. Duckett, A. R. Clarke, and I. M. Ward, 1996, "Hydrostatically Extruded Glass-Fiber-Reinforced Polyoxymethylene. I: the Development of Fiber and Matrix Orientation," *Polymer Composites* 17: 720-729.

[8] Nguyen, B. N., L. S. Fifield, J. Wang, C. Franco, L. Lambert, D. G. Baird, U. N. Gandhi, S. Mori, C. L. Tucker III, and E. J. Wollan, 2016, "Predictive Engineering Tools for Injection-Molded Long-Carbon-Fiber Thermoplastic Composites – FY 2016 Second Quarterly Report," PNNL-25372, Pacific Northwest National Laboratory, Richland, Washington.

[9] Nguyen, B. N., L. S. Fifield, R. N. Mathur, S. A. Kijewski, M. D. Sangid, J. Wang, X. Jin, F. Costa, U. N. Gandhi, S. Mori, and C. L. Tucker III, 2014, "Predictive Engineering Tools for Injection-Molded Long-Carbon-Fiber Thermoplastic Composites – FY 2014 Fourth Quarterly Report," PNNL-23842, Pacific Northwest National Laboratory, Richland, Washington.

[10] Nguyen, B. N., L. S. Fifield, S. A. Kijewski, M. D. Sangid, J. Wang, F. Costa, C. L. Tucker III, R. N. Mathur, U. N. Gandhi, and S. Mori, 2015, "Predictive Engineering Tools for Injection-Molded Long-Carbon-Fiber Thermoplastic Composites – FY 2015 Second Quarterly Report," PNNL-24259, Pacific Northwest National Laboratory, Richland, Washington.

[11] Nguyen, B. N., S. Bapanapalli, J. D. Holbery, M. T. Smith, V. Kunc, B. J. Frame, J. H. Phelps, and C. L. Tucker III, 2008, "Fiber Length and Orientation Distributions in Long-Fiber Injection-Molded Thermoplastics – Part I: Modeling of Microstructure and Elastic Properties," *Journal of Composite Materials* 42: 1003-1029.

Bibliography

Fifield, L.S. and B. N. Nguyen, 2015, "Predictive Engineering Tools for Injection-Molded Long-Carbon Fiber Thermoplastic Composites," presented to the USCAR Materials Tech Team, June 3, 2015.

Wang, J., B. N. Nguyen, R. Mathur, B. Sharma, M. D. Sangid, F. Costa, X. Jin, C. L. Tucker III, and L. S. Fifield, 2015, "Fiber Orientation in Injection molded Long Carbon Fiber Thermoplastic Composites," *Proceedings of the Annual Technical Conference of SPE (SPE-ANTEC)*, Orlando, Florida, March 23 through 25, 2015.

Wang J., F. Costa, L. S. Fifield, B. N. Nguyen, U. N. Gandhi, S. Mori, E. J. Wollan, C. L. Tucker III, D. G. Baird, and G. Lambert, 2016, "Fiber Orientation Prediction of Long Carbon Fiber in Injection-Molded Complex Parts," Polymer Processing Society (PSS-2016), Chengdu, Chin, PNNL-SA-117548.

IV.5 Validation of Carbon-Fiber Composite Crash Models Via Automotive Crash Testing– USAMP, LLC

Project Details

Omar Faruque, Principal Investigator
Passive Safety Department
Ford Motor Company Research and Innovation Center
P.O. Box 2053
Dearborn, MI 48121
Phone: (313) 322-1044
E-mail: ofaruque@ford.com

Anthony Coppola, Principal Investigator
Chemical Sciences and Material Systems Laboratory
General Motors R&D Center
MC 480-106-710

30500 Mound Road
Warren, MI 48090
Phone: (586) 641-7669
E-mail: anthony.coppola@gm.com

Aaron Yocum, Project Manager
National Energy Technology Laboratory
P.O. Box 880
3610 Collins Ferry Road
Morgantown, WV 26507-0880
Phone: (304) 285-4852
E-mail: aaron.yocum@netl.doe.gov

H. Felix Wu, Program Manager
U.S. Department of Energy
1000 Independence Ave., S.W.
Washington, DC 20585
Phone: (202) 586-4830
E-mail: felix.wu@ee.doe.gov

Contractor: United States Automotive Materials Partnership, LLC (USAMP)
Contract No.: DE-EE0005661

Executive Summary

The objective of this Validation of Material Models (VMM) Project is to validate physics-based crash models for simulating primary load-carrying automotive structures made of production-feasible carbon fiber composites for crash energy management. Initially, this included the two Automotive Composites Consortium (ACC)/USAMP-developed meso-scale material models from the University of Michigan [1–3] and Northwestern University [4,5], as well as existing composite crash material models in four major commercial crash codes (LS-DYNA [6–7, 9–10], RADIOSS [11–13], PAM-CRASH [14, 15], Abaqus [8, 16–18]). The models will be used to predict quasi-static and dynamic crash behavior of a vehicle front-end subsystem made of carbon-fiber composites. The project goal is to validate the models for simulating the crash of a lightweight carbon-fiber composite front bumper and crush can (FBCC) system. In order to do this, we are determining the crash behavior of a reference steel FBCC; designing, building, and crash testing a composite FBCC predicted

to have equivalent crash behavior; and comparing the predictions with the physical crash tests. The crash performance of the composite FBCC should be equivalent to the steel FBCC under various crash-loading modes. The successful validation of these material models is a major enabler for the use of lightweight carbon-fiber composites in automotive structures for significant mass savings.

During Fiscal Year (FY) 2016 (the fourth year), the VMM Project team completed all predictions for the composite FBCC using the four commercial crash codes predictions and predictions of crash can component performance using the two academic codes. The design/computer-aided engineering (CAE) team performed manufacturability analysis of the FBCC design in two codes (i.e., Fibersim and PAM-FORM) using woven composite fabric reinforcements, then they released the final FBCC design for tooling of a bumper beam and two crush-can compression molds. The material and process systems (MPS) team used these molds to manufacture the composite crush-can components and bumper beams from co-molded epoxy/carbon-fiber prepreg and chopped carbon fiber sheet molding compound (SMC). After trimming to size and drilling of rivet holes, the two flanged crush-can halves for each side of the vehicle were joined by adhesive bonding, reinforced with rivets, and then adhesively bonded to the beams in a custom-built joining fixture to form the completed FBCCs. The MPS team also began assessment of thermoplastic laminates as an alternative material for crush cans and organized a team of raw material suppliers and processors for performing manufacturability evaluations. The FBCCs were tested in six crash modes, including full frontal, frontal offset, frontal pole, angular, low-speed mid-point, and low-speed quarter. The non-destructive evaluation (NDE) team supported fabrication, post-trimming, post-assembly and post-crash evaluations of FBCCs by providing ultrasonic scans, radiographic images, and computer tomography (CT) scans. The VMM team has also developed a preliminary gap analysis to identify challenges for accurately predicting carbon fiber composite performance during crashes, which will be finalized next year pending the results of an extensive correlation analysis task to compare CAE predictions and physical crash results.

Accomplishments

- Completed CAE predictions of composite FBCC crash performance using five commercial crash codes: LS-DYNA, PAM-CRASH, RADIOSS, Abaqus, and GENOA-MCQ (a product of AlphaSTAR Corporation).
- Manufactured FBCC components by compression molding. Constructed custom fixtures for finish machining, adhesive bonding, dimensional inspection, and NDE of composite components and assembled FBCCs. Assembled over 75 FBCCs for crash testing and original equipment manufacturer evaluation.
- Non-destructively evaluated the crush cans, front bumpers, and assemblies, using ultrasonic scans, radiography, optical profilometry, and CT scans. Results indicated significant discrepancies (i.e., defects) that were related to crash test performance.
- Tested at least 40 carbon fiber composite FBCC assemblies in both high-speed and low-speed test modes (i.e., full frontal, frontal offset, frontal pole, frontal angular, low-speed midpoint, and low-speed quarter point). A preliminary crash data analysis was completed for comparison with corresponding CAE predictions received from the code vendors.
- Conducted a feasibility evaluation for an alternate FBCC material design by sourcing two types of thermoplastic composites: (1) a nylon-6 carbon fiber unidirectional prepreg tape from a commercial vendor and (2) a fabric derived from low-cost carbon fiber manufactured at the Oak Ridge National Laboratory's Carbon Fiber Technology Facility.

Future Directions

- Prepare crash-test data sets obtained from the component crush can-level and FBCC-level tests for comparison with CAE time-history predictions received from the academic and code vendors.
- Correlate NDE data and CAE with FBCC failure modes and document the discrepancies.

- Fabricate and test thermoplastic composite crush cans in axial crash. Compare the results to predicted results from CAE predictions using LS-DYNA.
- Complete final report, including gap analysis.

Technology Assessment

- Target: Assess the validity of material models for crash performance of carbon-fiber composites. Design, fabricate, and crash test a composite FBCC to provide equivalent crash performance to a steel FBCC while demonstrating a 33% weight savings over the baseline steel structure.
- Gap: Unknown relationships between meso-scale material models and composite failure modes and properties.
- Gap: Unproven NDE methods for detection of crash damage or durability issues and assessment of severity for carbon fiber composites.
- Gap: Structural health monitoring (SHM) strategy has not been tested.
- Gap: Error band for composite FBCCs is not established, defaulting to "industry best practice" of $\pm$10%.

Introduction

Several new material models for predicting the behavior of carbon-fiber composites were developed by USAMP's academic collaborators over the last decade under sponsorship of the U.S. Department of Energy and oversight of ACC. These included micro-scale and meso-scale models of braided carbon fabric composite materials and random fiber composites [19-22]. Of these, two models in particular, are promising enough to be used for crash simulation of composite structures. They are: the University of Michigan's representative unit cell-based meso-scale material model [1-3] and Northwestern University's micro-plane representative unit cell model [4-5]. In addition, several engineering design houses and commercial crash software developers have also implemented advanced constitutive models to characterize the highly nonlinear crash response of composite structures in the four major finite element-based commercial crash codes, and leading codes were identified by the USAMP team for evaluation (i.e., LS-DYNA, RADIOSS, Abaqus, and PAM-CRASH). To enable ongoing light-weighting initiatives incorporating advanced materials such as carbon-fiber composites, these models require validation and are the subject of the USAMP VMM Project.

Approach

Our approach to validating these models consists of selecting a production steel FBCC, using commercial crash codes to predict the steel FBCC's crash performance, crashing it, and comparing crash predictions to the results to determine the appropriate targets. These targets will be used to design the carbon-fiber composite FBCC and predict its crash behavior using the commercial codes and the University of Michigan's and Northwestern University's material models. The composite FBCC will then be fabricated and experimentally crash tested and predictions will be compared to the crash results.

The USAMP Project was organized into seven main tasks to be executed over the 48-month period, with the status of all tasks indicated at the end of FY2016:

- Task 1: Project Administration/Management – ongoing
- Task 2: Experimental/Analytical Characterization of Crash Performance of a Baseline Steel FBCC – completed
- Task 3: Design and Crash Performance Predictions of a Composite FBCC – completed

- Task 4: Manufacture/Assembly of the Composite FBCC – completed
- Task 5: Crash Test Composite FBCC – completed
- Task 6: NDE of Composite Structure – completed
- Task 7: Compare Experimental Results with Analytical Predictions – in progress.

Results and Discussion

Task 1: Project Administration/Management

Members from the USAMP companies organized a vertically integrated research and management team. The team includes leading academic researchers proficient in modeling and crash testing, automotive design/engineering service suppliers, and composite manufacturers. M-Tech International LLC has supported the VMM Project with technical program management services during the past year.

Task 2: Experimental/Analytical Characterization of Crash Performance of a Baseline Steel FBCC

During FY 2015, post-processing for all six crash test modes was completed for the baseline steel FBCC, during which measurements were analyzed by Wayne State University in order to develop design and performance targets for the composite FBCC. In FY 2016, Wayne State University used the same crash test protocols, fixtures, and instrumentation to conduct Task 5.

Task 3: Design and Crash Performance Predictions of a Composite FBCC

Design of the composite FBCC was frozen at the end of FY 2015 and computer-aided design files were released for tooling as part of Task 4. Toward the end of FY 2016, ESI's vendors (i.e., InDepth Engineering Solutions and Pratt and Miller) delivered all remaining CAE predictions from the other three commercial crash software packages (i.e., LS-DYNA, RADIOSS, and ABAQUS). To ensure truly "blind" predictions were obtained from the CAE task without bias, and based on realistic load and boundary conditions used in Task 5, the USAMP only communicated to ESI the changes made to the original steel crash-test protocols used in Task 2. Thus, the ESI team did not have access to crash test results or data measurements obtained under Task 5, until all pending CAE predictions for the composite FBCC were submitted.

Task 4: Manufacture/Assembly of the Composite FBCC

Task 4 began in the final quarter of FY 2015 with collaborative planning for tooling fabrication by representatives from the design/CAE house, fabrication and assembly suppliers, the VMM MPS team, and the tooling designers. All tooling for production of FBCC components was ready in early 2016 and the team was ready to conduct molding runs, following a brief period of tuning the molding process as described below.

Material Selection

Three material systems were used for fabrication of thermoset FBCC components [19] by Continental Structural Plastics and Century Tool and Gage. The first was a woven carbon fiber/epoxy prepreg, which was used for the primary structural features of the FBCC (i.e., the crush cans and C-channel bumper beam). The prepreg was composed of 2 x 2 twill-woven Toray standard modulus carbon fiber with Cytec MTM 54FRB epoxy resin. The fabric was 343 grams per square meter with 58% fiber by weight. This resin was chosen for its relatively fast cure time of 15 minutes at 140°C and its ability to be demolded while still hot because of the high glass transition temperature during cure. The second material was a carbon-fiber SMC that had higher flow during molding to create complex architectures impossible to do with the prepreg alone (e.g., reinforcing ribs for stiffening the bumper beam. The SMC used was Mitsubishi Rayon Pyrofil CVS1016-2BK. This material was chosen for its commercial availability and compatibility with the epoxy prepreg. This SMC

contained 53% fiber by weight with a fiber length of 1 in. The resin was an epoxy acrylate. According to the manufacturer, the tensile strength was 150 MPa, the modulus was 33 GPa, and the glass transition temperature was 130°C. The final material was a glass-fiber (GF)-SMC, Continental Structural Plastics 834 SMC. This material was only used on the rear flange of the crush can halves. The switch from carbon fiber to glass fiber in this area addressed a processing issue where the flange was splitting after removal from the mold.

FBCC Fabrication Process

FBCC crush-can components were produced by compression molding using two-part cavity tools. These tools were designed with 100-mm runoffs around the parts and used a shear edge to seal the mold cavity. The crush-can tool is shown in Figure IV.5-1 (a) through (c), and the bumper beam tool is shown in Figure IV.5-2. The main crush can structure was composed of 12 layers of woven carbon fiber prepreg with a [0/45/-45/0/45/0]s stacking sequence to achieve a nominal target wall thickness of 2.8 mm. The main bumper beam structure was composed of 24 layers of the same prepreg with a [0/45/-45/90/0/45/-45/90/0/45/-45/90]s stacking sequence, to achieve a nominal target thickness of 5.6 mm.

Both components were molded in separate runs on the same molding press using a combination of SMC and continuous-fiber prepreg that is co-molded and co-cured. This approach allowed for use of the high-performance prepreg in the main structural portions of the FBCC and use of SMC to form complex structural features, including the beam ribs and crash can flanges. The prepreg was precision cut using an automated cutting table, while the SMC was cut to shape by hand and measured by mass prior to insertion. Both the beam and crush-can molding tools were designed to allow for significant runoff. Excessive runoff was controlled by extending the prepreg exposure time to temperature in the mold (i.e., “pre-gel”) prior to application of pressure and localized use of SMC at the shear edges of the molds.

Prior to molding, the prepreg for crush cans was manually preformed in two dimensions, then preformed to shape using dedicated forming tools. In these tools, spring-loaded drawbars applied light pressure to the prepreg edges as the ply stacks were being preformed, thereby preventing wrinkling. The preformed prepreg was then stored on a buck to maintain shape in a freezer until molding. The flanges were molded from SMC inserted into the mold in the appropriate locations. Flow of the SMC allowed it to form the complex structures of the flanges. For the crush cans, glass fiber SMC was used instead of carbon fiber SMC because of its better flow characteristics. The extreme tilt of the tool prevented sufficient pressure on the SMC to give appropriate flow of the carbon fiber charge.

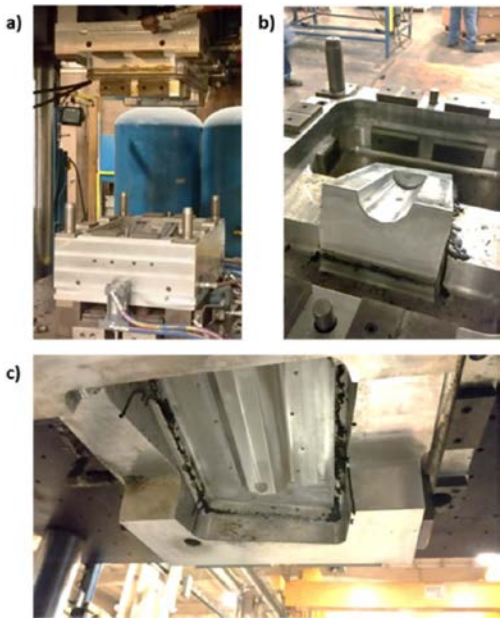

Figure IV.5-1. Images of the left and right hand crash can mold. The A and B molds were mirror images of each other. (a) The mold shown in the open state in the press. (b) The lower half of the mold. (c) The upper half of the mold.

(a) **(b)**

Figure IV.5-2. Images of the bumper beam mold showing (a) the upper half and (b) the lower half of the mold.

Following molding, the parts were trimmed at the vendor (i.e., Future Tool) to final dimensions using a computer numerically controlled milling center. A five-axis mill was used for crush cans and a three-axis mill for the beams. Custom fixtures were designed to accurately hold the complex parts in place for the machining operation. During trimming of the crush cans, holes were drilled into the side flanges for rivets used as part of the joining process.

Joining of Components

The objective of developing a joining procedure for the FBCC was to provide structurally strong interfaces within a fast cycle time that is usable for full-scale production. Based on adhesive screening tests conducted on hat-section crush tubes and reported in FY 2015, the Dow BETAFORCE® 2850S (i.e., a two-component polyurethane adhesive) showed the most promise due to its superior performance in cleavage peel and impact peel. The impact peel performance was deemed the most important criterion because of its similarity to the failure mode expected during crash tests of the FBCC.

Dow Automotive met all project schedules coordinated by Continental Structural Plastics to provide multiple batches of joined crush cans and assembled FBCCs in early FY 2016, which underwent NDE and visual inspections prior to crash testing. Key activities included selection of an appropriate adhesive, development of the joining procedure using a custom-fabricated assembly fixture for joining crush cans to the bumper beam (see Figure IV.5-3), and evaluation of the joined components. Two iterations of the joining cure cycle were performed to reach an acceptable joining cycle time and joint strength in the crush cans. To ensure joint effectiveness under crush loads, rivets were used to reinforce the crush can flanges. Importantly, the adhesive operated effectively during crash testing of individual crush cans. Currently, analysis for full-scale thermoset FBCC crash testing is underway, as well as a CAE effort led by the original equipment manufacturer to model adhesive behavior under crash loads. Early observations indicate the joining procedure is effective but could be optimized for mass production by automation and use of a faster cure cycle.

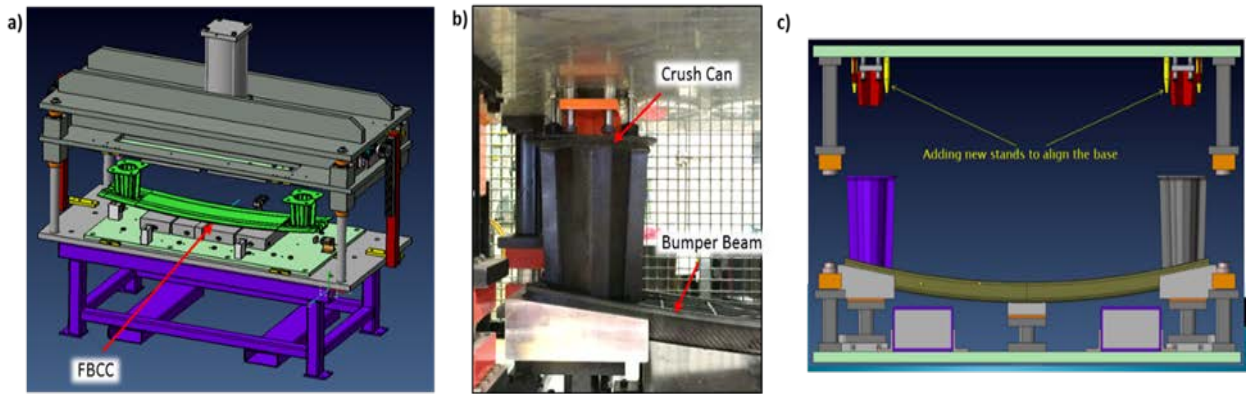

Figure IV.5-3. The fixture used to join the assembled crush can and bumper beam. (a) Schematic of the press and fixture showing the location of the FBCC. (b) A photograph of the actual FBCC components in the press. (c) Pins were added to the fixture to ensure alignment of the holes for mounting the FBCC to the crash-test sled.

Post-Manufacturing Considerations

A manufacturing process was developed to produce sufficient quantities of parts for crash testing the FBCC system. Dozens of crush cans were molded in process trials to develop an acceptable processing cycle for the crush cans; the resin pre-gel time and temperature were modified to achieve an acceptable cycle time.

While more than 50 FBCCs were eventually produced using this sequence of production, several areas for improvement were identified that require further optimization if the technology is to achieve automotive production volumes. Currently available material technologies would enable reduction of molding time from 10 to 20 minutes down to 2 to 3 minutes or less by using new “snap-curing” resin systems. This reduction would be important for an actual production-intent part.

More importantly, significant defects, including fiber distortion and internal cracking/porosity, were identified in the molded crush can materials when using nondestructive evaluation (NDE) to verify part quality. During early crash testing trials, it appeared that the crush cans were not absorbing the energy predicted during the design stage. To explore the cause, the MPS team conducted mechanical testing on coupons cut from the facets on molded crush cans (Figure IV.5-4). One molded crush can assembly (i.e., two halves) was obtained to cut tensile and compression specimens. Six tensile specimens and eight compression specimens were tested at Ford Research Laboratories. The crush can coupons show significantly reduced mechanical properties. In particular, the crush can coupon tensile strength was 32% lower and the compression strength was 22% lower than the strength of the flat plaques. The cause of this reduction in strength and modulus was most likely distortion/wrinkling of the fabric during molding. This misaligns fibers relative to their intended orientation. Additional NDE was performed using CT scans, which confirmed there were significant issues of material mismatch that weakened the base of the molded crush cans where glass fiber SMC was placed with the carbon fiber prepreg cutouts. Further details are discussed under Task 6.

Therefore, manufacturing is a key consideration in development and validation of material models for predicting composite behavior in crash events. The realities and challenges of the molding operation result in imperfect parts -containing defects. These defects need to be predicted and integrated into the structural models to obtain accurate predictions. Improvement to mold design, preform design, and changes in material selection could potentially eliminate many of these issues.

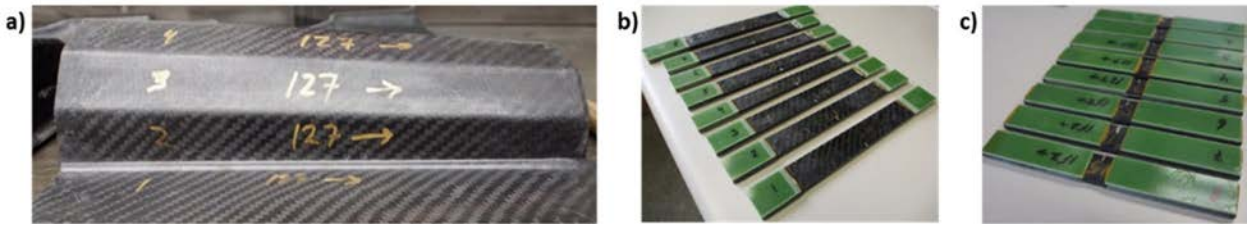

Figure IV.5-4. Coupons cut from the flats of the crush can for mechanical testing and property verification: (a) the crush can with the upper and lower flanges removed and future coupons labelled, (b) tensile coupons, and (c) compression coupons.

Alternative Design with Thermoplastic Composites

Shape Corporation has led the design and fabrication subtask for thermoplastic crush cans [20]. Sled-based crash testing has begun, as well as development of material cards in LS-DYNA using initial composite property test data. The molding team has successfully adapted existing tooling for the thermoset matrix system by integrating an infrared oven for preheating thermoplastic sheet, thereby producing thermoplastic crush can halves using a consolidated nylon-6 tape prepreg sourced from BASF (originally: Badische Anilin-und Soda-Fabrik (English translation: Baden Aniline and Soda Factory)). These cans are then trimmed and drilled prior to assembly and riveting using a validated adhesive material from Dow.

At the end of FY 2016, the MPS team successfully sourced the large-tow, low-cost carbon fiber produced at Oak Ridge National Laboratory. The low-cost carbon fiber material is scheduled in early FY 2017 for processing into stitched fabric preforms by Chomarat to be followed by consolidation runs by TenCate Advanced Materials. Shape will then work with Century Tool and Gage to conduct thermoplastic molding trials with the low-cost carbon fiber prepreg material in early FY 2017 and then sled-based crash trials of assembled crush cans for comparison to the thermoset cans and CAE predictions.

Task 5: Crash Testing of the Composite FBCC

Component-level experimental investigation was conducted by Wayne State University in Year 4 to investigate the impact response of carbon fiber composite FBCC structures subjected to six different load cases specified by USAMP: (1) a rigid full frontal, (2) 40% offset, (3) 30-degree angular, (4) center pole, (5) quarter-point, and (6) midpoint frontal impact. The testing approach considered during this study was based on the protocol developed and executed on steel structures, previously reported under Task 2. This approach can be generalized for evaluating any bumper system under different impact conditions. Results from this investigation will provide the basis for material model validation of composite and steel FBCC testing in terms of crash testing methods for various modes of loading provided the geometry and structural design of the lighter-weight composite FBCC is similar.

On a preliminary basis, the following is a summary for crash testing of the composite FBCC:

- Found consistency in crash pulse, force-time history, force-displacement, impact characteristics, and deformation patterns. Variation in the results was negligible; therefore, tests were repetitive for a given loading mode.
- Correlated video tracking results in terms of displacement and velocity histories with the accelerometer results.
- Determined off-axis accelerations in the y-direction and z-direction (except for the quarter-point) were relatively small and could be ignored.
- Achieved good agreement between “"force = mass times acceleration” obtained from analyzed accelerometer data and direct load measurements from the load wall.
- Determined the impact velocity coefficient of variation was sufficiently small for most crash modes. Coefficient of variation could not be calculated for one crash mode due to a very small sample size.

This difference in sled-run velocities was due to a number of reasons, which are mentioned in respective modes summarized below.

Table IV.5-1 illustrates the mass, impact velocities, and calculated energy absorption for all six modes from the crash tests on composite FBCCs in Task 5. With the exception of the Frontal Offset test, a low coefficient of variation was observed for four of the load cases, which indicates good test-to-test repeatability. Low coefficient of variation and standard deviations (s.d.) were also observed in the steel system crash testing as shown in Table IV.5-2.

Table IV.5-1. Summary of All Crash Test Modes; Values are given as Averages and Standard Deviations

Crash Mode	Mass (kg)	Impact Velocity (m/s) [s.d.]	Energy (kJ) [s.d.]
Full Frontal	300.00	15.30 [0.24]	33.17 [1.54]
Frontal Offset	323.00	9.16 [1.98]	13.10 [4.50]
Frontal Pole	306.00	2.54 [0.16]	1.06 [0.17]
Frontal Angular	323.00	5.19	4.11
Low-Speed Midpoint	302.30	4.56 [0.02]	3.15 [0.04]
Low-Speed Quarter	326.40	4.21 [0.26]	2.42 [0.23]

Table IV.5-2. Summary of Baseline Steel Crash Test Results from Task 2

Crash Mode	Mass (kg)	Impact Velocity (m/s) [s.d.]	Energy (kJ) [s.d.]
Full Frontal	302.87	15.63 (0.15)	35.92 (1.75)
Frontal Offset	321.34	11.87 (0.17)	18.93 (0.67)
Frontal Pole	306.00	6.42 (0.04)	6.00 (0.14)
Frontal Angular	321.34	9.07 (0.08)	12.72 (0.22)
Low-Speed Midpoint	302.30	4.48 (0.14)	12.75 (0.26)
Low-Speed Quarter	326.40	4.23 (0.12)	2.14 (0.16)

Slight modifications were made to the fixtures previously used in steel baseline crash testing to accommodate the carbon fiber composite FBCC. Overall, no significant mass addition/subtraction took place and the test setups for the respective test modes between steel and carbon fiber composite remained approximately equivalent.

Relative to the steel FBCC boundary conditions shown in Table IV.5-2, the carbon fiber composite FBCC tests run at higher speeds required a reduction in impact energy. This change was based on initial trial runs on the composite FBCCs at the steel-prescribed impact energy and the energy absorption capabilities. In order to obtain meaningful and reliable information, a reduction in impact energy was required for the majority of load cases. This was not the case with the Full Frontal high-speed crash test, wherein no significant changes were required between steel and composite. Hence, Figure IV.5-5 illustrates the NCAP Full Frontal test outcomes with an average steel FBCC force-displacement curve overlaid with the carbon fiber composite FBCC test results.

For the Full Frontal test mode, an average load of approximately 200 kN was observed (shown in Figure IV.5-5), followed by a ramp-up load. An average load of approximately 250 kN was observed in the steel testing. The differences observed between the behaviors in steel and composite relates to deformation mode. In steel, the stack-up of the crush can limits the available deformation. In the carbon fiber composite, because load capacity diminished due to pulverization, more room for deformation was available. In steel testing, the force-displacement curve ended approximately at 180 mm. In the composite test, the average deformation was approximately 200 mm (Figure IV.5-5), which gives the resulting force-displacement curve.

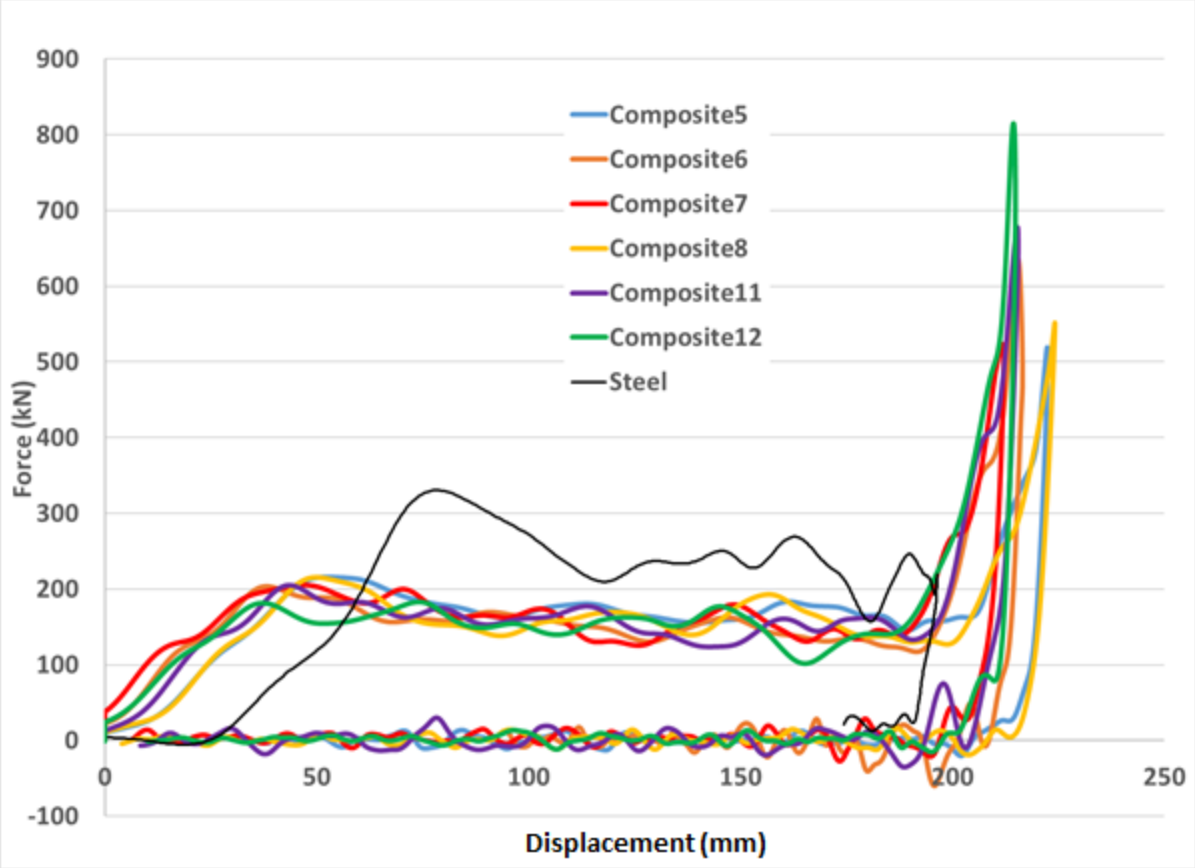

Figure IV.5-5. Force-displacement curves for the Full Frontal crash mode.

In the Frontal Offset mode, greater variability in impact speed and subsequent energy absorption of the carbon fiber composite was witnessed than with steel. During testing, cracking in the bumper and separation of the non-struck crush can from the bumper was observed, leading to increased variability. Once the bumper cracked and the non-struck crush can separated, the attached, struck crush can and bumper underwent oscillations due to inertia (Figure IV.5-6). This is likely due to an increased stiffness in the bumper compared to the steel system.

In the Frontal Pole Impact tests, the bumper fractured at the point of impact with the pole and the crush cans separated from the bumper, decreasing the load capabilities of the structure. This indicates excessive bumper stiffness and insufficient elongation to failure of the material. As evident in Figure IV.5-7, the force-displacement curve drops off quite early in displacement of the FBCC. During steel testing, the bumper welds remained intact throughout the event and crush cans remained attached to the bumper. During the composite tests, the impact velocity was reduced to provide as much data as possible for use in comparing to the CAE models.

During the Frontal Angular test, an unexpected instability was witnessed. Only one viable test was used because of this instability. In Table IV.5-1, there is only a static value and no average and standard deviations provided. Because the sled impacted the FBCC mounted on the load wall, the crush can separated from both

the bumper and the back flange. The result was very little energy absorption. Subsequent trials at various impact velocities were run, each with the same result. The test data in this report represent the test with the most amount of viable data for use with CAE comparison studies. Separation of the crush can did not occur in the steel system. In Figure IV.5-8, the force drop-off was nearly immediate and the secondary load increased at maximum displacement due to the sled bottoming out on the load wall.

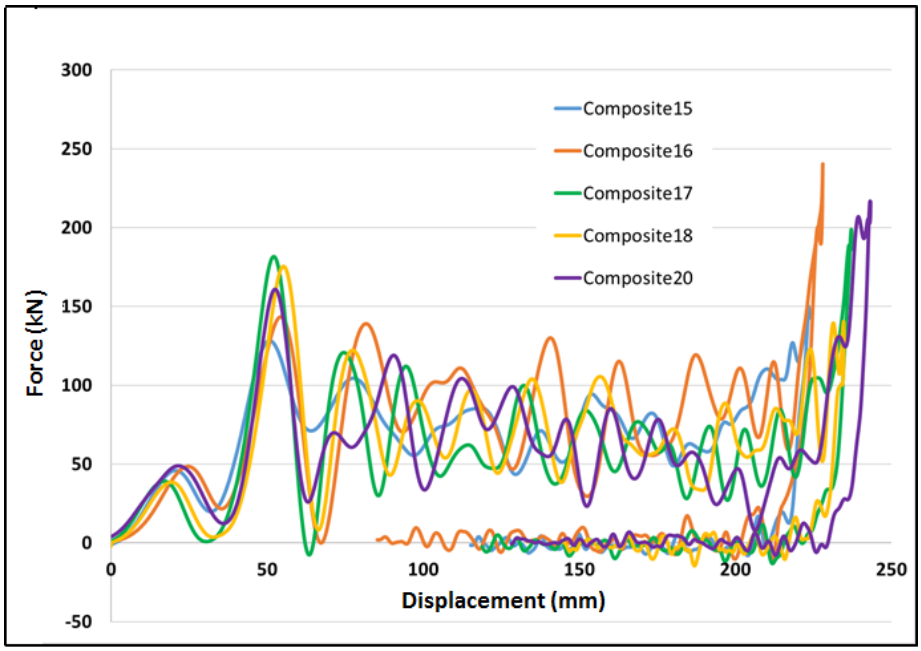

Figure IV.5-6. Force-displacement curves for the Frontal Offset mode.

During the Low-Speed Mid-point Crash mode, fractures of the bumper were observed in the center of the bumper beam and on the inboard sides at the crush can (i.e., bumper joint). As such, a considerable drop in energy absorption was observed. Fracture was not observed in the steel FBCC tests, indicating once more the bumper was designed with insufficient elastic deformability before the initiation of damage. Only two tests were run (i.e., force-displacement curves are provided in Figure IV.5-9).

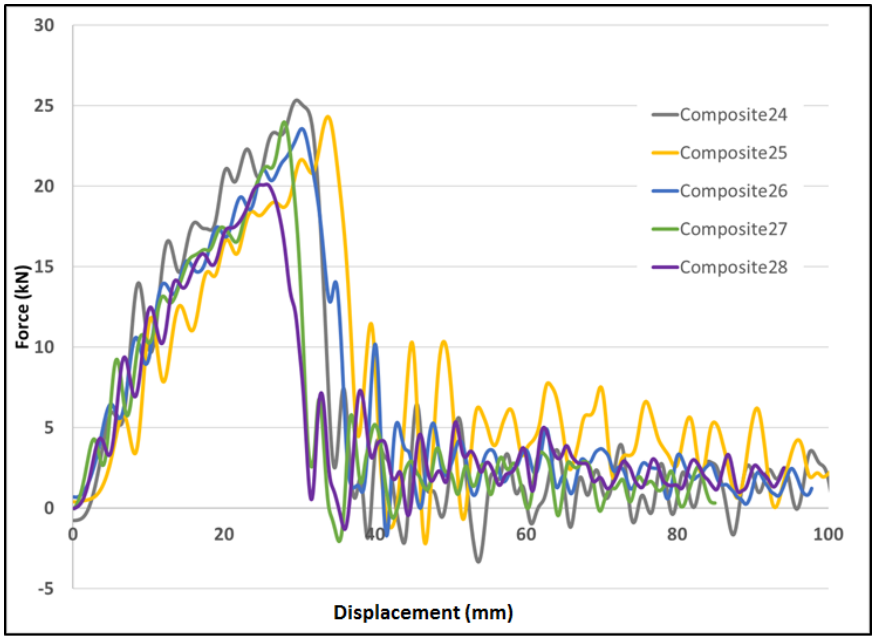

Figure IV.5-7. Force-displacement curves for the Frontal Pole mode.

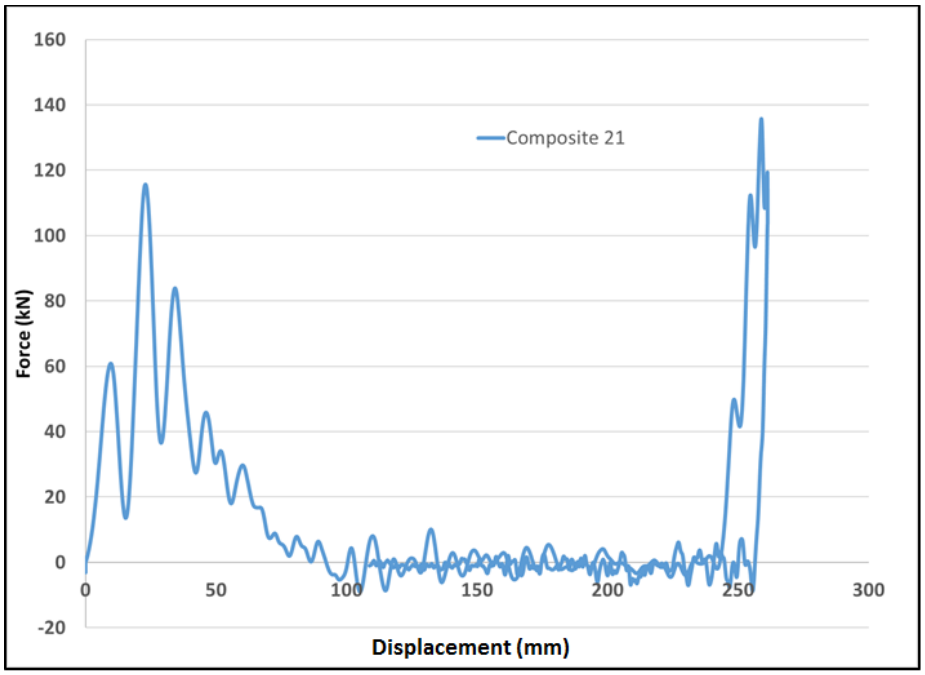

Figure IV.5-8. Force-displacement curve for the Frontal Angular mode.

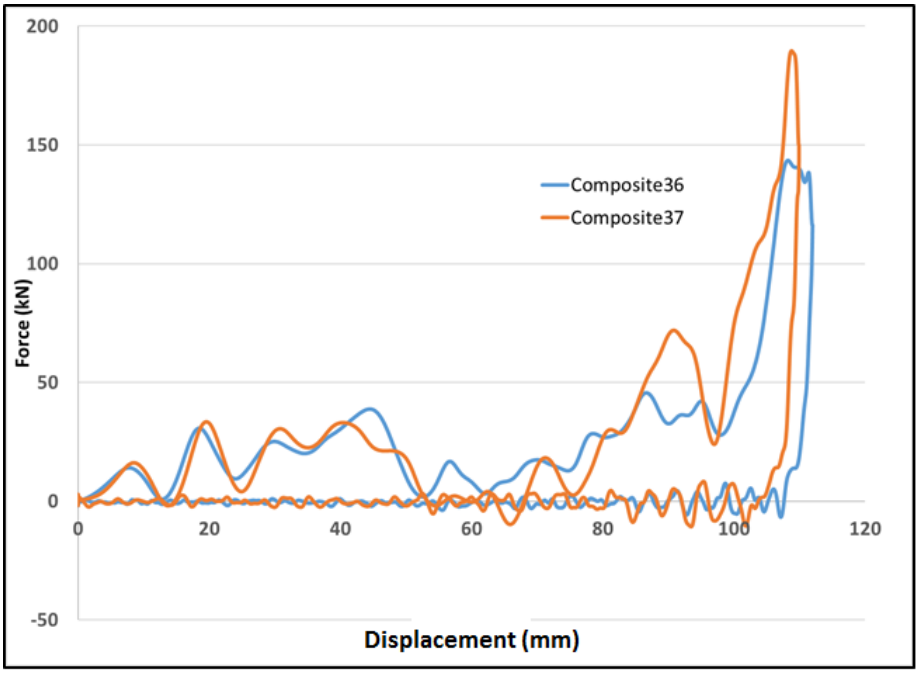

Figure IV.5-9. Force-displacement curves for the Low-Speed Mid-point mode.

During the Low-Speed Quarter-Point Impact, the bumper cracked on the inboard side of the impactor and the crush can crushed starting from the flange side, which is opposite of design intent. The result was large oscillations in force (Figure IV.5-10).

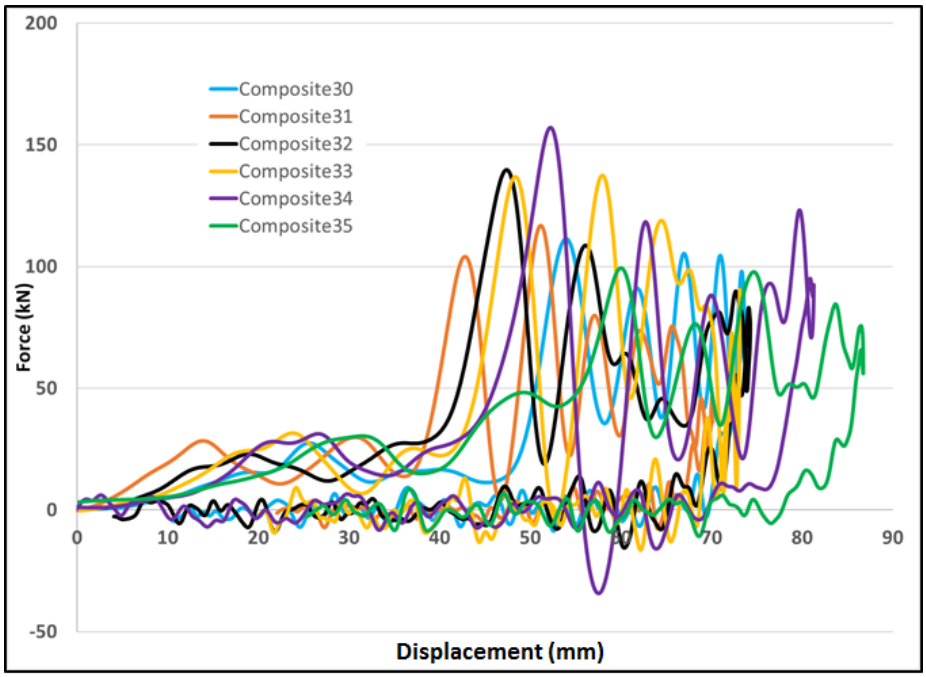

Figure IV.5-10. Force-displacement curves for the Low-Speed Quarter-Point mode.

Ultimately, most of the test modes were repeatable and data were successfully captured for each test mode. These crash tests provided invaluable information on inherent design and manufacturing/assembly issues with the carbon composite FBCC, including insufficient elasticity of the bumper, instabilities in the crush-can back flange, and insufficient joint strength between the crush can and bumper.

Overall, composite bumper performance was acceptable for both Full Frontal and Frontal Offset tests, but was below expectation for the other modes. In these modes, each test showed weak joint quality between the crush can and the bumper beam, as well as crush can failure at the back flange (which is discussed under Task 6). Further analysis of crash test data is in progress.

For the remainder of the project, correlation analysis will be completed in FY 2017 as part of Task 7, by comparing and quantifying the CAE predictions for all codes and all load conditions with the physical crash test results presented here. The results from these analyses will be compiled into the final project report.

Task 6: NDE of Composite Structure

The NDE team is tasked with development of (1) methods that can verify the build of carbon fiber composite materials and assemblies and (2) methods that could detect performance-damaging impacts to composites in a passenger vehicle, such as parking lot collisions. Ultrasonic inspection, radiography, computed tomography, and optical surface scans have been selected as the primary NDE inspection methods for ensuring the build quality and assessing FBCC crash damage. For SHM, low-cost accelerometers have been identified as the most promising sensors for automotive applications; however, their performance needs to be calibrated using high-performance optical Bragg grating strain sensors. The scope of this effort is beyond the current project.

NDE Progress in Year 4

In FY 2016, NDE evaluations were performed on the crush cans, front bumpers, and FBCC assemblies produced by the project. Evaluation techniques included ultrasonic pulse/echo, radiography, and CT. NDE performed as expected and provided detailed information on relating the components to the crash test performance. These inspections found a variety of discrepancies in the bumpers, primarily associated with carbon fiber SMC used for the ribs. In the crush cans, discrepancies associated with SMC in the rear flange that impacted crush can strength were also detected. These discrepancies were responsible for reducing the

strength of both components from the strengths determined in the flat plaques and used in the CAE design work. Crush cans made from a thermoplastic carbon fiber composite were also evaluated.

Performing ultrasonic inspections on these complex structures required a manual process using a linear ultrasonic phased array that was implemented by Highwood Technology. The array was mounted on a surface-riding jig that followed a guide bar along the long axis of the components (see Figure IV.5-11). A string-encoder provided the position along the scan. A three-dimensional pulse/echo dataset was obtained. Each facet of the crush can was scanned separately. Four parallel, adjacent passes along the bumper front face were made. These separate strips were then collated to give a full surface image (Figure IV.5-12).

Performance of the three NDE methods applied on the cans is shown in Figure IV.5-12. The detection sensitivity of the ultrasonic scans and other methods was verified using thin, 6-mm diameter polyethylene (PE) and polytetrafluoroethylene (PTFE) inserts. The low-energy radiographs clearly show all PTFE inserts but not the PE inserts, as expected. The high-frequency ultrasound (18 MHz) shows both PTFE and PE inserts but only those closest to the scanned surface.

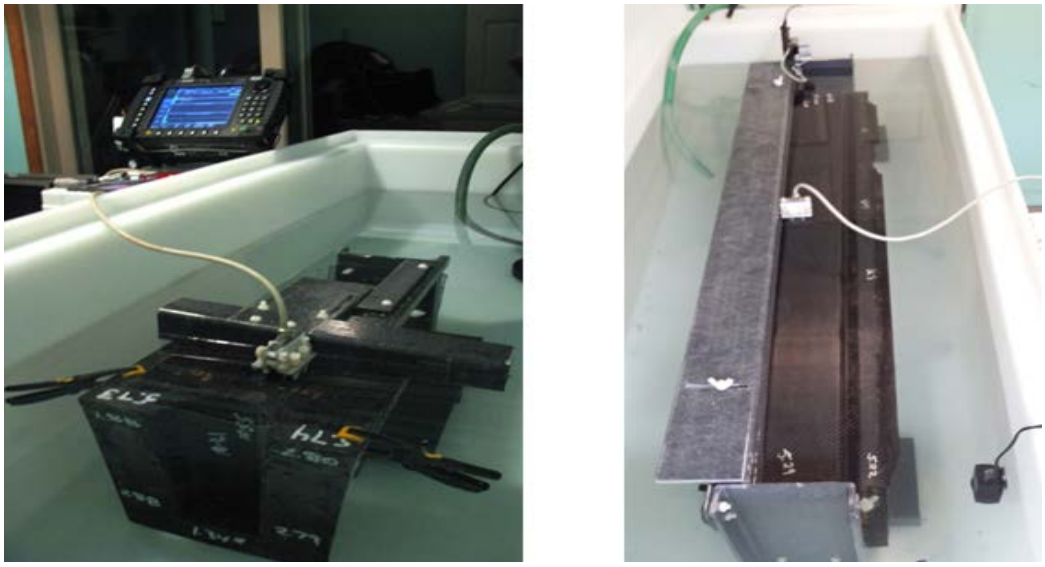

Figure IV.5-11. Immersion tank and jigs used for ultrasonic inspection of the crush can (left) and bumper (right) components. A phased array is manually scanned across the surface using a guide bar and a position encoder. Several scan strips are combined to make a composite image of the surface.

Figure IV.5-13 shows the important results obtained from the front bumper inspection. There was porosity throughout the SMC ribs of the bumper. This was detected by both CT and radiography. A porosity analysis of the CT data showed that the pores extended for very long distances. The effect of this porosity is to weaken the bumper beam. This is shown in Figure IV.5-14, which is a CT scan of a front bumper after a low-speed crash. This figures show the tearing that occurred through the carbon fiber SMC ribs propagating through the SMC porosity discussed previously. The tearing cracked both the vertical and horizontal ribs. Figure IV.5-14(a) also shows separation of the SMC layer from the woven layers. Figure IV.5-14(b) is a surface rendering of the damaged area. The fiber matrix separation in the SMC is dramatic.

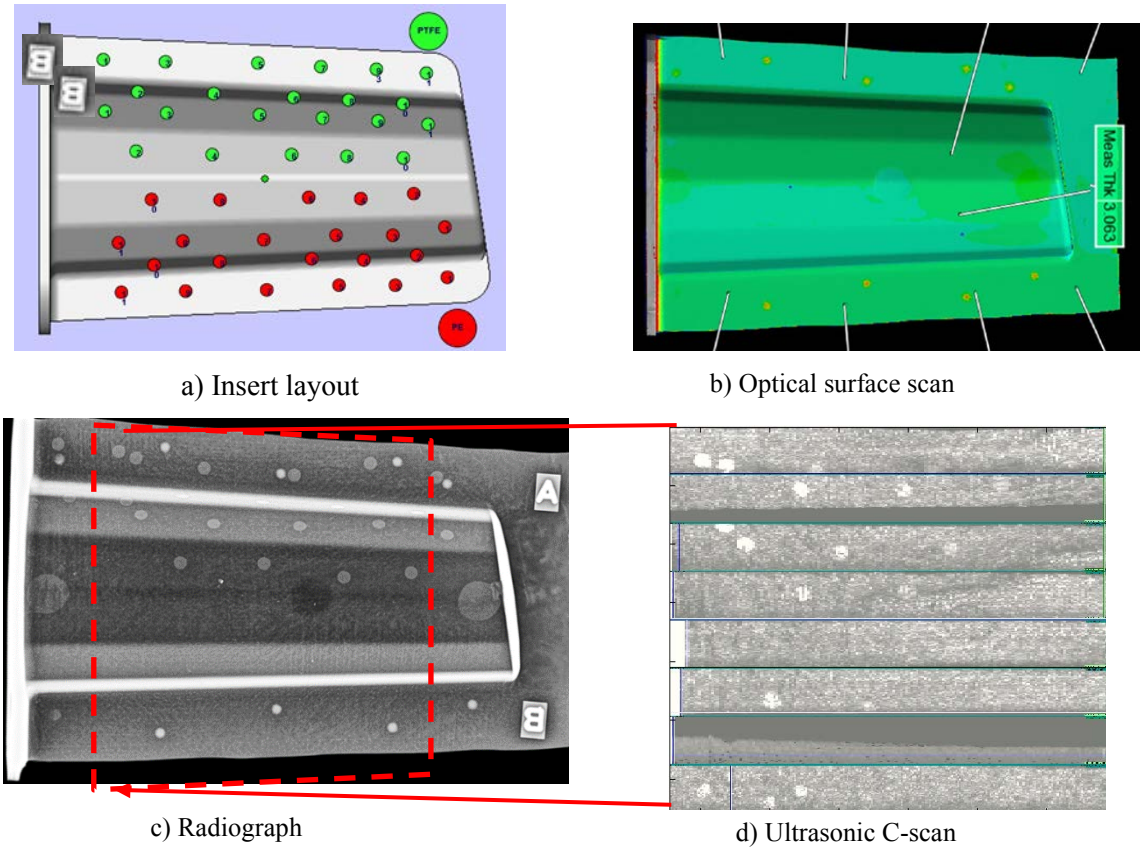

a) Insert layout

b) Optical surface scan

c) Radiograph

d) Ultrasonic C-scan

Figure IV.5-12. Non-destructive imaging of a crush can section with thin film phantoms. (a) Layout of PTFE and PE inserts. (b) Optical surface scan showing variation in thickness (range from 2.8 to 3.2 mm). (c) Low-energy radiograph show PTFE inserts. (d) Collage of ultrasonic C-scans showing both PTFE and PE inserts.

a) FB-CC Assembly #5 showing sections marked for tomography.

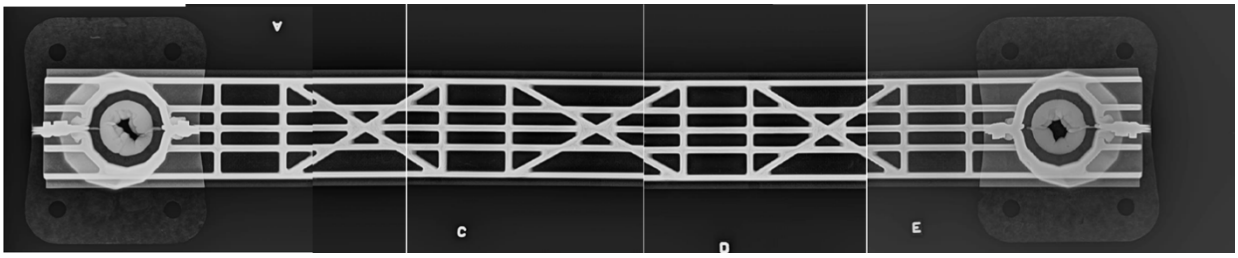

b) Collage of low-energy x-ray radiographs.

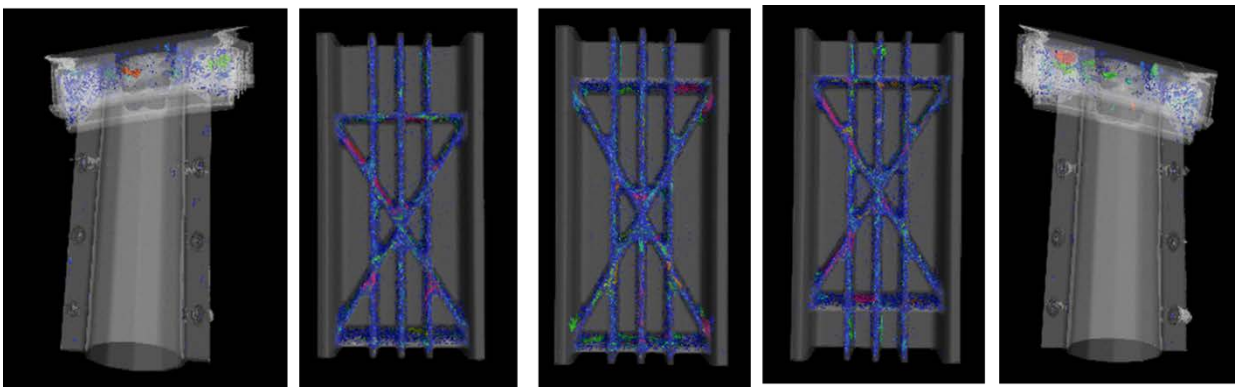

c) CT of individual sections with porosity analysis.

Figure IV.5-13. Non-destructive imaging of a front-bumper/crush can assembly. (a) Picture of assembly with separate CT sections marked. (b) Low-energy radiography of assembly before sectioning. (c) CT of individual sections with superimposed porosity analysis shown in color.

a)

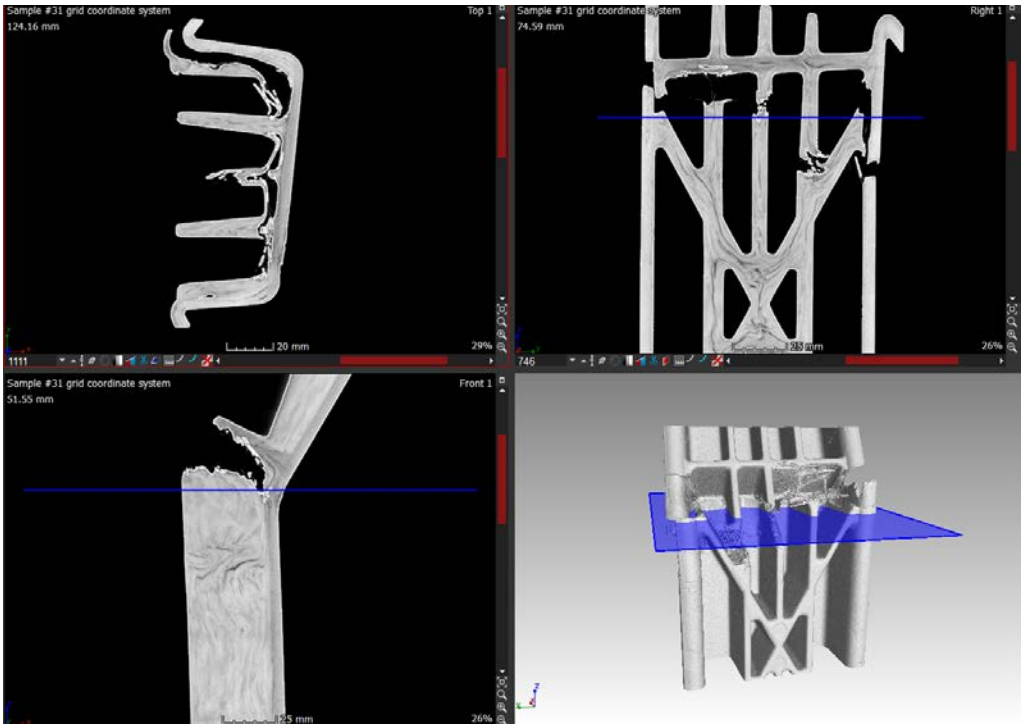

b)

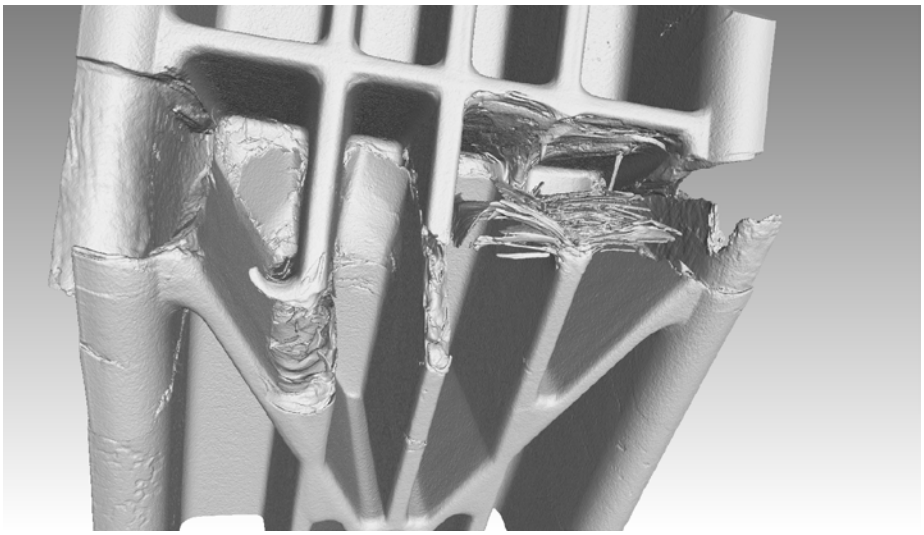

Figure IV.5-14. CT inspection of a front bumper after a center pole crash. (a) Three orthogonal view through the center fraction site, showing tearing through the glass fiber (GF)-SMC ribs. (b) Surface rendering showing matrix fiber damage.

The major discrepancy found in the crush cans is shown in Figure IV.5-15 [21]. The GF-SMC that is molded into the rear flange is shown to infiltrate into the fabric area in the facets of the molded cans. This infiltration caused the fabric to distort, including thinning, bunching, stretching, and twisting of the fabric. The microstructural effects are shown in Figure IV.5-16, which shows both sectioning and CT results. This SMC infiltration causes the region between the facets and the rear flange to be weakened due to these distortion mechanisms. Premature failures in this region observed during crash testing, particularly during the angular impact test, were likely a result of this discrepancy. This issue is likely a result of the differing rheological properties of the prepreg and the SMC, causing the materials to exhibit very different flow behaviors during mold. Improvements to the process could be achieved by tuning the flow and cure properties of the materials.

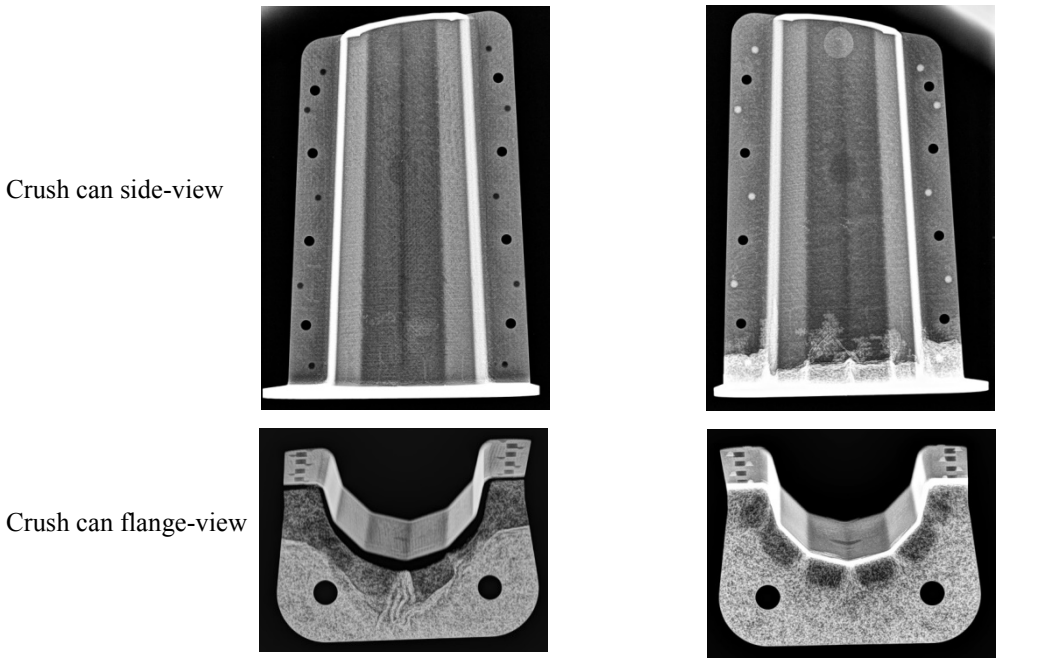

Figure IV.5-15. Low-energy radiographs of crush can sections showing GF location (light areas) and dart locations, with (a) no GF intrusion and (b) extensive GF intrusion.

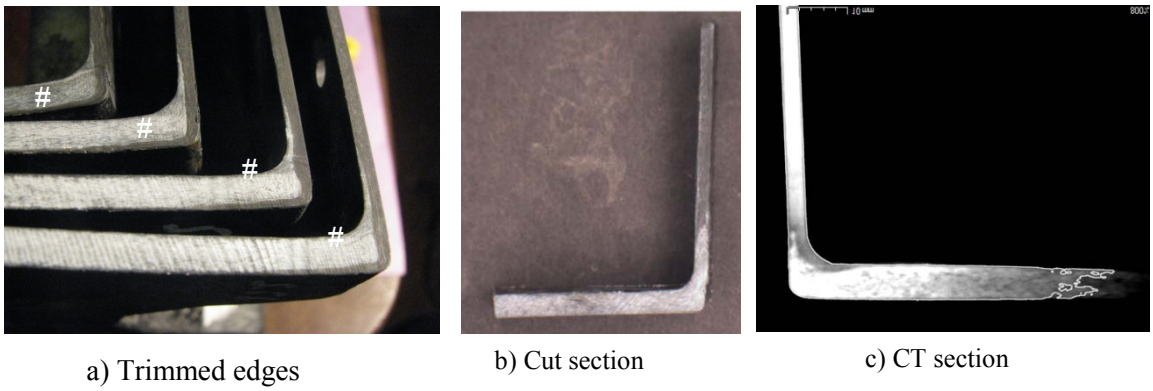

Figure IV.5-16. Images of the GF intrusion and fabric thinning in the crush can rear fillet. The rear flange is the thicker section. GF is lighter material. (a) Trimmed edges of four crush cans. (b) Cut section through a can fillet. (c) CT section of a can fillet.

Two thermoplastic crush cans made with nylon PA-6 were also examined with ultrasonic pulse/echo, radiography, and CT (Figure IV.5-17). The ultrasonic C-scans for delamination do not show any delamination or the striations found in the thermoset parts; however, evidence of fabric bunching is seen in the radiographs. Both ultrasonically and in the CT images, the thick layer structure of the PA-6 parts are seen. This is due to the thick weave of the re-enforcements and the addition of inter-ply film of PA-6 to get the full thickness of the mold (2.8 mm). The CT also indicates there is minor porosity in the rear fillet.

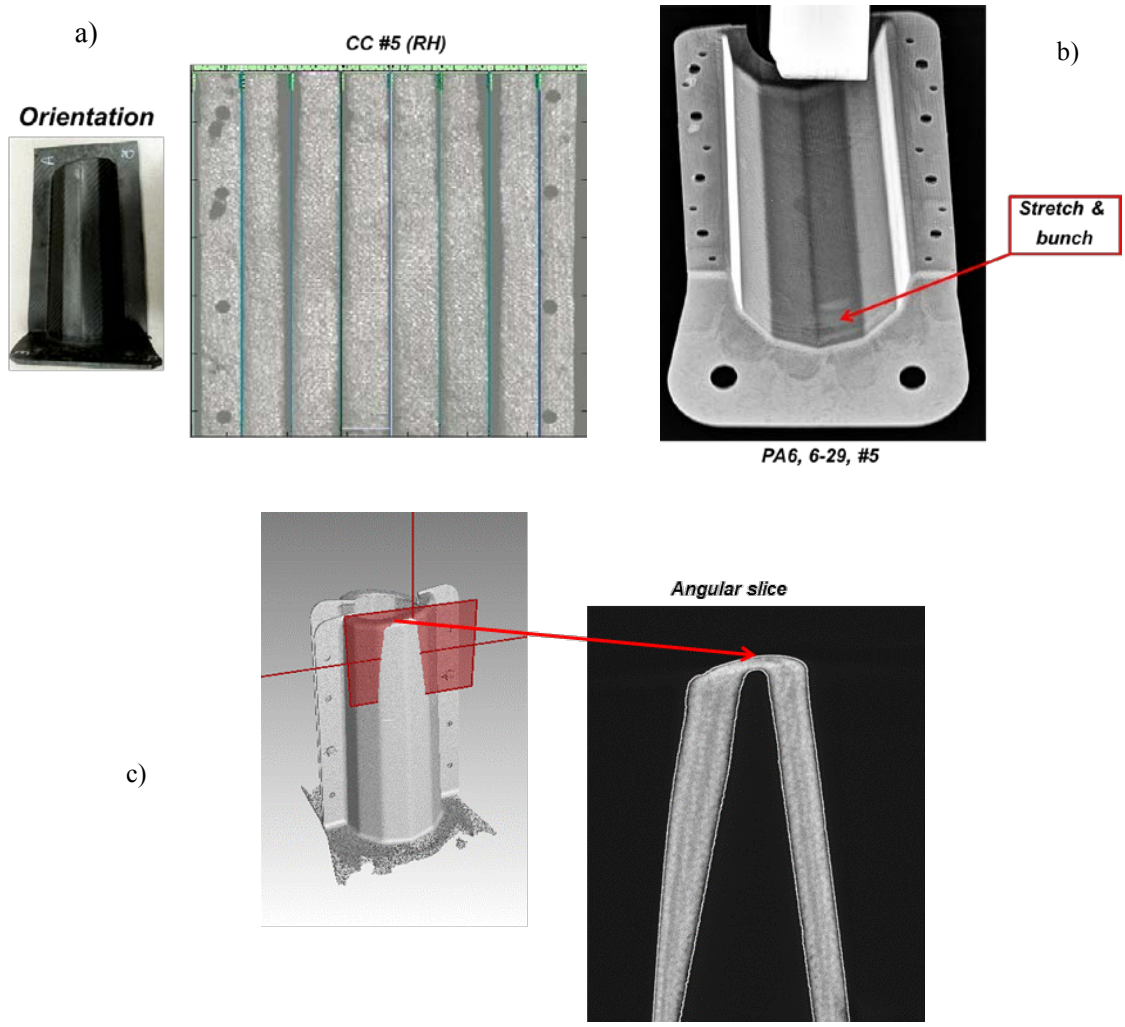

Figure IV.5-17. Inspection of a thermoplastic (nylon PA-6) carbon tape composite showing good uniformity of the fabric. (a) Ultrasonic pulse/echo C-scan showing no evidence of delamination. (b) Radiograph showing some bunching/stretching near the rear flange. (c) CT cross-section showing some of the ply structure.

Structural Health Monitoring (SHM)

A general strategy for SHM in the automotive environment was developed during the project. While traditional NDE methods (such as tap tests and ultrasound) can be used in the manufacturing environment, they require too much training to reduce subjectivity and impose capital expense for most repair shops. This drives the need for onboard sensors to detect in-service impacts that may have damaged the composites. While there is a deep literature base available for SHM of composites, most of these methods are considered too expensive for the automotive market. Our current, primary strategy was to evaluate very low-cost microelectromechanical accelerometers (such as those found in cellphones) to determine optimal detector locations and the range of impact conditions that can be detected. These sensors could be mounted as self-powered, remotely accessible devices. Although an extensive plan to compare these devices to an optical-fiber Bragg grating strain sensor using a pendulum impact stand was developed, this was not pursued. There was no SHM work done during FY 2016.

Task 7: Comparison and Correlation of FBCC Crash Tests with CAE Predictions

The USAMP original equipment manufacturer-led correlation study of composite FBCC commercial code predictions with results of physical crash testing is in progress. This methodology uses the objective International Organization for Standardization's standard proposal rating metrics for dynamic systems to quantify goodness of fit, using measures such as force, displacement, and acceleration versus time histories.

Technology Transfer Path

The FBCC was selected because it is a primary energy-absorbing structural member in frontal crashes and is a challenging structural application of composites for crash energy management. Data for six load cases are being evaluated for the crush cans and bumper beam application in predictive modeling, followed by validation with fabricated structures via crash and physical testing and analyses. At all levels, a broad group of technology stakeholders were involved in modeling with academic material models and five commercial codes (i.e., LS-DYNA, RADIOSS, PAM-CRASH, Abaqus, and GENOA-MCQ). These help accelerate evaluation of the models for early identification of key knowledge gaps and develop best practices in crash modeling. Advances made in crash modeling will be quickly implemented by the respective crash code vendors into the major commercial crash codes for crash analyses of carbon composite structures. During FY 2016, ESI implemented the University of Michigan's Waas-Pineda [22] meso-scale representative unit cell material model in its latest release of Virtual Performance Solution/PAM-CRASH code, for broader evaluation by industry.

Successful demonstration of challenging crash structures such as FBCCs opens new light-weighting application opportunities for composites in passenger vehicles and light trucks, with the near-term potential to drive U.S. industrial capacity and economies of scale in carbon fiber production. The project outcomes are presently undergoing extensive analyses. The USAMP team expects to identify key gaps and remaining barriers and to propose pathways for advancing the readiness levels of composite design and predictive crash modeling tools, as well as identify improvement needs in associated manufacturing and joining technologies to prove their feasibility for broader application of primary automotive composite structures.

Conclusion

During FY 2016, the USAMP team completed all CAE predictions of composite FBCCs using five commercial crash codes (LS-DYNA, RADIOSS, PAM-CRASH, Abaqus and GENOA-MCQ) and also completed all FBCC fabrication and assembly-related tasks, followed by the completion of all planned crash tests of FBCC assemblies. A detailed NDE methodology was demonstrated for characterization of the fabricated composite FBCCs and adhesive joining. Final comparison and correlation of crash-test data with CAE predictions will be completed during FY 2017; however, all initial results from the project point to the critical role that NDE plays in enabling successful product development and application of carbon fiber composites for structural components. NDE has to be conducted on manufactured and assembled parts prior to testing to ensure no damage that could compromise performance (e.g., delaminations or excessive voids) is present. The team also made good progress in evaluating alternative thermoplastic composite materials (including low-cost carbon fiber from Oak Ridge National Laboratory's Carbon Fiber Technology Facility). Axial crush tests remain to be completed and the final documentation of technology gaps in CAE capability, design, manufacturing, joining, and NDE considerations remains. This project has received a no cost extension till the first half of FY 2017.

References

[1] Song, S., A. M. Waas, K.W. Shahwan et al., 2007, "Braided Textile Composites under Compressive Loads: Modeling the Response, Strength and Degradation," *Composites Science and Technology* 67(15): 3059–3070.

[2] Quek, S. C., A. M. Waas, K. W. Shahwan, and V. Agaram, 2003, "Analysis of 2D Triaxial Flat Braided Textile Composites," *International Journal of Mechanical Sciences* 45(6): 1077–1096.

[3] Song, S., A. M. Waas, K. W. Shahwan, and O. Faruquec, 2009, "Compression Response, Strength and Post-Peak Response of an Axial Fiber Reinforced Tow," *International Journal of Mechanical Sciences* 51(7): 491–499.

[4] Caner, F. C., Z. P. Bazant, C. G. Hoover, A. M. Waas, and K. W. Shawan, 2011, "Microplane Model for Fracturing Damage of Triaxially Braided Fiber-Polymer Composites," *Journal of Engineering Materials and Technology* 133(2).

[5] Cusatis, G., A. Beghini, and Z. P. Bazant, 2008, "Spectral Stiffness Microplane Model for Quasibrittle Composite Laminates – Part 1: Theory," *Journal of Applied Mechanics* 75(2).

[6] Chang, F. K. and K. Y. Chang, 1987, "A Progressive Damage Model for Laminated Composites Containing Stress Concentrations," *Journal of Composite Materials* 21: 834–855.

[7] Feraboli, P., B. Wade, F. Deleo, M. Rassian, M. Higgins, and A. Byar, 2011, "LS-DYNA MAT54 Modeling of the Axial Crushing of a Composite Tape Sinusoidal Specimen," *Composites (Part A)* 42(11): 1809–1825.

[8] Matzenmiller, A, J. Lubliner, and R. L. Taylor, 1995, "A Constitutive Model for Anisotropic Damage in Fiber-Composites," *Mechanics of Materials* 20(2): 125–152.

[9] Xiao, X., 2008, "Simulation of Composite Tubes Axial Impact with a Damage Mechanics Based Composite Material Model," presented at the *10th International LS-DYNA Users Conference*, June 2008.

[10] Goldberg, R. K. and K. S. Carney, 2004, "Modeling the Nonlinear, Strain Rate Dependent Deformation of Shuttle Leading Edge Materials with Hydrostatic Stress Effects Included," presented at the *8th International LS-DYNA Users Conference*.

[11] Gatti, M., L. Vescovi, M. Sperati, P. Pagano, and L. Ferrero, 2007, "Characterization of Composite Materials, Unidirectional and Fabric Samples," presented at the *Autosim Technology Workshops & CSC*.

[12] Tsai, S. W. and E.M. Wu, 1971, "A General Theory of Strength for Anisotropic Materials," *Journal of Composite Materials* 5(1): 58–80.

[13] Daniel, I. M. and O. Ishai, 2006, *Engineering Mechanics of Composite Materials*, 2nd ed., New York: Oxford University Press: 122–147.

[14] Ladevèze, P. and E. Le Dantec, 1992, "Damage Modelling of the Elementary Ply for Laminated Composites," *Composites Science and Technology* 43(3): 257–267.

[15] Johnson, A. K., A. K. Pickett, and P. Rozycki, 2001, "Computational Methods for Predicting Impact Damage in Composite Structures," *Composites Science and Technology* 61(15): 2183–2192.

[16] Hashin, Z., 1980, "Failure Criteria for Unidirectional Fiber Composites," *Journal of Applied Mechanics* 47(2): 329–334.

[17] Dassault Systemès Simulia Corp., 2011, *ABAQUS Analysis User's Manual*, Revision 6.11.

[18] Heimbs, S., 2011, "Bird Strike Simulations on Composite Aircraft Structures," presented at the *2011 Simulia Customer Conference*.

[19] Coppola, A. M., L. Berger, G. Smith, D. Armstrong, and C. J. Dasch, 2016, "Validation of Material Models: Thermoset Composite Materials and Processing for a Composite Bumper Beam System," presented at the *Society of Plastics Engineers Automotive Composites Conference and Exhibition (SPE-ACCE)*.

[20] McHenry, J. and J. Tao, 2016, "Validation of Material Models: Development of Carbon Fiber Reinforced Thermoplastic Composites for a Front-Bumper/Crush-Can System," presented at the *Society of Plastics Engineers Automotive Composites Conference and Exhibition (SPE-ACCE)*.

[21] Dasch, C., G. Harmon, and M. Jones, 2015, "Ultrasonic and X-ray Inspection of a High Performance Carbon Fiber Composite for Automotive Applications," presented at the *2015 American Composites Society Technical Conference*.

[22] Pineda, E. J., B. A. Bednarcyk, A. M. Waas, and S. M. Arnold, 2013, "Progressive Failure of a Unidirectional Fiber-Reinforced Composite Using the Method of Cells: Discretization Objective Computational Results," *International Journal of Solids and Structures* 50(9): 1203–1216.

Bibliography

Board, D., Y. Chen, O. Faruque, G. Newaz, P. Begeman, A. S. Yaghoubi, and Y. Dixit, 2016, "Physical Crash Testing of Composite Bumper Beams," presented at the *Society of Plastics Engineers Automotive Composites Conference and Exhibition (SPE-ACCE)*, Novi, Michigan, September 8, 2016.

Cawley, A., J. Truskin, A. Coppola, M. Mehta, and contributor H. Stevens, 2016, "Joining and Assembly System for Thermoset and Thermoplastic Composite Materials," presented at the *Society of Plastics Engineers Automotive Composites Conference and Exhibition (SPE-ACCE)*, Novi, Michigan, September 8, 2016.

Coppola, A., L. Berger, G. Smith, D. Armstrong, and C. Dasch, 2016, "Thermoset Composite Materials and Processing for a Composite Bumper Beam System," presented at the *Society of Plastics Engineers Automotive Composites Conference and Exhibition (SPE-ACCE),* Novi, Michigan, September 8, 2016.

Dasch, C., M. Jones, and contributor G. Harmon, 2016, "Non-Destructive Testing Throughout the Development of a Carbon Fiber Composite Automotive Crash Structure," presented at the *Society of Plastics Engineers Automotive Composites Conference and Exhibition (SPE-ACCE)*, Novi, Michigan, September 8, 2016.

Dasch, C., G. Harmon, and M. Jones, 2015, "Ultrasonic and X-ray Inspection of a High Performance Carbon Fiber Composite for Automotive Applications," *2015 American Composites Society Technical Conference,* Michigan State University, East Lansing, Michigan, September 28–30, 2015.

Faruque, O., A. Coppola, D. Board, J. Truskin, M. Jones, and M. Mehta, 2016, "Validation of Material Models for Crash Testing of Carbon Fiber Composites," presented at the *Society of Plastics Engineers Automotive Composites Conference and Exhibition (SPE-ACCE)*, Novi, Michigan, September 8, 2016.

McHenry, J. and contributor Jian Tao, 2016, "Development of Carbon Fiber Reinforced Thermoplastic Composites," presented at the *Society of Plastics Engineers Automotive Composites Conference and Exhibition (SPE-ACCE)*, Novi, Michigan, September 8, 2016.

Pasupuleti, P., M. Doroudian, R. Dwarampudi, A. Coppola, L. Berger, O. Faruque, J. Truskin, and M. Mehta, 2016, "Design of a Composite Bumper and Assessment of Current Composite Crash Simulation Capabilities," presented at the *Society of Plastics Engineers Automotive Composites Conference and Exhibition (SPE-ACCE)*, Novi, Michigan, September 8, 2016.

Pasupuleti, P., X. Jin, H. Yu, M. Doroudian, D. Armstrong, A. Coppola, L. Berger, O. Faruque, and J. Truskin, 2016, "Composite Fabric Manufacturing Studies by Simulation and Experiment," presented at the *Society of Plastics Engineers Automotive Composites Conference and Exhibition (SPE-ACCE)*, Novi, Michigan, September 8, 2016.

Yaghoubi, A. S., P. Begeman, G. Newaz, D. Board, Y. Chen, and O. Faruque, 2016, "Generic Steel Vehicle Front Bumper and Crush Can Assemblies Subjected to a Rigid High Speed Offset Frontal Impact," *Proceedings of the ASME 2016 International Mechanical Engineering Congress & Exposition*, Phoenix, Arizona, November 11–16, 2016.

IV.6 Integrated Computational Materials Engineering Development of Carbon Fiber Composites for Lightweight Vehicles – Ford Motor Company

Project Details

Xuming Su, Principal Investigator
Ford Research and Advanced Engineering
Ford Research and Innovation Center
2101 Village Road
Dearborn, MI 48124
Phone: 313-845-5643
E-mail: xsu1@ford.com

David Wagner, Principal Investigator
Ford Research and Advanced Engineering
Ford Research and Innovation Center
2101 Village Road
Dearborn, MI 48124
Phone: 313-845-2547
E-mail: dwagner6@ford.com

Walter (Jerry) Parker, Project Manager
National Energy Technology Laboratory
626 Cochrans Mill Road
P.O. Box 10940
Pittsburgh, PA 15236
Phone: 412-386-7357
E-mail: walter.parker@netl.doe.gov

Sarah Kleinbaum, Technology Area Development Manager
U.S. Department of Energy
1000 Independence Avenue, SW
Washington, DC 20585
Phone: 202-586-8027
E-mail: sarah.ollila@ee.doe.gov

Executive Summary

The project will develop integrated computational materials engineering (ICME) techniques for carbon fiber reinforced polymer (CFRP) composites and use ICME tools to design a structural carbon fiber composite subframe to support immediate weight reduction in light-duty vehicles and reduce development-to-deployment lead time.

During the current Phase 1 of the project, the focus is on developing ICME tools. The numerical tools intended here are to predict material performance of CFRP based on fiber architecture, molding process, and curing history, with consideration of uncertainties and the probabilistic nature of materials, processes, and in-service conditions. Great progress has been made during Fiscal Year (FY) 2016. A non-orthogonal model has been established for preforming analysis for woven fabrics. The model has been validated and shown to accurately predict fiber orientation and wrinkling. By inverse engineering, a reliable viscosity of sheet molding compound (SMC) has been obtained, which is still difficult to be precisely characterized, allowing Moldflow to predict the filling pattern of SMC molding correctly. Multi-scale material models are being developed and validated to

predict material stress-strain behavior based on material design and material microstructures, which are the results of manufacturing simulations. These computer-aided engineering (CAE) tools have been integrated by using modeFRONTIER® for performance and weight analyses and optimization.

Molecular dynamic (MD) analysis is also integrated into the ICME multi-scale models to predict relevant properties of pure resin and the interphase between resin and fibers. Material property variations are studied at the fundamental level (such as waviness of the fibers and local fiber volume fractions).

The tools are and will be implemented in popular software packages such as LS-DYNA for stress and crash analysis, nCode for durability, Moldflow for molding, and modeFRONTIER® for optimization. With these tools, engineers can optimize component design, material design, and manufacturing processes and can optimize them simultaneously to achieve the most efficient usage of the material.

The project is on schedule and meets every milestone established at the start of the project. Building on the above-mentioned success, the majority of ICME work is expected to be implemented during FY 2017 when design of the subframe with target weight savings will be initiated.

Accomplishments

- Met and exceeded all milestones of the project: completed models and methodology for preforming, SMC molding, and curing analyses; established multi-scale representative volume element (RVE) models for unidirectional (UD), woven, and chopped fiber composites; improved CAE models for crash analysis; and integrated all modes for design optimization (FY 2015, FY 2016).
- Molded 80 UD and 110 woven CFRP plaques (with thicknesses of 1.2 mm, 2.5 mm, and 5 mm, respectively, and a fiber volume fraction of about 55%) and distributed for characterization at Northwestern University, the National Institute of Standards and Technology (NIST), and Ford Motor Company (FY 2016).
- Completed two trials of compression molding of chopped fiber SMC for over 100 plaques with various process parameters. Tensile properties and fiber orientations of the molded plaques will be used to calibrate and improve the Moldflow analyses (FY 2016).
- Molded 72 UD, 24 woven hat sections, and 30 back plates with different layouts for crash model validation (FY 2016).
- Completed static tensile tests and viscosity measurements on neat resin. Performed static and high-strain rate tests and fracture toughness tests on UD composites and tensile and shear tests on woven composites. Test data are used for calibration of multi-scale modeling and input for structural and crash analyses (FY 2016).
- Completed development of the non-orthogonal material model for preforming analysis. The model was validated using single-dome tests and proven to be able to predict fiber orientation and wrinkling during preforming process for woven prepregs. The model is programmed as a LS-DYNA user subroutine and is ready for implementation in LS-DYNA (FY 2015, FY 2016).
- Completed a multi-scale model for CFRP using RVE for woven fabric. The model is being validated using test data. The model is used to study the effects of the geometric layout of fiber tow on the mechanical properties of the material (FY 2016).
- Developed multi-scale models for compression-molded chopped fiber SMC using RVE. RVE is generated using either a Voronoi diagram or a chip-packing algorithm for reconstruction of three-dimensional microstructures, which are based on predictions from Moldflow. The anisotropic elastic properties predicted using the model are consistent with test data (FY 2016).

- Linked Moldflow analysis, multi-scale material model, and structural analysis for optimized design of structural parts. Completed a preliminary study on the integrated tools for a CFRP subframe based on current steel design. Material thickness and fiber layout are assumed as design variables. The results gave 18% weight savings in a subframe built with SMC material and more than 40% weight savings in a UD-laminated design compared to the steel baseline (FY 2016).
- Discovered that the newly developed approach using a modified self-learning metabasin escape (SLME) algorithm for the MD simulation produces stress-strain behavior of resins at a strain rate achievable at conventional laboratories. At a very high strain rate, SLME predictions are consistent with traditional MD results (FY 2016).
- Established an uncertainty analysis framework to study material property variations due to fiber waviness and variations of local fiber volume fraction (FY 2016).

Future Directions

- Further validate the robustness of the multi-scale models for UD composites by studying the impact of fiber volume fraction on the mechanical properties of CFRP. Plaques of different fiber volume fractions between 48 and 58% will be molded and tested and their properties will be compared with model predictions.
- Further validate the robustness of multi-scale models for woven fabrics by studying the impact of fiber tow size and geometry on mechanical properties. Plaques of different tow size and geometry will be molded and tested and their properties compared with model predictions.
- Further validate the robustness of multi-scale models for SMC by studying the impact of SMC chip size on mechanical properties. Plaques of SMC chip size varying from 12 to 50 mm will be molded and tested and their properties will be compared with model predictions.
- Further validate a preforming analysis tool set by studying the impact of process variations on preforming product. Double domes will be molded with a different temperature and forming speed. Local fiber orientations and wrinkling patterns will be measured and compared with predictions.
- Further validate an SMC compression molding tool set by studying the impact of process variations. Plaques will be molded with different displacement and force profiles and different mold temperatures. Local fiber orientation and tensile properties will be measured and compared with model predictions.
- Complete process integration, linking all ICME tools using modeFRONTIER®. The tool set will be used for a simultaneous design and process optimization. Subframe design will be used as the targeted demonstration.
- Design of the CFRP subframe using ICME tools will be initiated. The design aims at a carbon fiber composite subframe capable of achieving a greater than or equal to 25% weight reduction and less than or equal to $4.27/lb of weight saved when compared to the baseline technology to be replaced.
- Establish ICME crash models for safety analysis. While current RVEs are able to provide material inputs for the material stress-strain relationship in LS-DYNA, improvements/new material relations shall be developed and implemented in LS-DYNA to describe special failure modes in CFRP crash tests, including material degradation and delamination.
- Complete fatigue tests of UD specimens and establish fatigue analysis procedures/models for UD CFRP. Establish fatigue models for non-crimped laminates that correlate the fatigue strength of laminates to prepreg stack-ups. Start fatigue tests of woven CFRP and chopped fiber SMC.
- Perform an extensive analysis of microstructure for both continuous and chopped fiber composites. Statistically define material uncertainty through multi-scale modeling of local variations of microstructures, especially fiber waviness and local fiber volume fraction.

- Continue to improve SLME approach and use MD analysis to predict resin curing behavior and the interphase strength between resins and fibers.

Technology Assessment

- Target: Comprehensive material characterization of CFRP and ICME database to establish and validate ICME models.
- Gap: High-strain rate tests of both resin and composite need to be completed, as well as tests studying the temperature dependency of the material. Extensive microstructural image analysis is needed for a comprehensive characterization of failure mechanisms and uncertainty.
- Gap: Plaques of CFRP with different fiber volume fraction for UD, different tow size and geometry for woven, and different chip size for SMC still need to be produced to verify ICME models.
- Target: Preforming models accurately predicting fiber orientations and wrinkling.
- Gap: Robustness of the established models needs further validation by more experimental cases.
- Gap: The current model is developed specially for woven prepregs. The model needs to be extended for UD prepregs.
- Target: Using an MD analysis to predict the thermomechanical behavior of resins, explore mechanisms of resin and interphase failures and provide key data for micro and macro-scale material models.
- Gap: MD simulation with strain rate lowered by applying SLME algorithm needs to be further validated with experimental data.
- Gap: Fiber fragmentation tests need to be completed to validate MD interphase model.
- Target: RVE for UD and woven composites relating mechanical properties of composite to properties of its constituents.
- Gap: RVE robustness of a multi-scale model needs to be further verified.
- Gap: Current RVE is not able to predict material failures, which is critical for performance analysis.
- Target: A Moldflow module for compression molding simulation of chopped fiber CFRP.
- Gap: Fiber orientation predictions are not fully verified.
- Target: Fracture models and energy absorption models for vehicle component safety analysis.
- Gap: Failure models are not yet well developed for crash analysis.
- Target: Fatigue and durability models to predict component life.
- Gap: Available test data are not comprehensive. Further test development must be conducted to generate a comprehensive data set.
- Target: Full integration of all ICME models.
- Gap: Preforming analysis is not included in the current ICME integration process.
- Gaps: Simultaneous optimization of design and the manufacturing process does not include optimization of manufacturing processes.
- Target: Design of CFRP subframe using ICME tools.
- Gaps: Preliminary design is not available.
- Target: Models capable of characterizing material uncertainty.

- Gap: Multi-scale models describing local material microstructure variations have not been completed.
- Gap: Because of limited design freedom in material architectures that can be realized in experiments, validation of statistical schemes to describe material uncertainty is challenging.
- Gap: Uncertainty transfer from one scale to another is yet to be explored.

Introduction

Vehicle lightweighting is very important for automotive manufacturers to meet the ever-increasing demand of fuel efficiency in order to reduce greenhouse gas emissions and dependency on foreign oil. CFRP composites, with a density of 1.55 g/cm^3 and tensile strength of about 2,000 MPa in the fiber direction, are among the most promising candidates to replace metals for structural components. The project will design, develop, and optimize, using CAE only, a light-duty vehicle carbon fiber subframe capable of achieving a greater than or equal to 25% weight reduction and less than or equal to $4.27/lb of weight saved when compared to the baseline technology to be replaced.

Unlike many metals typically used in automotive vehicles, the mechanical properties of CFRP are highly direction-dependent. The strength of the material in the fiber-reinforced direction could be an order of magnitude higher than in the direction perpendicular to it. More importantly, the fiber orientation in a component is decided not only by the initial fabric layout, but also by the preforming and molding processes. An optimized vehicle component design will need tools that predict the performance of CFRP based on fiber architecture, molding process, and curing history, with considerations of uncertainties and the probabilistic nature of materials, processes, and in-service conditions. The current project will develop these ICME tools to meet the design challenge.

ICME tools developed during the project will be robust, accurate, and reliable constitutive models for each constituent material and the composite assembly under expected service conditions, including high-strain rates using physics-based models. The manufacturing process (including variability from both process and material) are simulated to predict fiber orientation and other microstructural features of manufactured products. This information is passed to performance analysis, with the material design, manufacturing simulation, and performance analysis integrated. Local material properties are related to the composite architecture and microstructure by multi-scale models. Design and manufacturing processes are optimized simultaneously to achieve the most efficient usage of the material.

Approach

The project will design, develop, and optimize, using CAE only, a light-duty vehicle carbon fiber subframe capable of achieving a greater than or equal to 25% weight reduction and a less than or equal to $4.27/lb of weight saved when compared to the baseline technology to be replaced. This objective is achieved by developing ICME tools and numerical procedures for optimizing both the design and manufacturing process so CFRP is most efficiently used.

The ICME tools relate the performance requirements of a vehicle to the material design and processes. While material performances are expressed at the continuum macroscale, they are decided by material microstructures and microstructural features at the microscale and again by molecular bonds and crosslinking at the nanoscale. The material microstructures and microstructural features, bonding, and crosslinking are results of material design and manufacturing processes. ICME tools are multi-scale models and approaches that bridge the different material scales. The models are based on the physical principles, testing measurements, and observations. Test data are also needed to validate material models. Modeling and testing are always hand-in-hand in successful development of ICME tools. The project team, which consists of Ford Motor Company (i.e., an automotive manufacturer), Dow Chemical (i.e., a material manufacturer), Northwestern University (i.e., an institution of highly regarded academics), and NIST (i.e., a world-renowned test laboratory), has all the elements for making a breakthrough in developing ICME tools. The research team also includes software developers from Livermore Software Technology Corporation (LSTC) (LS-DYNA),

Autodesk (Moldflow), ESTECO (modeFRONTIER®), and HBM (nCode). The ICME tools developed during the project can be numerically implemented and disseminated through available engineering software.

The project is conducted in four budget periods. The budget periods are (1) CFRP material characterization and ICME model development, (2) ICME model database and validation, (3) ICME model integration and validation, and (4) ICME-based design and optimization. The first two budget periods constitute Phase I, Model Development and Model-Level Validation. The remaining two budget periods constitute Phase II, ICME Integration and System Design. FY 2016 is the second year of Phase I.

Results and Discussion

The project was organized into four main tasks: Task 1 was material characterization and ICME database development, Task 2 was ICME model development and validation, Task 3 was ICME model integration and validation, and Task 4 was ICME-based design and optimization. FY 2016 is the second year of Phase I. Only Task 1 and Task 2 were active during FY 2016.

Task 1. Material Characterization and ICME Database

Experimental characterization of each CFRP constituent and characterization at the coupon level were conducted during this task. Results were collected and stored in the ICME database and used to correlate with models in Task 2. The tested materials were produced by Dow Chemical. The matrix of the composite is epoxy resin and the fibers are DowAksa A42 and AC1101 for continuous and SMC, respectively. A vacuum-assisted compression molding process was used in order to achieve aggressive cycle time and cost requirements.

Task 1.1. Resin Characterization

Notched beam in bending tests were performed according to American Society of Testing and Materials E399 to obtain the critical Mode I stress intensity factor (K_{Ic}) and critical strain energy release rate (G_{Ic}) for the cured epoxy resin. Initial cracks were formed by first machining a thin notch of about 3 mm (0.12 in), followed by razor-blade tapping to produce a true crack of approximately equal length beyond the machined notch, so the final effective crack length was nominally 6.3 mm (0.25 in). The average results are summarized in Table IV.6-1. Resin characterization work was completed as requested. More tests may be conducted if requested for validation in FY 2017.

Table IV.6-1. Average Mode I Fracture Properties for Neat Epoxy

Property	Value	Coefficient of Variation
K_{Ic}	1.172 Mpa-$m^{(1/2)}$	9.68%
G_{Ic}	314 J/m^2	19.20%

Task 1.2. Carbon Fiber and Fabric Characterization

Tests were conducted to determine the ply-to-ply resistance-to-sliding at various rates of relative displacement and temperatures to support the preforming simulation. The resistance-to-sliding comes from a combination of friction between the sheets and adhesion from the resin. The results indicate that the resin viscosity does not have a significant impact on the ability of plies to slide against each other for the normal loads considered. However, temperature does have a significant effect on the apparent resistance to sliding as the resin becomes stickier and then softer as the temperature increases. Carbon fiber and fabric characterization will continue during FY 2017.

Task 1.3. Interfacial/Interphase Property Characterization

Single-fiber fragmentation specimens were successfully molded at NIST in Gaithersburg, Maryland, using the silicon mold shown in Figure IV.6-1. Single carbon fibers were extracted from a tow using specialized tools affixed to an optical microscope. Cast specimens were found to be opaque on the side of the specimen facing the mold. Further work is ongoing to improve the optical properties of the cast specimens. Interface and interphase property characterization will continue in FY 2017.

Figure IV.6-1. Silicon mold used to cast single-fiber fragmentation specimens.

Task 1.4. Composite Plaque Characterization

Over 300 12 × 12-in. plaques, including 170 UD, 110 woven fabric, and over 100 SMC, were molded for material characterization. Completed tests include tensile and compression tests of pure resin, UD and woven composites, and compression tests of pure resin and UD. Shear tests included pure resin, UD, and woven composites. High-strain rate tests were also done on UD. Many of the tests were repeated at two or three different laboratories to confirm accuracy.

Mode I and Mode II interlaminar fracture toughness tests were performed. Plaques formed by Dow Chemical incorporated a thin Teflon layer at two edges to serve as a pre-crack at the center of the plaque. Width-tapered (Figure IV.6-2a), double-cantilever beam (DCB) specimens were used for Mode I fracture toughness testing at Northwestern University. The edge-notched flexure specimen (Figure IV.6-2b) was chosen for Mode II.

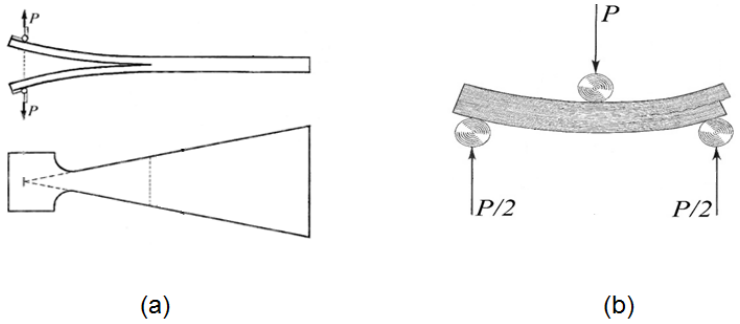

Figure IV.6-2. Illustration of specimen geometry for fracture tests: (a) Mode I and (b) Mode II.

Digital image correlation was used for tests conducted at NIST with constant width DCB geometry to track the advance of the crack front. The edge of the sample was decorated and imaged using digital image correlation, which allowed detailed measurement of the sample's crack tip opening angle and an accurate measurement of the crack length (Figure IV.6-3). Experiments were performed on UD composite in the fiber direction. Tests results are summarized in Table IV.6-2, showing acceptable coefficient of variation values for both modes of fracture.

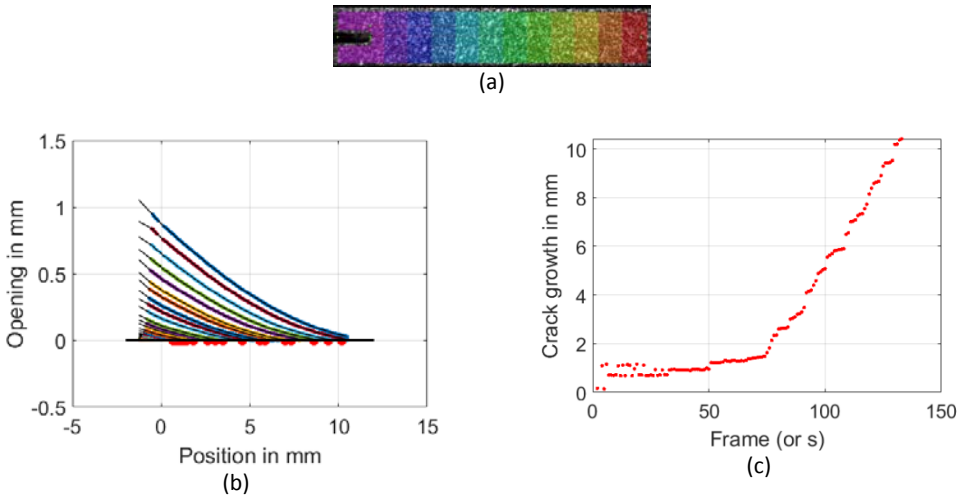

Figure IV.6-3. (a) DCB specimen patterned for digital image correlation. (b) Raw deflection data from digital image correlation. (c) Crack growth rate as a function of time from DCB test.

Table IV.6-2. Mode I and Mode II Interlaminar Fracture Test Data

Property	Value	Coefficient of Variation
G_{Ic}	536 J/m^2	12.8%
G_{IIc}	913 J/m^2	17.6%

Composite plaque molding was completed for initial characterization. Mechanical testing will continue in FY 2017. Further composite plaque molding will be conducted in FY 2017 to provide variations of materials needed to validate ICME models.

Task 2. ICME Model Development and Validation

A collection of process and material computational models and methodologies for predicting/optimizing CFRP performance in vehicle application were identified and/or developed and integrated into the ICME process during this task.

Figure IV.6-4 is a flowchart of the processes to be modeled in the ICME framework. They include process modeling of preforming and curing for UD and woven laminates, compression molding, and curing modeling for chopped fiber SMC. Bridging process models and performance analyses are RVE models that predict material constitutive and failure behaviors based on constituent properties. Performance analyses will be performed for crash, durability and noise, vibration, and harshness. MD will provide a fundamental understanding of thermomechanical behavior and failure mechanisms of resins and resin and fiber interface. Statistical tools are needed to describe distributions of process defects and uncertainties of processes.

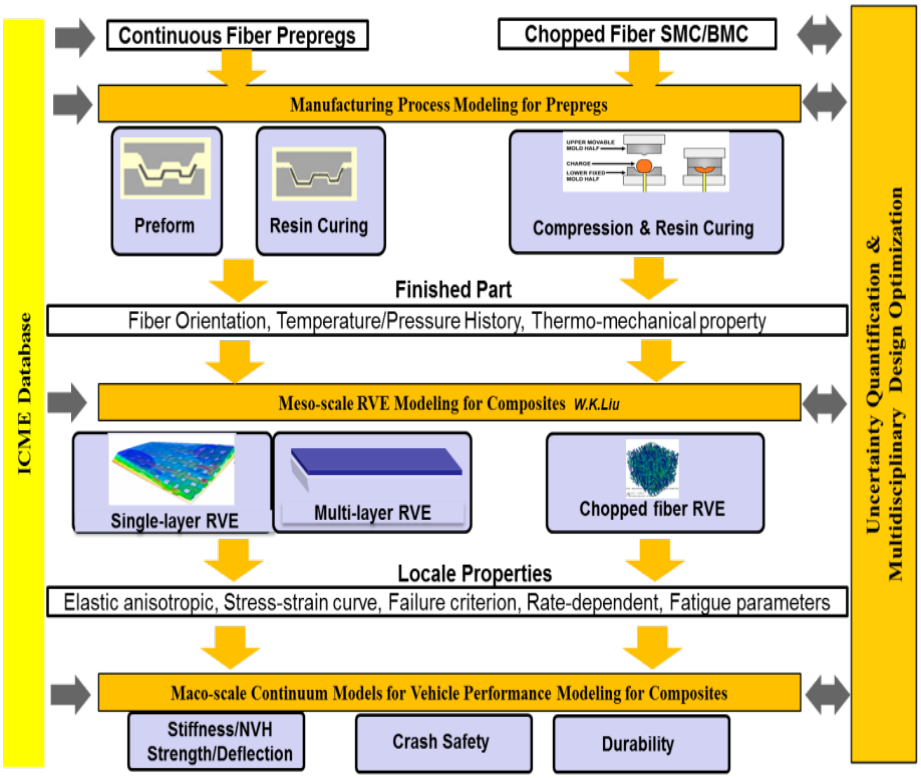

Figure IV.6-4. Models to be developed during the current project.

Task 2.1. Atomistically Informed Resin Infusion Models

A combined MD simulation with a continuum fracture mechanics modeling approach was proposed to investigate the onset of crack propagation and calculate the macroscopic fracture energy of epoxy. Stress-strain relationship, yield stress, and maximum stress predicted by MD were used in the continuum fracture mechanics model to calculate fracture energy. The fracture properties of two epoxy systems (Epon 825™ and 3501-6) were evaluated using the developed method. The results demonstrate that increasing the functionality of the epoxy decreases the fracture energy; this trend was consistent with experiment observations. The effect of conversion degree and amount of curing agent on the fracture properties were investigated. Predicted fracture energy was found to increase with conversion degree.

The most critical challenge in using an MD analysis in ICME work flow is the computation efficiency; real time achieved during an analysis is in terms of nanoseconds. In most MD analyses, including our earlier work, predictions of the resin stress-strain relation were computed for strain rates larger than $10^6 s^{-1}$. A newly developed method [1] that couples a SLME algorithm for potential energy surface exploration and the standard Monte Carlo approach has the potential to increase computational efficiency and study material behavior at strain rates seen in conventional mechanical tests laboratories. SLME was modified and applied to cured epoxy resin Epon 825™ for different strain rates at a constant temperature of 300 K, where strain rates range from $10^2 s^{-1}$ to $10^{10} s^{-1}$. Figure IV.6-5 shows results where the modified SLME method was not only able to reproduce conventional MD results at a very-high strain rate, but, at the same time, also predicted yield stress at a strain rate achievable by physical testing.

Further work will investigate the effect of strain rates on shear viscosities using the modified SLME method coupled with shear deformation.

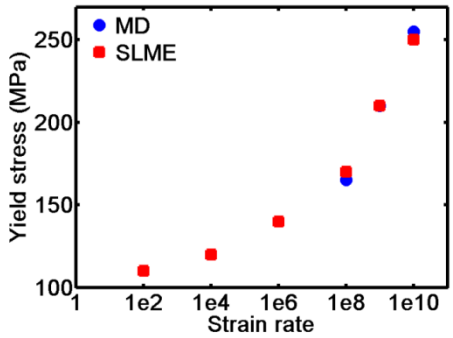

Figure IV.6-5. SLME predictions of yield stress at different strain rates.

Task 2.2. Preform and Compression Molding Process Models

This task includes preforming simulation and compression modeling simulation; the results are discussed below for each subtask.

Task 2.2.1. Preforming Analysis

A number of new tests were designed and performed to increase the accuracy of the material input for the preforming analysis, including gravity bending of prepreg for compression modulus and friction testing for friction coefficients between prepregs under different temperatures and relative speeds. The test data were calibrated and used in a non-orthogonal model for the preforming analysis.

Single-dome tests (Figure IV.6-6) were performed to validate the non-orthogonal model for preforming. A comparison of test results and predictions showed that the model accurately predicts fiber reorientation and wrinkling.

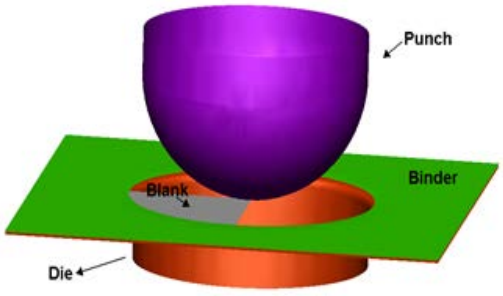

Figure IV.6-6. Single-dome preforming validation tests.

Two binders were used during preforming model validation: cardboard binder and steel binder. The preforming products with the two binders are very different. The ones formed with the cardboard binders have no wrinkle and the shear deformation is larger when compared to the one formed by the steel binders (Figure IV.6-7). Because the material is strongly dependent on temperature, the difference in deformation mode is related to the difference of heat conductivity between cardboard and steel. Performance of a single dome was simulated with different shear modulus curves: one for cardboard binder corresponding to a higher temperature and the other for steel binder with a lower temperature. The temperatures of the cardboard and steel binders were measured during tests using infrared cameras. Simulation results (Figure IV.6-8) show that the model predicts test results, especially deformation (i.e., fiber orientation) and the wrinkling, correctly.

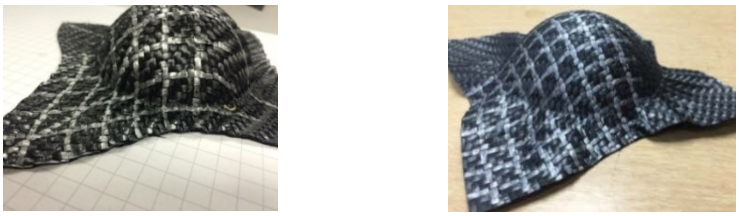

(a) (b)

Figure IV.6-7. Single-dome formed parts with (a) cardboard binder and (b) steel binder.

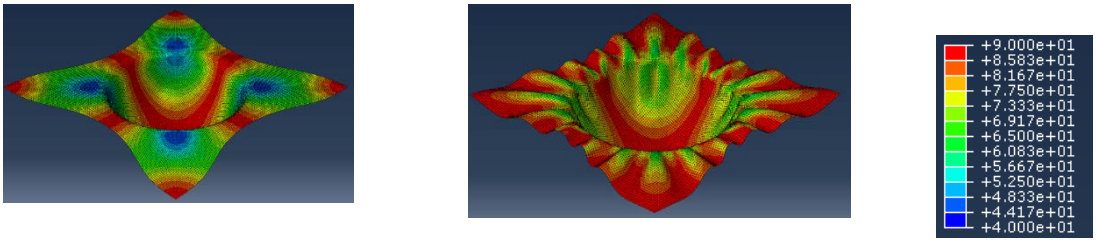

(a) (b)

Figure IV.6-8. Single-dome simulations (a) for cardboard binder and (b) for steel binder.

The preforming tools will be further validated using more complicated double-dome simulations during FY 2017.

A user material subroutine of the model has been programmed and used in the LS-DYNA analysis. The model will be implemented in LS-DYNA as a built material model once fully validated.

Task 2.2.2. Curing Models for Compression Molding

The implemented curing model MAT278 will be further validated during FY 2017.

Task 2.2.3. Compression Molding Modeling for Chopped Fiber Composites

Two sets of molding trials have been completed for the SMC material provided by Dow Chemical. In the first molding trial, 12 SMC plaques were molded under different processing conditions. The initial charges were cut and preheated in an oven to 60°C and then placed in the center of the molding tool, which has planar dimensions of 12 × 18 in. The compression molding on the charges was performed at 150°C for 3 minutes using different press speeds and force profiles. Pressure and displacement sensors were plugged into the mold to provide testing data that were later used for comparison with predictions in Moldflow simulations.

The second molding trial was later performed to provide additional sample plaques and molding data for Moldflow validation. A total number of 89 plaques molded with six different processing conditions were obtained from the molding trial to provide tensile and microstructure characterization samples. Also obtained from the second molding trial were the unfilled plaques to compare with filling pattern evolution predicted by Moldflow. The metal shims with designed thickness were inserted into the machine to stop the tool at certain locations. The initial charge thus stopped flowing and kept the shape at the moment when the moving mold met with the metal shims. These short-filling patterns would be compared with pattern prediction at the corresponding filling time in Moldflow.

A set of the tensile tests on bar samples cut from the molded plaques from the first trial were performed to compare with the predicted Young's modulus using the fiber orientation results from Moldflow. The cut design for the tensile test bars are shown in Figure IV.6-9a. On the sample locations marked on the plaque, the samples along 0, 45, and 90-degree directions were cut from three plaques that were all molded with the same force profile, with the peak force equal to 1,500 kN. As shown in Figure IV.6-9b, differences between

experiments and predictions are observed. Work to improve the orientation models and the prediction of directional Young's modulus is still ongoing.

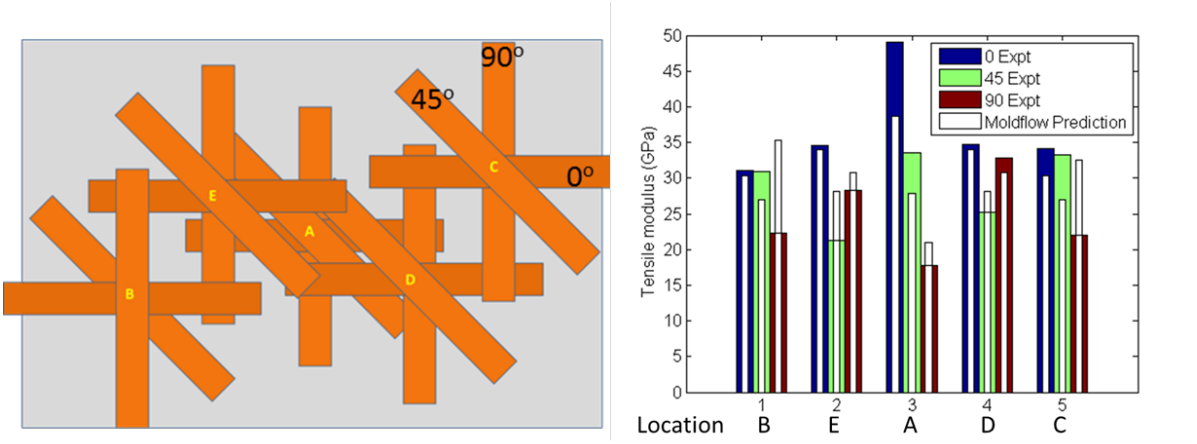

(a) (b)

Figure IV.6-9. Predicted and measured Young's modulus of molded SMC plaque: (a) sample locations, and (b) Young's modulus at 0, 45, and 90 degrees.

Viscosity was of critical importance in the Moldflow simulation. Two sets of measured viscosity, one by Dow Chemical and another by Autodesk, were used in the simulation. Neither of them produced satisfactory results. Realizing current viscosity characterization procedures may not be suitable for CFRP SMC because of chip size, a set of viscosity was inverse modeled using molding results. Two sets of the processing conditions with different maximum press forces were used for this purpose. With the reverse modeled viscosity parameters, the Moldflow prediction showed filling patterns that matched experimental observations. Also, the press force predictions matched the experimental data.

Task 2.3. Multi-Scale Models for CF Composites

Figure IV.6-10 illustrates the multi-scale approach adopted to derive macroscopic mechanistic continuum models for the different carbon fiber reinforced composites of interest to this project: UD fibers, woven fabrics, and chopped fiber composites. The goal was to find a macroscopic constitutive law with minimum experimental inputs by using a bottom-up hierarchical multi-scale approach.

RVE for UD CFRP was completed during FY 2015. RVE for woven CFRP and chopped fiber SMC were completed during FY 2016. The three models were further improved and used to study various aspects of material properties.

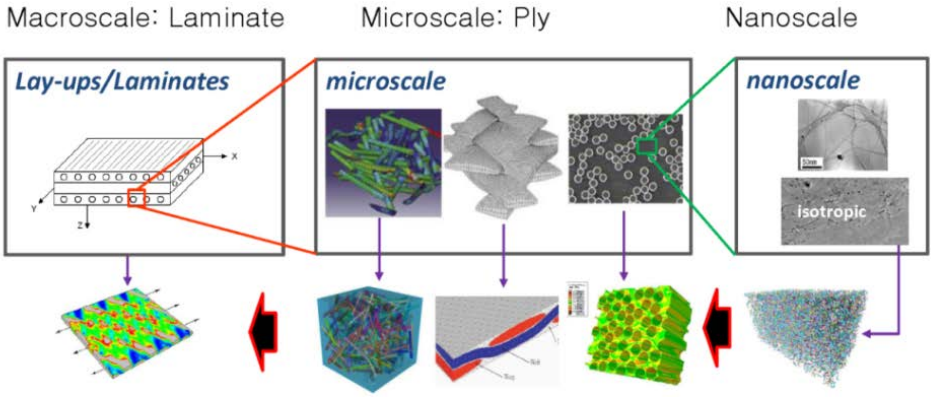

Figure IV.6-10. A multi-scale approach toward mechanistic continuum models for CF composites.

Task 2.3.1. Micro-Scale Model (Continuous Fiber)

Previously, the RVE fibers for UD laminates were assumed to be perfectly straight and parallel to one another, as well as aligned with the boundaries of the RVE. However, fibers are not straight in real material and this waviness of fiber has a great impact on both material modulus and failure behavior. It is also one of the root causes of material uncertainty. Efforts are continuing to quantify the impact of waviness on material properties.

The effects of waviness and variations of volume fraction have also been studied using woven RVE modeling. As can be seen in Figure IV.6-11, the waviness was controlled by changing the thickness of the RVE, where the tow width was fixed at 2.5 mm. Table IV.6-3 lists the moduli with respect to different thicknesses. It is obvious that moduli E11, E22, and G12 were decreased when the thickness was enlarged (i.e., equivalent to enlarging the waviness), while G12 was changed in an opposite trend.

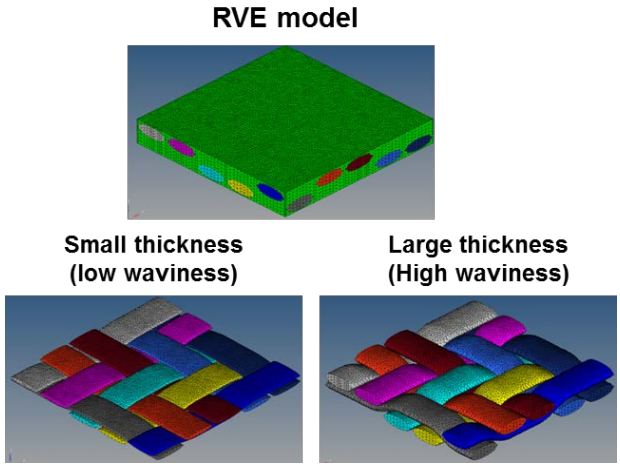

Figure IV.6-11. Woven RVE for different thicknesses.

Table IV.6-3. Material Moduli for Different Tow Thicknesses

Case #	0	1	2	3
Tow width/mm	2.5	2.5	2.5	2.5
Thickness/mm	1.65	0.814	0.6875	0.55
VF in tow/%	77.36	75.60	78.05	77.87
E11/MPa	5.58E+04	6.55E+04	6.64E+04	6.69E+04
E22/MPa	5.58E+04	6.55E+04	6.64E+04	6.71E+04
G12/MPa	4.55E+03	4.88E+03	5.07E+03	5.12E+03
G13/MPa	3.45E+03	3.17E+03	3.13E+03	3.05E+03
v12/MPa	5.35E-02	4.01E-02	4.09E-02	4.18E-02
v13/MPa	6.27E-01	5.82E-01	5.74E-01	5.67E-01

On the other hand, the volume fraction effect of the woven fabric structure is shown in Figure IV.6-12. The volume fraction varies from 30% to 60% with fixed waviness. As can be seen from Figure IV.6-12, a 10% change of volume fraction results in around a 20% change of E11 and E22, while for G12, the change is up to 30%. This means volume fraction variation is a very important factor for material properties.

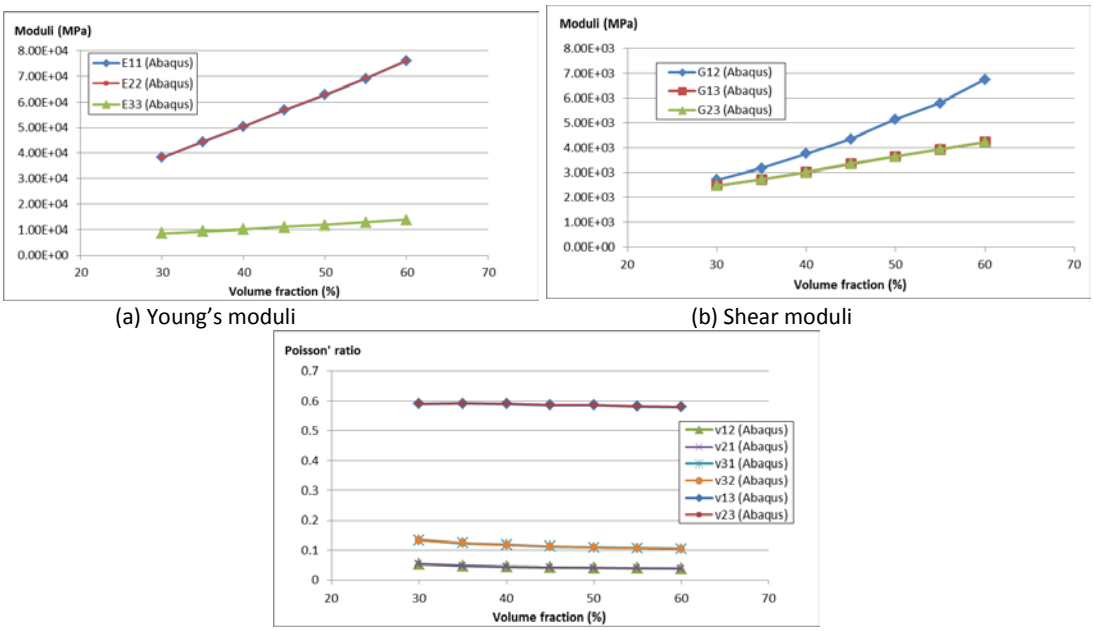

(a) Young's moduli (b) Shear moduli

(c) Poisson's ratios

Figure IV.6-12. Material constants of woven RVE for various volume fractions.

The studies of waviness and volume fraction effects will be continued during FY 2017 and used for optimized material design.

Task 2.3.2. Micro-Scale Model (Chopped Fiber SMC)

The foundation of chopped fiber RVE is the stochastic microstructure reconstruction algorithm. On the surface plane of the SMC plaque, the microstructure can be partitioned into cells (Figure IV.6-13a). Within a cell, all fibers are aligned in the same direction. In the through-thickness direction, clear-layered structural features can be seen (Figure IV.6-13b).

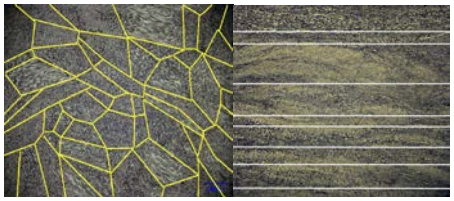

(a) (b)

Figure IV.6-13. (a) Partitioning of SMC in plane with cells, (b) layer-like structure in thickness.

Two methods have been developed to reconstruct the cell structure: the Voronoi diagram-based method and chip packing-based method. A Voronoi diagram involved partitioning a plane into convex polygons based on predefined points in the plane following two rules: (1) each polygon (called "cell") contains one point (also called "seed") and (2) every point in the polygon is closer to its corresponding seed than to any other. Each cell contained aligned, UD fibers. As a result of fiber alignment, a fiber orientation angle needed to be assigned to each cell. The aggregated orientation tensor of the RVE was approximated as the weighted mean of the orientation tensors of all cells (i.e., volume of cells were chosen as weights) in the RVE. The aggregated orientation tensor should agree with the target orientation tensor obtained from process simulation.

An optimization approach was developed using the simulated-annealing algorithm to align fiber orientations based on the given target. A typical result of this algorithm is shown in Figure IV.6-14a. Each cell contains a solid color to show the main diagonal of the orientation tensor of its fibers (Figure IV.6-14b).

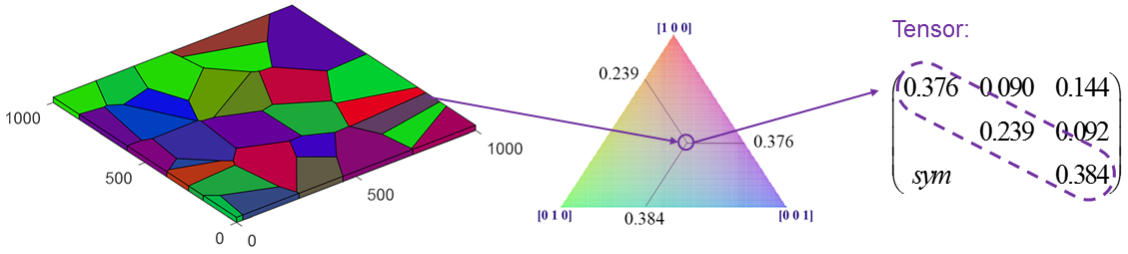

(a) (b)

Figure IV.6-14. (a) Visualization of fiber orientation alignment result, and (b) how solid colors are associated with orientation tensors.

A Voronoi diagram approach required microstructure images and was incapable of modeling certain microstructures (e.g. bent fibers), which has restricted the use of this approach. A new chip packing-based approach was recently developed. Development of this new approach was motivated by SMC's chip-type structure, which was observed in the three-dimensional microstructure feature study by auto polishing and microscopic imaging. This algorithm took information from the manufacturing process (such as chip size, orientation tensor, and volume fraction parameters) as inputs and generated the mathematical representation of the multi-layer plates packed with chips (i.e., coordinates of chips) as outputs. The reconstructed RVE satisfied the modeling requirements: (1) RVE's orientation tensor matched the fiber orientation output from the processing simulation, (2) a high-volume fraction (i.e., about 80%) of chips could be achieved, (3) the interaction between chips (i.e., bending) could be modeled, and (4) the results were finite element analysis compatible.

The RVEs of chopped fiber SMC have been developed to calculate local elastic modulus of SMC based on the two microstructure reconstructions discussed above. The predicted modulus is in the range of the measured data. Because the modulus is fiber-orientation dependent, the RVE model will be further validated, along with Moldflow predictions of fiber orientations.

Task 2.4. Fracture Models and Energy Absorption Models

RVEs have been used to provide material properties for crash analysis. The automatic modeling of the UD composite RVE has been built through a package program, including Matlab and ABAQUS. The RVE results of the linear elastic moduli were compared with the experiments and estimation from the rule of mixtures for the composite with 51.4% volume fraction of fiber as shown in Table IV.6-4.

Table IV.6-4. Material Moduli Predicted by RVE and Comparison With Measurements

	E11	E22	E33	G12	G13	G23
Rule of Mixtures	127.792	8.264	8.264	3.782	3.782	2.567
Experiment (Gpa)	125.255	8.894	**8.894**	4.846	**4.846**	
Calculated (Gpa)	125.906	8.615	8.556	4.867	4.584	2.735
Difference (%)	0.52%	3.14%	3.80%	0.43%	5.41%	
	v12	**v21**	**v13**	**v31**	**v23**	**v32**
Rule of Mixtures	0.3274	0.0212	0.3274	0.0212	0.6094	0.6094
Experiment	0.3267	0.0232	**0.3267**	**0.0232**		
Calculated	0.3214	0.022	0.3227	0.0219	0.6056	0.6015
Difference (%)	1.62%	5.17%	1.22%	5.60%		

*Note: **Bold** numbers are from the assumption of transverse isotropy.

As can be seen in Table IV.6-4, the results from RVE analyses were very close to the ones from experiments, where the maximum difference was around 5.60% from the Poisson ratio v_{31}.

While crash tests of the section of the current project's Dow Chemical material have been planned to improve and validate crash material models, test data are not yet available. Efforts have also focused on analysis of test data from another U.S. Department of Energy validation of materials and models project.

Task 2.5. Fatigue and Durability Models

Fatigue tests were started for different R-ratios with the objective of completing the constant life diagrams for different orientations: longitudinal (0 degrees), transverse (90 degrees), and 10 degrees off-axis. Tests at R=0.1 are mostly completed and Figure IV.6-15 shows the results in the longitudinal direction.

The "critical R-ratio" for CFRP materials was defined as the compressive strength divided by the ultimate tensile strength. For the UD material provided by Dow Chemical, the critical R-ratio was estimated as follows:

$$R_{crit} = \frac{-1100}{1800} \cong -0.6$$

Therefore, fatigue tests were attempted to be performed with R = -0.6 and the preliminary results are reported in Figure IV.6-15. The scatter in the fatigue life at R = -0.6 was very large because the material does not fail consistently within the gauge length. The reason for this issue is currently being investigated, but it seems to be related to the failure of the adhesive material that bonds the tabs to the CFRP material. Alternative tabbing and gripping methods are currently being evaluated to try to overcome this problem, which includes use of a different type of adhesive and optimization of the gripping pressure. Results will be presented in future reports.

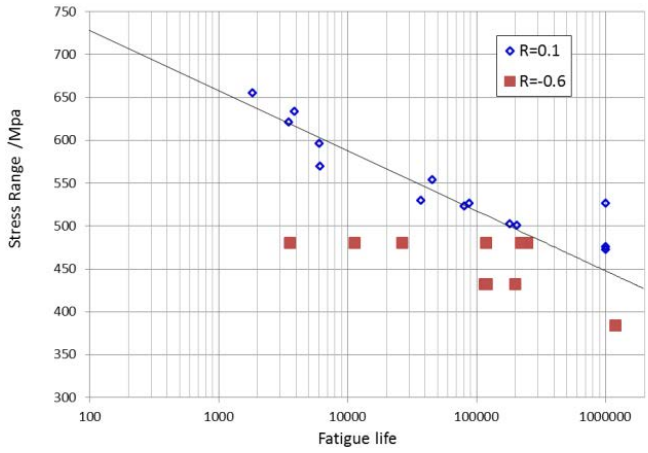

Figure IV.6-15. Fatigue S-N curve for the UD laminate in the longitudinal direction (7 Hz).

Task 2.6. Stochastic Multi-Scale Characterization

Process integration was conducted with the currently available subframe models to demonstrate the design process and potential of ICME. This integrated process was established in modeFRONTIER® and is schematically represented in Figure IV.6-16.

The inputs are the parameters that can be treated as design variables or the parameters that will be supplied by the material processing simulation results. During the current process, there are two sets of input parameters: (1) the thicknesses of each part (i.e., structural parameters and P-shell), which are the design variables, and (2) the material parameters (i.e., material selection for each part). During this case study, the layouts of the UD laminates are identified as material parameters. The outputs of the process are the structure stiffness and mass, which are obtained from the NASTRAN simulation of the vehicle subframe.

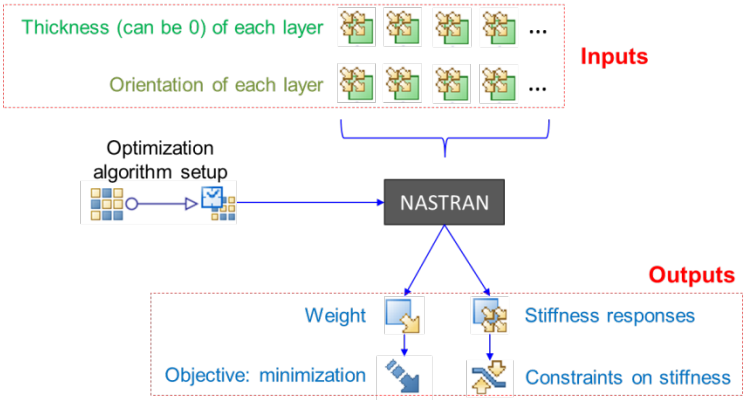

Figure IV.6-16. The integrated design process of subframe optimization: minimizing weights and maximizing stiffness.

Two types of design representation methods describing the laminate layout were developed for material optimization. Optimization results of two design representation methods are plotted in Figure IV.6-17. The optimization history of Type 1 design representation is shown on the left and the optimization history of Type 2 design representation is shown on the right. Ten thousand design evaluations were taken in the entire optimization history. The feasible designs were marked using gray squares. The best solution of both optimization jobs appear between 8,000 and 9,000 runs. For Type 1, the optimal design is 14.85 kg, which achieves a 43.6% weight reduction compared to the baseline design of steel; for Type 2, the optimal design is 15.84 kg, which achieves a 40.2% weight reduction compared to the baseline design of steel.

The next step is to further investigate the performance of the optimization methods and establish an optimization workflow that includes design variables of processing, RVE, structure, and responses from multi-disciplinary functions.

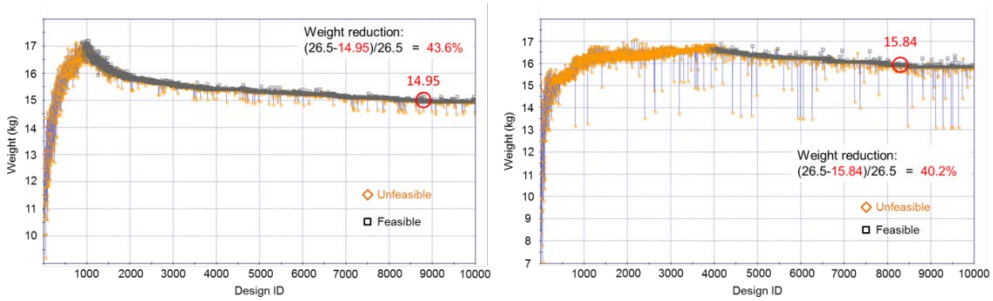

Figure IV.6-17. Optimization history of the two different design representation methods (left: Type 1; right: Type 2).

Technology Transfer Path

The project team includes primary software developers in every aspect of the ICME application chain. LSTC's LS-DYNA is a popular finite element analysis package for stress analysis and is especially dominating in vehicle safety analysis. Moldflow has the largest user group in polymer molding analysis. The same is true for HBM's nCode for fatigue and ESTECO's modeFRONTIER® for optimization. All models developed by the project are results of cooperation between the above-mentioned software developers, researchers in academia, and end users in original equipment manufacturers and suppliers. The models are being implemented in the respective software programs when developed and are available to the general public once validated.

As mentioned in the results and discussion section, the curing model developed during this project has already been implemented in LSTC LS-DYNA as MAT278. The non-orthogonal model for preforming analysis will be implemented during FY 2017.

The second path of technology transfer is through infrastructure and methods identified by NIST. All test data and material models are being stored at the NIST datacenter and will open to the public once the project has

been completed. The research results will also be published in respective technical journals and conference proceedings.

The third path of technical transfer is direct usage of the results at Ford and Dow Chemical.

Conclusion

FY 2016 was the second year of this project for developing ICME tools for CFRP composites and using ICME tools to design structural carbon fiber composite subframes to support immediate weight reductions in light-duty vehicles and reduce development-to-deployment lead time.

Great progress has been made during FY 2016, building on the success of FY 2015. A non-orthogonal model has been established for preforming analysis for woven fabric. The model has been validated and shown to accurately predict fiber orientation and wrinkling. Moldflow prediction of SMC compression molding has been improved by the viscosity profile tuned through inverse engineering; the predicted local material properties are compared with tensile testing results of samples cut from plaques. Multi-scale material models (e.g., RVE) are developed for UD, woven fabric laminates, and compression-molded SMC. These RVEs were validated to predict material stress-strain behavior based on composite architecture and microstructure, which are results of manufacturing simulations. MD analysis is also integrated into multi-scale models to predict relevant properties of pure resin and the interphase between resin and fibers. RVEs are used to study material property variations in the fundamental level (such as waviness of the fibers and local fiber volume fractions).

Material design information, manufacturing process simulation, and multi-scale models tools have been integrated into engineering structural CAE analyses by using modeFRONTIER®. In this way, local anisotropic material properties are predicted based on local material microstructures and engineers can optimize component design, material design, and manufacturing processes, and can optimize them simultaneously to achieve the most efficient usage of the material.

The developed ICME tools are and will be implemented in popular software packages such as LS-DYNA for stress and crash analysis, nCode for durability, Moldflow for molding, and modeFRONTIER® for process integration and optimization.

The project is on schedule and meets every milestone established at the start of the project. Building on the above-mentioned success, a majority of the ICME work is expected to be implemented during FY 2017, which is also the year that design of the subframe with target weight savings is to be initiated.

References

[1] Cao, P., X. Lin, and Park, H. S., 2014, “Strain-rate and temperature dependence of yield stress of amorphous solids via a self-learning metabasin escape algorithm,” Journal of the Mechanics and Physics of Solids 68: 239-250.

Bibliography

Bai, X., Bessa, M.A., Melro,A.R., Camanho, P.P., Guo, L., and Liu, W.K., 2016, “Corrigendum to High-fidelity micro-scale modeling of the thermo-visco-plastic behavior of carbon fiber polymer matrix composites,” Composite Structures.

Bessa, M. A., 2016, “Data-driven Multi-scale Analyses of Materials and Structures,” PhD thesis, Northwestern University.

Daniel, I. M., 2016, “Yield and Failure Criteria for Composite Materials under Static and Dynamic Loading,” invited review in Progress in Aerospace Sciences 81: 18-25.

Daniel, I. M., Fenner, J.S., and Werner, B.T., 2016, "Characterization and Modeling of Composite Sandwich Core Foam under Static and Dynamic Loading," presented at Conference on Experimental Mechanics, Orlando, Florida.

Daniel, I. M., Fenner, J.S., Werner, B.T., and Cho, J.M., 2016, "Characterization and Modeling of Polymeric Composite Sandwich Core Material under Multi-Axial Static and Dynamic Loading," Paper No. 335, XIII International Congress on Solid Mechanics, Orlando, Florida.

Fenner, J. S. and Daniel, I.M., 2017, "Mixed-Mode and Mode-II Fatigue Crack Growth in Woven Composites," in Fracture, Fatigue, Failure and Damage Evolution, Volume 8, Springer International Publishing: 63-73.

Li, Y., Chen, W. and Xu, H., 2016, "3D Representative Volume Element Reconstruction of Fiber Composites via Orientation Tensor and Substructure Features," 31st Annual Technical Conference, American Society for Composites.

Li, Y., Zhao, Q., Mirdamadi, M., Zeng, D. and Su, X., 2016, "Finite Element Simulation of Compression Molding of Woven Fabric Carbon Fiber/Epoxy Composites: Part I Material Model Development" SAE International Journal of Materials Manufacturing 9(3): 729-736, doi: 10.4271/2016-01-0498.

Liu, Z., Bessa, M.A. and Liu, W.K., "Self-consistent clustering analysis: an efficient multiscale scheme for inelastic heterogeneous materials," CMAME, accepted.

Meng, Z., Bessa, M.A., Xia, W., Liu, W.K. and Keten, S., "Predicting the Macroscopic Fracture Energy of Epoxy Resins from Atomistic Molecular Simulations." In submission.

Wang, Z., Cheng, P., Liu, W.K. and Chen, W., 2016, "Stochastic Multiscale Material Modeling of Unidirectional Carbon Fiber Reinforced Composites," Materials Research Society (MRS) Verification, Validation and Uncertainty Quantification Symposium, Phoenix, Arizona.

Zhang, W., Ren, H., Wang, Z., Liu, W.K., Chen, W., Zeng, D., Su, X. and Cao, J., 2016, "An Integrated Computational Materials Engineering Method for Woven Carbon Fiber Composites Preforming Process," ESAFORM 2016.

Zhang, W., Ren, H., Lu, J., Zhang, Z., Su, L., Wang, Q.J., Zeng, D., Su, X. and Cao, J., 2016, "Experimental methods to characterize the woven composite prepreg behavior during the preforming process," 31st Annual Technical Conference, American Society for Composites.

IV.7 Development and Integration of Predictive Models for Manufacturing and Structural Performance of Carbon Fiber Composites in Automotive Applications – General Motors, LLC

Project Details

Venkateshwar Aitharaju, Principal Investigator
Chemical Sciences and Material Systems Laboratory
General Motors R&D Center
MC 480-106-710
30500 Mound Road
Warren, MI 48090
Phone: 248-343-9500
E-mail: venkat.aitharaju@gm.com

Walter Parker, Project Manager
National Energy Technology Laboratory
PO Box 880
3610 Collins Ferry Road
Morgantown WV 26507-0880
Phone: 412-386-7357
E-mail: walter.parker@netl.doe.gov

Carol Schutte, Technology Area Development Manager
U.S. Department of Energy
1000 Independence Ave., SW
Washington, DC 20585
Phone: 202-586-1022
E-mail: carol.schutte@ee.doe.gov

Contractor: General Motors, LLC
Contract No.: DE-EE0006826

Executive Summary

The goal of this project is to develop an integrated suite of state-of-the-art computational modeling tools that are critically needed to enable structural carbon fiber (CF) applications in automobiles. These tools help to predict the manufacturing and structural performance of CF composites, including stochastic effects. The project team comprised of researchers from General Motors (GM), Engineered Solutions, Inc. (ESI) Group (i.e., software company owner of composite manufacturing tools PAM-RTM for resin transfer molding and PAM-FORM for forming of composites), Altair (i.e., software company owner of the multi-scale structural performance predictive tool for composites), Continental Structural Plastics (CSP; i.e., molder/material supplier for composite materials and GM-Corvette composite parts supplier), and the University of Southern California (i.e., leader in uncertainty quantification of the DOE-funded Scientific Discovery through Advanced Computing Institute for Uncertainty Quantification). During the first phase of the project, both the manufacturing and structural performance tools, including a stochastic driver, will be calibrated and validated against coupon and component level tests. The difference between the predictions and experimental results is to be limited to less than 15%. During the second phase of the project, the manufacturing and performance tools will be integrated by mapping the manufacturing outcome (e.g., fiber angles, residual stresses, degree of cure, and defects [voids, dry patches, and wrinkles]) into structural models. Further, these integrated manufacturing and structural performance tools will be used to design a composite CF automotive assembly for a high-volume, medium-duty automobile currently made of steel.

Various CF formats friendly to high-volume automotive manufacturing (e.g., non-crimp, woven, and chopped systems) and manufacturing processes (e.g., such as resin transfer molding [RTM] and compression molding) will be studied. Cost models will be developed in parallel for these high-volume manufacturing processes. The total number of parts in the CF assembly will be reduced through part consolidation and weight will be reduced through strategic thickness optimization at critical and noncritical locations for each of the components. Each of the CF composite components in the assembly will be optimized for weight, cost, and performance. The optimized CF automotive assembly will be certified and the developed numerical models will be validated by comparing the numerical and experimental results for performance of the assembly. Finally, for the optimized CF assembly design, the weight, cost, and performance will be compared with the existing steel design. Availability of integrated computational tools to predict stochastic manufacturing and structural performance of structural composites to an original equipment manufacturer (like GM) can potentially eliminate significant bottlenecks that currently exist with large-scale implementation of CF composites in an automobile.

Accomplishments

- Completed benchmark testing of a reference assembly in the 2016 GM-Malibu to derive the performance requirements of the future CF assembly.
- Selected and ranked manufacturing processes suitable for high-volume automotive manufacturing for each of the components in the assembly.
- Developed preliminary design ideas for the CF assembly that were considered unique advantages of composite manufacturability.
- Selected 17 different material systems suitable for high-volume automotive manufacturing and completed the material characterization required for ranking them.
- Generated experimental data for RTM of flat plaques using an instrumented tool and the GM Research and Development RTM machine at a constant injection pressure for panels with defects.
- Designed and fabricated an experimental setup to demonstrate compression RTM (C-RTM).
- Conducted C-RTM experiments for the truncated pyramid mold and created an experimental database for correlating with the simulations.
- Measured fabric mechanical properties for two classes of woven fabrics (i.e., twill and satin) to provide data for simulations.
- Conducted draping experiments for twill and satin weaves using a GM-draping tool to collect the angle change data after draping.
- Conducted draping simulations for (0/90) twill and satin weaves; excellent correlations were observed.
- Developed a framework for stochastic manufacturing simulation and conducted stochastic simulations to predict the fill time and cure for the resin transfer molding process. A total of 18 parameters were considered for stochastic simulations.
- Determined the multi-scale structural performance tool predicts excellent correlation results for twill non-crimped fabric (NCF) CF composites for 0-degree tension, 0-degree flex, and 90-degree flex experiments.
- Developed a hybrid elastic plastic material model for resin to accurately capture damage progression in the resin for axial and shear loading. This capability will help predict the energy absorption capability of off-axis plies.
- Developed a parametric unit cell for non-orthogonal weave and implemented it in the HYPERMESH framework.

- Generated preliminary results for the stiffness and strength of sheared fabrics, which require experimental results for correlation.
- Developed the capability to account for thermal strain in the structural performance model.
- Developed a stochastic framework for conducting stochastic performance simulations by upscaling the physics across the scales (i.e., fiber scale, tow scale, meso-scale, and macro-scale). Using this framework, the stochastic elastic properties of NCF laminates were estimated.

Future Directions

- Complete the C-RTM experiments planned at the component level to generate the required data to validate the stochastic process simulation tools.
- Validate the draping simulation for 45-degree twill and satin fabrics.
- Develop a computationally efficient delamination model for multi-layer composites. The development is expected to reduce the computational expense of the current state of modeling through cohesive zone modeling.
- Complete validation of structural performance predictions for NCF and woven composites with crush data.
- Develop mapping technology to map out the manufacturing outcome (e.g., residual stresses) and fiber angle changes in structural performance models.
- Finalize the design of automotive assembly manufacturing that is friendly to high-volume automotive manufacturing.

Technology Assessment

- Target: Develop an integrated stochastic manufacturing and structural performance computation tool to design structural automotive composites and predict performance within 15% of experimental results.
- Gap: Unknown manufacturing effects on structural performance of automotive composites.
- Gap: Commercial software package capability to predict combined manufacturing and structural performance, including stochastic effects.
- Gap: Manufacturing process optimized to yield lower costs and higher quality for automotive composites.
- Gap: Certification procedure for an automotive composite assembly based on computer modeling alone.

Introduction

GM was the first North American automotive original equipment manufacturer to develop and commercialize CF composites for Class-A body panel (i.e., closure) applications. Going forward, our objective is to look beyond closure components and implement CF composites in body structural panels that undergo the complex loading conditions represented in crash and durability. To enable these broader automotive structural applications of CF composites, three key issues must be addressed. First, significant variability in material properties incurred during the manufacturing process need to be understood and predicted. Second, prediction of the structural performance of composites undergoing complex loading (i.e., crash) and environmental conditions is required. Third, the effect of manufacturing on performance of the final components needs to be understood and predicted. Without a good handle on the above issues, automotive designs can be overly

conservative, thereby increasing cost significantly and limiting the weight reduction potential of CF composites. The present project addresses all above needs by developing a suite of integrated computational tools to predict manufacturing performance and structural performance of CF composites, including stochastic effects.

Approach

Four key components of probabilistic integrated computational materials engineering will be at the core of our approach, namely model integration, optimization, validation, and design certification. The computational engine will be constructed by integration of state-of-the-art tools and capabilities from specific domains, namely, composites manufacturing (from GM and CSP), process simulation software for composites (from ESI), integrated multi-scale/multi-physics structural software (using the multi-scale design system [MDS] of Altair), probabilistic methods and probabilistic software (from the University of Southern California), and, finally, the largest U.S. automaker with considerable expertise and a record of accomplishment in the design and manufacturing of composite cars (e.g., the Chevrolet Corvette [from GM]) leads the project and integrates these modules. By model validation, we refer to making a prediction of the variables of interest and comparing the specific variables under the same conditions. By certification of a component we mean assurance that, once designed, manufactured, and loaded (i.e., crash tested), these components will perform satisfactorily up to preset specifications. Enabling model validation and component certification requires retooling of the deterministic scientific process, specifically by requiring evidential attributes to be attached to model-based predictions. During this project, we will identify the limitations of existing software components comprising the computational engine and offer alternative technologies and solutions that facilitate integration for design optimization. Once the computational engine has been developed and validated, the chosen CF assembly will be designed, optimized, tested, and certified and the resulting composite component will be compared to the current steel design.

The present CF integrated computational materials engineering project is organized into 10 tasks executed over a 48-month period. An outline of the tasks carried out during the current fiscal year is given as follows:

- Task 1.0: Project planning, coordination, and reporting – ongoing
- Task 2.0: Select the automotive assembly preliminary design – in progress
- Task 3.0: Identify preliminary CF material systems and manufacturing processes – completed
- Task 4.0: Develop and validate the manufacturing and crash simulation engines – in progress
- Task 5.0: Integrate the manufacturing and structural models – started
- Task 6.0: Design and optimize automotive assembly for manufacturing and performance – not started
- Task 7.0: Design and fabricate assembly and the test fixture – completed
- Task 8.0: Manufacture the automotive assembly – not started
- Task 9.0: Certify the automotive assembly – not started
- Task 10.0: Assessment of the assembly: correlations of predictions and experimental results – not started.

Results and Discussion

Task 1.0 Project Planning, Coordination, and Reporting

Project team members are leading industrial and academic researchers, computational modeling professionals, experimental specialists, and management teams from GM, CSP, ESI, Altair, and the University of Southern California. The tasks in the project were divided into three major subtasks: (1) manufacturing modeling, (2) structural performance modeling, and (3) stochastic modeling. Biweekly project meetings are held on these

subtasks to track progress of the project. GM coordinates technical and management tasks for the entire project. Table IV.7-1 provides the schedule and timing for the project.

The objective of this task is to determine the baseline performance requirements for the future design of an automotive assembly by simulating the side pole impact on the baseline vehicle. A light-duty, high-volume automobile (i.e., GM Malibu, model year 2016) was chosen as the baseline.

During FY 2016, a study of strain rate for the reference steel automotive assembly was conducted to understand the influence of strain rate on side impact. The value of maximum strain rate is very important because it will be used to guide the experiments (i.e., quasi-static and dynamic) in the project. The maximum strain rate was computed for side impact for the vehicle level and local level models developed in this project.

Table IV.7-1. Project schedule.

WBS ID #	Phase, Task, Subtask, and Milestone Descriptive Names	months	Q1	Q2	Q3	Q4	Q5	Q6	Q7	Q8	Q9	Q10	Q11	Q12	Q13	Q14	Q15	Q16
			Mar-15 Apr-15 May-15	Jun-15 Jul-15 Aug-15	Sep-15 Oct-15 Nov-15	Dec-15 Jan-16 Feb-16	Mar-16 Apr-16 May-16	Jun-16 Jul-16 Aug-16	Sep-16 Oct-16 Nov-16	Dec-16 Jan-17 Feb-17	Mar-17 Apr-17 May-17	Jun-17 Jul-17 Aug-17	Sep-17 Oct-17 Nov-17	Dec-17 Jan-18 Feb-18	Mar-18 Apr-18 May-18	Jun-18 Jul-18 Aug-18	Sep-18 Oct-18 Nov-18	Dec-18 Jan-19 Feb-19
- Task 1.0	Project Planning, Coordination, and Reporting	48	PROJECT MANAGEMENT - GM / CSP - ESI - MDS - USC															
* Milestone 1.1 *	Go/No-Go #1 Decision Point	1				X												
* Milestone 1.2 *	Go/No-Go #2 Decision Point	1							X									
* Milestone 1.3 *	Phase 1 Topical Report Completed	1							X									
* Milestone 1.4 *	Go/No-Go #3 Decision Point	1										X						
* Milestone 1.5 *	FEP Models Delivered to DOE	1																X
* Milestone 1.6 *	Phase 2 Topical Report Completed	1																X
Phase 1	**Model Development and Model-Level Validations**	21	PHASE 1 - MODEL DEV+VAL															
- Task 2.0	Select the Automotive Assembly Preliminary Design	9	GM															
* Milestone 2.1 *	Performance Requirements (loads, energy absorption) Determined	1			X													
- Task 3.0	Identify Preliminary CF Material Systems & Manufacturing Process	9	GM / CSP - ESI															
* Milestone 3.1 *	Appropriate Materials Selected (2-3 material systems)	1			X													
* Milestone 3.2 *	Appropriate Manufacturing Processes Selected	1			X													
- Task 4.0	Develop and Validate the Manufacturing and Crash Simulation Engines	21	GM / ESI - MDS - USC															
- - Subtask 4.1	Develop Stochastic Process Simulation Engine	21	USC / MDS															
- - Subtask 4.2	Develop & Validate Manufacturing Process & Link Simulation Models	21	ESI / MDS - USC - CSP - GM															
* Milestone 4.2.1 *	Manufacturing of Small Plaques Completed and Data Generated	1				X												
* Milestone 4.2.2 *	Development of Manufacturing Process & Linking of Models Completed	1							X									
- - Subtask 4.3	Develop & Validate Stochastic Performance Model	18		MDS / USC														
* Milestone 4.3.1 *	Development of Mechanical Tests for Model Development Completed	1				X												
* Milestone 4.3.2 *	Stochastic Performance Model Developed & Compared with Experiments	1							X									
Phase 2	**Integration and Design**	30							PHASE 2 - INTEGRATION+DESIGN									
- Task 5.0	Integrate the Manufacturing and Structural Models	6							ESI / MDS - USC									
* Milestone 5.1 *	Mapping of Manufactured Properties to Structural Models Achieved	1								X								
- Task 6.0	Design & Optimize Automotive Assembly for Manufacturing & Performance	12							GM / MDS - ESI - USC - CSP									
* Milestone 6.1 *	Design and Optimization for Manufacturing and Performance Completed	1										X						
- Task 7.0	Design and Fabricate the Assembly and Test Fixture	6											CSP / GM					
* Milestone 7.1 *	Assembly and Test Fixture Designs Completed	1											X					
- Task 8.0	Manufacture Automotive Assembly	12										CSP / GM						
- - Subtask 8.1	Design and Build Tools	6										CSP						
- - Subtask 8.2	Fabricate the Components	6											CSP					
- - Subtask 8.3	Assemble the Components	6												CSP				
* Milestone 8.3.1 *	Build of Ten Assemblies for Testing Completed	1													X			
- Task 9.0	Certify Automotive Assembly	6											GM / MDS - CSP - ESI - USC					
- - Subtask 9.1	Certify Manufacturing Process	6											GM / MDS - CSP - ESI - USC					
* Milestone 9.1.1 *	Certification of Manufacturing Process Completed	1															X	
- - Subtask 9.2	Certify Automotive Assembly and Components	6											GM / MDS - CSP - ESI - USC					
* Milestone 9.2.1 *	Certification & Validation of Components and Assembly Completed	1															X	
- Task 10.0	Assessment	9												GM / MDS - ESI - USC				
* Milestone 10.1 *	Final Cost & Performance Comparison of Composite & Steel Completed	1																X

Task 2.0 Select the Automotive Assembly Preliminary Design

Strain Rate Study for the Vehicle Level Model

Strain rate was evaluated for a few critical elements of the automotive assembly in the vehicle level model. Effective plastic strain values at mid-plane of the critical shell elements were written out with a time frequency of 0.05 milliseconds (msec). Further, the strain output was post-processed using a differentiation function to evaluate strain rate. Figure IV.7-1 shows the plot of the strain rate for those chosen critical elements with time. In all of the plots for strain rate, the units for the x-axis is msec and the unit for the y-axis is $msec^{-1}$.

Table IV.7-1 shows that strain rate values for most of the elements are below 40/sec, except for two elements. Those two elements show a huge jump around a time equal to 25 msec and a detailed study showed they can be waived. During FY 2016, seven reference steel assemblies were procured and impact-tested to determine

baseline performance requirements. These baseline data will help to design the future CF assembly. More details of this task were provided in the protected document submitted to DOE.

Task 3.0 Identify Preliminary CF Material Systems and Manufacturing Processes

The objective of this task is to select appropriate materials and manufacturing processes for high-volume automotive manufacturing. GM and CSP, based on their experience and following state-of-the-art in composite manufacturing technologies, broadly selected RTM and compression molding as the preferred choices for high-volume manufacturing methods for the chosen CF assembly.

Corresponding to the manufacturing processes chosen above, GM appropriately selected 17 candidates for CF material systems and completed material characterization. Based on material characterization, these material systems were ranked (protected data) based on strength, stiffness, and cost for each of the components in the future CF assembly.

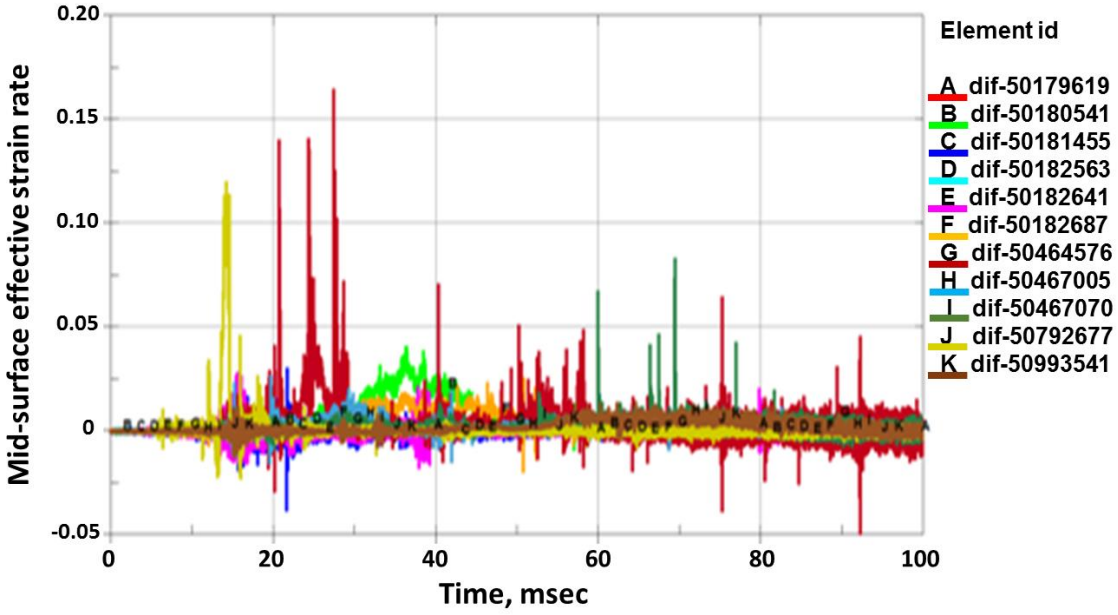

Figure IV.7-1. Strain rate of critical elements of the assembly (global model) – time step = 0.005

Task 4.0. Develop and Validate the Manufacturing and Crash Simulation Engines

The objective of this task is to develop and validate stochastic manufacturing and structural performance models.

Subtask 4.1 involves development of a stochastic driver and Subtask 4.2 involves development of a manufacturing process performance model.

A framework for development of tools for an integrated stochastic manufacturing and structural performance engine was developed and is shown in Figure IV.7-2.

Subtask 4.1. Develop the Stochastic Process Simulation Engine

Credible uncertainty quantification for the lightweight composite vehicle project requires a comprehensive exploration of the parameter space in order to identify critical parameter combinations, understand the mechanistic justification for their fluctuations, and mitigate the associated risks through proper geometry and process optimization. Generally, the greater the uncertainty in the design objective function, the more iterations

are required in the corresponding optimization algorithm. This uncertainty can be reduced for the present problem by taking advantage of multi-scale modeling capabilities while honoring experimental data obtained from several spatial scales. This clearly involves a prohibitive computational and analysis burden that is alleviated along two fronts: first, the feasible domain of the parameter space is constrained by first principles (e.g., elastic moduli are bounded) and by observed experimental data that add statistical dependence constraints (e.g., elastic moduli or axes of tows are statistically dependent). These experimental data induce a generally non-uniform probability measure on the feasible set, thus permitting a further reduction by ranking the parameter space according to this measure. This reduction directly impacts the computational cost by reducing the volume of parameter space. This involves a close interplay between experiments, physics, mechanics, and computational science. Second, computational algorithms are developed to efficiently explore the reduced parameter set, taking into account the non-standard shape of the set (e.g., non-cubic and non-spherical) and the empirical form of the probability over it (e.g., non-uniform and non-Gaussian). These algorithms involve a tight integration between the various analysis codes used for analysis and design optimization. In preparation for a full-scale simulation task to be conducted during FY 2017, it is imperative that as much efficiency be built into the stochastic drivers as possible. With that perspective in mind, we are pursuing efforts along both fronts described above.

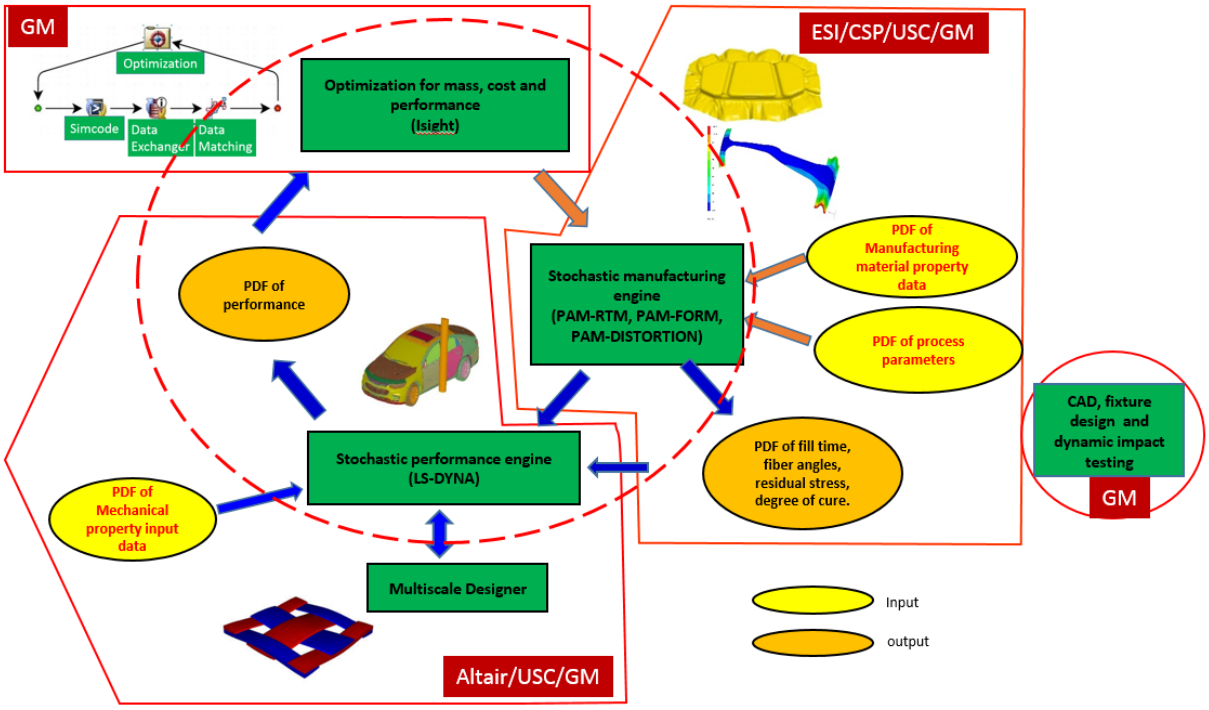

Figure IV.7-2. Framework of integrated tool development

Efforts along both directions have been initiated with specific attention to manufacturing process characterization and structural performance assessment. First, we developed stochastic representations of quantities of interest in terms of irreducible uncertainties. Second, we updated procedures that permit us to update both the models of the irreducible uncertainties and those of the quantities of interest as observations are made. As part of our machinery, we will also be able to ascertain the worth of additional information (data and simulation) on the certification of intermediate quantities of interest or on the final design. We coupled the stochastic representations across scales and across physics with a cross-scale parameterization using a cross-scale polynomial chaos construction. This involves both propagating the stochastic representations from PAM-RTM to PAM-DISTORTION and across scales in Multi-Scale Designer and LS-DYNA. During the next phase, we will couple the PAM-suite with Multi-Scale Designer/LS-DYNA. In the next two subsections, we discuss the manufacturing process, the effect of permeability, upscaling coefficients of thermal expansion, and the structural performance assessment.

Stochastic Modeling of Manufacturing Process

Irreducible uncertainties for the manufacturing process consist of the permeability of fabric, permeability in racetracking and injection channels, volume fraction in laminate, and coefficients of thermal expansion. Current quantities of interest for the manufacturing process include resin fill/cure times and localized residual stresses following curing and distortion processes. During the next phase, the most critical quantities of interest will be failure criteria appearing in the design optimization objective function.

A first comprehensive stochastic model was developed by introducing uncertainty in the following parameters: two principal permeabilities of the fabric and racetracking channel, density, specific heat and thermal conductivity of resin, density, specific heat and two principal thermal conductivities of fabric, specific heat and thermal conductivity of the laminate, thickness of the layers, porosity, density, injection channel, thermal conductivity and specific heat. Statistical constraints on permeability were obtained by propagating constraints on volume fraction available from experimental observations. High-order polynomial approximations in these variables are achieved using basis adaptation with respect to fill time. This has permitted the accurate evaluation of the polynomial chaos expansion (PCE) of fill time using a high-order, one-dimensional polynomial expansion.

Given that observations of temperature and pressure are available at sensors within the injection mold, a fill time representation was sought in terms of these observables that were treated as random variables. The observed temperature was treated as a random boundary condition and parameterized by eight random variables representing temperature at the observed locations. A PCE of the RTM process was then conducted in 13D parameter space, which included, in addition to these boundary conditions, porosity, injection channel permeability, and three fabric permeabilities. The stochastic pressures at the sensor locations were computed and their values compared to the observed pressures. Figure IV.7-3 shows realizations of the predicted stochastic pressure profiles with the observed experimental profiles.

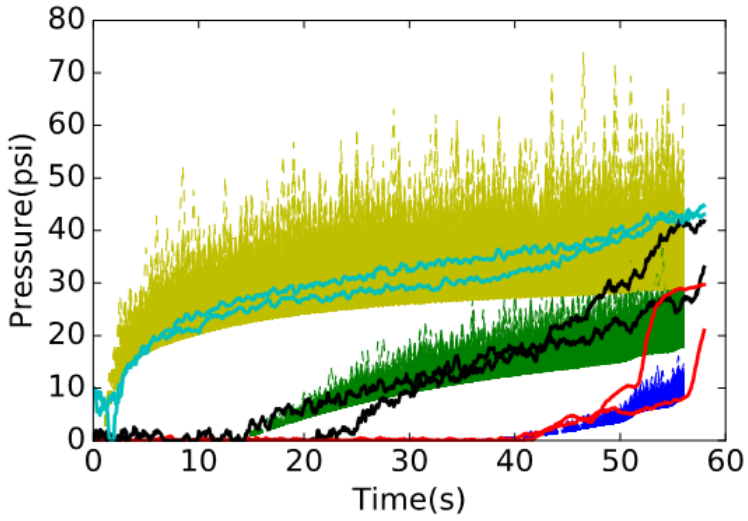

Figure IV.7-3. Pressure as function of time at three sensor locations; comparison of stochastic predictions with measurements

Figure IV.7-4 shows the predicted cure at three sensor locations at various stages during the manufacturing process. These results entail a coupling of uncertainty across PAM-RTM and PAM-CURE (i.e., the injection and curing software). Additional coupling with PAM-DISTORTION enables prediction of displacements associated with curing and ensuing residual stresses. This last step was performed while assuming the coefficients of thermal expansions of the fibers and resin to be random variables constant over the simulation domain.

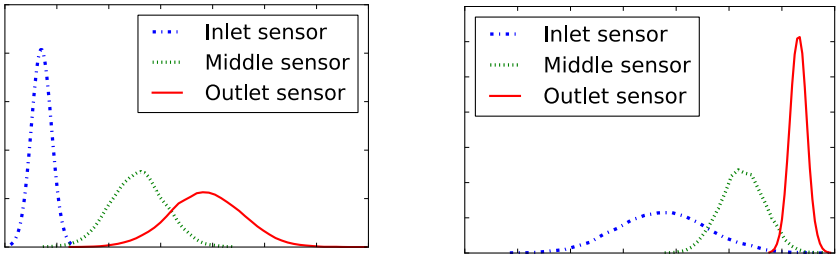

Figure IV.7-4. Probability distribution function (pdf) of cure at three sensor locations. Left figure shows results at 300 seconds after injection begins. Right figure shows results at 300 seconds after curing begins.

As seen in Figure IV.7-5, scatter in the coefficient of thermal expansion induces significant scatter in the displacement and stresses. We will be pursuing this effort to better reflect uncertainty in residual stresses to which the structure-scale simulator will be subjected.

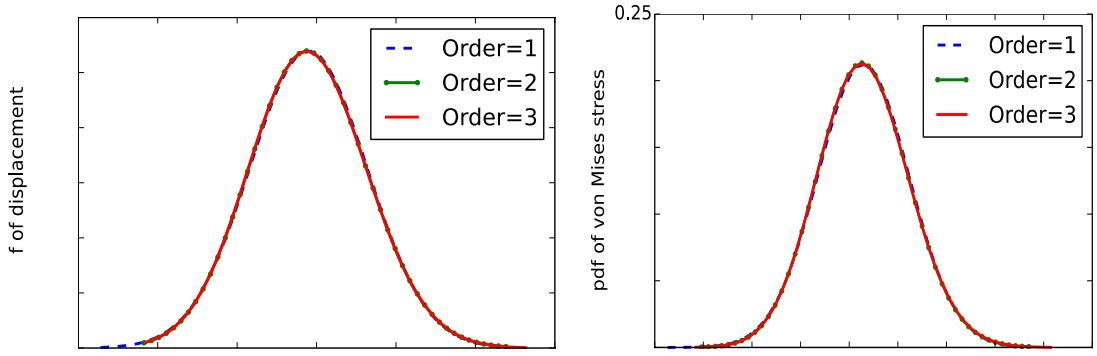

Figure IV.7-5. Probability density function of displacement norm and von Mises stress; only random input is coefficient of thermal expansion.

Effect of Permeability as a Stochastic Process

By allowing permeability to exhibit spatial fluctuations (i.e., modeling it as random processes instead of random variables), the probability distribution of the predicted fill time is significantly reduced while encompassing measured values. A comparison of these results between the random variable and the random process models is shown in Figure IV.7-6. The range of predicted values is reduced from 45 to 75 seconds to 54 to 58 seconds. This reduction has implications on the number of samples required for accurate stochastic computations. These will be much more significant in the full-scale model; it will make the difference between "prohibitively expensive" and "expensive but manageable."

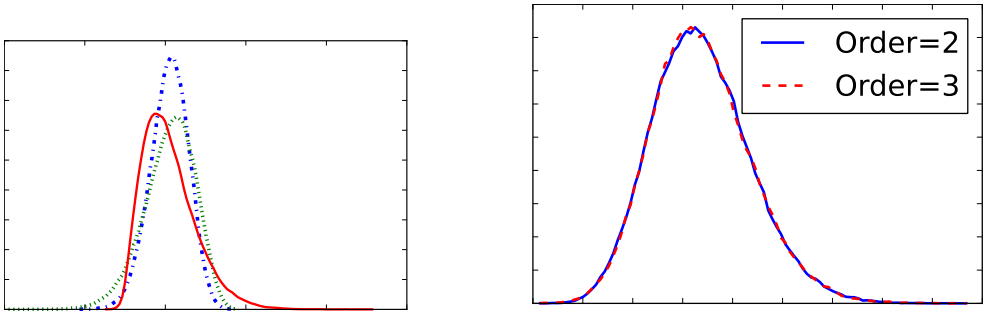

Figure IV.7-6. PDF of fill time. Left: random process model for permeability using one-dimensional, two-dimensional, and three-dimensional adaptations, all with polynomial order 3. Right: random variable model for permeability.

At the present stage, only the permeability tensor in the fabric is modeled as a random process and all other variables in the manufacturing process are described as random variables. During the next phase, the volume fraction of fiber in the laminate will also be extended to be a stochastic process, while permeability in the racetracking channels and the coefficients of thermal expansions will remain as random variables constant over the spatial domain. This choice is driven both by software considerations and by physical considerations concerning relative rates of flow in fabric and channels. However, adding the stochastic process capability significantly increased the stochastic dimension of the problem (number of uncertain parameters); specialized algorithms, using basis adaptation in PAM-RTM, were developed to tackle this challenge. This consists of implementation of a basis adaptation procedure for polynomial chaos representations. These adapted bases permit an accurate representation of the quantity of interest (in this case the fill time of the RTM process), using a much smaller stochastic dimension. Figure IV.7-6 shows results associated with one-dimensional, two-dimensional, and three-dimensional reductions. It is observed that the particular correlation length used for spatial fluctuations does not significantly affect the predict fill time, and the mere introduction of spatially varying permeability reduces the variance of the predicted fill time. However, varying the correlation length of the permeability field is observed to have some effect on the gradients of the curing degree. To better calibrate the spatial fluctuations of the permeability tensor and have better control over the predicted residual stresses and void formation, we are performing calibration of the correlation function of permeability and void ratio against experimental measurements of void formation in the presence of hard inclusions within the fiber domain. Experimental observations indicate significant fluctuation in the location of these voids even under nominally identical fabrics. These experimental data will be used to infer the spatial structure of permeability.

Upscaling Coefficients of Thermal Expansion

In addition to treating permeability as a stochastic process, we have also started developing the PCE representation of the coefficients of thermal expansion of the tows, laminae, and laminates in terms of the uncertainty at the finest scale (fiber volume fraction and elasticity parameters of fiber and resin). This will help us develop statistical dependence between the manufacturing parameters and the structural performance parameters. This is expected to significantly reduce uncertainty in the optimization objective function and have an impact on computational cost. Figure IV.7-7 shows the histograms obtained from PCE representations of the transverse and longitudinal thermal coefficients. We also compute the Sobol indices, identifying the mean effect sensitivities. This is ongoing work because we have still not converged to matching experimentally derived values of these coefficients.

The purpose of this work is to develop statistical dependence between the thermal properties and the elastic properties of the laminate, thus providing a more rational accounting for uncertainties feeding into the design optimization logic.

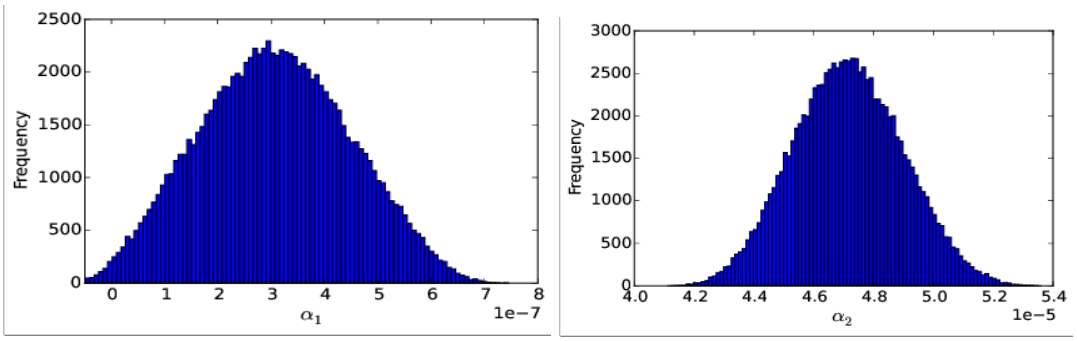

Figure IV.7-7. Histogram of the axial (left) and transverse (right) coefficient of thermal expansion and obtained from the samples of PCE of dimension = 11 and order = 3.

Stochastic Modeling of Structural Performance

This task has similar objectives to the previous task. One difference is that in the structural performance context, the stochastic representation is carried out across scales and not across physical models. The stochastic representations are thus done in stages, with observables and constraints specified at different scales. For example, observations on the volume fraction of a tow are used to construct a statistical dependence model for the geometric parameters of the fibers. We have developed the machinery to propagate polynomial chaos representations across three scales. We have also developed the capability to estimate a random matrix for the elasticity tensor model at any scale using either experimental data or simulations from a finer scale. This random matrix model will serve in development of model error estimates during calibration and model update.

With regards to structural performance modeling, we have dedicated a significant part of FY 2016 to investigate the extent to which modeling can shape the probability model at the smallest available scale, namely the fibers and the tows. Specifically, we developed models for statistical dependence between the dimensions of tows that are both consistent with available experimental data on tow geometry while not violating available data on volume faction within a tow. This effort is particularly important because, given our computational multi-scale framework, uncertainty at these smallest scales is an essential driver of the uncertainty at the structural scale. Figure IV.7-8 shows the geometry of a tow and its constituent fibers used during this analysis.

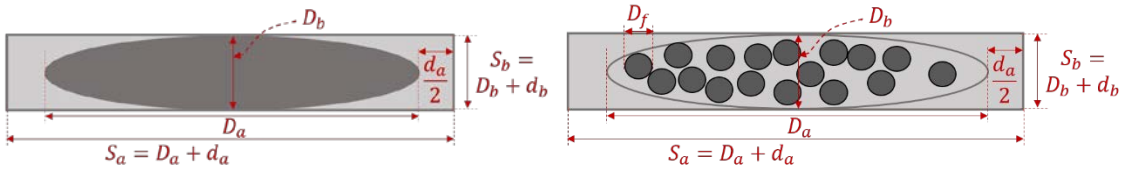

Figure IV.7-8. Geometry of tow and fibers used to constrain the probabilistic model.

Figure IV.7-9 shows experimental data for dimensions for the tow major diameter, $\mathbf{D_a}$, and the tow minor diameter, $\mathbf{D_b}$. These are currently being used to constrain the probability model of these dimensions and to propagate these constraints to the probability measure of structural performance indicators.

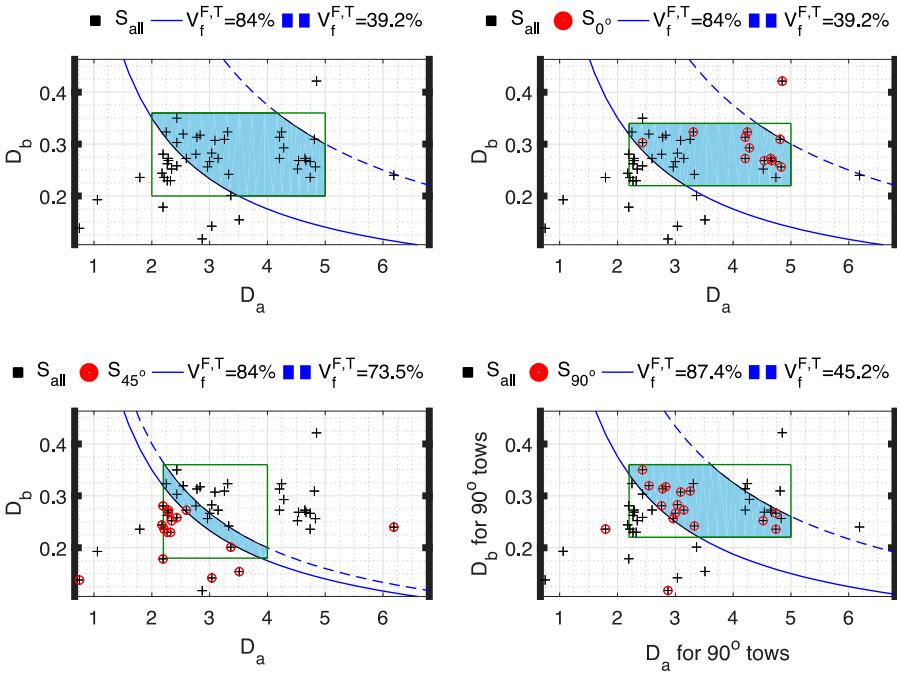

Figure IV.7-9. Domains of definition of $\boldsymbol{D_a}$ and $\boldsymbol{D_b}$.

Applying the framework shown in Figure IV.7-10, we obtained a functional representation of the coarser scales in terms of the finer-scale uncertainties and model errors introduced through each upscaling process. The modeling errors are the subject of next fiscal year's efforts. For FY 2016, we demonstrated the propagation of uncertainty from the fiber scale to the structural composite scale. All parameters shown in Table IV.7-2 are assumed to have a uniform distribution with the indicated bounds.

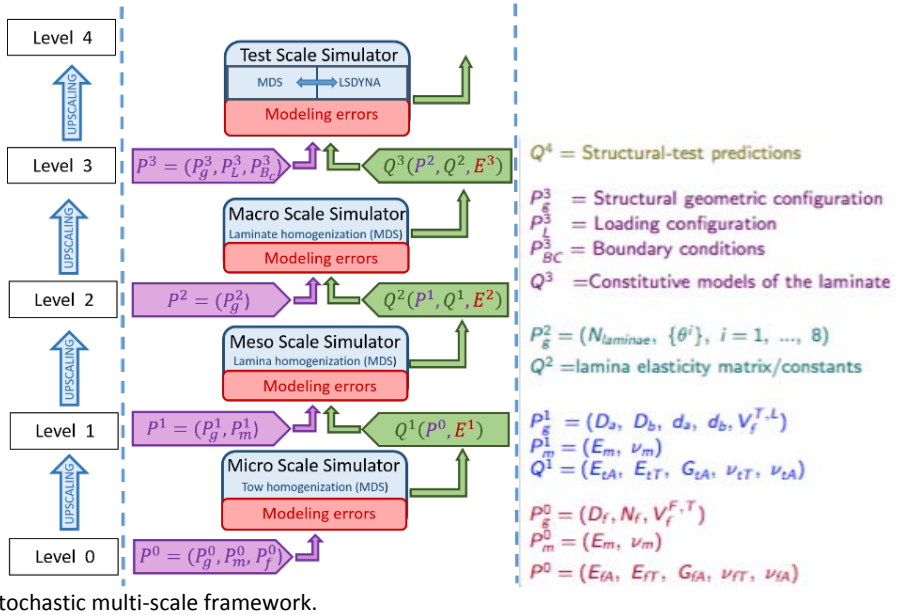

Figure IV.7-10. Stochastic multi-scale framework.

Table IV.7-2. Random Parameters from Across Three Scales used During the Demonstration

Variables	Mean value	Lower limit	Upper limit	Coefficient of variation
Tow axial modulus	230 GPa	220 GPa	240 Gpa	2.51%
Tow transverse modulus	20 GPa	14.8 GPa	25.2 GPa	15%
Tow Shear Modulus	25 GPa	20.7 GPa	29.3 Gpa	10%
Poisson's ratio (1-2)	0.016	0.013	0.019	10%
Poisson's ratio (2-1)	0.4	0.331	0.469	10%
Matrix modulus	0.335	0.294	0.376	7%
Tow Major diameter	3.47	0.74	6.2	45.4%
Tow Minor diameter	0.505	0.1	1.0	56.6%
Clearance	0.27	0.12	0.42	32.1%

Subtask 4.2. Develop and Validate the Manufacturing Process and Link Simulation Models

The objective of this task is to develop and validate the stochastic manufacturing simulation models. Simulation tools for the following manufacturing methods for high-volume automotive manufacturing were developed.

1. Resin transfer molding (traditional RTM, C-RTM, and HP-TRM)
2. Prepreg compression molding.

During the present performance period, the following items were completed:

Resin Transfer Molding (RTM/C-RTM)

1. Revision of inverse calculation for permeability
2. Validation of the exothermic model
3. Prediction of defects
4. Prediction of the residual stresses and warpage of the plaque after curing
5. C-RTM experimental tool design and experiments
6. C-RTM analysis using three-dimensional solid elements
7. Draping simulation of twill and satin weaves.

Prediction of Defects

During this task, the manufacturing simulation engine was validated for predicting the voids common to RTM. The ability to accurately predict the void formation will help to optimize the process parameters and help to reduce the costs of manufacturing. Novel experiments were devised to create voids and simulations were conducted to mimic those experimental conditions. One method used in this exercise was to create a local area

with a drastic change in permeability inside the mold. It was expected that the permeability difference would cause a non-uniform flow in the mold, causing entrapment of air. For lowering permeability in a local region, a metal plate $244.5\ mm \times 100\ mm \times 0.45\ mm$ was placed under the preform, creating a high-volume fraction area and thus a low-permeability region. Figure IV.7-11 shows the schematics of the metal obstacle in the mold.

In the corresponding numerical model, the preform in the area of the obstacle was modeled with a lower permeability value. Because there is no experimental permeability value available for this condition, the value of permeability was determined from empirical relation between the volume fraction and permeability using Gebart's model [1].

$$k = \frac{8r^2}{c}\frac{(1-V_f)^3}{{V_f}^2} \quad (1)$$

Where k is permeability, r the radius of the tow, c constant depending on fiber packing inside the tow, V_f is the volume fraction of the tow.

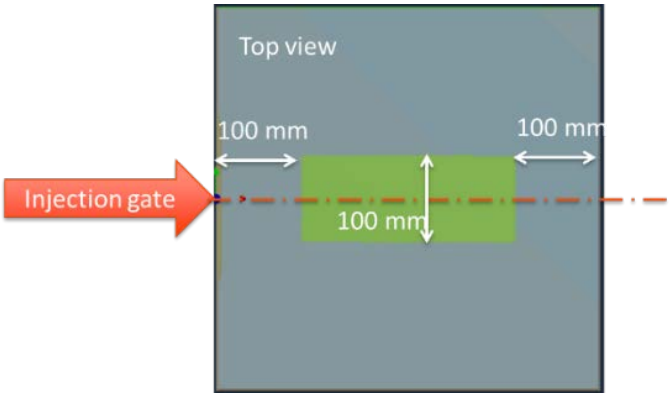

Figure IV.7-11. Schematic for location of the metal obstacle.

The above value of permeability for the preform was used as an initial guess in the area of the obstacle. This value was iterated to match the pressure versus time for Sensor 2, located at the middle of the obstacle. The pressure versus time with the iterated permeability value in the area of the obstacle matched closely with the experiments.

In the above experimental setup, with racetracking around the obstacle, the resin reaches the vent earlier than in the experiments without obstacle. The time at which the fluid reaches the vent was measured to be 42 seconds compared to 55 seconds without obstacle. The permeability of the obstacle area was iterated to match the fluid arrival time of 42 seconds at the vent. The value of permeability for the racetracking region around the obstacle area was determined to be $k_{race} = 2 \times 10^{-9} m^2$.

Figure IV.7-12 shows the dry spots obtained from the experiments and the analysis. The location of the dry spot predicted from numerical simulation agrees well with the experiments. The area of the void predicted from the simulation is around 3,750 mm^2, which is close to the experimental measurement of 3,600 mm^2.

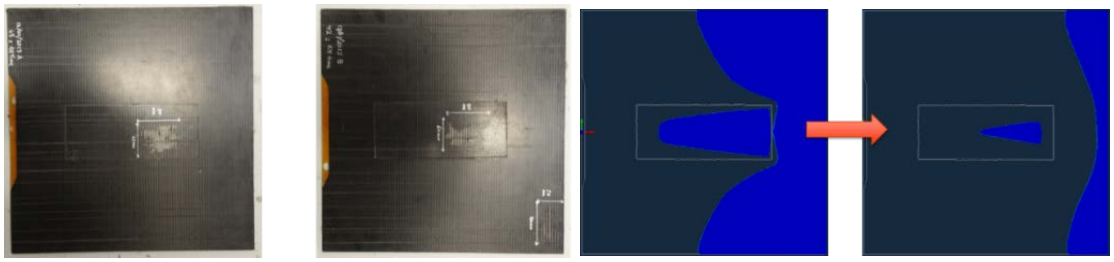

Figure IV.7-12. Voids observed in the experiment (left) and voids predicted in the simulation (right).

Prediction of Residual Stresses and Warpage of the Plaque after Curing

During this task, the distortion and residual stresses were calculated after curing for the panel without any obstruction. For the simulation, enthalpy was assumed to be 350,000 J/kg and the Kamal-Sourour kinetic model [2] given below was used to model the curing reaction:

$$\frac{d\alpha}{dt} = (0.1179e^{-\frac{4117}{T}} + 3.32E6 * e^{-\frac{7836.3}{T}}\alpha^{0.457})(1-\alpha)^{1.199} . \quad (2)$$

The temperature field is governed by the general equation:

$$\rho C_p \frac{\partial T}{\partial t} + \rho_r C_{pr} V \cdot \nabla T = \nabla \cdot (k \cdot \nabla T) - \rho_r \Delta h \frac{d\alpha}{dt} \quad (3)$$

where $d\alpha/dt$ denotes the change in degree of cure with time, α is the resin degree of cure, t denotes the time, T denotes the temperature, ρ is the density, C_p is the specific heat, $\partial T/\partial t$ denotes the temperature change with time, V is the velocity, ∇T is the gradient of the temperature field, ∇ is the gradient operator, k is the thermal conductivity tensor, the subscript r designates the resin, and Δh is the total enthalpy of the polymerization of the resin.

Following the filling and curing simulation analyses, a plaque distortion analysis was performed using the computer program PAM-DISTORTION. The distortion simulation model is based on the orthotropic, homogeneous, solid element formulation proposed by Svanberg [3] and implemented in PAM-DISTORTION. This model is a non-coupled, thermo-chemical, and mechanical transitory model with an incremental constitutive model based on linear viscoelasticity, but the rate dependence is replaced by a path dependence on the state variables.

Figure IV.7-13 shows distortion results for the case of an unsymmetric lay-up (0/-45/45/90/90/-45/45/0). The warpage predicted in the simulation is around 25.8 mm compared to the 20 mm measured during the experiment. The simulation predicts higher distortion, which is attributed to the fact that the distortion solver is linear (no geometric nonlinearity accounted). Currently, ESI is linking their nonlinear solver to PAM-DISTORTION.

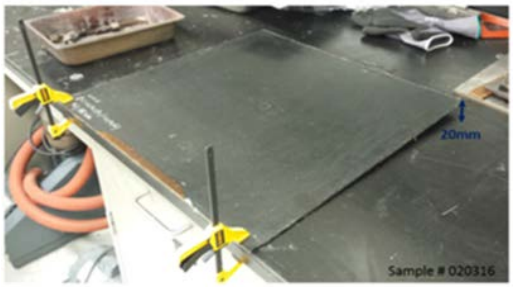

Figure IV.7-13. Distortion simulation result for the eight-layer unsymmetrical laminate with [0/45/-45/90/90/45/-45/0] layup.

Figure IV.7-14 shows the distortion predicted and measured for the plaque lay-up of [0/45/-45/90/100/-35/55/10]. The simulation predicted an upward displacement of 12 mm and experiments show the value of 8 mm. Again, the simulation is predicting higher values than the experiment. It is believed that once the solver is improved, the correlations will be very close.

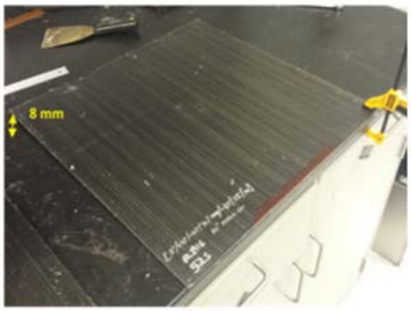

Figure IV.7-14. Distortion simulation result for the eight-layer unsymmetrical laminate with [0/45/-45/90/100/-35/55/10] layup.

C-RTM Experimental Tool Design and Experiments

C-RTM is a hybrid molding process ideal for many composite parts. The key difference between C-RTM and conventional RTM is that the mold is held open by a few millimeters during the injection of the resin. The extra mold gap provides an area of permeability that can be several times higher than with the mold fully closed. Higher permeability allows for extremely fast resin injection without a large pressure gradient in the mold and without the problems of preform washout.

A truncated pyramid part shape was designed and fabricated in GM to demonstrate the C-RTM process. An instrumented steel mold and a transparent acrylic mold with identical shapes will be used to generate experimental datasets for validating the models. Figure IV.7-15 shows a cross-section of the steel truncated pyramid mold.

The mold uses an outer O-ring for a vacuum seal and an inner O-ring for the resin seal. The vacuum seal is engaged at mold gaps as large as 10 mm above full closed position, enabling evacuation of the mold for C-RTM. The resin inlet is centered in the top mold half. The injected resin must fill the floor of the mold cavity before flowing up the 45-degree angled side walls and finally into the flange. The bottom mold half is equipped with a pressure transducer centered under the injection port and a 1-in. diameter dielectric cure sensor positioned halfway between the pressure transducer and the side wall. The thermocouple locations were chosen to allow the advancing resin flow front to be sensed by the timing of small temperature differences.

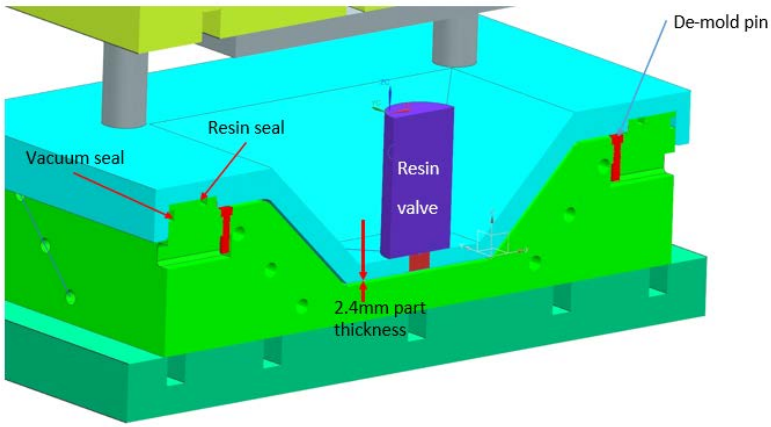

Figure IV.7-15. Truncated pyramid mold for C-RTM experiments.

GM Research and Development's RTM apparatus was used to meter and mix a two-part epoxy/anhydride resin system and pump the resin into the inlet line of the RTM inlet valve. The overall resin flow rate was chosen so

that all of the resin needed to fill the mold was pumped in 20 seconds. After the resin was injected into the mold cavity, the press was closed using its low-rate setting for 15 seconds, followed by high-pressure closing. Several experiments were planned with different gap openings and measurements for pressure, and resin arrival times were provided to the simulation for correlations.

C-RTM Analysis Using Three-Dimensional Solid Elements

During this compression RTM process analysis, two main issues need to be addressed: the resin gap evolution during forming due to the moving tool and preform deformation due to compression and resin flow. Numerically, the analysis is a two-step process: first, resin is injected in a gap located between mold and preform; then, in a second stage, resin injection is closed and the top mold begins its displacement in order to close the gap and compress the preform until a final desired thickness is reached. Several material parameters are to be defined for running three-dimensional C-RTM simulations. Alongside traditional RTM input data (such as resin viscosity and reinforcement permeability tensor) the fluid/solid coupled solver requires mechanical compression data. Moreover, in C-RTM simulations, reinforcement permeability tensor values Kx, Ky, and Kz have to be defined as a function of fiber volume content to capture with significant precision the effect of reinforcement compression on flow front evolution. A solid-element mesh was used for simulations.

Variations of permeability tensor values are given in Figure IV.7-16 based on the experimental data for in-plane permeability of the woven fabric and extrapolation approximation.

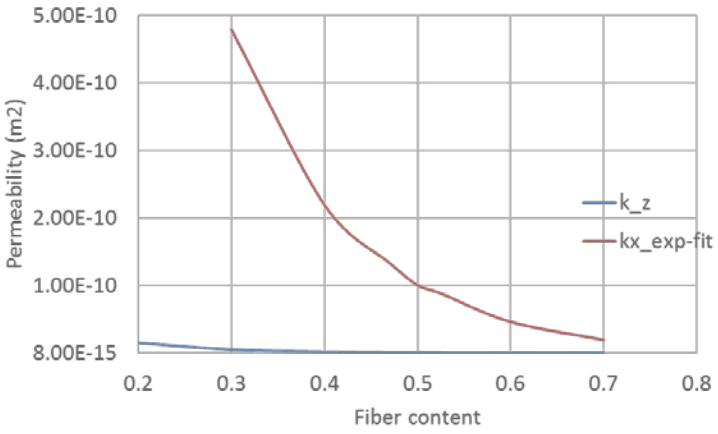

Figure IV.7-16. Permeability tensor as a function of fiber content for the woven fabric.

The mold opening was assumed to be 5 mm and the initial thickness of the preform to be 3 mm. The target thickness is 2.4 mm.

The injection time is kept as 20 seconds and the compression velocity is set to 1 mm/second. From results shown in Figure IV.7-17, it can be seen that the resin flow initially within the gap was due to the much higher permeability value when compared with preform permeability values. Once the total amount of resin needed to mold the part at the desired fiber content is injected (after 20 seconds), the inlet is closed and the mold begins its displacement.

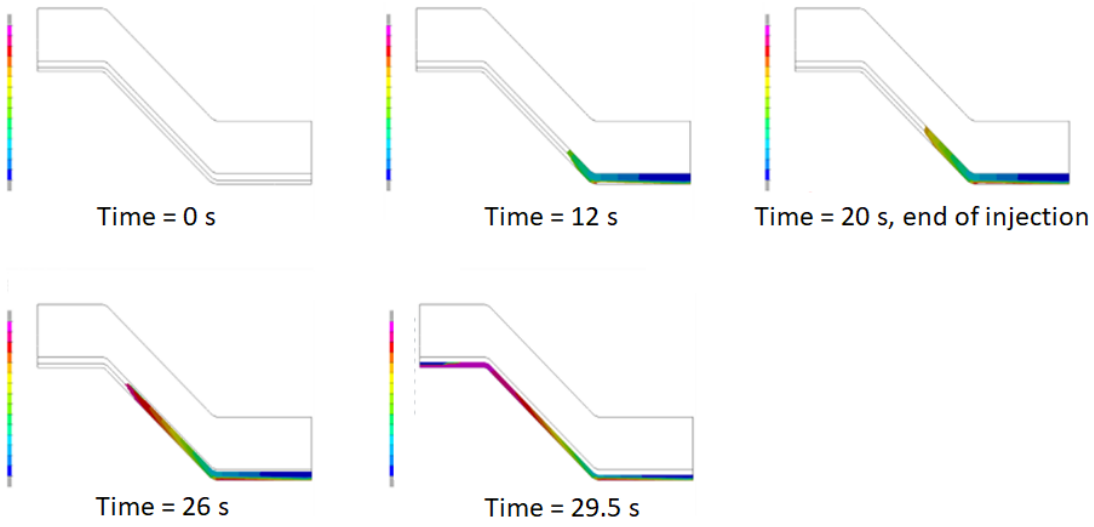

Figure IV.7-17. Resin flow history in the gap and preform for the quarter model during the injection-compression process.

The permeability and fiber content values of the gap do not evolve due to current limitations. The gap has vanished in the end. The mold compresses the preform as the deformed mesh. Fiber volume content in the preform has increased to the targeted 52.5%. Because of a solver instability issue, it is not always guaranteed that the analysis will converge due to the complex coupling between the solid and fluid solver.

Fabric Deformation Studies

The deformation studies involved use of a tool (shown in Figure IV.7-18) built from clear polycarbonate, which allows visual examination of the deformed fabrics while deformed in the tool. This tool is designed to be mounted in an Instron tensile test fixture to allow deformation of the fabrics at controlled deformation rates. Two types of fabric were evaluated: (1) a 2 x 2 twill woven material (TC411) and a five-harness satin woven material (SC685). Samples of a stitch-bonded quadraxial fabric (MC933) were also investigated, but due to the large folds that occurred in the material on deformation, further investigation on this fabric was discontinued. All fabrics were woven by Sigmatex, Inc., of 12K Toray T700 CF. The fiber crossing angles of the twill and satin fabrics begins as 90 degrees. In other words, the weft (or fill) tows cross the warp tows at an angle of 90 degrees. Although numerous global orientations are possible for the fabric in the tool, only two orientations (0/90, and ±45) were investigated to date.

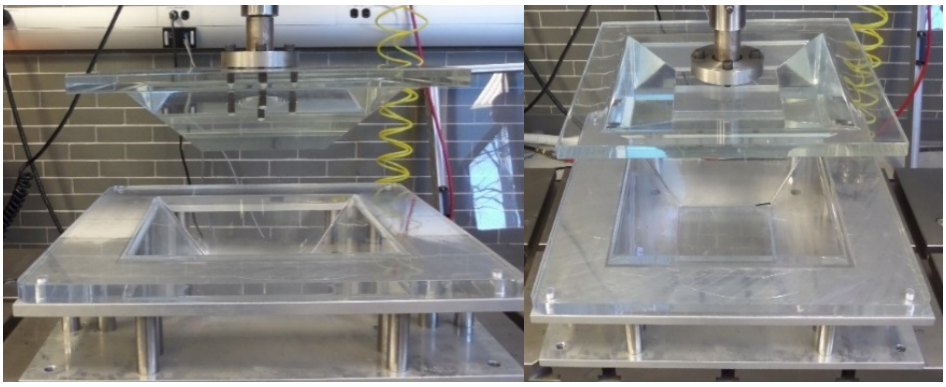

Figure IV.7-18. Truncated pyramid deformation tool.

The global performance of both fabrics was similar. Therefore, only a single orientation is shown for each material. Figure IV.7-19 shows the global appearance of the 2 x 2 twill fabric following deformation in the

0/90-degrees global orientation and the five harness satin fabric following deformation in the ±45-degree global orientation.

Initially, there are some obvious differences in how the fabrics perform in each global orientation. In the 0/90-degree orientation, the corners of the material appear to stay in their original location, while the center of the material pulls in significantly. This seems to be due to the angle change in the fabrics coupled with the difference in the line length between the straight line across the fabric and the longer line length produced by following the contour of the tool. For the ±45-degree orientation, the fabric pulls in uniformly from all sides. This may be an indication the fabric is more deformable in this orientation or perhaps another mechanism is working.

Figure IV.7-19. Global view of 2 x 2 twill fabric 0/90-degree and satin ±45-degree orientation deformation.

The fiber angles were measured using an image analysis program (Image-J [http://imagej.nih.gov/ij/]). This tool allows the user to manually draw angles, tracing the edges of the intersecting tows and measure them. Using this tool, angles were measured on the deformed fabric at multiple locations for each global orientation and were used to correlate with the simulations.

Draping Simulations of Twill and Satin Weaves

Material model 140 was used to model the dry woven fabric during the draping operation. This material data type has all the major features to simulate the bending and shear behavior of the fabric during draping. The shear stiffness is an independent property and is the most important factor because fabrics predominantly deform in this mode. A non-linear shear stiffness can be imposed via three parameters: (1) for initial shear modulus, (2) locking angle and locking modulus, or (3) via a more accurate user-defined curve function. Fabric-bending stiffness is decoupled from in-plane stiffness and may be properly characterized via different methods. Before proceeding to the draping simulation, the material model was calibrated to two distinct characterization tests (e.g., Pierce cantilever test [bending stiffness] and a picture frame test). The cantilever bending test and picture frame test were conducted by the University of Tennessee.

Draping Simulation for 0|90-Degree Twill and Satin Woven Fabrics

From the literature covering the shear behavior of fabrics, we can be reasonably certain of two noticeable factors:

1. The shear modulus is not a constant.
2. The initial shear modulus $(G_i)_{is}$ very small.

Preliminary simulation for fabric draping of 45-degree twill and satin fabric were conducted using the material parameters in previous studies of 0/90-degree fabric. Shear angles measured at certain locations on the formed part were used as a basis to compare against simulations. Figures IV.7-20 and IV.7-21 show various sections on the truncated pyramid used for measurements and correlations. These figures also define the measured locations for the M-line, the P-line, the U-line and the Z-line from the center of the bottom edge used for the shear angle measurement and prediction. Figures IV.7-22a shows the comparison of the experimental and the simulated results for the shear angle distributions along the M-line and the U-line in the twill fabric.

Figure IV.7-22b provides the results for the shear angle distributions along the P-line (above) and Z-line (below) in satin 5H fabric.

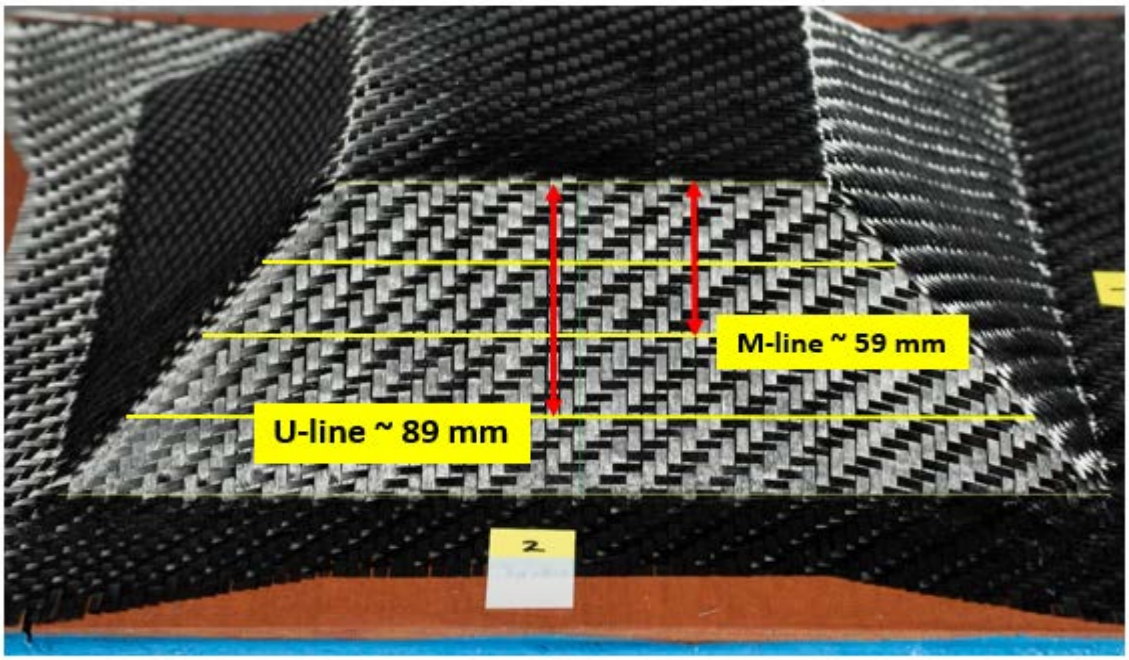

Figure IV.7-20. Description of M and U line sections used for the shear angle measurement and prediction.

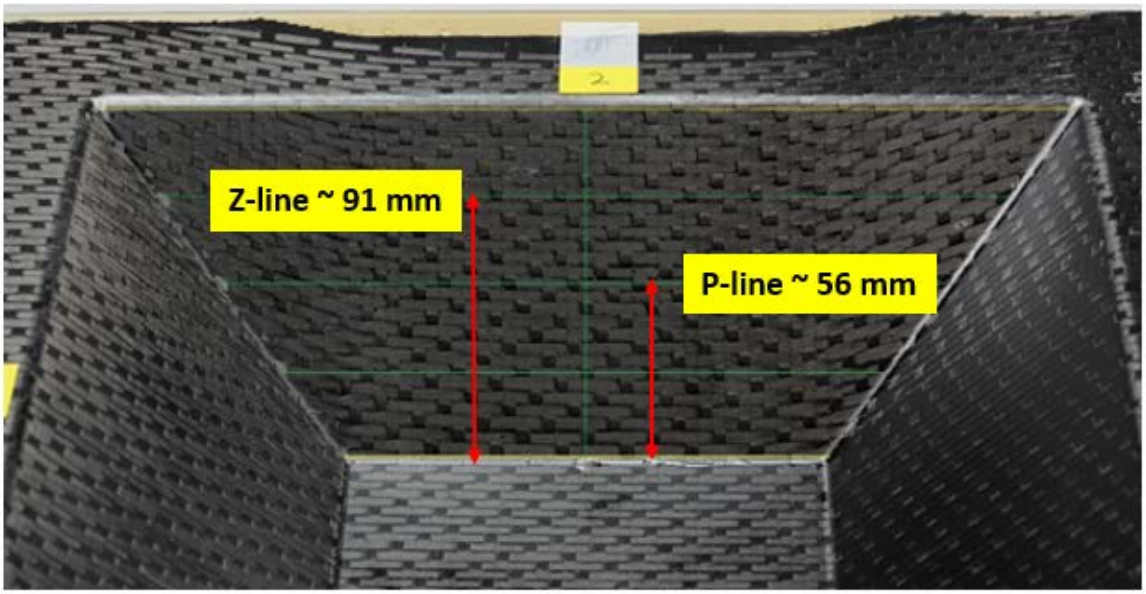

Figure IV.7-21. Description of P and Z line sections used for the shear angle measurement and prediction.

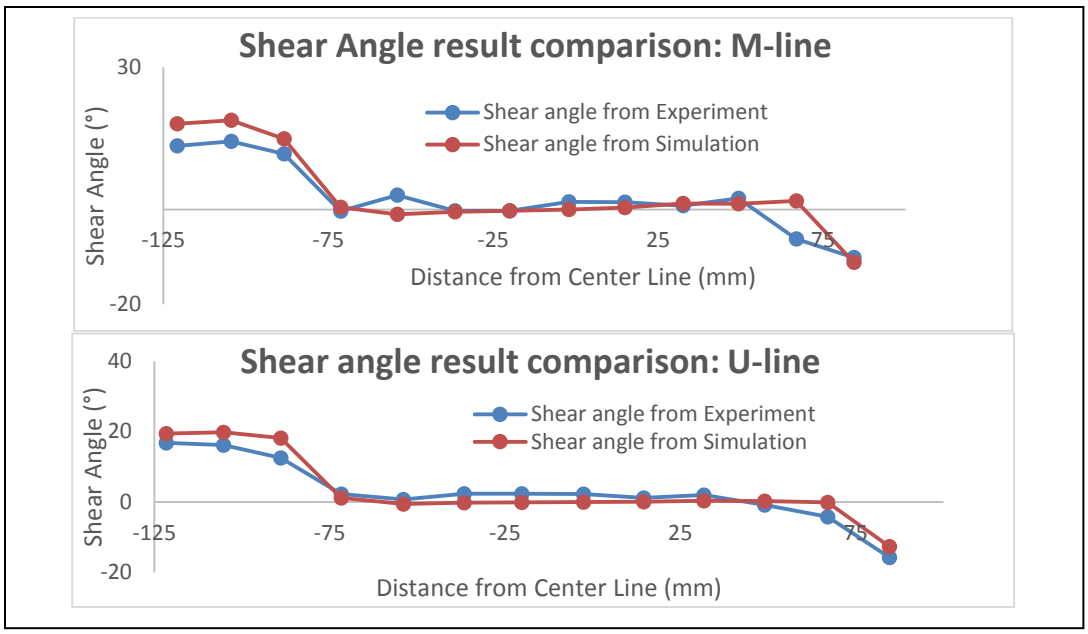

Figure IV.7-22a. Comparison of shear angle distributions along the m-line (above) and u-line (below) in twill fabric

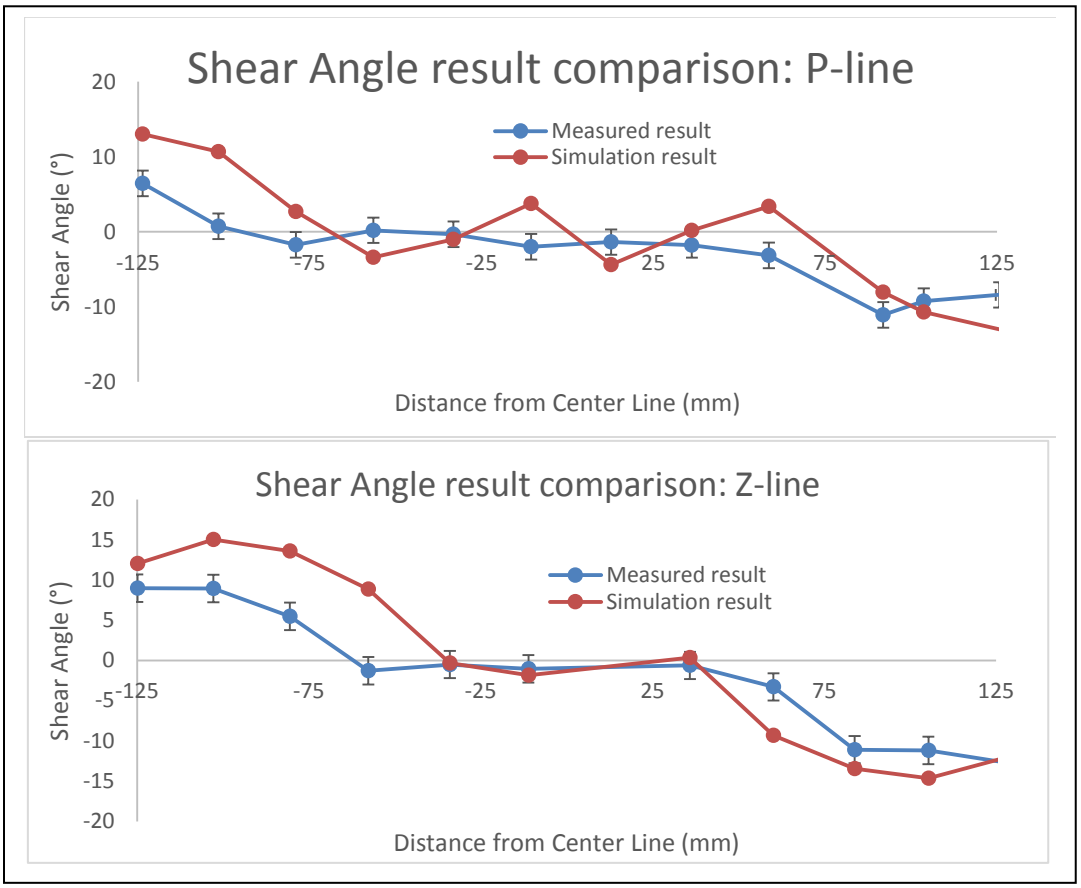

Figure IV.7-22b. Comparison of shear angle distributions along the p-line (above) and z-line (below) in satin 5H fabric.

The material parameters, which yielded good agreement with 0/90-degree ply, did not provide the same for ±45-degree ply. This was true for both twill and satin fabrics and is due to the fact that the material parameters obtained from the current inverse analysis may not be always optimum. In order to investigate

further, a wider test matrix was created with different material data sets. Table IV.7-3 provides details for the test matrix.

Table IV.7-3. Design of Experiment Matrix for Draping Simulation

Configuration	Initial Shear Modulus Gi (GPa)	Locking Angle TLock (Degrees)	GLock (GPa)	B1 (GPa)	B2 (GPa)	Notes
Configuration 1	0.001	14	0.05	0.5	0.5	Mesh oriented in fiber direction with adaptive mesh refinement
Configuration 2	0.050	14	0.50	2.0	2.0	
Configuration 3	0.001	6	0.10	2.0	2.0	
Configuration 4	0.001	6	0.50	2.0	2.0	
Configuration 5	0.001	6	0.50	0.5	0.5	
Configuration 6	0.001	4	0.05	2.0	2.0	
Configuration 7	0.050	14	0.50	2.0	2.0	Mesh oriented in fiber direction with no adaptive mesh refinement

Figure IV.7-23 shows comparison of simulation results using different test matrix configurations and experimental results. A general trend observed in simulations from different configuration runs is that higher shear angles on the wall at the corner than in the center, whereas experiments show a constant shear along various measured lines. This dip at the center in simulations is being further investigated. From the plots, it can be seen that Configuration 7 (basically Configuration 2 without the adaptive mesh technique) for satin fabric yielded better correlation for shear angles. The dip reduces and shear angles at the center now seem to align close to the experimental curve.

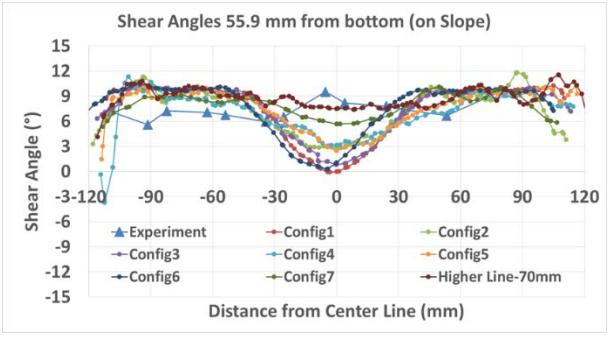

Shear angle comparison for satin fabric at 55-mm line.

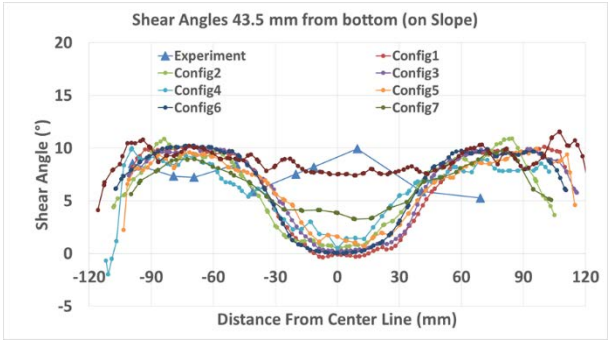

Shear angle comparison for satin fabric at 43-mm line.

(a)

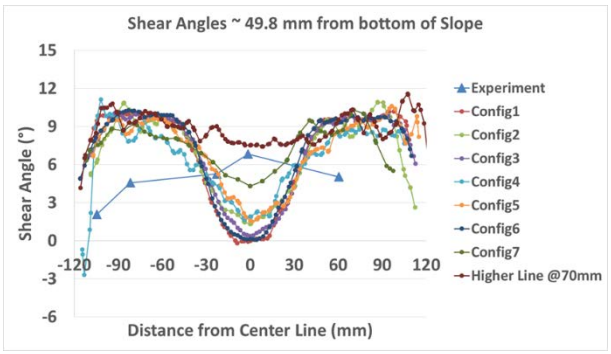

Shear angle comparison for twill fabric at 50-mm line.

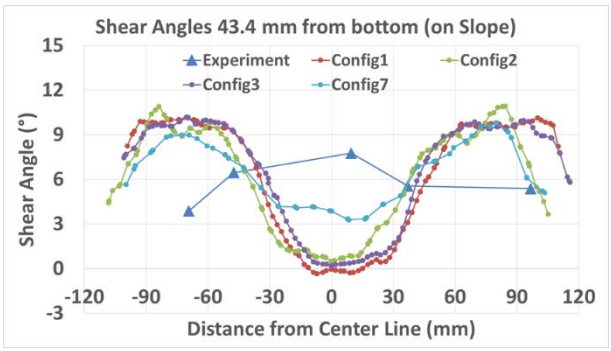

Shear angle comparison for twill fabric at 43-mm line.

(b)

Figure IV.7-23. Shear angle comparisons for (a) twill and (b) satin fabrics.

Further investigation is required to confirm if this is an isolated issue arising from the adaptive mesh technique. On the other hand, there was not so much success correlating twill fabric because there is still some discrepancy. It is possible that there may be more than one factor affecting this analysis; this needs to be studied further. Additional measurements on other sides of the truncated cone could remove suspicion on experimental measuring techniques.

Furthermore, an alternate test method (i.e., bias-extension) to obtain ply shear properties is planned. Data from bias-extension tests can be used to further validate both 0/90-degree and ±45-degree plies on a truncated cone draping analysis.

Subtask 4.3. Develop and Validate a Stochastic Performance Model

Contributions to this project from Altair this year consisted of the following items:

1. Calibration of MDS multi-scale material models for simulation of a twill weave and non-crimp fabric CF composite material system
2. Development and validation of a hybrid plasticity-damage model for nonlinear epoxy behavior for composite modeling
3. Transition to a LS-DYNA plugin from ABAQUS
4. Investigation of the relevance of rate dependence in epoxy-dominated loading modes
5. Incorporation of manufacturing effects into performance simulations
6. Modeling of sheared fabrics.

Calibration of MDS Multi-scale Material Models for Simulation of a Twill Weave and Non-Crimp Fabric CF Composite Material System

Automated calibration for nonlinear parameters follows the same steps as the linear case, but is generally more complicated because more parameters need to be identified and the underlying physics are more complex. Progress to date resulted in partial automation of the nonlinear parameter identification process. The main challenges to full automation are the computation time required for rail shear and flexural tests and the mesh sensitivity associated with these tests. Regardless, the partially automated nonlinear calibration process has led to excellent agreement between model and experiments for the twill. Figure IV.7-24 shows modeled versus experimental four-point flexure simulations. The simulation shows some softening during the loading due to some damage at the microscale level. At this time, it is not accounted in simulation. The modeled peak load and failure strain match with the experimental data very well. In addition, there is a slight degradation of the

flexural stiffness before ultimate failure as the epoxy and transverse tows begin to develop cracks in the bending direction. This loss of stiffness is also appropriately captured by the model. In the case of strength-based design criteria, this loss of stiffness could be justifiably ignored, but for crash prediction of energy absorbing automotive components this stiffness loss represents a secondary but non-negligible source of energy dissipation during failure. Accounting for every available energy dissipation source is crucial for designing composite components that are competitive with their metal counterparts.

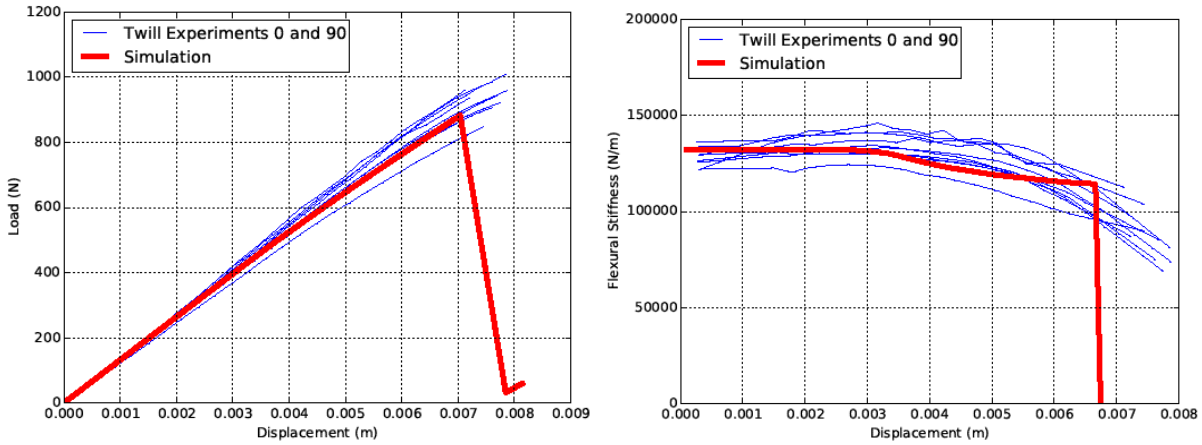

Figure IV.7-24. Load displacement and flexural stiffness versus displacement for twill in four-point bending.

The same four-point flexure simulation has been run in LS-DYNA using the Multi-scale Designer plugin. The load displacement curve is shown in Figure IV.7-25, which again matches well with the experiments. The matrix develops damage in the axial and delamination directions, which contributes to the loss of stiffness observed in the model and experiments. Additionally, transverse damage in the transverse tows contributes to this stiffness loss. Note that transverse damage in the transverse tows refers to cracking in the global axial direction of the matrix material inside the transverse tows.

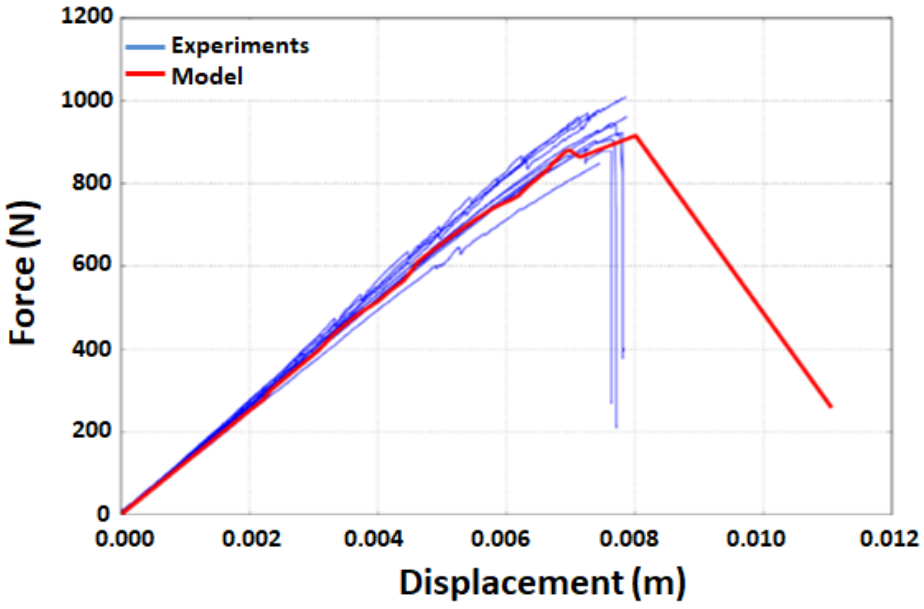

Figure IV.7-25. Load displacement curve for LS-DYNA simulation of the twill four-point bending.

Development and Validation of a Hybrid Plasticity Damage Model for Nonlinear Epoxy Behavior in Composites Modeling

The model for neat epoxy developed during FY 2016 is a combination of classical plasticity and isotropic damage. The plasticity formulation is based on a von Mises yield criterion. Note that such a formulation was originally developed for metals where the carrier of plasticity is dislocation motion along crystallographic slip planes. For amorphous materials (such as polymers), no such crystal structure exists and the plasticity arises from so-called shear transformations. However, the von Mises framework is entirely phenomenological in the sense that it makes no distinction between different micromechanical mechanisms of plasticity. As long as inelastic deformation may be regarded permanent and driven by deviatoric strain measures, von Mises criteria may apply. This can be confirmed for epoxy through examination of cyclical loading data on pure epoxy and carbon epoxy composites.

This decoupling confers a significant advantage with regards to parameter identification because common experiments, for example, unnotched tension on 90-degree and ±45-degree laminates, will independently expose the behavior of the damage and plasticity portions of the model, respectively. Plots of model behavior simulating plain epoxy under different loading conditions are shown in Figure IV.7-26. The model reproduces experimentally observed behavior (e.g., distortion and very-high strain to failure under shear), yielding uniaxial tension followed by fracture at around 5 to 7% strain and fracture at 1% strain or less in a highly triaxial "poker chip" test (also known as short-wise tension). Formulation is also amenable to modifications that may account for temperature and rate effects, which may become relevant as the project moves forward.

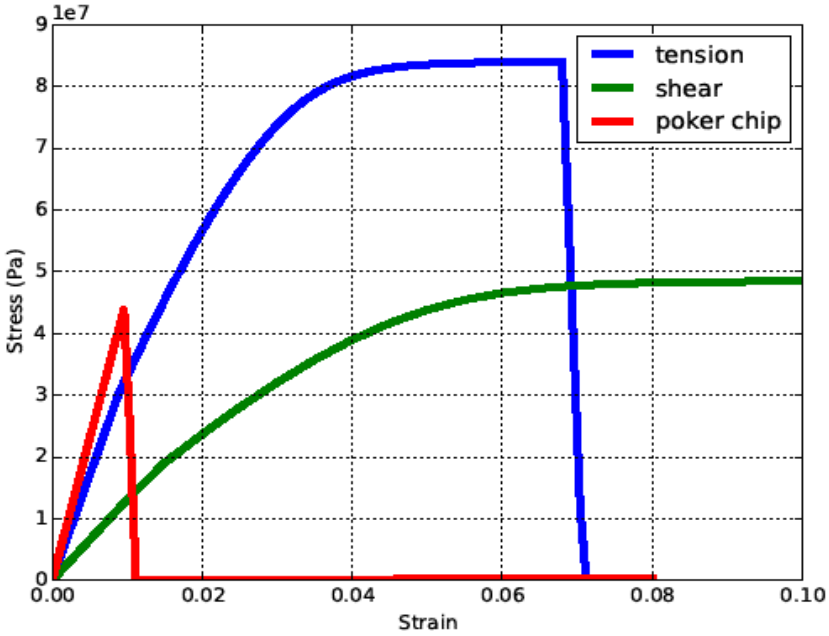

Figure IV.7-26. Behavior of the hybrid model for plain epoxy under different loading states.

Performance of the Hybrid Model for the Twill Material System

Performance of the hybrid model for CF epoxy material systems was demonstrated as follows. First, deeply notched rail shear data provided to Altair by GM was used to identify parameters for the hybrid model. These parameters were used by Altair to make a blind prediction of the stress-strain curve of a 45-degree unnotched tension test. Subsequently, experimental data for this test were provided by GM to Altair, which confirmed the blind prediction. Aside from building confidence in the predictive capability of the Altair models, this exercise shows that unnotched tension on 45-degree specimens can replace notched rail shear. Both tests expose the same physics in the composite but the unnotched tension test is easier to conduct, both from a modeling and an experimental point of view. This has potentially significant implications for the composites industry at large, because cost, time, and difficulty associated with testing, qualifying, and model development for composite

material systems can be reduced by eliminating notched rail shear testing and replacing it with unnotched tension testing.

Parameters for the hybrid model were identified from rail shear experiments provided by GM. Modeling a notched rail shear specimen presents several challenges, primarily due to uncertainty that is introduced by considering idealized boundary conditions. These idealized boundary conditions are necessary to reduce the computational cost of the parameter identification process, but they may introduce systematic errors. Here, we have modeled the test using a single element model in pure shear. An additional difficulty with the rail shear data is that the material failed well after the strain gauges exceeded their limit. This means the parameter identification process was conducted with a partial shear stress strain curve and an ultimate strength but without any measurements of strain-to-failure and a significant portion of the stress-strain curve missing (Figure IV.7-27).

Despite these difficulties, a sensitivity analysis of the nonlinear response in shear versus 45-degree tension demonstrated that model properties that control the closeness of the fit to the given partial shear stress-strain curve also influence the shear strain-to-failure. Similarly, the properties that govern the shear strength also govern the 45-degree tensile strength. Therefore, based on this analysis, we expect that if the model matches well with the given rail shear data, it contains the requisite information to make a reasonable prediction of the 45-degree tensile data. The missing portions of the shear stress-strain curve and the approximate numerical model contribute to uncertainty of the prediction, but this uncertainty is not significant enough to render the prediction invalid.

The prediction step then consisted of a stochastic analysis that sampled from the feasible parameter set to predict possible responses for the 45-degree tensile data. The results are shown in Figure IV.7-28, along with experimental data that were provided to Altair after the computational prediction was made. Comparing the blind prediction versus actual experimental data, the match to the strength and failure strain is good, while the model systematically over-predicts the yield strength of the actual material (Table IV.7-4). These differences can most likely be attributed to the highly idealized computational model of the complex rail shear test setup. Given the success of these predictions, we propose that notched rail shear testing can be replaced by unnotched tension experiments on 45-degree specimens.

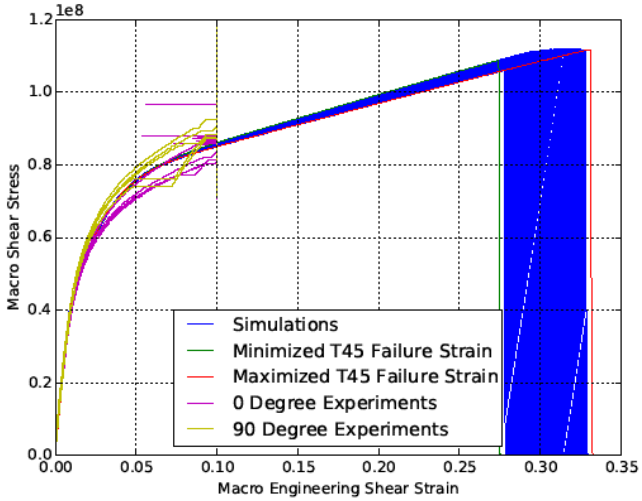

Figure IV.7-27. Parameter identification phase: a set of feasible parameters is constructed using constrained optimization techniques and the available rail shear experimental data.

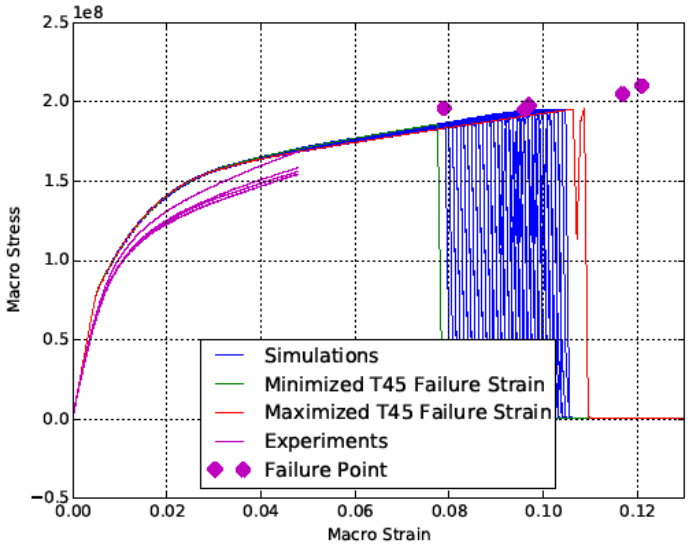

Figure IV.7-28. Prediction phase: a blind prediction of the 45-degree tensile data was made using the feasible set of parameters. The true experimental behavior is shown in purple.

Table IV.7-4. Comparison of Blind Prediction with Experiments

45-Degree Tensile Macro Property	Average Simulated Result	Simulated Result Range	Average Experimental Result	Experimental Result Range
Failure Strain Percent	9.27	7.9 to 10.5	10.2	7.9 to 12.1
Ultimate Stress MPa	191	186 to 195	201	195 to 210
Modulus	15.3	—	13.7	13.4 to 14.1

Investigation of the Relevance of Rate Dependence for Epoxy-Dominated Loading Modes

Rate dependence for the response of composite materials is widely regarded as a negligible effect. This is due to the fact that composite failure modes dominated by axial fiber failure have been observed to be rate independent. This is true not only for the rates sustained in side impact, which are presently under consideration, but also for the higher rates sustained in front impact and even for much higher ballistic loading rates that are often of interest for military applications. This is the result of the CF itself having negligible rate dependence.

In contrast, the yield strength of epoxy is strongly rate dependent, even at loading rates that are nominally quasi static and, therefore, well below the rates sustained in side impact. Therefore, it is expected that the response of a composite in a loading mode dominated by the yielding response of the epoxy should also be rate dependent. Exploiting epoxy yielding and maximizing the strain in the matrix during impact are promising techniques for design of efficient energy-absorbing composite structures. However, to avoid potentially non-conservative designs for crashes, rate dependence requires a thorough re-examination. Based on experimental evidence and some preliminary numerical analysis, it appears that rate dependence may be a relevant phenomenon for composite structures in side impact conditions.

Evidence for and Analysis of Rate Dependence for Epoxy-Dominated Loading Modes

Rate dependence is typically not considered relevant for analysis of CF composite systems because CFs appear to have negligible rate dependence. However, designing composite structures to exploit the tendency of epoxy to yield under distortional loading appears to be a highly promising strategy for increased composite energy absorption. Because of the inherent rate sensitivity of epoxy yield strength, this strategy is expected to become less effective with increasing strain rate. The results of this study indicate that rate effects may indeed be

relevant for side impact if the designer wishes to accurately account for epoxy yielding in energy-absorbing automotive structures.

The twill material system also shows rate dependence for 45-degree tensile loading, which is an epoxy yielding dominated mode (Figure IV.7-29). An increase in strain rate increases the yield strength of the epoxy and the overall strength of the composite. The strain-to-failure decreases with increasing strain rate, which is consistent with expectations because the strain-to-failure is controlled by the epoxy reaching a critical tensile state, the development of which is inhibited by yielding. Because the energy absorption capacity of this loading mode appears to diminish with strain rate, some understanding of the extent of this phenomenon is needed.

A multi-scale analysis may be used to first infer the rate dependence of the epoxy yield strength and to estimate how the composite yield strength will change for strain rates beyond the available coupon tests and into rates that will be sustained in side impact. The results of the inference step are shown in Figure IV.7-30. A multi-scale analysis is used to determine the stress and strain rate in the epoxy in the twill at the onset of yield. Assuming the commonly used log linear relationship between yield stress and strain rate, the yield strength is expected to increase by 8.7 MPa per decade of strain rate. In the work of Gilat et al. [4], a different type of epoxy is used but the observed rate sensitivity was similar. After this determination, the composite yield strength for any strain rate may be estimated. This is shown in Figure IV.7-31, where a macro strain rate of 100 $^{sec-1}$ results in a composite yield strength that is roughly double that for a macro strain rate of 10E-4 sec^{-1}. For side impact, the macro strain rate is unlikely to exceed 100 sec^{-1}, but is likely to be greater than 10 sec^{-1}. Given this preliminary result, rate dependence for energy-absorbing composite structures is relevant. Further, a full nonlinear analysis is needed to quantify how energy absorption is affected by strain rate.

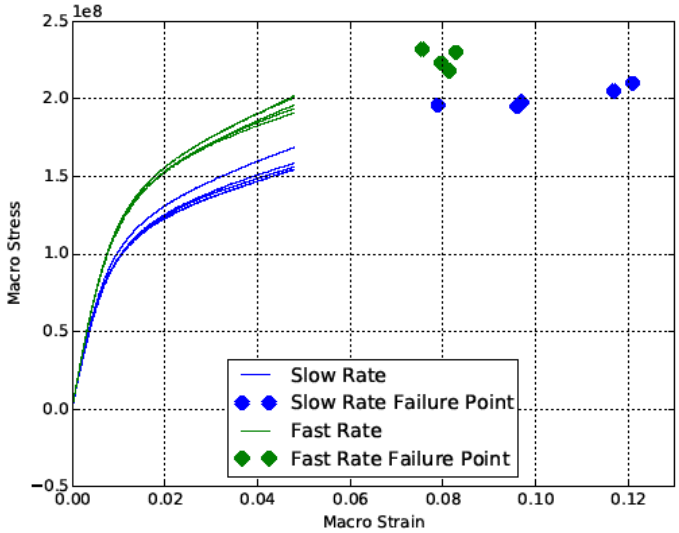

Figure IV.7-29. Twill material system loaded in 45-degree tension. Remarkable energy absorption capacity is observed, but this capacity is diminished by increases in strain rate.

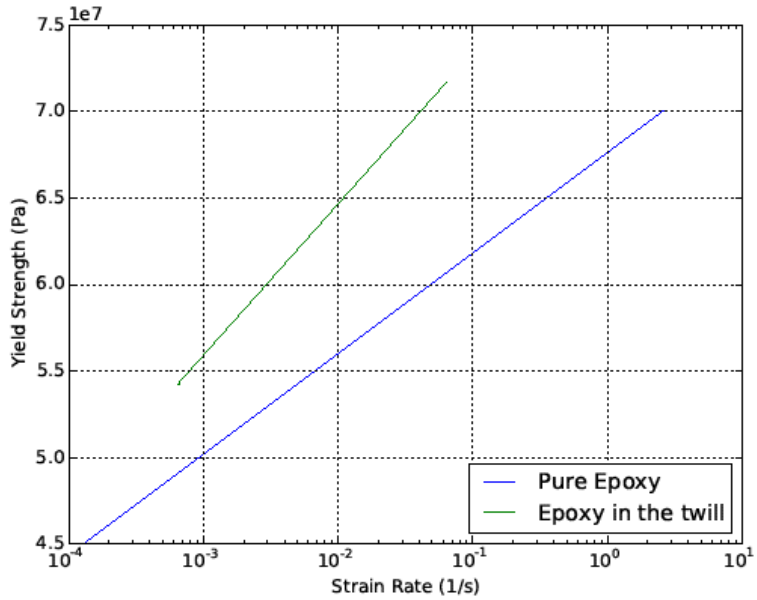

Figure IV.7-30. Yield strength versus strain rate for the epoxy in the twill inferred from 45-degree tensile tests. As a point of comparison, the epoxy studied in Gilat et al. [4] is also shown, where pure epoxy was loaded in torsion.

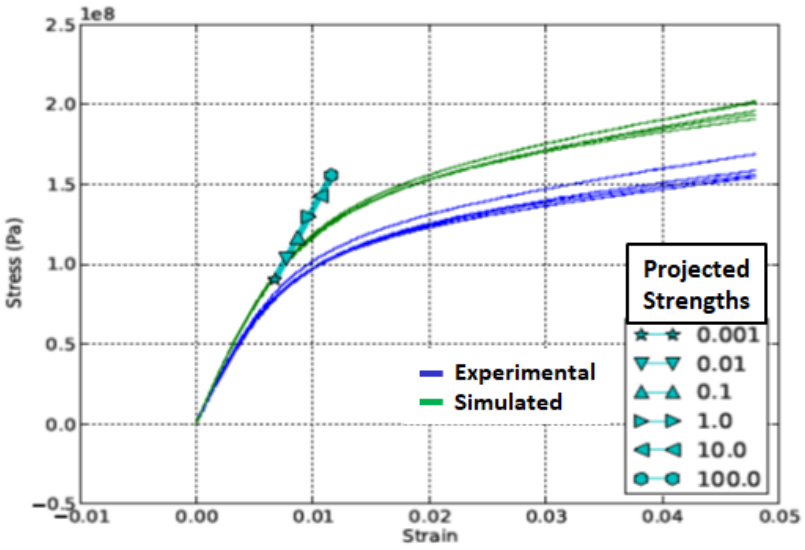

Figure IV.7-31. Estimated composite yield strength for several strain rates - light blue points show the projected strengths, assuming a log linear dependence of epoxy yield strength on strain rate inferred from the coupon experiments.

Modeling of Sheared Fabrics

Non-Orthogonal Weave Modeling

Draping a dry textile often results in a sheared weave where the warp and weft fiber directions are not orthogonal. Manufacturing solvers for modeling draping provide warp and weft fiber directions as output. To integrate this information with performance solvers, first a model for a sheared weave must be available, then fiber angles from the manufacturing solver must be used to construct the local material coordinate systems for the part.

To develop sheared weave models, Altair HyperMesh mesh morphing capability is used to map the mesh of an orthogonal weave onto a non-orthogonal one given a prescribed shearing angle. This approach has numerous advantages; the first is that it is a very accurate representation of the sheared geometry that can be generated in a simple and quick manner. In addition, multi-scale calculations proceed as usual on the morphed mesh without any modification to the multi-scale procedures themselves. Therefore, this process is applicable to any particular weave geometry (e.g., plain, twill, and satin weaves) and, further, the process does not place any restrictions on the particular fiber or matrix materials that may be of interest. Figure IV.7-32 shows the unit cell of the sheared fabric created following this new approach.

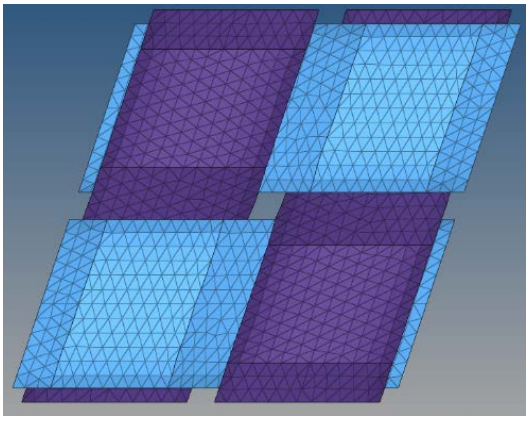

Figure IV.7-32. Unit cell of the sheared fabric.

To understand the properties of the non-orthogonal weaves computed according to the current approach with a common approach of representing a weave as two layers of unidirectional composite called classical lamination theory (CLT), stiffness and strengths were compared for both methods. Preliminary results are shown in Figure IV.7-33. Stiffness computed by both methods is very close to one another, but the trend in the transverse strength is very different between the two approaches. The non-orthogonal weave unit cell shows a precipitous drop in transverse strength with increasing shearing angle. In contrast, the method of modeling a weave as two layers of unidirectional composite shows a much more gradual strength decrease. The sudden drop in strength for the non-orthogonal weave is due to the fact that at that particular angle, matrix failure leads to a failure mechanism in the composite. The different geometrical representations of the material microstructure will lead to differences in the way these mechanisms form. GM will be conducting experiments on non-orthogonal weave coupons and the results will be used to validate this modeling approach.

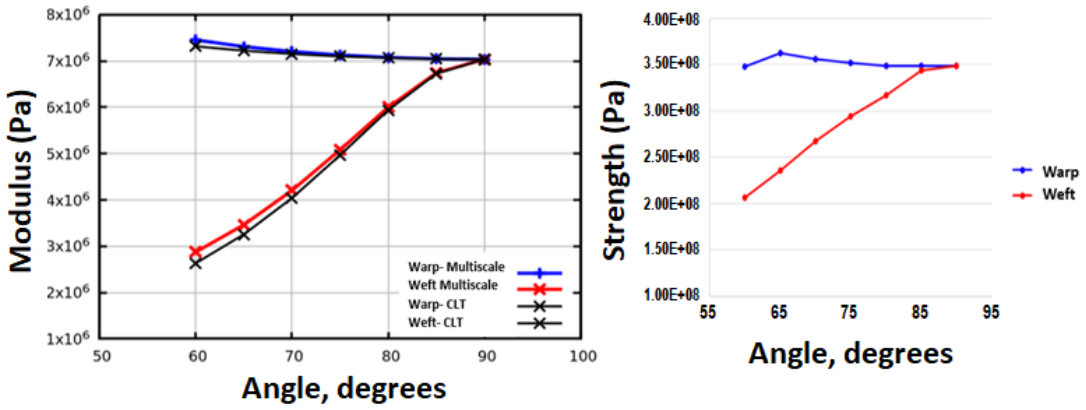

Figure IV.7-33. Stiffness and strength of a non-orthogonal weave represented by a non-orthogonal weave unit cell versus an approximation of the weave as two layers of unidirectional composite.

Conclusion

During the FY 2016, the project team has designed and completed several experiments to validate the stochastic manufacturing simulation and structural performance tool developed in this project. Also, a new simulation tool to predict the manufacturing outcome for a compression resin transfer molding (C-RTM) is being developed. From the structural modeling side, new models were developed to include the plasticity in the resin to predict more accurately resin dominant ductile behavior which is useful in energy absorbing applications. Also, a parametric unit cell for non-orthogonal fabric model to predict the performance of sheared fabrics was developed. A mapping procedure is being developed to map the manufacturing outcome onto the structural models. The manufacturing outcome includes the angle changes during draping, residual stresses after molding and unfilled dry areas. A stochastic framework was developed based on upscaling the physics across the scales (fiber, tow, unit cell, and component level) for both manufacturing and structural performance.

References

[1] Gebart, B.R., 1992. "Permeability of unidirectional reinforcements for RTM", *Journal of Composite Materials*, Vol 26, No. 8, pp 1100-1133.

[2] Kamal, M. R. and S. Sourour, 1973, "Kinetics and thermal characterization of thermoset cure," *Polymer Engineering and Science* 13(1): 59–64, DOI: 10.1002/pen.760130110.

[3] Svanberg, J. M., and Holmberg, J. Anders, 2004. *Prediction of shape distortions Part I. FE-implementation of a path dependent constitutive model*, Composites Part A: Applied Science and Manufacturing, Vol. 35, Issue 6, Pages 711-721.

[4] Gilat, Goldberg, R., Roberts, G.D., "Strain Rate Sensitivity of Epoxy Resin in Tensile and Shear Loading", NASA TM—2005-213595.

Bibliography

Aitharaju, V, 2016, "Stochastic Modeling for Performance and Design Across Scales," invited talk to the *IUTAM Symposium on Integrated Computational Structure-Material Modeling of Deformation and Failure under Extreme Conditions*, Baltimore, Maryland, June 20 through 22, 2016.

Aitharaju, V., H. Yu, S. Zhao, J. Owens, P. Pasupuleti, and M. Doroudian, 2016, "Modeling of Resin Transfer Molding of carbon fiber composites," presented at the *American Society of Composites*, Williamsburg, Virginia, September 19, 2016.

Mehrez, L., R. Ghanem, C. McAuliffe, W. R. Rodgers, and V. Aitharaju, 2016, "A Multiscale Framework for the Stochastic Assimilation and Modeling of Uncertainty Associated with NCF Composite Materials," presented at *VII European Congress on Computational Methods in Applied Sciences and Engineering Congress (ECCOMAS)*, Crete, Greece, June 2 through 10, 2016.

Rodgers, W. R., X. Jin, J. Zhu, T. Wathen, M. Doroudian, and V. Aitharaju, 2016, "Draping Simulation of Woven Fabrics," presented at the *Society of Plastics Engineers Automotive Composites Annual Conference & Exhibition (SPE ACCE)*, Novi, Michigan, September 2016.

IV.8 Spider Silk MaSp1 and MaSp2 Proteins as Carbon Fiber Precursors – Utah State University

Project Details

Randolph V. Lewis, Principle Investigator
Utah State University
9820 Old Main Hill
Logan, UT 84322-9820
Phone: 435-797-9291
e-mail: randy.lewis@usu.edu

Felix L. Paulauskas, Co-Principle Investigator
Oak Ridge National Laboratory
Building 5800, Rm A107
Post Office Box 2008
Oak Ridge, TN 37831-6053
Phone: 865-576-3785
e-mail: paulauskasfl@ornl.gov

Soydan Ozcan, Co-Principle Investigator
Oak Ridge National Laboratory
Building 5800, Post Office Box 2008
Oak Ridge, TN 37831-6053
Phone: 865-576-3785
e-mail: ozcans@ornl.gov

Cheryl Hayashi, Co-Principle Investigator
University of California, Riverside
2318 Spieth Hall
Riverside, CA 92521
Phone: 951-827-4322
e-mail: cheryl.hayashi@ucr.edu

H. Felix Wu, Program Manager
U.S. Department of Energy
1000 Independence Ave., S.W.
Washington, DC 20585
Phone: 202-586-4830
e-mail: felix.wu@ee.doe.gov

Contractor: Utah State University
Contract No.: DE-EE0006857/0002

Executive Summary

The objective of this project is to develop an unconventional non-petroleum based carbon fiber precursor that has the potential for production in high yield and quantities. Methods will be developed to produce pilot-scale quantities of fibers from spider silk proteins with mechanical properties at least 75% that of the natural dragline silk fibers in tensile strength and elongations of less than 5%. The precursor fibers will be converted to carbon fibers, with a goal of greater than 250-Ksi strength and 1 to 2% elongation. Cost analysis will be performed and the process optimized.

Task 1: Fiber Synthesis

Subtask 1: Protein Production

The go/no-go milestone of 1.0 g/L of one spider silk protein (MSp2) purified was exceeded last year and fermentations have increased from 5 to 500 L. A series of changes to the purification protocol were made since the initial report last year. These changes led to a reduction in the time needed for the purification and reduced purification costs by nearly 90%. In addition, a rapid assay using the Waters Corporation ultra performance liquid chromatography to determine both concentration and purity of the spider silk proteins is under development, which will eliminate two of the time-consuming and costly analysis steps.

Subtask 2: Fiber Spinning

The major focus has been to produce more material to send a 24-fiber thread to ORNL. The methodology for successfully spinning 24-fiber yarns is still under development. This involves both spinning dope solutions and methods for keeping the fibers from fusing during the post spin stretch. The second area of focus has been to standardize the spin dopes for making the fibers. The conductivity (indicative of salt remaining with the protein after purification) is an important factor in successful spinning, as is pH. There is a need to be below 600 micro Siemens (μS) conductivity and the most effective pH is protein dependent.

Subtask 3:, Silkworm Silk

The transgenic silkworms made using gene replacement at the fibroin light chain instead of the heavy chain have a higher tensile strength. This tensile strength is the same as the average for spider dragline silk.

Task 2: Carbonization

The major effort for carbonization was that Oak Ridge National Laboratory successfully heated the spider silk protein fibers to 1700°C and still maintained a useable fiber. These initial trials produced several important findings: (1) ramp speed for increasing the temperature is critical, (2) maintaining tension on the fiber during the heating process is critical because the fiber expands as it is heated, and (3) having a narrow temperature window when stretching the fiber during heating leads to much better final materials.

Task 3: Techno-Economic Analysis

The techno-economic analysis was expanded to determine the relative cost of production with the bacterial production system compared to the transgenic alfalfa and goat production systems. For all systems, the key factor in the final price is the amount of spider silk protein produced for whatever measure of volume or weight is used. Alfalfa can be the cheapest, but it is subject to possible regulatory control unless the United States develops a more comprehensive approach to genetically modified organisms. The silkworm analysis was not completed due to a variety of confounding factors. The primary one was that if the production were shifted overseas, then the cost would likely be nearly equivalent to current silk prices of $5 to $15/kg. However, if concerns about the location of production are important, then production would need to be done in the United States and initial costs would be much higher. However, if the later scenario is utilized, the cost would be lowered, but it would not be possible to calculate exact costs for this analysis.

Accomplishments

- Completed all Task 1 milestones and exceeded the go/no-go milestone for producing 1.0 g/L of one of the spider silk protein (MSp2) purified, which has now been scaled to 500 L of fermentation.
- Carbonized the spider silk protein fibers to 1700°C and still maintained a useable fiber with excellent tensile strength.

- Made transgenic silkworms using gene replacement at the fibroin light chain instead of the heavy chain, which generates fibers with higher tensile strength and at the average of spider dragline silk.
- Created a techno-economic model that describes the relative percent costs of all the inputs to spider silk protein production via fermentation with the latest modifications to the process.

Future Directions

- Increase spider silk protein production via fermentation.
- Improve further tensile strength of the transgenic silkworm silk.
- Generate methods for increasing the tensile strength of the thermally stabilized spider silk derived from carbon fibers.

Technology Assessment

- Target: Increase spider silk protein production to 2 g/L recovered protein.
- Gap: Bacterial production and purification technology need to be improved.
- Target: Increase the tensile strength of carbon fibers by stabilizing spider silk fibers by crosslinking.
- Gap: The best crosslinking method needs to be identified.

Introduction

This project uses unconventional, non-petroleum precursors that are high-strength, low-cost, and high-yield for developing carbon fibers that are more efficient. To our knowledge, the use of spider silk as a carbon fiber precursor is entirely novel. Specifically, during this 2-year project, the project will assess the feasibility of spider silk fiber as a model for engineering biomimetic polymer precursors to replace petroleum-based polyacrylonitrile precursors. Use of this unconventional precursor has several potential impacts. From a material science perspective, spider silk has many desirable properties, including tensile strength as high as Kevlar and elongation equivalent to nylon, that would impart new properties to carbon fiber. From a sustainability perspective, silks are proteins; therefore, they are renewable resources. Finally, from the perspective of national competitiveness and security, unlike polyacrylonitrile precursors, spider silk can be sourced in the United States. Techno-economic modeling will be performed to understand the commercial feasibility of production processes being investigated with data feedback that is used to highlight key areas for research focus for improving the process economics.

The technical target for this feasibility project is to produce carbon fibers with uniform mechanical properties of at least 250 Ksi (1.72 GPa) tensile strength, 25Msi (172 GPa) tensile modulus, and 1% ultimate tensile strain. Spider silk protein will be produced via E. coli fermentation at a pilot-scale level of multiple 500-L fermenters. Recent advances in fermentation and protein expression indicate that this production level at the pilot scale will produce in excess of 1 kg per fermentation, resulting in about 330,000 m of silk fiber.

There are the following three major goals for this project:

1) Develop methods for producing pilot-scale quantities of fibers from spider silk proteins having mechanical properties with at least 75% that of the natural dragline silk fibers in tensile strength and elongations of less than 5%,
2) Develop procedures for converting these fibers into carbon fibers with mechanical properties of 250 Ksi and elongations of 1 to 2%
3) Conduct a techno-economic assessment of key process cost points to determine where to minimize costs with the most cost-effective alternative method.

Approach

Task 1: Fiber Synthesis

Task 1 evaluated spider silk protein-based fiber production. There are two separate approaches for producing sufficient spider silk protein-based fibers (Project Objective 1): (1) spin fibers from *E. coli*-produced protein and (2) create transgenic silkworms producing cocoon silk fibers with mechanical properties similar to spider silk. Figure IV.8-1 shows the flowchart for this process. Our major deliverable depends on successfully completing this task.

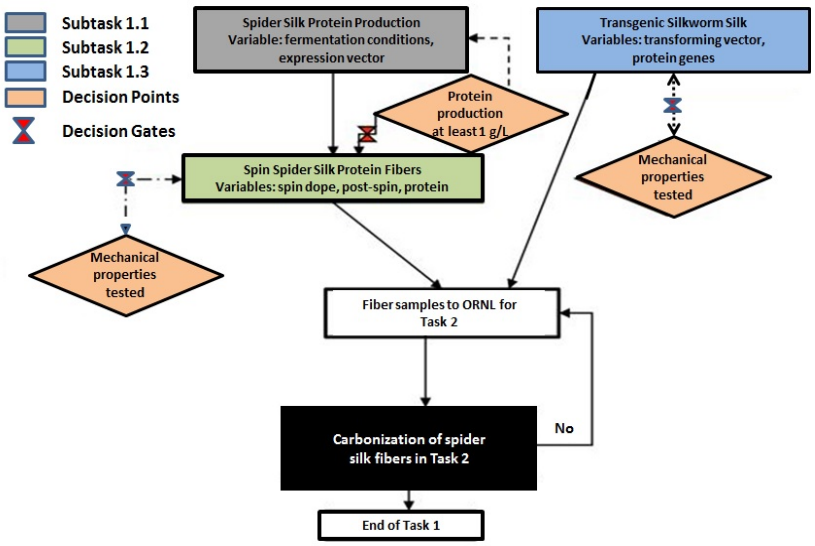

Figure IV.8-1. Flowchart for Task 1.

Initial production methods for spider silk fibers had two deficits: (1) lack of production capacity and (2) inferior mechanical properties. The project improved bacterial production to meet the initial go/no-go milestone in Fiscal Year (FY) 2015 and continued to improve the production process. In theory, the transgenic silkworm system is infinitely expandable and at a low cost, but the fibers produced lack the needed mechanical properties. To overcome this, the silkworm light chain protein gene was replaced with a spider silk protein gene.

A number of changes to the initial protocols were made. This led to a substantially more efficient and less costly process. Specifically, the flow-through homogenizer is operating as designed, which allows the project to lyse up to 100 L/hour of fermentation liquid; this can be directly passed to the flow-through centrifuge. This system added two more key steps that greatly decreased the time and cost of purification. As previously shown, the spider silk proteins are highly stable, even at temperatures exceeding 90°C. Therefore, while still in the fermentation tank, the tank temperature increases to 80°C and the fluid passes through the homogenizer, which increases the temperature to about 85°C. In order to remove as much of the insoluble material as possible, 0.2% polyethylenimine is added after the homogenization step and the mix is cooled near room temperature before centrifugation. These steps created a decrease in the suspended solids from over 2% to less than 0.1%, making all the downstream steps more efficient.

Ammonium sulfate ($AmSO_4$) was immediately added to the supernatant from the centrifuge to precipitate the spider silk protein and a small amount of bacterial proteins. This suspension passed through the flow-through centrifuge and the collected precipitate that contains the spider silk protein. Based on the previously described heat/pressure method for solubilizing the spider silk proteins, a Paar Instrument Company vessel is used for larger volumes (i.e., greater than 300 mL) to resolubilize the spider silk proteins; this prevents the remaining bacterial proteins from solubilizing due to the high temperature. This solution is cooled and the $AmSO_4$ precipitation is repeated to generate a very high purity spider silk protein preparation.

The precise recoveries and purity of the final proteins will be assessed in FY 2017 because the complete process only evolved near the end of FY 2016. In addition, the project is developing a rapid assay using the Waters ultra performance liquid chromatography to determine both concentration and purity of the spider silk proteins, which will eliminate two time-consuming and costly steps in the analysis process.

Task 2: Carbonization

Task 2 involved developing the spider silk fiber conversion technology to obtain low-cost carbon fiber for automotive and commodity applications. The overall technical objective of the proposed research is to demonstrate continuous mode conversion of spider silk protein fiber precursors to obtain carbonized fibers that are applicable in automotive industries. The specific objectives for this work include (1) develop modified spider silk protein fiber that can be rendered infusible, (2) demonstrate accelerated stabilization using thermal in air or thermochemical methods with a residence time comparable to traditional polyacrylonitrile fiber residence time, and (3) obtain carbonized fiber from the stabilized precursors by applying optimal conversion parameters. Figure IV.8-2 shows the process flowchart for this task. A systematic approach was conducted to optimize the conversion parameters with an overarching goal of producing renewable source spider silk-based, low-cost carbon fiber for automotive applications. The final project deliverable will be a continuously processed spider silk-based carbon fiber with satisfactory mechanical properties.

Subtask 2.1, Development of Chemical/Physical Pretreatment

At this point, the project is still exploring two methods for protein crosslinking. The first is a visible light-induced photo crosslinking process that can be initiated during the fiber spinning process. The other is chemical crosslinking that uses specific amino acids in the protein. There are several alternatives for this that are still under investigation. Several methods for crosslinking are still under study.

Task 3: Techno-Economic Analysis

The scope of the modeling work is focused on critical evaluation of the proposed process for the metrics of economics and environmental impact. A critical component of the modeling work is integration of experimental data for validation and data feedback to experimental systems. The scope has two performance periods. The first focuses on development of engineering process models and integration with economic evaluation. The second performance period will continue to refine economic modeling while leveraging engineering process models for life-cycle assessment. The results from the first performance period will be an economic assessment of the proposed process and data feedback highlighting areas for improvement. The results from the second performance period will include updating economic models based on experimental results and quantifying the environmental impact of production and use of the proposed technology.

The techno-economic analysis was expanded to determine the relative cost of production of the bacterial production system compared to the transgenic alfalfa and goat production systems.

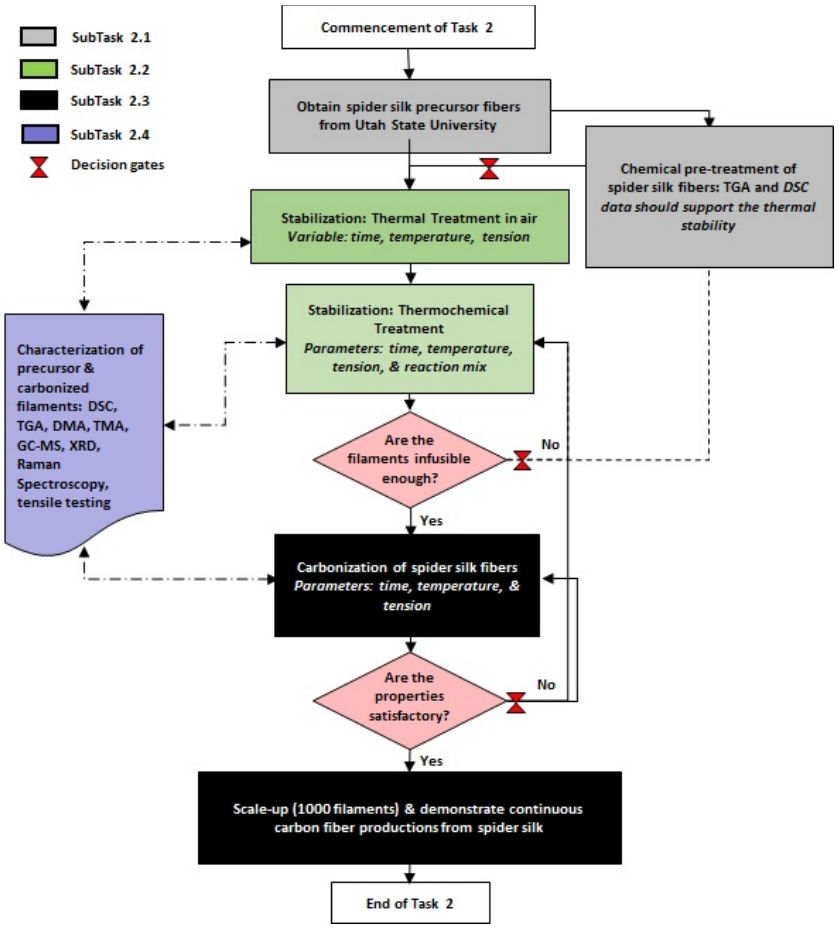

Figure IV.8-2. Flowchart for Task 2.

Results and Discussion

Task 1: Fiber Synthesis

The transgenic silkworms made using gene replacement at the fibroin light chain instead of heavy chain have a higher tensile strength. Figure IV.8-3 illustrates the increase of strength for the transgenic silkworm cocoon fibers (an average of 10 fibers), which is the same as the average for spider dragline silk.

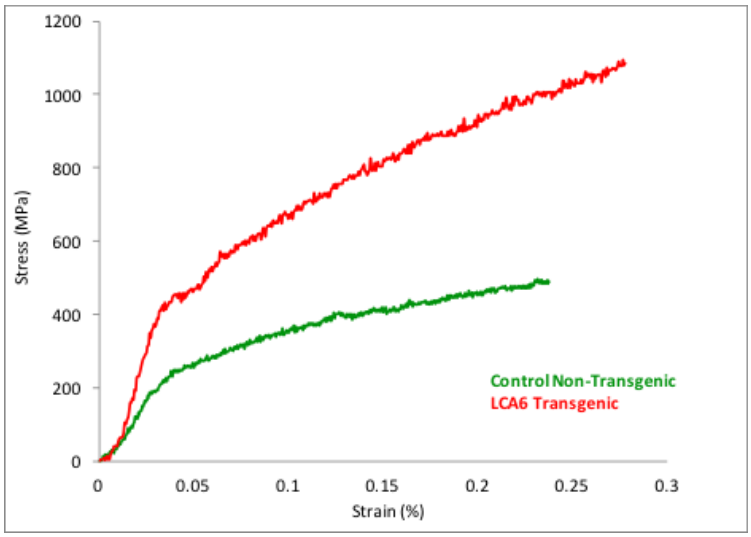

Figure IV.8-3. Stress-strain curve for silkworm silk fibers.

Task 2: Carbonization

Utah State University and ORNL continue to work on chemical crosslinking methods in addition to photo crosslinking to provide modifications to the synthetic spider silk protein. Studies are not complete enough to provide results.

During the conversion of the spider silk fibers to carbon fiber, several important factors were discovered: (1) the ramp speed for increasing the temperature is critical; (2) maintaining tension on the fiber during the heating process because it tends to expand as it is heated; and (3) narrow temperature window in which stretching the fiber during heating leads to much better final materials. Figure IV.8-4 presents results for some of the initial studies and illustrates the performance characteristics of the new carbon fiber over the previous fiber produced in FY 2015.

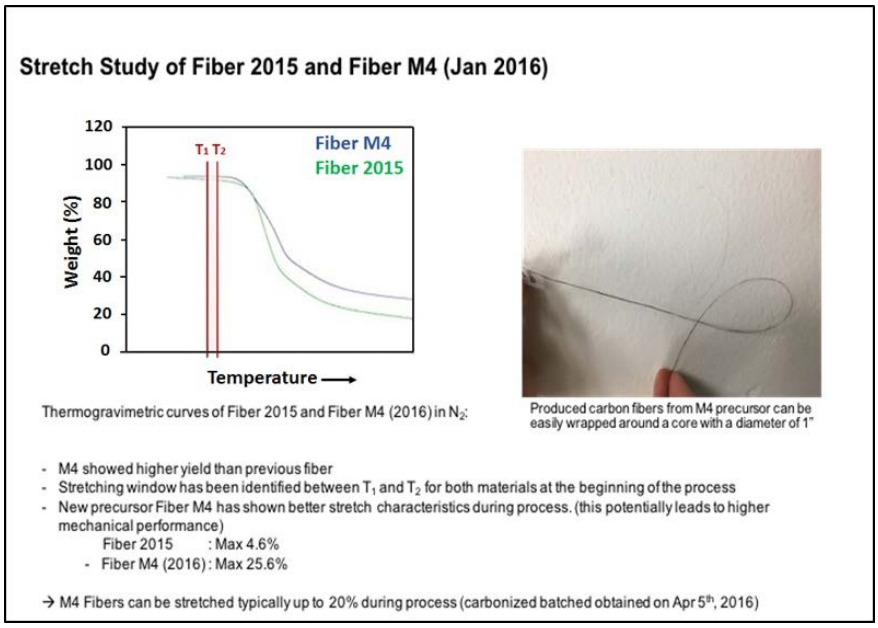

Figure IV.8-4. Initial carbon fiber studies from spider silk protein fibers.

Further analyses of the fibers at various final heating temperatures showed that the higher temperature leads to better fiber mechanical properties (see Table IV.8-1). For these tests, the assumption was that each bundle

contains eight filaments. The diameter of one individual filament was evaluated and measured for each bundle (around 10 µm at 1300°C and 9 µm at 1700°C). The "equivalent diameter" shown in Table IV.8-1 is a calculation for a "virtual large filament" that would have the same surface of cross section compared to the bundles of eight filaments that were tested. The tensile strength, in particular, is higher at 1700°C than at the lower temperatures and the diameter is only slightly smaller, indicating very little loss of mass when going from 1300 to 1700°C. The initial modulus and the ultimate strain are relatively unchanged with increasing temperature. As shown in Figure IV.8-4, the fibers are still pliable and not brittle even after 1700°C. The minimum for the second go/no-go milestone to produce fibers with greater than 50 ksi for the peak stress was achieved. These fibers also exceeded the peak stress of most carbon fibers (50 to 70 ksi) and the modulus values (1 to 2 Msi).

Several microstructural analyses by ORNL that are shown in Figure IV.8-5 include scanning electron microscope images of improved fiber shape and uniformity. The image on the left side of Figure IV.8-5 shows a precursor made of transgenic silkworm/spider silk blend in April 2015. The filaments are not fused, but the shape of their cross section is irregular. The longest dimension is mostly in the 15 to 22-µm range. On the right side of Figure IV.8-5, a precursor made of spider silk proteins in January 2016 shows that the cross section is almost perfectly circular with a diameter around 28 µm; however, these filaments are fused in bundles of usually eight filaments, which is the maximum.

Table IV.8-1. Mechanical Tests on the Fused Material Produced in FY 2016; Numbers in Parentheses are the Standard Deviations from 10 Tests

Sample ID	Maximum Temperature (°C)	Equivalent Diameter (µm)	Peak Stress (ksi)	Modulus (Msi)	Strain at Break (%)
Bundle 1	1300	29.37 (1.58)	99.7 (41.0)	7.5 (0.9)	1.28 (0.42)
Bundle 2	1300	29.34 (1.51)	77.3 (41.1)	7.3 (1.1)	1.06 (0.67)
Bundle 3	1500	28.52 (1.35)	69.2 (43.6)	8.9 (1.4)	0.78 (0.50)
Bundle 4	1700	26.08 (3.11)	101.9 (61.9)	7.4 (2.0)	1.32 (0.67)

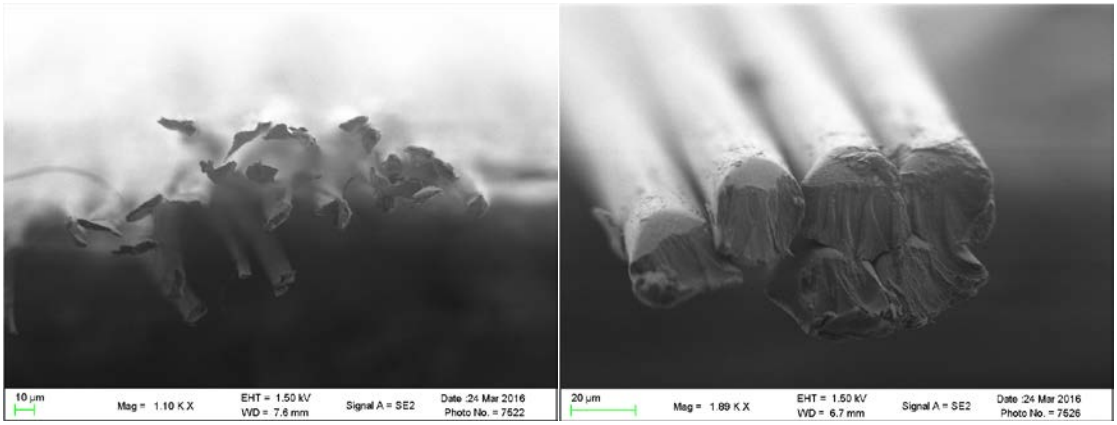

Figure IV.8-5. Scanning electron microscope images emphasizing improvement in the production of the precursor between FY 2015 (left) and FY 2016 (right).

The Raman spectra presented in Figure IV.8-6 show the D-band (1,350 cm^{-1}) and G-band (1,580 cm^{-1}) have smaller peak widths, which indicates they are better ordered in relationship to the fiber axis. Figure IV.8-7

shows that the micro-Raman, when overlaid on the visual fiber cross sections, demonstrates the same conclusion as the bulk Raman in Figure IV.8-6. The D/G peak ratio is lower at the higher temperatures, indicating higher order and, especially at the highest temperature, a very uniform ratio compared to the lower temperatures.

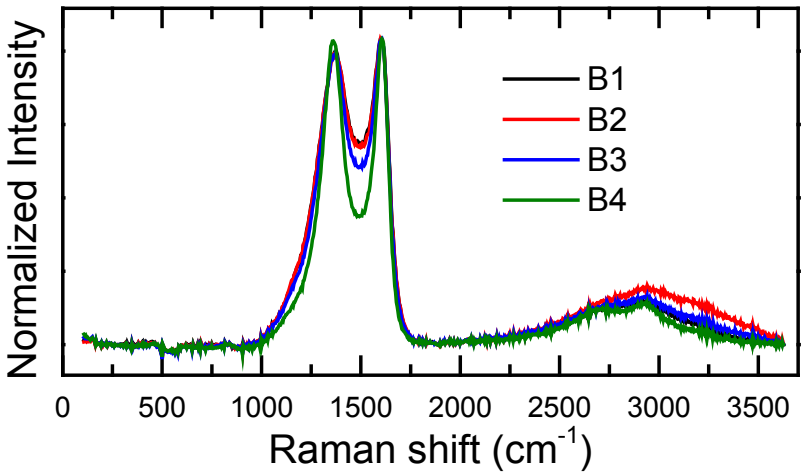

Figure IV.8-6. Average Raman spectroscopy of the cross section of the carbonized fiber with mechanical properties displayed in I. The sample B4 shows much narrower D and G-bands than the other batches and means ordering is better at higher temperatures.

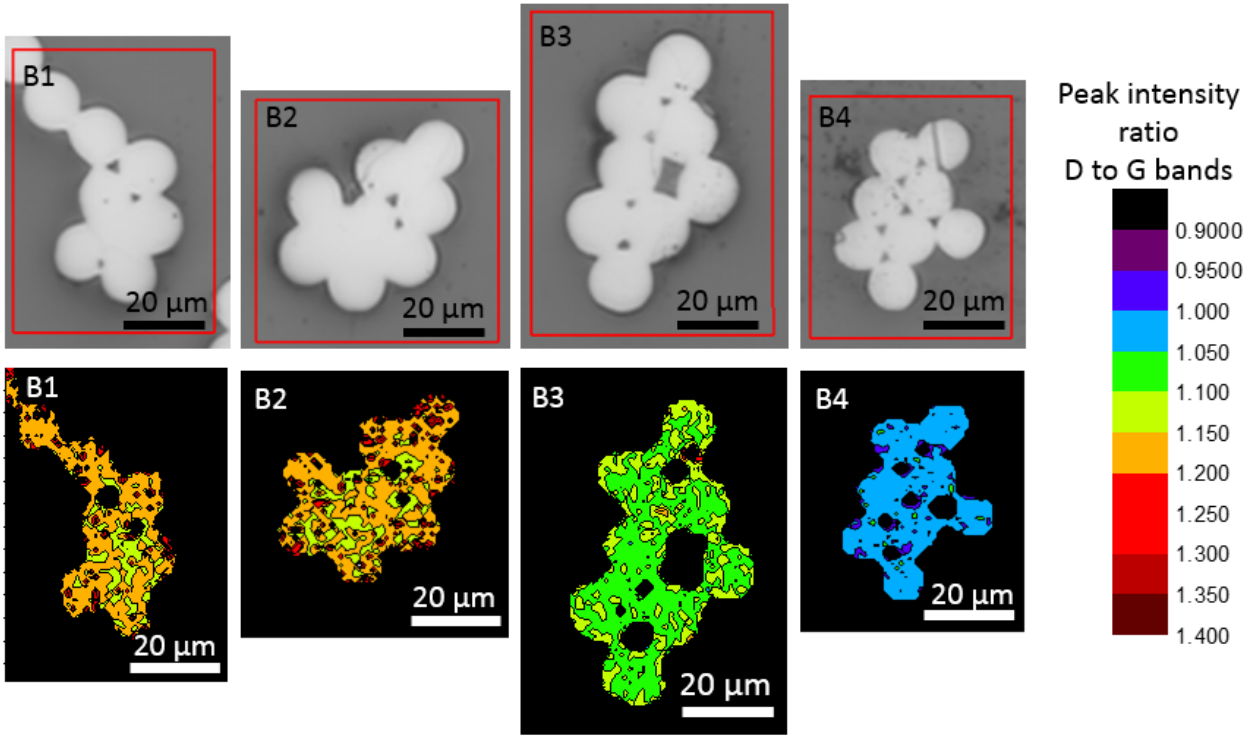

Figure IV.8-7. Optical and resonance Raman spectroscopy images of the cross sections of the bundles B1 to B4 presented in Table IV.8-1. The map of D/G shows that this ratio is decreasing with the increased temperature of thermal treatment, which means that ordering is better at higher temperature (lower D/G ratio).

Task 3: Techno-Economic Analysis

An expanded techno-economic analysis determined the relative cost of production with the bacterial production system shown in Figure IV.8-8 compared to the transgenic alfalfa and goat production systems shown in Figure IV.8-9.

The comparisons show two important things. First, for all systems, the key factor in the final price is the amount of spider silk protein produced for whatever measure of volume or weight is used. Second, alfalfa can be the cheapest but is subject to the possible regulatory control unless the United States develops a more comprehensive approach for genetically modified organisms. The silkworm analysis is complete due to a variety of confounding factors. The primary one was that if the production shifted overseas, then the cost would likely be nearly equivalent to current silk prices of $5 to $15/kg. However, if concerns about the location of production were important, then it would need to be done in the United States and initial costs would be much higher; however, if the later scenario were utilized, then the cost would be lowered. Calculations for exact costs were not possible.

Technology Transfer Path

Utah State University is negotiating a joint research effort with an automobile parts designer in California.

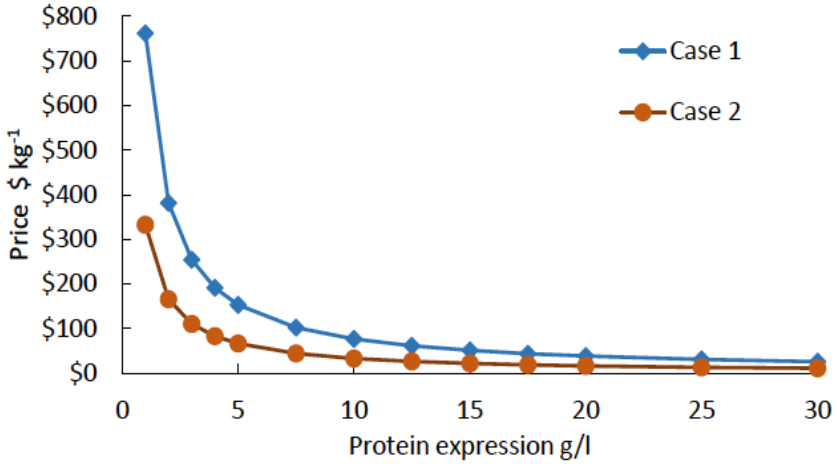

Figure IV.8-8. Product sales price as a function of protein expression in *E. coli* for the initial purification scenario, Case 1 (initial costs), and the new optimized purification scenario, Case 2.

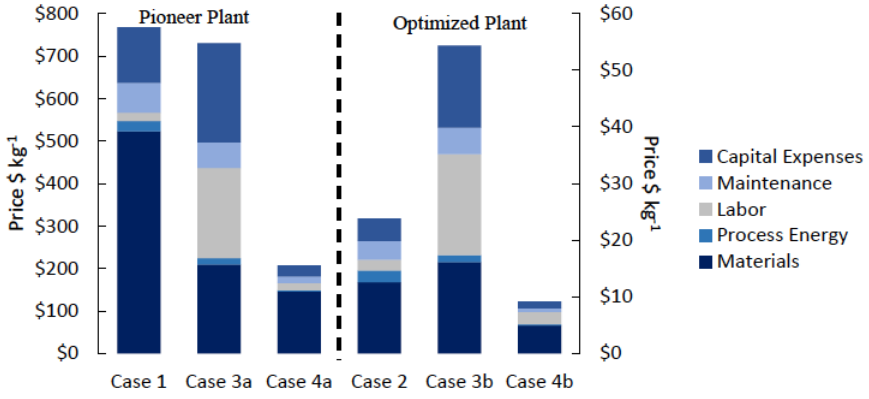

Figure IV.8-9. Synthetic spider silk sales price estimates from various facilities and levels of optimization. Cases 1 and 2 are from Figure 5 at low protein production from *E.coli*. Cases 3a and 3b are the initial and optimized goat milk production and Cases 4a and 4b are for alfalfa production initial and optimized.

Conclusion

Task 1: Fiber Synthesis

For the protein production subtask, 1.0 g/L of purified spider silk protein (MSp2) was produced, which exceeds the go/no-go milestone from FY 2015 and fermentations were increased from 5 to 500 L. Changes were made to the purification protocol, which led to a reduction in the purification time needed and reduced the purification costs by nearly 90%.

The major focus for fiber spinning was to produce sufficient material to send several 24-fiber thread to ORNL for carbonization. The methodology is under development to successfully spin 24-fiber yarns. This involves both spinning solutions and methods for keeping the fibers from fusing during the post-spin stretch.

A second area of focus was to standardize the spin dopes for making the fibers. Conductivity is an important factor in successful spinning and needs to be below 600 μS. The most effective pH is protein dependent.

The transgenic silkworms made using gene replacement at the fibroin light chain instead of heavy chain have a higher tensile strength. This tensile strength is the same as the average for spider dragline silk.

Task 2. Carbonization

ORNL successfully carbonized the spider silk protein fibers up to 1700°C and maintained a useable fiber, which is a major accomplishment. There was discovery of several important factors during these initial trials: (1) ramp speed for increasing the temperature is critical; (2) tension on the fiber needs to be maintained during the heating process because it tends to expand as it is heated; and (3) a narrow temperature window where stretching the fiber during heating leads to much better final materials. Different spider silk proteins and crosslinking methods need developed to achieve higher tensile strengths of the carbonized fibers.

Task 3. Techno-Economic Analysis

An expanded techno-economic analysis determined the relative cost of production, with the bacterial production system being compared to the transgenic alfalfa and goat production systems. The comparisons show two important things. First, for all systems, the most important factor in the final price is the amount of spider silk protein produced. Second, alfalfa can be the cheapest, but may be subject to regulatory issues (see Figures IV.8-8 and IV.8-9). The silkworm analysis is incomplete due to a variety of confounding factors, including intellectual property issues if the production shifts from the United States.

The project was approved for a no cost extension until 09/30/2017 to allow for completion of the project.

Bibliography

Copeland, C. G., E. Brianne, B. E. Bell, C. D. Christensen, V. Randolph, and R. V. Lewis, 2015, "Development of a Process for the Spinning of Synthetic Spider Silk," *ACS Biomaterials Science and Engineering* 1(7): 577–584, accessed December 13, 2016, http://pubs.acs.org/doi/abs/10.1021/acsbiomaterials.5b00092?src=recsys&journalCode=abseba.

V. Multi-Material Joining

V.1 Friction Stir Scribe Joining of Aluminum to Steel – Pacific Northwest National Laboratory

Piyush Upadhyay, Principal Investigator
Pacific Northwest National Laboratory (PNNL)
902 Battelle Boulevard
PSL/424
MSIN K2-03
Richland, WA 99352 USA
Phone: 509-375-6591
E-mail: piyush.upadhyay@pnnl.gov

Sarah Kleinbaum, Technology Area Development Manager
U.S. Department of Energy
1000 Independence Avenue, SW
Washington, DC 20585
Phone: 202-586-8027
E-mail: sarah.ollila@ee.doe.gov

Contractor: PNNL
Contract No.: DE-AC05-00OR22725 & DE-AC06-76RL01830

Executive Summary

The purpose of this project is to develop a joining technology needed to demonstrate the fabrication of dissimilar aluminum (Al)-steel assemblies that can enable direct replacement of steel components with lightweight Al alternative for high-volume applications. The objectives of the proposed work are to mature friction stir scribe (FSS) technology for implementation and to demonstrate the required Al-steel mechanical properties in industrially relevant components. Specifically, the project will develop the critical process technology, models, and tools necessary to advance the friction FSS method through experimentation, validation at the laboratory scale, and integration into a production-like environment to demonstrate viability of FSS technique on industrially relevant components. Additionally, the project also aims to transfer technological understanding, tool designs, and parameters to the participating original equipment manufacturers (OEMs) and suppliers to aid in direct joining of Al and steel assemblies and components.

Accomplishments

- Produced FSS joint between cast Al (3 mm) to mild steel (2 mm) and AA6022 (1 mm) to mild steel (0.7 mm); also supplied joint coupons to corresponding OEM for individual evaluation, including corrosion and impact testing (Fiscal Year [FY] 2016).
- Established welding parameters and tool design to produce FSS joints with quasi-static strength greater than 70% of weaker base metal for dissimilar joints between an Al alloy (Surfalex 6s, 1.1 mm) and transformation-induced plasticity (TRIP 590) steel (1.6 mm) for body and chassis application (FY 2016).
- Integrated stationary shoulder with FSS technique and initiated implementation of FSS and stationary shoulder for AA6022 mild steel dissimilar joining application for prototypical demonstration (FY 2016).

- Developed computational model of Al-steel FSS joint and investigated effects of hook morphology on mechanical property and fracture mode (FY 2016).

Future Directions

- Demonstrate the capability of the FSS process to extend to alternative material combinations, including progressively higher-strength steels up to and including fully martensitic steels.
- Evaluate the feasibility of extending advanced technologies (e.g., adjustable pin technology and stationary shoulder) to the FSS process to allow for greater process flexibility to industrial partners interested in implementing the process for multi-material joining.
- Demonstrate the ability to predict joint properties, failure mechanisms, and failure locations of FSS joints in aluminum/steel.
- Complete prototypical technology demonstrations at the facilities of an industrial partner.

Technology Assessment

- Target: Achieve 70% joint efficiency for dissimilar Al-steel joints between various combinations of Al and steel in production environments.
- Gap: Conventional linear solid-state joining techniques for dissimilar material combinations rely on bonding mechanisms that rarely approach the structural strengths of the base materials and cannot adequately manage the interfacial heat of dissimilar materials like Al and steel to remain truly solid state. The temperatures required to plastically form steel are higher than the melting temperature of Al; therefore, intermetallic formation at the joint interface cannot be managed to produce quality, uniform joints.
- Target: Demonstrate the FSS technique in a production environment.
- Gap: FSS has yet to be demonstrated in production environments.

Introduction

This project addresses the joining aspects of lightweight dissimilar metal structures made with Al and steel with the aim of achieving the U.S. Department of Energy's goal of increasing the efficiency of vehicle transportation by enabling more efficient multi-material solutions. Project collaborators include General Motors, Honda R&D America, and Fiat Chrysler Automobiles. They are actively involved in the project by providing materials, demonstration parts, and unique expertise related to the specific hybrid joining needs. Kuka Systems (i.e., an automotive supplier and robotic integrator) is another project collaborator that provides robotic implementation of the FSS technique in the automotive supply chain.

The technology to be developed, if successful, will provide a new method for enabling low-cost joining of Al alloy components to existing steel structures. Success in the project will enable direct replacement of steel components with Al that can achieve a mass savings of more than 40% while maintaining the form and function of existing steel structures. The project provides direct integration of joining technology to participating automotive OEMs for Al-steel assembly. PNNL will develop, characterize, and transfer unique joining parameters for specific applications provided by participating collaborators. This includes applications ranging from body structures to assembly of Al chassis components onto a steel substructure. Each specific application will be developed sufficiently to determine the overall properties, welding parameter operating window, tooling and fixture requirements, and computational design specifications. Upon successful completion of development at the laboratory-scale, each participant will demonstrate a prototypical application-specific mock-up using the FSS process.

Approach

To develop joining technology that enables hybrid Al-steel structures and assemblies for high-volume automotive production lines, the project is divided into four main task areas. The first task focuses on initial joint development and characterization for each of the selected Al-steel combinations associated with the demonstration needs of each OEM. This includes developing weld parameters, tool design, and other process requirements for achieving acceptable joint performance. The second task is designed to expand overall application of FSS, optimize tooling, introduce stationary shoulder and retractable pin technologies, and provide applicability across numerous alloys, thicknesses, and material combinations. This task ultimately will lead to a decision gate for use of the developed knowledge base in prototypical demonstrations associated with Task 3 by providing the information necessary to justify capital investments and product design using Al-steel joints.

Task 3 is divided into several subtasks that will emphasize the preparation process for commercialization and demonstrating the process in a production-like environment. This task focuses on supporting transfer of technology into each of the OEM's facilities/suppliers to allow for prototypical demonstrations by each industrial participant. The final task will use the information developed in Tasks 1 and 2 to calibrate a numerical modeling tool for prediction of joint performance, failure location, and failure mode, and, finally, to validate the predictive tool against new material combinations and demonstration parts. Figure V.1-1 shows the Al-steel combinations selected by each OEM for investigation in task 1 and demonstrated in task 3.

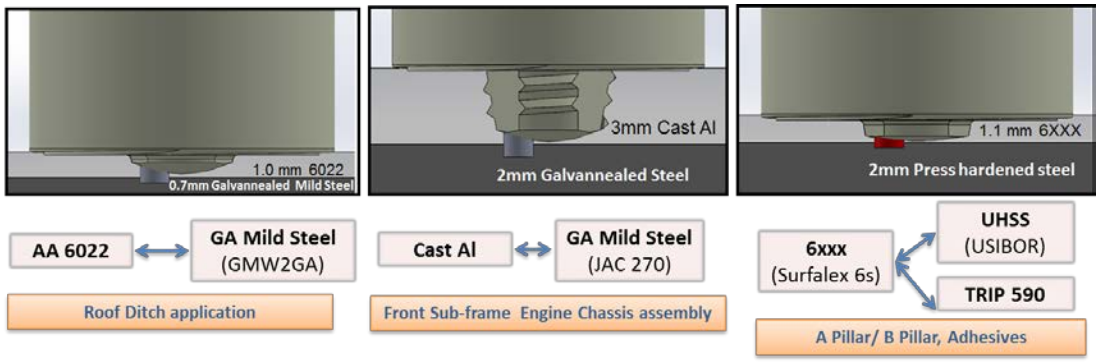

Figure V.1-1. A snapshot of Al-steel combinations being evaluated in this project, including welding tool setup and OEM-intended applications.

During FY2015, the FSS tools were optimized for initial material sets desired and supplied by participating OEMs. The efforts during FY 2016 began with evaluating the repeatability of the process in a specific material set and fabricating joints for evaluation by individual OEMs. Additionally, an FSS technique was further evaluated in high-strength steel, including TRIP 590 and ultra-high-strength steel (UHSS). This led to the discovery of a tool durability challenge associated with UHSS that is discussed in the results section. The PNNL project team, in association with participating OEMs, also made progress in selecting near-prototype parts where the FSS technique could be demonstrated as the process is matured beyond the coupon levels.

Results and Discussion

Experimental Work

Figure V.1-2 shows representative welded panels produced using an FSS technique for a variety of Al and steel combinations. For two combinations, (a) AA6022 (1 mm) to mild steel (0.7 mm) and (b) cast Al (3 mm) to mild steel (2 mm), a large number of welded coupons amounting to a linear weld length of about 100 in. were sent to the corresponding OEM (General Motors in Warren, Michigan and Honda R&D America in Raymond, Ohio, respectively). The OEM partners have begun joint testing, including, but not limited to, impact and corrosion testing for internal evaluation and comparison with existing technology.

Figure V.1-2. Representative Al-steel welded panels produced using the FSS technique.

An initial set of results obtained from lap shear testing of weld transverse samples (i.e., cast Al [3 mm] to mild steel [2 mm] from Honda R&D America) that were extracted from three locations along the length of a weld are shown in Figure V.1-3 and are represented in terms of load per unit weld length versus measured displacements. The obtained lap shear strength value (i.e., about 270 to 340 N/mm) exceeds the OEM requirement. In addition to lap shear strength, the mode of fracture and resulting elongation (i.e., representative of energy absorption) are also of interest in light of specific automotive applications. Figure V.1-3 shows fractured lap shear samples and corresponding joint cross-sections extracted from locations near each of the lap shear samples. For ease of comprehension, the three sample locations will be referred in the following paragraph as "near start" (S+52), "near middle" (S+138) and "near end" (S+209) samples.

The measured displacement, indicative of energy absorption of the FSS joint, is greater in "near start" and "near end" samples, that fracture through the Al nugget, compared to the interfacial fracture of the "near middle" sample. The joint cross-section from nearby locations can be used to understand this difference in the failure mode. In all three cross-sections (Figure V.1-4), the machining of steel surface by the FSS scribe is apparent. However, the extent of machining and morphology of resulting features are different. At the outset, the extent of machining is significantly greater in the "near end" sample compared to the other two cross-sections. Presence of hook like features are apparent in the "near end" cross-section, smaller hook like features are also present in the "near start" sample. In contrast, hook like features are absent on either side of the "near middle" sample despite evidence of machining. This suggests that the fracture mode of lap shear samples correlates well with the presence of hook. While the "near start" and "near end" samples fractured through the welded Al (i.e., near the advancing side nugget/hook interface), the sample in the middle failed in the interface, which resulted in much smaller elongation. It is also important to note that although the mode of failure is the same in both the "near end" and "near start" cases, the resulting elongation at peak strength is significantly larger for the "near end" perhaps due to a larger hook-like feature in the "near end" sample.

Thickness of the cast Al coupon was found to vary from 2.98 to 3.06 mm, with the thickest location being in the middle of the plate. Because the FSS tool position was controlled relative to the top surface of the Al, the scribe depth (or "z" position) was reduced at the mid-section and resulted in lesser scribe engagement on the steel. For the same reason, the sections of weld with thinner Al showed excessive hook formation even though the strength requirement set by OEM was met.

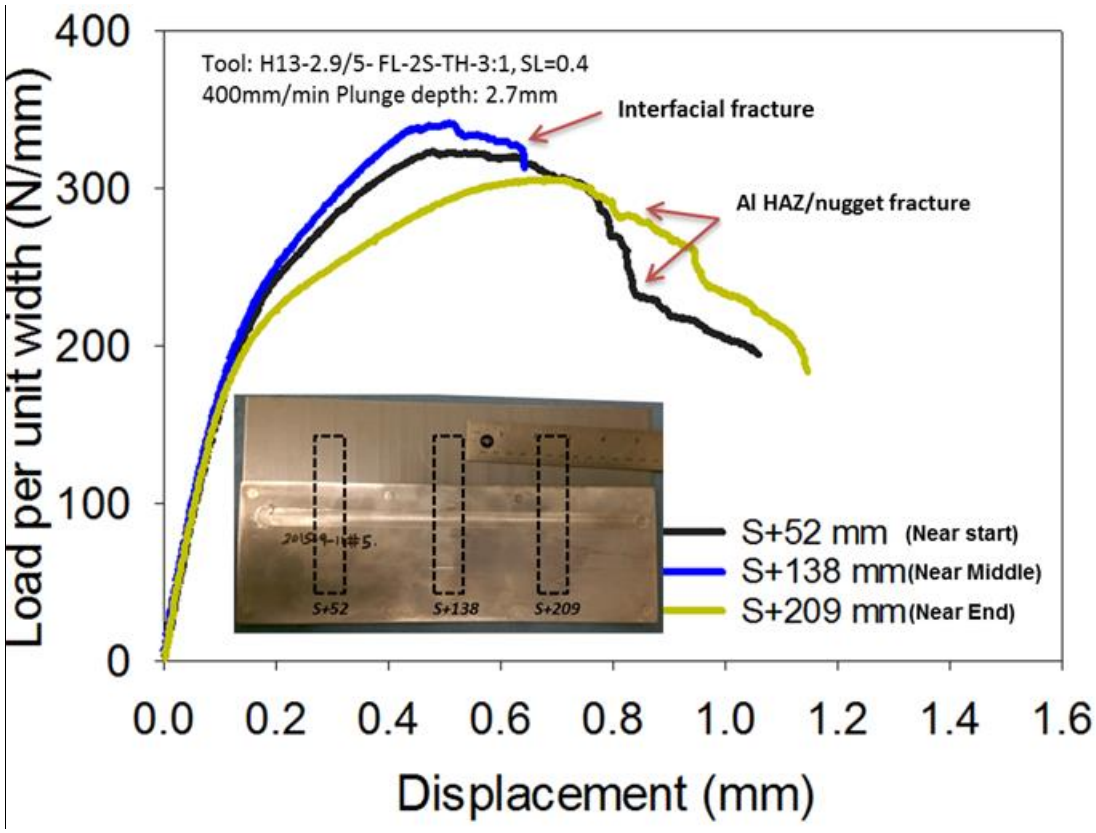

Figure V.1-3. Load per unit weld length plotted against measure displacement during lap shear testing of the FSS joint between cast Al (3 mm) to mild steel (2 mm). The locations where lap shear samples were extracted are shown using dotted boxes. The mode of fracture (interfacial or in the heat affected zone (HAZ)) is indicated for each sample.

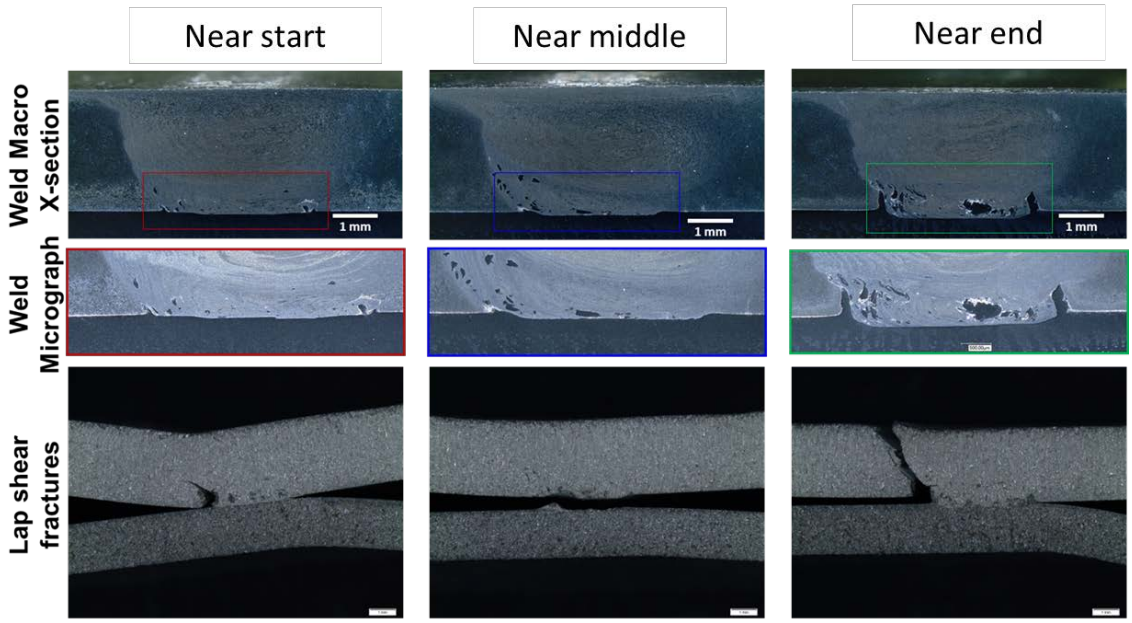

Figure V.1-4. Weld macro cross sections, micro graphs, and fracture location (i.e., corresponding rows) for welded specimens at different distances from the start (i.e., corresponding columns). Lap shear strength results for this weld are shown in Figure V.1-3

Figure V.1-5 shows load per unit weld length obtained from three tested samples for welds made at three different welding conditions arranged in the order of heat input per unit weld length. The heat index is defined as $\frac{\text{Welding Speed}^2}{\text{Tool RPM}}$ [1]. For the lower heat index of 1340, the reduced heat input has resulted in uniform lap shear strength. The load versus extension curves for the welds corresponding to the lowest heat index of 1340 (1,100 rpm at 900 mm/min) are given in Figure V.1-6. This shows a higher and more consistent load-bearing capacity and elongation values compared to the results for cast Al and mild steel weld shown previously in Figure V.1-3 where the heat index of 9500 (950rpm at 400mm/min) was significantly higher. Figure V.1-7 illustrates the joint cross sections from an optimized FSS joint shown in Figure V.1-6 and right-most bar chart in Figure V.1-5. This is in line with consistent mechanical properties for the joint cross section and also shows consistent hook formation from the beginning to the end of the weld.

As reported in FY 2015, the project has demonstrated joint strength greater than 70% of the weaker Al in precipitation-hardened Al (i.e., Surfalex 6s) joined to UHSS (i.e., USIBOR). Upon further repeatability examination, a rapidly built-up edge formation was observed around the cutter scribe, thus significantly affecting repeatability using the current choice of the H13 tool material. The problem discovery can be summarized in Figure V.1-8. Figure V.1-8(a) shows the FSS tool after several FSS joints between Al and mild steel containing a layer of Al around the shoulder pin and scribe cutter. The Al layer was then cleaned off from the tool using a caustic solution to reveal the cutting edge of the scribe with a relatively intact cutting edge shown in Figure V.1-8(b). A similar tool was used to make a FSS joint with UHSS and is shown in Figure V.1-8(c).

Unlike the tool used for mild steel, a significant amount of material build-up has been observed with UHSS. At high temperatures, the plasticized steel "welds" on the surface of the tool pin (i.e., H13 material) likely because of some iron-carbon bonding, thus blunting the cutting edge. While some amount of built-up edge is seen even with softer steels after numerous welding runs, the result is lot more severe with UHSS because the cutting characteristics are modified. In order to reduce susceptibility of material build-up, a uni-body tool design is required that incorporates both a cutting scribe and FSS tool into a single manufacturing process. A scribe and FSW tool made of harder material (e.g., tungsten-carbon-cobalt) has been designed and is currently being prepared for evaluation. It is anticipated that use of uni-body tools will reduce the built-up edge and increase the tool's life in joining UHSSs.

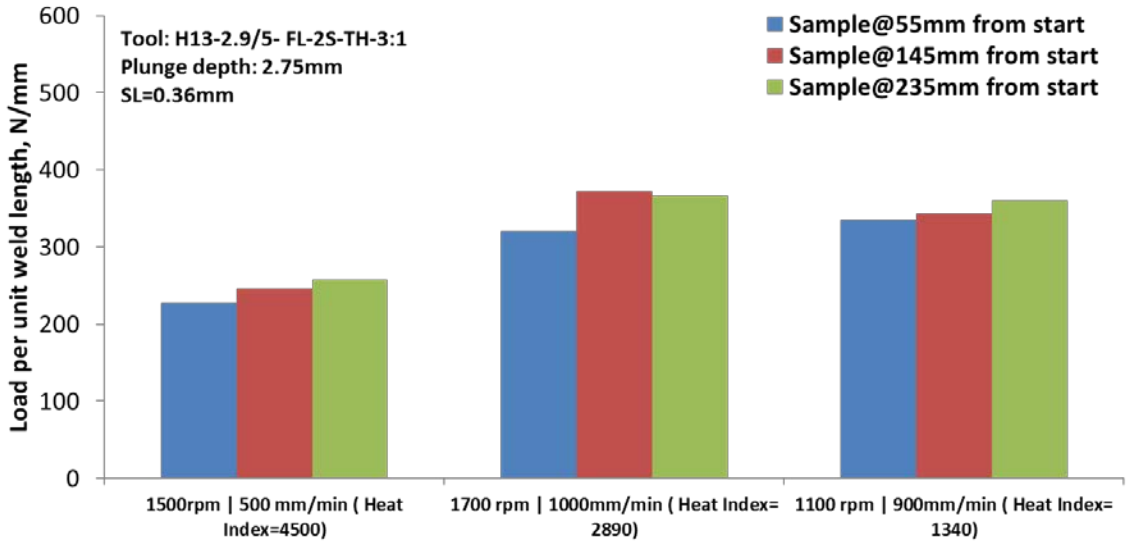

Figure V.1-5. Load per unit weld length corresponding to the top three sets of welding parameters arranged in descending order of heat input. Welds made between cast Al (3 mm) to mild steel (2 mm).

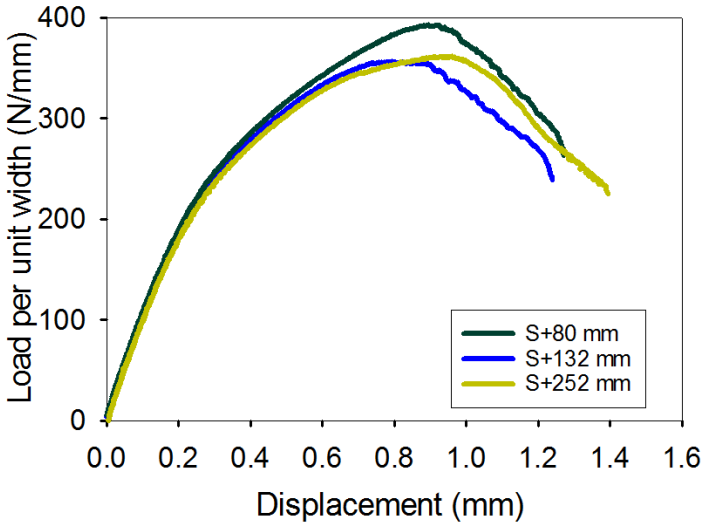

Figure V.1-6. Load per unit weld length plotted against the measure displacement during lap shear testing of an optimized FSS joint (between cast Al [3 mm] to mild steel [2 mm]) (1,100 rpm at 900 mm/min).

Figure V.1-7. Joint cross sections from an optimized FSS joint shown in Figure V.1-6 and right-most bar chart in Figure V.1-5.

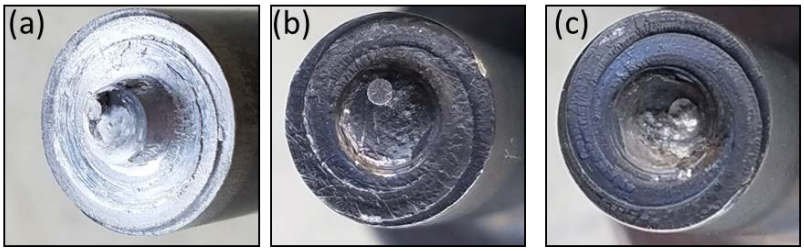

Figure V.1-8. (a) FSS tool after several welds between Al and mild steel. (b) Cleaned tool after several welds between Al and mild steel, revealing the cutting edge of the scribe cutter. (c) Cleaned tool after three welds between Al and UHSS (i.e., USIBOR), showing the built-up edge around the scribe region.

In addition to UHSS, we also evaluated the FSS process for joining Surfalex 6S with TRIP 590 steel (a steel of choice for A pillar/B pillar designs). Load versus displacement curves for these joints are shown in Figure V.1-9. For the samples tested, fractures occurred outside the weld region in the base Al (see Figure V.1-10). The joint cross section shows relatively small amounts of hook formation, which suggests that an intermetallic compound formation may be providing some extent of bond strength. As repeatability in this material is evaluated in FY 2017, the project plans to characterize intermetallic compounds between the interfaces.

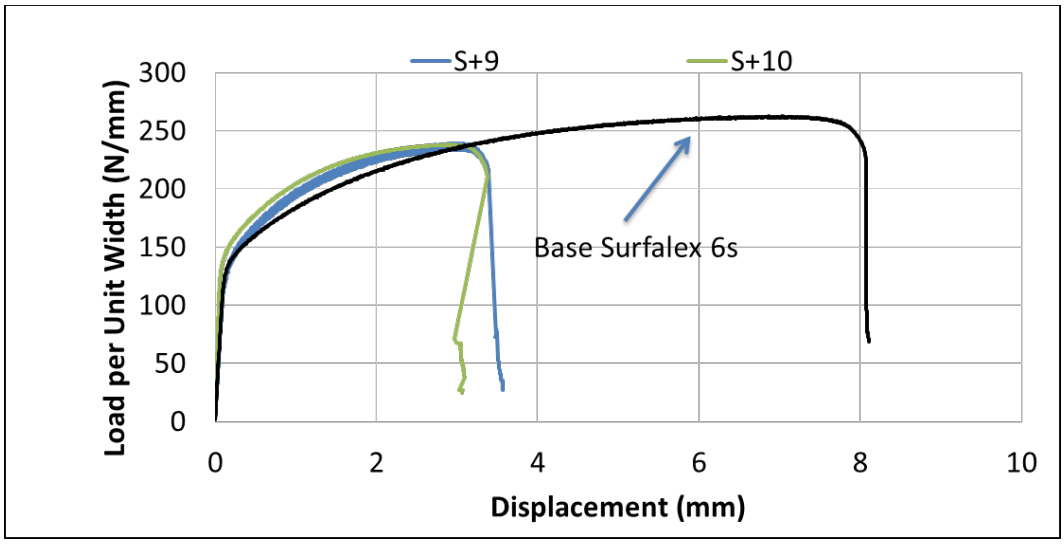

Figure V.1-9. Load per unit weld length versus displacement for the welded joint (Surfalex 6S TRIP 590 steel) and base Al.

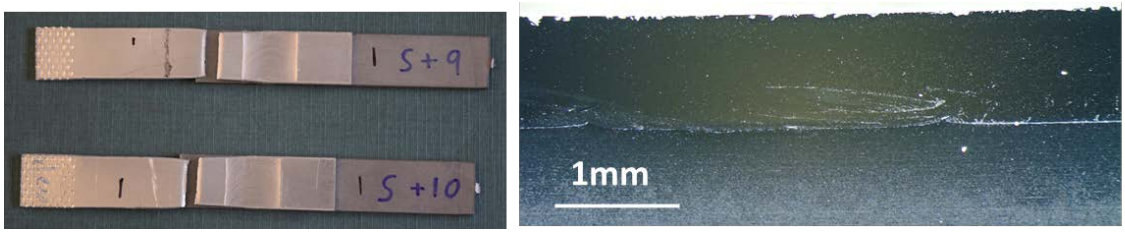

Figure V.1-10. The fractured samples and a representative joint cross section.

As the project moves beyond coupon-level evaluation of FSS technology, a stationary shoulder design is integrated with FSS technology in PNNL's facility. Because of the absence of bulk material movement and heat at the shoulder, the stationary shoulder FSS technology allows for a significantly smoother weld crown surface [2]. For the AA6022 (1 mm) to mild steel (0.7 mm) material set with intended use in a roof ditch application, the ability to produce welds with a smooth crown is critical. To this end, a stationary shoulder setup was designed and implemented in FY 2016 (see Figure V.1-11). A comparison between weld crown surfaces obtained with a stationary shoulder and a conventional rotating shoulder is also presented. In initial lap shear-tested samples, an equivalent load bearing capacity of greater than 50% of the base mild steel was observed. This value is less than previous values obtained with a conventional rotation shoulder [3]. It is anticipated that after weld and shoulder design optimization is completed during FY 2017, joint strength closer to the rotating shoulder welds can be achieved. Note that use of a stationary shoulder required greater heat input per unit weld length for a defect free weld; therefore, a much slower welding speed is needed if everything else remains constant when compared to a conventional method.

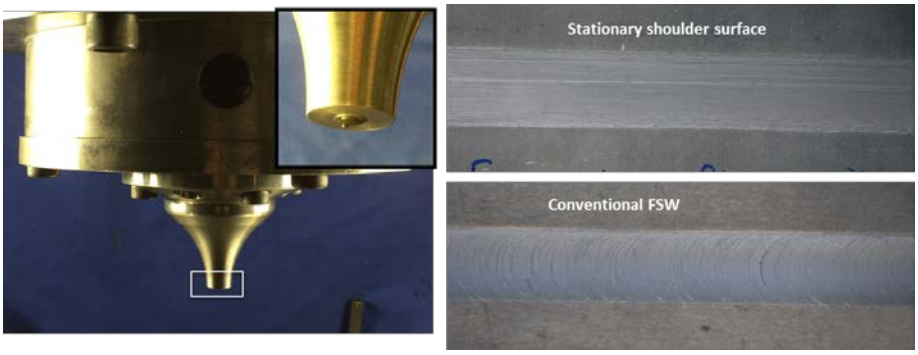

Figure V.1-11. Stationary shoulder setup integrated with FSS technology (left). Comparison between weld crown surfaces obtained with stationary shoulder and conventional rotating shoulder (right).

In addition to evaluation and optimization of a stationary shoulder, we also initiated joining trials with steel sheets to a non-uniform surface. General Motors provided sandwich steel coupons containing spot welds and/or adhesives with an irregular surface (thickness variation from 20 to 100% of Al thickness). Process optimization and assessments are underway to evaluate the extent of thickness variation in the steel layer the FSS technique can accommodate.

Modeling Work

The experimentally measured load versus displacement curves for FSS lap joints show consistent yield stress and tensile strength across samples; however, some variations in elongation to failure are observed. Visual inspection of the FSS joint region shows consistent formation of hook features. However, the morphology of the hooks can vary along the length of a given weld. Initial modeling of FSS lap joints investigated the impact of hook morphology on joint strength in order to build a predictive modeling capability.

A two-dimensional finite element model of the lap joint was built using LS-DYNA. The initial hook morphology was based on an actual joint cross section. Figure V.1-12(a) shows the initial joint model for a 1-mm thick sheet of 6022 Al on top of a 0.7-mm sheet of galvanized mild steel. Hardness values extracted through micro-indentation tests on joint cross sections also indicate variation in material properties in the heat-affected zone beyond the nugget in the Al top sheet. Hardness variations in the steel bottom sheet also indicate a heat-affected zone. Therefore, the initial model was modified to include these different material property regions (see Figure V.1-12(b)). Additional versions of the model were generated with specific modifications to the hook morphology to study the impact on joint strength.

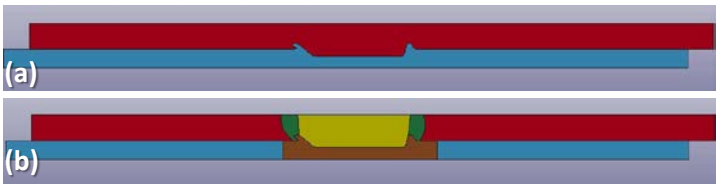

Figure V.1-12. Two-dimensional finite element model geometry made using LS-DYNA: (a) initial FSS joint geometry with Al top plate and steel bottom plate and (b) modified joint geometry to include multiple material property regions.

Based on multiple FSS joint cross sections, variations to the left hook morphology were generated. Figure V.1-13 shows the various hook morphologies. Boundary conditions for the model include fixing the left end of the bottom plate and applying a displacement to the right end of the top plate. This simulates pulling the model to the right. The boundary conditions can be flipped to simulate pulling to the left.

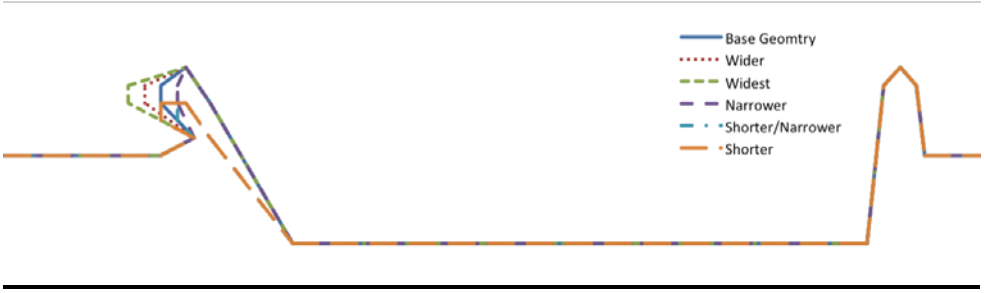

Figure V.1-13. Variations of left hook morphology.

Figure V.1-14 shows load versus displacement for each of the hook morphologies. The solid black line is the base hook morphology and the dashed black line is an example experimental measurement. The simulated yield strength and tensile strength compare well to experimental results. However, the current model setup demonstrates ductility at the low end of the experimentally observed values. This may be related to modeling the joint in two dimensions rather than three dimensions. The impact of model thickness is currently being investigated. The simulated lap joints failed in the Al top sheet along the interface between the nugget and the heat affected zone on the loaded side as seen in experimental results.

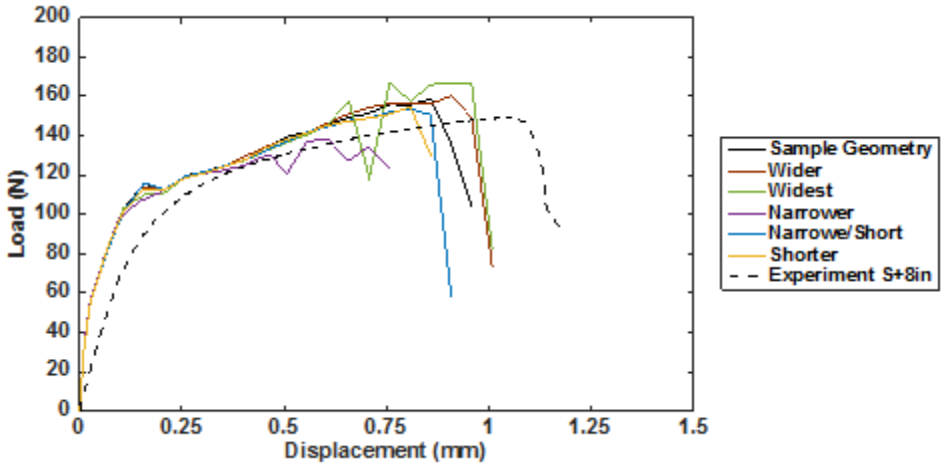

Figure V.1-14. Load versus displacement for FSS lap joint model with various hook morphologies.

Additional analyses are being conducted with boundary conditions that simulate pulling the model to the left. The direction of loading determines which hook is primarily loaded. Initial results show that changing the loading direction alters which side of the nugget the Al top sheet fails on. It should also be noted that including the hardness variation (seen in the bottom sheet after welding) have been observed to affect failure locations from interfacial failure to failure occurring through the aluminum weld nugget. This effect will be investigated further with welding samples with different hardness variation to ascertain the effect of local property changes in predictability of joint strength and failure modes.

Technology Transfer Path

As one of the primary goals of this project, transferring the FSS process to the industrial participants is part of everyday project execution. First, the team brings together multiple automotive OEMs and a robotic supplier into a single team to evaluate FSS of Al to steel in various and unique applications. The project team develops the welding process and provides mechanical testing and characterization throughout development to demonstrate how the technology is applied to various applications. This ranges from thin wrought Al alloys being joined to mild sheet steels to high-pressure vacuum die-cast Al being joined to advanced high-strength steels. Monthly calls bring together the team to evaluate the process, provide opportunities to educate and discuss the nuances of the process, and provide updates on the latest development. This forum provides design guidelines that establish a methodology for applying the FSS process across a more diverse set of materials and, ultimately, strengthens the ability for industrial partners to make informed decisions regarding where and how to implement the FSS joining process for optimized multi-material designs.

Conclusion

Working in association with three automotive OEMs and a supplier, a large window of welding parameters and tool geometry was investigated across several sets of Al and steel combinations. During the process, a large collection of data sets, including joint cross sections, resulting hook features, lap shear strength, weld forces, and torque, have been generated and analyzed. With the inherent thickness variations in the cast Al sheet used, some variation in hook features was observed. Use of relatively lower-heat input provided better uniformity in the joint property, including the crown flash level and hook geometry. Tool build-up around the edge of the scribe region of the FSS tool tip was identified as a tool durability issue in joining UHSS (1,500 MPa) to Al. A potential solution with uni-body tool design is being considered to minimize edge build-up. Work has also begun in evaluating the FSS technology to produce prototype components in association with participating OEMs and suppliers, including development of stationary shoulder FSS technology. Modeling efforts are underway to develop a predictive capability to ascertain fracture mode and joint strength.

References

[1] Mishra, R. S. and M. W. Mahoney, 2007, "Friction Stir Welding and Processing," *ASM International*.

[2] Russell, M. J., M. E. Nunn, and J. Martin, 2008, "Recent Developments in the Stationary Shoulder FSW of Titanium Alloys," *Proceedings of Seventh International Symposium on Friction Stir Welding*, TWI, Japan.

[3] Upadhyay, P., Y. Hovanski, S. Jana, and L. S. Fifield, 2016, "Joining Dissimilar Materials Using Friction Stir Scribe Technique," Journal of Manufacturing Science and Engineering 139(3): 034501–034501.

Bibliography

Hovanski, Y., P. Upadhyay, S. Jana, and L. S. Fifield, 2015, "Joining Dissimilar Materials with Friction Stir Scribe Technology," *4th International Conference on Friction Stir Welding and Processing – 2015*, Ordizia, Spain, October 1, 2015.

Hovanski, Y., P. Upadhyay, S. Jana, and L. S. Fifield, 2015, "Joining Dissimilar Materials with Friction Stir Scribe Technology," *Aeromat 2016*, Bellevue, Washington, May 24, 2016.

Hovanski, Y., G. J. Grant, S. Jana, and K. F. Mattlin, 2013, "Friction Stir Welding Tool and Process for Welding Dissimilar Materials," US8434661 B2, May 7, 2013.

Upadhyay, P., Y. Hovanski, B. Carlson, R. Ruokolainen, P. Busuttil, and E. Boettcher, 2015, "Solid-State Joining of Aluminum to Steel Using Friction Stir Scribe," *Materials Science & Technology,* Columbus, Ohio.

Upadhyay, P., Y. Hovanski, S. Jana, and L. S. Fifield, "Joining Dissimilar Materials Using Friction Stir Scribe Technique," Material.

V.2 High-Strength, Dissimilar Alloy Aluminum Tailor-Welded Blanks – Pacific Northwest National Laboratory

Project Details

Piyush Upadhyay, Principal Investigator
Pacific Northwest National Laboratory (PNNL)
902 Battelle Boulevard
PSL/424
MSIN K2-03
Richland, WA 99352 USA
Phone: 509-375-6591
E-mail: piyush.upadhyay@pnnl.gov

Sarah Kleinbaum, Technology Area Development Manager
U.S. Department of Energy
1000 Independence Avenue, SW
Washington, DC 20585
Phone: 202-287-5371
E-mail: sarah.ollila@ee.doe.gov

Contractor: PNNL
Contract No.: DE-AC05-00OR22725 and DE-AC06-76RL01830

Executive Summary

The purpose of this project is to further develop high-speed friction-stir welding (FSW) to accommodate dissimilar aluminum alloy combinations in both linear and curvilinear geometries. This includes combinations that accommodate mixtures of work-hardenable alloys that demonstrate deep drawing capabilities, with precipitation-hardenable alloys that can be hardened after joining and forming to develop the high strengths required for body skins and structural supports. This work will develop the novel material coefficients needed to support formability modeling of dissimilar alloy structures that have properties ranging from strain hardening to heat-affected zone (HAZ) property degradation across a fixed panel. These material coefficients will be combined with properties of the base materials to allow for simulation of forming dissimilar alloy and dissimilar thickness aluminum tailor-welded blanks (TWBs). Simulated results will be validated on prototypical parts produced by the supplier to demonstrate production deployability within the duration of the 3-year effort. In Fiscal Year (FY) 2016, the project completed fundamental characterization of various aluminum alloys made at high welding speeds. The project also began technology transfer by successfully transferring welding parameters and scheduling production of a specific set of dissimilar thickness/alloy combinations using FSW equipment at the supplier's facility in both linear and curvilinear two-dimensional paths.

Accomplishments

- Generated and compiled data sets for advanced characterization of aluminum TWB (5xxx, 6xxx, and 7xxx), including nugget and HAZ texture and scanning electron microscopy analysis for a range of high welding speeds.
- Developed welding parameter sets to produce dissimilar thickness/alloy FSW joints between: (a) AA7075-T6 (2 mm) and AA5182-O (1.1 mm); (b) 6022-T4 (2 mm) and AA5182-O (1.1 mm); and (c) AA7085-T6 (2 mm) and AA5182-O (1.1 mm).

- Transferred welding parameters and tooling designs to produce dissimilar thickness/alloy FSW joints to original equipment manufacturers (OEMs) and supplier for demonstration trials with production equipment.
- Developed optimum joining parameter window and tooling requirements for curvilinear high-speed FSW in both similar and dissimilar alloy combinations (5182-O [1.1 mm] and 6022-T4 [2 mm]) at the supplier facility, using a commercial production FSW machine.
- Developed correlations between welded and naturally aged TWB panels (similar thickness precipitation-strengthened alloy) at the supplier's facility to address the ability to adequately evaluate welds in high-volume production environments.
- Produced and provided welded joint test panels to General Motors (GM) for Barlat coefficient determination in the weld region.

Future Directions

- Determine process sensitivity in producing repeatable welds for dissimilar alloy/thickness FSW and increasing the welding speed for high-volume production.
- Characterize coefficients of the Barlat yield criterion for weld regions in association with GM and Alcoa for similar and dissimilar alloy FSW.
- Expand formability model to include weld metal properties of similar and dissimilar alloy combination (i.e., results from above bullet point) and validate using actual joined panels.
- Determine tool durability and influence of tool material and coatings on weld quality, process repeatability, and production readiness.
- Validate process parameters, demonstrating near-term deployability by the supplier for high-volume commercial production.

Technology Assessment

- Target: Achieve FSW speeds for dissimilar aluminum TWBs in excess of 3 m/minute with repeatable quality and surface finish.
- Gap: While similar and dissimilar alloy aluminum TWBs have been demonstrated to be weldable above 3 m/minute, developments are needed to ascertain repeatability because of the inherent problem of different high-temperature flow stress for dissimilar materials.
- Target: Develop high-speed welding parameters so the soft zone typically present at the HAZ in precipitation hardening alloys is recrystallized.
- Gap: Commercially relevant welding speeds are higher than demonstrated at the research scale and robust processing parameters need to be developed that produce quality parts.
- Target: Develop material constitutive relationships, including Barlat coefficients for the welded region for use in the formability model.
- Gap: While Barlat coefficients have been established for base materials in the past, this is the first time the coefficients for a non-homogenous welded region are obtained. New methods of characterization will need to be developed.
- Target: Demonstration of a formability model in prototypical welded parts and demonstration of predictability.
- Gap: Current modeling practices do not take into account non homogenous weld properties.

Introduction

This work will develop high-strength, high-speed FSW of dissimilar aluminum alloy combinations in linear and curvilinear geometries. The alloy combinations considered in this project include work hardenable alloys (i.e., 5xxx series) capable of deep drawing and precipitation hardenable alloys (i.e., 6xxx and 7xxx series), which can be hardened post joining and forming to yield high strength for application in outer body panels and structural supports of automobiles. FSWs made at welding speeds greater than 1 m/minute are considered high speed for this work. Figure V.2-1 shows a comparative chart that includes a large number of aluminum FSWs reported in literature over the last 15 years [1]. Welding speeds already implemented in the current project are also shown.

The current project intends to significantly increase the welding speed, thus enabling high-volume application of FSW in TWB applications. The effects of high welding speed and the resulting weld properties were investigated. In addition, ways to exploit the high-speed FSW to the advantage of strength and ductility enhancements will be defined. This research will develop material coefficients required to support formability modeling of dissimilar alloy combinations with different hardening mechanisms (i.e., strain hardening in 5XXX and precipitation hardening and HAZ degradation due to coarsening in 6XXX and 7XXX). The resulting material coefficients will be used to develop a formability model capable of simulating combinations of dissimilar alloys and dissimilar thicknesses of TWBs. Ultimately, the formability model will be validated against formability performance of welds made at the supplier's facility.

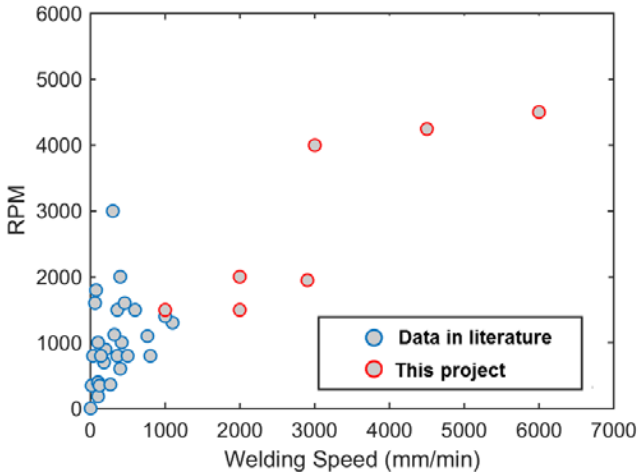

Figure V.2-1. Comparative chart showing welding speed and tool rpm used by a large number of aluminum alloy FSW reported in literature. The parameters used so far in the current project are also shown.

Approach

The work scope is divided into four main task areas. The first task is concerned with obtaining relationships between the weld parameters, process conditions, and weld properties. The second task focuses on developing high-speed parameter sets to produce sound welds in dissimilar alloy combinations for Aluminum Association (AA) 5XXX to 6XXX and 7XXX series in similar or dissimilar thicknesses. The third task of the project pertains to production readiness and deployability, including an FSW repeatability and tool durability study. The fourth task concerns weld formability modeling and validation, including development of material and weld region constitutive coefficients and simulation of sheet formability in dissimilar material and thickness of TWBs.

Welds in both bead-on-plate and dissimilar alloy combinations necessary to accomplish the first task were produced during FY 2015. Most of the characterization and data analysis were completed. Relationships of

welding parameters on resulting properties, including strength, ductility, through-thickness full-field hardness, and texture variations (via electron backscatter diffraction) in the HAZ and nugget were analyzed. Weld parameter development at laboratory-scale pertaining to this task was completed during FY 2015. During FY 2016, the focus was on transferring laboratory development process parameters and tooling designs to the supplier's site for use with commercial production equipment and cycle times. Additionally, progress was made in development of tooling, transitional weld parameters, and fixtures to support curvilinear high-speed FSW at the supplier's facility. Material combinations (alloy and thickness variations) were down selected and progress was made on the logistics necessary to assess repeatability and tool durability at the supplier's facility for high speed FSW. Development of formability modeling efforts continued with transition to LS-DYNA; and ensuring that model is capable to incorporate Barlat coefficients to account for non-homogeneity in the weld region. This was done with the participation of GM [2].

Results and Discussion

To expand on the FY 2015 efforts to understand the effects of welding parameters on process variables (e.g., peak welding temperature and resulting weld properties), advanced characterization of aluminum TWB FSW was accomplished. Figure V.2-2 shows pole figures and orientation distribution function extracted from the approximate nugget zone center (i.e., red cross) for three data sets corresponding to welding speeds of 1, 2, and 3 m/minute for 2mm thick AA7075. The data set has been rotated to match the theoretical shear texture direction (i.e., shear direction and shear plane normal direction) corresponding to face-centered cubic metal. At higher welding speeds of 2 m/minute and 3 m/minute, the shear texture appeared to be stronger than with 1 m/minute, as indicated by the high intensity in the pole figures, especially in the {1 1 1} plane. This may be indicative of a change in the material flow regime as the welding speed increases.

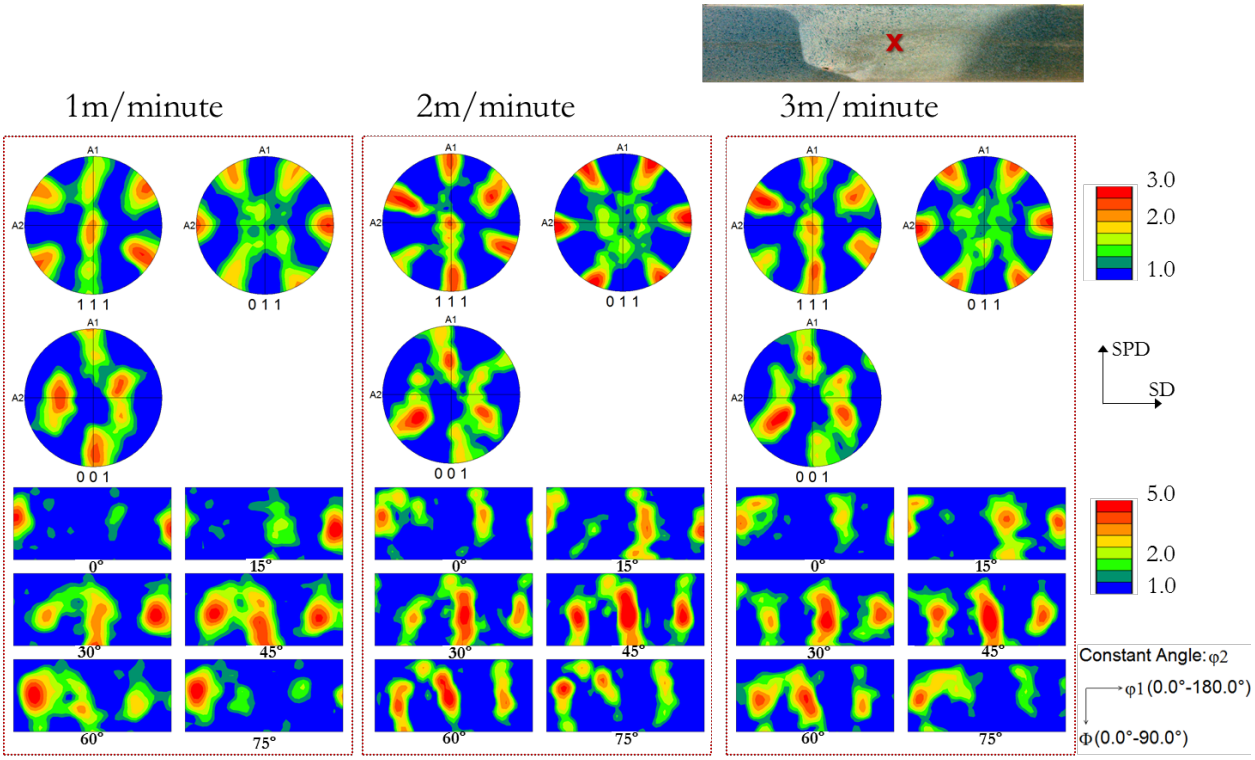

Figure V.2-2. Pole figures and orientation density function corresponding to the weld nugget center for three different welding speeds.

Figure V.2-3(a) shows hardness line plots in the transverse direction, across the nugget, for welds made with AA7075-T6 at varying welding and rotation speeds for comparison. The minimum average HAZ hardness and average nugget hardness extracted from each curve are shown in Figure V.2-3(b) and Figure V.2-3(c). There is

a relatively large decrease in nugget hardness and a small but distinctive decrease in the HAZ minimum average hardness as the measured peak pin temperature increases (observed for a variety of welding conditions across alloys in FY 2015). It is well known that the welding speed and rate of cooling can significantly affect the HAZ minimum hardness [3,4]. However, data sets like these can be helpful in understanding and predicting weld properties using process variables (e.g., peak temperature) that can be readily measured in comparison to destructive and time-consuming hardness testing. The combination of data sets generated in FY 2015 and data sets gathered in FY 2016 resulted in a wealth of information that can be used to relate process parameters, welding process conditions, and resulting joint properties. These results are helpful to welding engineers to make educated decisions on welding parameters for a desired outcome in a variety of conditions at a relatively high welding speed. This information is not currently available in literature.

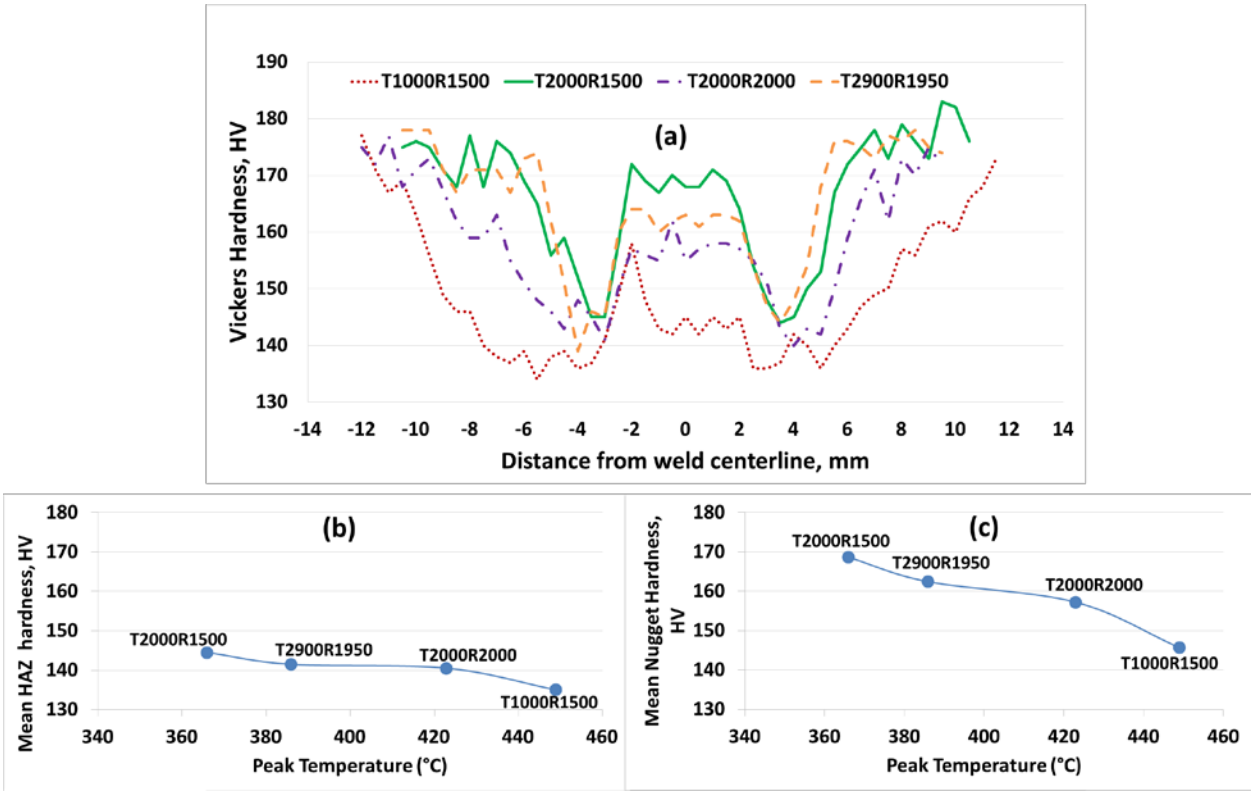

Figure V.2-3. (a) Transverse micro-hardness data set obtained from weld mid-plane. (b) Average HAZ hardness versus measured peak temperature during welding. (c) Average nugget hardness versus measured peak temperature. (The number after "T" indicates welding speed in mm/minute, while the number after "R" indicates tool rotation per minute [rpm].) For example, T2000R1500 means weld run at 2 m/minute and 1,500 rpm.

Aside from the fundamental weld characterization discussed above, progress was made this year on transferring welding parameters and tooling to the OEM supplier's facility. In FY 2015, the project reported on successful development of parameters and a process schedule to produce welds that passed quasi-static tensile tests for a variety of dissimilar thickness/alloy combinations. During FY 2016, we worked with engineers and technicians from the supplier's facility, both onsite and offsite to begin the process of transferring the welding parameters to a commercial production gantry-based FSW machine. Transferring welding parameters is far from trivial and requires careful tuning of several parameters based on the process condition recorded during welds made at the original FSW machine. This is because there are inherent differences in compliance and control between research FSW machine designs and commercial gantry-type and robotic machines at the supplier's facility. Machine stiffness, tool movement control strategies, and thermal boundary conditions are the primary concerns [5]. After a series of informed trial and error experiments in collaboration with engineers at the supplier's facility, welding parameters for both linear and curvilinear joint lines were transferred for TWB joints of AA6022 (2 mm) to AA5182-O (1 mm).

Several trial and error runs were conducted before a defect free weld parameter set, developed for a linear pathway, could result in a sound weld in the curvilinear case. This is because as the tool articulated a curve, the effective velocity vectors of material transfer between the advancing and retreating side of the tool were uneven in contrast to linear pathways. Therefore, robotic FSW command had to compensate for the associated changes. The pictures in Figure V.2-4 are representative of a gradual development of a welding parameter in chronological order, showing weld development for dissimilar thickness AA5182-O (i.e., strain hardening alloy) in Figure V.2-4(a), AA6022 (i.e., precipitation hardening alloy) in Figure V.2-4(b), and, eventually, in dissimilar thickness/dissimilar alloy combinations in Figure V.2-4(c). The curvilinear panel developed this year included one corner with a 50-mm radius and two corners with a 60-mm radius.

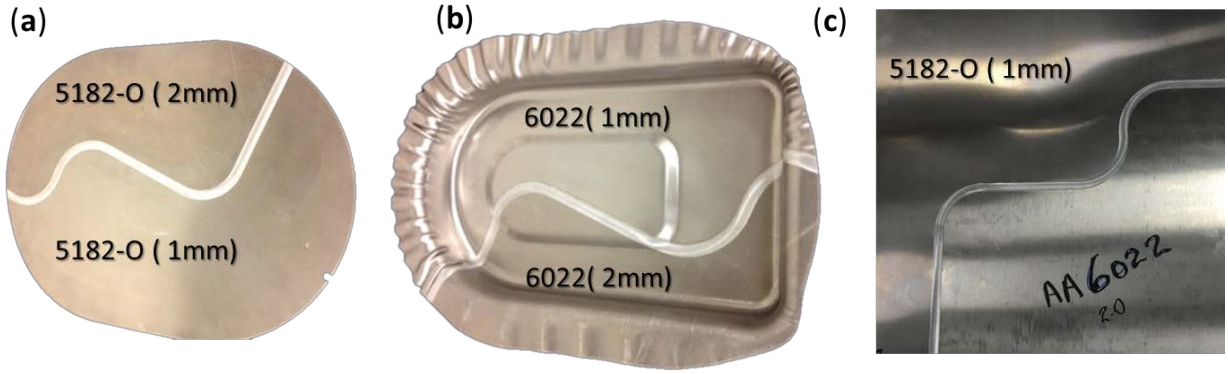

Figure V.2-4. Representative curvilinear welds made at TWB facility between (a) AA5182-O (1 to 2 mm), (b) AA6022-T4 (1 to 2 mm), and (c) AA5182-O (1 mm) to AA6022 (2 mm).

Future tasks will focus on assessing process parameters and conducting sensitivity analyses for varying combinations of sheet thickness and alloy based on the supplier's market needs. This will require process repeatability and tool wear studies, as well as coatings effects on tool life, which will be the focus for FY 2017.

In addition to transferring the developed FSW technology to industry partners, PNNL also aided the supplier in tackling practical issues that arose as the process was being assessed for implementation in a commercial manufacturing plant. As an illustrative example, a large batch of FSW TWBs was made at the supplier's facility using precipitation-hardened alloys in similar thicknesses. Based on the kinetics of the precipitates, a 96-hour hold at room temperature was necessary before performing a stamping operation in order to allow the aluminum to age naturally. However, high-volume production demands the ability to evaluate weld quality and ensure performance in real-time so that any necessary changes in the process can readily be made on the production floor. If welds sit for nearly 100-hours prior to testing, thousands of parts would have been completed prior to evaluation, leading to waste and low-production yields.

PNNL worked with the supplier to develop correlations between as-welded and naturally aged properties in order to predict final weld properties pre and post-stamping. Evaluations of as-welded TWB samples were made using limiting dome height (LDH) measurements. Destructive evaluations of welds produced at 4.5 m/minute are shown in Figure V.2-5 and Figure V.2-6. Representative LDH samples (as tested) that fractured inside the weld nugget resulted in a relatively low dome height and failed at lower load, owing to a partially brittle fracture in the middle of the weld region (see Figure V.2-5(a)). With parameters adjusted, optimized welds were repeatedly produced that showed good performance and fractured away from the nugget region in the HAZ (see Figure V.2-5b and Figure V.2-6b). The result for LDH testing was a significantly higher dome height (i.e., 14.5 mm in Figure V.2-5(a) compared to 25 mm in Figure V.2-5(b)). Additionally, the fracture mode was ductile throughout the thickness, suggesting thickness homogeneity. A number of welded samples were tested, using this test method with as-welded and after natural aging of samples for 96 hours to develop correlations between the two cases. Welds could be produced with confidence and without having to wait for 96 hours before testing. The LDH testing parameters for as-welded and naturally aged conditions are shown in Table V.2-1.

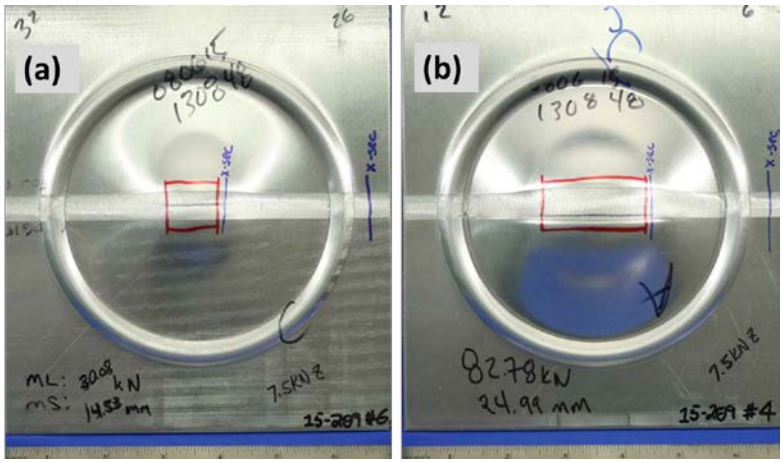

Figure V.2-5. Representative tested LDH samples with fracture at the nugget (a) and HAZ (b).

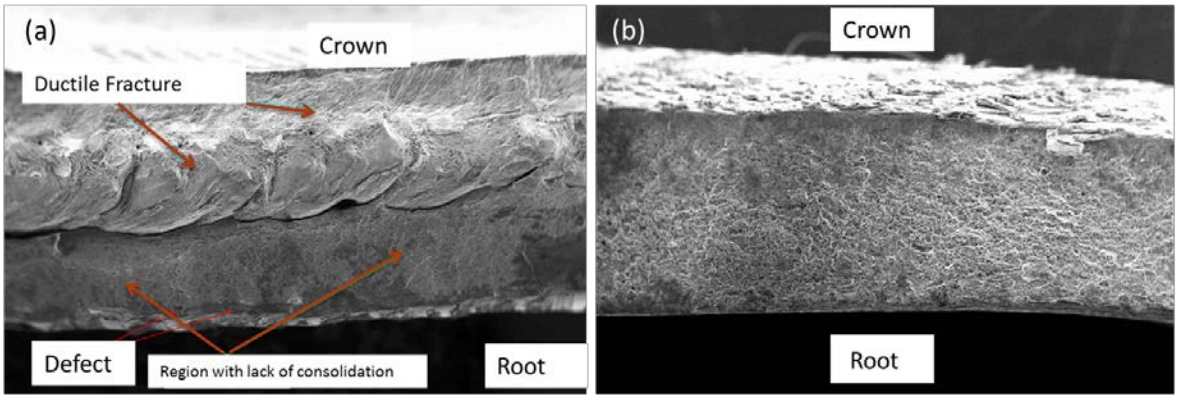

Figure V.2-6. Fracture morphologies of fractured samples showing contrast between fracture at weld nugget (a) and that at the HAZ (b) for welds made in a precipitation hardening alloy at 4.5 m/minute.

Table V.2-1. Limiting Dome Height Characteristics of TWB Joints As-Welded versus After Aging

Test Parameters	As-Welded	Aged 96 hours
LDH (mm)	16.53, 16.03	24.57,24.41
Load (kN)	35.62, 33.7	80.78,79.95

In addition to experimental work, progress was made in numerical simulation of formability. Based on the industrial partner's need, the ABAQUS formability model developed at PNNL was transitioned to LS-DYNA in the beginning of FY 2016. This commercial finite element software was used to simulate the LDH test in order to validate the model. Joints of similar/dissimilar alloys and varying thicknesses were simulated using either forming limit diagram bi-axial stretching data or limit strain failure criteria. Barlat's material behavior model was implemented using coefficients obtained from mechanical uni-axial and equi-biaxial tests conducted on the base material. Additional tests are scheduled to occur during FY 2017 to generate Barlat's coefficients for various alloys of interest in the base material, in the weld, and in the HAZ. The use of fully discretized joints is expected to improve the model's accuracy and increase its predictive strength, which is critical when simulating complex shape forming.

Figure V.2-7 shows comparison between experimental and predicted dome heights for dissimilar thicknesses of joints for 5182-O sheets. In order to validate the developed model with experimental results (square symbols) two failure criteria were used in simulation to extract dome heights 1) maximum strain of 18% of Base material (diamond symbols) and 2) Reduced Formability Limit Diagram (FLD) criteria. The simulation predictions use Barlat's model with coefficients from literature for 5182-O. [2] The experimental results match well with the simulation results corresponding to the 18% base metal strain criterion, however, the project

observed an over-prediction of the model using FLD failure criteria. It is expected that formability simulations run using Barlat coefficients that are obtained from weld regions and the base material (anticipated from partnering OEM in FY 2017) will provide improved predictability. An image of the equivalent plastic strain contours extracted from formability model for a joint dissimilar thickness sheet (2mm-1mm, 5182-O) with 18% maximum strain failure criterion is shown in Figure V.2-8. The failure location occurs just outside of obtained with the failure location just outside the sheet adjoining line.

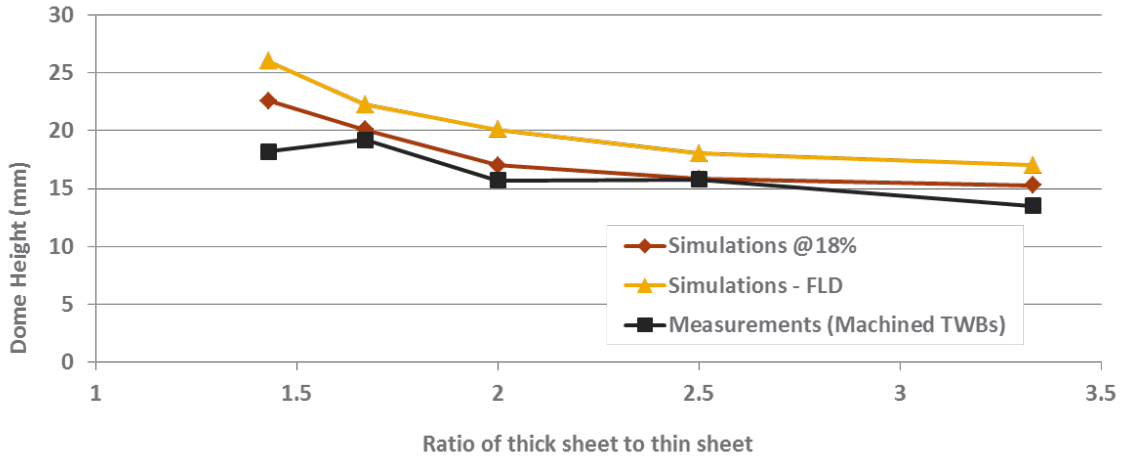

Figure V.2-7. Numerically predicted versus experimental dome heights for AA5182-O joints with various thickness ratios. The Barlat model was used for material behavior.

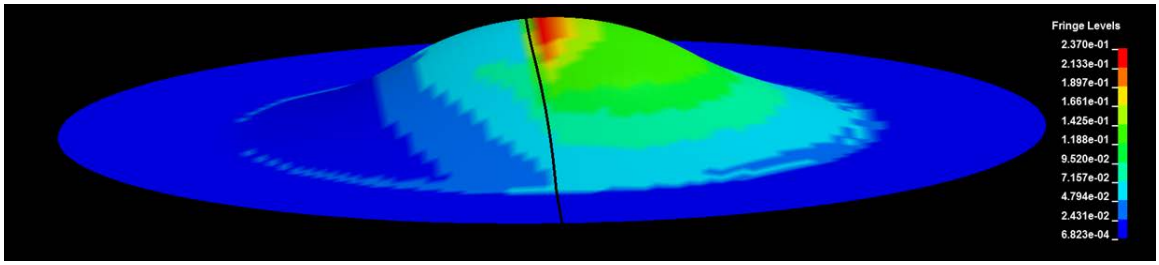

Figure V.2-8. Equivalent plastic strain contours of AA5182-O (2 to 1-mm joint).

Technology Transfer Path

Technology transfer will be made directly through the project participants (i.e., GM, TWB, and Alcoa), who will be the implementers of the technology. TWB Company (i.e., a tier 1 supplier to the automotive industry) will be able to use the joining technology developed during the project to address a wide range of automotive market light-weighting needs by implementing TWB technology for aluminum alloys. During FY 2016, welding parameters for both linear and curvilinear joint lines were transferred for TWB joints of AA6022 (2 mm) to AA5182-O (1 mm) to an OEM supplier.

Conclusion

During FY 2016, the project continued efforts under this scope of work to enable the OEM and TWB supplier to develop and integrate FSW of TWB aluminum into their production lines. Aside from fundamental characterization, we were able to successfully transfer welding parameters and processing schedules for producing a specific set of TWB dissimilar thickness/alloy combination using FSW equipment at the OEM supplier in both linear and curvilinear two-dimensional paths. Three industrial partners contributed in-kind efforts, including materials by Alcoa, experimental formability by GM, and joining and testing facilities and labor investments by TWB Company.

References

[1] Zhang, J., P. Upadhyay, Y. Hovanski, and D. P. Field, 2016, "Quantitative Microstructure Study of High Speed FSW Aluminum Alloy," *Material Science and Technology 2016*, Salt Lake City, Utah.

[2] Barlat, F., J. M. Ferreira Duarte, J. J. Gracio, A. B. Lopes, and E. F. Rauch, 2003, "Plastic Flow for Non-Monotonic Loading Conditions of an Aluminum Alloy Sheet Sample," *International Journal of Plasticity* 19(8): 1215–1244.

[3] Upadhyay, P. and A. P. Reynolds, 2010, "Effects of Thermal Boundary Conditions in Friction Stir Welded AA7050-T7 Sheets," *Materials Science and Engineering: A* 527(6): 1537–1543.

[4] Threadgill, P. L., A. J. Leonard, H. R. Shercliff, and P. J. Withers, 2009, "Friction Stir Welding of Aluminum Alloys," *International Materials Reviews* 54(2): 49–93.

[5] Hovanski, Y., P. Upadhyay, B. Carlson, T. Luzanski, D. Marshall, and R. Szymanski, 2014, "FSW of Aluminum Tailor Welded Blanks across Machine Platforms," *2015 TMS Annual Meeting & Exhibition,* Orlando, Florida, March 16, 2015.

Bibliography

Davies, R. W., M. T. Smith, M. A. Khaleel, S. G. Pitman, and H. E. Oliver, 2000, "Weld Metal Ductility in Aluminum Tailor Welded Blanks," *Metallurgical and Materials Transactions A* 31(11): 2755–2763.

Hovanski, Y., P. Upadhyay, J. Carsley, T. Luzanski, B. Carlson, M. Eisenmenger, A. Soulami, D. Marshall, B. Landino, and S. Hartfield-Wunsch, 2015, "High-Speed Friction-Stir Welding to Enable Aluminum Tailor-Welded Blanks," *Journal of Materials* 67(5): 1045–1053.

Hovanski, Y., P. Upadhyay, A. Soulami, B. Carlson, M. Eisenmenger, and B. Landino, 2015, "Enabling High Volume Production of Aluminum Tailor Welded Blanks," *The 4th International Conference on Friction Stir Welding and Processing,* Ordizia, Spain, October 2015.

Hovanski, Y., J. Carsley, B. Carlson, M. Eisenmenger, S. Hartfield-Wunsch, and B. Landino, 2014, "Aluminum Tailor Welded Blanks – Preparing for High Volume Production," *2015 TMS Annual Meeting and Exhibition*, Orlando. Florida, March 16, 2015.

Mishra, R. S. and Z. Y. Ma, 2005, "Friction Stir Welding and Processing," *Materials Science and Engineering Reports* 50(1–2): 1–78.

Murr, L. E., 2010, "A Review of FSW Research on Dissimilar Metal and Alloy Systems," *Journal of Materials Engineering and Performance* 19(8): 1071-1089.

V.3 Understanding Protective Film Formation by Magnesium Alloys in Automotive Applications – Oak Ridge National Laboratory

Project Details

Michael P. Brady, Principal Investigator
Materials Science and Technology Division
Oak Ridge National Laboratory
1 Bethel Valley Road
Oak Ridge, TN 37831-6156
Phone: 865-425-0231
E-mail: bradymp@ornl.gov

Sarah Kleinbaum, Technology Area Development Manager
U.S. Department of Energy
1000 Independence Avenue, SW
Washington, DC 20585
Phone: 202-586-8027
E-mail: Sarah.Ollila@ee.doe.gov

Contractor: Oak Ridge National Laboratory (ORNL)
Contract No.: DE-AC05-00OR22725

Executive Summary

The objective of this project is to enhance fundamental understanding of magnesium (Mg) corrosion to provide the basis for designing improved Mg alloys and coatings to permit more widespread automotive adoption of Mg. Two classes of Mg alloys are under study: (1) conventional Mg-aluminum (Al) base alloys and (2) state-of-the-art rare-earth (RE)–modified Mg alloys of interest for their improved formability characteristics, particularly in sheet form. The project is devoted to understanding the impact of alloying additions on film formation and hydrogen (H) migration into the underlying Mg alloy during aqueous exposures of uncoated (bare) alloys, as well as the impact of substrate alloying segregation tendencies on surface coating formation when treated by electro-ceramic and electro-coatings. New insights are achieved through application of advanced electron microscopy and neutron and isotopic tracer characterization tools not previously widely applied to Mg corrosion. Efforts during Fiscal Year (FY) 2016 focused on the discovery of unexpected H species penetration beyond the corrosion film and into the underlying Mg alloy on aqueous exposure. Depth profiling and time-of-flight (TOF) secondary ion mass spectrometry (SIMS) imaging revealed that the H penetration behavior was significantly impacted by alloying additions and alloy microstructure.

Accomplishments

- Completed SIMS depth profiling data acquisition experiments for seven cast model alloys (i.e., binary, ternary, and quaternary) in the Mg–zinc (Zn)–neodymium (Nd)–calcium (Ca) system (collaboration with University of Manitoba and McGill University). Also acquired data for cast Mg alloy AZ91 and wrought Mg alloy WE43 for comparison of Al and RE level effects, respectively, with Mg alloys AZ31B and E717 (collaboration with University of Manitoba, Magnesium Elektron North America, and McMaster University) (FY 2016).

- Demonstrated capability of TOF-SIMS cross-section imaging to locate deuterium (D) species in both film and metal for deuterated water (D_2O)–exposed Mg alloys. Microstructural features relative to D ingress successfully imaged for pure Mg; model cast Mg-Al, Mg-zirconium (Zr), and Mg-Nd alloys; wrought AZ31B; cast AZ91; wrought E717; and wrought WE43 (FY 2016).
- Completed initial data acquisition for a vibrational neutron spectroscopy experiment at the ORNL Spallation Neutron Source facility in an attempt to identify H speciation in aqueous-exposed pure Mg and Mg RE-modified alloy E717. To our knowledge, such techniques have not previously been applied in this manner to Mg corrosion (FY 2016).
- Completed an advanced characterization study of as-conversion coated and conversion coated plus e-coated metal-coating interface structures for Mg alloys E717 and AZ31B. Substrate alloy composition influenced the as-conversion coated structure, which was modified both compositionally and morphologically by subsequent e-coating (FY 2015).
- Demonstrated via D_2O exposure studies that the addition of Zr and Nd to Mg alloys significantly enhances uptake of H into the alloy on aqueous exposure, whereas Al additions do not (FY 2015).
- Completed isotopic tracer study of aqueous film formation growth on Mg alloys in the presence of salt species, which was shown to result in a transition to an outward oxygen (O) film growth mechanism (FY 2015).
- Completed and published a $D_2{}^{16}O$ and $H_2{}^{18}O$ isotopic tracer study for aqueous film formation growth mechanism by commercial Mg alloys AZ31B and E717 relative to ultra-high purity Mg. This is the first isotopic tracer study of Mg corrosion ever reported (FY 2014).
- Demonstrated small-angle neutron scattering as a new tool for providing insights into Mg corrosion. Small-angle neutron scattering was found to be sensitive to formation of nanoporous, filamentous magnesium hydroxide ($Mg(OH)_{2)}$ that results from the accelerated corrosion of Mg alloys in salt solutions. The small-angle neutron scattering data indicated extremely high surface areas in the $Mg(OH)_2$ corrosion product, which has implications for understanding film growth and breakdown (FY 2014).
- Completed an advanced transmission electron microscopy characterization study of ambient immersed aqueous film formation as a function of exposure time (4 to 48 hours) and alloy type (AZ31B, E717, and ultra-high purity Mg), elucidating nanoscale film segregation tendencies of Al, RE, Zn, and Zr alloy additions (FY 2013).
- Demonstrated SIMS/$D_2{}^{16}O$ and $H_2{}^{18}O$ isotopic tracer studies for film formation by Mg alloys under immersed aqueous and air plus steam exposure conditions, providing new insights into film growth mechanism and relative penetration of H and O species (FY 2013).

Future Directions

- Complete data analysis and post-exposure sample characterization for the FY 2016 vibrational neutron spectroscopy experiment and determine whether the technique can be used to identify the speciation of H introduced into Mg alloys on aqueous exposure (FY 2017).
- Complete aqueous corrosion film cross-section study/elemental segregation assessment by x-ray photoelectron spectroscopy and scanning transmission electron microscopy of WE43 and AZ91 alloys for comparison with lower-level RE addition E717 alloy and lower Al level AZ31B alloy previously studied. This information will also provide a basis for future comparison of segregation tendencies of these alloys after coating (FY 2017).
- Complete as-coated structure cross-section study/elemental segregation assessment by x-ray photoelectron spectroscopy and scanning transmission electron microscopy for E717, WE43, AZ31B, and AZ91 alloys with state-of-the-art electro-ceramic coatings (collaboration with Henkel Corporation) (FY 2017).

- Complete as-coated structure cross-section study/elemental segregation assessment by x-ray photoelectron spectroscopy and scanning transmission electron microscopy for E717, WE43, AZ31B, and AZ91 alloys with state-of-the-art electro-ceramic coatings and electro-coat top coats (collaboration with Henkel Corporation) (FY 2018).
- Complete corrosion assessment and microstructural correlations of electro-ceramic and electro-ceramic plus electro-coat top coats as a function of alloy substrate for E717, WE43, AZ31B, and AZ91 alloys (collaboration with McMaster University and Henkel Corporation) (FY 2018).

Technology Assessment

- Target: Gain improved understanding of film and coating formation by Mg alloys as a function of alloy chemistry and microstructure.
- Target: Provide a fundamental basis for designing and optimizing new Mg alloys and/or coating processes to improve corrosion resistance under automotive-relevant conditions.
- Gap: The lack of corrosion prevention strategies is a key limiting factor for more widespread use of Mg alloys in automotive applications.
- Gap: Alloying has been shown to modify surface film and coating performance; however, a detailed understanding of how and why is currently lacking. This understanding is needed to develop improved alloys and surface treatments/coatings to permit more widespread adoption of Mg alloys.

Introduction

Mg alloys are of great interest to automotive manufacturers due to their attractive combination of low density, good strength, amenability to casting, and ease of recycling. A major obstacle to widespread adoption of Mg alloys is their susceptibility to corrosion [1–3]. Surface treatments and/or coatings are needed for many applications [3], which results in increased cost and can be a source of component durability issues. The inability of Mg alloys to establish a continuous and fully protective surface film under many exposure conditions is a key factor underlying their susceptibility to corrosive attack. Alloying has been shown to modify surface film performance and impact the nature and protectiveness of reactive-based coating processes typically used for Mg alloys; however, a detailed understanding of how and why is currently lacking. This understanding is needed to provide a basis for developing improved alloys and coatings to permit more widespread adoption of Mg alloys in automotive applications.

Approach

This project is using advanced electron microscopy, neutron scattering and spectroscopy, and isotopic tracer characterization tools not previously widely applied to Mg corrosion to provide the improved fundamental insights needed to successfully design Mg alloys and coatings with improved corrosion resistance. The project is focusing on select state-of-the-art commercial Mg alloys and coatings relevant to automotive applications and chosen in consultation with project collaboration partners Magnesium Elektron North America (i.e., a Mg alloy producer), Henkel Corporation (i.e., coating producer), Magna International (i.e., Tier 1 automotive supplier), McMaster University (i.e., electron microscopy and electrochemistry), McGill University (i.e., developmental Mg sheet alloys), and the University of Manitoba (i.e., SIMS sputter depth profile analysis of isotopic tracers). The effort recently pursued film formation and coating studies for a representative alloy from two key classes of Mg alloys: conventional Mg-3Al-1Zn (all compositions in weight percent [wt %]) base alloy AZ31B and state-of-the-art RE and Zr-modified Mg alloy ZEK100 type (ZE10A) E717 from Magnesium Elektron North America (Mg-1.5Zn-0.25Zr-(<0.5)Nd base alloy, which is of interest for its improved formability characteristics, particularly in sheet form).

Efforts in FY 2016 through 2018 are devoted for expansion of this work to permit assessment of the impacts of higher levels of alloying additions and second phases on film and coating formation through study of automotive relevant alloys AZ91 (Mg-9Al-1Zn base) for comparison with AZ31B and WE43 (Mg-(3.7–4.3)Y-

(2.3–3.5) (RE)->0.2Zr) for comparison with E717. This effort is focused on the following two key corrosion aspects:

1. Defining the impacts of Al, Zr, Ca, and RE alloy additions on film structure and enhanced H migration phenomena into Mg alloys during aqueous exposures, which are potentially relevant to stress corrosion cracking (SCC)/embrittlement susceptibility and dissimilar metal interface corrosion. Understanding H uptake is also needed to more fully describe and successfully model aqueous corrosion processes for Mg alloys.
2. Establishing substrate alloying segregation tendencies on state-of-the-art electro-ceramic coating formation and performance with electro-coat top coat to provide a basis for optimally designing alloys for coating processing. The focus will be on determining why coating protectiveness varies with substrate alloy in these composition ranges.

Results and Discussion

Efforts in FY 2016 focused on H migration uptake-related phenomena during aqueous corrosion. SIMS isotopic tracer sputter depth profile studies performed during FY 2013 through 2015 using D_2O indicated that H/D penetrated through the mixed hydroxide/oxide film formed during corrosion of Mg and into the underlying alloy metal on room temperature aqueous exposure, particularly for the Zr and Nd-containing E717 alloy [4, 5]. Much less H penetration beyond the film and into the underlying Mg alloy metal was observed for the Mg-Al-Zn base alloy AZ31B and pure Mg [4]. To our knowledge, this H penetration phenomenon during aqueous corrosion of Mg has not previously been reported. It is potentially relevant not only to H embrittlement and/or SCC behavior of Mg alloys, but also to the fundamental understanding of how Mg reacts with water. This effect is illustrated in Figure V.3-1 for pure Mg and cast Mg-0.19Z, Mg-0.14Nd, and Mg-2.1 Al alloys (FY 2015 SIMS sputter depth profiling results). Compared to the baseline as-polished condition, exposure for 4 hours in D_2O resulted in elevated residual D levels to a depth of at least 20 µm for all alloys (the hydroxide/oxide surface films were less than 1-µm thick). However, the D levels in the underlying Mg alloy metal were far higher in the Mg-0.14Nd and Mg-0.19Zr alloys.

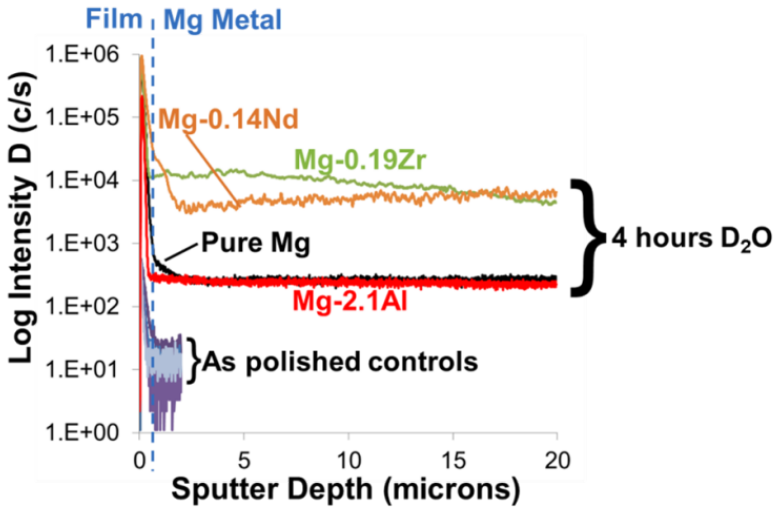

Figure V.3-1. SIMS D tracer data sputtered from film surface into the alloy for cast pure Mg, Mg-2.1Al, Mg-0.19Zr, and Mg-0.14Nd in weight percent. As-polished and after 4 hours of exposure in room-temperature D_2O.

Figure V.3-2 shows results in FY 2016 from initial attempts at TOF-SIMS D imaging of 4-hour D_2O-exposed samples in polished cross sections. The enhancement of D penetration with Zr additions to Mg was confirmed relative to that of pure Mg and Mg-2.1Al. These results are critical because they strongly suggest that top-down sputtering artifacts are not responsible for differences in H/D penetration tendencies observed among the different alloys in the SIMS depth profile data (Figure V.3-1).

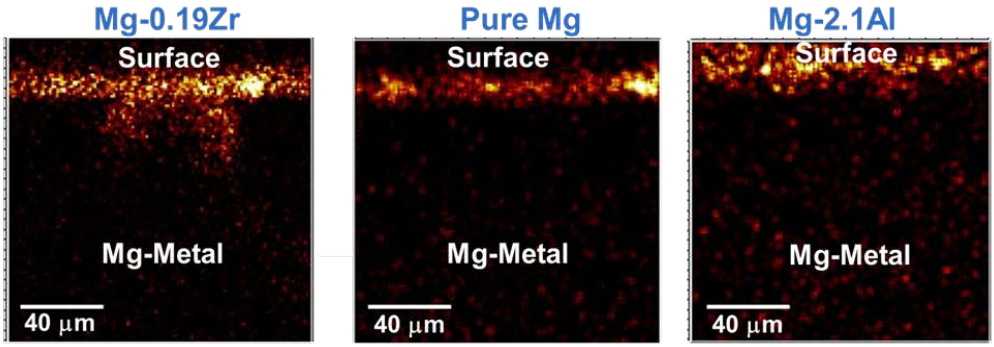

Figure V.3-2. TOF-SIMS imaging of polished cross sections for 4-hour D_2O-exposed pure Mg, cast Mg-2.1Al, and Mg-0.19Zr (D-enriched regions are bright contrast).

Figure V.3-3 shows TOF-SIMS cross-section imaging for a cast Mg-0.46Zr alloy after 4 hours in D_2O. Elevated D penetration of 50 µm was observed in the mapping, indicating very rapid uptake of D despite only 4 hours of exposure at room temperature. The distribution of D penetration was found to be non-uniform and correlated with Zr-enriched residual casting features in the alloy (backscatter electron image in Figure V.3-3, with Zr levels locally measured at the micron scale to be in the range of 1 to 5 wt % by electron probe microanalysis). It is postulated that these Zr-rich microstructural features act as a fast diffusion path for inward D penetration during aqueous corrosion and that it is driven, in part, by the greater thermodynamic stability of H/D with Zr relative to Mg. Whether this phenomenon is detrimental or beneficial is not yet clear. For example, preferential segregation of H/D species to Zr-rich regions in the alloy microstructure (or possibly even a coating containing Zr) could conceivably mitigate, rather than enhance, the potential detrimental impacts of H embrittlement or SCC.

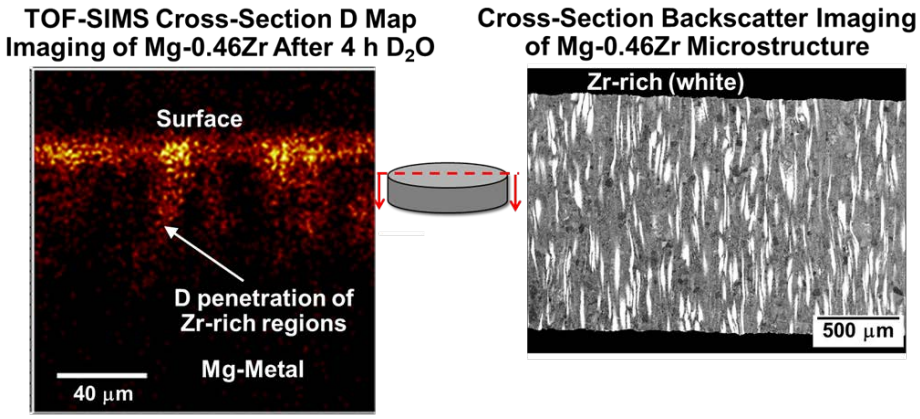

Figure V.3-3. TOF-SIMS imaging of the polished cross sections for 4-hour D_2O-exposed cast Mg-0.46Zr and a backscatter electron mode image of the cast microstructure (D-enriched regions are bright contrast).

D profiles from top-down SIMS sputtering of E717 (i.e., primarily single-phase alloy, low levels of RE additions) and WE43 (i.e., significant second-phase content, high levels of RE additions) are shown in Figure V.3-4. The E717 data [4] show significant D penetration compared to an as-polished control beyond the submicron-thick hydroxide-oxide corrosion film and well into the underlying alloy following 4 hours of exposure to D_2O at room temperature. The WE43 alloy showed a very high intensity of D in the near-surface regions, extending to nearly 10-µm deep, at which point the D signal reduced to that of the baseline as-polished WE43, with less overall depth of penetration than the E717 despite higher levels of RE additions (i.e., the film thickness on the 4-hour D_2O-exposed WE43 was submicron). It should be noted that the baseline D level for as-polished WE43 was quite high, presumably due to higher alloy H impurity levels from the high level of RE in this alloy. TOF-SIMS imaging (Figures V.3-5 and V.3-6) showed markedly different D penetration features for the wrought E717 versus wrought WE43 alloys. Segregation of D in the E717 was apparent in discrete bands in the alloy underneath the film, extending to nearly 100-µm deep (Figure V.3-5). Backscatter electron imaging in a microstructure region adjacent to the TOF-SIMS analyzed region revealed

that the D segregation correlated with bands of Zr-rich microstructure in the extruded E717, consistent with the similar Zr-enhanced D segregation observed in the cast Mg-0.46Zr alloy (Figure V.3-3). In contrast, consistent with the sputter profile data (Figure V.3-4), extensive D enrichment near the film surface was observed for WE43, but only to shallow depths (Figure V.3-6). Mapping of H suggested appreciable H content in the starting WE43 alloy microstructure, consistent with the high baseline D (and H, not shown in Figure V.3-5) level observed in the as-polished sample, likely corresponding with the second-phase alloy precipitate structure.

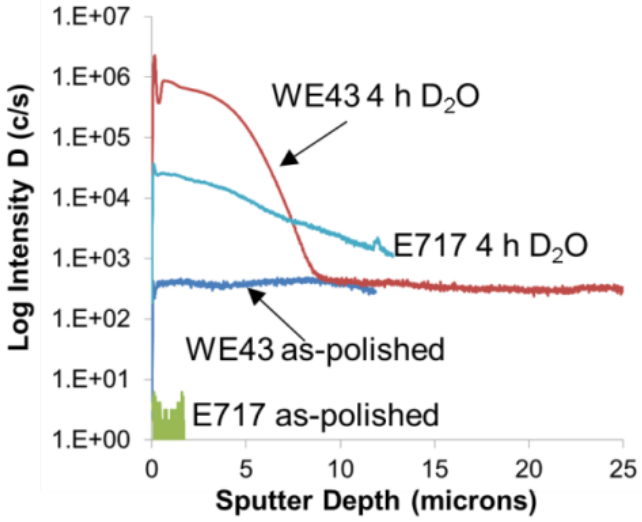

Figure V.3-4. SIMS tracer data sputtering profiles from film surface into the alloy for wrought E717 and WE43 as-polished and after 4-hour exposure in room-temperature D_2O.

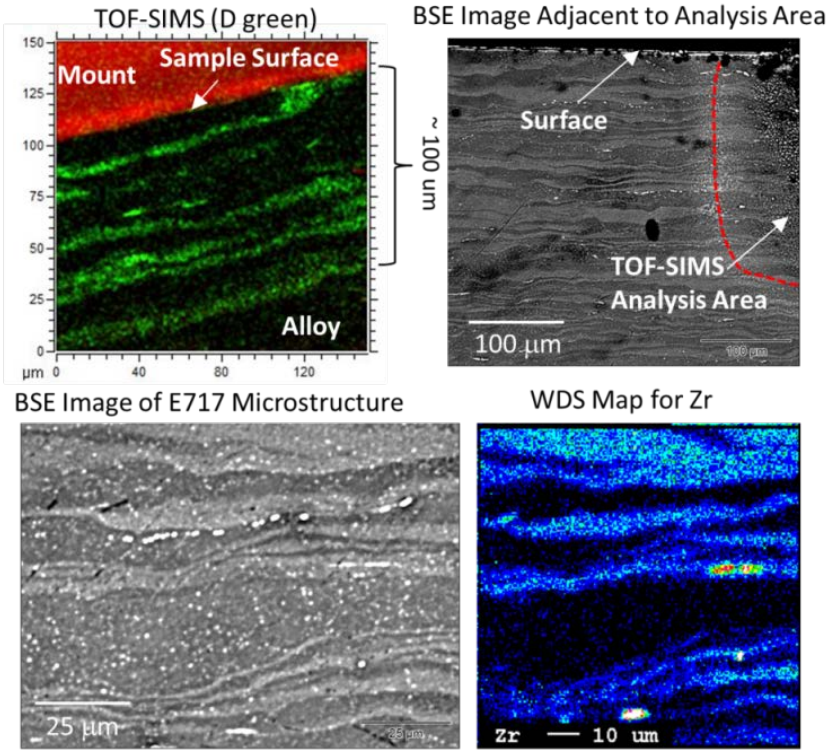

Figure V.3-5. TOF-SIMS D imaging of the polished cross section for 4-hour D_2O-exposed E717 and backscatter electron (referred to as BSE in the figure) mode imaging of the extruded E717 microstructure and corresponding wavelength dispersive x-ray spectroscopy (referred to as WDS in the figure) Zr map adjacent to the TOF-SIMS analysis region.

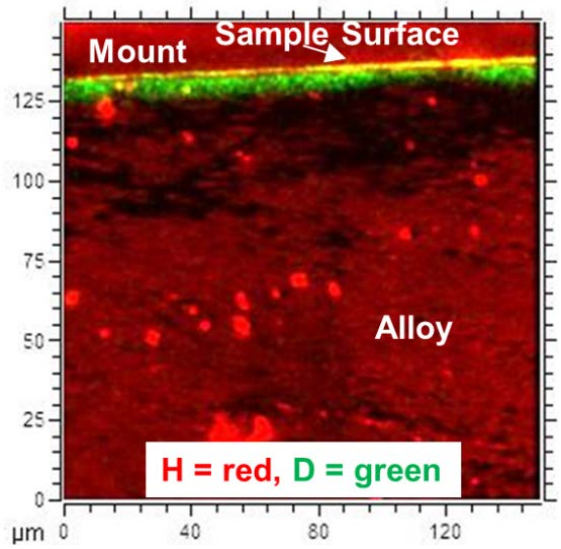

Figure V.3-6. TOF-SIMS imaging of the polished cross sections for 4-hour D_2O-exposed wrought WE43 (D-enriched regions are bright contrast).

Figure V.3-7 shows D profiles from top-down SIMS sputtering of wrought AZ31B (primarily single-phase alloy, low level of Al addition) and cast AZ91 (significant second-phase content, high level of Al). The AZ31B data [4] show rapidly decreasing D levels in the first few microns of sputtering, with a baseline D level only modestly above that of the as-polished control. This result initially suggested that Al additions do not enhance D penetration into the alloy, as was observed with Zr and RE additions. However, AZ91with higher levels of Al additions, which also result in appreciable second-phase content in the alloy, did result in enhanced D penetration, albeit with an irregular intensity profile versus sputter depth. TOF-SIMS imaging confirmed the low D penetration for AZ31B (Figure V.3-8). For the AZ91, significant, irregular D intensity was observed in the near-surface regions (possibly related to oxide inclusions and second phases), with lower D intensity also observed deeper into the alloy, likely associated with second phases and/or casting segregation.

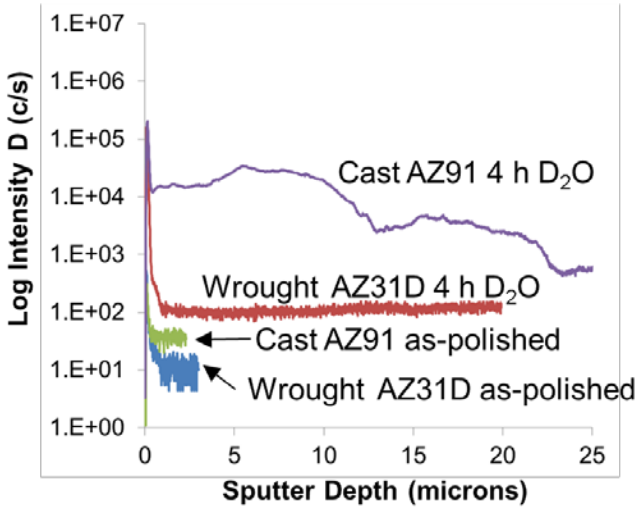

Figure V.3-7. SIMS tracer data sputtering profiles from film surface into the alloy for cast AZ91 and wrought AZ31D as-polished and after 4 hours of exposure in room-temperature D_2O.

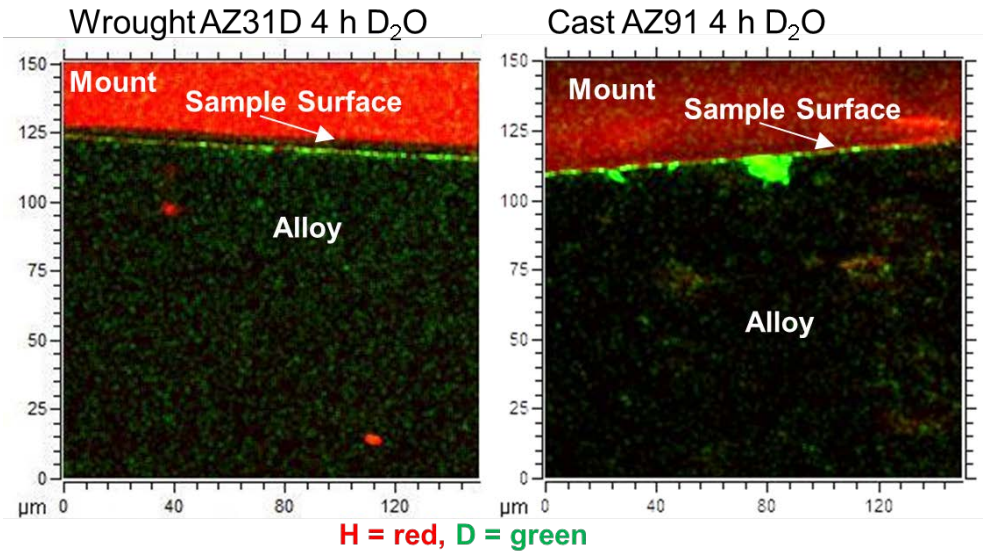

Figure V.3-8. TOF-SIMS imaging of the polished cross sections for 4-hour D_2O-exposed wrought AZ31B and cast AZ91.

Collectively, these new results indicate the complex impact of alloy additions and second-phase alloy structure and precipitates on D/H penetration into the alloy underlying the corrosion films formed on aqueous exposure of Mg and its alloys. An understanding of the form of this D/H penetration (i.e., hydride, atomic D/H in solution, and other) would provide a more complete picture of this phenomenon. Unfortunately, characterization of H speciation in Mg is quite challenging. During FY 2016, an attempt at such characterization was initiated using unique vibrational neutron spectroscopy techniques available at the ORNL Spallation Neutron Source facility. To our knowledge, these techniques have not previously been applied in this manner to Mg corrosion. To achieve a detectable level of H in the Mg alloy regions, multiple pieces of Mg foil about 100-μm thick were exposed in water and then stacked together for vibrational neutron spectroscopy analysis. It was possible to commercially procure pure Mg in foil form, but not for an alloy with Zr and RE additions such as E717. Therefore, E717 foil was manufactured internally using ORNL metal processing facilities by warm rolling at 300°C with 20 feet of foil successfully manufactured. This material was sufficient to obtain about 40 foil pieces each of water-exposed and unexposed control foil. Four sample sets were assembled: (1) as-received pure Mg, (2) 4-hour–exposed pure Mg, (3) as-received E717, and (4) 4-hour–exposed E717. The initial vibrational neutron spectroscopy data acquisition was successfully conducted in August 2016. These data will be analyzed in FY 2017.

Technology Transfer Path

Basic understanding of film formation on Mg alloys will provide insights into how improvements can be made to design and optimize new Mg alloys and coatings to improve corrosion resistance under conditions relevant to automotive applications. The current gap in basic understanding of film and coating formation mechanics and kinetics and correlation with alloy chemistry and microstructure are key factors limiting achievement of improved corrosion resistance to permit more widespread use of Mg alloys in automotive applications. Teaming with Magnesium Elektron North America (i.e., an Mg alloy producer) and Henkel Corporation (i.e., a coating company) provides a direct path for incorporating insights from this effort into practice. Project planning has also benefited from input by Magna International, a Tier 1 automotive supplier.

Conclusion

During FY 2016, this project focused on application of advanced characterization approaches to both confirm and gain a better fundamental understanding of H species penetration beyond the corrosion film and into the underlying Mg alloy metal on aqueous exposure. Depth profiling and TOF-SIMS imaging revealed that H penetration behavior was significantly impacted by alloying additions and alloy microstructure. In particular,

enhanced H species penetration was observed along Zr and/or RE- rich microstructural zones in the alloys to a depth of 50 to 100 μm in some cases after only 4 hours of aqueous exposure at room temperature. To our knowledge, these findings are unique to this project and represent a potentially important and under-considered aspect of the aqueous corrosion mechanisms for Mg and its alloys. These results are potentially relevant not only to structural Mg alloy design from an H embrittlement and SCC perspective, but also to functional applications of Mg alloys (e.g., in batteries or H storage). Such H uptake phenomena will also need to be considered during fundamental mechanistic and modeling studies of Mg corrosion with regard to how Mg reacts with water.

References

[1] Song, G.-L. and A. Atrens, 2007, "Corrosion Mechanisms of Magnesium Alloys," *Advanced Engineering Materials* 9(3): 177–83.

[2] Song, G.-L., 2005, "Recent Progress in Corrosion and Protection of Magnesium Alloys," *Advanced Engineering Materials* 7(7): 563–86.

[3] Gray, J. E. and B. Luan, 2002, "Protective Coatings on Magnesium and Its Alloys—a Critical Review," *Journal of Alloys and Compounds* 336(1–2): 88–113.

[4] Brady, M. P. et al., 2014, "Tracer Film Growth Study of Hydrogen and Oxygen from the Corrosion of Magnesium in Water," *Journal of the Electrochemical Society* 161(9): C395–C404.

[5] Unocic, K. A. et al., 2014, "Transmission Electron Microscopy Study of Aqueous Film Formation and Evolution on Magnesium Alloys," *Journal of the Electrochemical Society* 161(6): C302–C311.

Publications and Presentations

Brady, M. P., W. J. Joost, and C. D. Warren, "Insights from a Recent Meeting: Current Status and Future Directions in Magnesium Corrosion Research," (forthcoming).

Brady, M. P., D. N. Leonard, H. M. Meyer, J. K. Thomson, K. A. Unocic, H. H. Elsentriecy, G.-L. Song, K. Mitchen, and B. Davis, 2016, "Advanced Characterization Study of Commercial Conversion and Electrocoating Structures on Magnesium Alloys AZ31B and ZE10A," *Surface and Coatings Technology* 294: 164–176.

Brady, M. P., G. Rother, L. M. Anovitz, K. C. Littrell, K. A. Unocic, H. H. Elsentriecy, G.-L. Song, J. K. Thomson, N. C. Gallego, and B. Davis, 2015, "Film Breakdown and Nano-Porous $Mg(OH)_2$ Formation from Corrosion of Magnesium Alloys in Salt Solutions," *Journal of the Electrochemical Society* 162(4): C140–C149.

Brady, M. P., M. Fayek, H. M. Meyer, D. N. Leonard, H. H. Elsentriecy, K. A. Unocic, L. M. Anovitz, E. Cakmak, J. R. Keiser, G.-L. Song, and B. Davis, 2015, "Tracer Study of Oxygen and Hydrogen Uptake by Mg Alloys in Air with Water Vapor," *Scripta Materialia* 106: 38–41.

Brady, M. P., M. Fayek, H. H. Elsentriecy, K. A. Unocic, L. M. Anovitz, J. R. Keiser, G.-L. Song, and B. Davis, 2014, "Tracer Film Growth Study of Hydrogen and Oxygen from the Corrosion of Magnesium in Water," *Journal of the Electrochemical Society* 161(9): C395–C404.

Leonard, D. N. and M. P. Brady, 2016, "Advanced Characterization of Corrosion Films & Coatings on Magnesium Alloys" presented at the Henkel Corporation event *The Role of Surface Treatments in Achieving Lightweighting & Sustainability Goals within the Paint Shop*, Warren, Michigan, September 20, 2016.

Song, G.-L. et al. 2014, "Advanced Characterization of Mg Alloy Surface Films," invited presentation at *CORROSION 2014, NACE*, San Antonio, Texas, March 9 through 13, 2014.

Song, G.-L. et al., 2014, "Film Evolution on Mg Alloys," presented at *Materials Science & Technology 2014*, Pittsburgh, Pennsylvania, October 12 through 16, 2014.

Unocic, K. A., H. H. Elsentriecy, M. P. Brady, H. M. Meyer, G.-L. Song, M. Fayek, R. A. Meisner, and B. Davis, 2014, "Transmission Electron Microscopy Study of Aqueous Film Formation and Evolution on Magnesium Alloys," *Journal of the Electrochemical Society* 161(6): C302–C311.

Unocic, K. A. et al., 2013, "Characterization of Film Formation on Commercial and Model Magnesium Alloys," poster presented at *2013 TMS Annual Meeting*, San Antonio, Texas, March 4, 2013.

V.4 Solid-State Body-in-White Spot Joining of Al to AHSS at a Prototype Scale – Oak Ridge National Laboratory

Project Details

Zhili Feng, Principal Investigator
Oak Ridge National Laboratory
One Bethel Valley Road
Oak Ridge, TN 37831
Phone: 865-576-3797
E-mail: fengz@ornl.gov

Sarah Kleinbaum, Technology Area Development Manager
U.S. Department of Energy
1000 Independence Avenue, SW
Washington, DC 20585
Phone: 202-586-8027
E-mail: sarah.ollila@ee.doe.gov

Contractor: Oak Ridge National Laboratory
Contract No.: DE-AC05-00OR22725

Executive Summary

This project aims to develop, mature, and validate near-production readiness of a solid-state spot joining technology to join prototype-scale auto body-in-white (BIW) subsystems made of advanced high-strength steel (AHSS) and 7000/6000 series high-strength aluminum (Al) alloys (HSA alloys) to meet the dissimilar metal joining challenges in high-volume mass production. Development of the proposed technology is built on the project team's previous success in developing and demonstrating two emerging, solid-state, friction-heating-based spot joining processes—friction bit joining (FBJ) and friction stir spot welding (FSSW)—to join AHSS to Al alloys at a coupon scale. The project is led by Oak Ridge National Laboratory, with participations from Honda R&D Americas, Alcoa, DOW Chemical, L&L, Cosma Engineering, G-NAC, Mega-Stir Technologies, Brigham Young University, and The Ohio State University.

Accomplishments

- Brought the FBJ process past the Phase 1 go/no-go decision point by meeting or exceeding all performance targets at the coupon level specified by industry team members (Fiscal Year [FY] 2016).
- Determined that weld bonding further increases joint strength and provides a potentially practical and effective means for corrosion avoidance (FY 2016).
- Completed a number of iterative studies on joining bit geometry, material, and heat treatment combinations for joint strength, cost, and manufacturability (FY 2016).
- Completed joint performance evaluation of FBJ, adhesive bonding, and weld bonding (adhesive + FBJ) on dual phase (DP) 980 (DP 980), galvannealed DP 1180 (DP 1180GA), and 7xxx series Al alloys (FY 2016).
- Designed and demonstrated a prototype automated joining bit feed system (FY 2016).
- Developed a process model of FBJ with reasonable prediction of process conditions and temperature distribution (FY 2016).

- Demonstrated initial success of a thermal buckling modeling tool to understand and predict thermally induced buckling of spot-weld and adhesively bonded Al-steel components due to mismatch of the coefficient of thermal expansion (FY 2016).

Future Directions

- Pass the corrosion test per OEM requirements at the coupon and subcomponent level (FY 2017).
- Complete high-strain-rate testing of FBJ, adhesive-bonded, and weld-bonded coupons (FY 2017).
- Determine the interactive effects of multiple spot welds on mechanical performance with multi-spot-weld large coupons (FY 2017).
- Develop a prediction model for part distortion due to the material thermal expansion mismatch effect (FY 2017).
- Complete an automated joining bit feed system for FBJ (FY 2017).
- Complete hardware system integration for prototype-scale trials (FY 2017).
- Complete integrated model for joint performance prediction and validation (FY 2017).
- Complete project validation and verification by prototype-scale testing and demonstration (FY 2018).

Technology Assessment

- Target: Joining of ultra-high-strength steels (such as DP1180) with HSAs (such as 7xxx series Al alloys) to enable use of the highest strength steel and Al alloys for auto-body light-weighting. Refine and optimize the solid-state spot weld process to meet or exceed all performance targets, including combination with adhesive bonding. Examples of specific performance targets for weld bonding (combining solid-state spot welding with adhesive bonding) are 15-kN tensile shear strength (TSS), 4.5-kN cross-tension strength (CTS), 10 million fatigue lifecycles at 0.75 kN, and a 10-week corrosion test per original equipment manufacturer (OEM) testing specifications. The material combination evaluated will be 1.2-mm DP1180 AHSS and 2.0-mm 7xxx series HSA alloy.
- Gap: Conventional joining processes (such as resistance spot welding and self-piecing riveting) are not suitable or possible for joining these material combinations in a cost-effective manner for high-volume production vehicles.
- Gap: Part dimensional changes (i.e., distortion) and damage to joint strength due to thermal expansion mismatch are major technical hurdles that must be solved for successful use of different materials such as HSA alloys and AHSSs in auto-body structures.

Introduction

This project focuses on developing and demonstrating two emerging solid-state, friction-heating-based spot joining processes—FBJ and FSSW—to join AHSS to HSA alloys from the coupon scale to the prototype part level. Application of these joining processes to HSA and AHSS in the BIW production environment requires further research and development to address a number of technical obstacles (e.g., joint performance, productivity, maintaining consistency of joint quality under expected dimensional variations of stamped and/or formed parts, and cost-effectiveness).

The project consists of two phases. During Phase 1, both FBJ and FSSW were developed and evaluated at a coupon scale. Furthermore, because corrosion management is a primary concern for joining of dissimilar materials, both FBJ and FSSW were combined with adhesive bonding as an isolation approach to protect the spot joint from galvanic corrosion. Finally, an integrated computational welding engineering modeling framework, developed by the project team over the years, is being adopted, refined, and applied. The purpose of the integrated computational welding engineering model is (1) to refine and optimize the solid-state joining

process, (2) understand microstructure changes in the weld region and their effects on the strength/properties of an individual joint, and (3) optimize joinability and joint performance at the prototype assembly level. During Phase 2, the "winning" process will be selected for further development using prototype-scale BIW assembly level joining. Hardware of the winning joining process will be integrated with an assembly-line welding robot. Prototype BIW subsystems, selected by the OEM, will be welded and assembled with the robotic joining system to evaluate and validate production readiness of the joining technology for high-volume mass production BIW assembly. Al-steel joints, at both the coupon scale and the prototype scale, will be tested and characterized to determine performance of the joints in accordance with the requirements in the funding opportunity announcement and a set of process and performance criteria from the OEM, Tier 1 supplier, and industry partners. The project assembled an excellent project team composed of automotive manufacturers and auto-part suppliers to carry out the proposed process research and development; engineering testing; joining system integration; and eventual commercialization and implementation.

Approach

FBJ is a newly invented solid-state joining process particularly suitable for dissimilar materials. FBJ creates a metallurgical bonded spot joint in two or more sheets of dissimilar metals through a combination of frictional drilling and bonding action of a high-strength consumable joining bit. FSSW is a derivative of the friction stir welding (FSW) process. A rotating fixed-pin tool is plunged into the upper sheet with normal force to generate frictional heat. The heated and softened material adjacent to the tool deforms plastically and a solid-state bond is made between two dissimilar metals such as Al and steel. Figure V.4-1 illustrates both processes.

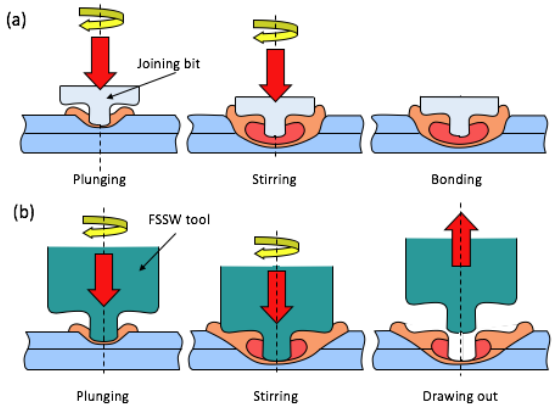

Figure V.4-1. Schematic of two emerging solid-state spot joining processes: (a) FBJ and (b) FSSW.

Development of joining technology must be coupled with corrosion management, which is critical for automotive applications, especially for any joint between dissimilar materials. An adhesive was applied at all proposed contact locations between HSA and AHSS components to serve as an insulator. The solid-state joining techniques, adhesive bonding, and combination of the two were initially assessed using laboratory-scale coupons.

Modeling the joining process provides insights on physical phenomena (e.g., thermal and deformation histories) during joining projects. This model is a prerequisite for subsequent weld microstructure and performance modeling and understanding the effect of temperature rise due to joining on the thermal expansion coefficient mismatch of two different metals. In addition, component level modeling provides an analytical modeling tool for assisting in design optimization to reduce welding distortion and stresses to a tolerance level. The integrated computational welding engineering approach has been adapted to refine the joining process and to predict joint performance under manufacturing conditions (e.g., paint baking).

Results and Discussion

FBJ, Adhesive-Bonding, and Weld-Bonding Process Development

FBJ process development was conducted on a number of combinations of steels and Al alloys. AHSS included GA DP 1180 and uncoated DP 980 and two types of HSA alloy (i.e., 7xxx-1 and 7xxx-2) were used. In addition, three different joining bit materials were used as part of FBJ process optimization to meet the performance target. The final target material combinations identified by project industry partners were the first choice for the prototype subsystem for the project. The joining bit material was selected taking into account its low cost and ability for mass production. The joining bit design was further refined to meet or exceed the coupon-level performance criteria. Table V.4-1 shows a summary of mechanical testing results for FBJ joints, without the use of adhesive bonding, indicating that joints of all target material combinations have successfully met all evaluation criteria. The average lap shear strength is 10 kN for the material combinations, while the targeted value is 5 kN. Cross-tension and T-peel strength also exceeded the evaluation criteria of 1.5 kN. Finally, the fatigue life of FBJ specimens also met the evaluation criteria of 10^7 cycles.

Table V.4-1. Summary of FBJ Joint Performance with Different HSA-AHSS Combinations with Different Joining Bit Materials and Designs (P = pass, F = fail)

Material Combination		Target Strength	7xxx-1–DP1180-GA	7xxx-1–DP1180-GA	7xxx-2–DP1180-GA	7xxx-2–DP1180-GA	7xxx-2–DP1180-GA	7xxx-2–DP1180-GA (target)	7xxx-1–DP980	7xxx-1–DP980
Thickness (mm)		—	2.0/1.2	2.0/1.2	2.0/1.2	2.0/1.2	2.0/1.2	2.0/1.2	1.6/1.2	2.0/1.2
FBJ Design/Material		—	1	1	1	2	2	3	1	3
TSS (kN)	FBJ-A	>5	10.0 (P)	9.7 (P)	8.3 (P)	9.0 (P)	9.9 (P)	10.0 (P)	10.3 (P)	12.85 (P)
	FBJ-B		—	—	—	—	—	—	10.5 (P)	12.9 (P)
CTS (kN)		>1.5	1.91 (P)	—	—	—	—	2.54 (P)	2.77 (P)	2.82 (P)
T-Peel (kN)		>1.5	—	—	—	—	—	1.79 (P)	—	1.63 (P)
TSS Fatigue (10^7)		0.75	P	—	—	—	—	P	—	P

Adhesive bonding has been used increasingly in the auto industry in the past few years to increase the strength and other performance of auto body structures made of AHSS. Our previous research also revealed the benefit of using adhesive bonding as insulation barrier for galvanic corrosion protection in dissimilar metal welds [1, 2]. In this project, weld bonding, which combines solid-state spot welding (FBJ or FSSW) with adhesive bonding, is considered essential for meeting performance requirements at the component level. It is also an effective means for corrosion prevention in joining dissimilar metals. The team evaluated two different types of adhesives from two adhesive suppliers (i.e., DOW Automotive and L&L Products). Later, the adhesives were combined with FBJ for weld bonding. The project evaluated different steel and Al combinations and tested three different adhesive bond-line thicknesses to find the optimum bond-line thickness. Joint performance was evaluated by means of tensile shear test, cross-tension test, peel strength test, and tensile shear fatigue test. Table V.4-2 summarizes mechanical testing results for adhesive bonding only. Because of the business sensitive nature of this work, we only present results with pass (P) or fail (F) criteria rather than actual data. For the target material combinations, TSS and CTS using both adhesive A and adhesive B passed the performance evaluation criteria. Peel strength was measured using both adhesives. The fatigue life of adhesively bonded specimens for both adhesives passed the evaluation criteria (10^7 cycles). Furthermore, the project evaluated weld-bonded (FBJ + adhesive) target material combinations for two different types of adhesives from the two adhesive suppliers. Table V.4-3 provides a summary of mechanical testing results for weld-bonded specimens. TSS and CTS of weld-bonded test specimens using both adhesive A and adhesive B successfully passed the evaluation criteria. The T-peel strength of both weld-bonded specimens was measured. The next annual report will report the measured fatigue life of both weld-bonded specimens.

Table V.4-2. Summary of Joint Performance for Adhesive-Bonded Specimen HSA/AHSS with Different Adhesives (P = pass, F = fail)

Material Combination		Target Strength	Adhesive A			Adhesive B		
			7xxx-2–DP1180GA	7xxx-1–DP1180	7xxx-1–DP980GA	7xxx-2–DP1180GA	7xxx-1–DP1180	7xxx-1–DP980GA
Thickness (mm)		—	2.0/1.2	2.0/1.2	2.0/1.2	2.0/1.2	2.0/1.2	2.0/1.2
TSS (kN)	Adhesive Bond-Line Thickness: A	>10	P	—	P	P	—	—
	Adhesive Bond-Line Thickness: B		–	P	P	–	P	P
	Adhesive Bond-Line Thickness: C		P	P	P	P	P	P
CTS (kN)		>3	P	P	F	P	P	P
T-Peel (kN)		Measure	Measured	—	—	Measured	—	—
TSS Fatigue (10^7)		0.75 kN	P	P	—	P	—	—

Table V.4-3. Joint Performance Summary of a Weld-Bonded (FBJ + adhesive) Specimen HSA/AHSS with Different Adhesives (P = pass, F = fail)

Material Combination	Target Strength	Weld Bonding (Adhesive A)	Weld Bonding (Adhesive B)
		7xxx-2–DP1180GA	7xxx-2–DP1180GA
Thickness (mm)	–	2.0/1.2	2.0/1.2
TSS (kN)	>15	P	P
CTS (kN)	>4.5	P	P
T-Peel (kN)	Measure	Measured	Measured
TSS Fatigue (10^7)	0.75 kN	To be tested	To be tested

FBJ Process Modeling Development

FBJ process modeling can provide insights on physical phenomena (e.g., thermal and deformation histories) during the joining process. This model is a prerequisite for subsequent weld microstructure and performance modeling and for understanding the effect of temperature rise due to joining and thermal expansion mismatch of two different materials. In this project, FBJ process model was developed based on ALE finite element formulation. It was capable of predicting the temperature field away from the bonding interface in FBJ (Figure V.4-2). The temperature profiles closely matched measured temperature histories at three different locations, which were measured by thermocouples. The peak Z-axis force from the simulation is similar to the peak force measured from the experiment. These modeling results are considered sufficient for simulation of the overall thermal expansion mismatch effect at the component level. The FBJ modeling results are being incorporated in modeling the dimensional changes of weld bonded auto body component based of AHSS and HSA. However, additional development and refinement of the FBJ process model is needed before use for microstructure modeling. The details of the modeling approach and experimental validations are being prepared for a publication.

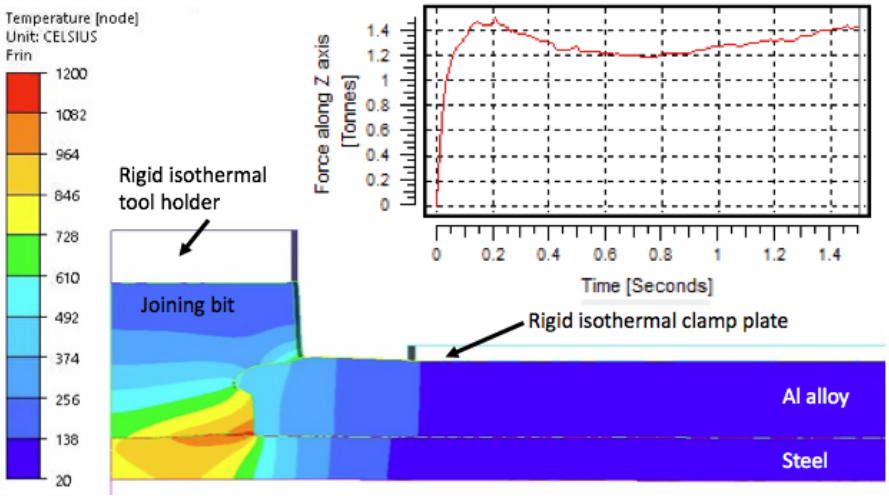

Figure V.4-2. Temperature and Z-axis force profiles from FBJ modeling.

Automated Joining Bit Feed System Development for FBJ

Automated joining bit feed system is being developed as part of FBJ system integration for demonstration of prototype part joining during Phase 2. The conceptualized automated joining bit feed system was fabricated, assembled, and successfully demonstrated. This is one of the major milestones and deliverables leading to Phase 2 of the project. Figure V.4-3 illustrates the parts of the system. A brief description of the working mechanism follows.

First, the joining bits start in the hopper (highlighted in red in Figure V.4-3(a)) and are moved by a corkscrew across a hole that lets the bits drop through a trap door one at a time. Next, the single bit is pushed through a tube via compressed air into the orientation drum (indicated by the red arrow in Figure V.4-3(b)). Once the bit is in the drum, the magnetic carriage (the red assembly in Figure V.4-3(c)) rotates around the stationary orientation drum (the green assembly in Figure V.4-3(b)). This allows the magnet located in the magnet block (pink block near the top of the picture) to sweep the drum and pick up and orient the bit. Once the sweep is complete and the bit is oriented, the carriage returns to the top position. Finally, when the bit is in the top-center position, a pneumatic ram pushes the reloading tray (light blue in Figure V.4-3(d)) out to present the bit to the driver. Once the driver is loaded, the tray retracts and the process begins again because the current bit is in service. To date, the front magnetic carriage assembly has been built. Figure V.4-3(e) is an isometric view of the integrated FBJ machine with automated joining bit feed system.

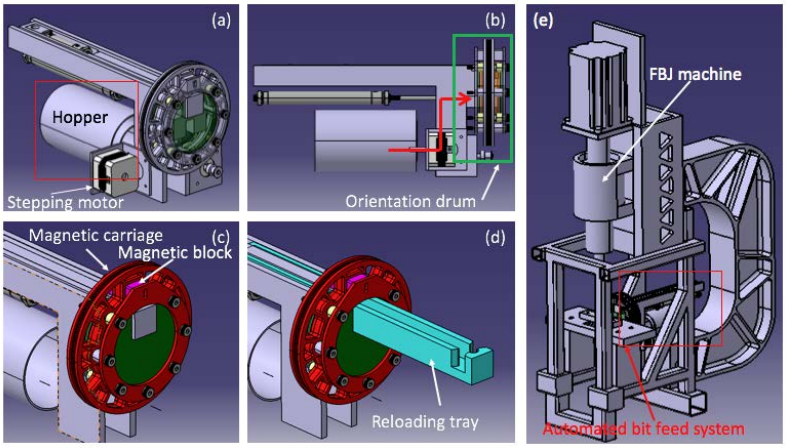

Figure V.4-3. Three-dimensional drawings of the automated joining bit feed system: (a) hopper, (b) orientation drum, (c) magnetic carriage and block, (d) reloading tray, and (e) isometric view of the whole system.

FSSW Process Development

Development of FSSW process in Phase I was carried out on two machines available to the project team: the FSW process development system (PDS) and the FBJ machine that was also used for FBJ process development. Each machine has different process parameter windows and other features (such as maximum tool rotational speed and Z-axis force). The use of two different machines made it possible to explore a wider range of process conditions for FSSW process development. FSSW process development was based on the target material combinations (HSA 7xxx–2/DP1180GA) with different surface conditions.

Initially, the development of FSSW was on FSW-PDS system. A maximum TSS of 3.55 kN was achieved when the surface oxide and zinc coating was removed, and 2.43 kN was achieved with the samples in the as-received surface conditions. When the oxide/coating was removed, only a marginal improvement in joint strength was achieved. Increasing the plunge depth into the steel resulted in higher joint TSS. These results are in large comparable with the results of FSSW Al to steel in open literature.

We later decided to use the FBJ machine (with modification) for FSSW development. The FBJ machine has much higher tool rotating speed and better controls of certain process aspects compared with the FSW-PDS system. We have carried out several rounds of process development, with each being refined based on the results from the previous rounds. Considerably higher joint strength was obtained. So far, we have passed initial lap shear joint strength target (5kN) with a specially designed tool and other process innovations. A summary of TSS data is provided in Table V.4-4. A maximum TSS of 7.46 kN was achieved, which is much higher than the strength values of FSSW in open literature for Al to steel FSSW of similar thicknesses. The average TSS is 5.44 kN, with a standard deviation of 1.37 kN. Bottom pullout failure of Al sheet was obtained, which indicate strong metallurgical bonding between Al and steel. Although the average TSS met the evaluation criteria of 5 kN, more consistent results with less scattered data are required. Further process refinement and optimization are being carried out to improve the strength and consistency of the FSSW process.

Table V.4-4. Summary of TSS for FSSW on the Target Material Combinations using FBJ Machine

Sample ID	Tensile Shear Strength (kN)
20160915#12	7.46
20160919#00	5.5
20160919#01	7.24
20160920#01	4.49
20160920#02	4.48
20160920#04	4.11
20160920#05	4.76
Average	5.44
STDEV	1.37

Component Level Modeling Development

The primary objective of component-level modeling is to understand the potential buckling failure of the bimetallic structure during the paint bake process. A structural model was developed based on ABAQUS software to simulate the thermal buckling condition. The model has two channels, one for Al and another for steel, which were bolted together (Figure V.4-4(a)). To reduce computational time, a quarter of the bimetallic structure was modeled (Figure V.4-4(b)).

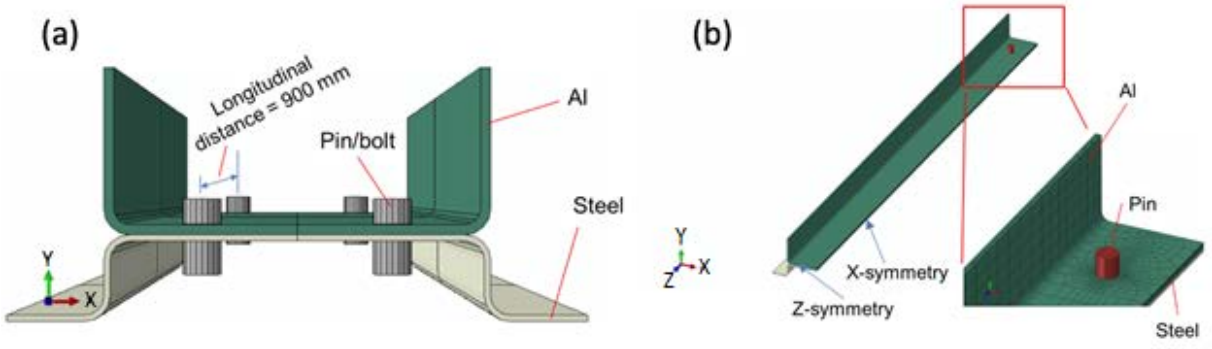

Figure V.4-4. Thermal buckling model setup: (a) overview of the entire geometry and (b) zoomed-in view of the pin region.

The calculated results at the paint-bake peak temperature after Al alloys are paint-bake hardened are shown in Figure V.4-5. As shown in Figure V.4-5(a), a compressive stress is formed in the Al alloy sheet, while a tensile stress is formed in the steel sheet. Both the Al and steel sheets bend upward and the maximum gap at the center of the two sheets is about 7.5 mm. This large separation would potentially lead to adhesive debonding if a layer of adhesive were present. The residual deflection predicted by the thermal buckling model was measured experimentally in the project. Although the shape of the deflection profile is consistent, the magnitude of the calculated deflection is much smaller in the measured sample than in the model. The cause for the discrepancy in the deflection magnitude is currently under investigation. One factor may be the experimental measurement was done after the bimetallic structure was completely disassembled (i.e., bolts removed), while the calculation was done before disassembling. Another factor for under-prediction of residual deflection is constraint and interaction locally between the pinholes and the bolt. To accurately capture interactions between the pinholes and the bolt, the complete geometry of the bolt was introduced. The calculated residual deflection profile of the bimetallic structure conformed better to the experimental result than that obtained in the previous baseline model. Particularly, the largest gap in the current model, considering the full bolt geometry, was about 1.1mm (60% larger than the previous result). However, it was still five times smaller than those in the experimental value of 5.07mm were. Further improvements to the paint bake model are necessary.

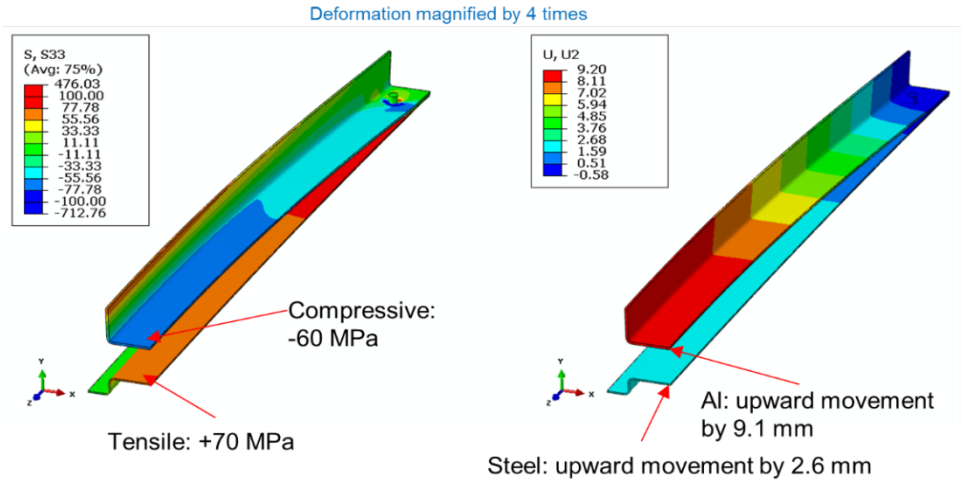

Figure V.4-5. Distribution of (a) longitudinal stress (MPa) and (b) vertical displacement (mm) at the paint bake peak temperature after the Al alloy is paint-bake hardened.

Model Development of Adhesive Bond

The lap shear model was designed with an Al sheet adhesively bonded on top of a steel sheet. For boundary and loading conditions, the steel's end is fixed and the aluminum end pulled with a constant velocity. The adhesive was modeled using cohesive elements with traction and separation failure behavior.

Results calculated using a preliminary model are shown in Figure V.4-6, where the corresponding experimental data tested are superimposed. A comparison between the calculated and measured data shows that traction and separation behavior can predict the load-displacement profile, particularly, the peak displacement at which the adhesive failure initiates. However, the calculated load-displacement curve is overly stiff prior to peak load when compared to experimental data. This is likely due to the assumption that thickness is indiscernibly thin for the adhesive in the finite element method.

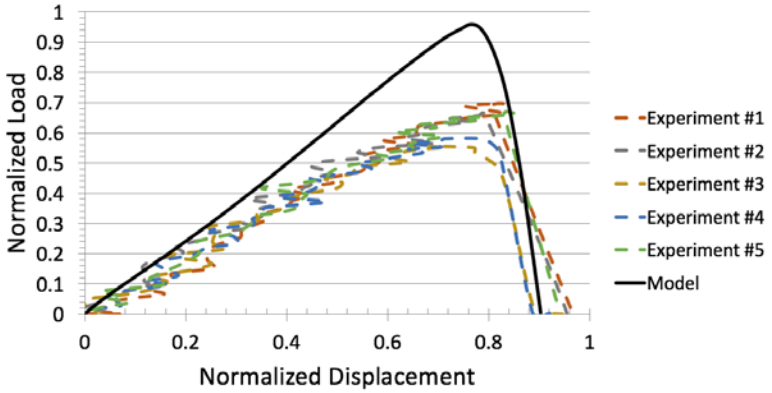

Figure V.4-6. Comparison of calculated and experimentally measured load-displacement curves for the lap shear tensile testing.

Technology Transfer Path

This project focuses on spot joining—the most common form of joining in BIW structures for high-volume production vehicles. Thus, it enables the broadest insertion of lightweight materials in BIW and has the highest potential among joining technologies for reduction of petroleum consumption, environmental impacts, and costs in the transportation sector.

The project has an excellent team comprising OEM, Tier 1 suppliers, welding equipment manufacturers, national laboratories, and research universities for both technology development and technology transfer. Participation of potential end users, material suppliers, and manufacturers from the outset allows the project to address various hurdles associated with commercialization, while providing a pathway for transfer of results to industry. The vertically integrated team provides an effective channel for technology transfer and commercialization.

Conclusion

The team is nearing completion of Phase 1 FBJ, adhesive-bonding, and weld-bonding (FBJ + adhesive) process development. The target material combination (Al alloy 7xxx-2–DP1180GA) has met or exceeded all coupon-level performance target evaluation criteria set forth by the OEM and industry partners. This is one of the major milestones and deliverables for Phase 1 of the project. Considerable progress has been made on FBJ process modeling, showing good agreement with the experiment. This is critical for microstructural modeling and component-part modeling. A prototype of the automated joining bit feed system was integrated with the FBJ process and successfully demonstrated at the MegaStir facility. The overall design of the automated joining bit feed system was further refined and finalized and is currently being fabricated and integrated with electronic and control systems. This is a major milestone and deliverable leading to Phase 2 of the project. Significant progress on component level modeling, including distortion and adhesive bonding, has been made.

References

[1] Lim, YC, Squires, L, Pan, T-Y, Miles, M, Song, G-L, Wang, Y, Feng, Z. (2015) Study of mechanical joint strength of aluminum alloy 7075-T6 and dual phase steel 980 welded by friction bit joining and weld-bonding under corrosion medium. *Materials & Design*, **69**(0):37-43

[2] Lim, YC, Squires, L, Pan, T-Y, Miles, M, Wang, Y, Feng, Z. (2014) "Mechanical and Corrosion Properties of Aluminum/Steel Spot Welded by Friction Bit Joining Process for Automotive Applications." in *67th IIW Annual Assembly & International Conference: Advanced Technology in Welding and Joining for Heavy, Automotive and Electronic Industries*. Seoul, South Korea.

Bibliography

Cardanini, A., Z. Feng, E. Boettcher, and W. Zhang, 2016, "Computational Study of Thermal-Buckling in a Mechanically Fastened Aluminum Steel Bi-Metal Structure," *FabTech/AWS Professional Program Conference*, Las Vegas, Nevada, November 16 through 18, 2016.

Feng, Z., 2016, "Solid-State Body-in-White Spot Joining of Al to AHSS at Prototype Scale," *U.S. Department of Energy Hydrogen and Fuel Cells Program and Vehicle Technologies Office Annual Review and Peer Evaluation Meeting*, Washington, D.C., June 6 through 10, 2016.

Lim, Y. C., L. Squires, T.-Y. Pan, M. Miles, G.-L. Song, Y. Wang, and Z. Feng, 2015a, "Study of Mechanical Joint Strength Of Aluminum Alloy 7075-T6 and Dual Phase Steel 980 Welded by Friction Bit Joining and Weld-Bonding under Corrosion Medium," *Materials and Design* 69: 37–43.

Lim, Y. C., L. Squires, T.-Y. Pan, M. Miles, Y. Wang, and Z. Feng, 2015b, "Joining of Aluminum/Dual Phase 980 Spot Welded by Friction Bit Joining and Weldbonding: Study of Mechanical Integrity under Corrosion Medium," presented at *Materials Science and Technology*, Columbus, Ohio, October 4 through 8, 2015.

Lim, Y. C., L. Squires, T.-Y. Pan, M. Miles, J. K. Keum, G.-L. Song, Y. Wang, and Z. Feng, 2016, "Corrosion Behavior of Friction Bit Joined and Weld-Bonded AA7075-T6/Galvannealed DP980," *Science and Technology of Welding and Joining,* doi:10.1080/13621718.2016.1255404.

Miles, M., Y. C. Lim, L. Atwood, and Z. Feng, 2016, "Mechanical Properties and Modeling of Friction Bit Joined AA7075 and DP 980," presented at the *International Symposium on Plasticity*, Big Island, Hawaii, January 3 through 9, 2016.

Squires, L., Y. C. Lim, M. Miles, and Z. Feng, 2015, "Mechanical properties of Dissimilar Metal Joints Composed of DP 980 Steel and AA 7075-T6," *Science and Technology of Welding and Joining*, 20(3): 242–248.

V.5 Chrysler Upset Protrusion Joining Techniques for Joining Dissimilar Metals – FCA US LLC

Project Details

Stephen Logan, Principle Investigator
FCA US LLC
800 Chrysler Drive
Auburn Hills, MI 48326
CIMS #482-00-13
Phone: (248) 512-9485
E-mail: stephen.logan@fcagroup.com

Chuck Alsup, Project Officer
National Energy Technology Laboratory
3610 Collins Ferry Road, P.O. Box 880
Morgantown, WV 26507-0880
Phone: (304) 285-5432
E-mail: charles.alsup@netl.doe.gov

Sarah Kleinbaum, Technology Area Development Manager
U.S. Department of Energy
1000 Independence Ave., S.W.
Washington, DC 20585
Phone: (202) 586-8027
E-mail: sarah.ollila@ee.doe.gov

Contractor: FCA US LLC
Contract No.: DE-EE0006442

Executive Summary

The overall project goal is to develop and demonstrate a robust, cost-effective, and versatile joining technique, known as upset protrusion joining (UPJ) for joining challenging dissimilar metal combinations. UPJ is well suited for joining metal combinations where one of the metals is die cast magnesium (Mg). This project has developed process variants that enable joining Mg die castings to aluminum (Al) and steel sheet components of various thicknesses, strengths, and coating configurations. A variant of the UPJ process, known as upset cast riveting (UCR) has been evaluated for joining mixed metals that do not include die cast components.

Joints produced from these techniques are evaluated with conventional microstructure characterization, joining-induced defect characterization, tensile lap-shear testing, cross-tension testing, fatigue energy tests, and drop tower impact energy tests. The joint's galvanic corrosion performance is evaluated using FCA US LLC's prescribed accelerated corrosion testing procedure (i.e., American Society for Testing Materials [ASTM] G85-A2). This is a cyclic salt fog test that incorporates a small amount of acetic acid. At the end of the corrosion test, selected configurations are re-evaluated for quasi-static, fatigue, and impact performance.

Accomplishments

- Completed accelerated corrosion exposure of all 350 round boss UPJ joints per the ASTM G85-A2 (i.e., acidified salt fog testing) schedule. 218 samples successfully completed the prescribed 12-week corrosion evaluation (Fiscal Year [FY] 2015, FY 2016).

- Completed post-corrosion testing of 7 and 8-mm round boss UPJ joints. Most of the results for 8-mm round boss UPJ Mg to steel and Mg to Al joint corrosion tests were reported previously in the FY 2015 Annual Report (FY 2015, FY 2016).
- Continued coating activities to support production of coated round boss UCR assemblies for testing and evaluation (FY 2015, FY 2016).
- Completed production of all 384 round boss UCR assemblies and pre-corrosion structural/mechanical testing and evaluation of 180 assemblies; initiated and completed accelerated corrosion evaluation of 204 assemblies per the ASTM G85-A2 schedule (FY 2015, FY 2016).
- Completed post-corrosion structural/mechanical testing and evaluation of all 204 round boss UCR assemblies after exposure to the ASTM G85-A2 schedule (FY 2016).
- Obtained 75 steel test coupons coated with the military specification chemical agent-resistant coating process from the U.S. Army Tank Automotive Research Development and Engineering Center to see if this coating could provide improved galvanic isolation between the steel and Mg samples compared to previously evaluated conventional automotive coating processes (FY 2016).
- Obtained 40-Mg AM60B test coupons treated with Henkel's new MGC-2.0 pretreatment to determine if this coating could provide improved corrosion performance of the Mg samples compared to the previously evaluated conventional Henkel Alodine 5200 automotive pretreatment process (FY 2016).

Future Directions

- Finish production and corrosion testing of round boss UPJ samples with alternative coatings (FY 2017).

Technology Assessment

- Target (Project): Develop a robust, low-cost method for joining Mg die castings to dissimilar metal components such as Al and steel sheet.
- Gap: No method is currently available for joining Mg die castings to dissimilar metals.
  - Fusion welding cannot be used to join Mg to dissimilar metals because of the formation of brittle intermetallic structures.
  - Although solid state welding should theoretically offer some advantages for joining Mg to dissimilar metals without forming brittle intermetallic formations, experimentation has shown that the processing windows must be very narrow in order to be successful.
  - Mechanical joining of Mg die castings with steel fasteners creates a strong potential for galvanic corrosion between the materials. Attempts to rectify this effect were only partially successful because (1) any coatings on the steel fastener typically get damaged during the fastener insertion and (2) attempts to use Al fasteners are typically cost-prohibitive.
- Target (Task 1): Develop optimized joint geometry and process parameters for producing robust UPJ joints between Mg and dissimilar metals at industry-acceptable cycle times without damaging coatings (where applicable) on the cathodic material.
- Gap: Robust boss and electrode design and process parameters have not been developed to ensure UPJ can be used reliably in volume production applications.
- Gap: Insufficient thermo-mechanical compression material data exist for common die cast Mg alloys.

- Gap: Most common die cast Mg alloys do not have ideal forming characteristics and may be susceptible to cracking during the forging process, even with substantial heat application.
- Target (Task 2): Produce joined assemblies for testing and evaluation.
- Gap: No joined assemblies are currently available for testing and evaluation.
- Target (Task 3): Conduct initial (pre-corrosion) mechanical/structural testing and evaluation.
- Gap: Data do not exist to compare performance of the UPJ process to existing joining processes for strength and durability.
- Target (Task 4): Conduct accelerated corrosion testing and evaluation on benchmark self-piercing riveting (SPR) joints and UPJ variants.
- Gap: Data do not exist to compare corrosion performance of the UPJ process to existing joining processes.

Introduction

The UPJ process (shown conceptually in Figure V.5-1) is similar to heat staking of plastic components. The simplest form of the process uses a cast-in protrusion on a die cast component, which is aligned with a clearance hole in a mating component. An application of force and heat are used to upset forge the protrusion into a larger diameter boss that fills the clearance hole and forms a mushroom-shaped head that solidly locks the two components together.

Die casting is the most common and cost-effective process for producing lightweight Mg components. The UPJ process was conceived primarily for joining Mg die castings to each other and for joining Mg die castings to dissimilar metals. However, prior to this study, there has been relatively little work, other than bolting, aimed at joining components produced from this process.

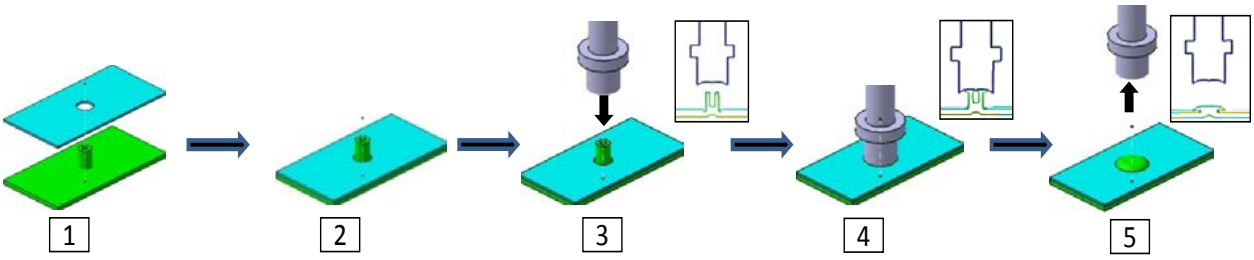

Figure V.5-1. Initial conceptual UPJ process schematic – assembling parts, applying heat and force, and completing the assembly

Alternative dissimilar metal joining processes have been investigated with varying levels of success. However galvanic corrosion has consistently been demonstrated to be a key challenge, particularly, the following:

1) Metallic bonding (such as fusion or solid state welding processes) require a clean (i.e., either no coatings or a specific coating that is designed to improve intermetallic bonding rather than corrosion performance) surface on both metals and does not allow for any isolation between the two metals.
2) Fasteners (e.g., rivets or bolts), which are typically made of steel for high strength and low cost, tend to promote galvanic corrosion in Al and aggressively promote galvanic corrosion in Mg. The galvanic activity is increased if one of the two light metals is joined to a steel component. Coatings intended for corrosion protection on steel fasteners tend to get damaged during the installation process. Fasteners also typically damage coatings on the components being joined. One result is that the preliminary coatings are rendered useless because galvanic isolation has been broken. Another result is the galvanic attack on the anode can be magnified if a small defect is created in the anode coating. Figure V.5-2 shows an example of this magnified galvanic attack where coated steel screws were driven into a coated Mg component and then exposed to a corrosive environment.

Figure V.5-2. Galvanic corrosion effects of steel screws in an Mg component exposed to 240 hours of ASTM B117 salt spray testing.

The UPJ process, by contrast, relies on a robust mechanical joint rather than intermetallic bonding; therefore, the cathodic material can be coated prior to joining to protect against galvanic attack on the anodic material. Additionally, because the UPJ protrusion is going through a hole that is drilled or punched prior to coating, the UPJ process is much less likely to damage the coating when the joint is being made. Furthermore, there is no joining-induced galvanic activity beyond that between the two parent materials because no additional cathodic material (such as a steel fastener) is used to create the joint.

Approach

The project technical approach is summarized as follows:

1. Establish the benchmark performance of Mg to Al joints produced with SPR, which is a currently available commercial process, for comparison purposes only.
2. Obtain additional knowledge and understanding of thermo-mechanical behavior of Mg alloys through Gleeble® testing conducted in Canada at no cost to the U.S. Department of Energy.
3. Supplement existing FCA UPJ process knowledge with computer-aided engineering forming simulation results based on knowledge gained through Gleeble® testing. Use this information to develop optimized cast protrusion and welding electrode shapes to reduce electrical current requirements and provide more robust, repeatable forming performance for each of the joint configurations being considered.
4. Evaluate all material configurations (e.g., AM60B to Al6022, Al6013, and high-strength steel [HSS] materials in bare, pre-treated, and coated conditions for round and oval shaped joints). For each configuration, produce tensile shear and cross-tension test coupons. Apply additional coating layers to select joint configurations prior to the mechanical/structural and corrosion evaluations.
5. Subject five samples of each configuration to the initial mechanical/structural tests described above.
6. Subject a substantial number of samples to FCA's accelerated corrosion tests, reviewing visually every 2 weeks and removing three samples of each configuration at 4-week intervals for quasi-static testing.
7. Finally, at the end of the 12-week accelerated corrosion exposure, subject select configurations to fatigue and impact testing for comparison to pre-corrosion performance.

Validate the joint performance through the following:

- Characterization of material microstructure in the joint region
- Characterization of joining-induced defects in the joint region
- Quasi-static tensile shear tests
- Quasi-static cross-tension tests

- Drop tower impact tests of select tensile shear and cross-tension samples
- Cyclic fatigue testing of select tensile shear and cross-tension samples
- FCA's 12-week accelerated corrosion test (ASTM G85-A2) with quasi-static lap-shear failure and cross-tension failure being evaluated after each 4-week increment and fatigue testing and impact testing to be re-evaluated on select samples at the end of the corrosion exposure
- Characterization of failure mechanisms for each of the mechanical tests described above.

Results and Discussion

This report focuses on performance results of UPJ joints developed and produced in FY 2014 and FY 2015, and UCR joint produced in FY 2016. During FY 2016, the team completed accelerated corrosion testing and post-corrosion mechanical testing of all round boss UPJ joints, as well as production, accelerated corrosion exposure, and post-corrosion testing of all round boss UCR joints. After completion of this pre-defined work, the team began to investigate alternative corrosion coatings.

The sample material/coating configuration descriptions for all round boss UPJ joints discussed in this report are shown in Table V.5-1. The configuration numbers defined in Table V.5-1 will be used throughout the report.

Table V.5-1. Round Boss UPJ Material and Coating Configurations

Configuration Number	Upper Sheet			Bottom Sheet			Assembly Coating Configuration
	Material	Thick-ness (mm)	Coating	Material	Thick-ness (mm)	Coating	
UPJ7-1	Al 6016	1.1	Bare	Mg AM60B	4.0	Bare	Uncoated
UPJ7-2	Al 6016	1.1	Alodine 5200	Mg AM60B	4.0	Alodine 5200	Powder-coated
UPJ7-3	Al 6016	1.1	Powder-coated	Mg AM60B	4.0	Alodine 5200	Uncoated
UPJ7-4	Al 6016	1.1	Powder-coated	Mg AM60B	4.0	Alodine 5200	Powder-coated
UPJ8-1	HSS DP-590	2.0	Armorgalv®	Mg AM60B	4.0	Alodine 5200	Uncoated
UPJ8-2	Al 6013-T4	2.2	Bare	Mg AM60B	4.0	Bare	Uncoated
UPJ8-3	HSS DP-590	2.0	Armorgalv®	Mg AM60B	4.0	Alodine 5200	Powder-coated
UPJ8-4	Al 6013-T4	2.2	Alodine 5200	Mg AM60B	4.0	Alodine 5200	Powder-coated
UPJ8-5	Al 6013-T4	2.2	Powder-coated	Mg AM60B	4.0	Alodine 5200	Uncoated
UPJ8-6	Al 6013-T4	2.2	Powder-coated	Mg AM60B	4.0	Alodine 5200	Powder-coated

The ***impact lap-shear tension*** test results for configurations UPJ8-2 and UPJ8-4 are shown in Figure V.5-3 prior to corrosion testing and after 12-weeks of accelerated corrosion exposure (left) and the failure mode for UPJ8-4 after corrosion is shown in Figure V.5-3 (right). This sample failed through shearing of the protrusion, which was consistent with pre-corrosion impact failure modes. Although there is not a substantial drop in impact performance after corrosion exposure, the data ***range*** for the results has increased substantially, possibly due to inconsistencies in coating applications and unidentifiable corrosion mechanisms.

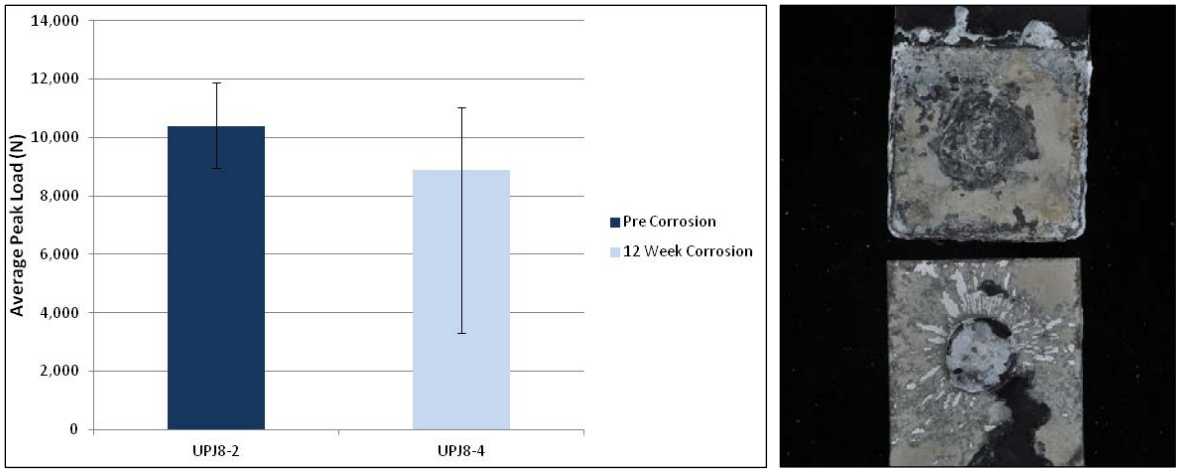

Figure V.5-3. 8-mm round boss UPJ lap-shear tension impact performance prior to corrosion testing and at 12 weeks of exposure (left) and failure mode (right).

The ***impact cross-tension*** test results for configurations UPJ8-1 and UPJ8-2 are shown in Figure V.5-4 prior to corrosion testing, while UPJ8-3 and UPJ8-5 are shown after 12-weeks of accelerated corrosion exposure. These samples failed through a range of mechanisms, including partial thickness protrusion pull-out, head of protrusion fracturing, and base of protrusion fracturing.

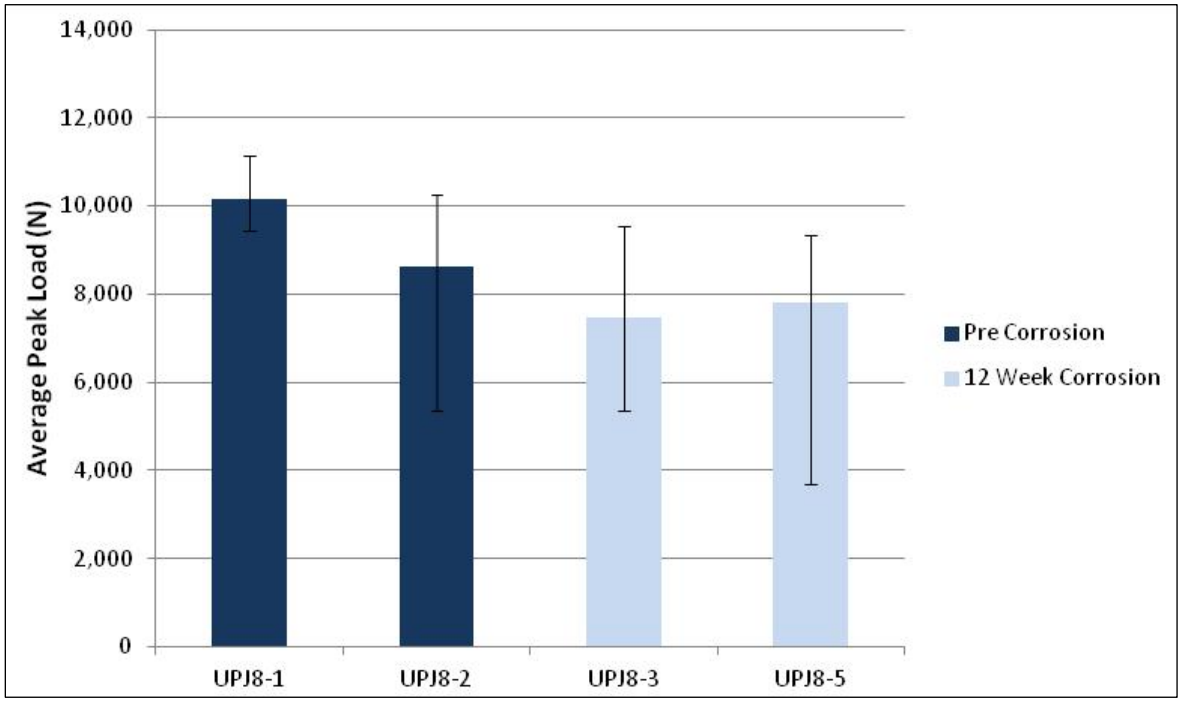

Figure V.5-4. 8-mm round boss UPJ cross-tension impact performance prior to corrosion testing and at 12 weeks of exposure.

Lap-shear tension fatigue results prior to corrosion and at 12 weeks of corrosion exposure are shown in Figure V.5-5. It is interesting to note that the post corrosion samples (shown in purple) failed at significantly lower levels than pre-corrosion samples in low-cycle fatigue, but not in high-cycle fatigue.

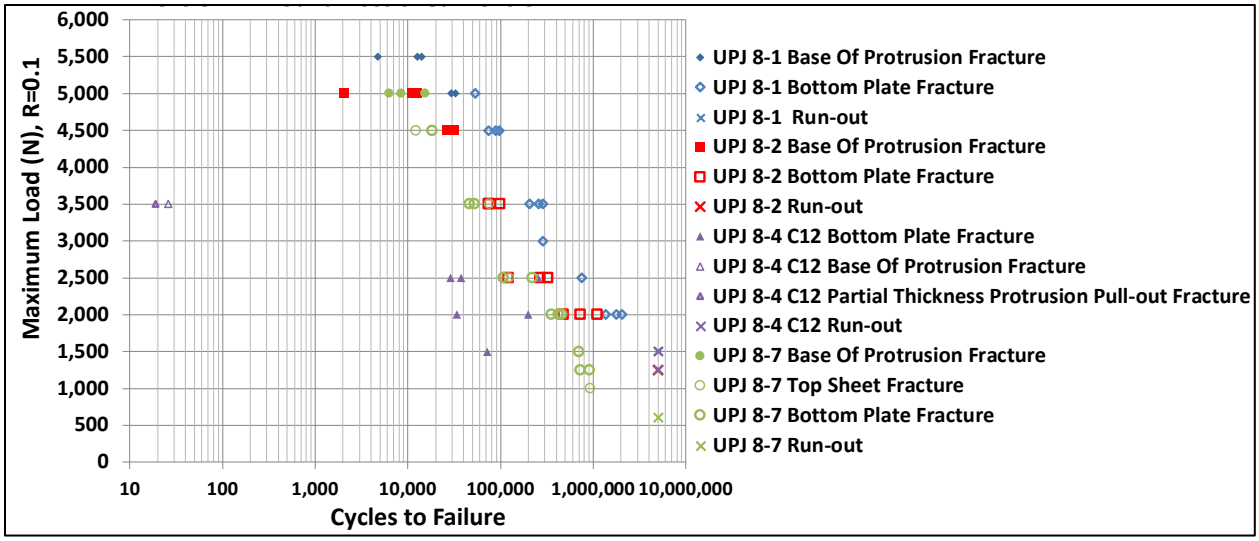

Figure V.5-5. Comparison of 8-mm round boss UPJ lap-shear tension fatigue performance prior to corrosion testing and after 12 weeks of exposure.

Cross-tension fatigue results are shown in Figure V.5-6. Unlike the lap-shear tension fatigue results, the post-corrosion cross-tension samples (again shown in purple) did not experience a significant drop in low-cycle fatigue performance and surprisingly failed at dramatically ***higher*** levels (2 to 3 times higher) compared to the pre-corrosion samples in high-cycle fatigue. This was completely unexpected and investigation of several possible theories was unable to verify the reason for the increase.

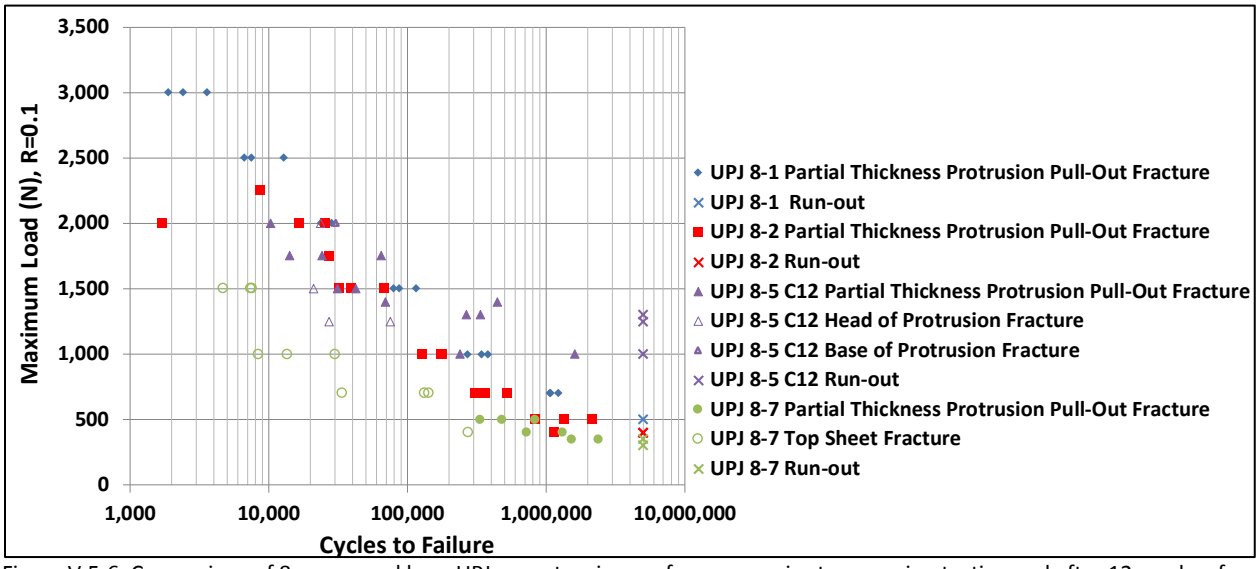

Figure V.5-6. Comparison of 8-mm round boss UPJ cross-tension performance prior to corrosion testing and after 12 weeks of exposure.

Figure V.5-7 shows the results of 12 weeks of accelerated corrosion exposure for Mg AM60B to Al 6016 lap-shear tension test configurations UPJ7-1, UPJ7-2, and UPJ7-3. None of the lap-shear samples separated as a result of the 12-week corrosion test, even the bare Mg to bare Al UPJ7-1 samples. The significantly improved corrosion test results for these samples compared to the 8-mm round boss samples that were discussed in FY 2015 is primarily due to the different Al alloy composition. For the FY 2015 report, the Al coupons were Al 6013, which is a high copper content Al alloy. For the samples discussed in this report, the Al coupons are Al 6016, which is a very low copper content Al alloy. Copper is well known to be aggressive to Mg when exposed to an acidic environment and has also been shown to have a very detrimental effect on the

intergranular exfoliation corrosion of Al sheet material. In each of the photos of Figure V.5-7, the upper panel is Al 6016 while the lower panel is Mg AM60B.

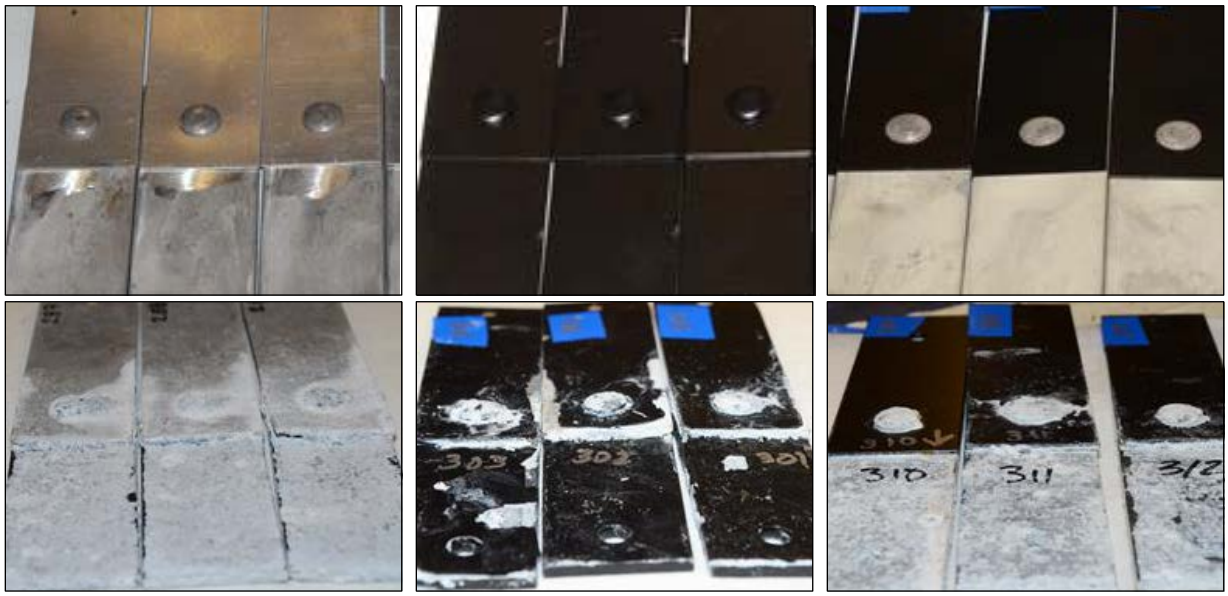

Figure V.5-7. UPJ7-1 (left), UPJ7-2 (center), and UPJ7-3 (right) Mg to Al lap-shear tension test coupons before corrosion exposure (top) and after 12 weeks of exposure (bottom).

Interestingly, while none of the cross-tension samples separated during the 12-week corrosion exposure, one sample from each coating configuration did experience substantial corrosion of the Mg coupons well away from the joint. Figure V.5-8 shows some of the cross-tension samples with damage to the Mg coupons. The reason for this is not completely clear because (a) none of the lap-shear samples experienced the same type of damage and (b) this particular type of damage was not observed in previous corrosion testing with the Mg to Al 6013 or Mg to steel joints. However, a likely explanation is that water may have pooled in the areas of the trays in the corrosion chamber where those samples were positioned.

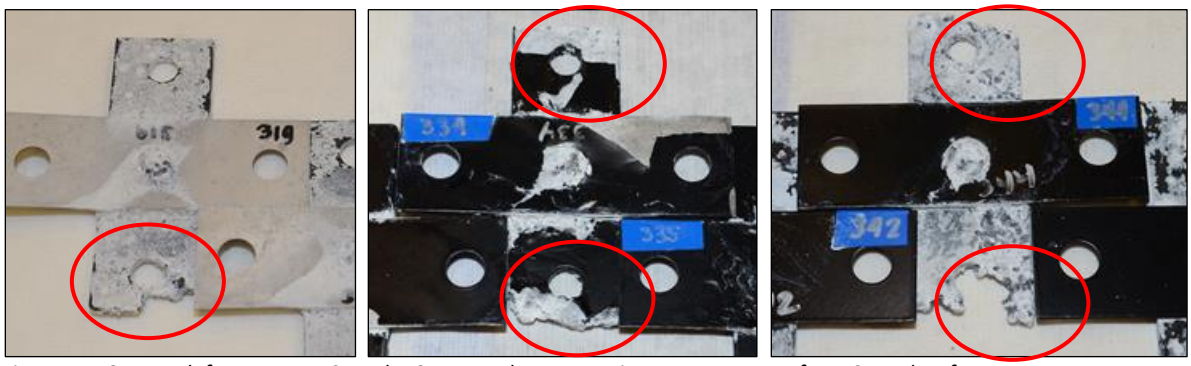

Figure V.5-8. From left, UPJ7-1, 7-2, and 7-3 Mg to Al cross-tension test coupons after 12 weeks of exposure.

The ***quasi-static lap-shear tension*** results for UPJ7-1, UPJ7-2, UPJ7-3, and UPJ7-4 are shown in Figure V.5-9 prior to corrosion testing and after 4 weeks, 8 weeks, and 12 weeks of accelerated corrosion exposure while ***impact lap-shear tension*** results for UPJ7-1 and UPJ7-4 are shown in Figure V.5-10 prior to corrosion testing and after 12 weeks of accelerated corrosion exposure. As previously mentioned, all of these configurations incorporated an Al 6016 alloy that has a lower level of copper than the Al 6013 alloy used in the UPJ8-2, UPJ8-4, UPJ8-5, and UPJ8-6 configurations; therefore, the general level of performance degradation (especially related to exfoliation corrosion) after corrosion exposure is expected to be less, and in fact, none of these joints separated during the accelerated corrosion testing. Even the UPJ 7-1 configuration, which consists of bare Al joined to bare Mg with no pretreatments or coatings on either material, remained intact throughout the full test procedure. Failures occur consistently by deformation and tearing in the thin 1.1-mm Al top sheet.

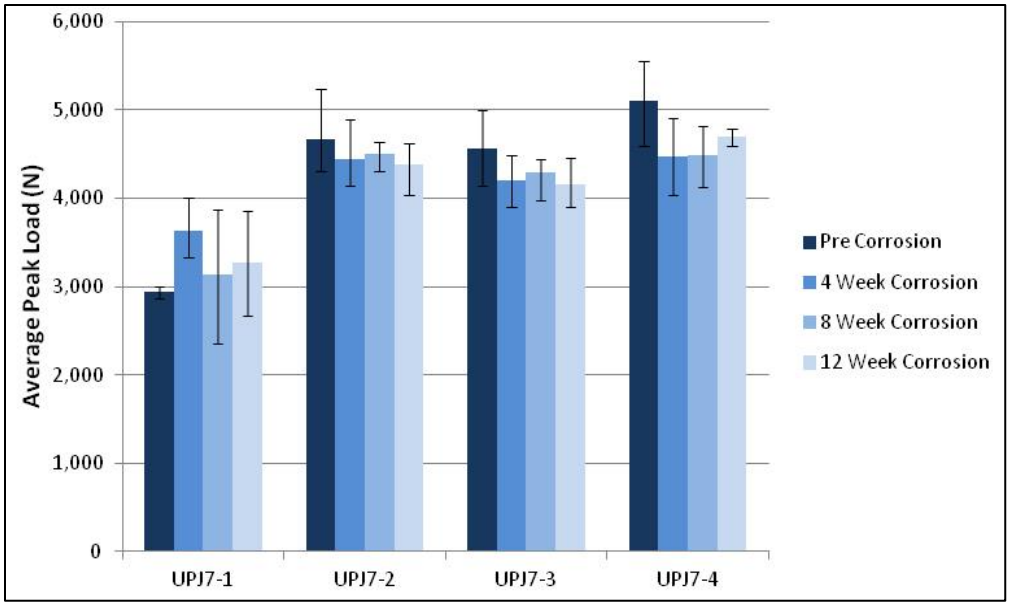

Figure V.5-9. 7-mm round boss UPJ quasi-static lap-shear tension performance prior to corrosion testing at 4 weeks, 8 weeks, and 12 weeks accelerated corrosion exposure.

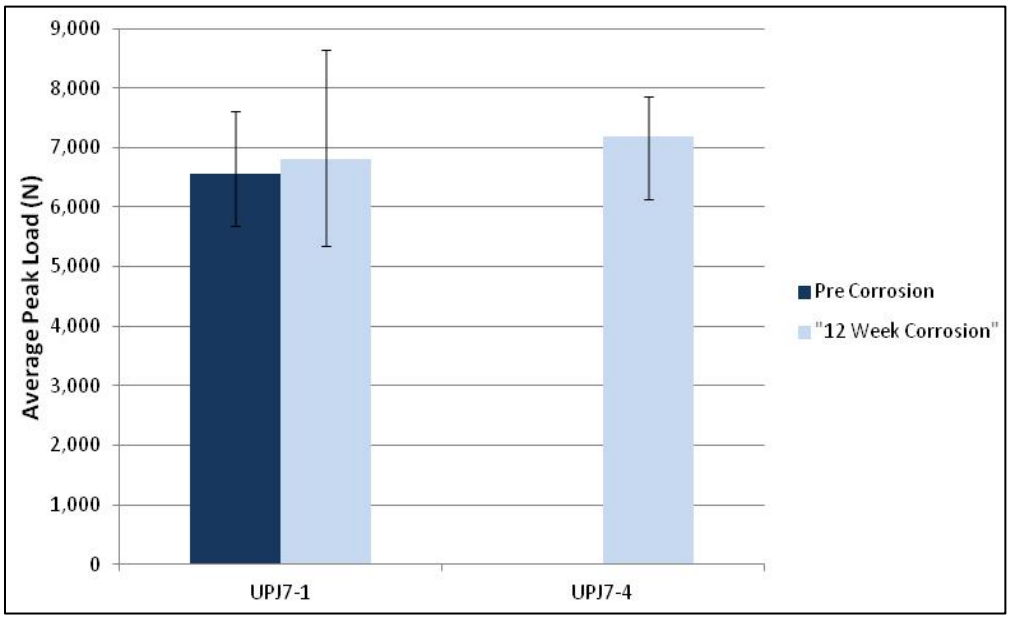

Figure V.5-10. 7-mm round boss UPJ impact lap-shear tension performance prior to corrosion and at 12 weeks accelerated corrosion exposure.

The Al panel in this configuration is only 1.1-mm thick; therefore, the overall strength levels in both lap-shear tension testing and cross-tension testing are lower than for the 8.0-mm diameter Mg-Al UPJ (UPJ8-2, UPJ8-4, UPJ8-5, and UPJ8-6) configurations reported in FY 2015. The reason for the overall lower level of performance of the UPJ7-1 configuration compared to the UPJ 7-2, UPJ 7-3, and UPJ 7-4 configurations is that this particular configuration is the only one that was not painted. Because all of these samples failed in the Al panel and Al 6016 is a bake-hardening alloy, the increased strength of the Al 6016 alloy after paint baking in UPJ 7-2, UPJ7-3, and UPJ7-4 resulted in higher joint strength.

The ***quasi-static cross-tension*** results for UPJ7-1, UPJ7-2, UPJ7-3, and UPJ7-4 are shown in Figure V.5-11 prior to corrosion testing and after 4 weeks, 8 weeks, and 12 weeks of accelerated corrosion exposure while ***impact cross-tension*** results for UPJ7-1 and UPJ7-4 are shown in Figure V.5-12 prior to corrosion testing and

after 12 weeks of accelerated corrosion exposure. Failures occurred by deformation in the thin 1.1-mm Al top sheet and by partial protrusion pull-out.

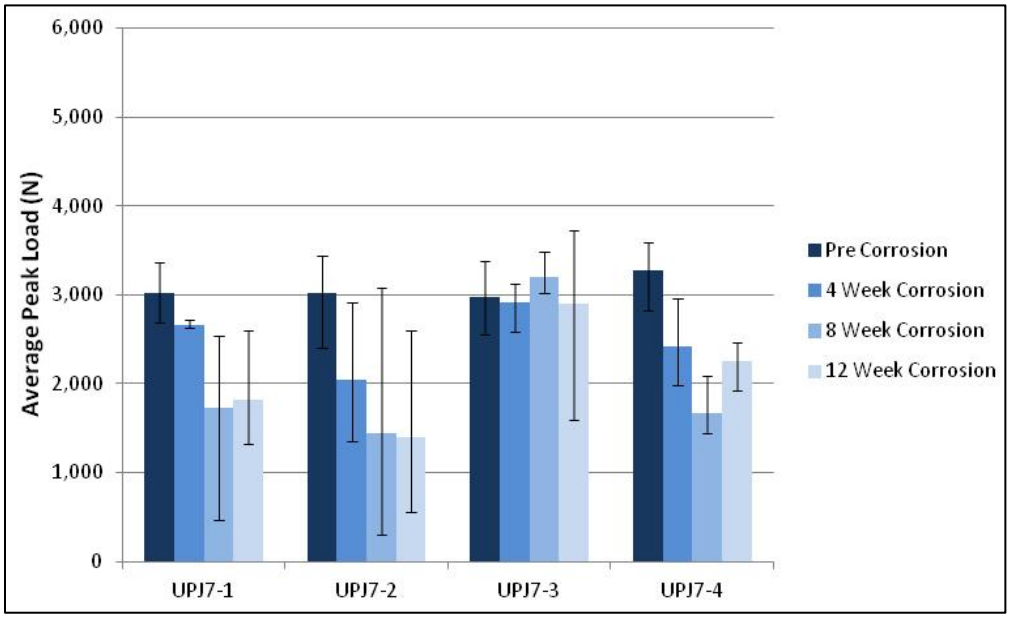

Figure V.5-11. 7-mm round boss UPJ quasi-static cross-tension performance prior to corrosion testing and at 4 weeks, 8 weeks, and 12 weeks accelerated corrosion exposure.

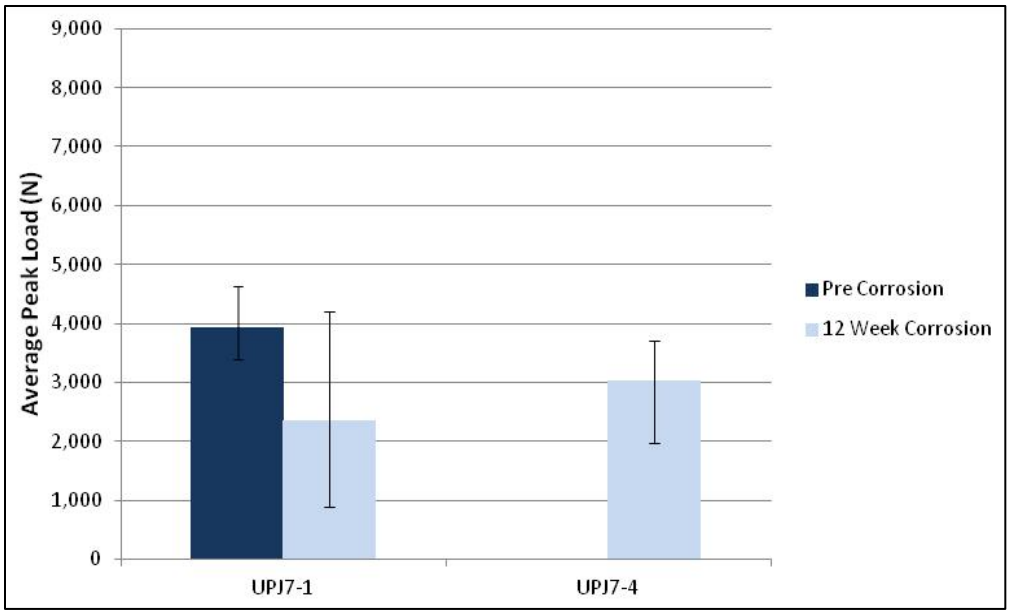

Figure V.5-12. 7-mm round boss UPJ impact cross-tension performance prior to corrosion testing and at 12 weeks accelerated corrosion exposure.

Again, as in the case of the lap-shear tension testing, due to the lower level of copper in the Al-6016 coupons versus the Al-6013 alloys evaluated with the 8-mm round boss UPJ joints, none of the joints separated during accelerated corrosion testing, even the UPJ 7-1 configuration, which consists of bare Al joined to bare Mg with no pretreatments or coatings on either material.

Note that unlike the lap-shear tension testing, in cross-tension testing, the UPJ7-1 configuration did not exhibit significantly lower joint strength than the other configurations. This is because in cross-tension, the joint strength is more dependent on the material stiffness than in lap-shear; therefore, additional strength gained through paint baking has less effect on overall joint strength.

For the UCR evaluations, all configurations incorporated a 1.3-mm thick Al 6016 alloy coupon joined to either a 1.0-mm thick (UCR 1-4) or 1.4-mm thick (UCR 5-8) HSS DP590 coupon. Because earlier evaluation of Mg to steel round boss UPJ assemblies had demonstrated that these joints would not pass the full 12-week test with the current coating configurations, the test protocol for the UCR Al to steel joints with Mg rivets was reduced to only 6 weeks and the samples were evaluated on a weekly basis instead of a bi-weekly basis. All configurations, except for the e-coated assemblies with sealed edges, were also tested at 1 week. The sample material/coating configuration descriptions for all round boss UCR joints discussed in this report are shown in Table V.5-2.

Table V.5-2. Round Boss UCR Material and Coating Configurations

Configuration Number	Upper Sheet			Bottom Sheet			Assembly Coating Configuration
	Material	Thickness (mm)	Coating	Material	Thickness (mm)	Coating	
UCR-1	DP590	1.0	Bare	Al 6016-T4	1.3	Bare	Uncoated
UCR-2	DP590	1.0	Armorgalv	Al 6016-T4	1.3	Bare	Uncoated
UCR-3	DP590	1.0	Armorgalv	Al 6016-T4	1.3	Pretreated	Uncoated
UCR-4	DP590	1.0	Armorgalv, e-coat, sealed	Al 6016-T4	1.3	Pretreated	Coated
UCR-5	DP590	1.4	Bare	Al 6016-T4	1.3	Bare	Uncoated
UCR-6	DP590	1.4	Armorgalv	Al 6016-T4	1.3	Bare	Uncoated
UCR-7	DP590	1.4	Armorgalv	Al 6016-T4	1.3	Pretreated	Uncoated
UCR-8	DP590	1.4	Armorgalv, e-coat, sealed	Al 6016-T4	1.3	Pretreated	Coated

Figure V.5-13 shows close-up views of the actual joint for UCR lap-shear tension configurations 1 through 4 prior to corrosion exposure and at 1, 2, 4, and 6 weeks of exposure. In all of these views, the rivet head on the steel side is shown. Clearly, when joining Al to steel with a Mg rivet, it is imperative to provide a substantial coating on the steel, sealing around the head and between the panels, and coating the assembly afterward as was done for UCR-4. Although UCR-4 displayed dramatically improved performance over UCR configurations 1 through 3 after 6 weeks, this is still only about half of the desired longevity in this corrosive environment; therefore, improved coating processes (especially for steel) are required for joining of Al to steel with a Mg rivet.

Quasi-static lap-shear tension results for all UCR joints are shown in Figure V.5-14 prior to accelerated corrosion exposure and at 1 week, 2 weeks, 4 weeks, and 6 weeks of exposure while ***impact lap-shear tension*** results for UCR-4 and UCR-8 prior to corrosion and at 1 week, 2 weeks, 4 weeks, and 6 weeks of accelerated corrosion exposure are shown in Figure V.5-15. Similar to the previously evaluated round boss UPJ Mg to steel assemblies, with the exception of UCR-4 and UCR-8 (the e-coated samples with sealed edges), all of the samples displayed a dramatic drop in strength after only 2 weeks of exposure. UCR-4 and UCR-8, however, both maintained good joint strength levels even after 6 weeks of exposure.

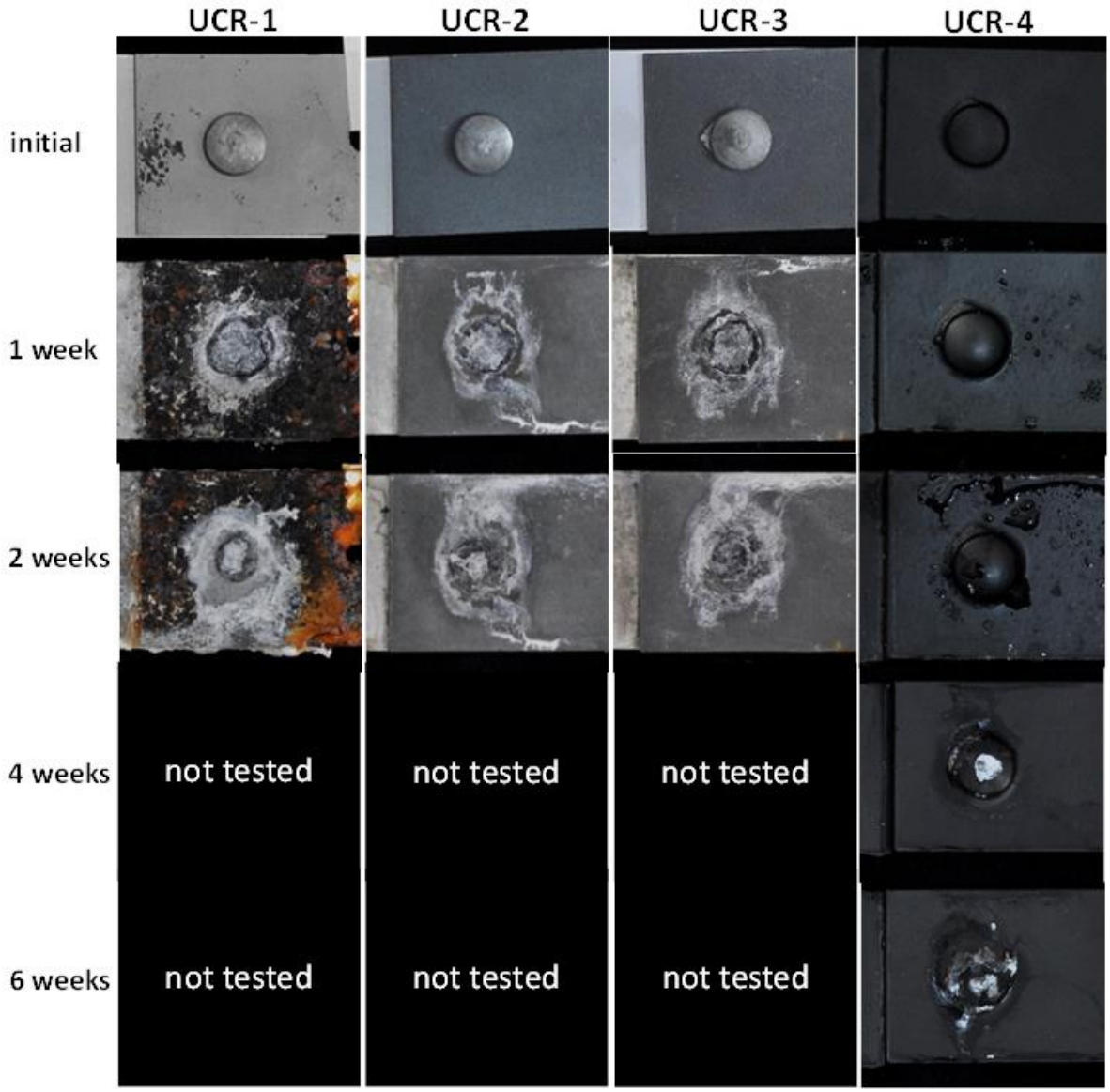

Figure V.5-13. Photos of UCR lap-shear joint configurations before and after ASTM G85-A2 accelerated corrosion exposure.

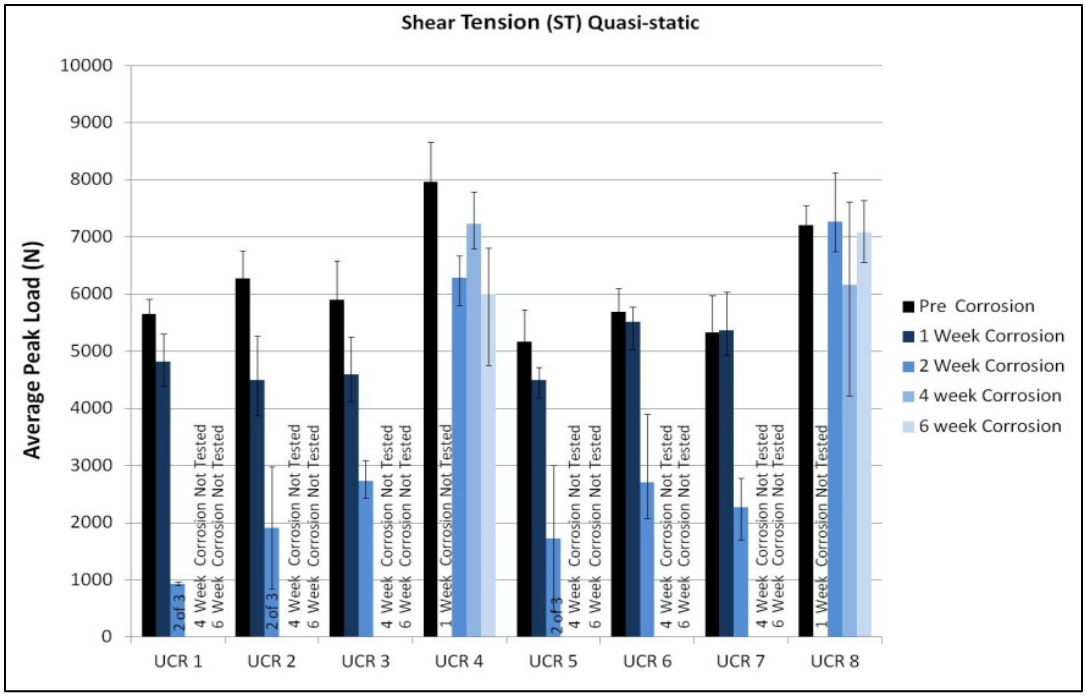

Figure V.5-14. UCR quasi-static lap-shear tension (ST) test results prior to corrosion testing and at 1 week, 2 weeks, 4 weeks, and 6 weeks of accelerated corrosion exposure.

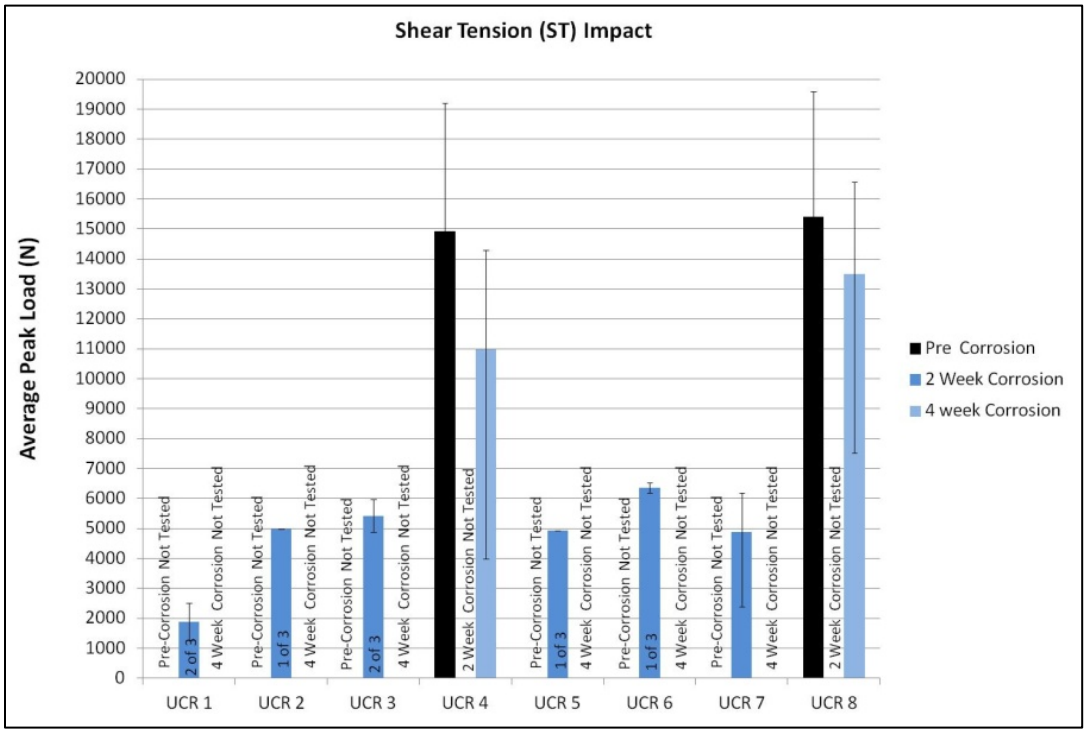

Figure V.5-15. UCR impact lap-shear tension (ST) test results prior to corrosion testing and at 1 week, 2 weeks, 4 weeks, and 6 weeks of accelerated corrosion exposure.

Quasi-static cross-tension results for all UCR joints are shown in Figure V.5-16 prior to accelerated corrosion exposure and at 1 week, 2 weeks, 4 weeks, and 6 weeks of exposure while ***cross-tension impact*** results are shown in Figure V.5-17. Similar to the lap-shear tension testing described above, with the exception of UCR-4 and UCR-8, all samples displayed a dramatic drop in strength after only 2 weeks of exposure. UCR-4 and

UCR-8, however, both maintained good joint strength levels even after 6 weeks of exposure. All pre-corrosion samples and most post-corrosion samples failed at the base of the rivet.

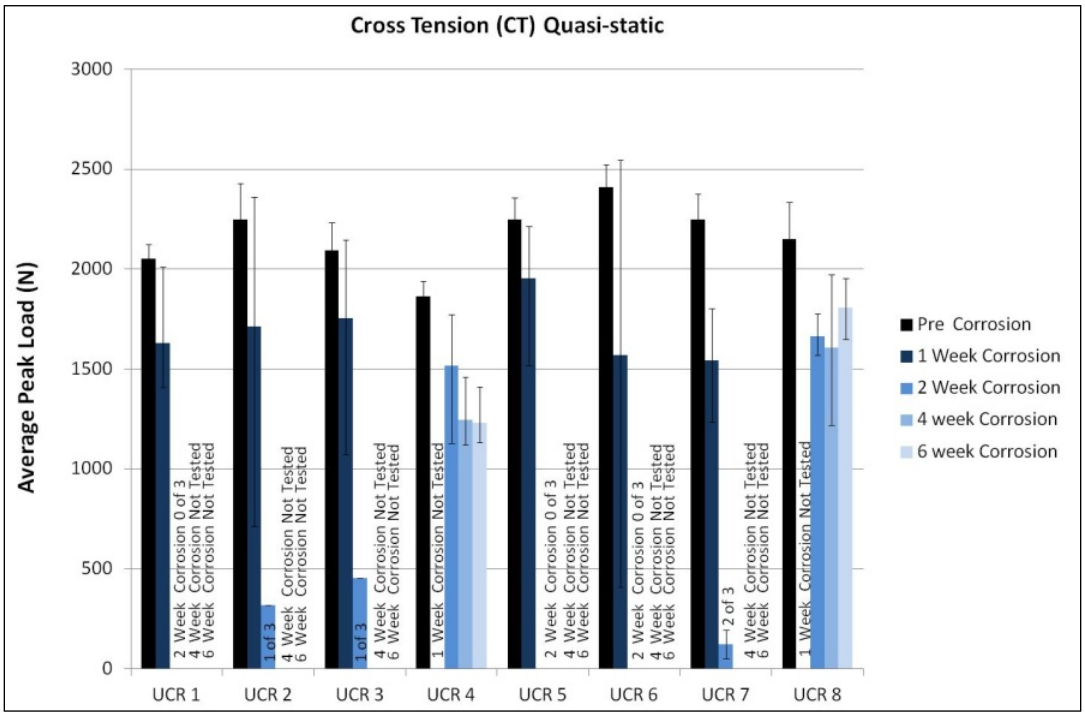

Figure V.5-16. UCR quasi-static cross-tension (CT) test results prior to corrosion testing and at 1 week, 2 weeks, 4 weeks, and 6 weeks of accelerated corrosion exposure.

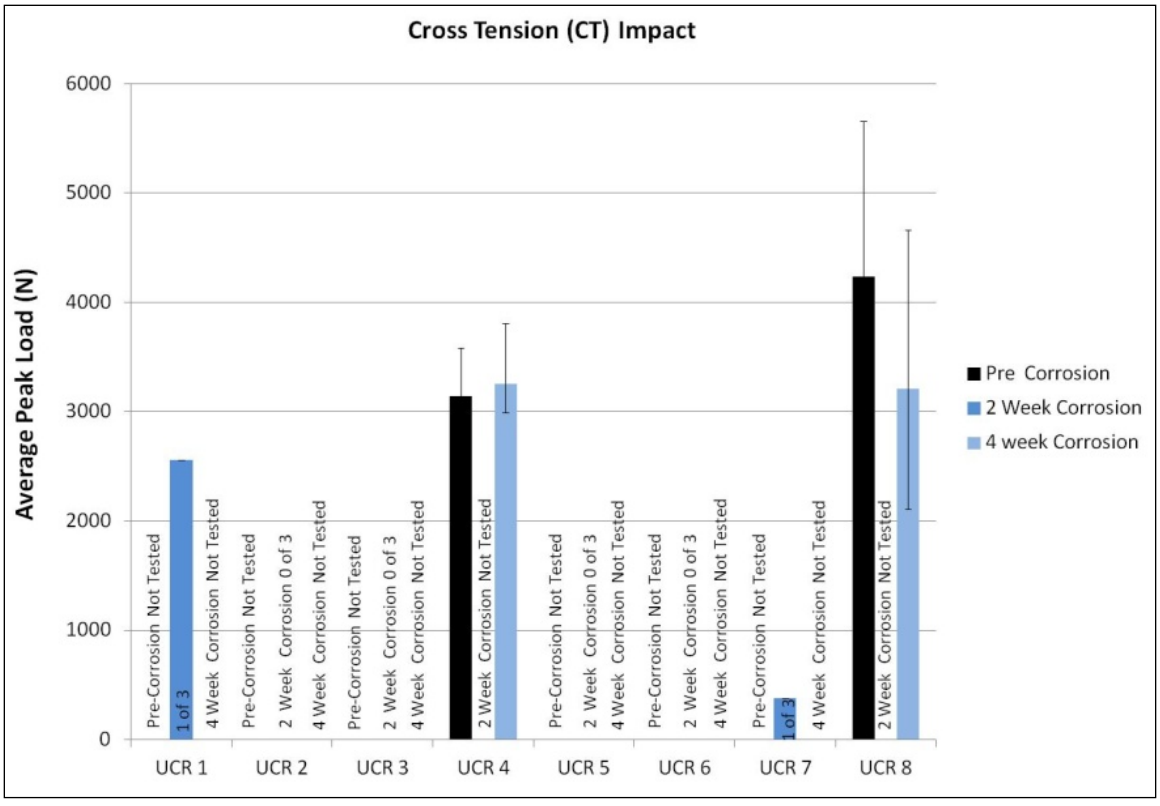

Figure V.5-17. UCR impact cross-tension (CT) test results prior to corrosion testing and at 1 week, 2 weeks, 4 weeks, and 6 weeks of accelerated corrosion exposure.

Lap-shear tension fatigue results prior to corrosion (shown in light blue) and after 4 weeks of corrosion exposure (shown in dark blue) are shown in Figure V.5-18. Results are generally consistent with previously reported results for UPJ lap-shear tension fatigue testing, although the high-cycle fatigue results are higher because the actual base materials are steel and Al and only the rivet is Mg. In previous UPJ lap-shear fatigue testing, many of the pre-corrosion, high-cycle fatigue failures had occurred in the die cast Mg plate, whereas ***all*** pre-corrosion UCR-8 lap-shear test samples failed in the parent material of the lower 1.3-mm Al sheet. However, while some of the post-corrosion UCR samples failed in the Al parent material, others failed in the actual rivet head.

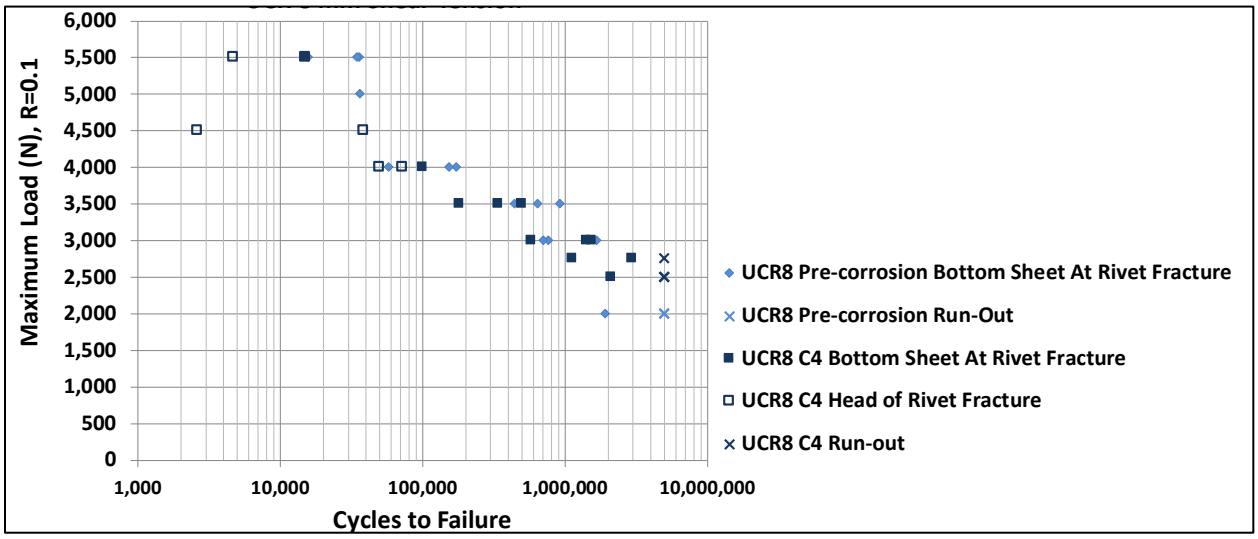

Figure V.5-18. Comparison of UCR8 lap-shear tension fatigue test results prior to corrosion exposure and at 4 weeks of exposure.

Cross-tension fatigue results are shown in Figure V.5-19. Again, results are generally consistent with previously reported results for UPJ cross-tension fatigue testing, with the exception there is not a dramatic increase in post-corrosion (again shown in dark blue), high-cycle fatigue versus pre-corrosion (again shown in light blue), high-cycle fatigue. All test samples failed at the base of the rivet.

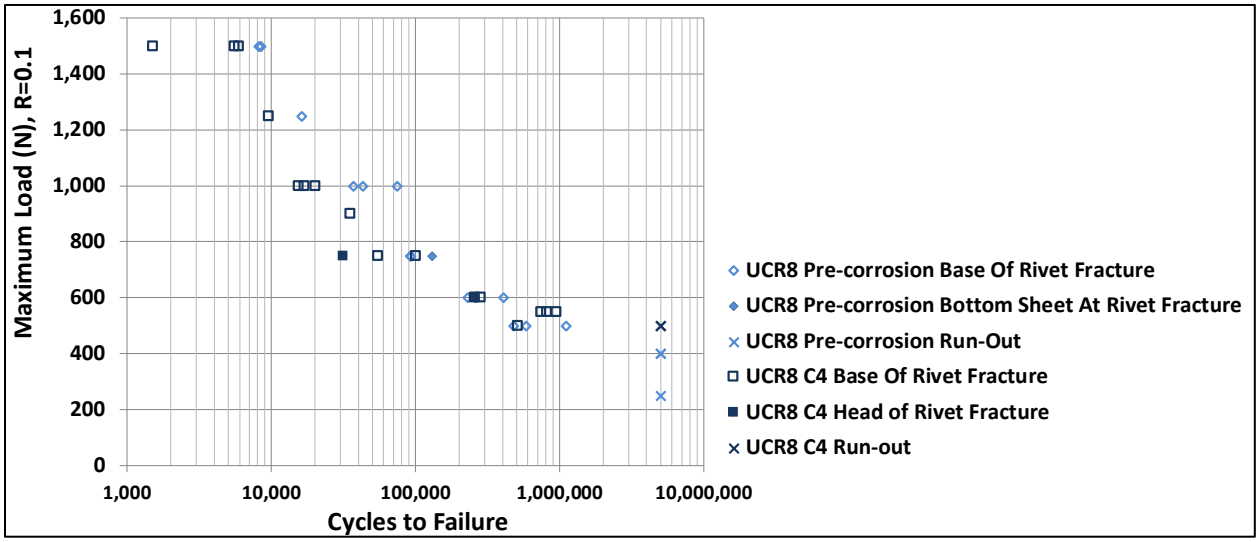

Figure V.5-19. Comparison of UCR8 cross-tension fatigue test results prior to corrosion exposure and at 4 weeks of exposure.

An alternative coating, known as chemical agent-resistant coating, was provided by TARDEC. Unfortunately, this coating was unable to withstand the UPJ process temperatures and forces (see Figure V.5-20). Because of the extensive coating damage in the area of the UPJ joint, no corrosion testing was conducted.

Figure V.5-20. Photo of two joined lap-shear tension assemblies using the chemical agent-resistant coating on the steel coupons.

The MGC-2.0 Mg pretreatment provided by Henkel converts the outer layer of the Mg material to a ceramic. However, this coating was unable to withstand UPJ process forces (see Figure V.5-21(a) and (b)), where most of the black MGC-2.0 coating flaked away from the boss in the form of a very fine powder when the UPJ force was applied prior to application of heat. This did not prevent the formation of a good mechanical joint (see Figure V.5-21(c)). Parts were returned to Henkel for evaluation, where it was determined that even though most of the black color was gone from the boss, approximately 50 to 75% of the actual coating thickness still remained. Nevertheless, subsequent corrosion testing at AET Integration showed no improvement over the previous results with Alodine 5200 for joints where the assembly was not powder coated post-assembly.

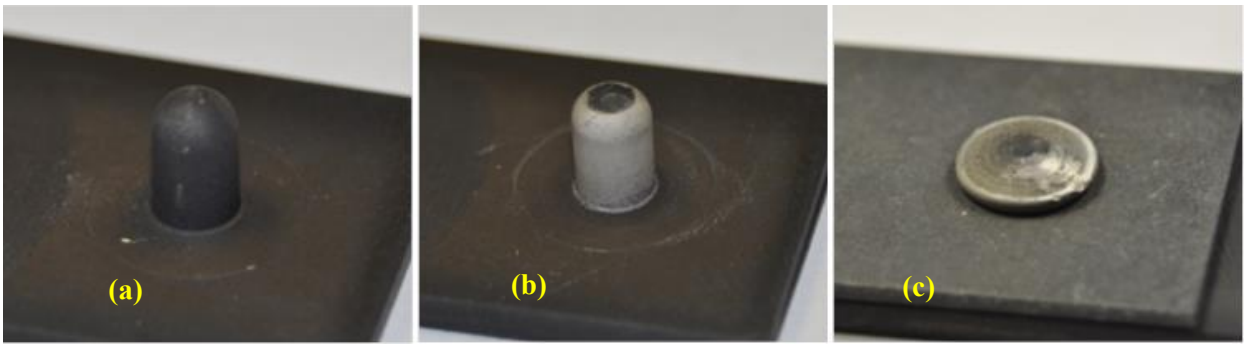

Figure V.5-21. Photos of MGC-2.0-treated Mg lap-shear tension coupons (a) prior to contact by the electrode, (b) after application of initial contact force by the electrode but prior to application of electrical current, and (c) after a full forming operation with force and current.

Technology Transfer Path

Two of the key obstacles preventing more widespread use of light metals in high-volume automotive applications are lack of robust joining techniques (especially for dissimilar metal joining) and susceptibility to galvanic corrosion. Successful completion of this project will provide a key enabler to high-volume application of lightweight materials. This will allow FCA (and ultimately other manufacturers) to accelerate development of new lightweight vehicle designs that use multiple lightweight materials in order to aggressively reduce mass on future vehicle programs.

Conclusion

During FY 2016, the team has continued evaluation of corrosion performance and post-corrosion structural/mechanical performance of 7.0 and 8.0-mm diameter round boss UPJ joints of Mg to Al-6013, Mg to Al-6016, and Mg to HSS DP590 steel. While there was substantial corrosion damage to joints produced with the uncoated Mg to Al-6013 joints and to all Mg-steel joints reported in FY 2015, the corrosion

degradation of the Mg to Al-6016 joints discussed in this report was minimal even in the uncoated configuration.

Additionally, the team produced round boss UCR Al-steel joints and conducted pre-corrosion structural mechanical testing, corrosion testing, and post-corrosion mechanical testing of these joints. While the pre-corrosion performance of these joints was on par with the UPJ joints, the corrosion and post-corrosion performance posed a substantial challenge due to the galvanic coupling of the three metals (i.e., Mg rivet, Al, and steel plates).

Finally, two alternative coating processes were evaluated for their performance as galvanic corrosion protection between Mg and steel. However, neither of these alternative coating processes showed an improvement over the current state-of-the-art processes.

References

None

Bibliography/Presentations

Logan, S. D., 2016, "Upset Protrusion Joining Techniques for Joining Dissimilar Metals," presented at the *2016 U.S. DOE Hydrogen and Fuel Cells Program and Vehicle Technologies Office Annual Merit Review and Peer Evaluation Meeting*, Washington, DC, June 8, 2016.

Logan, S. D., 2016, "Evaluating the Upset Protrusion Joining (UPJ) Method to Join Magnesium Castings to Dissimilar Metals," *3rd Global Lightweight Vehicle Manufacturing Summit*, Detroit, Michigan, February 24, 2016.

V.6 Brazing Dissimilar Metals with a Novel Composite Foil– Johns Hopkins University

Project Details

Timothy P. Weihs, Principal Investigator
Johns Hopkins University
Department of Materials Science and Engineering
3400 North Charles Street
Baltimore, MD 21218
Phone: 410-516-4071
E-mail: weihs@jhu.edu

David Ollett, Project Manager
National Energy Technology Laboratory
626 Cochrans Mill Road
Pittsburgh, PA 15236-0940
Phone: 412-386-7339
E-mail: david.ollett@netl.doe.gov

Sarah Kleinbaum, Technology Area Development Manager
U.S. Department of Energy
1000 Independence Avenue, SW
Washington, DC 20585
Phone: 202-586-8027
E-mail: sarah.ollila@ee.doe.gov

Contractor: Johns Hopkins University
Contract No.: DE-EE0006441

Executive Summary

Reactive brazing is a novel technique in the joining industry that uses reactive materials to produce locally the substantial amounts of heat to join components. In this project, mechanically processed dilute thermite foils (i.e., redox foils) were created, where, upon ignition, exothermic reactions self-propagate to produce molten metal capable of joining dissimilar metal combinations. Because of the transient nature of the reaction, thermal damage to base materials is limited. In addition, novel component combinations that cannot be joined via traditional furnace brazing (e.g., magnesium alloys to steel) can be produced. Redox foils are produced by mechanically processing and consolidating constituent powders. By adjusting the fabrication pathway and chemistry, reaction products can be tailored to join specific material combinations. In addition to producing mechanically processed foils, this project produces vapor-processed foils with controlled, model microstructures to characterize some of the reaction mechanisms.

This fiscal year, the project worked to identify the sources of gas formation during propagation and to reduce the amount of gas generated by adjusting the fabrication process. Gas generation is detrimental to the strength of the resulting bonds because it can cause mass ejection from the bond area, creating pores in the resulting braze. Local hot spots can create copper (Cu) vapor in ball-milled Al:Cu_2O redox foils; however, if the diluent is homogeneously distributed within the ball-milled powder, Cu gas production is suppressed. These foils have been used to successfully join dissimilar metal combinations, but there is still porosity in the foil products due to other gas production mechanisms that are still under investigation.

Accomplishments

- Identified Cu vapor as the gaseous species during propagation of reactions within ball-milled, mechanically processed redox foils with an Al:Cu_2O:Cu chemistry (Fiscal Year [FY] 2016).
- Produced vapor-deposited Al:Cu_2O:Cu foils with five different diluent amounts to identify an idealized microstructure (FY 2016).
- Increased homogenization of the diluent in redox foils by incorporating the diluent into the ball-milling process, resulting in suppression of Cu vapor during propagation (FY 2016).
- Reduced the solidification temperature on cooling by over 100°C by replacing the Cu diluent with silver (Ag), thereby producing a braze alloy and stronger bonds (FY 2016).

Future Directions

- Determine mechanisms and species of non-metal vapor produced by the reaction (FY 2017).
- Add oxygen getters to the foil chemistry to absorb oxygen at low temperatures (FY 2017).
- Create statistically significant data sets for shear strengths of bonds and determine the modes of failure in the joint (FY 2017).
- Determine corrosion susceptibility of bonds produced with redox foil (FY 2017).
- Analyze braze and components being joined for any changes in mechanical properties of base component metals due to heating from the reaction of the redox foil (FY 2017).

Technology Assessment

- Target: Bonds with a lap shear strength of 20 MPa.
- Gap: Current bonds fabricated with redox foil are approximately 10 MPa; shear strength can be increased by decreasing porosity of the bond area and improving wetting of samples during reaction.
- Target: Gasless propagation of redox foils.
- Gap: Current bonds fabricated with redox foil show significant porosity, which is likely due to evolution of gases upon reaction and heating.

Introduction

Reactive materials have been used to join metals for over 100 years; ever since Hans Goldschmidt discovered that reactive aluminum (Al) and iron oxide could produce molten iron capable of joining railroad lines. [1,2] This is called the thermite process, where Al reduces a metal oxide and creates molten metal, alumina, heat, and often gaseous products. Initial joining uses of these chemistries involved using powdered mixtures and a mold so the created molten braze could flow into the joints. More recently, reactive multilayer foils using intermetallic formation reactions have been used as local heat sources for joining. [3-5] The reactive foils do not produce their own braze; therefore, they require pre-wet solder or braze layers to enable joining. Reactive joining provides a fast, efficient bonding approach that allows use of high temperature brazes that cannot be used on certain alloys.

This project aims to combine the concepts of the two types of reactive joining described above. By utilizing a thermite composition, the exothermic reaction can create its own braze without requiring any pre-coated solder or braze layers on the components. Furthermore, by creating a fully dense foil, the joint can be formed without any mold or complicated fixture. The braze is created at the location of the joint and does not need to flow into the joint area as is the case with typical thermite joining (see Figure V.6-1). In order to reduce the amount of gas produced by thermite reactions, the mixture is diluted with excess metal. Adding diluent decreases reaction velocity, the total amount of heat, and the reaction temperature. Adding diluent also has the benefit of increasing the quantity of molten metal braze in the products when compared to undiluted thermites. [6]

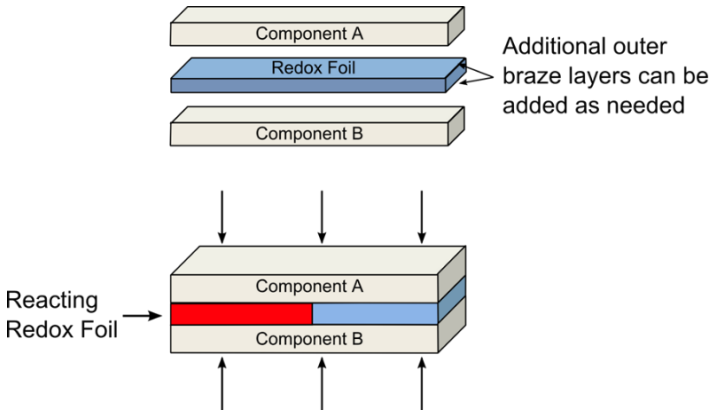

Figure V.6-1. Schematic of the joining process with redox foil. As the reaction propagates, molten braze is produced.

The chemistry and microstructure of the redox foil determines how the reaction will propagate. The chemistry also determines the characteristics of the braze that is formed. By engineering the reaction properties of the foil, the reaction to join many dissimilar metal combinations can be tailored. Because the reactions propagate quickly (approximately 1 m/s), heat is produced for a short period of time and very locally. This allows for brazing of dissimilar combinations that cannot be joined with traditional furnace brazing (e.g., joining steel to magnesium alloys).

Approach

To develop a redox foil capable of joining dissimilar metals, the project has produced two different types of foils. The first foil is made by mechanically processing constituent powders (i.e., redox foil), [6,7] and the other is made by physical vapor deposition (PVD) and is considered to be a model material. The redox foil is the economical solution that can be easily scaled for automotive applications. PVD foils, on the other hand, have well-defined geometries for scientific inquiry. These ideal microstructures are critical for understanding the processes that occur during propagation and for identifying the best microstructure to emulate in the redox foils. During the past fiscal year, the project has determined that the Al:Cu_2O system is the most promising system for joining, with the diluent typically being Cu (some Ag dilutions have been prepared) as will be described.

The redox foil mechanical fabrication process involves three steps. First, constituent powders are ball-milled to produce nanocomposite powders. This step was added in FY 2015 to reduce reactant spacing between the Al fuel and oxide. Initially, only the Al and metal oxide were ball-milled together to produce thermite composites (these foils are labeled BM). However, due to analysis from the PVD foils in FY 2016, it was determined that the diluent needs to be more uniformly incorporated into the final structure. Therefore, the diluent was added to the ball milling process (BM+D). After milling, the powders are packed into a tube and compacted by swaging, which is a radial reduction technique. Finally, the swaged tubes are rolled flat and the tube encasing the material is removed, leaving the fully dense redox foil.

The PVD foils are made using magnetron sputtering. The sputtering chamber contains three targets: Al, Cu2O-Cu, and Cu. Inside the chamber, substrates are rotated past each target, producing multilayered foils with a planar geometry.

To analyze the materials, a variety of techniques was employed. For understanding the characteristics of reaction propagation in the foils, high-speed videography coupled with emission spectroscopy was used. High-speed videos allowed us to determine propagation velocity, which was a key metric for how fast the reaction was producing heat. Emission spectroscopy was used to identify if vapor species were produced by the reactions and approximate reaction temperatures. Slow-heating experiments, including differential scanning calorimetry and thermogravimetric analysis, were also used to characterize the thermal properties of reactive materials and the resulting braze. Finally, the redox foils were used to join Al 3003, Mg AZ31, and hot-stamped boron steel; the shear strengths of resulting bonds were tested.

Results and Discussion

For FY 2015, we found that by utilizing BM powders, we could increase the propagation velocity of the initial redox foils that were produced with single-phase powders instead of BM powders (Figure V.6-2a). However, qualitatively, it was observed that many of the BM foils disintegrated during propagation, resulting in lots of mass ejected from the reaction front. To investigate the cause of mass ejection, emission spectra was obtained during the reactions to detect any gaseous species.

Elements and gaseous molecules emit light at known wavelengths; therefore, peaks in the emission spectra can be attributed to certain evolved species. The emission spectra for Al:Cu_2O:Cu BM foils are presented in Figure V.6-2b (red traces). For the 20 and 30 wt.% foils, there are multiple peaks, including broad peaks at 490 and 500 nm. These correspond to CuO and possibly AlO emissions. The sharper peak at 510 nm corresponds to Cu emissions. The 40 wt.% BM foil does not show any peaks and has a smooth emission curve. These results indicate that BM foils produce Cu vapor during the propagation process. This vapor can create pressure that causes much of the material to be ejected. Ejected material will be detrimental to the joining process because it will create pores in the resulting braze.

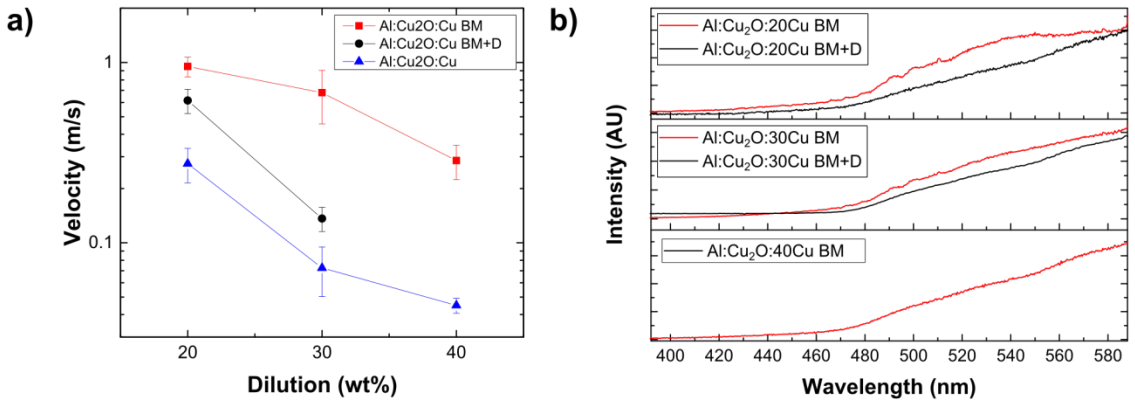

Figure V.6-2. a) Propagation velocity of the Al:Cu_2O:Cu system for three different processing paths: conventional (FY 2014), BM (FY 2015), and BM+D (FY 2016). b) Emission spectroscopy as a function of wavelength for BM (red) and BM+D (black) foils of the Al:Cu_2O:Cu system.

To understand why the BM foils produced Cu vapor, we examined the microstructure of the resulting foils. Multiple scanning electron microscopy (SEM) images for each chemistry were obtained at two magnifications, and then analyzed via Matlab image processing. For each image, a threshold was set for each constituent powder (i.e., Al, Cu_2O, and Cu); only the thresholding for Cu will be discussed here (Figure V.6-3). The number of threshold Cu pixels was summed in each image to provide an area fraction of diluent. The area fraction can be compared to the theoretical value for a given dilution percentage to locally determine how far the microstructure is from the desired chemistry. In this analysis, we observe that locally the amount of dilution can be lower than the theoretical value. This is clear for the 30 wt.% foil, where the area fraction can

be well below 30 wt.% and even dips below the thermodynamic limit of the boiling point of Cu. We believe this local inhomogeneity in dilution, being far from the desired area fraction, leads to hot regions in the foil during propagation, which leads to mass ejection.

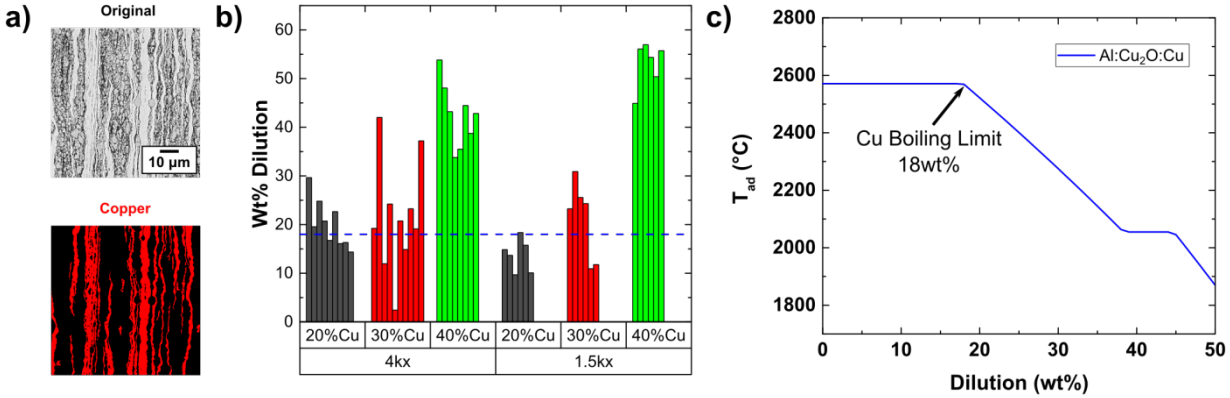

Figure V.6-3. a) SEM cross section of Al:Cu_2O:30Cu BM foil and the image processed for the Cu dilution. b) Equivalent weight percent dilutions based on area fraction of Cu in image analysis for BM foils of 20, 30, and 40 wt.% Cu at two magnifications (i.e., 1.5 kx and 4 kx). Each bar represents an individual image. The dotted line represents the wt.% of Cu that yields an adiabatic flame temperature plot equal to the thermodynamic boiling point of Cu. The adiabatic temperature is shown in c) as a function of wt.% Cu dilution.

Bonds formed with the BM foils that produce Cu vapor can be porous. An example of a dissimilar bond with Al:Cu_2O:20Cu BM is given in Figure V.6-4. The resulting bond has many pores, including pores at the surface of the metallic component being bonded, which can cause delamination of the braze from the substrate when sheared. These pores are weak points that can significantly limit the strength of the resulting bonds. Despite the resulting mass ejection and porosity from gas production, bond strengths approximately 5 to 10 MPa can be reached with BM redox foils.

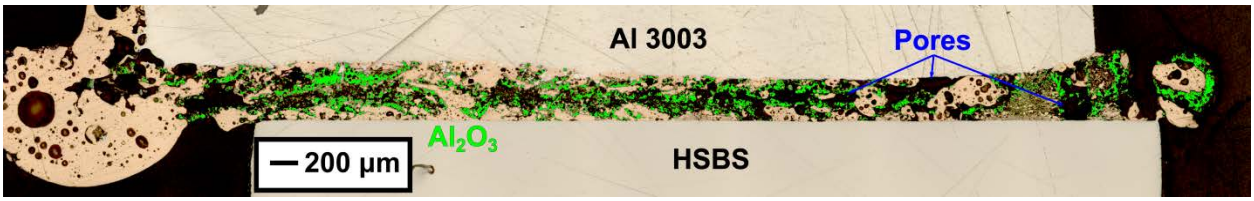

Figure V.6-4. Cross section of dissimilar Al 3003/hot-stamped boron steel bond made with Al:Cu_2O:20Cu BM Foils; the alumina has been false colored green for clarity.

To understand what is causing gas production and how to suppress it, we fabricated PVD foils of Al:Cu_2O chemistry and added different amounts of Cu diluent into the foils. Five different foils were made (i.e., a bilayer structure, with no excess Cu layers, but excess Cu in the Cu_2O layer, and four quad layer structures). The quad layer structures had layers of Cu at each Al/Cu_2O interface. The four foils are denoted by the Cu thickness layer: 0 nm (Bilayer), 25 nm, 50 nm, 75 nm, and 100 nm. The Al and Cu_2O layer thickness remained constant throughout. As the thickness of the Cu layers increased, the peaks in the emission spectra decreased (Figure V.6-5). The bilayer had very prominent emission peaks and the high-speed video displayed lots of gas and particulate spray. The 25-nm foil had some spray and a few peaks. The other foils showed no sign of emission peaks and no sign of spray or gas vapor.

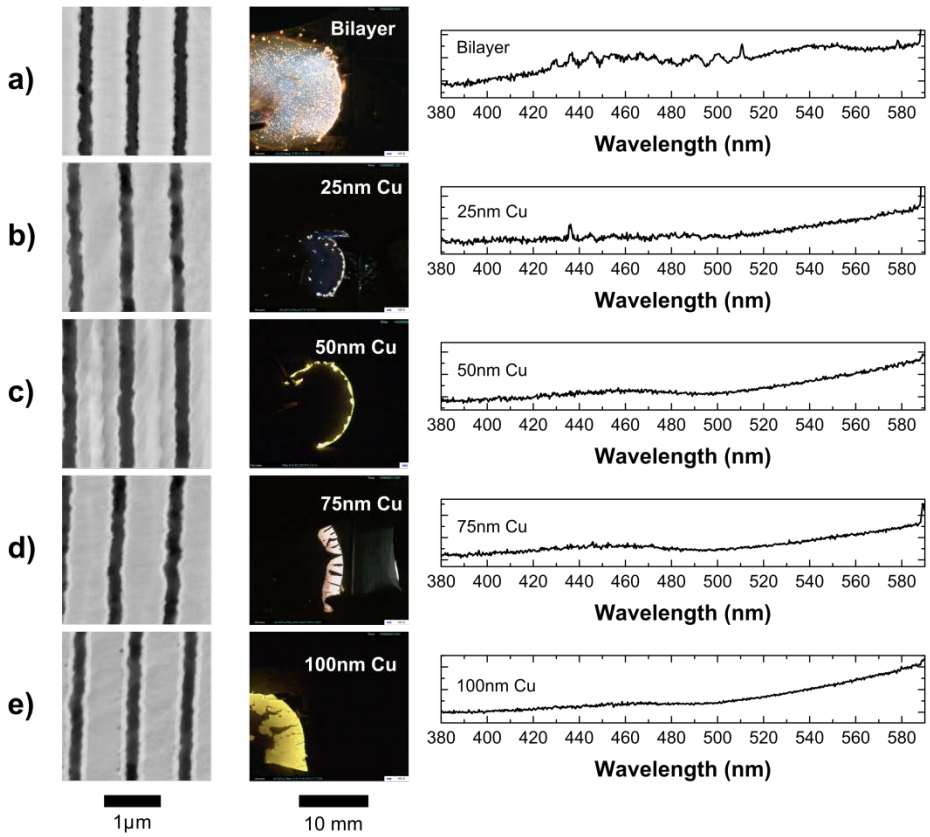

Figure V.6-5. SEM image, high-speed video snapshot, and emission spectroscopy of a) bilayer, b) 25-nm, c) 50-nm, d) 75-nm, and e) 100-nm PVD foils. In the SEM images, dark is Al, grey is Cu_2O-Cu, and the thin white layer between the two is the Cu layer.

These ideal PVD foils suggest that Cu vapor production can be suppressed if the diluent is evenly distributed throughout the foil. In order to accomplish this in the mechanically processed foils, the diluent was ball-milled with the fuel and oxide to produce three-phase composite particles. With this fabrication, the diluent is more intimately mixed with the Al and Cu_2O resulting in finer Cu evenly dispersed in the resulting BM+D redox foil microstructures (see Figure V.6-6). Adding the diluent during milling does reduce the propagation velocities when compared to BM foil (see Figure V.6-6a), but it also suppresses Cu vapor production. The emission spectra of BM+D foils do not exhibit any peaks Figure V.6-6b), suggesting that homogenization of diluent did eliminate gaseous Cu products as was seen with the PVD foils.

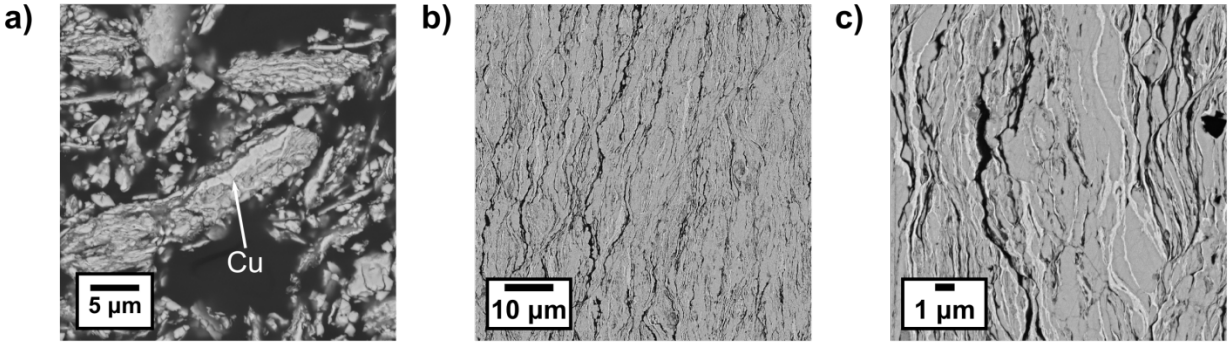

Figure V.6-6. SEM cross sections of a) BM+D powder with Cu inclusion highlighted and images of Al:Cu_2O:30Cu BM redox foil at low magnification b) and high magnification c).

For Al:Cu_2O:Cu BM+D foils, bond strength goes down as dilution increases. At 20 wt.% dilution, the fracture occurs within the braze, whereas for 30 wt.% dilution, the fracture location moves from within the braze to the substrate interface. Strengths and fracture surfaces are shown in Figure V.6-7. This change in fracture location indicates that the molten Cu produced by the reaction did not adequately wet the substrates at higher dilutions. We believe the higher amount of dilution for 30 wt.% reduces the reaction temperature; therefore, the braze remains molten for a shorter period of time, which is detrimental to wetting of the substrate.

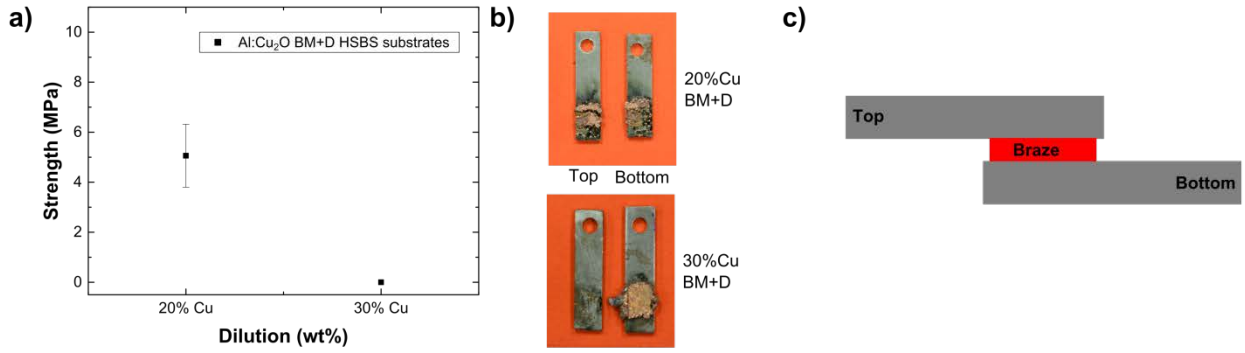

Figure V.6-7. a) Shear strengths of Al:Cu_2O:Cu BM+D foils joining hot-stamped boron steel with representative fracture surfaces in b) and a schematic of the lap shear joint for fracture location in c).

To overcome these wetting issues, the amount of dilution is increased, the project substituted Ag for Cu as the diluent. This produces an alloy braze that has a lower solidification temperature. The lower melting temperature should increase the amount of time the braze is molten. The Ag substitution was done with both BM and BM+D fabrication methods. In both cases, the Ag-diluted sample melted at a lower temperature than the Cu-diluted sample (Figure V.6-8), suggesting that Ag diluted redox foils will stay molten for a longer period of time, which is believed will promote wetting of the surfaces. In FY 2016, only BM foils produced with Ag diluent were used to create bonds. Preliminary strength data (Figure V.6-9) for the 30 Ag BM foil shows an increase in strength in comparison to the 20 Cu BM+D foils, for all three substrates tested. We believe this enhanced strength is due in part to the improved wetting enabled by the lower solidification temperature.

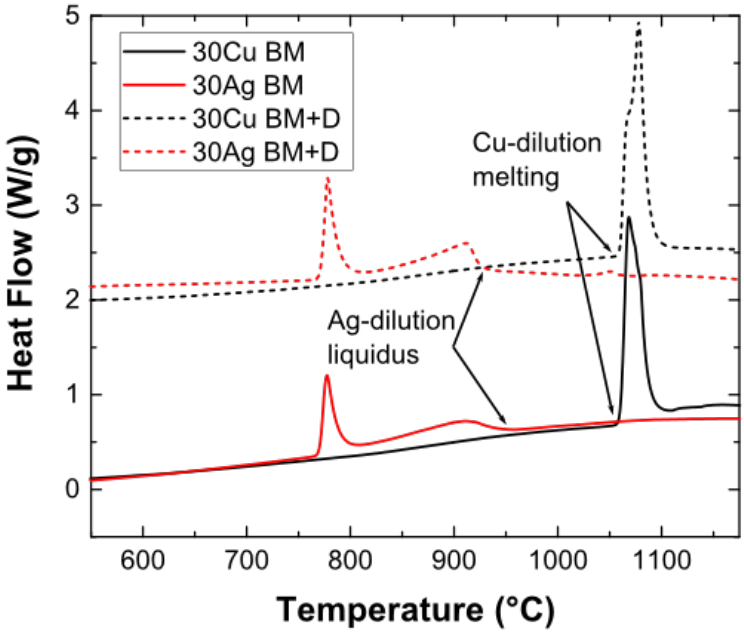

Figure V.6-8. Differential scanning calorimetry traces of the second heating of redox foils that indicates the melting temperatures of the resulting braze are lower when diluted with Ag when compared to Cu.

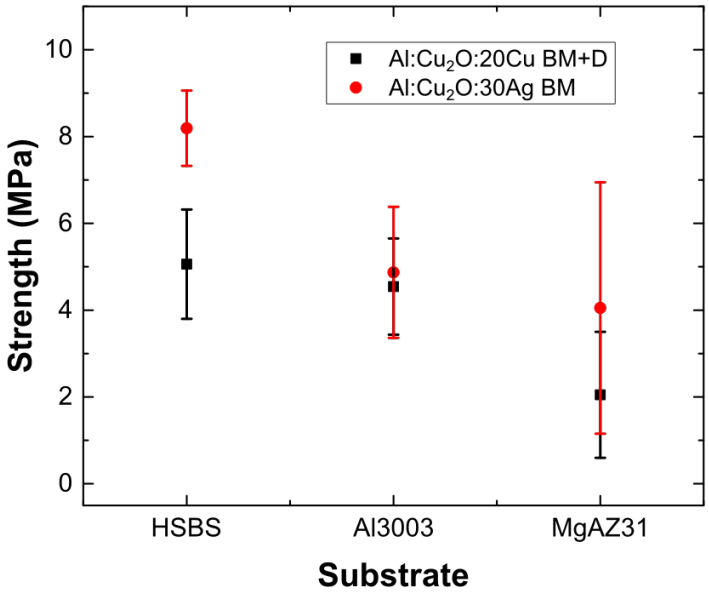

Figure V.6-9. Strengths of bonds formed with Al:Cu_2O:20 Cu BM+D and Al:Cu_2O:30 Ag BM on all three substrates, hot-stamped boron steel (HSBS), aluminum 3003, and magnesium AZ21.

Even with these improvements in suppressing metal vapor and tailoring the braze to effectively wet the bonding substrates, bonds formed with Ag-diluted foils and Cu-diluted BM+D foils still exhibit porosity. Preliminary data suggests that there may be some form of gas generation other than metal vapor formation. Figure V.6-10 shows an SEM cross section of a 100-nm PVD foil, before and after reaction. The post reaction image contains large pores, which are suspected to be formed by vapor not detected via emission spectroscopy (i.e., not metal vapor). The project has also performed thermogravimetric analysis experiments for both PVD foils and redox foils, which show mass loss at low temperatures and slow heating rates. This mass loss could be indicative of oxygen release, which may also occur at the faster rates and higher temperatures of propagating foils. This sort of oxygen release has been seen for other thermite systems [8] and must be overcome in order to produce non-porous brazes with limited mass ejection during propagation. The project aims to determine the mechanism causing this porosity and adjusts the fabrication process accordingly to mitigate it.

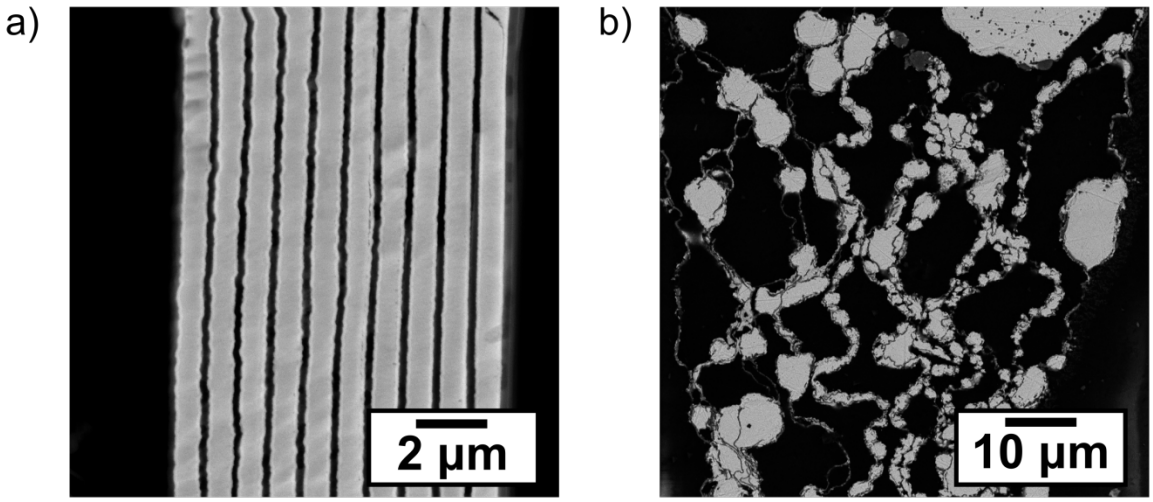

Figure V.6-10. SEM of (a) initial 100-nm PVD foil showing regular layer spacing and total thickness of approximately 15 µm and (b) SEM of reacted foil with large pores causing an increase in foil thickness.

Technology Transfer Path

A patent application covering the redox foil materials has been submitted to the U.S. patent office and is under review. The project will look to license the patent as the technology becomes viable.

Conclusion

In order to produce strong joints, the braze produced by propagating redox foil should have low porosity and mass ejection. Our efforts in FY 2016 focused on identifying the sources of gas production and altering our fabrication process to eliminate it. We determined that BM redox foils produced Cu vapor species due to localized hot spots in the foil, resulting in higher temperatures capable of boiling the Cu. Using the ideal microstructure of the PVD foils, we discovered that Cu gas production can be suppressed with uniform distribution of the diluent, which led us to produce BM+D foils. These BM+D foils had no signs of Cu vapor, but still showed high degrees of porosity. Additionally, lower reaction velocities at higher dilutions resulted in poor wetting of the substrates and low bond strengths. To overcome this limitation, Ag was substituted for Cu, which produced a lower melting temperature braze in the reactant products. Despite the suppression of Cu vapor produced during propagation, bonds still exhibit porosity, which appears to be due to another gaseous species not detected via emission spectroscopy. This will need to be investigated further to eliminate the gas production completely that results in porous joints.

References

[1] Goldschmidt, H., 1903, "Process of Joining Metal Pieces," Google Patents, January 6, 1903.

[2] Wang, L. L., Z. A. Munir,and Y. M. Maximov, 1993, "Review Thermite Reactions: Their Utilization in the Synthesis and Processing of Materials," *Journal of Materials Science* 28: 3693–3708.

[3] Wang, J., E. Besnoin, A. Duckham, S. J. Spey, M. E. Reiss, O. M. Knio, T. P. Weihs, 2004, "Joining of Stainless-Steel Specimens with Nanostructured Al/Ni Foils," *Journal of Applied Physics* 95(1): 248–256.

[4] Duckham, A., S. J. Spey, J. Wang, M. E. Reiss, T. P. Weihs, E. Besnoin, and O. M. Knio, 2004, "Reactive Nanostructured Foil Used as a Heat Source for Joining Titanium," *Journal of Applied Physics* 96(4): 2336.

[5] Weihs, T. P., 2014, *Fabrication and Characterization of Multilayer Films and Foils*.

[6] Kinsey, A. H., K. Slusarski, K. Woll, D. Gibbins, and T. P. Weihs, 2016, "Effect of Dilution on Reaction Properties and Bonds Formed Using Mechanically Processed Dilute Thermite Foils," *Journal of Materials Science* 51(12): 5738–5749.

[7] Woll, K., J. D. Gibbins, K. Slusarski, A. H. Kinsey, and T. P. Weihs, 2016, "The Utilization of Metal/metal Oxide Core-Shell Powders to Enhance the Reactivity of Diluted Thermite Mixtures," *Combust. Flame* : 259–267.

[8] Zhou, L., N. Piekiel, S. Chowdhury, and M. R. Zachariah, 2010, "Time-Resolved Mass Spectrometry of the Exothermic Reaction between Nanoaluminum and Metal Oxides: The Role of Oxygen Release," *Journal of Physical Chemistry C* 114(33): 14269–14275.

Bibliography

Kinsey, Alex H., Kyle A. Slusarski, John Gibbins, Karsten Woll, and Timothy P. Weihs, 2015, “Brazing with Mechanically Processed Diluted Thermite Foils for Joining Dissimilar Metals,” *Materials Science and Technology 2015,* Columbus, Ohio, October 7,2015.

Kinsey, Alex, Kyle Slusarski, Karsten Woll, and Tim Weihs, 2015, "Exothermic Brazing with Mechanically Processed Diluted Thermite Foils for Joining Dissimilar Metals" *AIAA Young Professional, Student and Education Conference 2016*, Laurel, Maryland, November 13, 2015.

Kinsey, Alex, Kyle A. Slusarski, Karsten Woll, and Timothy P. Weihs, 2016, "Enhancing Reactivity of Fully Dense, Diluted Al:Cu_2O:Cu Thermite Foils," *Gordon Research Conference*, Stowe, Vermont, June 4, 2016.

Slusarski, Kyle A., Alex H. Kinsey, Karsten Woll, Evan Krumheuer, and Timothy P. Weihs, 2015, "Effects of Dilution on the Reactive Properties of Thermite Composite Foils," *Materials Science and Technology 2015*, Columbus, Ohio, October 7, 2015.

VI. Crosscutting

VI.1 Assessment of NHTSA's Updated Analysis of the Relationship between Fatality Risk, Mass, and Footprint in Model Year 2003 through 2010 Passenger Cars and LTVs – Lawrence Berkeley National Laboratory

Project Details

Tom Wenzel, Principal Investigator
Environmental Technologies Area
Lawrence Berkeley National Laboratory (LBNL)
90R2000
1 Cyclotron Road
Berkeley, CA 94720
Phone: 510-486-5753
E-mail: TPWenzel@lbl.gov

Sarah Kleinbaum, Technology Area Development Manager
U.S. Department of Energy
1000 Independence Ave., S.W.
Washington, DC 20585
Phone: (202) 586-8027
E-mail: sarah.ollila@ee.doe.gov

Contractor: LBNL
Contract No.: DE-AC02-05CH11231

Executive Summary

LBNL completed an updated analysis of the relationship between vehicle weight, size (i.e., footprint or wheelbase times track width), and societal fatality risk per vehicle miles of travel, using data for model year 2003 through 2010 light-duty vehicles from 2005 to 2011. The analysis replicated the methodology used by the Volpe Transportation Center for the National Highway Transportation Safety Administration (NHTSA) using the same public database and analyzed 33 alternative regression models to better understand the relationship between vehicle mass, size, and fatality risk. LBNL concurs with NHTSA's finding that every 100-lb reduction in vehicle mass is associated with a small increase in societal fatality risk for lighter-than-average cars; however, there are small reductions in fatality risk for every 100-lb reduction in the mass of heavier-than-average light trucks and all crossover utility vehicles (CUVs)/minivans. These changes in fatality risk are statistically significant based on standard errors generated by logistic regression models, but are not statistically significant at the 95% confidence level using the jack knife method employed by NHTSA to estimate uncertainty. In statistics, the jackknife is a resampling technique especially useful for variance and bias estimation. LBNL notes that the estimated effect of mass or footprint reduction on societal fatality risk is substantially smaller than other control variables included in the regression model; the results are sensitive to changes in data or variables included in the analysis. There is a wide range of risk for vehicle models of similar mass, even after accounting for differences in vehicle attributes, driver characteristics, and crash circumstances.

Accomplishments

- Participated in monthly discussions by the interagency working group (i.e., the U.S. Department of Energy [DOE], NHTSA, U.S. Environmental Protection Agency [EPA], and the California Air Resources Board) on updating research on the relationship between vehicle weight/size and safety in support of federal agency rulemakings on fuel economy/greenhouse gas emission standards for new light-duty vehicles (Fiscal Year [FY] 2016).

- Completed an assessment of NHTSA's updated analysis of the relationship between mass and footprint reduction and societal fatality risk per vehicle mile of travel (VMT), based on model year 2003 through 2010 light-duty vehicles from 2005 to 2011 (Phase 1 analysis). Performed additional analyses to better understand the relationship between mass reduction and fatality risk (FY 2016).

- Began developing a model to simulate the effect over time of mass reduction from the standards on the mass difference between two vehicles involved in a crash and the resulting estimated change in societal fatalities.

- Began analysis of the relationship between mass and footprint reduction and the two components of fatality risk per VMT: crashes per VMT (i.e., crash frequency) and fatality risk once a crash has occurred (i.e., crashworthiness). This Phase 2 analysis involves analyzing police-reported crash data from 13 states and uses a simultaneous two-stage regression model developed by Dynamic Research Institute, Inc.

Future Directions

- Complete simulation of the effect of standards on the difference in masses of two vehicles involved in a crash and the resulting change in societal fatalities over time (FY 2017).

- Complete the update of the 2012 Phase 2 analysis using more recent state data on police-reported crashes (FY 2017).

- Begin updating analyses using more recent data for the final rule due in 2018 (FY 2017 and FY 2018).

Introduction

Reducing vehicle mass is perhaps the easiest and least-costly method of reducing fuel consumption and greenhouse gas emissions from light-duty vehicles. However, the extent to which government regulations should encourage manufacturers to reduce vehicle mass depends on what effect, if any, light-weighting of vehicles is expected to have on societal safety. As part of an interagency analysis effort between NHTSA, EPA, and DOE, LBNL has been examining the relationship between vehicle mass and size and U.S. societal fatality and casualty risk, using historical data on recent vehicle designs. This research effort informs the agencies about the extent that vehicle mass can be reduced in order to meet fuel economy and greenhouse gas emissions standards, without compromising the safety of road users.

Approach

LBNL replicated the method NHTSA used in their baseline regression model for their 2016 analysis, which used fatality data from NHTSA's Fatality Analysis Reporting System from 2005 to 2011 for model years 2003 through 2010. [1] This involved running a separate logistic regression model for each of three vehicle types (i.e., passenger cars, comprised of two and four-door cars; light trucks, comprised of pickup trucks and truck-based sport utility vehicles [SUVs]; and car-based CUVs and minivans) and for each of nine crash types; this led to a total of 27 regressions. Crashes with other light-duty vehicle were categorized into a combination of

four types based on the type and weight of the crash partner: a car, CUV or minivan lighter or heavier than average (i.e., 3,157 pounds), and a pickup or truck-based SUV lighter or heavier than average (i.e., 4,303 pounds). Because all fatalities in the crash were used, the risks reflect societal risk, rather than just risk to occupants of the case vehicle. Induced exposure cases were derived from the non-culpable vehicle in a two-vehicle crash; this is taken from police-reported crash records from 13 states. The induced exposure cases were weighted by the number of vehicle registrations and average annual mileage by vehicle age and make/model; therefore, the models estimate the effect of changes in the control variables on U.S. fatalities per VMT. As in its previous analyses, NHTSA excluded three types of cars (i.e., models used as sports cars, police cars, and models with all-wheel drive, as well as full-size passenger and cargo vans) from its baseline regression analyses.

For cars and trucks, NHTSA used two variables (i.e., UNDRWT00 and OVERWT00) for vehicle weight, allowing the relationship between mass and risk to vary for lighter and heavier cars and trucks. Determination of the two weight classes was based on the median weight for each vehicle type: 3,197 lb for cars and 4,947 lb for light-duty trucks. Because there are fewer CUVs and minivans in the database, NHTSA used a single variable, LBS100, for CUV/minivan weight. NHTSA included control variables for vehicle types (i.e., two-door cars, SUVs, heavy-duty pickups, and minivans), vehicle technologies (i.e., all-wheel drive, anti-lock braking system, electronic stability control, and two methods for making light-duty trucks more crash-compatible with cars), eight variables for driver age and gender, crash circumstances (i.e., whether the crash occurred in a rural county, at night, on a high-speed road, or in a high fatality state), vehicle age, and calendar year.

NHTSA reported a single weighted average of the coefficients from the regression models run for each of the nine crash types, based on the expected distribution of fatalities after 2012, when all vehicles were required to have electronic stability control installed. The assumptions used for this adjustment were taken from an updated NHTSA study that found electronic stability control reduced fatal rollovers by 60% in cars and 74% in light trucks; fixed-object impacts by 31% in cars and 45% in light trucks; and other non-pedestrian crashes by 7% in cars and by 6% in light trucks. [2] The “post-electronic stability control” distribution of fatalities by crash type was multiplied by the regression coefficients for each crash type to create the weighted average effect of each variable on risk.

LBNL replicated the 2016 NHTSA analysis, and reproduced their main results; LBNL also examined the NHTSA data in slightly different ways to get a deeper understanding of the relationship between vehicle weight, footprint, and safety. [3] The NHTSA baseline results and these alternative analyses are summarized in Table VI.1-1 under the Results and Discussion section. Statistically significant estimates, based on confidence intervals output by the logistic regression models, are shown in red.

Results and Discussion

Using the updated databases, NHTSA estimated that reducing vehicle mass by 100 lb while holding a fixed footprint is associated with an increase in societal fatality risk per VMT of 1.49% for lighter-than-average cars and of 0.50% for heavier-than-average cars; however, it also results in a reduction in risk of 0.10% for lighter-than-average light-duty trucks, 0.71% for heavier-than-average light-duty trucks, and 0.99% for CUVs/minivans as shown in Figure VI.1-1. Using a jack knife method to estimate the statistical uncertainty of these point estimates, NHTSA found that none of these estimates are statistically significant at the 95% confidence level; however, the 1.49% increase in risk associated with mass reduction in lighter-than-average cars and the 0.71% and 0.99% decreases in risk associated with mass reduction in heavier-than-average light trucks and CUVs/minivans are statistically significant at the 90% confidence interval. The 2016 NHTSA analysis estimated that reducing vehicle footprint by 1 ft^2 while holding mass constant would increase fatality risk per VMT 0.28% in cars, 0.38% in light trucks, and 1.18% in CUVs and minivans; only the increases in risk in light trucks and CUVs/minivans are statistically significant, as shown in Figure VI.1-1.

The 2016 estimated effects of a reduction in car mass are essentially unchanged from the 2012 estimated effect; however, mass reduction in lighter-than-average light trucks is now associated with a slight reduction in fatalities (as opposed to an increase in fatalities in the 2012 analysis), while mass reduction in heavier-than-

average light trucks and CUVs/minivans are associated with larger decreases in fatality risk than in the 2012 analysis (see Figure VI.1-2).

Many of the control variables NHTSA included in its baseline logistic regressions are statistically significant and have a much larger estimated effect on fatality risk than vehicle mass. For example, installing torso side airbags, electronic stability control, or an anti-lock braking system in a car is estimated to reduce fatality risk by about 7 to 14%; cars driven by men are estimated to have a 50% higher fatality risk than cars driven by women; and cars driven at night, on rural roads, or on roads with a speed limit higher than 55 mph are estimated to have a fatality risk over twice that of cars driven during the daytime on low-speed, non-rural roads. While the estimated effect of mass reduction may result in a statistically significant increase in risk in certain cases, the increase is small and is overwhelmed by other known vehicle, driver, and crash factors.

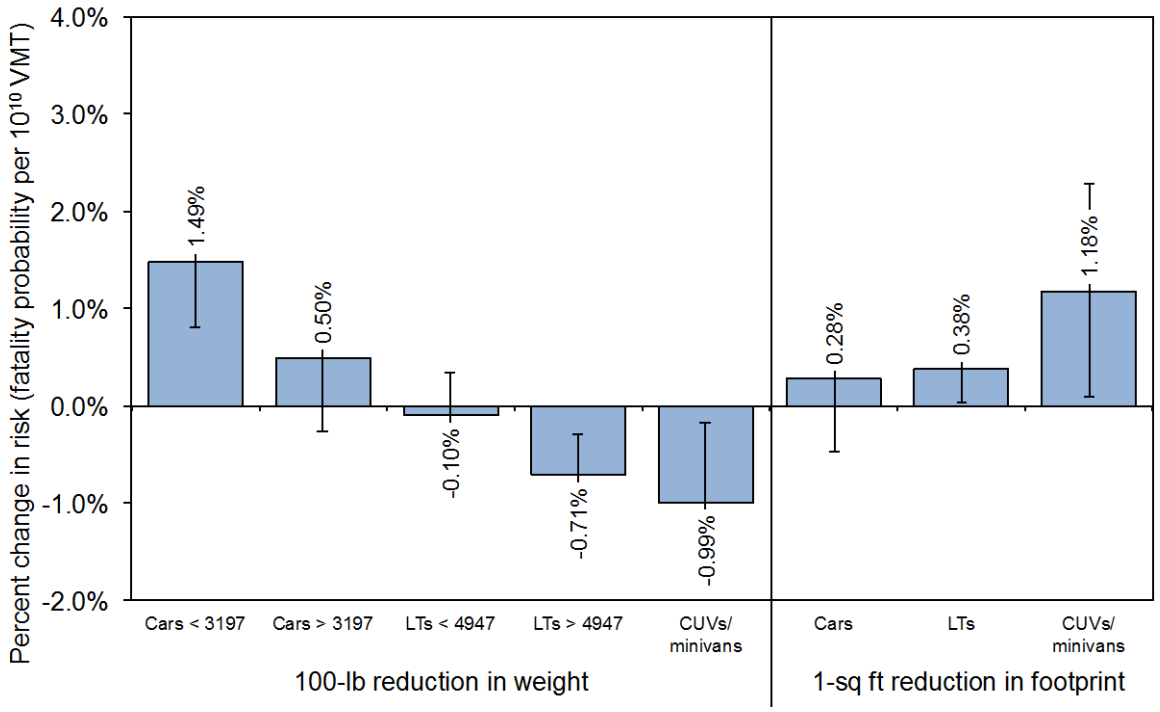

Figure VI.1-1. Estimated effect of mass or footprint reduction on U.S. societal fatality risk per VMT, from the NHTSA baseline model, by vehicle type.

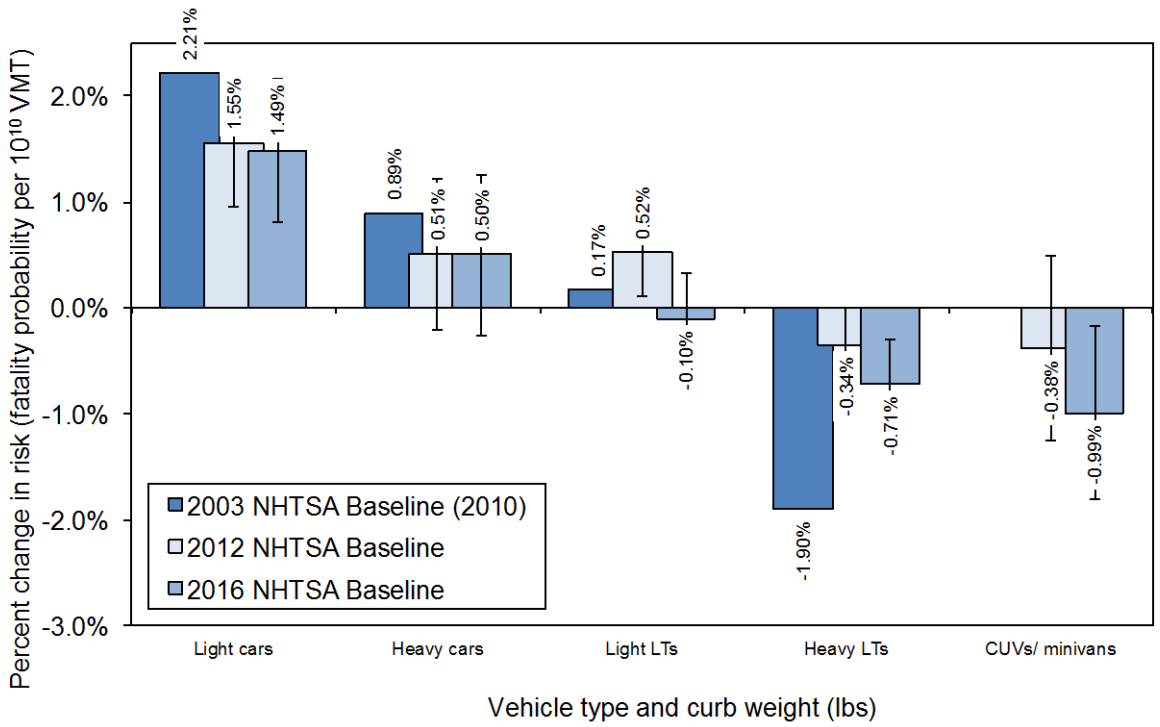

Figure VI.1-2. Estimated effect of 100-lb mass reduction on U.S. fatality risk per VMT by vehicle type from NHTSA baseline models in 2003, 2012, and 2016 analyses.

Using two or more variables that are strongly correlated in the same regression model (referred to as multicollinearity) can lead to inaccurate results. However, correlation between vehicle mass and footprint may not be strong enough to cause serious concern. NHTSA included several analyses to address the possible effects of near-multicollinearity between mass and footprint. First, NHTSA ran a sensitivity case where footprint is not held constant, but rather allowed to vary as mass varies (i.e., NHTSA ran a regression model that includes mass but not footprint); LBNL recreated this analysis as Model 6 in Table VI.1-1. If the multicollinearity was so great that including both variables in the same model gave misleading results, removing footprint from the model would give much different results than keeping it in the model. NHTSA's sensitivity test estimates that when footprint is allowed to vary with mass (i.e., removing footprint as a control variable in the regression model), the effect of mass reduction on risk increases for all vehicles types: from a 1.49 to a 1.71% increase for lighter cars; from a 0.50 to a 0.68% increase for heavier cars; from a 0.10 to a 0.26% increase for lighter light trucks; from a 0.71 to a 0.55% decrease for heavier light trucks; and from a 0.99 to a 0.25% decrease for CUVs and minivans.

Table VI.1-1. Estimated Effect of Mass Reduction on U.S. Fatalities, Baseline Model, and 33 Alternative Regression Models Analyzed in this Report

Regression model	Cars		Light trucks[1]		CUV/ minivan
	<3,197 lbs	≥3,197 lbs	<4,947 lbs	≥4,947 lbs	
Baseline model	1.49%	0.50%	-0.10%	-0.71%	-0.99%
1.Weighted by current distribution of fatalities	1.37%	0.46%	-0.13%	-0.56%	-1.30%
2.Single regression model across all crash types	1.36%	0.46%	-0.13%	-0.56%	-1.31%
3.Fatal crashes per VMT	1.67%	0.58%	-0.02%	-0.72%	-1.28%
4.Fatalities per induced exposure crash	1.14%	-0.85%	-1.66%	-1.06%	-0.16%
5.Fatalities per registered vehicle-year	1.45%	2.90%	-0.56%	-1.24%	-0.42%
6.Allow footprint to vary with mass[2]	1.71%	0.68%	0.26%	-0.55%	-0.25%
7.Account for 14 vehicle manufacturers	2.39%	1.37%	0.32%	-0.09%	0.00%
8.Account for 14 manufacturers + 5 luxury brands	2.65%	2.96%	0.30%	0.00%	-0.43%
9.Account for initial vehicle purchase price	1.42%	0.70%	-0.39%	-0.99%	-1.65%
10.Exclude CY variables	0.53%	0.10%	-0.10%	-0.52%	-1.13%
11.Exclude crashes with alcohol/drugs	2.08%	1.09%	0.21%	-0.83%	-1.01%
12.Exclude crashes with alcohol/drugs, and bad drivers	2.72%	1.57%	0.42%	-0.55%	-1.00%
13.Account for median household income	1.42%	-0.11%	-0.08%	-0.62%	-1.43%
14.Include sports, police, and AWD cars, and full vans	1.44%	0.62%	-0.05%	-0.94%	-0.99%
15.Use stopped instead of non-culpable vehicles	1.58%	-0.42%	-0.09%	-1.80%	-0.61%
16.Replace footprint with track width & wheelbase	0.93%	0.48%	-0.66%	-0.97%	-1.15%
17.Above two models combined (15 & 16)	0.88%	-0.43%	-0.85%	-2.13%	-0.66%
18.Reweight CUV/minivans by 2010 sales	1.49%	0.50%	-0.10%	-0.71%	-0.27%
19.Exclude non-significant control variables	1.47%	0.54%	-0.13%	-0.70%	-0.84%
20.Exclude LTs over 10k GVWR[3]	1.49%	0.50%	0.06%	-0.80%	-0.99%
21.Small pickups and SUVs only[3]	1.49%	0.50%	-0.01%	-0.24%	-0.99%
22.Large pickups only[3]	1.49%	0.50%	-4.27%	0.52%	-0.99%
23.Large pickups only, exclude those > 10k GVWR[3] (20 & 22)	1.49%	0.50%	-6.49%	1.31%	-0.99%
24. Include AWD, but not muscle or police, cars	1.29%	0.77%	-0.10%	-0.71%	-0.99%
25. Include muscle and police, but not AWD, cars	1.66%	0.40%	-0.10%	-0.71%	-0.99%
26. Exclude 3 high-risk car models	1.38%	0.29%	-0.10%	-0.71%	-0.99%
27. Include AWD cars, exclude 3 high-risk car models (24 & 26)	1.15%	0.53%	-0.10%	-0.71%	-0.99%
28. 2-piece variable for CUV weight[4]	1.49%	0.50%	-0.10%	-0.71%	-0.31% -1.21%
29. 2-piece variable for PC and LT footprint	1.31%	0.72%	-0.75%	-0.89%	-1.07%
30. 2-piece variable for weight and for footprint[4] (28 & 29)	1.31%	0.72%	-0.75%	-0.89%	-0.20% -1.21%
31. Remove kinks in NHTSA VMT schedules	1.47%	0.49%	-0.10%	-0.72%	-0.99%
32. Use Texas rather than Polk odometer ratios	1.21%	0.15%	-0.25%	-0.87%	-0.99%
33. Both adjustments to NHTSA VMT (31 and 32)	1.19%	0.13%	-0.26%	-0.87%	-1.00%

Red font indicates estimate is statistically significant at 95% confidence interval.
Gray shading indicates estimate is not changed from baseline regression model in alternative regression model.
[1] Light trucks includes pickups and truck-based SUVs, and excludes car-based CUVs and minivans.
[2] In model 6 footprint is allowed to vary with mass.
[3] The median weights used for Models 20-23 are: 4,870 pounds for Model 20; 4,704 pounds for Model 21; 6,108 pounds for Model 22; 6,062 pounds for Model 23.
[4] The two estimates for CUV/minivan mass in Models 28 and 30 are for vehicles under and over the median mass (3,939 pounds).

Second, NHTSA conducted a stratification analysis of the effect of mass reduction on risk by dividing vehicles into deciles based on their footprint and running a separate regression model for each vehicle and crash type, for each footprint decile (i.e., three vehicle types times nine crash types times 10 deciles equals 270

regressions). This analysis estimates the effect of mass reduction on risk separately for vehicles with similar footprint. LBNL replicated this analysis and found that reducing vehicle mass does not consistently increase risk across all footprint deciles for any combination of vehicle type and crash type. Risk increases with decreasing mass in a majority of footprint deciles for only 11 of the 27 crash and vehicle combinations, but few of these increases are statistically significant. On the other hand, risk decreases with decreasing mass in a majority of footprint deciles for 10 of the 27 crash combinations; in some cases, these risk reductions are large and statistically significant.[1] If reducing vehicle mass while maintaining footprint inherently leads to an increase in risk, the coefficients on mass reduction should be more consistently positive and have a larger R^2 across the 27 vehicle/crash combinations, than shown in the analysis. LBNL conducted a separate analysis using multiple bins of curb weight for cars and light trucks (rather than the two bins NHTSA used in its baseline model), which found that the relationship between mass reduction and societal fatality risk is not consistent over the range in vehicle mass within a weight bin. [4] These analyses are consistent with the conclusion of the basic regression analyses; namely, the effect of mass reduction while holding footprint constant, if any, is small.

One limitation of using logistic regression to estimate the effect of mass reduction on risk is that a standard statistic for measuring the extent to which the variables in the model explain the range in risk, equivalent to the R^2 statistic in a linear regression model, does not exist. For this reason, LBNL conducted an analysis of risk versus mass by vehicle model for 246 models with at least 10 billion VMT or at least 100 fatalities (i.e., 90 car models, 113 light truck models, and 43 CUV/minivan models). These 246 models represent nearly 90% of all fatalities, vehicle registration years, and VMT. After accounting for all variables in NHTSA's logistic regression model, except for vehicle mass and footprint, we found that the correlation between estimated fatality risk by vehicle model and mass is very low. For example, while the correlation between actual risk and adjusted risk for two-door cars increased from 0.19 to 0.40 and for four-door cars increased from 0.02 to 0.36, after accounting for other vehicle attributes, driver age and gender, and crash circumstances, Figure VI.1-3 indicates that societal fatality risk varies by about a factor of two across four-door car models of similar mass (e.g. model A to model B, model C to model D, and model E to model F); one four-door car model (model B) has the same societal risk as models weighing at least 1,500 lb more (models G and H). These results indicate that even after accounting for many vehicle, driver, and crash factors, the variation in risk by individual vehicle model is quite large and unrelated to vehicle weight. The large remaining unexplained variation in risk by vehicle model could be attributable to other differences in vehicle design or how drivers who select certain vehicles drive them. It is possible that including variables that account for these factors in the regression models would change the estimated relationship between mass or footprint and risk. In a separate analysis, LBNL examined the trend in mass and societal fatality risk of the 10 most popular four-door car models over time, which accounts for differences in the characteristics and behavior of drivers of particular vehicle models. This analysis found that annual increases in mass from a redesign or refresh of a car model is not consistently associated with a reduction in societal fatality risk and that reductions in fatality risk can occur in the absence of increases in mass. [5]

[1] And in six of the 27 crash and vehicle combinations, risk increased in five deciles and decreased in five deciles with decreasing vehicle mass.

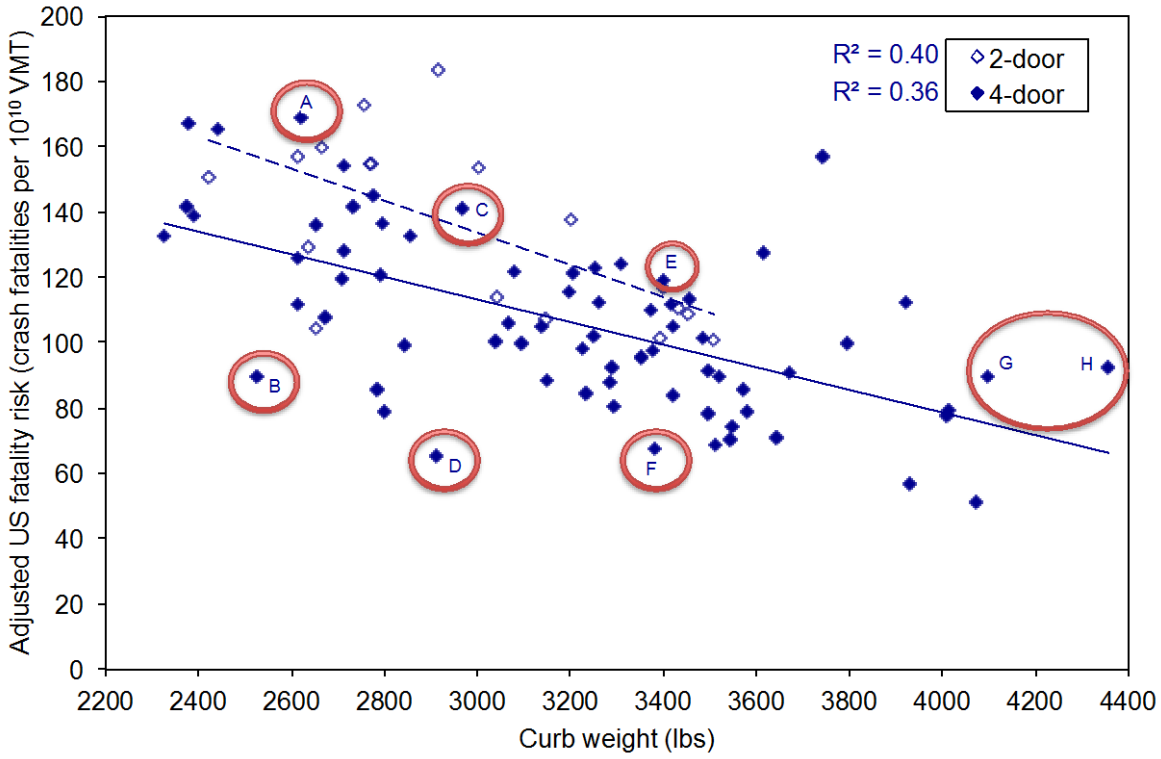

Figure VI.1-3. Adjusted U.S. societal fatality risk per VMT after accounting for all driver, crash, and vehicle variables, except mass and footprint versus curb weight car models.

LBNL tested the sensitivity of the NHTSA estimates of the relationship between vehicle weight and risk using 33 different regression analyses that changed the measure of risk, the control variables used, or the data used in the regression models. The intent in running the alternative regression models is not to develop a regression model that is "more correct" than the NHTSA baseline model; rather, the intent is to test how sensitive the results from the baseline model are to changes in the data and variables used, as well as to gain an understanding of how accounting for various factors (such as driver alcohol/drug use or driving behavior, or quality of vehicle design) influences the relationship between vehicle mass, size, and societal fatality risk. LBNL analyzed alternative models 1 through 19 in its 2012 assessment of the NHTSA 2012 report; the results from these models using data updated through 2011 are shown in Table VI.1-1. Table VI.1-1 also shows the results of the 14 new alternative regression models we conducted as part of our 2016 assessment. Models 20 through 23 explore two changes to how light trucks are classified: excluding light trucks with a GVWR rating over 10k pounds, and treating small (1/2-ton capacity) pickups and SUVs as a separate class distinct from large (3/4- and 1-ton capacity) pickups. As noted in the table footnotes, the median weight was recalculated for each alternate truck category. Models 24 through 27 test the sensitivity to which cars are included. Models 28 through 30 add a two-piece variable for CUV/minivan curb weight, based on the median CUV/minivan curb weight, as was done for cars and light trucks in the NHTSA baseline model, and two-piece variables for footprint for all vehicle types, based on the median footprint by vehicle type. Models 31 to 33 replace NHTSA's VMT weights with weights developed from annual odometer readings in Texas.

Table VI.1-1 indicates that, for cars < 3,197 pounds, all alternative models estimate that mass reduction is associated with an increase in societal fatality risk, ranging from a 0.53% increase (Model 10) to a 2.72% increase (Model 12). Nineteen of the 33 alternative models estimate a smaller increase in risk, and eight estimate a larger increase in risk, than the NHTSA baseline model (the remaining six alternative models, shaded in grey in Table VI.1-1 do not make changes to the regression model for cars). For cars ≥ 3,197 pounds, all but four of the alternative models estimate that mass reduction is associated with an increase in societal fatality risk, ranging from a 0.85% decrease (Model 4) to a 2.96% increase (Model 8). Thirteen of the 33 alternative models estimate a smaller increase, or a decrease, in risk, and 14 estimate a larger increase in

risk, than the NHTSA baseline model (six alternative models do not make changes to the regression model for cars).

For light trucks < 4,947 pounds, Table VI.1-1 indicates that only six of the 31 applicable alternative models[2] estimate that mass reduction is associated with an increase in fatality risk: ranging from a 1.66 percent decrease in risk (Model 4) to a 0.42 percent increase in risk (Model 12). 12 of the 31 applicable alternative models estimate a larger decrease in risk, 11 estimate a smaller decrease, or an increase, in risk, and two estimate the same change in risk, compared to the NHTSA baseline model (six alternative models do not make changes to the regression model for light trucks). In the two models restricted to analyses of large pickups, mass reductions in large pickups < 6,108 pounds (Model 22) and < 6,062 pounds (Model 23) are associated with decreases in fatality risk an order of magnitude larger than in the baseline NHTSA model (4.3 percent and 6.5 percent decreases in risk, respectively). The classification of relatively light (i.e., below the median) trucks in Models 22 and 23 is distinct to the classification of relatively light trucks in the other models.

For light trucks ≥ 4,947 pounds, none of the 31 applicable alternative models estimate that mass reduction is associated with an increase in fatality risk, and range from a 2.13 percent decrease in risk (Model 17) to no change in risk (Model 8). Fifteen of the 31 applicable alternative models estimate a larger decrease in risk, nine estimate a smaller decrease in risk, and one no change in risk, compared to the NHTSA baseline model (six alternative models do not make changes to the regression model for light trucks). In the two models restricted to analyses of large pickups, mass reductions in large pickups ≥ 6,108 pounds (Model 22) and ≥ 6,062 pounds (Model 23) are associated with increases in fatality risk (of 0.52 percent and 1.31 percent, respectively), compared to the decrease in the baseline model. The classification of relatively heavy (i.e., above the median) trucks in Models 22 and 23 is distinct to the classification of relatively heavy trucks in the other models.

For CUVs/minivans, all but one of the 31 applicable alternative models[2] estimate that mass reduction is associated with a decrease in fatality risk, and range from a 1.65 percent decrease in risk (Model 9) to no change in risk (Model 7). Eleven of the 31 applicable alternative models estimate a larger decrease in risk, and nine estimate a smaller decrease in risk, and two estimate no change in risk, than the NHTSA baseline model (nine alternative models do not make changes to the regression model for CUVs/minivans). In the two models that estimate the effect of mass reduction on risk separately for lighter- and heavier-than-average CUVs/minivans, mass reduction in lighter (< 3,939 pounds) CUVs/minivans is associated with smaller decreases in fatality risk (0.31 percent and 0.20 percent decreases in Models 28 and 30, respectively) than mass reduction in heavier (≥ 3,939 pounds) CUVs/minivans (1.21 percent decrease in both models). The fatality risk includes risk of fatality in any crash partner in a two-vehicle crash. The larger decrease in fatality risk from mass reduction in heavier CUVS/minivans is most likely a reduction in the number of fatalities in the (lighter/smaller) crash partner.

If the relationship between mass reduction and societal fatality risk is strong, one would expect that the estimated effects from NHTSA's baseline model would be robust to changes in the variables and data used. However this is not the case; the baseline results can be sensitive, especially for cars, to changes in the variables and data used. For instance, accounting for vehicle manufacturer (Model 8), or removing crashes involving alcohol, drugs, or bad drivers (Model 12), substantially increases the detrimental effect of mass reduction in cars on risk. On the other hand, the measures suggested by Dynamic Research Institute, Inc. (DRI) using stopped instead of non-culpable vehicles and replacing footprint with wheelbase and track width, (Model 17), including all-wheel drive (AWD) cars but excluding three high-risk sporty compact cars (Model 27), and using VMT weights based on Texas odometer data (Model 33) substantially decreases the detrimental effect of mass reduction in cars on risk.

The differences among the point estimates of the alternative regression models in Table VI.1-1 are within the uncertainty bounds NHTSA estimated using a jack knife method. However, NHTSA uses the Volpe model and EPA uses the Optimization Model for reducing Emissions of Greenhouse gases from Automobiles (OMEGA) model to estimate changes in energy consumption and carbon dioxide emissions from mass reduction and other technologies. Both use point estimates and not the uncertainty bounds. Using the estimates from one of the

[2] Not including Models 22 and 23, which apply to large pickups only, and use much higher median weights (6,108 and 6,062 pounds, respectively) to define lighter and heavier large pickups than in the baseline model.

alternative models could result in large changes in the estimated change in fatalities from mass reduction. For example, if NHTSA used the estimated relationship between mass reduction for lighter cars and societal fatality risk from Model 17 (0.88% reduction) rather than the estimate from the baseline model (1.49%), the Volpe and OMEGA models would enable manufacturers to make much larger reductions in mass without compromising safety. Figure VI.1-4 compares the estimates from the NHTSA baseline model with those from the DRI measures (Model 17), and an alternative model specification which combines Models 17, 18, and 33 in Table VI.1-1. This "LBNL baseline" model results in an even smaller increase in fatality risk in lighter-than-average cars, larger decreases in fatality risk in heavier-than-average cars and light trucks, and a smaller decrease in fatality risk in CUVs/minivans, than the NHTSA baseline or DRI recommended models.

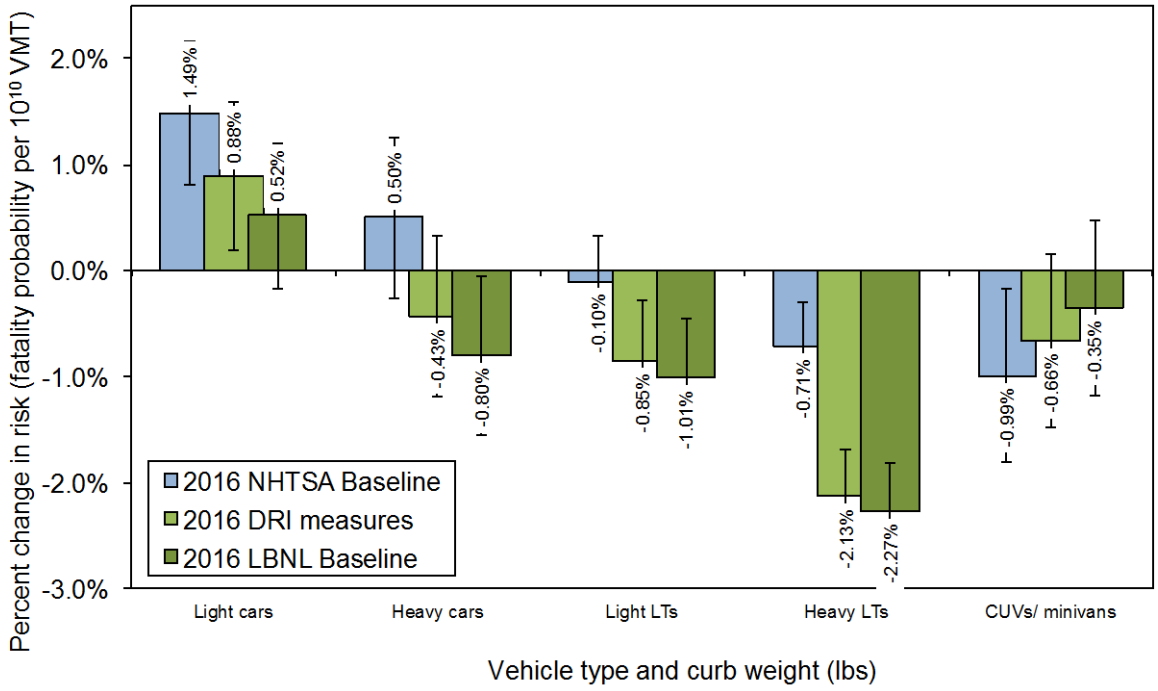

Figure VI.1-4. Estimated effect of mass reduction on U.S. fatality risk per VMT by vehicle type, NHTSA baseline, DRI measures, and LBNL baseline

In its 2012 report, NHTSA simulated the effect that four fleetwide mass reduction scenarios would have on the change in annual fatalities. NHTSA estimated that the most aggressive of these scenarios (reducing mass 5.2% in heavier light trucks and 2.6% in all other vehicles types except lighter cars) would result in a small reduction in societal fatalities. LBNL replicated the methodology NHTSA used to simulate six mass reduction scenarios, including the mass reductions recommended in the National Academy of Sciences (NAS) 2015 committee report using the updated data through 2011. [6] The analysis indicates that the estimated change in fatalities under each scenario based on the NHTSA and LBNL 2016 analyses is much smaller than in the NHTSA and LBNL 2012 analyses; for example, an across the board 100-lb reduction in mass would result in an estimated 157 additional annual fatalities based on the 2012 analysis, but would result in only an estimated 91 additional annual fatalities based on the 2016 analyses. The mass reductions recommended by the 2015 NAS committee report (5%, 10%, and 15% for small, midsize, and large cars, respectively, and 20% for light trucks, CUVs, and minivans) would result in 344 fewer annual fatalities (and roughly 2,000 lives saved using the coefficients after adopting the DRI measures, or from the LBNL baseline regression model, in Figure VI.1-4). These results support NHTSA's conclusion from its 2012 study that, when footprint is held fixed, "no judicious combination of mass reductions in the various classes of vehicles results in a statistically significant fatality increase and many potential combinations are safety-neutral as point estimates".

Conclusion

The 2016 NHTSA and LBNL reports conclude that the estimated effect of mass reduction while maintaining footprint on societal U.S. fatality risk is small, and statistically non-significant at the 95% confidence level for all light-duty vehicles, based on the jack-knife method NHTSA uses to estimate uncertainty. The LBNL report also finds that the estimated effects of other control variables, such as vehicle type, specific safety technologies, driver age and gender, and crash conditions on risk are much larger, in some cases two orders of magnitude larger, than the estimated effect of mass or footprint reduction on risk. Finally, the LBNL report shows that after accounting for the many vehicle, driver, and crash variables NHTSA used in its regression analyses, there remains a wide variation in risk for vehicle models of similar mass, and this variation is unrelated to vehicle mass.

Because the estimated relationships between mass reduction and societal fatality risk are not consistently statistically different from zero, and are sensitive to the data and variables used in the regression models, LBNL recommends that the agencies use a second set of regression coefficients, such as those used in the "LBNL baseline", that estimate the relationship between mass reduction and societal fatality risk. This second set of coefficients can be used as a sensitivity test when determining the extent to which manufacturers can use mass reduction as a strategy to meet fuel economy/greenhouse gas emission standards while minimizing costs in the NHTSA Volpe and EPA OMEGA models.

Although LBNL believes that the current analysis is the most comprehensive and thorough investigation to date of the relationship between vehicle mass/footprint and safety, there are limitations to the analysis. While the goal of the NHTSA and LBNL reports is to estimate the effect of vehicle mass reduction on societal risk, this is not exactly what the regression models are estimating. Rather, they are estimating the recent historical relationship between mass and risk, after accounting for most measurable differences between vehicles, drivers, and crash times and locations. In essence, the regression models are comparing the risk of a 2600-lb Dodge Neon with that of a 2500-lb Honda Civic, after attempting to account for all other differences between the two vehicles. The models are not estimating the effect of literally removing 100 pounds from the Neon, leaving everything else unchanged. In addition, the analyses are based on the relationship of vehicle mass and footprint on risk for recent vehicle designs (model year 2003 to 2010). These relationships may or may not continue into the future as manufacturers utilize new vehicle designs and incorporate new technologies, such as more extensive use of strong lightweight materials and specific safety technologies. As a result, the agencies should recognize that the findings from the regression analyses of the recent historical relationship between vehicle mass and fatality risk cannot accurately predict what effect mass reduction in future vehicle designs will have on societal fatality risk, especially in light of extensive use of stronger lightweight materials and adoption of new crash prevention technologies.

References

[1] Puckett, S.M. and Kindelberger, J.C. (2016). *Relationships Between Fatality Risk, Mass, and Footprint in Model Year 2003-2010 Passenger Cars and LTVs.* Preliminary report prepared for the National Center for Statistics and Analysis. (Docket No. NHTSA- 2016-0068). Washington, D.C.: National Highway Traffic Safety Administration.

[2] Kahane C.J. (2014). *Updated Estimates of Fatality Reduction by Electronic Stability Control*, NHTSA Evaluation Note No. DOT HS 812 020. Washington, DC: National Highway Traffic Safety Administration.

[3] Wenzel, T. (2016a). *Assessment of NHTSA's Report "Relationships Between Fatality Risk, Mass, and Footprint in Model Year 2003-2010 Passenger Cars and LTVs"*. Preliminary report prepared for the Office of Energy Efficiency and Renewable Energy, U.S. Department of Energy. LBNL-1005177. Berkeley, CA: Lawrence Berkeley National Laboratory.

[4] Wenzel, T. (2016c). *Effect of using Different Vehicle Weight Groups on the Estimated Relationship between Mass Reduction and U.S. Societal Fatality Risk per Vehicle Miles of Travel.* Final report

prepared for the Office of Energy Efficiency and Renewable Energy, U.S. Department of Energy. LBNL-1006317. Berkeley, CA: Lawrence Berkeley National Laboratory.

[5] Wenzel, T. (2016b). *Relationship between US Societal Fatality Risk per Vehicle Miles of Travel and Mass, for Individual Vehicle Models over Time (Model Year).* Final report prepared for the Office of Energy Efficiency and Renewable Energy, U.S. Department of Energy. LBNL-1006316. Berkeley, CA: Lawrence Berkeley National Laboratory.

[6] National Academy of Sciences (2015). *Cost, Effectiveness and Deployment of Fuel Economy Technologies for Light-Duty Vehicles.* Final report prepared by the Committee on the Assessment of Technologies for Improving Fuel, Economy of Light-Duty Vehicles, Phase 2; Board on Energy and Environmental Systems; Division on Engineering and Physical Sciences. Washington, D.C.: National Research Council.

VI.2 Magna/FCA Ultralight Door Design, Manufacturing, and Demonstration Project – Magna International

Project Details

Tim Skszek, Principal Investigator
Magna International
750 Tower Drive
Troy, MI 48098
Phone: 248-631-5375
E-mail: tim.skszek@magna.com

David Ollett, Project Manager
National Energy Technology Laboratory
626 Cochrans Mill Road
Pittsburg, Pennsylvania 15236-0940
Phone: 412-386-7339
E-mail: david.ollett@netl.doe.gov

Sarah Kleinbaum, Technology Area Development Manager
U.S. Department of Energy
1000 Independence Avenue, SW
Washington, DC 20585
Phone: 202-586-8027
E-mail: sarah.ollila@ee.doe.gov

Executive Summary

During Fiscal Year (FY) 2016, Magna International Inc., through a cooperative agreement with the U.S. Department of Energy (DOE) and partners Fiat Chrysler Automobiles US LLC (FCA US LLC0 and Grupo Antolin, developed a new Ultralight Door architecture that is 15.61 kg, or 40.35%, lighter than the 2014 baseline equivalent.

The project demonstrates a cost-effective means of realizing a 56-kg full vehicle mass reduction if all four doors of a 4-door, C-segment vehicle were lightweighted while maintaining the functionality and performance of the baseline production vehicle.

Accomplishments

Accomplishments during FY 2016 include:

Initiated the following:

- Product Design and Analysis – This included the architectural, concept, and prototype design associated with development of the Ultralight Door for the driver-side door. The prototype design release is 15.61 kg, or 40.35%, lighter than the baseline driver-side door. Characterized the mass and performance characteristics associated with the baseline door.
- Initiated an Incremental Cost Model – The incremental cost associated with the ultralight door is estimated to be $2.59 per pound saved, which is well under the DOE objective of $5 per pound saved.

Future Directions

Future activities scheduled to take place during FY 2017 include the following:

- Product Design and Analysis – Continue engineering and design efforts to realize the 42.5% mass reduction objective, reducing the door mass by an additional 800 g from 15.61 to 16.4 kg mass saved.
- Manufacture and Assembly of Prototype Components – Manufacture tooling, prototype component parts, and full-scale door assemblies.
- Vehicle Integration – Integrate prototype door assemblies with baseline production vehicles.
- Test – Validate performance of the ultralight door and demonstrate functional equivalence relative to the baseline driver's side door.

Technology Assessment

Initial efforts included material substitution, such as replacing steel components with carbon fiber and magnesium materials. This approach achieved the mass reduction objective, but it did not meet the incremental cost threshold of $5 per pound weight saved.

- Carbon fiber-reinforced composite materials are not included in the ultralight door design due to material and manufacturing cost constraints, which exceed the project objectives. Further research is needed to reduce the manufacturing cost of carbon fiber-reinforced composite components for high-volume commercial application.
- Magnesium sheet material is not included in the ultralight design due to material availability and manufacturing cost constraints, which exceed the project objectives. Further research is needed to reduce manufacturing cost and global availability of magnesium sheet components for high-volume commercial application.

Introduction

Magna International Inc., through a cooperative agreement with DOE and partners FCA US and Grupo Antolin, has developed a new, Ultralight Door architecture that is capable of meeting the DOE objective of 42.5% lighter than a current production door, offering a solution that will further enable automakers a means of achieving the proposed legislation regarding passenger vehicle emissions and fuel consumption regulation. The current Ultralight Door design is 15.61 kg, or 40.35%, lighter than the 2014 baseline equivalent.

Magna's advanced engineering team is a collaborative effort between the company's corporate research and development, body and chassis, closures, and exteriors groups. This team combined its unique, full-vehicle perspective on the design of a driver-side door with an inventive mix of materials and technology to tackle the challenge of achieving significant weight reduction in a cost-effective manner while maintaining all safety, durability, and functionality aspects relative to 2016 baseline driver-side door.

Approach

The project proposal included selection of a baseline "frame behind glass" door architecture, which is applicable to 70% of the lightweight vehicle market. Initial activities included characterization of the mass and performance characteristics associated with the baseline door and development of a performance target matrix for achieving a functionally equivalent Ultralight Door that is 42.5% lighter than the baseline driver's side door.

The design for the Ultralight Door realized the target performance and mass reduction objectives through functional integration of the various door components and subsystems, using multiple forms of aluminum, advanced molding processes, and innovative joining methods.

The significant mass reduction associated with the ultralight door is the result of a holistic design approach, enabling integration of the glass run channels with the module, application of advanced joining technologies to minimize the length of the flange, application of chemically toughened glass, Local Interconnect Network (LIN) Bus communications, and advanced molding technologies. The materials associated with the Ultralight Door are commercially available and suited for use in high-volume/low-cost manufacturing applications. The manufacturing and joining technologies are compatible with existing manufacturing processes and can be commercialized without a significant increase in production costs or changes in body-shop infrastructure. The project plan includes a prototype build of thirty prototype door assemblies, component-level testing, and full vehicle testing by FCA. The specifics and requirements for each type of test are given in Table VI.2-1.

Table VI.2-1. Ultralight Door Test Plan

Test Plan
Corrosion
Full Vehicle
Safety
20-mph side pole 50th male
38-mph side deformation - Side Impact New Car Assessment Program (SINCAP)
31-mph Insurance Institute for Highway Safety side impact
20-mph side pole fifth female
40-mph Insurance Institute for Highway Safety 25% small overlap frontal impact
Federal Motor Vehicle Safety Standards (FMVSS) 214 static
Structure/Durability
Hardware slam
Dynamic over check
Sag-set
Anti-theft
Static over check
Window cycle
Water testing
Denting and oil canning
Fit and Finish
Appearance
Noise, vibration, and harshness

Results and Discussion

During FY 2016, the Ultralight Door project team designed a complete driver's side door assembly that weighs 15.61 kg, or 40.35%, less than the 2016 baseline production door assembly. The breakdown for the weights of individual components and the percent of mass reduction for each are given in Table VI.2-2. The Ultralight Door is based on materials and manufacturing technologies that are commercially available or have been demonstrated for high-volume production applications. The project team continues to evaluate material, process, and design alternatives to achieve the remaining 0.83 kg required to achieve the 42.5% mass reduction objective defined in the funding opportunity announcement. The incremental cost per pound saved associated with the Ultralight Door design is estimated to be $2.59 per pound saved, which is well below the $5 per pound saved objective defined in the funding opportunity announcement.

Table VI.2-2. Mass Characteristics Associated with Baseline and Ultralight Door Systems

Door Subsystem	Baseline Door(kg)	Ultralight Door (kg)	Mass Reduction %
Door -In -White (DIW)	17.42	9.31	46.56%
Interior Trim Panel and Upper Trim	4.35	2.78	36.09%
Glass Assembly	4.12	2.15	47.82%
Window System/Door Module	3.38	2.13	36.98%
Sealing System	2.18	2.03	6.88%
Mirror Assembly	1.42	1.06	25.35%
Latch Assembly	0.81	0.45	44.44%
Exterior Handle Assembly	0.65	0.15	76.92%
Hinges	0.70	0.40	42.86%
Wiring Harness	0.73	0.63	13.70%
Speaker	0.96	0.50	47.92%
Other	1.97	1.49	24.37%
Total	**38.69**	**23.08**	**40.35%**

The engineering design effort included several computer-aided engineering (CAE) activities associated with structural performance, safety, and durability relative to the baseline production door. Results of the performance for each of the design parameters are shown in Table VI.2-3. Other assessment activities included closing effort, manufacturing feasibility, and cost.

Table VI.2-3. CAE Performance Results of Ultralight Door Relative to the Baseline Production Door

Design Performance Parameters	Status
Structural	
Modal	Pass
Stiffness	Pass
Strength	Pass
Abuse	Pass
Safety	
Dynamic 214	Pass
Static 214	Pass
Durability	Pass
Closing Effort	Pass
Manufacturing Feasibility	Pass

The key Magna innovations associated with development of the ultralight door include functional integration of the door-in-white assembly, SmartLatch^{tm}, carrier module, glass, hinges, speakers, and interior trim:

- The lightweight carrier module resulted from a unique design and assembly process enabled by the bolt-on beltline inner and beltline outer structural components.
- Integration of SmartLatch^{tm} eliminated the need for mechanical hardware and enabled local interconnect network bus control.
- Unique design of the window system/door module resulted in an 11% reduction in glass area and integration of the glass run channels, providing mass reduction and assembly benefits.
- Material selection and design optimization of the design door-in-white components resulted in an 8.11-kg mass reduction of the door assembly or approximately 52% of the total mass reduction.

Grupo Antolin U.S. leveraged its knowledge relative to design and manufacture of interior trim components, integrating additional functional requirements imposed by the electronic latch and lightweight door module.

Application of advanced molding technologies, polymers, and joining technologies contributed approximately 10% to the total mass reduction associated with the driver's side door.

The FCA US engineering team collaborated with the Magna team throughout the development process to ensure compatibility with existing assembly operations.

- FCA US developed lightweight cast aluminum door hinges and lightweight neodymium magnet speaker components that resulted in a 0.76-kg mass reduction.
- FCA US conducted CAE durability, fatigue, and safety analysis associated with the Ultralight Door to ensure functional equivalence to the baseline door.
- FCA US will conduct component and vehicle-level testing of prototype door assemblies and full vehicles to validate the results of the CAE predictive simulation in FY 2016 through FY 2017.

The DIW construction includes various grades and forms of aluminum, including a vacuum die cast A-pillar support, extruded upper support, and stamped inner panel, outer panels, and door beam. Figure VI.2-1 is an exploded view of the DIW components and materials of construction. Material grade, gauge, and cross-section geometry were optimized to achieve structural, safety, and durability requirements.

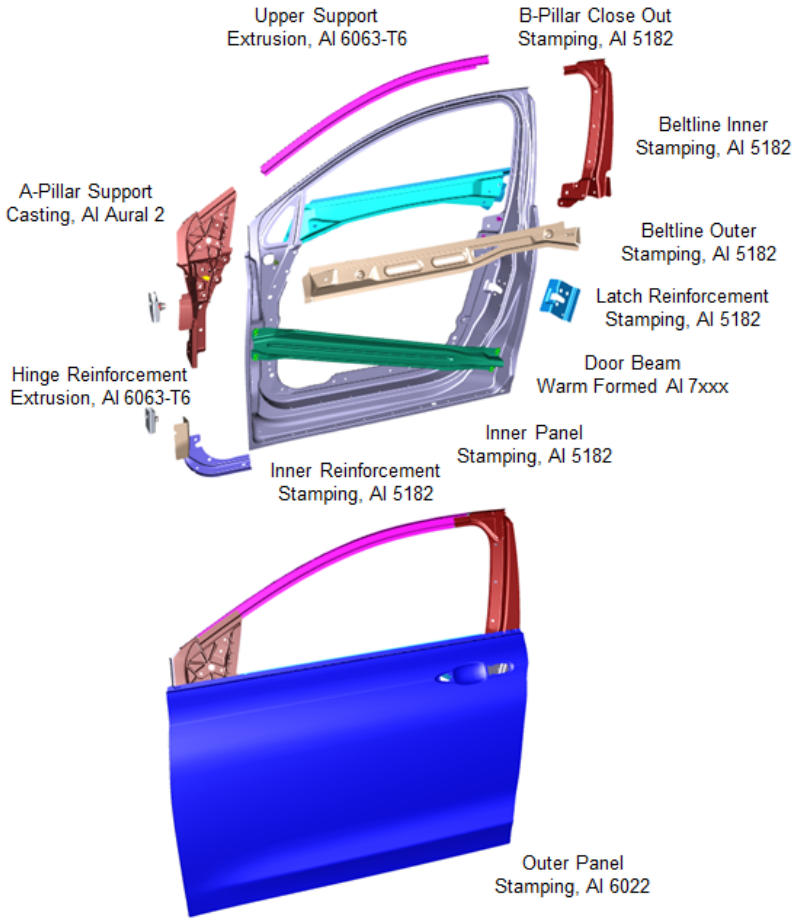

Figure VI.2-1. Door-in-white subsystem, 8.11-kg mass reduction.

The interior trim subsystem was developed by Grupo Antolin US. Light-weighting was achieved through part integration and application of advanced molding technologies and materials. Figure VI.2-2 shows a schematic

of this subsystem. The interior trim includes functional integration of the SmartLatch[tm], door module, and DIW subsystems.

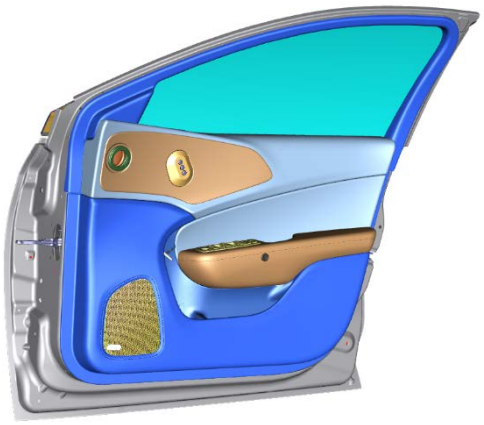

Figure VI.2-2. Interior trim subsystem, 1.57kg mass reduction.

The side glass developed by Magna includes application of a Corning® Gorilla® Glass laminate and an 11% reduction in surface area enabled by the carrier module.

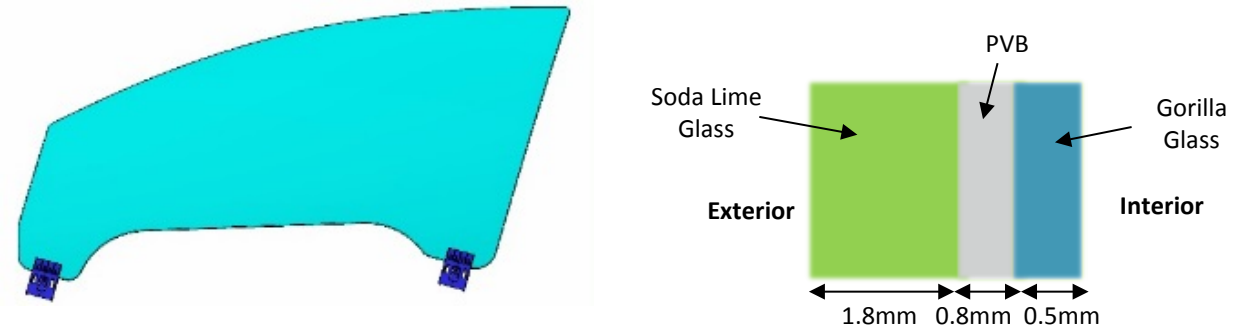

Figure VI.2-3. Side glass, 1.97-kg mass reduction.

The SmartLatch[tm] developed by Magna includes application of an electronic latch and lock as shown in Figure VI.2-4. Elimination of mechanical latch hardware enables application of the carrier module.

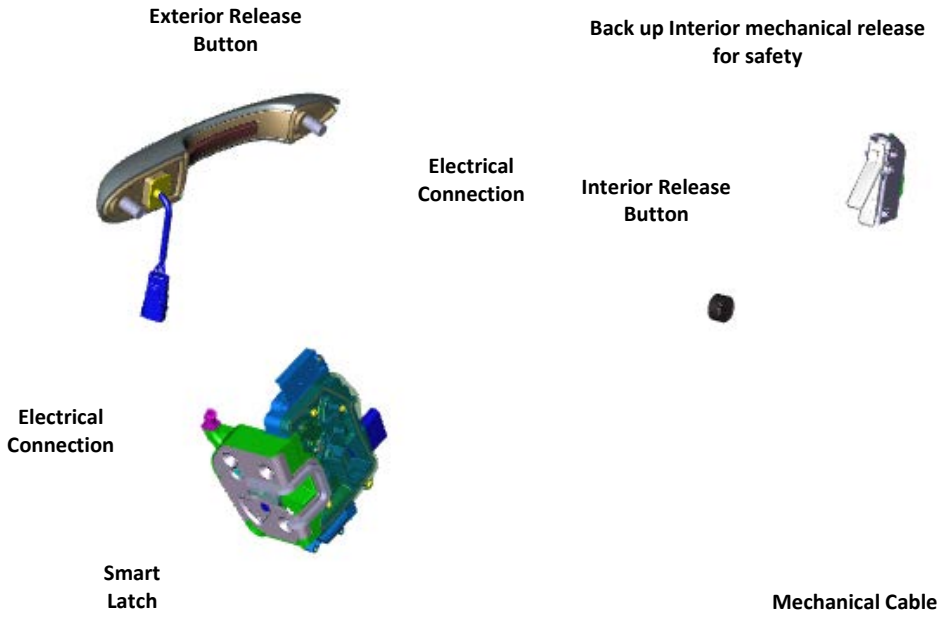

Figure VI.2-4. SmartLatch[tm] and handle exterior, 0.86-kg mass reduction.

Technology Transfer Path

Direct participation of FCA US, a global original equipment manufacturer, and Tier 1 suppliers Magna International, Grupo Antolin US, and Corning Glass provide a direct path for technology transfer and commercial application. Cost-effective mass reduction of automotive passenger car assemblies, which are compatible with existing manufacturing and assembly operations, are needed to meet Corporate Average Fuel Economy (CAFÉ) and Environmental Protection Agency legislation. The project includes both component and vehicle-level testing conducted by the original equipment manufacturer, which reduces the risk and timeline of commercial application.

Conclusion

Development of the Ultralight Door conducted by Magna's advanced engineering team, FCA US, and Grupo Antolin US during FY 2016 demonstrates the feasibility of reducing mass associated with a driver side door by over 40% relative to a 2016 baseline production door. In FY 2016 through FY 2017, the project will include component-level and full vehicle testing to enable high-volume commercialization of the technologies at a known cost and relatively low risk.

VI.3 Ultralight Hybrid Composite Door Design – TPI Composites, Inc.

Project Details

Nathan P. Gravelle, Principal Investigator
TPI Composites Inc.
373 Market St.
Warren, RI 02885
Phone: 401-247-4071 Fax: 401-247-2669
E-mail: ngravelle@tpicomposites.com

David Ollett, Project Manager
National Energy Technical Laboratory
DOE/NETL/PMC/VTP
626 Cochrans Mill Road
Pittsburg, PA 15236-0940
Phone: 412-386-7339
E-mail: david.ollett@netl.doe.gov

Sarah Kleinbaum, Technology Area Development Manager
Lightweight Materials
Vehicle Technology Office
U.S. Department of Energy
1000 Independence Ave
Washington, DC 20585
Phone: (202) 586-8027
Email: Sarah.Ollila@EE.DOE.Gov

Contractor: TPI Composites Inc.
Contract No.: DE-EE0007296

Executive Summary

This project is developing a comprehensive systems approach for designing, manufacturing, and demonstrating an ultra-light hybrid composite automotive door. Composite structural components are integrated with other functional systems to ***reduce part count and full-system weight by a minimum of 42.5%***. The approach will be demonstrated on a driver-side front door and will consider all fit, functional, safety, and cost requirements. Materials (i.e., fast-curing infusible epoxies developed by Hexion, non-crimp fabrics by Saertex, and acoustic foam/sealants/adhesives by Creative Foam) and processes (i.e., high-pressure resin transfer molding [HP-RTM] implemented by Krauss Maffei) will be demonstrated to meet the production rate and performance requirements established by the vehicle's original equipment manufacturer (OEM) (i.e., an approximate 4 to 5-minutes cycle time is required to meet annual production rate). TPI's expertise in system design and as a Tier 1 supplier will be complemented by the University of Delaware Center for Composite Materials (UD-CCM)'s modeling and simulation capabilities for HP-RTM, material response, and side-impact crash modeling of composites. Our team will use a systems approach for establishing door requirements, including geometry, environmental, structural, durability, and crash performance; assembly to vehicle structure; consumer preference (i.e., noise, vibration, and harshness); and weight and cost to meet or improve the metallic door. Concepts will be developed and include material selection and composite layups, geometries, light alternative glazing materials, and integration approaches to meet all requirements. These concepts will be evaluated using structural and crash simulations and linked to a manufacturing feasibility study, resulting in producible designs of an integrated door system. A cost model will evaluate part of the cost

for the various designs and will ensure the ***cost target of less than $5 per pound of weight saved*** is met. Hybrid composites consisting of carbon, glass, and metal components will be included in our trade-off studies to satisfy these cost and performance goals.

The front-side driver door consists of about 50% structural steel components (i.e., outer and inner sheet-metal panels, window frame, local steel reinforcement, fasteners, and hinges). Non-structural plastic molded panels and trims (about 15% of total weight) are attached and allow integration of subsystems such as speakers and controls. The remainder of the weight is the side window and mirror system (about 20%) and other components (e.g., sealants, lock, speaker, and others). Replacement of the steel parts and molded panels with carbon fiber-reinforced composites offer between 60 to 70% weight reduction potential over steel (i.e., 20 to 30% for glass fiber-reinforced composites will be designed to meet total weight reduction goals [1]). A hybrid glass/carbon composite at 48% weight reduction could reduce cost of the composite structure and meet the funding opportunity announcement (FOA) goal through additional part consolidation and other component light weighting. Geometries will need to be optimized to allow manufacturing feasibility and other materials can be strategically incorporated to allow improved structural performance coupled with other functionality (such as noise or vibration control). Fastener weights can be reduced through parts consolidation, co-molding and adhesive bonding while improving durability, and reducing secondary assembly steps that add to cost.

Accomplishments

- Agreed upon requirements for the door
- Transferred computer-aided design data
- Generated finite element analysis model, both steel baseline and composite models
- Completed laminate optimization
- Created test samples for material properties.

Future Directions

- Complete Material and Process Database
- Fabricate sub-component
- Conduct a detailed design review
- Demonstrate the projected manufacturing rate
- Demonstrate that the design meets FOA goals using a Predictive Engineering Environment
- Receive tooling for the full door build
- Verify that the door fabrication meets manufacturing quality
- Establish a full-scale door test procedure
- Complete testing of the full-scale door
- Demonstrate FOA goals are met by the full-scale vehicle test

- Validate that the full door test results meet requirements

Technology Assessment

- Target: Reduce part count and full-system weight by a minimum of 42.5%.
  - Gap: Current materials and methods utilize steel as the main structural component, adding mass to the overall structure, thereby reducing the vehicle fuel efficiency.
- Target: Cost increase will not exceed $5 per pound of weight saved.
  - Gap: one of the major light-weighting materials at our disposal, carbon fiber, is upwards of $10-15/lb. This material must be used judiciously in order to meet cost targets.
- Target: Materials and processes will be demonstrated to meet the production rate and performance requirements (an approximate 4 to 5-minute cycle time is required to meet annual production rate).
  - Gap: Standard composite manufacturing processes can process these parts at a cycle time of about 1 hour per part. New injection technologies and resin formulations have opened the possibility of faster cycle times.

Introduction

New Corporate Average Fuel Economy regulations will require improved fuel efficiency of the future vehicle fleet and weight reduction is key to achieving these targets. Replacing metallic body and chassis components with carbon fiber-reinforced composites offers the most weight reduction potential at up to 70%. Introduction of the BMW i3 and i8 in 2014 required mass production processes to meet 20,000+ units per year. Preforming with HP-RTM has been implemented and meets rate, cost, and performance requirements. Our team members, Krauss Maffei, Hexion, and Saertex, were extensively involved in technology development (i.e., manufacturing, materials, and preforming) with BMW and brought this experience to our team led by TPI, the vehicle OEM, and the UD-CCM. We will advance these technologies to develop an ultra-light driver-side door for the vehicle with production rates of 80,000 units annually per plant in Detroit, Michigan

TPI has over 40 years of experience in the design, testing, prototyping, and production of lightweight composite structures and is leading the team of industry and academic partners with knowledge in all aspects of vehicle design and composite materials. The OEM will provide system requirements, integrate the ultra-light door into the vehicle, and validate the design during vehicle testing. Krauss Maffei, Hexion, Saertex, and Creative Foam will demonstrate their next-generation material and process solutions, while UD-CCM is world-renowned for their composite expertise in all aspects of composites research and development. The team will implement the new composite door design and evaluate integration and manufacturing challenges to meet automotive rate and cost targets.

Approach

Development of a vehicle body-in-white is a very complex and time-consuming process, because various, often-conflicting, functional requirements have to be considered. Introducing new designs to reduce vehicle weight requires a systems approach where new designs can be quickly iterated and refined to evaluate their performance. This is particularly true when metals are replaced with composite materials because composite materials have significant potential to reduce weight when designs are fully optimized for parts consolidation and engineered properties using a variety of available material, fiber layups, and processing choices.

A typical automotive door is made from a combination of materials, including steel, plastic, and glazing. The structural materials are heavy, while the non-structural components do not contribute significantly to structural performance. Elements are joined together, increasing manufacturing and assembly cost and weight. We propose to replace all structural parts of the front side driver door with continuous reinforced composites (with a weight saving of up to 60%), reduce part count and system weight through part consolidation, and evaluate

alternative glazing materials. This approach has the potential to meet and exceed the goals of 42.5% system weight reduction compared to the steel door baseline and to meet cost targets of $5 per pound weight saved. The team will take a systems approach to meet the targets, as seen in the flow diagram in Figure VI.3-1.

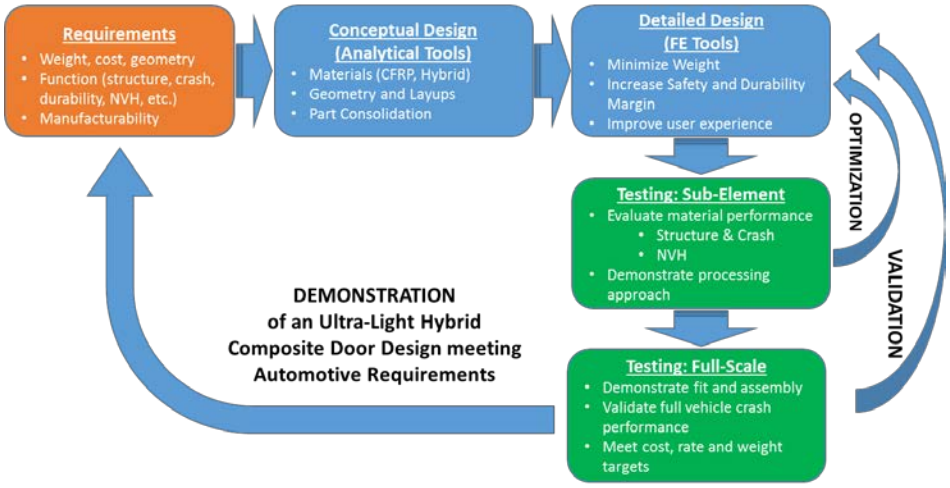

Figure VI.3-1. Systems approach for reducing weight in complex automotive structures.

This approach relies on use of computational engineering analysis and simulation tools combined with sub-element testing to rapidly develop and evaluate design changes while full-scale testing is used to proof out the final design. The program will define the design requirements (such as weight and cost targets), functional and topology constraints, and consider the ability to manufacture the door at the required rate and performance. Cost; structural; crash; noise, vibration, and harshness; and manufacturing simulations exist and will be utilized. These individual simulation tools are state-of-the-art, commercially available, and have been validated on numerous occasions. Conceptual designs will be evaluated at the sub-element level to evaluate material performance (i.e., structure, crash, and noise, vibration, and harshness) and to demonstrate the processing approach meets rate and quality targets. Full-scale test articles will be manufactured to validate form, fit, function and cost of all integrated structural and non-structural components. A small number of design iterations may be required to optimize the various configurations. The approach will allow (1) a shortened design cycle, resulting in reduced development time and costs, (2) elimination of trial-and-error process and part trials reducing tooling and manufacturing costs, and (3) an optimum door configuration at minimum weight leading to a more cost-competitive product. The overall approach will be demonstrated on a composite door solution for the vehicle, but it is applicable to a wide variety of automotive components. The comprehensive systems approach for designing, manufacturing, and validating a complex ultra-lightweight composite automotive component using a validated, multi-disciplinary design tool with a small number of manufactured components for validation will reduce risk to convert metal structures to composites.

Predictive engineering tools guide material and design down-selection and are critical for eliminating trial and error and reducing cost and time. Figure VI.3-2 shows the design environment the team will employ to evaluate the composite door structure.

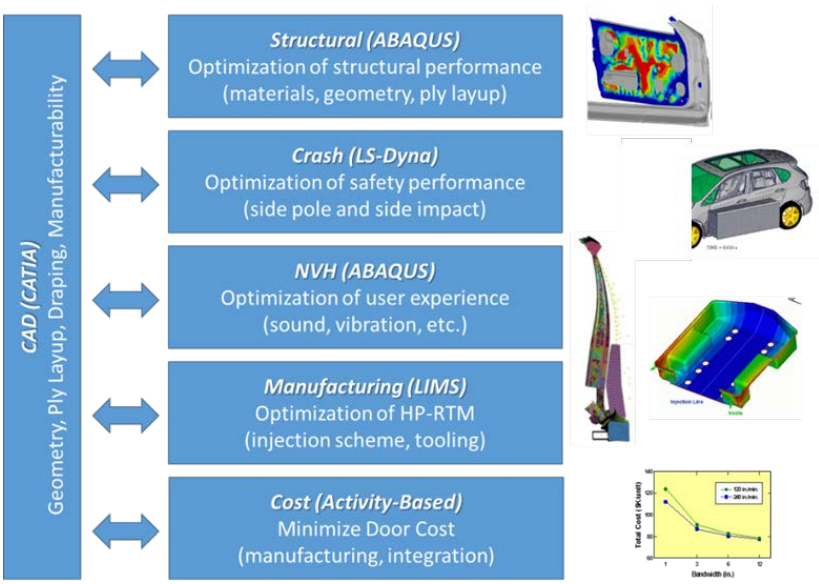

Figure VI.3-2. Integrated predictive engineering environment.

Dassault System's computer-aided three-dimensional interactive application (CATIA) product design solution is our product development platform that easily communicates with other simulation tools. This enables multiple disciplines to share geometry, ply layup, and manufacturing-induced fiber orientations. Thus, designs are developed in one environment and then evaluated in the specialist applications across all phases of the product development process. For example, an important aspect of composite manufacturing is the effect of draping the fiber layer onto the mold surface, resulting in changes of the local fiber orientation. This can affect the infusion behavior during resin injection and the structural and crash performance of the final part. Our approach captures manufacturing-induced variations in the design and feeds these properties into all sub-models. Another example is potential sandwich constructions where the design not only improves structural stiffness but also noise attenuation (improving ride experience) with novel foam solutions. Integration of other non-structural functional door items (e.g., speakers, glazing, and electronics) are captured in the design and are fed into the appropriate models and concepts.

The existing vehicle steel door is used as a baseline and the ability to reduce part count with a composite structure will be investigated. Part consolidation reduces weight and cost because a smaller number of parts has to be manufactured. Assembly time and associated labor costs can be significantly reduced as well. The HP-RTM process allows complex geometry part fabrication, which enables integration of features into one component. Figure VI.3-3 illustrates the potential part count reduction of a steel door with an equivalent composite structure. Part count reduction alone will not be able to meet our weight reduction goals of 42.5%, but in combination with hybrid and/or carbon fiber-reinforced composites material replacement and lower weight window solutions, it will reduce the weight of the door structure to the required levels.

Figure VI.3-3. Composites allow part consolidation, further reducing cost and weight [1].

Our hybrid solution will evaluate a variety of material solutions, including glass and carbon fibers. Fiber modulus and strength depend on the fiber selection with specific properties being the highest for carbon fibers. Design solutions without cost consideration will use 100% carbon fibers and provide the best structural performance at the lowest weight. A hybrid design will incorporate alternative fiber solutions at a lower cost and meet structural performance. Our optimal design will consider all options and will meet structural requirements and cost and weight targets.

Lower-density glazing (such as polycarbonate glazing) has been recently developed for automotive applications. Transparent polymers can be easily molded into complex shapes, and it offers a 50% weight savings compared to standard glass solutions. The new materials have been demonstrated in both concept and production cars, including the Chevrolet Volt and Hyundai European Design concept cars and the Mercedes SMART and Toyota V (station wagon version of the Prius) vehicles [2]. New window solutions also address the requirement for improved cabin comfort. Because glazing thicknesses have been reduced to save weight, the noise level within the car has increased. Integrating transparent acoustic layers within the glazing can be used to increase damping performance and thinner and lighter-weight glazing can be employed without compromising cabin comfort or safety. Polycarbonate glazing enables new design concepts because complex geometry windows can be fabricated. Polycarbonate glazing with integral ribs lock the parts onto the vehicle or support other features. This program will evaluate a polycarbonate solution, which should not only impact the weight of the glazing, but the overall design of the composite door solution. This will simplify assembly and have the potential to lower the cost and weight of the total door solution.

All considered concepts will be evaluated at the component and full door level using structural finite element analysis tools. The composite laminate structure can be varied and will change the anisotropic stiffness and strength behavior of the part. The selection of fiber materials will impact performance and cost. Optimization of the layups, materials, and geometries needs to result in a manufacturable design at minimum weight while meeting all design requirements. The team has significant experience in design and analysis using commercially available structural static and dynamic finite element analysis tools for vehicle structures that will be key for evaluating and optimizing the designs.

Crash worthiness will be evaluated using LS-DYNA, allowing simulation of the door and full vehicle under dynamic conditions. In particular, we will consider the crash performance under side impact meeting Federal Motor Vehicle Safety Standard 214's protection requirements (other FOA crash scenarios will be considered). The simulation will evaluate inward deflection as a function of time during impact for the baseline steel door and our composite solution. A conservative design goal would require the composite solution provide a deflection profile that stays below the transient intrusion levels of the steel baseline door. This would ensure the safety mechanisms (such as the side airbag) are able to be employed in time and space and the passenger is protected in case of a side collision. UD-CCM has significant experience with crash predictions and under a current National Highway Traffic Safety Administration program evaluates composites for a steel B-pillar replacement. Strain-rate-dependent material properties for composites are available; however, additional

properties for the HP-RTM resins and fibers may have to be determined using coupon and sub-scale element testing. The test data will provide the programs with a database of material properties for crash designs.

The program will implement the HP-RTM process to fabricate sub-elements and full-size components. The process has been proven to produce Class A finished structural components at automotive rates. Cycle times of less than 10 minutes have been demonstrated in production on the BMW i3 and i8; this program will further reduce cycle time and performance using the most recent advances in resins and reinforcements developed by our team members (i.e., a 4 to 5-minute cycle time would meet current vehicle production rates). Our partner, Krauss Maffei, has implemented a production cell to automate the process. Structural components, sidewall panels, floor pans, front-end carriers, crash boxes, and carbon-fiber design components are applications that have been implemented via HP-RTM. Fiber mats or fabrics are preformed and then positioned in the mold. A variety of low-viscosity polymers (such as polyurethane, epoxy, and polyamide) can be used as matrix material. The material components are mixed and heated in a metering system and injected into the heated mold. The resin quickly cures in the closed tool and the part can be demolded. Trimming occurs onsite. The HP-RTM process can produce parts with fiber content up to 70%. The process allows reuse of scrap material, improving material yield. Components manufactured using high-pressure RTM exhibit Class A surface quality and can produce high-quality (low-defect) parts with an aesthetically pleasing carbon appearance. The procedure has been fully automated and is suited for series production from the manufacturing of preforms up to post-mold processing. The program will use the existing HP-RTM as the baseline process, evaluate opportunities to reduce cycle time through innovative new materials (Saertex and Hexion), and evaluate new process improvements (Krauss Maffei, UD-CCM, and TPI).

New resin materials are currently being developed at Hexion and will be optimized for this program. These resins (EPIKOTE™ 05475) and appropriate curing agents have low initial viscosity (below 100 centipoise) and allow rapid infusion of reinforcement during the injection phase of the HP-RTM process [3]. The rheology of the EPIKOTE resin with three different curing agents is discussed in Reference [3] and shows the ability to control the viscosity profile while ensuring rapid cure without significant exothermic reaction of the polymer. Recent advances show full property translation and rapid (i.e., snap) cure in less than 2 minutes at elevated temperature. The low viscosity profile allows reduced injection pressure throughout the infusion cycle, relaxing the requirements of the preform, tool, mixer, and press. This, in turn, reduces preform distortion, cycle time, and capital cost.

Non-crimp fabrics provide the best fiber property translation and, through use of multi-axial systems, can be combined in a preform used in production of large series vehicle components. These preforms are manufactured to the correct geometry and fiber layup, allowing rapid placement of the reinforcement into the HP-RTM tool. This enables minimum cycle time during the process, paired with the high quality of the final product. It is important to optimize the preform to reduce scrap material and lower material cost. Our partner, Saertex USA, is the world-wide leader in tailor-made non-crimp fabric materials and they will support development of low-cost preforms for this program.

A key challenge of the HP-RTM is design of the mold and preform to ensure full infusion of the polymer into the reinforcement. Tooling cost is a significant capital expense, because applied pressures are high and the tool is expected to last over the entire production run. UD-CCM is an expert in modeling the infusion behavior in liquid molding of hybrid preforms with complex geometry. The permeability and drapability of the reinforcement, as well as the rheology of the resin, are key material properties and are needed to allow optimization of the injection port locations and resin pressure cycle during infusion processing. We will evaluate the feasibility of the proposed designs to be manufactured and optimize the mold features for successful infusion, eliminating any required tool changes due to resin infusion issues. The program will ensure manufacturability of the proposed concept with HP-RTM and use virtual process tools to optimize tooling and infusion approaches. Tooling cost for HP-RTM is a significant investment and can only be amortized over a large production run. Conventional RTM processing of prototypes with equivalent part properties will be conducted as part of our risk reduction strategy.

The performance of our designs will be evaluated at the coupon, sub-element, and full-door component level. This will include structural performance testing (i.e., static and crash) and other functionalities such as durability to environmental exposures and noise, vibration, and harshness. Our team has existing testing

capabilities in all of these areas and a comprehensive test plan will be developed as part of the program. Coupon testing is needed to characterize the mechanical and micro-structural (i.e., void content and fiber volume fraction) properties of the hybrid composite design made with the Hexion resin and HP-RTM process. Other data (such as durability, acoustical damping, and environmental performance) may need to be generated and may require larger component testing.

Results and Discussion

UD-CCM received a candidate door model from the OEM though TPI via a secure share process. Figure VI.3-4 shows screen shots of this model after import into CATIA. UD-CCM is in the process of establishing a simplified representation of this model that captures the design space available for analysis. The model will be segmented into primary components with a simple geometric form. Small holes and localized details will be removed to simplify the composite shape and coverage detail.

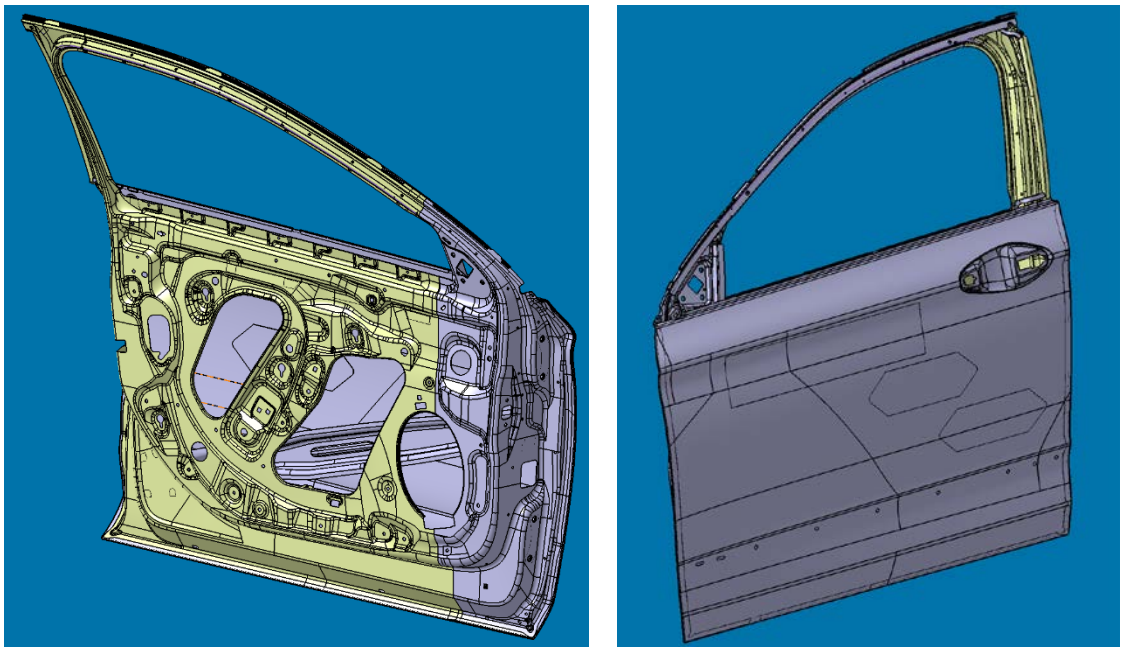

Figure VI.3-4. As provided computer-aided design model of baseline door for replacement composite design.

Figure VI.3-5 shows the model after import of the various subassemblies into CATIA. This model includes all internal components necessary to determine the available volume (Space Claim) for the composite model.

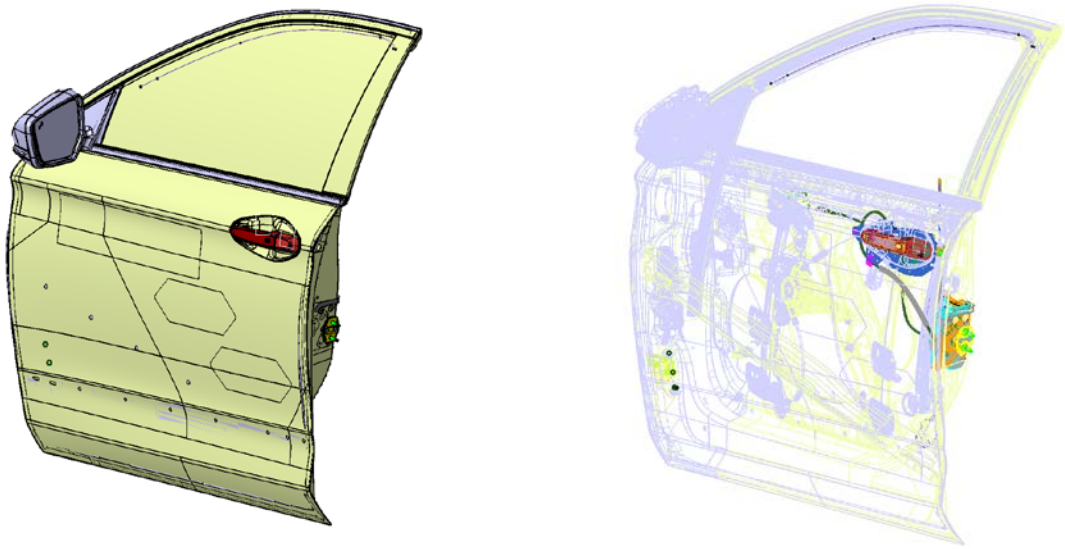

Figure VI.3-5. Complete computer-aided design model via the .step file format imported into CATIA to build the master baseline model.

To date, the interior and exterior surface geometries have been extracted and simplified to build a composite surface model. These steps are shown schematically in Figure VI.3-6. The cleaned up geometries provide an Outer Mold Line basis for design; further simplification of this geometry is expected upon discussion with the OEM. All through-holes have been removed and supplemental geometries have been created to ensure a closed surface on the interior geometry. The exterior panel geometry has undergone some minor surface cleanup and merging for baseline model development purposes.

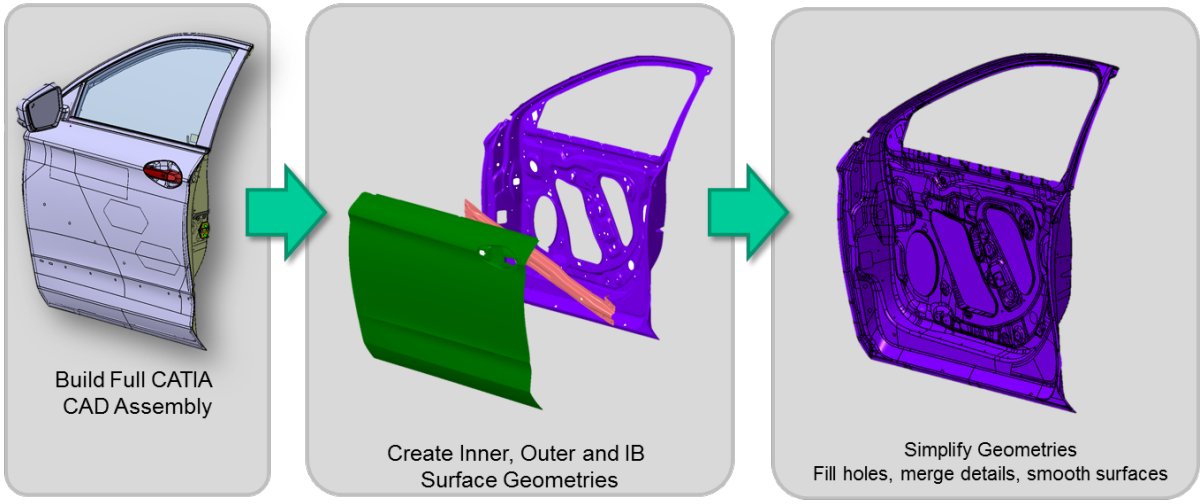

Figure VI.3-6. Model framework development.

Door Requirements

The vehicle OEM supplied the following list of key validation requirements for door design. These are not actual durability requirements. They have been modified to provide meaningful results without compromising the OEM's internal requirements. The static strength loads for the model are provided; however, the stiffness and other requirements have been removed because we will be relying solely on an A to B comparison of the steel computer aided engineering model and the proposed composite design.

Durability:

- Door slam
- Door check
- Inside and outside handle
- Inner panel interface durability (pull cup)

Safety:

- Crashworthiness and occupant protection
    - Dynamic
    - Static

Corrosion Resistance

Sound Transmission Loss

Strength/Stiffness:

- Header rigidity
- Torsional rigidity
- Vertical rigidity
- Abusive loads
- Beltline stiffness
- Dent resistance
- Molding and weather-strip retention
- Resonant frequencies
- Squeaks and rattles
- Mirror system mounting strength
- Inner panels stiffness
- Handle strength load

Quality:

- Sound levels – interior components
- Water leaks
- Body leakage

Function:

- Freeze performance
- Solar load performance.

Hyperworks Optistruct Model Implementation

The fiber lay-up optimization process in HyperWorks uses the Optistruct-solver and consists of three phases. All phases can be done individually, but it is recommended all three phases are used in conjunction. The

phases are (1) free-size optimization, (2) size optimization, and (3) shuffle optimization. Figure VI.3-7 shows the basic process for composite optimization in HyperWorks.

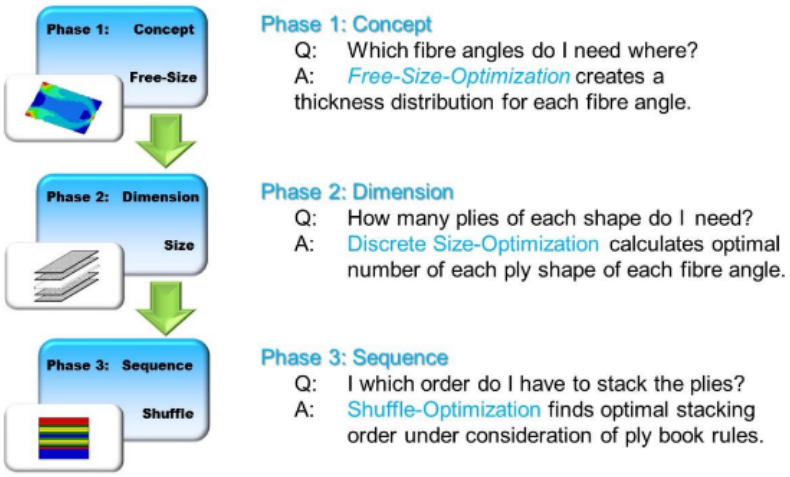

Figure VI.3-7. Basic flow chart for composite optimization in HyperWorks.

In each optimization model, responses and constraints can be introduced. All constraints and restrictions, once defined, will be carried through the following phases. Responses of the model include, but are not limited to, mass, volume, compliance, stresses, and displacements. One response will be the optimization objective (e.g., minimize mass). The other responses can be used as constraints (e.g., minimize mass and do not exceed a certain displacement). Other constraints not based on model responses include laminate structure (i.e., balanced, symmetric, maximum laminate thickness, and percentage of specific fiber orientations) and ply data (i.e., possible fiber orientations and ply thicknesses).

Phase 1 Free Size Optimization

The baseline model was created to validate the Optistruct finite element analysis model using steel geometry. Four point loads were applied to this geometry to perform initial optimization runs (Figure VI.3-8).

Figure VI.3-8. Point loads applied to door outer.

The objective of this phase is to generate the smallest theoretical plies in order to minimize weight and meet design needs (Figure VI.3-9). However, this goal creates some strange ply shapes that will be cleaned up in the latter phases.

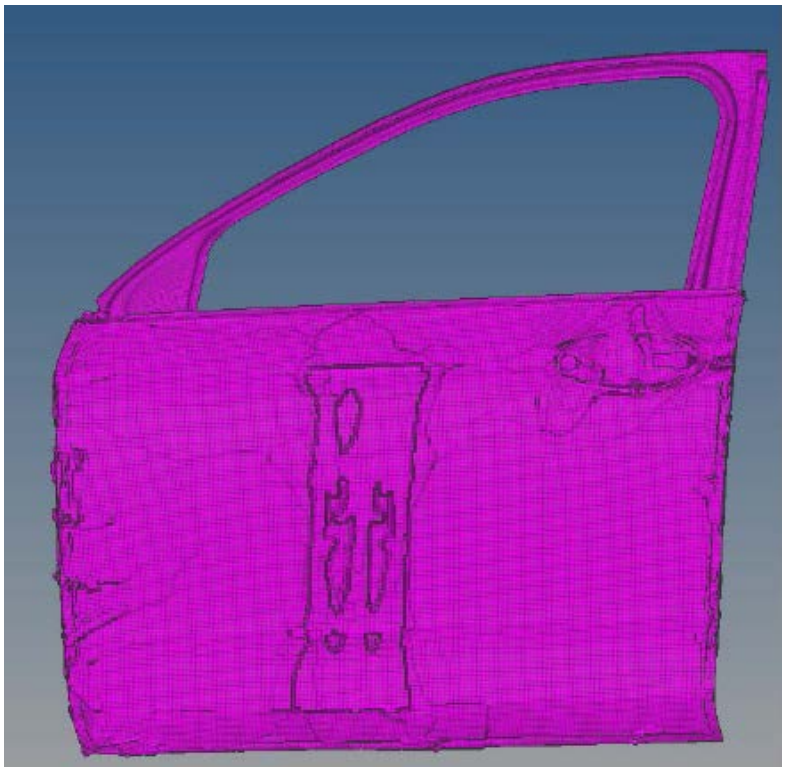

Figure VI.3-9. Zero degree ply shapes.

Phase 2 Size Optimization

This step takes the created ply shapes, the manufactured ply thicknesses, and calculates the number of single plies needed per shape. The solution is a laminate that uses exactly one ply of each shape.

Phase 3 Shuffling

Ply shuffling (Figure VI.3-10) places the plies into the laminate ply stack, where they are most effective for loading. This type of analysis has been accomplished for each of the load case types described earlier. The results will be combined to form the lightest optimized design for meeting all requirements.

Test Panels Fabricated at Hexion Duisburg

Panels were produced by Hexion at Duisburg and shipped to UD-CCM. Panels were inspected using ultrasonics. C-scans and visual inspection indicated high-quality parts with low attenuation variation. Infusion ports, ejector pin locations, and edges will not be used for mechanical testing because variation in quality are observed.

Some additional variations in quality were caused by the need for unidirectional fiber panels for tensile and compression testing. The unidirectional fibers are placed into the mold perpendicular to the gating in order to achieve a good resin flow along the fibers. As a result, fiber washout was created at the end of the gating. A unidirectional preform is not optimal for HP-RTM because the individual filaments nest next to each other, barely providing a path for the resin to flow in the transverse direction, which results in fiber wash. These

preforms were also not stabilized with binder prior to injection, allowing them to potentially move during injections.

Iteration 0	Iteration 1	Iteration 2	Iteration 3
11101	14101	12201	12201
11201	13101	12101	12101
11301	11101	14201	14201
11401	12101	13201	13201
12101	14201	11201	11201
12201	13201	11301	11301
12301	11201	14101	14101
12401	12201	13101	13101
13101	14301	11401	11401
13201	13301	11101	11101
13301	11301	14301	14301
13401	12301	13301	13301
14101	14401	12301	12301
14201	13401	12401	12401
14301	11401	14401	14401
14401	12401	13401	13401
15401	15401	15401	15401
15201	15301	15301	15301
15301	15201	15201	15201
15401	15101	15101	15101

Legend
90.0 degrees
60.0 degrees
45.0 degrees
0.0 degrees
-45.0 degrees

Figure VI.3-10. Ply shuffling for optimized layup.

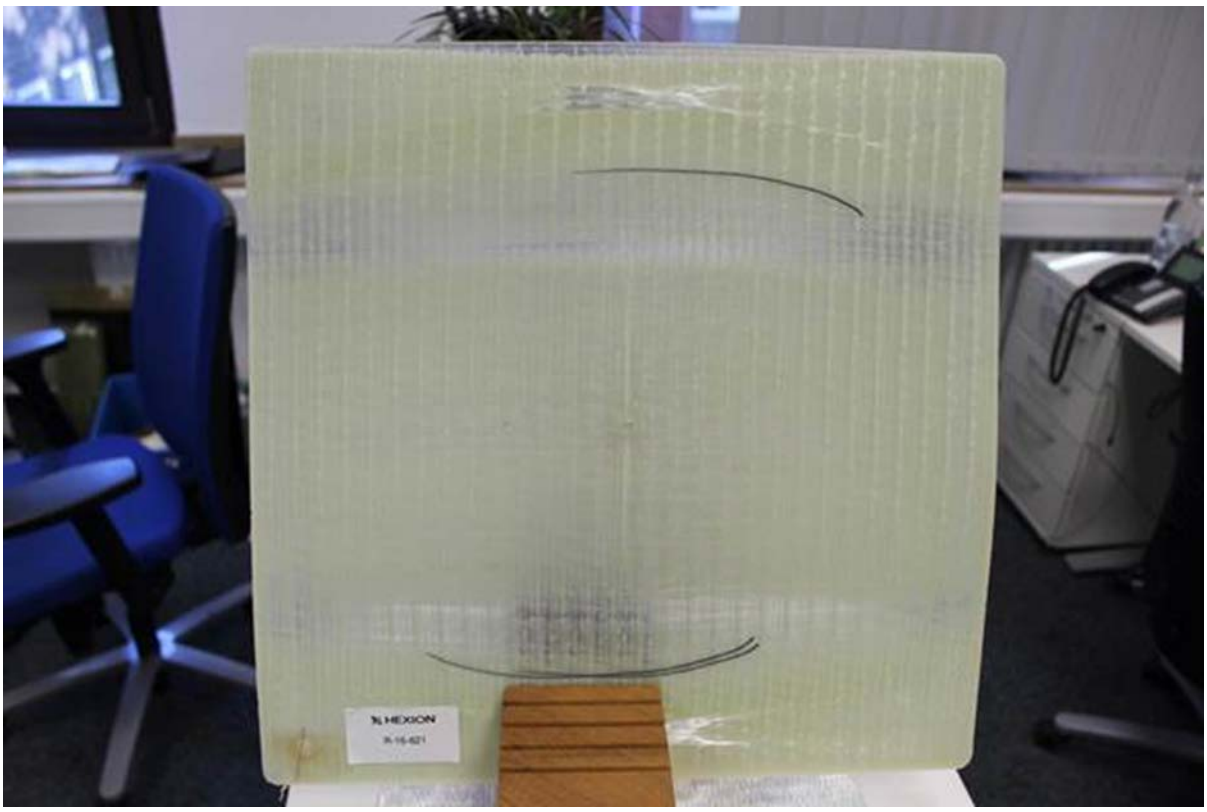

Figure VI.3-11. Test panels with fiber washout.

These panels will be remade at Hexion in October with binder applied and injected at a slower flow rate to minimize fiber wash in the test panels.

The panel matrix is given in Table VI.3-1 and images are shown in Figure VI.3-12 for the received samples.

Table VI.3-1. Panel Matrix for Test Samples

Panel No	Fabric	Lay up
R-16-609	Saertex, Carbon, UD, Zoltek Panex 35, 30003791	(0)6
R-16-610	Saertex, Carbon, UD, Zoltek Panex 35, 30003791	(0)6
R-16-611	Saertex, Carbon, UD, Zoltek Panex 35, 30003791	(0)6
R-16-612	Saertex, Carbon, Biax, Aska A-42, 30000987	(±45°)2s
R-16-613	Saertex, Carbon, Biax, Aska A-42, 30000987	(±45°)2s
R-16-614	Saertex, Carbon, Biax, Aska A-42, 30000987	(±45°)2s
R-16-615	Vectorply, Carbon, Biax, C-BX-0900	(±45°)3s
R-16-616	Vectorply, Carbon, Biax, C-BX-0900	(±45°)3s
R-16-617	Vectorply, Carbon, Biax, C-BX-0900	(±45°)3s
R-16-618	Saertex, Glass, UD, PPG 2002, VU800685	(±45°)3s
R-16-619	Saertex, Glass, UD, PPG 2002, VU800685	(±45°)3s
R-16-620	Saertex, Glass, UD, PPG 2002, VU800685	(±45°)3s
R-16-621	Owens Corning, Glass, UD, WRx0440, 36B00	(0)6
R-16-622	Saertex , Glass, Biax, PPG 2002, U32EX010	(±45°)3s
R-16-623	Saertex , Glass, Biax, PPG 2002, U32EX010	(±45°)3s
R-16-624	Saertex , Glass, Biax, PPG 2002, U32EX010	(±45°)3s
R-16-625	Vectorply , Glass, Biax, E-BX-1200	(±45°)3s
R-16-626	Vectorply , Glass, Biax, E-BX-1200	(±45°)3s
R-16-627	Vectorply , Glass, Biax, E-BX-1200	(±45°)3s
R-16-628	Owens Corning, Glass, Biax, BX0440lld, 05A02	(±45°)3s
R-16-629	Owens Corning, Glass, Biax, BX0440lld, 05A02	(±45°)3s
R-16-630	Owens Corning, Glass, Biax, BX0440lld, 05A02	(±45°)3s
R-16-631	Saertex, Glass, UD, PPG 2002, VU800685	(0)3
R-16-632	Saertex, Glass, UD, PPG 2002, VU800685	(0)3
R-16-633	Saertex, Glass, UD, PPG 2002, VU800685	(0)3

Grey: not received, yellow: received, and green: received and forwarded to the OEM

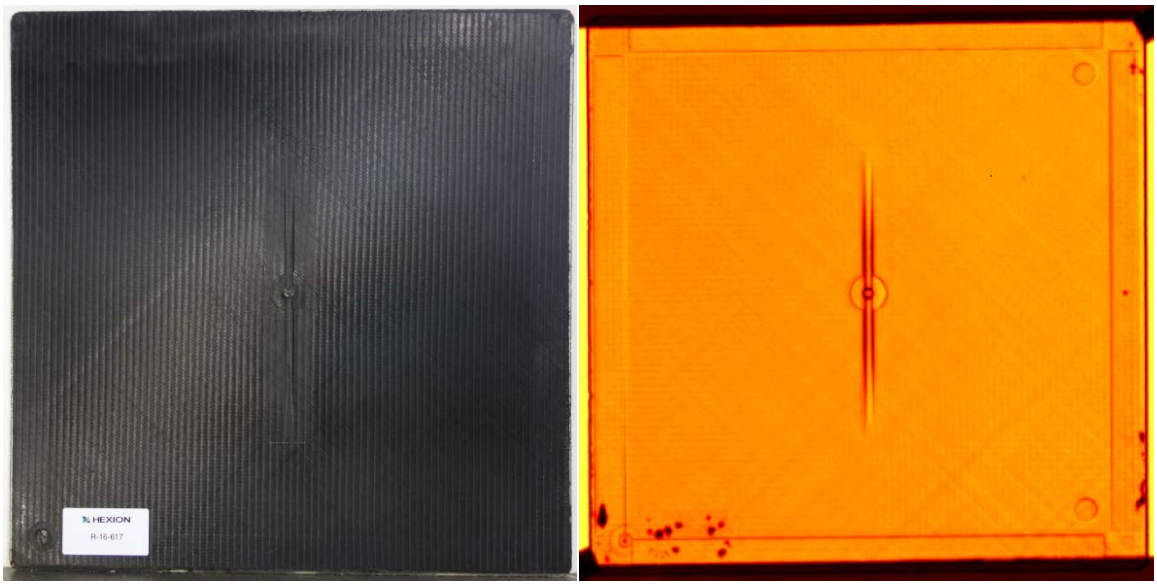

R-16-617

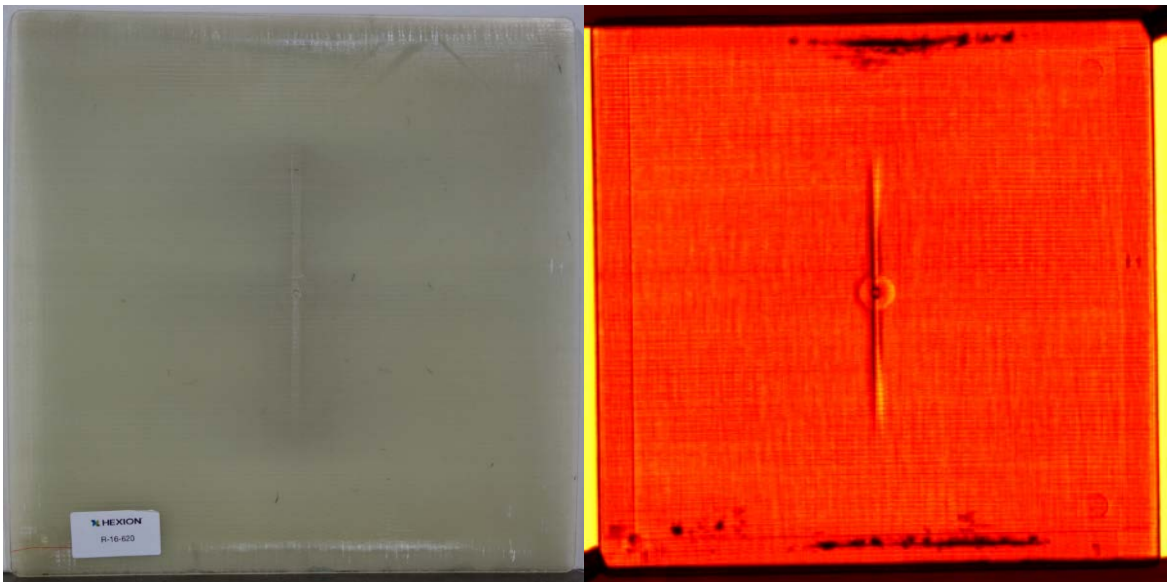

R-16-620

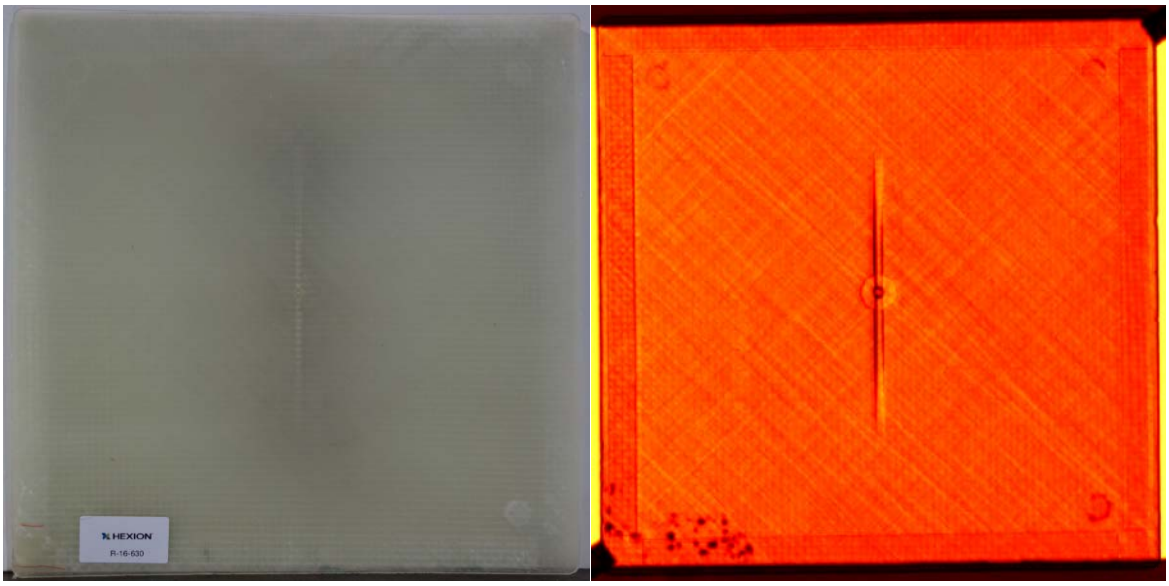

R-16-630

Figure VI.3-12. Images of test panels for the various fabric configurations in Table VI.3-1. The left image is a photograph and the right image is an ultrasonic C-scan. These C-scans are used to help select an area of the sample that is uniform with no voids for testing.

Technology Transfer Path

This HP-RTM technology and associated automation, demonstrated by European automakers, can be directly applied to U.S. manufacturers to reach and exceed 100,000 units per year.

Injection technology is the first step, part preforming is the second, and automation is the third part of the process to ensure good takt times are reached to make this process and its associated capital expenditure worthwhile.

Conclusion

Year one of this 3-year program is nearly completed. We have achieved our major goals of defining the technology gaps and performance requirements. Computer-aided design, loading, and testing requirements (both static and dynamic) were transferred from the OEM and a preliminary design review was completed.

References

[1] Sloan, Jeff, "Auto composites quest: One–minute cycle time?," Composites World (August 2012), http://www.compositesworld.com/articles/auto-composites-quest-one-minute-cycle-time.

[2] Motavalli, Jim, "Shattering Glass: Low-weight Plastic Car Windows are Coming," CBS Money Watch (July 2011), http://www.cbsnews.com/news/shattering-glass-low-weight-plastic-car-windows-are-coming/.

[3] Hillermeier, Dr. RomanW., Hasson Dr. Tareq, Friedrich, Lars and Ball, Cedric, "Advanced Thermosetting Resin Matrix Technology for Next Generation High Volume Manufacture of Automotive Composite Sstructures," SPE Automotive (2012), http://www.speautomotive.com/SPEA_CD/SPEA2012/pdf/TS/TS1.pdf.

VI.4 Functionally Designed Ultra-Lightweight Carbon Fiber-Reinforced Thermoplastic Composites Door Assembly – Clemson University

Project Details

Srikanth Pilla, Principal Investigator
Assistant Professor
Department of Automotive Engineering
Department of Materials Science and Engineering
Clemson University
4 Research Drive
Suite 340, Greenville, SC, 29607
Phone: 864-283-7216
E-mail: spilla@clemson.edu

David Ollett, Project Manager
Office of Energy Project Management
National Energy Technology Laboratory
626 Cochrans Mill Rd
Pittsburgh, PA 15236-0940
Phone: 412-386-7339
Email: david.ollett@netl.doe.gov

Carol Schutte, Technology Area Development Manager

U.S. Department of Energy
1000 Independence Avenue, SW
Washington, DC 20585
Phone: 202-287-5371
E-mail: carol.schutte@ee.doe.gov

Contractor: United States Automotive Materials Partnership, LLC
Contract No.: DE-EE0005661

Executive Summary

One of most promising routes for achieving the 2025 Corporate Average Fuel Economy standards involves decreasing vehicular weight by incorporating lightweight materials, coupled with component redesign, in order to improve overall fuel efficiency. Indeed, one recent study indicates that simple replacement of current metallic door frames with carbon fiber-reinforced plastic composites can reduce overall weight of the component by nearly 58% [1]. The objectives of this project are to achieve a weight reduction of at least 42.5%, compared to the baseline door structure, at the cost of less than $5/lb while saving on energy metrics without compromising the fit, function, crash, and noise, vibration, and harshness requirements. The strategy for achieving these targets involves a holistic systems approach through integration of unique designs, novel materials, manufacturing technologies, and joining/assembly of subsystems to ensure the developed technologies are ready for commercialization.

Accomplishments

- Identified six design criteria that were used in conceptual design trade studies to enable selection of materials, designs, and processes based on the discussions held with project partners, including original equipment manufacturers (OEMs) (Fiscal Year [FY] 2016).
- Investigated the baseline metrics of weight, cost, performance, manufacturing, and assembly by conducting a systematic teardown benchmarking and generating a bill of materials on an OEM-supplied driver side front door (FY 2016).
- Conducted preliminary tests and an evaluation of endless fiber thermoplastic composites comprising market-available carbon fiber-impregnated thermoplastic resins (FY 2016).
- Investigated the structural requirements for the door under static conditions representing daily use and misuse to identify strength and stiffness zones on the door via Finite Element Analysis (FEA) simulations and developed systems-level performance requirements for the door redesign (FY 2016).

Future Directions

- Develop conceptual designs for the prototype door that meets virtual targets.
- Identify and down-select technology solutions for weight-critical door components, including structure, glazing, and trim.
- Fabricate a low-cost, non-functional prototype to validate geometrically the conceptual design.
- Develop a material property database and material models for market-available carbon fiber thermoplastic systems.
- Design and fabricate tooling for the structural frame and subcomponents.
- Develop jigs and fixtures in order to simulate the loading conditions experienced.

Technology Assessment

- Target: To design, build, and test a complete driver's side front door with all trim, glazing, and other baseline features with a total weight of 42.5% less than a baseline structure.

- Gap: All current programs for light-weighting door assemblies approach this challenge by focusing on the structural frame with no emphasis on door subassemblies (which is approximately 50% of the door weight). The principal investigators are approaching the 42.5 % light-weighting target for the entire door as a holistic module.

- Target: To demonstrate via physical testing that the light door meets or exceeds baseline door performance with respect to noise, vibration, and harshness; fit/finish; structural performance; and performance of creature comforts like speakers and automatic windows (specific metrics are confidential).

- Gap: As higher mass corresponds to better noise, vibration, and harshness performance, conventional approaches for noise insulation and vibration damping may be inapplicable, thus requiring innovative solutions to manage these deficiencies.

- Target: To demonstrate via cost modelling the door assembly meets the indicated weight reduction for less than $5/lb of weight saved.

- Gap: Neither OEM's current cost-prediction models for baseline metallic doors nor conventional cost prediction tools for composite-intensive closure systems are effective, because production of the lightweight door involves non-traditional manufacturing systems and layouts.

Introduction

The objective of this project is to reduce the weight of a door assembly by at least 42.5% compared to a baseline driver's side front door with an expected cost increase of less than $5/lb in weight saved. A 2013 mid-sized sport utility vehicle's door from our OEM partner with an assumed production volume of 20,000 vehicles annually was the basis for design. These criteria will either meet or exceed the fit, function, crash, and noise, vibration, and harshness requirements of the baseline door.

The intent is to (1) enable the radical redesign of the baseline door via a holistic systems approach through the integration of unique designs, (2) use novel materials that render the door 100% recyclable, and (3) investigate manufacturing technologies and joining/assembly of subsystems to ensure the developed technologies are ready for commercialization. The partner organizations listed in Table VI.4-1 are providing highly leveraged knowledge expertise to ensure the success of this effort.

Table VI.4-1. Project Participants

Universities	Industry Partners	Computation Partners
Clemson University	Original Equipment Manufacturer (OEM)	Altair Engineering
University of Delaware	BASF	Core-Tech Systems (Moldex 3D)
	SABIC	MSC Software (Digimat®)
	Krauss Maffei	LS-Dyna
	Trexel Inc.	
	Corning	

Approach

The project uses a systems-level approach that began with systematic evaluation and benchmarking of the door and its subassemblies. In collaboration with our partnering companies and commercial suppliers, researchers are evaluating a variety of carbon fiber thermoplastic material forms for structural components (i.e., novel unidirectional and fabric prepregs, co-mingled fabrics, high aspect ratio discontinuous fibers, performance thermoplastic resins, novel fiber architectures, and localized reinforcements) and alternative solutions for glazing, trim, and other subcomponents. The initial focus is on creating the structural component and a materials database for all parts of the door structural assembly (i.e. outer shell, inner panel, carrier, and anti-intrusion beam(s)).

A two-phase integrated design and manufacturing optimization approach is being adopted to obtain the optimal manufacturing process parameters of the thermoplastic materials and the optimal structural design parameters of the door. The principal investigators also conducted a top-level trade study to determine at least two candidate designs for optimization. The design parameters will incorporate (a) thermoforming and injection molding parameters (e.g., pressure and temperature), (b) fiber parameters (e.g., material, length, diameter, and volume fraction), (c) matrix parameters (e.g., material and volume fraction), (d) structural wall thickness, and (e) material density distribution. The research team will use four analysis tools (i.e., Moldex3D, Digimat, and LS-DYNA Implicit and Explicit) to construct the manufacturing-to-response analysis pathway [2-4]. The team will fabricate a door based on this optimal design for testing in accordance with the performance requirements of the OEM.

Results and Discussion

Investigation of the Baseline Door

The focus of this fiscal year's research efforts involved a systematic evaluation, benchmarking of door subassemblies, and a top-level trade study for determining at least two candidate designs for optimization. Our OEM partner supplied a driver side front door for a teardown benchmarking study to better understand and set baseline metrics for our proposed door.

The doorframe shown in Figure VI.4-1a weighs 15.44 kg of the total mass of the door, which is 31.02 kg.

All parts shown in Figure VI.4-1b were weighed three times with the average of those values being recorded and the parts were classified as rigid polymers, metals, and elastomers. As shown in Figure VI.4-2, the metal components contribute to 62% of the mass.

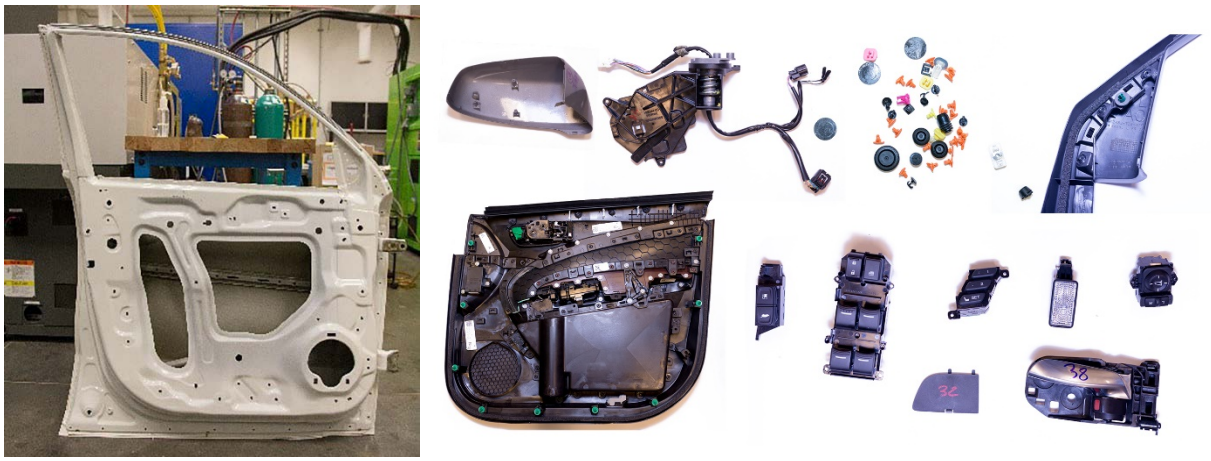

Figure VI.4-1. (a) Steel doorframe with hinges and (b) components from the OEM door.

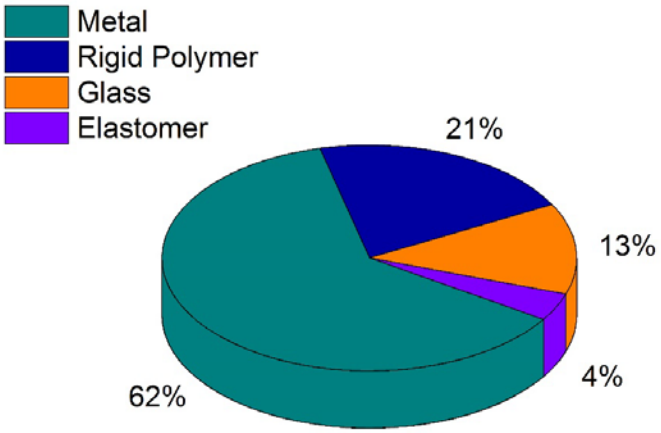

Figure VI.4-2. Weight distribution by material groups.

Test and Evaluation of Continuous Fiber Thermoplastic Composites

The team performed an initial assessment to select the commercially available carbon fiber and thermoplastic resins and material forms deemed most suitable for use in scalable automotive manufacturing processes. Of the available carbon fibers that come in a variety of specifications, the team selected polyacrylonitrile (PAN)-based fibers with Standard Modulus (i.e., T700 or equivalent, with about 34 Msi stiffness and 700 ksi strength)

because of their optimal mix of cost versus performance. Although more expensive, the option of selecting higher-performing fibers (at T800 or IM7) may be considered should that prove necessary.

A preliminary material screening strategy was used for all materials sourced in this effort to down select promising candidate systems for detailed assessment and material card development for design and analysis codes (i.e., Hyperworks and LS-DYNA). The strategy centered on the measurement of three key mechanical properties:

- 0 degrees of tension for translation of fiber properties
- 90 degrees of tension for processed laminate quality and sizing or fiber matrix adhesion
- ±45 degrees of tension for an in-plane shear and ductility assessment.

In addition to these tests, future efforts will involve ultrasonic scans for panel quality, fiber volume fraction, and density measurements for all material systems. Suppliers will be asked to provide either material forms and process conditions or the processed panels for these three properties. Preliminary mechanical test data are being generated for a host of high-performance carbon fiber-reinforced plastic, including those from Barrday, Cytec, and Tencate (data not shown). These systems are currently under evaluation for generation of full LS-Dyna material card data. Also, a preliminary trade study on material costs suggests a range of 17 to 19 $/lb for high-performance thermoplastics at the volumes desired for the production target. Discussions are also underway with other material suppliers and collaborators (i.e., BASF, SABIC, and Krauss Maffei) to obtain material forms and panels for further testing and evaluation.

Investigation of Static Structural Requirements for the Door

Prior to developing conceptual designs for the door, the team decided to first investigate the door's structural requirements under static conditions representing daily use and misuse. As a feasibility study, a generic door was selected to implement the static tests discussed in the following subsections for the boundary conditions shown in Figure VI.4-3.

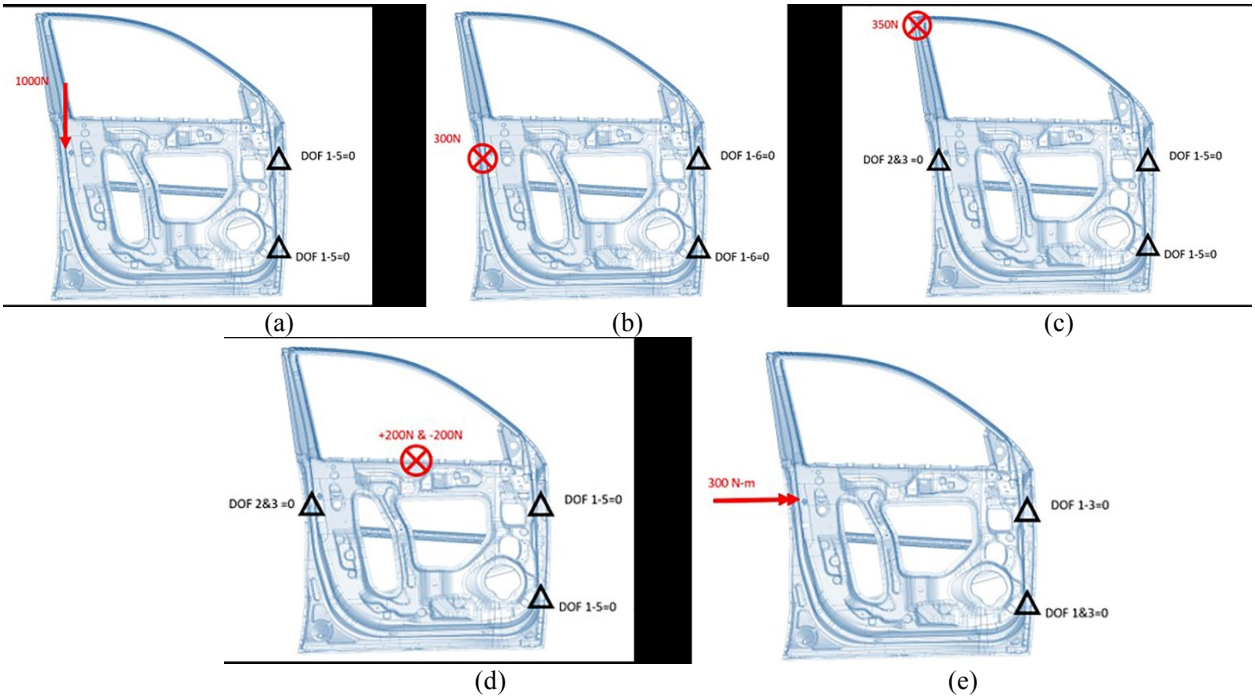

Figure VI.4-3. Representations of boundary conditions for (a) door sag (b) door over opening (c) door frame stiffness (d) door belt line stiffness, and (e) torsion stiffness.

Door Sag

A force of 1,000 N was applied in the vertical direction at the latch (Figure VI.4-3a). The stiffness value for the load case was calculated by dividing 1,000 N by total displacement at the latch.

Door Over Opening

The door was constrained in all degrees other than rotation on the Z axis at the mounting points of the hinges (designated by DOF values in Figure VI.4-3b). A force of 300 N was applied in the Y direction at the lock. The stiffness value for the load case was calculated by dividing 300 N by the total displacement at the force application point.

Door Frame Stiffness

The door was constrained in all degrees other than rotation on the Z axis at the mounting points of the hinges. In addition, translation in Y and Z are constrained at the latch (Figure VI.4-3c). A load of 300 N was applied on the top edge of the window frame. The stiffness value was calculated by dividing 300 N by displacement at the point of loading.

Belt Line Stiffness

All degrees of freedom were constrained, except for rotation around the Z axis. A force of 200 N each was applied in the Y direction on the door belt line at the center of the window opening (Figure VI.4-3d). The lock was constrained in the Y and Z directions in order to suppress global rotation of the door around the hinge axis and sagging. The stiffness value for the load case was calculated by dividing 400 N by the sum of total displacements at the force application points.

Door Frame Torsional Stiffness

The upper hinge was constrained for all translations in X, Y, and Z and the lower hinge in X and Z. The latch point was rotated in a clockwise direction (Figure VI.4-3e) and deflections at the top of the window frame and bottom of the door were measured.

A maximum stress of about 190 MPa was observed, which is within the elastic limit of steel. Stress plots from each individual load case were overlapped on each other to generate a heat map of the stress concentration (Figure VI.4-4). The heat map provides insight about the strength and stiffness requirements of the doorframe. These data were invaluable in designing non-uniform anisotropic laminates and local geometrical reinforcements for weight reduction.

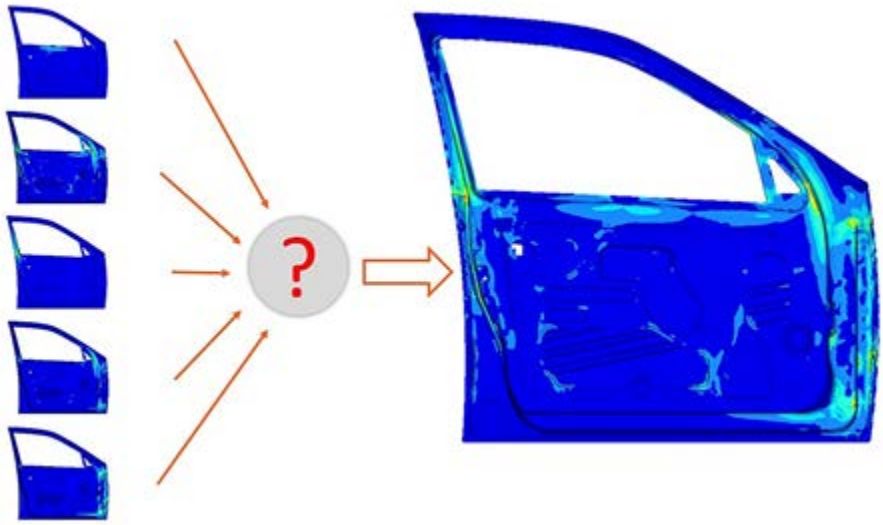

Figure VI.4-4. Combined stress concentration.

A summary of the study is shown in Figure VI.4-5. The inner frame (colored in red) toward the hinge pillar has to possess high stiffness and strength, unlike the belt-line and foot-line (colored in yellow). The latch side of the door is responsible for transmitting the crash loads and frame stiffness; therefore, this region (colored in orange) has to possess moderate stiffness, yet high strength.

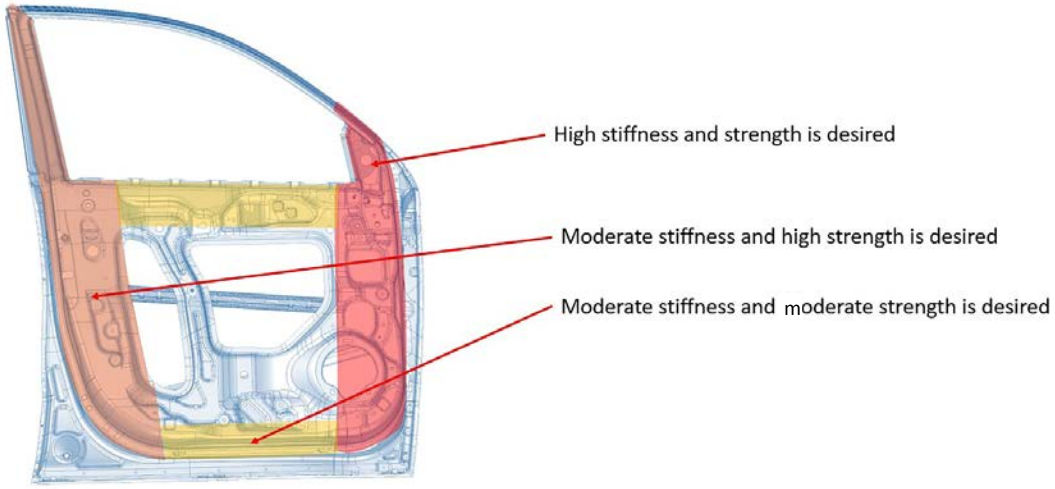

Figure VI.4-5. Strength and stiffness zones on the door.

Identifying the different strength and stiffness zones laid the foundation for our conceptual designs. Figure VI.4-6 presents an overview of the different attributes considered while designing the conceptual prototypes; these designs are absent from this report due to their confidential nature.

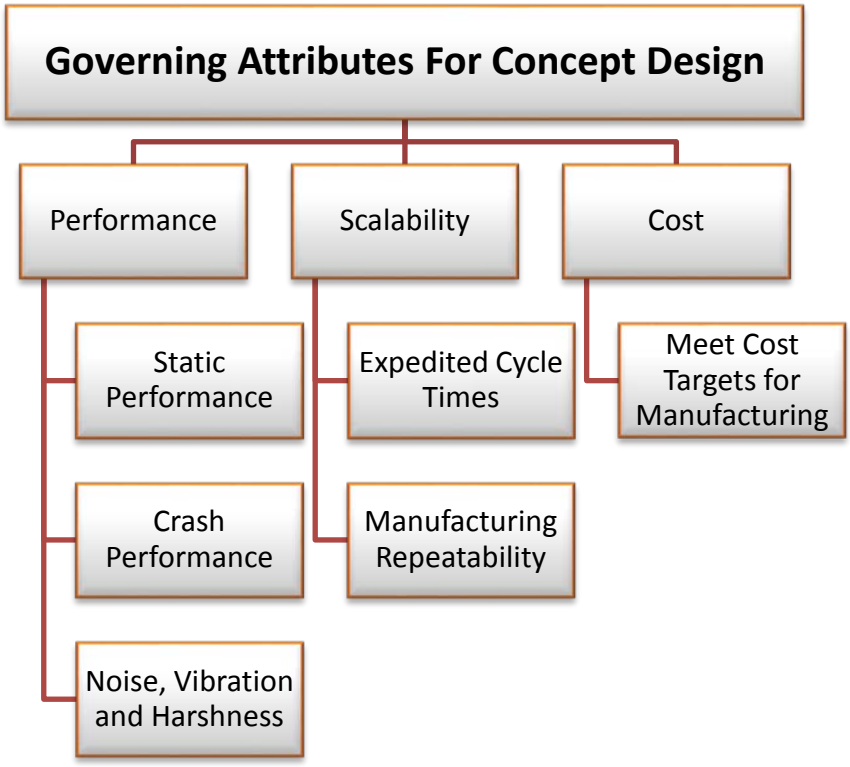

Figure VI.4-6. High-level approach to tackle.

Cost Modeling

For one of the developed conceptual designs, we decomposed the composite door concept into a set of structural and non-structural subsystems and developed process steps for each component of the subsystems. Then, based on the process steps, we have created an overall manufacturing and assembly process of the composite door concept. Four separate locations (Figure VI.4-7) were used for manufacturing and assembling the conceptual composite door, based on manufacturing requirements for the various subsystems. The large doorframe parts were manufactured and assembled in a doorframe shop; the smaller non-structural composite parts were manufactured in a component shop; the doorframe and some of the smaller composite parts were painted in a high-volume Carbon Fiber Reinforced Thermoplastics (CFRT) paint shop; and the composite doors were assembled on a separate assembly line adjacent to the car body assembly and trim lines.

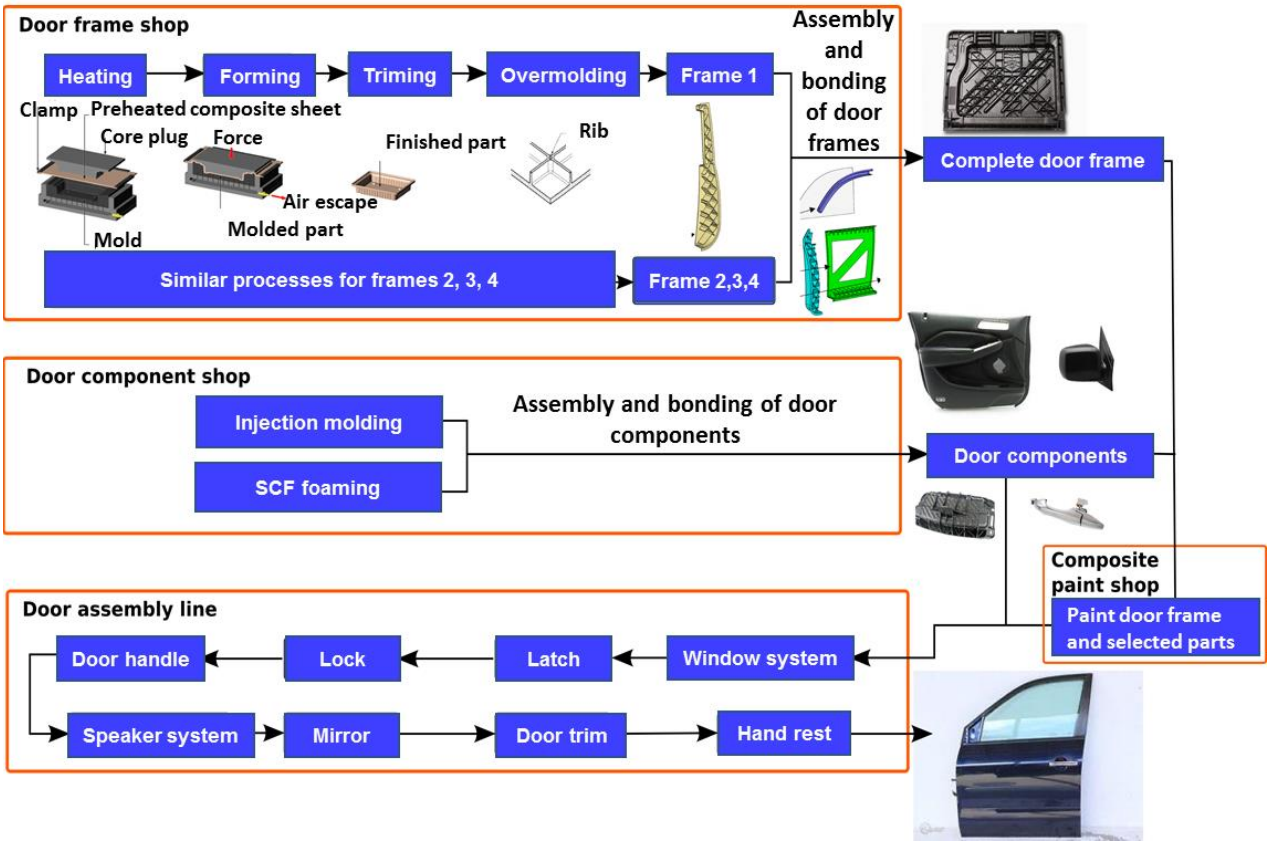

Figure VI.4-7. Manufacturing and assembling Version 1 of the composite door concept.

We next proposed integration of the manufacturing shops and assembly line of the composite door into the assembly plant of a baseline car factory (Figure VI.4-8). The green regions represent the current layout of the baseline car factory and the orange regions represent the shops and assembly line to be constructed for production of the composite doors. Note that the baseline factory layout (which is not the OEM factory layout) will be updated once relevant data are obtained from the OEM.

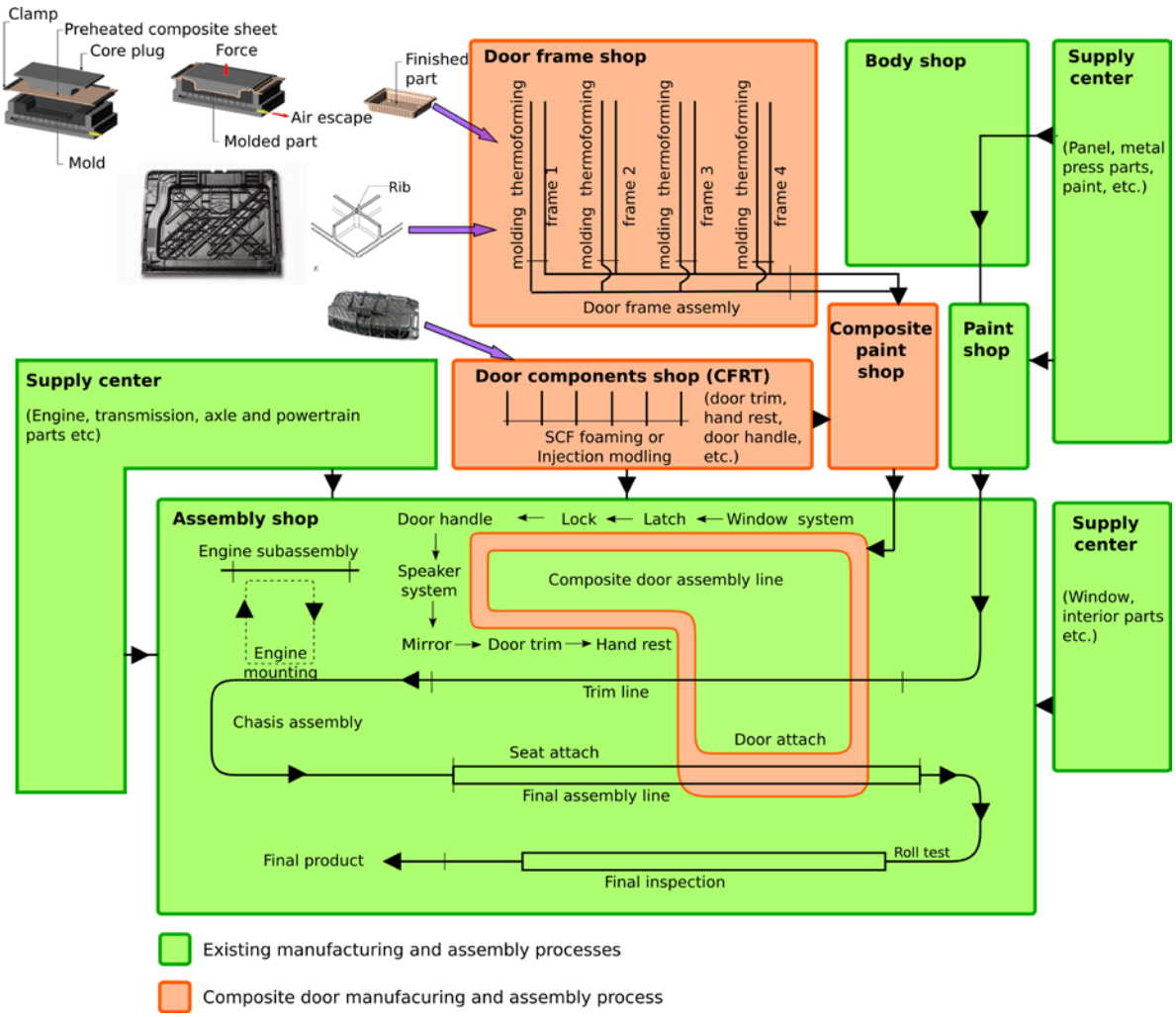

Figure VI.4-8. Top-level factory layout.

Technology Transfer Path

The design optimization process, coupled with the manufacturing-to-response pathway for computational analysis of proposed thermoplastic composite structures, serves as conduit for ensuring developed technologies are market-ready for commercialization among project partners.

Conclusion

In conclusion, the research focus during this fiscal year involved elucidating, systematically evaluating, and benchmarking the current baseline steel door and its various subassemblies to identify the requisite design attributes for the proposed conceptual designs. A preliminary strategy for testing, evaluating, and down-selecting promising thermoplastic composites systems for material card development was developed to virtually validate the proposed designs.

References

[1] Kelly, J. C., J. L. Sullivan, A. Burnham, and A. Elgowainy, 2015, "Impacts of Vehicle Weight Reduction via Material Substitution on Life-Cycle Greenhouse Gas Emissions," *Environmental Science Technology* 49: 12535–42, doi:10.1021/acs.est.5b03192.

[2] Mi, H.-Y., X. Jing, J. Peng, L.-S. Turng, and X.-F. Peng, 2013, "Influence and Prediction of Processing parameters on the Properties of Microcellular Injection Molded Thermoplastic Polyurethane based on an Orthogonal Array Test," Journal of Cellular Plastics 49: 439–458, doi:10.1177/0021955X13488399.

[3] Chang, S. H. and S. S. Cheon, 2006, "In-plane Directional Mechanical Properties of carbon Fabric Skins in sandwich Structures After Thermoforming," Composite Structures 75: 577–581, doi:10.1016/j.compstruct.2006.04.033.

[4] Yu, Y., J. Ye, Y. Wang, B. Zhang, and G. Qi, 2013, "A Mesoscale Ultrasonic Attenuation Finite Element Model of Composites with Random-Distributed Voids," Composites Science and Technology 89: 44–51, doi:10.1016/j.compscitech.2013.09.006.

U.S. DEPARTMENT OF
ENERGY
Energy Efficiency &
Renewable Energy

For more information, visit: vehicles.energy.gov

DOE/EE-1533 • October 2017